

# **NEW CONCEPTS AND ADVANCED STUDIES IN NATURAL SCIENCE AND MATHEMATICS**





*NEW CONCEPTS  
AND ADVANCED  
STUDIES IN  
NATURAL  
SCIENCE AND  
MATHEMATICS*

Editor  
Prof. Dr. Canan ÖZDEMİR





*New Concepts and Advanced Studies in Natural Science and Mathematics*  
**Prof. Dr. Canan ÖZDEMİR**

**Design:** All Sciences Academy Design

**Published Date:** October 2025

**Publisher's Certification Number:** 72273

**ISBN:** 978-625-5794-61-1

© All Sciences Academy

[www.allsciencesacademy.com](http://www.allsciencesacademy.com)

[allsciencesacademy@gmail.com](mailto:allsciencesacademy@gmail.com)



## CONTENT

<b>1. Chapter</b>	<b>8</b>
A Noteworthy Macro-algae: Sargassum (Phaeophyta)	
<i>Seher DİRİCAN</i>	
<b>2. Chapter</b>	<b>16</b>
Determination of Phenolic Compounds in Rubia Tinctorum Chloroform Extract by LC-MS/MS	
<i>Temine ŞABUBDAK</i>	
<b>3. Chapter</b>	<b>30</b>
Research on Multifocal Motor Neuropathy as a Rare Autoimmune Neuropathy	
<i>Emine DIRAMAN, Fatma Gönül SEZGIN, Birol SEZGIN</i>	
<b>4. Chapter</b>	<b>38</b>
Numerical Solution for Parabolic Equation	
<i>Armida BRAKAJ, Zhifka MUKA, Fizeleni LEKLI</i>	
<b>5. Chapter</b>	<b>53</b>
Electrical Conductivity Measurement System Design with Logarithmic Amplifier Based Electrometer and Modbus Featured Temperature Controller	
<i>Tayyar GÜNGÖR</i>	
<b>6. Chapter</b>	<b>68</b>
A Study on a Special Curve via Conformable Fractional Derivative	
<i>Burçin SALTİK BAEK</i>	
<b>7. Chapter</b>	<b>85</b>
Measurement of Clustering Performance in Enzyme Sequence Classification Using a Hybrid DbSCAN Spectral Ensemble	
<i>Çağın KANDEMİR ÇAVAŞ</i>	

<b>8. Chapter</b>	<b>102</b>
Laser Roughening of Metal Surfaces: An Exemplary Study on the Application of Surface Roughness Parameters	
<i>Timur CANEL</i>	
<b>9. Chapter</b>	<b>127</b>
Comparative and Hybrid Application of Ftir and HPLC-Rid For Sugar Analysis in Sugar-Free Products	
<i>Amirhosein OROUJIEGHBAL, Yücel KADIOĞLU</i>	
<b>10. Chapter</b>	<b>148</b>
Solvothermal Synthesis and Structural Characterization of A Dysprosium-Based Metal–Organic Framework	
<i>Adem DÖNMEZ, Uğur ERKARSLAN</i>	
<b>11. Chapter</b>	<b>163</b>
Equivalence in Action: Homotopy From Simplicial to Crossed Modules	
<i>Hatice GÜLSÜN AKAY, İlker AKÇA</i>	
<b>12. Chapter</b>	<b>176</b>
Eco-Friendly Tri-Layer Electrospun Nanofiber Filters: PVA–CS/Cellulose Architecture for High-Efficiency PM2.5 Removal	
<i>Kenan ISAZADE, Hülya KARA SUBAŞAT</i>	
<b>13. Chapter</b>	<b>190</b>
Fabrication of 3D PCL/GEL/NHA Scaffolds for Bone Tissue Engineering Applications	
<i>Özay EROĞLU, Hülya KARA SUBAŞAT</i>	
<b>14. Chapter</b>	<b>205</b>
Numerical solutions of the Caudrey-Dodd-Gibbon Equation	
<i>Melis ZORŞAHİN, Dursun IRK</i>	

<b>15. Chapter</b>	<b>220</b>
Geometry of Canal Surfaces Via Darboux Frame	
<i>Nural YÜKSEL, Nurdan OĞRAŞ</i>	
<b>16. Chapter</b>	<b>237</b>
A Study on TB-Smarandache Tube Surfaces in Three-Dimensional Euclidean Space	
<i>Nural YÜKSEL, Nurdan OĞRAŞ</i>	
<b>17. Chapter</b>	<b>255</b>
Double fractional integral inequalities including for functions whose higher-order partial derivatives are elements of the $L_1$ space	
<i>Samet ERDEN, Neslihan UYANIK</i>	
<b>18. Chapter</b>	<b>272</b>
DFT and Topological Insights into the Structural and Reactive Features of a Pyridine Based Hydrazone	
<i>Sevgi KANSIZ, Okan ŞİMŞEK</i>	
<b>19. Chapter</b>	<b>287</b>
On Desargues Theorem in The Smallest Cartesian Group Plane	
<i>Şümeyye Büşra YAMAN, Ziya AKÇA</i>	
<b>20. Chapter</b>	<b>306</b>
A Quick Overview on Electronic Structure, Solvatochromic Behavior and Optoelectronic Applications of Schiff Bases	
<i>Yadigar GÜLSEVEN SIDİR</i>	
<b>21. Chapter</b>	<b>323</b>
Toxicological Effects of Hexythiazox (Yoksorrun-5EC) on Ovarian Folliculogenesis in Zebrafish: A Histopathological Perspective	
<i>Yücel BAŞIMOĞLU KOCA</i>	
<b>22. Chapter</b>	<b>339</b>
Sectoral Analysis of Greenhouse Gas Emissions in Türkiye: Trends, Breakpoints, and Policy Recommendations (1990–2023)	
<i>Ece ÖZGÖREN ÜNLÜ</i>	

<b>23. Chapter</b>	<b>353</b>
Ionic Liquids in the Extraction of Flavonoids from Plants	
<i>Murat YILDIZ</i>	
<b>24. Chapter</b>	<b>377</b>
On the Apollonian Sets in the Chinese Checkers Plane	
<i>Süheyla EKMEKÇİ</i>	



# **A Noteworthy Macro-algae: *Sargassum* (Phaeophyta)**

**Seher DİRİCAN<sup>1</sup>**

1- Assoc. Prof. Dr. Seher Dirican; Sivas Cumhuriyet University, Faculty of Science, Department of Biology Sivas, Turkey. [sdirican@cumhuriyet.edu.tr](mailto:sdirican@cumhuriyet.edu.tr) ORCID No: 0000-0001-9130-5114

## ABSTRACT

Aquatic ecosystems, which constitute three-quarters of the world, have enabled the formation and development of many sectors. The blue economy creates a framework for developing new biotechnologies based on sustainable aquatic economic activities. In this process, the blue economy plays an important role not only in environmental sustainability but also in economic development and progress. With the rapidly increasing world population and global climate change, accessing food resources is becoming more and more difficult every day. It is thought that the importance of macro-algae will increase in terms of food security and health in the future. It is necessary to make more use of macro-algae. In this respect, macro-algae will have an even more important place in the future as they do today. *Sargassum* is a pelagic brown macro-algae species that swims in large masses. *Sargassum* plays a very important role in marine ecosystems. This study focuses on *Sargassum*, a macro-alga that attracts attention with its importance and potential to expand its area of use in the future.

*Keywords – Blue Economy, Brown Macro-algae, Sargassum.*

---

## INTRODUCTION

Algae are plant organisms of ecological and economic importance in aquatic ecosystems. Algae provide an organic food source for animal organisms and also provide oxygenation of the ecosystem by photosynthesis. Algae, which do not have real roots, stems and leaves, are divided into two main groups according to their size as microalgae and macro-algae. The sizes of macro-algae vary between one or two centimeters and forty or fifty meters depending on the species. They provide nutrition, shelter and reproduction environment for aquatic organisms. Macro-algae have a very good biochemical composition in terms of proteins, vitamins, carbohydrates, lipids and minerals. Macro-algae have quite good fat content, amino acid composition is close to legumes and vitamin and mineral content is high. While carbohydrate digestibility is 50 percent, protein digestibility is at the level of 80 percent in some algae classes. Today, macro-algae are used in the production of human food, cosmetics, medicine, animal feed, agricultural fertilizer, polysaccharides such as agar and alginate, and biofuels (Ak, 2015). *Sargassum* is also widely cultivated, especially in the Far East countries (Yangson et al. 2022).

Algae differ from other plants in terms of structure, cell aspect and natural selection reproduction. These organisms, which are the first producers, increase the amount of dissolved oxygen and nutritional value in aquatic ecosystems thanks to the pigments in their structures. Recently,

global warming, climate change, factors causing eutrophication due to domestic, industrial and agricultural wastes have affected the distribution of algae. At the same time, with the increase in algae populations, the ecological balance is disrupted due to changes in the odor and color of aquatic ecosystems. Algae, one of the important organisms of aquatic ecosystems, are of great importance for other aquatic organisms. Macro-algae are one of the golden resources of aquatic ecosystems. In the future, many biological properties of macro-algae such as anti-inflammatory, anti-cancer, anti-tumor, anti-viral, antioxidant, anticoagulant should be revealed and used more as an important source in biotechnological applications (Peksezer et al. 2022).

Due to reasons such as unconscious use of water resources, industrialization and uncontrolled release of chemical wastes into natural systems, usable water resources are rapidly polluted in the world. Blue economy is a holistic development approach that encourages growth by emphasizing the efficient use of optimum and effective water resources without compromising sustainability elements (Yılmaz, 2021). Blue economy aims to provide economic growth from water resources while leaving clean and healthy water resources to serve future generations. Accordingly, the evaluation of *Sargassum* and its potential to be transformed into an economic opportunity is important. This study is about *Sargassum*, a macro-alga that attracts attention with its importance and potential to expand its usage area in the future.

## **SOME BIO-ECOLOGICAL FEATURES OF *SARGASSUM***

*Sargassum* is a brown macro-algae genus in the Fucales order of the Phaeophyceae class. The Fucales order lives in the cold seas of the northern and southern hemispheres or in the warm seas between them. They are usually found attached to rocks and other surfaces. The thallus is usually in the form of a ribbon. In some species, the thallus is hard like leather. The thallus of some of them swim freely. The thallus of some of those living in the depths reaches five meters. The thallus of those living on the coasts is usually under one meter. The thallus shows a high degree of differentiation. In its structure, axis, leafy branches and swim bladders are distinguished. The *Sargassum* genus is very common in the region called the “Sargasso Sea” between the Bahamas and the Azores islands of the Atlantic Ocean. *Sargassum* is mostly observed after a depth of two meters in Turkish seas (Altuner, 1998). *Sargassum* macro-algae that develop in warm seas have a tree-like structure. There are three species of *Sargassum* that grow in



Turkish seas: *Sargassum vulgare*, *Sargassum linifolium* and *Sargassum hornschiui* (Güner and Aysel, 2011).

*Sargassum* species contain gas-filled tubes to facilitate swimming (Geldiay and Kocataş, 2002). *Sargassum* species have a high degree of morphological complexity and flexibility. *Sargassum* has a characteristic filamentous thallus with an attachment site that branches to form several main axes. However, it has distinct leaves, capillaries, and gas-filled tubes located in the axes near the leaves. These tubes are filled with oxygen. These tubes keep the *Sargassum* macro-algae afloat and enable them to photosynthesize. Sexual reproduction occurs by oogamy. Female oogonia are exposed outside a cavity sunken into the surface of the thallus that has an opening that opens to the outside containing the reproductive structures. Fertilization occurs when the sperm is chemically attracted to the oogonium and the zygote is released from the recipient, guided by light and temperature cues. The young thallus of benthic *Sargassum* then come into contact with a solid substrate, where rhizoids and growth axes are produced. In contrast to their benthic counterparts, clonal reproduction is the only known dispersal mechanism for holopelagic species today. This occurs by fragmentation of old thallus sections, allowing new fragments to regrow. *Sargassum* can continue to shed its offspring if its leaves are removed, and this strong dispersal mechanism explains the invasive success of the species. While the European Union does not consider any *Sargassum* species to be invasive, most member states affected by *Sargassum muticum*, such as Germany, France, Ireland, Spain, Belgium and the Netherlands, have classified the species as invasive (BBR, 2023).

## **SARGASSUM AS AN IMPORTANT MACRO-ALGAE**

*Sargassum* is a resource with a wide range of uses and cultivation. It can be produced, processed and has economic importance. *Sargassum* is a complex macro-algae containing hundreds of elements and compounds. Therefore, *Sargassum* has many potential benefits due to its biochemical composition. For example; It can be used as a natural fertilizer, building material, renewable biological energy source, carbon source and in the food industry (FAO, 2023).

*Sargassum* species provide essential biodiversity habitats. They have been called the “golden floating rainforest of the Atlantic Ocean” because they act as hotspots for biodiversity and productivity in substrate-poor, nutrient-poor offshore waters. As *Sargassum* drifts around, it contributes significantly to seasonally changing biodiversity. Particulate matter from

*Sargassum* feeds all levels of the marine food chain at all depths. It contributes to approximately 60 percent of total primary production in the upper one meter of water column. After losing its buoyancy after about a year, *Sargassum* sinks to the seabed and provides energy to marine life. Even small amounts of *Sargassum* that wash ashore have positive environmental effects, both on coastal fauna and by absorbing wave energy and preventing erosion (BBR, 2023). *Sargassum* blooms in coastal waters need to be assessed and economically managed, but this is very difficult and complex. These are: uncertainty surrounding *Sargassum* supply, insufficient knowledge about chemical components, challenges related to harvesting, transportation and storage, insufficient governance, and economic shortcomings for innovation.

Algal ecosystems play an important role in the marine carbon cycle. Algae act as net carbon sinks worldwide. There are significant natural marine algal ecosystems along European coasts. However, they account for less than 0.25% of global anthropogenic seaweed production. Efforts to integrate marine algae into climate policies have potential positive impacts on both climate and the environment. These include conservation, restoration and productivity. Knowledge gaps need to be addressed and filled to best exploit the climate mitigation potential of *Sargassum* macro-algae. Existing natural marine algal ecosystems in Europe should be assessed. The carbon footprint of marine algae-based products should also be assessed (BBR, 2023).

Global warming and climate change mitigation initiatives have recently attracted great interest in the role of natural carbon sinks, especially in coastal ecosystems. The *Sargassum* genus has a wide global distribution. Since these macro-algae provide a high amount of biomass, their contribution to global carbon stocks and thus to mitigating climate change as carbon dioxide sinks is important. The urgent demand for carbon dioxide reduction and the threats of increasing coastal urbanization have made *Sargassum* a prime target for conservation, management and eventual restoration efforts in a global context (Gouvea et al. 2020).

*Sargassum* uses carbon dioxide from surface waters. Since it decomposes in coastal waters and terrestrial environments, it can act as a carbon sink rather than a source of greenhouse gases going into the atmosphere. *Sargassum* can be collected from coastal waters and taken to deeper waters, where it can be sunk to a depth of approximately 150 meters. Here, the air pocket collapses due to pressure and becomes negatively buoyant. *Sargassum* therefore slowly decomposes its carbon over many years, gradually disperses in the water and slowly sinks to the benthic zone of the deep sea. This potentially supports the reduction of carbon dioxide and other greenhouse gases in the atmosphere. *Sargassum* management and utilization methods can be an important source of income. It can also make coastal areas healthier, more resilient and sustainable (FAO, 2023).

The increase in macro-algae belonging to the *Sargassum* genus on the Aegean and Mediterranean coasts of Turkey has begun to be observed in recent years. *Sargassum* lives in clean and deep waters and forms a habitat in marine ecosystems. For this reason, these *Sargassum* genus macro-algae seen on the Aegean and Mediterranean coasts are important beneficial species of the ecosystem and should be protected.

Blue biotechnology focuses particularly on aquatic organisms and involves the use of marine products to create new drugs, cosmetics, food or nutritional supplements. For the development of the blue economy, it is necessary to protect aquatic ecosystems and promote their sustainable use (Wenhai et al. 2019). Suluk (2022) reported that in Turkey's blue economy, only the fishing and aquatic products sectors stand out, and that its share in the shipbuilding and recycling sectors is insufficient, and that although it is a suitable country in terms of cruise tourism, it remains far from its potential. Accordingly, it is very important to utilize macro-algae belonging to the *Sargassum* genus, which has begun to increase on the Aegean and Mediterranean coasts of Turkey, within the scope of blue biotechnology.

## CONCLUSION

The benefits obtained from aquatic ecosystems are constantly increasing. It is extremely important to continue to obtain sustainable benefits from aquatic ecosystems due to the increasing population, food deficit and changes in consumption habits. Accordingly, *Sargassum* is a remarkable macro-alga to be evaluated as a product. As a result, *Sargassum* offers high economic potential because it is a very important and complex macro-alga that contains many elements and compounds. More research is needed to understand the importance of *Sargassum* and its use. In this context, *Sargassum* will have a very large place in the blue economy in the future.

## REFERENCES

- Ak, İ. (2015). Economic Plants of the Aquatic Environment; Macroalgae. World Food Journal, 88-97.
- Altuner, Z. (1998). *Seedless Plants Systematics*. First Volume, Özyurt Ofset and Tipo Printing, Ankara, pp. 186.
- BBR, (2023). *Blue Bioeconomy Report*. European Market Observatory for Fisheries and Aquaculture Products, Publications Office of the European Union, Luxembourg, pp. 117, DOI: 10.2771/223072.
- FAO, (2023). Impacts of *Sargassum* on Marine Resources in the Region and Utilization of Initiatives. Western Central Atlantic Fishery Commission (WECAFC), 19th Session, Barbados, 6-8 September 2023, pp. 1-14.
- Geldiay, R., Kocataş A. (2002). *Introduction to Marine Biology* (Textbook). Ege University Faculty of Science Book Series No: 31, 5th Edition, Ege University Press, İzmir, pp. 562.
- Gouvea, L.P., Assis, J., Gurgel, C.F.D., Serrao E.A., Silveira, T.C.L., Santos, R., Duarte, C.M., Peres, L.M.C., Carvalho, V.F., Batista, M., Bastos, E., Sissini, M.N., Horta, P.A. (2020). Golden Carbon of *Sargassum* Forests Revealed as an Opportunity for Climate Change Mitigation. Science of the Total Environment, 729 (138745), 1-10, DOI: 10.1016/j.scitotenv.2020.138745.
- Güner, H., Aysel, V. (2011). *Seedless Plants Systematics (Algae)*. First Volume Ege University Faculty of Science Publication No: 108, Ege University Press, İzmir, pp. 245.
- Peksezer, B., Alp, M.T., Ayas, D. (2022). Antimicrobial Effects of Extracts from *Ulva intestinalis* (Linnaeus 1753) and *Sargassum vulgare* (F. Furcatum (Kützinger) J. Agardh 1889) on Some Pathogenic Microorganisms. Mediterranean Fisheries and Aquaculture Research, 5(2), 54-64.
- Suluk, S. (2022). Colors of the Economy: An Evaluation of Turkey in the Context of the Sustainable Blue Economy. Dumlupınar University Journal of Social Sciences, 74, 132-150, DOI: 10.51290/dpusbe.1123257.
- Wenhai, L., Cusack, C., Baker, M., Tao, W., Mingbao, C., Paige, K., Xiaofan, Z., Levin, L., Escobar, E., Amon, D., Yue, Y., Reitz, A., Neves, A.A.S., Oroureke, E., Mannarini, G., Pearlman, J., Tinker, J., Horsburgh, K.J., Lehodey, P., Pouliquen, S., Dale, T., Peng, Z., Yufeng, Y. (2019). Successful Blue Economy Examples with an Emphasis on International Perspectives. Frontiers in Marine Science, 6(261), 1-14, DOI: 10.3389/fmars.2019.00261.
- Yangson, N.A.T., Edubos, J.I., Tahliluddin, A.B., Toring, C.C., Farquerabao, M.L.T. (2022). A Preliminary Study on the Cultivation of Brown Seaweed *Sargassum cristaefolium* Using Fixed-off Bottom and Raft Methods. Journal of Agricultural Production, 3(1), 17-29, DOI: 10.29329/agripro.2022.413.3.
- Yılmaz, T.Ö. (2021). Evaluation of Fisheries Support in Turkey for Sustainable Blue Economy. Academic Review of Economics and Administrative Sciences, 14(3), 906-923, DOI: 10.25287/ohuiibf.788879.



# **Determination of Phenolic Compounds in Rubia Tinctorum Chloroform Extract by LC-MS/MS**

**Temine ŞABUBDAK<sup>1</sup>**

1- Prof. Dr.; Tekirdağ Namık Kemal Üniversitesi Fen Edebiyat Fakültesi Kimya Bölümü.  
tsabudak@nku.ed.tr ORCID No: 0000-0003-4384-4265

## ABSTRACT

It's a known fact that the ethnobotanical applications of plants are as old as human history. Humankind has benefited from a vast number of plant secondary metabolites for the prevention and treatment of diseases. Among these, phenolic compounds constitute the most important group due to their health-promoting benefits. In this study, phenolic/flavonoid compounds in the chloroform extract of *Rubia tinctorum* L. were determined using the LC-MS/MS method. LC-MS/MS analysis of *R. tinctorum* root and aerial chloroform extract revealed the presence of 24 phytochemical compounds. Hesperidin, rutin, theaflavin and quercetin were identified as the main components among the detected compounds.

**Keywords:** *Natural Liquid Soap, Hot And Cold Process, Stability Testing, Microbiological Testing, Plant Oil, Essential Oil.*

---

## INTRODUCTION

Natural products are of great importance due to the presence of many secondary metabolites in their structure and their use in many different places in life. Their use in the food, drug and dye industries and the fact that many of them are obtained synthetically, has increased their importance. With the theoretical methods used today, many properties of molecules have begun to be calculated before these experiments or without the need for experiments. Calculations made using computer software in chemical research allow the properties of many substances obtained by experimental methods to be obtained in a shorter time and more reliably without the use of any chemicals.

Phenolic compounds represent the major class of secondary metabolites in plants (Vermerris and Nicholson, 2007). Owing to their beneficial effects on human health, these compounds have attracted growing scientific and industrial interest in recent years. Structurally, phenolic substances are characterized by the presence of one or more hydroxyl groups (-OH) attached to one or more aromatic rings, and they can range from simple low-molecular-weight molecules to highly complex macromolecular structures (Carocho and Ferreira, 2013:1236; Stewart and Stewart, 2008:2682). These compounds function as potent antioxidants and metabolic regulators, thereby contributing to the protection of human health against a wide range of diseases, including cardiovascular disorders, microbial infections, cancer, diabetes, osteoporosis, neurodegenerative diseases, and asthma. Due to these remarkable bioactivities, phenolic compounds have garnered increasing scientific and clinical interest in recent years (Zuiter, 2014).

Foods contain between 500 and 25,000 diverse phytochemical compounds. Among these, phenolic substances, which account for approximately 500 of them, are considered the most important group due to their health-promoting benefits (Acosta-Estrada et al., 2014:46). This significance arises from their wide range of biological activities, including anti-inflammatory (Zhang and Tsao, 2016:33), antioxidant (Albishi et al., 2013:930), antiviral (Zhang et al., 2014:300), antidiabetic (Asgar, 2013-930), anticancer (Wang et al., 2011:949), and antimicrobial properties (Cushnie and Lamb, 2005:343).

Flavonoids, a major class of polyphenolic secondary metabolites, are widely distributed in plants and human diets. Owing to their broad spectrum of bioactive properties-such as antiviral, antibacterial, anti-inflammatory, cardioprotective, antidiabetic, anticancer, and anti-aging effects-they have long attracted considerable scientific interest and are well supported by numerous studies (Krych and Gebicka, 2013:148; Ragab et al., 2014:506; Tian et al., 2014:34; Zhang et al., 2015:144). To date, more than 9,000 flavonoids have been identified (Wang et al., 2011:949), with an estimated daily intake ranging from 20 mg to 500 mg, primarily derived from dietary sources such as tea, red wine, apples, onions, and tomatoes (Rakers et al., 2014:4312; Giuliani et al., 2014:23).

*Rubia tinctorum* L., belonging to the Rubiaceae family, has historically been one of the most extensively cultivated dye plants in our country. Traditionally, it has been employed as a natural source of red dye, primarily for coloring textiles and various plant- and animal-based fibers (Dölen, 2008; Kayabaşıp et al., 1998:84). Beyond its use in traditional dyeing practices, *R. tinctorum* holds significant ethnobotanical value and has attracted attention for potential applications in the pharmaceutical, cosmetic, and food industries due to its bioactive secondary metabolites, particularly anthraquinones (Zhang and Tsao, 2016:33; Albishi et al., 2013:930). In this context, the present study determined the composition of phenolic and flavonoid compounds in the chloroform extract of *Rubia tinctorum* L., cultivated as a crop in Edirne-Havsa, using Liquid Chromatography–Tandem Mass Spectrometry (LC–MS/MS).



## BOTANICAL INFORMATION AND PHARMACOLOGICAL PROPERTIES

The Rubiaceae family, consisting of roughly 450 genera and 6500 species, is home to the genus *Rubia*. This diverse family includes a mix of trees, shrubs, and less commonly, herbs. The genus *Rubia* itself is widespread, with more than 60 species found across Africa, temperate Asia, and America. Approximately 15 of these species have been documented in India (Krishnan Marg, 1985). These plants are characterized as perennial, herbaceous climbers with long, cylindrical, and flexible roots covered by thin, reddish bark. Their stems often feature a long, rough, grooved, and woody base (Figure 1 and Figure 2). The plants within the *Rubia* genus are valued for their significant commercial, economic, and medicinal uses. They are particularly notable for containing large quantities of anthraquinones, which are especially concentrated in their roots (Thomson, 1996; Perkin and Everest, 1918).



Figure 1. *R. tinctorum* (Yavuzcanli, 2023)



Figure 2. Roots shoot of *R. tinctorum* (Yavuzcanli, 2023)

In Turkey, five species of *Rubia* grow naturally: *R. davisiana* Ehrend. (endemic), *R. peregrina* L., *Rubia rotundifolia* Banks & Sol., *R. tenuifolia* d'Urv. and *R. tinctorum* L. (Arı and Kahraman, 2020:1). *Rubia tinctorum* L. is a species classified within the genus *Rubia*. (Dölen, 20082). *R. tinctorum* is locally referred to by various names, such as kök boya, ‘bostan otu’, ‘boyacı kökü’, ‘boya çili’, ‘çubuk boya’, ‘yumurta boyası’, ‘boya pürü’, and ‘çöp boyası’ (Eşberk, 1947). *R. tinctorum* is naturally distributed across the Caucasus, Iran, Central West Asia, and as far as the Himalayas. As the most important dye plant for producing red color, madder has been cultivated for centuries. Its cultivation extended to North Africa and Europe, and it was even introduced to India by the British and the Portuguese. Despite its long history of cultivation, no new varieties of madder have been developed. There is no difference between the cultivated madder and the wild-growing forms of the plant. In Turkey, *R. tinctorum* occurs naturally in several provinces, including Manisa, Demirci, Gördes, Konya, Aksaray, Niğde, Kayseri, Kırşehir, Çorum, Yozgat, Malatya, Elazığ, Adıyaman, Amasya, Ankara, Tokat, Kahramanmaraş, Çanakkale and Muğla, and is also cultivated in certain regions ([https://www.naturaldyes.com.tr/kokboya/?utm\\_source](https://www.naturaldyes.com.tr/kokboya/?utm_source)).

Extracts of *R. tinctorum* contain some compounds of pharmacological interest. Crude extracts have been used for the treatment of bladder and kidney stones, especially those consisting of calcium oxalate and calcium phosphate in the urinary tract. *In vitro* experiments showed that ruberythric acid prevented the formation of calcium phosphate and calcium oxalate

(Schilcher 1984:2429; Murti et al., 1970:779; Poginsky et al.,1991:12656; Wijnsma and Verpoorte 1986:79).

*Rubia tinctorum* L. (Rubiaceae) has been traditionally used as a diuretic, in the treatment of jaundice, sciatica, and paralysis, as a postpartum menstrual regulator, and for the management of rheumatism, eczema, and fungal diseases (Güzel et al., 2015:118). *Rubia tinctorum* is a valuable source of raw materials for dyes used in the cosmetic, textile, food, and pharmaceutical industries. Additionally, it is recognized for its various beneficial biological properties (Kabaalioğlu and Tezcan, 2021:3573).

## EXPERIMENTAL

### *Experimental Chemical*

Methanol (Merck), hekzan (Merck) and kloroform (Merck) of chromatographic grade were purchased from labor chemistry Company.

### *Collection and Extraction of the Plant*

The cultivated *R. tinctorum* L. plant was collected in August 2024 from the garden of Trakya University Havsa Vocational School and dried in a well-ventilated shaded area. The dried plant material was separated into aerial and underground parts (root) and subjected to extraction by maceration with 80% methanol. Following evaporation of the solvent mixture in an evaporator, the methanolic extract was dissolved in a small amount of water and subsequently re-extracted first with hexane and then with chloroform. After extraction, the solvents were evaporated in a rotary evaporator, yielding hexane, chloroform, and aqueous extracts of both the underground (root) and aerial parts. Following the acidic hydrolysis of the underground and aerial chloroform extracts, the composition of phenolic and flavonoid compounds was determined by LC–MS/MS using a method developed with standard compounds. The measurements were performed at the TUTAGEM (Edine) Center.

### *Acidic Hydrolysis Procedure*

To 25 mg of the sample, 50 µL of 2 M HCl solution was added. The mixture was stirred for 30 seconds and then kept in an ultrasonic bath at 80 °C for 40

minutes. Subsequently, 200 µL of extraction solution (79% ultrapure water + 20% methanol + 1% formic acid) was added and mixed for 30 seconds using a vortex mixer. The sample was centrifuged at 9000 rpm for 5 minutes, and the clear supernatant was transferred into glass vials for injection.

### ***LC-MS/MS Analysis***

The analyses of phenolic compounds were carried out using an Agilent 1260 Infinity Liquid Chromatography system coupled with an Agilent 6460 Triple Quadrupole MS/MS system equipped with a Jet Stream Electrospray ion source.

Mobile Phase A: 5 mM Ammonium Acetate in ultrapure water

Mobile Phase B: Acetonitrile: Methanol (1:1) containing 0.1% Acetic Acid

Column: Agilent Zorbax SB-C18; 4.6 × 150 mm, 3.5 µm

Column Temperature: 35°C

Injection Volume: 5.0 µL

Gradient elution at 35 C was used in the following steps: 8 % B (0-3.5 min); 99 % B (3.5-8 min); 100 % B (8-10 min); 60 % B (10-11.8 min); 8% B (11.8-15 min).

## **RESULTS AND DISCUSSION**

LC-MS/MS analysis of *R. tinctorum* root chloroform extract revealed the presence of 9 phytochemical compounds. Of these, 2 were phenolic acids and 7 were flavonoids. Hesperidin, rutin, theaflavin and quercetin were identified as the main components among the detected compounds (Table 1).

LC-MS/MS analysis of *R. tinctorum* aerial chloroform extract revealed the presence of 15 phytochemical compounds. Of these, 3 were phenolic acids and 12 were flavonoids. Hesperidin, rutin, theaflavin and quercetin were identified as the main components among the detected compounds (Table 2).

In a study by Houari et al. (2022), phytochemical compounds in the aqueous extract of *R. tinctorum* roots collected from Northwest Algeria were investigated using LC-MS/MS. But, in this study, hesperidin, rutin, and theaflavin were not detected.

Table 1. LC-MS/MS analysis of *R. tinctorum* roots chloroform extract

Compound	Retention Time (min)	Concentration (ng/g)
Gallic Acid	3,221	nd
Protocatechuic Acid	3,747	nd
2,5-Dihydroxybenzoic Acid	4,045	nd
Chlorogenic Acid	4,964	nd
Epigallocatechin	5,058	nd
Galocatechin	5,206	nd
Rosmarinic acid	5,335	nd
Syringic Acid	5,301	nd
Epicatechin	5,365	nd
Caffeic Acid	5,302	3,4364
Epigallocatechin gallate	5,408	nd
Salicylic Acid	5,378	208,5875
Catechin	5,541	nd
Verbascoside	5,536	nd
Gibberellic Acid	5,688	nd
Catechin gallate	5,612	nd
Epicatechin gallate	5,603	nd
Hesperidin	5,611	3348,9623
Rutin	5,620	3076,3477
p-Coumaric Acid	5,637	nd
Naringin	5,844	nd
trans-Ferulic Acid	5,776	nd
Sinapic Acid	5,822	nd
Ethyl Gallate	5,832	nd
Phlorizin	5,882	nd
Oleuropein	6,011	nd
Theaflavin	5,955	7414,9807
Theaflavin-3-gallate	6,160	nd
Myricetin	6,004	nd
2-Hydroxytranscinnamic Acid	6,224	nd
Resveratrol	6,129	nd
Indole-3-acetic Acid	6,047	nd
Propyl Gallate	6,204	nd
Aloin A	6,274	nd
Quercetin	6,285	2803,5132
Luteolin	6,295	nd
Abscisic Acid	6,287	119,9448
Naringenin	6,388	nd
Genistein	6,463	192,9772
Kaempferol	6,499	nd
Apigenin	6,473	nd

Isorhamnetin	6,544	16,8073
Jasmonic Acid	6,632	nd
Jaceosidin	6,636	nd
CAPE	6,869	nd
Pinocembrin	6,946	nd
Galangin	7,156	nd
Chrysin	7,159	nd

Nd: not dedected

Table 2. LC-MS/MS analysis of *R. tinctorum* aerial chloroform extract

Compound	Retention Time (min)	Concentration (ng/g)
Gallic Acid	3,340	128,4147
Protocatechuic Acid	3,646	14944,6707
2,5-Dihydroxybenzoic Acid	3,925	1942,4420
Chlorogenic Acid	4,964	4418,5870
Epigallocatechin	5,327	nd
Gallocatechin	5,327	nd
Rosmarinic acid	5,270	nd
Syringic Acid	5,274	6677,6133
Epicatechin	5,225	nd
Caffeic Acid	5,395	32,8886
Epigallocatechin gallate	5,333	nd
Salicylic Acid	5,368	1736,3964
Catechin	5,234	nd
Verbascoside	5,490	nd
Gibberellic Acid	5,604	nd
Catechin gallate	5,575	nd
Epicatechin gallate	5,622	nd
Hesperidin	5,592	5302,8085
Rutin	5,592	6294,7960
p-Coumaric Acid	5,656	557,1139
Naringin	5,806	nd
trans-Ferrulic Acid	5,730	2909,3874
Sinapic Acid	5,784	nd
Ethyl Gallate	5,646	nd
Phlorizin	5,761	nd
Oleuropein	5,863	nd
Theaflavin	5,937	nd
Theaflavin-3-gallate	5,908	nd
Myricetin	6,013	nd
2-Hydroxytranscinnamic Acid	5,647	nd
Resveratrol	6,120	nd
Indole-3-acetic Acid	6,037	nd
Propyl Gallate	5,654	nd
Aloin A	6,199	nd
Quercetin	6,294	13,9057
Lutolein	6,304	2,4214
Abscisic Acid	6,324	494,0822
Naringenin	6,369	nd
Genistein	6,453	31,9472
Kaempferol	6,462	nd
Apigenin	6,519	nd

Isorhamnetin	6,572	nd
Jasmonic Acid	6,558	nd
Jaceosidin	6,590	80,3740
CAPE	6,527	nd
Pinocembrin	6,909	nd
Galangin	7,147	nd
Chrysin	7,113	nd

Nd: not dedected

## CONCLUSION

In this study, the composition of phenolic/flavonoid compounds in the root and aerial chloroform extracts of *Rubia tinctorum* L. was determined using the LC-MS/MS method. Hesperidin, rutin, theaflavin, and quercetin were observed as the main compounds in both the root and aerial extracts. Secondary metabolites in plants differ depending on the soil, its mineral content, and the climate. Therefore, a difference in the collection location of the plant leads to the presence of different secondary metabolites.

## REFERENCES

- Acosta-Estrada, B.A., Gutierrez-Urbe, J.A. and SernaSaldivar, S.O. (2014). Bound phenolics in foods, a review. *Food Chemistry*, 152, 46-55.
- Albishi, T., John, J. A., Al-Khalifa, A. S. and Shahidi, F. (2013). Antioxidant, anti-inflammatory and DNA scission inhibitory activities of phenolic compounds in selected onion and potato varieties. *Journal of Functional Foods*, 5(2), 930-939.
- Ari, N., and Kahraman, A. (2020). Anatomical and palynological investigations on *Rubia tinctorum* L. (Rubiaceae, Rubiaceae) from the Aegean Region of Turkey. *Commagene Journal of Biology*, 4(1), 1-4.



Carocho, M., and Ferreira, I. (2013). The role of phenolic compounds in the fight against cancer—a review. *Anti-Cancer Agents in Medicinal Chemistry (Formerly Current Medicinal Chemistry-Anti-Cancer Agents)*, 13(8), 1236-1258.

Cushnie, T. P. T., and Lamb, A. J. (2005). Antimicrobial activity of flavonoids, *International Journal of Antimicrobial Agents*, 26 (5), 343-356.

Dölen, E. (2008). *Kök boya (Rubia tinctorum L.) bitkisinden pigment eldesi, analizi ve uygulaması* (Yüksek Lisans Tezi). Marmara Üniversitesi Fen Bilimleri Enstitüsü.

Eşberk, T. (1947). Yurdumuzda yetişen boya bitkilerinden köy sanatlarında faydalanma usulleri; Kökboya. *Türk Tekstil Mecmuası*, 4, 11-13.

Giuliani, C., Bucci, I., Di Santo, S., Rossi, C., Antonino, G., Piantelli, M., Fabrizio, M., and Giorgio, N. (2014). The flavonoid quercetin inhibits thyroid-restricted genes expression and thyroid function. *Food and Chemical Toxicology*, 66, 23–29.

Güzel, Y., Güzelşemme, M., Miski, M. (2015). Ethnobotany of medicinal plants used in Antakya: A multicultural district in Hatay Province of Turkey. *Journal of Ethnopharmacology*, 174, 118-152.

[https://www.naturaldyes.com.tr/kokboya/?utm\\_source](https://www.naturaldyes.com.tr/kokboya/?utm_source) (Access date: 25 August 2025).

Kabaalioğlu, N., and Tezcan, H. (2021). The important of root dyeing in the ottoman period, The positive and negative effects of chemical dyes on the textile industry. *International Social Sciences Studies Journal*, 7 (86); 3573-3578.

Kayabaşıp, N., ARLI, M., and Erdoğan, Z. (1998). Kökboya (*Rubia tinctorum* L.)'dan elde edilen renkler ve bu renklerin yün halı iplikleri üzerindeki ışık ve sürtünme haslıkları, *Tarım Bilimleri Dergisi*, 4 (3), 84-90.

Krishnan Marg, K.S. (1985). *The Wealth of India: Raw Materials*, National Institute of Science Communication and Information Resources CSIR, New Delhi-110 012.

Krych, J., and Gebicka, L. (2014). Catalase is inhibited by flavonoids. *International Journal of Biological Macromolecules*, 58, 148–153.

Perkin, A. G., and Everest, A.E. (1918). *In the natural organic colouring matters*, Longmans-Green, London, p. 43.

Poginsky, B., Westendorf, J., Blomeke, B., Marquardt, H., Hower, A., Grover, P. L., and Phillips, D. H. (1991). *Carcinogenesis*, 72, 1265-1271.

Ragab, F. A., Yahya, T. A. A., El-Naa, M. M., and Reem, A. (2014). Design, synthesis and structure–activity relationship of novel semi-synthetic flavonoids as antiproliferative agents. *European Journal of Medicinal Chemistry*, 82(23), 506–520.

Rakers, C., Schwerdtfeger, S. M., Mortier, J., and Matthias F. M. (2014). Inhibitory potency of flavonoid derivatives on influenza virüs neuraminidase. *Bioorganic and Medicinal Chemistry Letters*, 24(17), 4312-4317.

Schilcher, H. (1984). Extracts of madder roots have been used as ingredients of phytopharmaceuticals, *Deutsche Apotheker-Zeitung*, 124, 2429-2436.

Stewart, A. J. and Stewart, R. F. (2008). *Phenols*. Editor: Jorgensen, S. E. and Fath, B. D., Encyclopedia of Ecology, pp. 2682–2689, Academic press.

Thomson, R. H. (1996). *Naturally occurring quinones*. Chapman & Hall, London.

Tian, S. S., Jiang, F. S., Zhang, K., Xue-Xin, Z., Bo, J., Jin-Jian, L., and Zhi-Shan, D. (2014). Flavonoids from the leaves of *Carya cathayensis* Sarg. inhibit vascular endothelial growth factor-induced angiogenesis. *Fitoterapia*, 92, 34-40.

Murti, V. V. S., Seshadri, T. R., and Sivakumaran, S. (1970). A study of madder, the roots of *Rubia tinctorum* Linn., *Indian Journal of Chemistry*, 8, 779-782.

Vermerris, W., and Nicholson, R. (2007). *Phenolic compound biochemistry*. Springer Science & Business Media.

Wijnsma, R., and Verpoorte, R. (1986). In-progress in the chemistry of organic natural products. Eds. Herz, W., Grisebach, H., Kirby, G. W., Tamm, C., Springer, Wien, Vol. 49, p. 79.

Wang, Y., Chen, S., and Yu, O. (2011). Metabolic engineering of flavonoids in plants and microorganisms. *Applied Microbiology and Biotechnology*, 91(4), 949–956.

Yavuzcanli, M. (2023). *Rubia tinctorum* L. (Kök boyası) bitkisinin ekstraktından partikül sentezi, yapısal karakterizasyonu ve biyoaktivite özellikleri (Yüksek Lisans Tezi). Van Yüzüncü Yıl Üniversitesi Fen Bilimleri Enstitüsü.

Zuiter, A. S. (2014). *Proanthocyanidin: Chemistry and biology: From phenolic compounds to proanthocyanidins*. Elsevier press.

Zhang, X., Huang, H., Zhao, X., and Kunsong, C. (2015). Effects of flavonoids-rich Chinese bayberry (*Myrica rubra* Sieb. et Zucc.) pulp extracts on glucose consumption in human HepG2 cells. *Journal of Functional Foods*, 14, 144-153.

Zhang, H., and Tsao, R. (2016). Dietary polyphenols, oxidative stress and antioxidant and antiinflammatory effects. *Current Opinion in Food Science*, 8, 33-42.

Zhang, X. L., Guo, Y. S., Wang, C. H., Li, G. Q., Xu, J. J., Chung, H. Y., Ye, W.C., Li, Y. L. and Wang, G. C. (2014). Phenolic compounds from *Origanum vulgare* and their antioxidant and antiviral activities. *Food Chemistry*, 152, 300-306.

Zohra, H. F., Erenler, R., Bakir, S., Capanoglu, E., and Hariri, A. (2022). LC-ESI-MS/MS analysis, toxicity and anti-anaemic activity of *Rubia tinctorum* L. aqueous extract. *Nova Biotechnol Chim*, 21(1): e978.



# **Research on Multifocal Motor Neuropathy as a Rare Autoimmune Neuropathy**

**Emine DIRAMAN<sup>1</sup>**

**Fatma Gönül SEZGIN<sup>\*2</sup>**

**Birol SEZGIN<sup>3</sup>**

<sup>1</sup>Department of Biology, Faculty of Science & Arts, Ondokuz Mayıs University, Samsun, Turkey

<sup>2</sup> Department of Biology, Faculty of Science & Arts, Ondokuz Mayıs University, Samsun, Turkey

<sup>3</sup>Department of Family Medicine Faculty of Medicine, Samsun University, Samsun, Turkey

<sup>\*</sup>(gonul.solmaz@omu.edu.tr)

## ABSTRACT

Multifocal motor neuropathy (MMN) is a rare, immune-mediated neuropathy characterized by chronic progression, selective motor involvement, and preservation of sensory function. The clinical hallmark is asymmetric weakness, most frequently affecting the distal upper limbs, often accompanied by fasciculations and muscle cramps. Unlike amyotrophic lateral sclerosis (ALS), MMN lacks upper motor neuron signs and bulbar involvement, while conduction block on nerve conduction studies serves as a key diagnostic marker. The pathogenesis involves autoantibodies—most notably anti-GM1 IgM—that activate the complement system at nodes and paranodes, leading to disruption of axonal conduction. Diagnosis is supported by electrophysiological studies, serology, and increasingly by high-resolution nerve imaging. First-line treatment is intravenous or subcutaneous immunoglobulin (IVIg/SCIg), which consistently improves strength and function, although lifelong maintenance is often required. Corticosteroids and plasma exchange have proven ineffective and may worsen outcomes. Emerging therapeutic approaches, particularly complement-targeted therapies, offer new promise for patients with partial or insufficient response to immunoglobulin therapy. Early recognition and initiation of treatment are crucial to prevent irreversible axonal degeneration and long-term disability. With timely and adequate management, most patients maintain functional independence, though the chronic course and high treatment burden underscore the need for innovative and cost-effective therapeutic strategies.

*Keywords – Multifocal Motor Neuropathy (MMN), Autoimmune Neuropathy, Anti-GM1 Antibody, Conduction Block, Rare Disease.*

---

## INTRODUCTION

MMN is a rare autoimmune polyneuropathy in which sensory fibers are largely preserved, while motor fibers are selectively affected. Clinically, it presents with asymmetric weakness, predominantly in the distal upper extremities, while objective sensory loss is absent or minimal. Electrophysiologically, the hallmark finding is partial motor conduction block in segments not prone to entrapment (1,2,5).

### Epidemiology

MMN typically begins in mid-adulthood, with a slight male predominance. Prevalence varies by region but is generally <1–2 per 100,000. The clinical hallmark is asymmetric distal upper-limb weakness (1).

## Pathophysiology

The immune-mediated pathogenesis of MMN centers on IgM antibodies directed against the ganglioside GM1 (with positivity ranging between ~20–80% depending on laboratory and methodology). These antibodies trigger complement activation at nodal/paranodal regions, disrupting sodium channel clustering and leading to conduction block. If untreated, progressive axonal loss may occur (3,6,7).

## Clinical Features

- Weakness: Asymmetric, multifocal, predominantly distal and upper-limb involvement; cramps and fasciculations may accompany.
- Sensory function: Objective sensory loss is typically absent; mild abnormalities may rarely occur in the lower limbs.
- Reflexes: Reduced in affected regions.
- Upper motor neuron and bulbar signs: Absent in MMN; their presence suggests ALS (5).

## Differential Diagnosis

- ALS: Widespread fasciculations/weakness with upper motor neuron signs; conduction block not characteristic.
- MADSAM/Lewis–Sumner variant of CIDP: Prominent sensory involvement.
- Entrapment neuropathies and radiculopathies: May show focal distribution, but electrophysiological patterns and imaging distinguish them (4,5).

## Diagnostic Approach

### *Electrophysiology (NCS/EMG):*

- Partial motor conduction block in non-compression-prone segments is highly suggestive of MMN; sensory conduction usually preserved.
- Over time, temporal dispersion and conduction slowing may occur (4).

### *Serology:*

- Anti-GM1 IgM positivity is common and supportive of MMN. Higher titers may correlate with severity and risk of axonal degeneration, though positivity is not mandatory for diagnosis.

Reported prevalence varies widely depending on testing method (6,7).

*Imaging:*

- High-resolution nerve ultrasound (HRUS) and MR neurography may reveal segmental nerve enlargement corresponding to conduction block sites and can aid in differentiating from CIDP (13).

*Guidelines and Criteria:*

- EFNS/PNS consensus guidelines (2006; updated 2010) remain the reference for diagnosis, investigation, and management, emphasizing conduction block with sensory preservation as key criteria (1,4).

*Treatment*

*Immunoglobulin (IVIg/SCIg):*

- First-line: IVIg is supported by randomized trials and systematic reviews as effective in improving muscle strength and function in the short term. Most patients require long-term maintenance (2).
- Subcutaneous immunoglobulin (SCIg): Demonstrated comparable efficacy to IVIg in maintenance therapy with improved convenience. Randomized crossover studies and long-term observational data support its use (class II–IV evidence). Facilitated SCIg (fSCIg) with hyaluronidase enables higher infusion volumes (9,10,11).

*Corticosteroids and Plasma Exchange:*

- Corticosteroids are typically ineffective and may worsen weakness; not recommended as first-line.
- Plasma exchange has not shown significant or sustained benefit in MMN (4,3).

*Other Immunotherapies:*

- Agents such as cyclophosphamide and rituximab have been trialed in limited cases/series but are not standard of care. Interest in complement-targeted therapies (e.g., C1s inhibitors) is increasing; DNTH103 entered phase 2 trials approved by the FDA in 2024, with results expected in late 2026. This approach directly targets the anti-GM1-mediated complement activation pathway (3,14).

### *Rehabilitation and Quality of Life:*

- Regular physiotherapy, energy-conservation strategies, and supportive devices (splints, ergonomic tools) help maintain function. Patients should avoid overexertion, which may exacerbate fatigue and transient weakness. Recommendations should be tailored to individual clinical status (5).

### Prognosis and Natural History

MMN usually progresses slowly. If untreated, axonal degeneration and permanent weakness may develop. Long-term cohort studies suggest worse outcomes with lower baseline MRC scores and absent reflexes. Most patients remain functional with ongoing IVIg/SCIg therapy, although lifelong maintenance is common (2,12).

## DISCUSSION

The distinct clinical and electrophysiological profile of MMN—motor predominance, conduction block, and sensory preservation—makes accurate differentiation from ALS and MADSAM critical, as IVIg responsiveness positions MMN as a treatable neuropathy. While anti-GM1 IgM seropositivity enhances diagnostic specificity, seronegative MMN is also frequent, reinforcing the need for integrated interpretation of serology, electrophysiology, and clinical findings. The burden and cost of lifelong IVIg/SCIg therapy (8) underscore the need for novel, targeted strategies. Complement inhibition offers a promising avenue, though high-level evidence of efficacy and safety remains necessary.

## CONCLUSION

MMN is a treatable neuropathy that responds well to timely immunoglobulin therapy, though most patients require long-term maintenance. Accurate diagnosis—based on careful clinical and



electrophysiological assessment, with supportive serology and imaging—is crucial. IVIg/SCIg should be initiated early, while corticosteroids and plasma exchange should be avoided. In the near future, complement-targeted and personalized therapeutic strategies may broaden the treatment spectrum.

## REFERENCES

- [1] Claytor, B.; Polston, D.; Li, Y. Multifocal Motor Neuropathy: A Narrative Review. *Muscle Nerve* **2025**, *71*, 512–534.
- [2] Keddle S, Eftimov F, van den Berg LH, Brassington R, de Haan RJ, van Schaik IN. Immunoglobulin for multifocal motor neuropathy. *Cochrane Database Syst Rev*. 2022 Jan 11;1(1):CD004429. doi: 10.1002/14651858.CD004429.
- [3] Yeh WZ, Dyck PJ, van den Berg LH, Kiernan MC, Taylor BV. Multifocal motor neuropathy: controversies and priorities. *J Neurol Neurosurg Psychiatry*. 2020 Feb;91(2):140-148. doi: 10.1136/jnnp-2019-321532.
- [4] Joint Task Force of the EFNS and the PNS. (2010). EFNS/PNS guideline on management of multifocal motor neuropathy (update). *European Journal of Neurology*, *17*(3), 356–363.
- [5] Allen JA, Clarke AE, Harbo T. A Practical Guide to Identify Patients With Multifocal Motor Neuropathy, a Treatable Immune-Mediated Neuropathy. *Mayo Clin Proc Innov Qual Outcomes*. 2024 Jan 8;8(1):74-81. doi: 10.1016/j.mayocpiqo.2023.12.002.
- [6] Pestronk A, Choksi R. Multifocal motor neuropathy. Serum IgM anti-GM1 ganglioside antibodies in most patients detected using covalent linkage of GM1 to ELISA plates. *Neurology*. 1997 Nov;49(5):1289-92. doi: 10.1212/wnl.49.5.1289.
- [7] Carpo M, Allaria S, Scarlato G, Nobile-Orazio E. Marginally improved detection of GM1 antibodies by Covalink ELISA in multifocal motor neuropathy. *Neurology*. 1999 Dec 10;53(9):2206-7. doi: 10.1212/wnl.53.9.2206.
- [8] Harbo T, Andersen H, Jakobsen J. Long-term therapy with high doses of subcutaneous immunoglobulin in multifocal motor neuropathy. *Neurology*. 2010 Oct 12;75(15):1377-80. doi: 10.1212/WNL.0b013e3181f735ce.
- [9] Al-Zuhairy A, Jakobsen J, Andersen H, Sindrup SH, Markvardsen LK. Randomized trial of facilitated subcutaneous immunoglobulin in multifocal motor neuropathy. *Eur J Neurol*. 2019 Oct;26(10):1289-e82. doi: 10.1111/ene.13978. Epub 2019 May 31.
- [10] Gentile L, Russo M, Rodolico C, Arimatea I, Vita G, Toscano A, Mazzeo A. Long-term treatment with subcutaneous immunoglobulin in multifocal motor neuropathy. *Sci Rep*. 2021 Apr 28;11(1):9216. doi: 10.1038/s41598-021-88711-9.

- [11] Al-Zuhairy A, Sindrup SH, Jakobsen J. Long-term follow-up of facilitated subcutaneous immunoglobulin therapy in multifocal motor neuropathy. *J Neurol Sci.* 2021 Aug 15;427:117495. doi: 10.1016/j.jns.2021.117495.
- [12] Herraets I, van Rosmalen M, Bos J, van Eijk R, Cats E, Jongbloed B, Vlam L, Piepers S, van Asseldonk JT, Goedee HS, van den Berg L, van der Pol WL. Clinical outcomes in multifocal motor neuropathy: A combined cross-sectional and follow-up study. *Neurology.* 2020 Oct 6;95(14):e1979-e1987. doi: 10.1212/WNL.0000000000010538. Epub 2020 Jul 30. Erratum in: *Neurology.* 2022 May 10;98(19):818. doi: 10.1212/WNL.0000000000012098.
- [13] Goedee HS, Jongbloed BA, van Asseldonk JH, Hendrikse J, Vrancken AFJE, Franssen H, Nikolakopoulos S, Visser LH, van der Pol WL, van den Berg LH. A comparative study of brachial plexus sonography and magnetic resonance imaging in chronic inflammatory demyelinating neuropathy and multifocal motor neuropathy. *Eur J Neurol.* 2017 Oct;24(10):1307-1313. doi: 10.1111/ene.13380.
- [14] URL: <https://www.nasdaq.com/articles/dianthus-gets-fda-clearance-initiate-phase-2-trial-dnth103-multifocal-motor-neuropathy> access: 21. 08. 2025



# **Numerical Solution for Parabolic Equation**

**Armida BRAKAJ<sup>1</sup>**

**Zhifka MUKA<sup>2</sup>**

**Fizeleni LEKLI<sup>3</sup>**

<sup>1</sup>Math Department, Polytechnic University of Tirana, Albania

<sup>2</sup>Math Department, Polytechnic University of Tirana, Albania

<sup>3</sup>Math Department, Polytechnic University of Tirana, Albania

<sup>1</sup>[brakaj\\_armida@yahoo.com](mailto:brakaj_armida@yahoo.com)

<sup>2</sup>[zhifkamuka24@yahoo.it](mailto:zhifkamuka24@yahoo.it)

<sup>3</sup>[fizelenilekli@yahoo.com](mailto:fizelenilekli@yahoo.com)

## ABSTRACT

Numerical methods for solving problems with differential equations are generally based on the local approximate representation of the solution using elementary functions, usually polynomials. Historically, and depending on the mathematical tools used, two main methods are distinguished: the finite difference method and the finite element method. The above methods reduce a differential problem to an algebraic one, respectively linear, if the differential problem is such. The finite difference method is based on the local replacement of derivatives with differences. In principle, the finite difference method for partial differential equations is a simple method, but it is rigid and encounters difficulties in handling boundary conditions when these are complex. In this paper, we have studied the numerical solution of one-dimensional parabolic equations with finite difference method for partial differential equation. The problem is solved using the Forward Difference method, the Backward Difference method, the Richardson method, and the Crank–Nicolson method. We have distinguished the advantages and disadvantages of the methods based on the accuracy and stability of each method for solving the parabolic problem. The conclusions reached have been verified by solving a parabolic problem with simple initial and boundary conditions using all the above methods. The numerical results demonstrate the advantages and disadvantages of the finite difference methods.

*Keywords – Parabolic Equation, Difference Method, Matlab Implementation, Numerical Results, Local Truncation Error.*

---

## INTRODUCTION

We formulate the diffusion equation in its canonical form (its simplest form). Find the function  $u(x, t)$  that satisfies the differential equation:

$$\frac{\partial}{\partial t} u(x, t) = \alpha^2 \frac{\partial^2}{\partial x^2} u(x, t), \quad 0 < x < l, \quad t > 0 \quad (1.1)$$

with initial condition and boundary conditions respectively

$$u(0, t) = 0, \quad u(l, t) = 0, \quad t > 0 \quad \text{and}$$

$$u(x, 0) = f(x), \quad 0 \leq x \leq l$$

In general, equation (1.1) appears in the study of heat conduction, gas diffusion, and single-phase flows. The finite difference method for the numerical solution of problem (1.1) is similar to that of other differential problems. Initially, we choose two constants  $h$  and  $k$ , which define the grid of nodes. The choice of  $h$  is made so that the size  $m = l/h$  is a natural

number. Therefore, the grid of nodes will be  $(x_i, t_j)$ , where  $x_i = ih$  for  $i = 0, 1, \dots, m$  and  $t_j = jk$  for  $j = 0, 1, \dots$ . Below, we will examine some variants of the difference method for problem (1.1).

## THE FORWARD-DIFFERENCE METHOD FOR THE SOLUTION OF STANDARD PARABOLIC PROBLEM

In this method, second-order central differences are used for the second derivative  $u_{xx}(x_i, t_j)$ , while first-order  $u_t(x_i, t_j)$  forward differences, also called progressive differences, are used for the first derivative.

$$\begin{aligned} \frac{\partial^2}{\partial x^2} u(x_i, t_j) &= \frac{u(x_i + h, t_j) - 2u(x_i, t_j) + u(x_i - h, t_j))}{h^2} - \frac{h^2}{12} \frac{\partial^4 u}{\partial x^4}(x_i + \phi_i h, t_j) \\ \frac{\partial}{\partial t} u(x_i, t_j) &= \frac{u(x_i, t_{j+1}) - u(x_i, t_j)}{k} - \frac{k}{2} \frac{\partial^2}{\partial t^2} u(x_i, t_j + \theta_j k) \end{aligned} \quad (1.2)$$

where above  $0 < \theta_j < 1$  and  $-1 < \theta_i < 1$ . Differential equation (1.2) at the interior node  $(x_i, t_j)$ ,  $i = 1, \dots, m-1$  and  $j = 1, \dots$ , written:

$$\frac{\partial}{\partial t} u(x_i, t_j) - \alpha^2 \frac{\partial^2}{\partial x^2} u(x_i, t_j) = 0$$

By substituting the derivatives according to the equations in (1.2), getting the finite difference method.

$$\frac{u_{i,j+1} - u_{i,j}}{k} - \alpha^2 \frac{u_{i+1,j} - 2u_{i,j} + u_{i-1,j}}{h^2} = 0 \quad (1.3)$$

Has local truncation error:

$$\tau_{ij} = \frac{k}{2} \frac{\partial^2}{\partial t^2} u(x_i, t_j + \theta_j k) - \frac{h^2}{12} \frac{\partial^4 u}{\partial x^4}(x_i + \phi_i h, t_j) \quad (1.4)$$

where  $0 < \theta_j < 1$  and  $-1 < \theta_i < 1$

Solving equation (1.3) for  $u_{i,j+1}$ , we obtain:

$$u_{i,j+1} = \left(1 - \frac{2\alpha^2 k}{h^2}\right) u_{i,j} + \alpha^2 \frac{k}{h^2} (u_{i+1,j} + u_{i-1,j})$$

(1.5)

For  $i = 1, \dots, (m-1)$  and  $j = 1, 2, \dots$ .

In matrix form it can be written as

$$\begin{bmatrix} u_{1,j+1} \\ u_{2,j+1} \\ \vdots \\ u_{m-1,j+1} \end{bmatrix} = \begin{bmatrix} (1-2\lambda) & \lambda & & 0 \\ \lambda & (1-2\lambda) & & \lambda \\ & \ddots & \ddots & \ddots \\ 0 & & 0 & (1-2\lambda) \end{bmatrix} \begin{bmatrix} u_{1,j} \\ u_{2,j} \\ \vdots \\ u_{m-1,j} \end{bmatrix}$$

where  $\lambda = \alpha^2 (k/h^2)$ .

In a shorter way  $\mathbf{u}^{(j+1)} = \mathbf{A} \mathbf{u}^{(j)}$  for  $j = 0, 1, \dots$

(1.6)

where

$$\mathbf{u}^{(j)} = \begin{bmatrix} u_{1,j} \\ u_{2,j} \\ \vdots \\ u_{m-1,j} \end{bmatrix} \quad \text{dhe} \quad \mathbf{u}^{(0)} = \begin{bmatrix} f(x_1) \\ f(x_2) \\ \vdots \\ f(x_{m-1}) \end{bmatrix}$$

The above method is known as the forward difference method or the progressive difference method. It's local error, according to (1.4), is of the form  $O(k + h^2)$ . The error propagation analysis for the above method reveals that this method is relatively stable. The stability condition of the method, the dependence of stability on the choice of  $k$  and  $h$  is a statement confirming that the forward difference method is relatively stable.

## BACKWARD DIFFERENCE METHOD FOR THE SOLUTION OF STANDARD PARABOLIC PROBLEM

To obtain a finite difference method that is absolutely stable, the backward differences are used. Instead of equation (1.2) for approximating the derivative we use the formula:

$$\frac{\partial}{\partial t} u(x_i, t_j) = \frac{u(x_i, t_j) - u(x_i, t_{j-1})}{k} - \frac{k}{2} \frac{\partial^2}{\partial t^2} u(x_i, t_j + \theta_j k)$$

where  $-1 < \theta_j < 0$ .

By substituting this last one, together with the difference (1.2) for  $u_{xx}(x_i, t_j)$ , into the differential equation (1.1), we obtain the backward difference method:

$$\frac{u_{i,j+1} - u_{i,j}}{k} - \alpha^2 \frac{u_{i+1,j} - 2u_{i,j} + u_{i-1,j}}{h^2} = 0$$

(1.7)

$$i = 1, 2, \dots, m-1 \quad \text{and} \quad j = 1, 2, \dots$$

In equation (1.7), a typical step includes the nodes:  $(x_i, t_j)$ ,  $(x_i, t_{j-1})$ ,  $(x_{i-1}, t_j)$  and  $(x_{i+1}, t_j)$

Schematically, these points are represented by filled circles in Figure 2.2 - a). The boundary and initial conditions of problem (1.1) determine it's solution only at the boundary nodes of the domain, represented by small circles in Figure 3.1-a. From this figure, it is clear that no explicit procedure can be constructed for solving equation (1.1). Meanwhile, recall that in the forward difference method, the nodes involved in one step were:

$$(x_{i-1}, t_j), (x_i, t_j), (x_i, t_{j+1}) \quad \text{and} \quad (x_{i+1}, t_j)$$



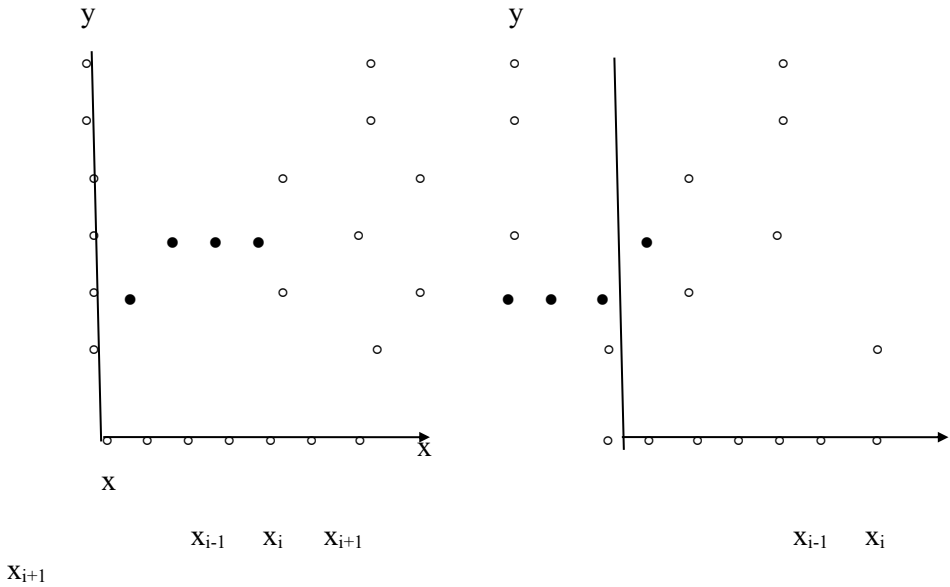


Fig 1. a)-The backward difference method b)- The forward-difference method

From their positions in Figure 3.1-b, the possibility of calculating the approximations sequentially is immediately apparent, by first using the initial condition and then the boundary conditions.

If we denote, as before,  $\lambda = \alpha^2(k/h^2)$ , then the backward difference method (1.7) takes the form:

$$(1 + 2\lambda)u_{i,j} - \lambda u_{i+1,j} - \lambda u_{i-1,j} = u_{i,j-1} \quad (1.8)$$

$$i = 1, 2, \dots, m-1 \text{ and } j = 1, 2, \dots$$

Using the fact that,  $u_{i,0} = f(x_i)$  for  $i = 1, 2, \dots, m-1$  (from the initial condition) and  $u_{0,j} = u_{m,j} = 0$ , for  $j = 1, 2, \dots$  (from the boundary conditions), the method (1.8) can be written in matrix form as:

$$\begin{array}{c}
 u_{1,j-1} \\
 u_{2,j-1} \\
 \vdots \\
 u_{m-1,j-1}
 \end{array}
 \begin{bmatrix}
 (1+2\lambda) & -\lambda & & 0 \\
 -\lambda & (1+2\lambda) & -\lambda & \\
 & 0 & \ddots & 0 \\
 0 & & & (1+2\lambda)
 \end{bmatrix}
 \begin{array}{c}
 u_{1,j} \\
 u_{2,j} \\
 \vdots \\
 u_{m-1,j}
 \end{array}
 =
 \begin{array}{c}
 \vdots \\
 \vdots \\
 \vdots \\
 \vdots
 \end{array}$$

or

$$(1.9) \quad A \mathbf{u}^{(j)} = \mathbf{u}^{(j-1)} \quad \text{for} \quad j = 1, 2, \dots$$

where  $\mathbf{u}^{(j)}$  and  $\mathbf{u}^{(0)}$  are the same as those appearing in equation (1.6).

The matrix  $A$  here is tridiagonal, symmetric, positive definite, and diagonally dominant. The left difference method (1.9) does not have stability problems. Thus, the backward difference method is absolutely stable.

## RICHARDSON METHOD FOR THE SOLUTION OF STANDARD PARABOLIC PROBLEM

The local error of the two finite difference methods (1.6) and (1.9) above was of the form  $O(k + h^2)$ .

Precisely, the presence of the  $O(k)$  component in the above form constitutes the main drawback of the backward difference method. The first-order local error with respect to  $k$ , compared to the second order with respect to  $h$ , indicates that the step  $k$  should be chosen qualitatively smaller than  $h$ . It would be better to have a procedure with local error of the form  $O(k^2 + h^2)$ .

Certainly, for this, another finite difference approximation of  $u_t(x_i, t_j)$  must be used. Specifically, the centered difference formula can be used, which here takes the form:

$$\frac{\partial}{\partial t} u(x_i, t_j) = \frac{u(x_i, t_{j+1}) - u(x_i, t_{j-1}))}{2k} - \frac{k^2}{6} \frac{\partial^3}{\partial t^3} u(x_i, t_j + \theta_j k)$$

where  $-1 < \theta_j < 0$ .

The finite difference method obtained by the above substitution and the known substitution (1.2) into the differential equation (1.1) is known as the Richardson method. The equation of this method is:

$$\frac{u_{i,j+1} - u_{i,j-1}}{2k} - \alpha^2 \frac{u_{i+1,j} - 2u_{i,j} + u_{i-1,j}}{h^2} = 0 \quad (1.10)$$

The Richardson method has a local error of the form  $O(k^2 + h^2)$ , but this method has serious stability problems. In fact, it can be observed that formula (1.10) is an "arithmetic average" of formulas (1.3) and (1.7), and figuratively speaking, it inherits about 50% of the poor stability characteristics of the forward difference method. This defect of the Richardson method is remedied by the following method.

### **CRANK-NICOLSON METHOD FOR THE SOLUTION OF STANDARD PARABOLIC PROBLEM**

It is known that Richardson's method has serious stability problems. A more rewarding method can be derived by averaging the forward-difference method written at its  $j$ th step in  $t$

$$\frac{u_{i,j+1} - u_{i,j}}{k} - \alpha^2 \frac{u_{i+1,j} - 2u_{i,j} + u_{i-1,j}}{h^2} = 0 \quad (2.1)$$

and the backward-difference method written at the  $(j+1)$ st step in  $t$ .

$$\frac{u_{i,j+1} - u_{i,j}}{k} - \alpha^2 \frac{u_{i+1,j+1} - 2u_{i,j+1} + u_{i-1,j+1}}{h^2} = 0 \quad (2.2)$$

The averaged difference method

$$\frac{u_{i,j+1} - u_{i,j}}{k} - \frac{\alpha^2}{2} \left[ \frac{u_{i+1,j} - 2u_{i,j} + u_{i-1,j}}{h^2} + \frac{u_{i+1,j+1} - 2u_{i,j+1} + u_{i-1,j+1}}{h^2} \right] = 0$$

(2.3)

has local truncation error of order  $O(k^2 + h^2)$ . This method is known as Crank-Nicolson method. In matrix form it can be written as

$$A\mathbf{u}^{(j+1)} = B\mathbf{u}^{(j)}, \quad \text{for } j = 0, 1, 2, \dots$$

(2.4)

Where the three-diagonal matrix A and B can be specified.

$$A = \begin{bmatrix} (1+\lambda) & -\frac{\lambda}{2} & 0 & \cdots & 0 & 0 \\ -\frac{\lambda}{2} & (1+\lambda) & -\frac{\lambda}{2} & \cdots & 0 & 0 \\ 0 & -\frac{\lambda}{2} & (1+\lambda) & \cdots & 0 & 0 \\ \vdots & \vdots & \vdots & \vdots & \vdots & \vdots \\ 0 & 0 & 0 & \cdots & (1+\lambda) & -\frac{\lambda}{2} \\ 0 & 0 & 0 & \cdots & -\frac{\lambda}{2} & (1+\lambda) \end{bmatrix}$$

$$B = \begin{bmatrix} (1-\lambda) & \frac{\lambda}{2} & 0 & \cdots & 0 & 0 \\ \frac{\lambda}{2} & (1-\lambda) & \frac{\lambda}{2} & \cdots & 0 & 0 \\ 0 & \frac{\lambda}{2} & (1-\lambda) & \cdots & 0 & 0 \\ \vdots & \vdots & \vdots & \vdots & \vdots & \vdots \\ 0 & 0 & 0 & \cdots & (1-\lambda) & \frac{\lambda}{2} \\ 0 & 0 & 0 & \cdots & \frac{\lambda}{2} & (1-\lambda) \end{bmatrix}$$

$$\lambda = \alpha^2(k/h^2), \quad \mathbf{u}^{(j)} = (u_{1,j}, u_{2,j}, \dots, u_{m-1,j})^T$$

The Crank-Nicolson method is unconditionally stable and it has order of convergence  $O(k^2 + h^2)$ . In many applications it results to be a very efficient numerical method.

## NUMERICAL EXPERIMENTS AND RESULTS FOR THE ABOVE DIFFERENCE METHODS

Example 1: We consider the parabolic differential problem

$$\frac{\partial u}{\partial t} - \frac{\partial^2 u}{\partial x^2} = 0, \quad 0 < x < 1, \quad t > 0$$

$$u(0,t) = u(1,t) = 0, \quad t > 0;$$

$$u(x,0) = \sin \pi x, \quad 0 \leq x \leq 1$$

It can be verified that the function  $u(x,t) = e^{-\pi^2 t} \sin \pi x$  is the theoretical solution of the problem. First, we will find the approximate solution of the problem using the forward difference method with:

$$\begin{array}{ll} \text{a) } h = 0.1, \quad k = 0.0005, \quad T = 0.5 \quad (\lambda = 0.05) & \text{b) } h = 0.05; \quad k = 0.0005; \\ T = 0.5; \quad (\lambda = 0.2) & \end{array}$$

c)  $h = 0.1$ ,  $k = 0.01$ ,  $T = 0.5$  ( $\lambda = 1$ ).

Executing code in Matlab for the three cases a), b), and c) above yielded the following results:

Table 1. Forward difference method for the three cases a), b), and c)

$h=0.1, k=0.0005$	$h=0.05, k=0.0005$	$h=0.1, k=0.01$
U      u U-u	U      u U-u	U      u      U- u
0.0023   0.0022   - 0.0001	0.0022   0.0022   0.0000	2.0e+06*
0.0043   0.0042   - 0.0001	0.0042   0.0042   0.0000	-0.5420   0.0000 0.5420
0.0060   0.0058   - 0.0002	0.0058   0.0058   0.0000	2.0337   0.0000   - 2.0337
0.0070   0.0068   - 0.0002	0.0068   0.0068   0.0000	-2.4287   0.0000 2.4287
0.0074   0.0072   - 0.0002	0.0068   0.0068   0.0000	2.6884   0.0000   - 2.6884
0.0070   0.0068   - 0.0002	0.0058   0.0058   0.0000	-2.7857   0.0000 2.7857
0.0060   0.0058   - 0.0002	0.0042   0.0042   0.0000	2.7081   0.0000   - 2.7081
0.0043   0.0042   - 0.0001	0.0022   0.0022 0.0000	-2.4606   0.0000 2.4606
0.0023   0.0022   - 0.0001		2.0655   0.0000   - 2.0655
		-0.5617   0.0000 0.5617
<b>a)   <math>\lambda = 0.05</math></b>	<b>b)   <math>\lambda = 0.2</math></b>	<b>c)   <math>\lambda = 1</math></b>

From Table 1, the increased accuracy when moving from step  $h=0.1$  to step  $h=0.05$  is clearly evident. Meanwhile, the calculation in case c) fails because ( $\lambda=1$ ) and the forward difference method becomes unstable. We repeat the solution of Example 1 in case c) using the backward difference method.

Table 2. Backward and forward difference methods for case c)

h=0.1, k=0.001			h=0.1, k=0.01		
U	u	U-u	U	u	U-u
			2.0e+06 *		
0.0023	0.0022	-0.0001	-0.5420	0.0000	0.5420
0.0045	0.0042	-0.0002	2.0337	0.0000	-2.0337
0.0061	0.0058	-0.0003	-2.4287	0.0000	2.4287
0.0072	0.0068	-0.0004	2.6884	0.0000	-2.6884
0.0076	0.0072	-0.0004	-2.7857	0.0000	2.7857
0.0072	0.0068	-0.0004	2.7081	0.0000	-2.7081
0.0061	0.0058	-0.0003	-2.4606	0.0000	2.4606
0.0045	0.0042	-0.0002	2.0655	0.0000	-2.0655
0.0023	0.0022	-0.0001	-0.5617	0.0000	0.5617
c) $\lambda = 1$			c) $\lambda = 1$		

The failed computation of the forward difference method for case c) becomes successful using the backward difference method.

It can be observed that the Richardson method has not been presented in its matrix form. In fact, the attempt to do this seems difficult. But in fact, it is not necessary to find the matrix form of the Richardson method. As a combination (average) of the forward and backward difference methods, its result and code can be obtained easily, without requiring the matrix form of Richardson.

The corresponding results of the Richardson and Crank-Nicolson method codes are presented in Table 3 below, where it can be seen that the results of the Richardson method code are absurd.

Table 3: Richardson method and Crank-Nicolson method.

h=0.05, k=0.01			h=0.05, k=0.01		
u	U	U-u	u	U	U-u
2.0e+26 *					
0.6931	0.0000	-0.6931	0.0011	0.0011	-0.0000
-2.4367	0.0000	2.4367	0.0022	0.0022	-0.0000
2.2651	0.0000	-2.2651	0.0033	0.0033	-0.0000
-2.1826	0.0000	2.1826	0.0043	0.0042	-0.0000
4.1563	0.0000	-4.1563	0.0051	0.0051	-0.0000
-5.1152	0.0000	5.1152	0.0059	0.0058	-0.0000
5.9589	0.0000	-5.9589	0.0064	0.0064	-0.0000
-6.5738	0.0000	6.5738	0.0069	0.0068	-0.0000
6.8559	0.0000	-6.8559	0.0071	0.0071	-0.0000
-6.7343	0.0000	6.7343	0.0072	0.0072	-0.0000
6.1918	0.0000	-6.1918	0.0071	0.0071	-0.0000
-5.2768	0.0000	5.2768	0.0069	0.0068	-0.0000
4.1013	0.0000	-4.1013	0.0064	0.0064	-0.0000
-2.8241	0.0000	2.8241	0.0059	0.0058	-0.0000
2.6221	0.0000	-2.6221	0.0051	0.0051	-0.0000
-0.6532	0.0000	0.6532	0.0043	0.0042	-0.0000
0.0217	0.0000	-0.0217	0.0033	0.0033	-0.0000
0.2460	0.0000	-0.2460	0.0022	0.0022	-0.0000
-0.2094	0.0000	0.2094	0.0011	0.0011	-0.0000
$\lambda = 4$			$\lambda = 4$		



## CONCLUSIONS

Many applied mathematics problems lead to solving ordinary differential equations with boundary conditions or even partial differential equations. Since exact solutions of these equations are difficult or almost impossible to obtain, finding approximate methods for these equations provides significant ease.

The numerical solution of differential problems involves various difficulties, such as challenges during algebraic procedures or problems related to discretizing the integration domain. Another issue is the stability and convergence of the numerical method used. Finite difference methods have better characteristics and are stable, but generally require more effort and mental resources for their practical implementation. The Crank–Nicolson method is accurate and unconditionally stable for solving parabolic partial differential equations.

## REFERENCES

- [1] Fausett L.: Applied Numerical Analysis Using Matlab, Prentice Hall, New Jersey, (1999; 596 pages).
- [2] Smith, G.D.: Numerical solution of partial differential equations, Oxford, (1983).
- [3] Smith, G.D.: Numerical solution of partial differential equations, Oxford, (1983).
- [4] <https://www.researchgate.net/publication/326476591>
- [5] SIGMON K., DAVIS T.: Matlab Primer, Sixth edition, CRC Press LLC – USA, (2002; 162 pages).
- [6] Burden, R.L. and Faires, J.D. and Reynolds, A.C. (2007). Numerical Analysis. Prindle, Weber & Schmidt, Massachusetts 0211.
- [7] Golub.G.H, Ortega.J.M, Scientific Computing and Diferential Equation, Standford Califonia, USA(1992,337 pages).



# **Electrical Conductivity Measurement System Design with Logarithmic Amplifier Based Electrometer and Modbus Featured Temperature Controller**

**Tayyar GÜNGÖR<sup>1</sup>**

1-Prof. Dr.; Burdur Mehmet Akif Ersoy University Energy Systems Engineering Department.  
tgungor@mehmetakif.edu.tr ORCID No: 0000-0003-2518-9535

## ABSTRACT

In this study, an electrical conductivity measurement system was developed using a logarithmic amplifier (LOG-114) designed for low-current measurements, a microcontroller (Arduino UNO), a 16-bit analog-to-digital converter (ADS1115), and a temperature controller (Elimko E72P) operating via the MODBUS communication protocol. The ADS1115 ADC, capable of reading both positive and negative voltage values with 16-bit resolution, was used to measure the output voltage from the LOG-114, covering a wide current range spanning approximately 7.5 orders of magnitude (from 100 pA to 10 mA). Corresponding current values were then calculated using the appropriate transfer function. A LabVIEW program was integrated with the temperature controller and the microcontroller to enable synchronized operation, providing both precise temperature control and real-time data acquisition. The designed system allows for the monitoring of current variation with temperature or equivalently, conductivity change with temperature by considering film thickness and electrode geometry. Moreover, the setup can be employed to measure wavelength-dependent photoconductivity at a given temperature and/or time-dependent currents at fixed temperature conditions.

*Keywords –Electrometer, Logarithmic Amplifier, Electrical Conductivity, Arduino Uno, MODBUS.*

---

## INTRODUCTION

In semiconductor device technology, material production is fundamentally essential, but characterizing its physical properties is equally important. Perhaps the most significant of these properties is the variation in electrical conductivity with temperature. To analyze this, the current passing through the sample must be measured as a function of temperature. The measurement system consists of three main components: a heating unit that allows the sample temperature to be varied by applying current, a voltage source that provides a constant voltage to the sample, and a suitable ammeter to measure the current passing through the sample. The voltage sources used to apply an electric field to the sample are generally analog; however, modern models with computer communication capabilities are increasingly being used. To measure low currents passing through the sample, a device called an electrometer can be utilized. Unlike a conventional current meter, an electrometer can measure extremely low currents, typically in the picoampere (pA) to milliampere (mA) range (Rajput, 2002:3644, Rajput, 2003:3120, Chui, 2006:1501). Keithley introduced its first electrometer in 1951 for precision high resistance and low current measurements (Keithley).

In earlier years, current-to-voltage converters built using operational amplifiers were commonly used. Later, highly advanced and expensive commercial electrometers with computer communication capabilities (e.g., GPIB, Serial, USB) became available. As the temperature increases, the current passing through the sample can change by several orders of magnitude. Logarithmic amplifiers can be employed to measure such large variations in current. These amplifiers can be designed using operational amplifiers (OP-AMPs) and transistors.

A sensitive logarithmic amplifier is used to measure the electric current flowing from the tip through the sample for Atomic Force Microscope (Kuntze, 2005:71, Aguilera, 2017:342). However, due to the components and connections involved in these designs, increased reading errors may occur. To address this, specialized single-chip logarithmic amplifiers have been developed, such as the LOG-112 and LOG-114 (LOG-112, LOG-114). A study in the literature describes an electrometer design incorporating the LOG-112 logarithmic amplifier integrated circuit and the C8051F006 microcontroller (Khairurrijal, 2007:3019). The LOG-112 operates with an error of 0.2% over approximately five orders of magnitude. In contrast, the LOG-114, which offers more advanced features than the LOG-112, can achieve an accuracy of 0.1% over a range of 100 pA to 10 mA, spanning 7.5 orders of magnitude. Logarithmic amplifiers can provide either positive or negative output voltages, depending on the input current value. Normally, an analog-to-digital converter (ADC) can read positive voltage values, but using a special ADC called ADS1115 with high resolution (16 bits) that can communicate with the I2C protocol, both negative and positive voltage values can be read. For this, the ADC must be used with a microcontroller.

One of the most important components of an electrical characterization system is the unit responsible for controlling the sample temperature. This sample holder unit is heated using either a cartridge heater or a resistance wire to adjust the sample's temperature. The semiconductor material, with electrical contacts mounted on the sample, is cooled or heated under vacuum inside a chamber known as a cryostat, allowing its temperature to be modified. The temperature range can vary depending on the electrical behavior of the sample. For instance, temperatures as low as a few kelvins can be achieved using liquid helium, while liquid nitrogen can be used to maintain temperatures between 77 K and room temperature. Special diodes serve as temperature sensors in extremely low-temperature ranges, whereas thermocouples are commonly used for liquid nitrogen temperatures, room temperature, and higher temperature ranges. This enables real-time monitoring of the sample temperature.

Various temperature controllers are available to regulate the sample temperature. These controllers operate using different techniques, such as simple on/off control or more advanced methods that consider three

fundamental coefficients: proportional (P), integral (I), and derivative (D), commonly known as PID control. Some controllers also utilize binary combinations of these coefficients for more precise temperature regulation. In addition to basic temperature control systems, where the user manually sets the target temperature and monitors the process temperature on a display, more advanced temperature controllers exist. These advanced controllers can communicate with a computer, allowing both the set temperature and read process temperature to be adjusted and analyzed automatically through interface software. Controllers capable of communication via GPIB, TCP, or serial protocols tend to be quite expensive. However, an alternative is using controllers that support the Modbus protocol, which enables bidirectional communication for both retrieving real-time temperature data and adjusting the set temperature.

In this study, considering the aforementioned points, an electrometer was designed to measure low currents. The design includes a logarithmic amplifier (LOG-114) with improved performance, a microcontroller (Arduino UNO), and a 16-bit resolution ADC. This electrometer was integrated with a temperature controller (Elimko E72P) supporting the Modbus protocol and a graphical programming language (LabVIEW) to obtain real-time temperature data from the sample. Additionally, the set temperature could be sent to the controller as a variable. Thus, an economical electrical conductivity measurement system different from previous study (Güngör, 2023:163) was developed and tested for analyzing current variations under a desired temperature profile in thin films or bulk materials, particularly semiconductor materials.

## **MATERIALS AND METHODS**

### ***Modbus Protocol***

Modbus (Endustriyel) is one of the oldest serial communication protocols used to facilitate communication between different devices in industrial environments. It was developed by Modicon in 1979 for programmable logic controllers (PLCs). In the early years of industrial automation, Modbus was a preferred protocol because it required minimal hardware resources (RAM, ROM) and had simple implementation requirements. However, it has evolved alongside advancements in microprocessor technology, adapting to modern communication needs. Modbus enables communication between smart devices and sensors. This is achieved by sending a request message to a remote terminal unit (RTU),

which responds based on the master/slave principle. If the communication is broadcast-type, the connected device does not send a response. Modbus communication requires only a two-wire connection, and data from sensors can be safely read and recorded in real-time using appropriate software. This is accomplished through fast and cyclic redundancy check (CRC) error detection.

Within a Modbus network, a master can control up to 247 devices, each identified by a unique address ranging from 1 to 247. RS-232 or RS-485 protocols are used for Modbus ASCII and Modbus RTU communication, while a standard internet connection is used for Modbus TCP/IP. RS-232 and RS-485 define the physical layer for serial communication, whereas Modbus itself is a protocol that establishes the format and rules for data exchange between devices. With specialized software capable of reading and analyzing Modbus data, real-time logging can be performed. Additionally, Modbus data can be visualized and analyzed, enabling efficient monitoring and decision-making based on recorded information.

### ***Temperature Controller (E72P)***

The E72P, a temperature controller developed by Elimko, operates with a 220V AC input voltage. It is equipped with a K-type thermocouple input for temperature sensing, with alternative options available for platinum resistance thermometers and other thermocouple sensors, selectable via the controller. The device provides a 0–10V analog output and includes an RS485 Modbus RTU Slave interface with integrated PID control functions.

For register operations, the following Modbus function codes are employed: 03 for reading registers, 05 for writing a single coil, 06 for writing a single register, and 16 for writing multiple registers. The temperature setpoint can be adjusted via register address 12 (read/write), while the process value is accessible at register address 2. Using these set and measured values, the setpoint can be modified in defined increments.

Communication with the device is established through a USB-to-RS485 converter, in combination with a Modbus library integrated into a LabVIEW environment. The corresponding LabVIEW program developed for the Elimko E72P controller is presented in Figure 1. In Figure 1-a, the controller is configured in RTU mode, with a serial communication speed of 38,400 bps, even parity, and no flow control. During the transmission of the temperature setpoint, the value is multiplied by a factor of ten prior to being sent to the recorder (Figure 1-b). Conversely, the measured value is divided by ten in order to obtain the actual temperature (Figure 1-c).

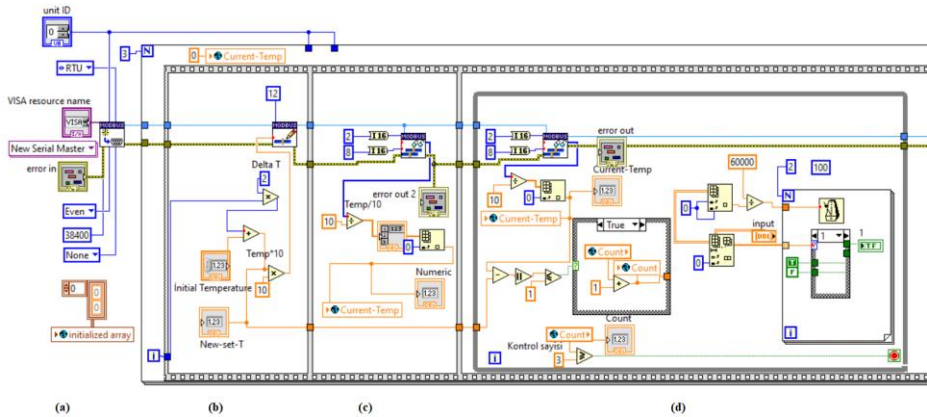


Figure 1: Labview program for use with Elimko 72P model temperature controller with Modbus protocol

System stability at the set temperature is defined as the condition in which the absolute deviation between the instantaneous process temperature and the setpoint remains below a predefined threshold for a specified number of consecutive measurements. When this condition is satisfied, the counter variable *count* is incremented; otherwise, the counter is reset, and the temperature monitoring process continues. The logic module responsible for this operation is depicted in Figure 1-d. Upon reaching the predetermined counter threshold, the system proceeds to the next step, which consists of measuring the current passing through the sample.

### ***Logarithmic Amplifier (LOG-114)***

Logarithmic amplifier circuits can be designed using diodes, single transistors, or paired transistors. The number of external components used in such designs, as well as their temperature compensation, significantly impact amplifier performance. Therefore, using integrated single-chip amplifiers such as the LOG-112 or LOG-114 provides a more stable output voltage. The LOG-114 (Figure 2-a), an improved version of the LOG-112, features an increased upper current limit of 10 mA and includes two independent operational amplifiers, making it suitable for various applications. For a reference voltage of 2.5 V and a reference current of 1  $\mu$ A, the LOG-114 provides excellent linear output between 100 pA and 1 mA (Figure 2-b).



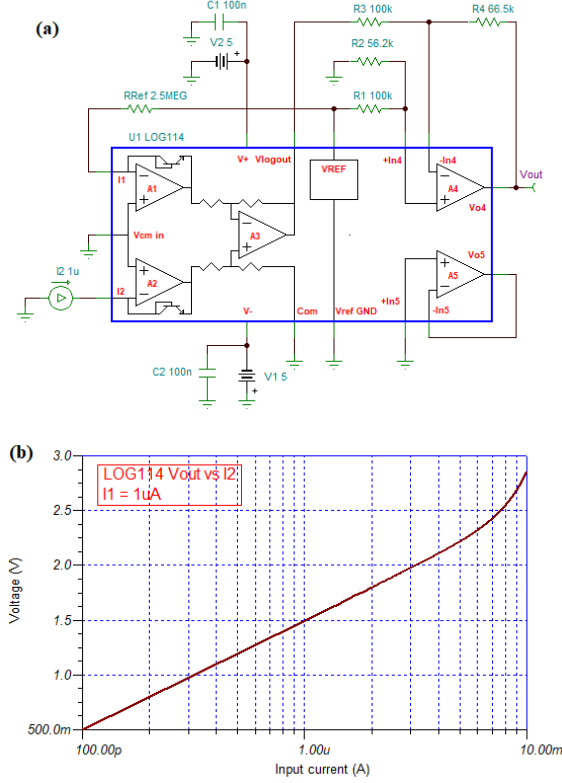


Figure 2: a) The configuration of LOG-114 to use low currents, b) Output voltage depending on the input current for 2.5 V reference voltage and 1 μA reference current value [9]

The LOG-114 features two transfer functions for the current to be measured such as  $V_{out}=V_{04}=-0.249 \log(I_1/I_2) + 1.5 \text{ V}$  or  $V_{logout}=0.375 \log(I_1/I_2)$ . Depending on the current, these voltage values can be either negative or positive (ranging from -4.4 V to 4.4 V). Since analog-to-digital converters (ADCs) are generally designed for positive input voltages, modifications may be required to accommodate negative voltage measurements. Typically, this adjustment can be made by adding an operational amplifier and summing circuit to the system, or by applying an offset voltage to the LOG-114 terminal indicated by  $V_{com}$ . In this case, the output voltage value is calculated using Eq. (1):

$$V_{logout}=0.375\log(I_1/I_2)+V_{com} \quad (1)$$

where,  $I_2$  current value is calculated using the reference  $I_1$  value, the measured  $V_0$  voltage value and Eq. (1).

Before starting the electrometer design, the LOG-114 integrated circuit in the QFN16 structure with 16 pins and 0.65 mm pitch was first converted to the dip3 case with the QFN16-dip3 converter printed circuit board. The electrometer and its components, designed using the LOG-114 and Arduino Uno, are shown in Figure 3. Figure 3-a displays the power supply stage with the symmetrical sources required for the operation of the LOG-114, while Figure 3-b presents the LOG-114 logarithmic amplifier circuit. Figure 3-c shows the Arduino UNO, Figure 3-d illustrates the 16-bit resolution ADS1115 ADC, and Figure 3-e displays the 2x16 I2C LCD screen used to monitor the output voltage of the logarithmic amplifier. The Arduino UNO's 10-bit ADC, which can only measure positive voltages, is insufficient for capturing the output voltage proportional to the current from the LOG-114, especially considering that LOG-114 is used to measure low currents and can produce negative voltages depending on the input current. Therefore, an ADC with higher resolution and the capability to read negative voltages was required. For this reason, the ADS1115 was chosen. It features a 4-channel gain adjustment and can sample 860 times per second through an I2C-compatible serial interface.

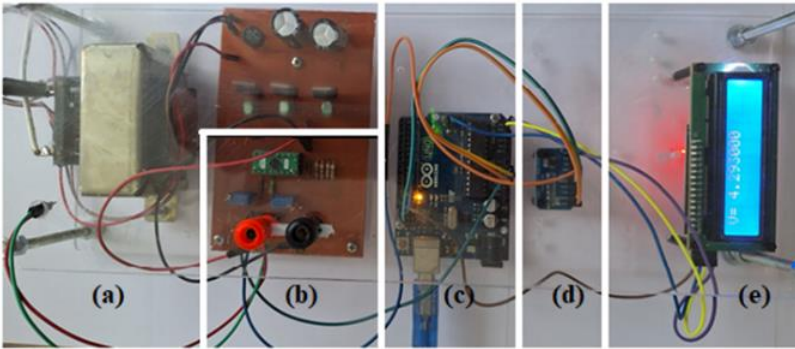


Figure 3: Electrometer and its components designed with LOG114 and Arduino Uno: a) Power supply stage, b) LOG-114 integrated circuit, c) Arduino UNO, d) 16 Bit ADC and e) 2x16 I2C LCD screen.

The program for ADS1115 given in Figure 4 was uploaded to Arduino UNO so that the LOG-114 output voltage values associated with the current values passing through the sample can be sent via the serial port.

```

#include <Adafruit_ADS1X15.h>
Adafruit_ADS1115 ads;
int16_t readings[50]; float total;
void setup(void)
{ Serial.begin(9600); if (!ads.begin()){
Serial.println("Failed to initialize ADS.");
while (1); } }
void loop(void)
{ total=0;
int16_t adc0;float volts0;
for (int i=0;i<50;i++)
{ adc0=ads.readADC_SingleEnded(0);
total=total+ ads.computeVolts(adc0); }
volts0=total/numReadings;
Serial.println(volts0); delay(1000);
}

```

Figure 4: Program uploaded to Arduino Uno to read voltage with ADS1115

Then, the LabVIEW program (Figure 5) was used to read data from the specified serial port, with a serial communication baud rate of 9600 bits per second. Depending on the resistance of the semiconductor sample, the LOG-114 output voltage may be either positive or negative. Therefore, the default gain setting of the ADS1115's PGA (Programmable Gain Amplifier) was used with a multiplier of 2/3. In this configuration, the ADC operates within a range of  $\pm 6.144$  V, and each step corresponds to 0.1875 mV (calculated as  $2 \times 6.144 / 65536$ ). In other words, each ADC value is multiplied by 0.1875 mV to recalculate the LOG-114 output voltage. Thus, the logarithmic output voltage corresponding to the current passing through the sample—that is, the voltage value from the ADS1115 ADC—is read via the USB port through the Arduino UNO.

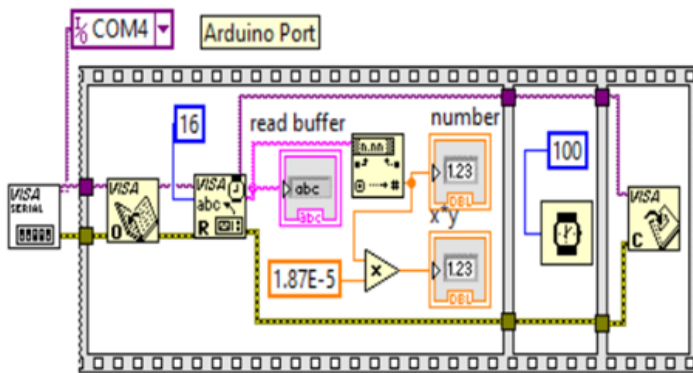


Figure 5: Labview program that transfers the voltage value read by ADS1115 to the computer via serial port

Temperature-controlled cryostat and auxiliary devices are shown in Figure 6. A  $25\ \Omega$  heater, connected to the sample holder, and a K-type thermocouple, used for temperature control, are mounted inside the cryostat. A voltage-controlled current source—capable of delivering a current in the range of 0–2 A with a 0–10 V input—is designed to adjust the sample temperature. This current source can be selectively configured to operate in a 0–0.5 A mode for low power and a 0–2 A mode for high power, thereby reducing temperature fluctuations in the sample holder system.

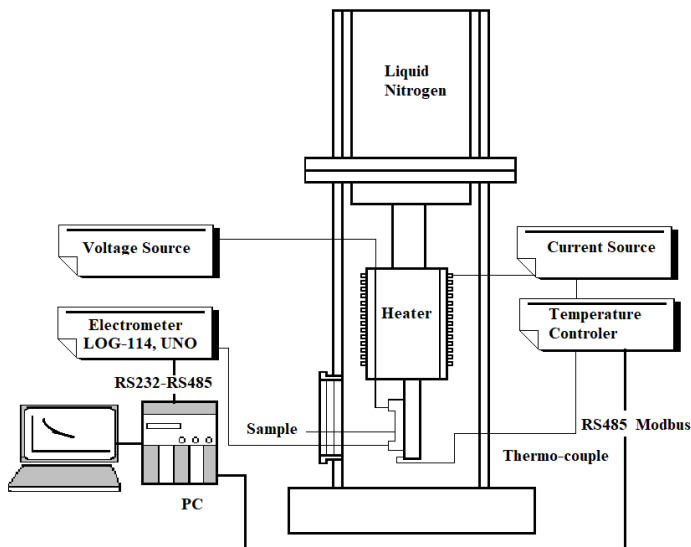


Figure 6: Temperature dependent electrical characterization system and its auxiliary components

The 0–10 V PWM output signal from the temperature controller, which communicates via the Modbus protocol, is directly connected to this current source. When desired, the sample holder's temperature can be reduced to 130 K using liquid nitrogen, facilitated by a specialized 250 mL capacity chamber attached to the cryostat. This chamber is connected to the sample holder via a cold-finger arrangement. Additionally, the cryostat is linked to a vacuum pump and auxiliary electronic devices using dedicated connection elements.

## RESULTS AND DISCUSSION

The current through the 100 k $\Omega$  load resistor was measured with the designed electrometer. The relative error between the current values measured by the commercial electrometer (Keithley 6487 Electrometer) and the designed electrometer is around 2% for approximately six orders of magnitude (Güngör, 2023). At room temperature and higher, conduction in semiconductors generally arises from electrons transitioning from donor levels to the conduction band or from the valence band to acceptor levels. To measure conductivity ( $\sigma$ ) or resistivity ( $\rho = 1/\sigma$ ), parameters such as sample thickness and surface area must be known. Typically, electrical contacts are formed by evaporating metal onto the sample in a specific geometry. For the region between the contacts, a geometric factor ( $GF = l/wt$ ) is defined, considering by the electrode length ( $l$ ), sample thickness ( $t$ ), and electrode width ( $w$ ). In this case, conductivity can be calculated using the formula  $\sigma = GF \cdot (I/V)$ . Assuming that the applied voltage and GF are constant, conductivity is proportional to the current ( $I$ ) flowing through the semiconductor. Depending on the applied voltage, the current flowing through the sample is usually in the order of nA,  $\mu$ A, or even mA. Moreover, it can vary significantly over the measured temperature range. These variations provide insights into the conduction mechanisms. In this case, the relationship between the current ( $I$ ) flowing through the sample and the temperature ( $T$ ) can be expressed as follows:

$$I(T) = I_0 \exp(-E_a/kT) \quad (2)$$

here,  $I_0$  is a pre-exponential factor,  $E_a$  is the activation energy,  $k$  is the Boltzmann constant, and  $T$  is the absolute temperature in Kelvin.

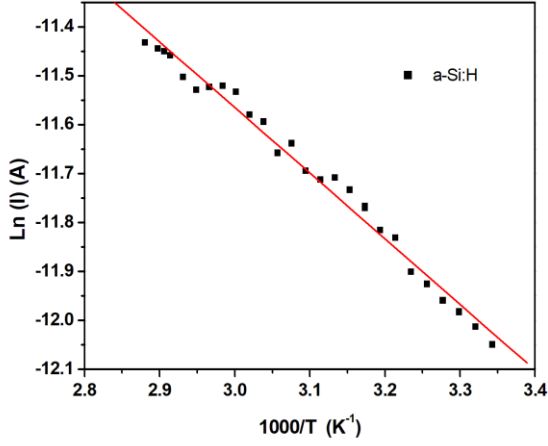


Figure 7:  $\ln(I) - 1000/T$  plot for a-Si:H sample

Using the system shown in Figure 6 and the designed logarithmic amplifier-based electrometer, the current through a test sample of hydrogenated amorphous silicon (a-Si:H) was measured in 2 K temperature steps. Considering the thickness of the a-Si:H film ( $t = 1079$  nm), the electrode width ( $l = 100$   $\mu\text{m}$ ), and the electrode length ( $w = 10$  mm), the GF was calculated as  $92.6$   $\text{cm}^{-1}$ . For the temperature-dependent change of the dark current (Figure 7), the Arrhenius equation given in Eq. (2) was used, and from the  $(\ln(I) - 1000/T)$  plot, the activation energy  $E_a$  was calculated as 115 meV. Accordingly, dark conductivity measurements show a single activation energy behavior up to room temperature (Figure 7). Similar values have been reported in the literature (Güngör, 2001). This activation energy may vary depending on the preparation technique of the a-Si:H sample and the parameters used in those techniques.

## CONCLUSION

In summary, a cost-effective alternative to commercial temperature control and current measurement systems has been developed. By integrating a voltage-controlled current source, a Modbus-based temperature controller, and the LOG-114 logarithmic amplifier, the system provides reliable dark and photocurrent measurements under both continuous and

pulsed illumination. Its flexibility and low cost make it a valuable tool for semiconductor and optoelectronic research.

## REFERENCE

- Aguilera, Lidia, and Joan Grifoll-Soriano. Design and Fabrication of a Logarithmic Amplifier for Scanning Probe Microscopes to Allow Wide-Range Current Measurements, In *Conductive Atomic Force Microscopy*, 243–62. Weinheim, Germany: Wiley-VCH Verlag GmbH & Co. KGaA, 2017. DOI:10.1002/9783527699773.ch11
- Chui, C.O., Ito, F., Saraswat, K.C. (2006). Nanoscale germanium MOS dielectrics: Part I. Germanium oxynitrides. *IEEE Transactions. Electron. Devices*, Vol. 53(7), p. 1501–1508. DOI: 10.1109/TED.2006.875808
- Endustriyel, <https://www.3eendustriyel.com.tr/BlogModbus> (Access Date: 04.03.2025)
- Evangelou, E.K., Mavrou, G., Dimoulas, A., Konofaos, N. (2007). Rare earth oxides as high-k dielectrics for Ge based MOS devices: An electrical study of Pt/Gd2O3/Ge capacitors. *Solid-State Electronics*, Vol. 51(1), p.164-169. DOI: 0.1016/j.sse.2006.10.011
- Güngör, T. (2001). Comparison of Experimental Methods\_ Used for Determination of Optical Constants of Hydrogenated Amorphous Silicon, PhD, Hacettepe University, Ankara, Turkey
- Güngör, T., Kılıçaslan, A., Güngör, E. (2023). Arduino-Based Electrometer Design and Metal Oxide Semiconductor, *The Journal of Graduate School of Natural and Applied Sciences of Mehmet Akif Ersoy University*, Vol. 14(1), p. 163-170. DOI: 10.29048/makufebd.1266216
- Keithley, <https://www.tek.com/en/products/keithley/low-level-sensitive-and-specialty-instruments> (Access Date: 04.03.2025)
- Khairurrijal, M.A., Suhendi, A., Munir, M.M., Surachman, A. (2007). A simple microcontroller-based current electrometer made from LOG112 and C8051F006 for measuring current in metal-oxide-semiconductor devices. *Measurement Science and Technology*, Vol.18 (9), 3019-3024.
- Kuntze, S. B., Ban, D., Sargent, E. H., Dixon-Warren, S. J., White, J. K., & Hinzer, K. (2005). Electrical Scanning Probe Microscopy: Investigating the Inner Workings of Electronic and Optoelectronic Devices. *Critical Reviews in Solid State and Materials Sciences*, Vol. 30(2), 71–124. doi:10.1080/10408430590952523
- LOG-112, <https://www.ti.com/lit/ds/symlink/log2112.pdf> (Access Date: 04.03.2025)
- LOG-114, <https://www.ti.com/product/LOG114> (Access Date: 04.03.2025)
- Rajput, S.S., and Jamuar, S.S. (2002). Low voltage, low power, high performance type II current conveyor-based linear current electrometers, *Review of Scientific Instruments*, Vol.73 (10), p. 3644-3651. DOI: 10.1063/1.1505095

Rajput, S.S. (2003). An improved multigain range linear current electrometer, *Review of Scientific Instruments*, Vol. 74(6), p.3120-3126. DOI: 10.1063/1.1573743





# **A Study on a Special Curve via Conformable Fractional Derivative**

**Burçin SALTİK BAEK<sup>1</sup>**

- 1- Res. Asst. Gör.; Erciyes Üniversitesi Fen Fakültesi Matematik Bölümü. [burcinsaltik@erciyes.edu.tr](mailto:burcinsaltik@erciyes.edu.tr)  
ORCID No: 0000-0001-5174-6484

## ABSTRACT

This study examines the behavior of curves in 3D Euclidean space using conformable fractional derivatives, comparing their properties with those from standard differentiation. It focuses on adjoint curve, which undergo significant changes when viewed through fractional derivatives. In the paper, it is given the definition of a conformable adjoint curve of the curve. The construction of the conformable adjoint curve and the connections between curvatures and Frenet frame vectors are shown in this paper. It also examines the Darboux vector and the circumstances in which the adjoint curve forms a general helix. Through theoretical analysis and graphical representations, the new method provides a thorough illustration of the conformable adjoint curve and illustrates how fractional derivatives affect its shape.

*Keywords – Conformable Fractional Derivatives, Adjoint Curve, Darboux Vector.*

---

## INTRODUCTION

Gottfried Wilhelm Leibniz initially proposed fractional calculus in 1695. It is a field of mathematics that examines integrals and derivatives of any order. It is used to model physical phenomena and was created by mathematicians like as Riemann, Abel, and Liouville.

Khalil et al. (2014:264) offered a present definition different from the previously used Riemann-Liouville and Caputo fractional derivatives. This idea is closer to the concept of classical derivatives and provides a more sensitive approach to the discontinuities of functions. Abdeljawad (2015:279) explored a new approach known as "conformable fractional calculus" and examined the mathematical properties and advantages of the concept of conformable derivatives. The conformable derivative, a simpler base for fractional differentiation, preserves key characteristics of classical derivatives, making it easier to solve differential equations and describe dynamic systems. Its applications include kinematics, computer-aided design, and physical simulations. Yajima et al. (2018:1493) explored the geometric properties of Frenet-Serret formulas of a curve. Gözütok et al.(2019) were the first to redefine the Frenet frame using conformable derivatives. In this study, the classical Frenet-Serret formulas were expanded within the framework of conformable derivatives, and the tangent, normal, and binormal vectors of curves were redefined using conformable derivatives. Has and Yılmaz (2022:132) investigated the effects of conformable derivatives on curves in Euclidean 3-space and revealed new and important results. In this study, fundamental differential properties such as curvature and torsion of curves were examined using conformable derivatives. By applying conformable derivatives to curves studied with

classical differential geometry (such as helices and Bertrand curves), the dynamic properties of these curves were addressed. Aydın and Kaya (2023:67) explored fractional equiaffine curvatures of curves in 3-D affine space, extending the concepts of classical affine geometry within the framework of fractional calculus, and examined how curves could be analyzed using this new geometric structure. Apart from these, there are also studies on fractional calculus in various fields. For detailed information, relevant reference can be examined to see how fractional derivatives affect disciplines such as biology, engineering and physics (Boulaaras, 2022:2347).

Adjoint curve holds a significant place in the study of differential and algebraic geometry. The concept of adjoint curve has been extended to various contexts, including Euclidean and Minkowski spaces. These curves are defined in relation to a given curve, provide information about the geometric and algebraic characteristics of a particular curve. Recently, conformable derivatives have been used to expand the idea of adjoint curve into the field of fractional calculus (Nurkan et. al, 2019:155, Arıkan and Nurkan, 2020:54, Yüksel et. al., 2017:203, Yüksel and Saltık, 2023:11132).

This paper aims to define and analyze adjoint curve according to conformable fractional derivatives. We suggest a new formulation for conformable adjoint curves by adding fractional scaling effects to the curve's binormal vector. The proposed method bridges the gap between classical differential geometry and fractional calculus, providing a unified framework for fractional geometric analysis.

According to the classical adjoint curve, the integral of the binormal vector defines the position of the adjoint curve in space. In conformable derivatives  $t^\alpha$  factor represents the fractional effect of the conformable derivative. Depending on the fractional parameter of the curve ( $\alpha$ ), this can change the structure of the adjoint curve in space, offer a new geometry. In the last part, we showed this analysis on a graph.

## **METARIALS AND METHODS**

In this section, some fundamental definitions and theorems of the conformable fractional derivative and integral are provided.

**Definition 1.** (Khalil et al., 2014:264) Let  $f: [0, \infty) \rightarrow \mathbb{R}$  be a function.

Then the conformable fractional derivative for  $f$  of order  $\alpha$ , for each  $t > 0, 0 < \alpha < 1$ , is defined by

$$D_\alpha(f)(t) = \lim_{\epsilon \rightarrow 0} \frac{f(t + \epsilon t^{1-\alpha}) - f(t)}{\epsilon}.$$

If  $f$  is  $\alpha$ -differentiable in some  $(0, \alpha)$ ,  $\alpha > 0$  and  $\lim_{t \rightarrow 0^+} f^{(\alpha)}(t)$  exists, then  $f^{(\alpha)}(0) = \lim_{t \rightarrow 0^+} f^{(\alpha)}(t)$  occurred.

**Theorem 2.** (Khalil et al., 2014:264) Let  $f: [0, \infty) \rightarrow \mathbb{R}$  be a function  $\alpha$ -differentiable at  $t_0 > 0, 0 < \alpha < 1$ , then  $f$  is continuous at  $t_0$ .

Accordingly, it is readily apparent that the conformable fractional derivative offers each of the characteristics listed in the following theorem.

**Theorem 3.** (Khalil et al., 2014:264) Let  $t > 0, 0 < \alpha < 1$ , and let  $f, g$  be  $\alpha$ -differentiable. Below we have listed the properties of the conformable derivative

- For all  $k, m \in \mathbb{R}$ ,  $D_\alpha(kf + mg)(t) = kD_\alpha(f)(t) + mD_\alpha(g)(t)$
- For all  $k \in \mathbb{R}$ ,  $D_\alpha(t^k) = kt^{k-\alpha}$
- For all constant functions  $f(t) = \mu$ ,  $D_\alpha(\mu) = 0$
- $D_\alpha(fg)(t) = f(t)D_\alpha(g)(t) + g(t)D_\alpha(f)(t)$ .
- $D_\alpha\left(\frac{f}{g}\right)(t) = \frac{f(t)D_\alpha(g)(t) - g(t)D_\alpha(f)(t)}{g^2(t)}$ .
- If  $f$  is a differentiable function, then  $D_\alpha(f)(t) = t^{1-\alpha} \frac{df}{dt}$ .

**Theorem 4.** (Abdeljawad, 2015:279) Let  $f, g: [0, \infty) \rightarrow \mathbb{R}$  be  $\alpha$ -differentiable at  $t > 0, 0 < \alpha < 1$ . If  $f \circ g$  is  $\alpha$ -differentiable and for all  $t$  with  $t \neq 0$  and  $f(t) \neq 0$ , we have

$$D_\alpha(g \circ f)(t) = f(t)^{\alpha-1} D_\alpha(f)(t) D_\alpha(g)(f(t)).$$

**Definition 5.** (Abdeljawad, 2015:279) Let  $f: (0, \infty) \rightarrow \mathbb{R}$  be a function. The expression of a conformable fractional integral is given by

$$I_0^\alpha f(t) = \int_a^t \frac{f(x)}{x^{1-\alpha}} dx$$

where  $a > 0$ .

**Theorem 6.** (Abdeljawad, 2015:279) Let  $f: (0, \infty) \rightarrow \mathbb{R}$  be a function.

$$D_\alpha I_\alpha^\alpha f(t) = f(t), \text{ for } t \geq a.$$

**Definition 7.** (Gözütok et al., 2019) In Euclidean 3-space  $E^3$ , let

$x: I \subseteq \mathbb{R} \rightarrow E^3$  represent a unit speed curve. The curve  $x$  is referred to as a conformable fractional general helix, if, according to the conformable fractional derivative, its unit tangent

vector forms a fixed angle with any  $u$  fixed direction.

**Definition 8.** (Nurkan et. al, 2019:155) Let  $\alpha$  be a unit speed curve in  $E^3$

with non-zero torsion, and let  $\{T, N, B\}$  be its Frenet frame. According to ,

the adjoint curve of  $\alpha$  is given by

$$\beta(s) = \int_{s_0}^s B(u) du.$$

**Definition 9.** (Gözütok et al., 2019) Let  $x$  be a curve. The curve

$x: [0, \infty) \rightarrow \mathbb{R}^3$  is referred to as a conformable curve if it is  $\alpha$ -differentiable.

**Definition 10.** (Gözütok et al., 2019) Let  $x: [0, \infty) \rightarrow \mathbb{R}^3$  be a conformable curve in  $\mathbb{R}^3$ . Velocity vector of  $x$  is determined by

$$v(t) = \frac{\|D_\alpha(x)(t)\|}{t^{1-\alpha}}$$

for all  $t \in (0, \infty)$ . If  $v(t) = 1$  for all  $t \in (0, \infty)$ , it is said that  $x$  has unit speed.

**Definition 11.** (Has and Yılmaz, 2022:132) In Euclidean 3-space, let  $x = x(s)$  be a unit speed conformable curve, with  $s$  denoting the arc-length. Additionally, let  $t = \frac{D_\alpha(x)(s)}{s^{1-\alpha}}$  be its unit tangent vector,  $n = \frac{D_\alpha(t)(s)}{\|D_\alpha(t)(s)\|}$  be its principal normal vector, and  $b = t \times n$  be its binormal vector. The conformable Frenet frame of the curve  $x$  is the triple  $\{t, n, b\}$ . Then, the curve's conformable Frenet formula is given as follows:

$$\begin{pmatrix} D_\alpha(t)(s) \\ D_\alpha(n)(s) \\ D_\alpha(b)(s) \end{pmatrix} = \begin{pmatrix} 0 & \kappa_\alpha(s) & 0 \\ -\kappa_\alpha(s) & 0 & \tau_\alpha(s) \\ 0 & -\tau_\alpha(s) & 0 \end{pmatrix} \begin{pmatrix} (t)(s) \\ (n)(s) \\ (b)(s) \end{pmatrix} \quad (1)$$

where  $\kappa_\alpha(s) = \|D_\alpha(t)(s)\|$  and  $\tau_\alpha(s) = \langle D_\alpha(n)(s), b(s) \rangle$  are curvature and torsion of  $x$ , respectively.

**Corollary 12.** (Has and Yılmaz, 2022:132) The connection between  $\kappa, \tau$  of a regular unit speed conformable curve  $x$  and its conformable curvature  $\kappa^\alpha$  and torsion  $\tau^\alpha$  as exists  $\kappa^\alpha = s^{1-\alpha}\kappa, \tau^\alpha = s^{1-\alpha}\tau$ .

**Definition 13.** (Has and Yılmaz, 2022:132) A Fractional Bertrand curve is a regular conformable curve if there is a conformable curve  $y$  and a bijection  $\gamma$  such that the principal normal vectors of  $x(s)$  and  $y(s)$  match.

## RESULTS AND DISCUSSION

In defining the conformable adjoint curve of a curve, the choice of including  $t^{1-\alpha}$  as a divisor reflects a more precise adherence to the principles of conformable derivatives and their impact on geometry. Because conformable derivatives inherently introduce fractional scaling factors. For example, conformable curvature and torsion are scaled in Corollary (12).

By dividing  $b^\alpha(t)$  by  $t^{1-\alpha}$ , the adjoint curve explicitly reflects the inverse scaling behavior of conformable Frenet frame components. This ensures the geometry of the adjoint curve remains consistent with conformable fractional principles. The divisor  $t^{1-\alpha}$  emphasizes the fractional effects of conformable derivatives. As  $t$  increases, the fractional scaling diminishes the contribution of the binormal vector, creating tighter adjoint curves. This effect is aligned with the conformable framework, where fractional derivatives gradually reduce their influence at higher parameter values. Using  $t^{1-\alpha}$  as a divisor ensures that the integrand remains well-behaved for small values of  $t$  (provided  $a > 0$ ). In contrast, multiplication by  $t^{1-\alpha}$  may amplify the binormal vector excessively, leading to geometric distortions. The choice of division highlights the diminishing influence of the binormal vector as  $t$  increases, reflecting the fractional framework's gradual "memory loss" effect.

**Definition 14.** Let  $x: (0, \infty) \rightarrow E^3$  be a unit speed conformable curve in  $E^3$  with  $\tau^\alpha \neq 0$  and the conformable Frenet frame of the curve  $x$  be  $\{t^\alpha, n^\alpha, b^\alpha\}$ . The conformable adjoint curve of the curve  $x$  is defined as

$$\gamma^\alpha(s) = \int_a^s \frac{b^\alpha(t)}{t^{1-\alpha}} dt. \quad (2)$$

where  $a > 0, 0 < \alpha < 1$ .

**Theorem 15.** Let  $x(s)$  be a conformable curve with arc length parameter  $s$ , and let  $\gamma^\alpha(s)$  be the conformable adjoint curve of  $x(s)$ . The parameter  $s$  of  $x(s)$  is related to the arc length parameter  $\tilde{s}$  of  $\gamma^\alpha(s)$  by the following

relationship:  $\tilde{s} = \frac{s^\alpha - a^\alpha}{\alpha}$ , where  $a > 0, 0 < \alpha < 1$ . Thus, the parameter  $s$  is

not directly the arc length parameter of  $\gamma^\alpha(s)$ , but it is proportional to it through a fractional scaling factor.



*Proof.* Let the conformable adjoint curve of  $x$  be  $\gamma$ . If we take a  $\alpha$ -conformable fractional derivative of Eq. (2) with respect to parameter  $s$ , we have

$$D_\alpha \gamma^\alpha(s) = b^\alpha, \quad \| b^\alpha(s) \| = 1, \quad (3)$$

where  $b^\alpha$  is the conformable binormal vector. Hence the conformable speed of  $\gamma^\alpha$  is

$$v_\gamma(s) = \frac{\| D_\alpha \gamma^\alpha(s) \|}{s^{1-\alpha}}. \quad (4)$$

By calculating the arc-length parameter of the curve  $\gamma^\alpha(s)$ , we obtain

$$\tilde{s} = \int_a^s \frac{1}{u^{1-\alpha}} du. \quad (5)$$

If we solve Eq.(5), the proof is done.

**Theorem 16.** Let  $x$  be a unit speed conformable curve and  $\gamma$  be the conformable adjoint curve of  $x$ . If the conformable Frenet vectors of  $x$  and  $\gamma$  are  $t^\alpha, n^\alpha, b^\alpha$  and  $T^\alpha, N^\alpha, B^\alpha$ , respectively, then the following relations provide:

$$\begin{aligned} T^\alpha &= b^\alpha \\ N^\alpha &= -n^\alpha \\ B^\alpha &= t^\alpha \end{aligned} \quad (6)$$

**Theorem 17.** Let  $x$  be a unit speed conformable curve and  $\gamma$  be the conformable adjoint curve of  $x$ . The curvatures of the conformable curve  $\gamma$

with  $\alpha$  conformable fractional derivative are given as follow:

$$\kappa_{\gamma}^{\alpha} = \tau^{\alpha}, \quad \tau_{\gamma}^{\alpha} = \kappa^{\alpha} \quad (7)$$

where  $\kappa^{\alpha}, \tau^{\alpha}$  are the conformable curvatures of the curve  $x$ .

*Proof.* By  $\alpha$ -conformable fractional differentiating Eq. (3) with respect to parameter  $s$  and using Eq. (1), we get

$$D_{\alpha}(T^{\alpha})(s) = \tau^{\alpha}(s)n^{\alpha}(s). \quad (8)$$

If we take the norm of the Eq. (8) both sides, we have

$$\kappa_{\gamma}^{\alpha}(s) = \tau^{\alpha}(s).$$

From Eq. (6), we can find the following calculation simply;

$$D_{\alpha}(N^{\alpha})(s) = -D_{\alpha}(n^{\alpha})(s) \quad (9)$$

$$\kappa_{\alpha}^{\alpha}T^{\alpha} + \tau_{\gamma}^{\alpha}B^{\alpha} = -(-\kappa^{\alpha}(s)t^{\alpha}(s) + \tau^{\alpha}(s)b^{\alpha}(s))$$

where  $\kappa^{\alpha}, \tau^{\alpha}$  are curvatures and  $t^{\alpha}, b^{\alpha}$  are conformable tangent vector and binormal vector of the curve  $x$ . If Eq. (9) is applied scalar product by  $B^{\alpha}$  and using the definition of torsion, we get

$$\tau_{\gamma}^{\alpha} = \kappa^{\alpha}.$$

**Theorem 18.** Let  $x$  be a unit speed conformable curve with arc length parameter  $s$  and  $\gamma$  be the conformable adjoint curve of  $x$ . If the curve  $x$  is a general helix, then the conformable adjoint curve  $\gamma$  of the conformable curve  $x$  is a general helix.

*Proof.* Let  $x$  be a helix. Therefore,  $\frac{\tau^\alpha}{\kappa^\alpha} = \text{cons}$  such that  $\kappa^\alpha, \tau^\alpha$  are curvatures of the curve  $x$ . For the conformable adjoint curve  $\gamma$  of the conformable curve  $x$ , using Eq. (7), we have

$$\frac{\kappa_\gamma^\alpha}{\tau_\gamma^\alpha} = \frac{\tau^\alpha}{\kappa^\alpha} = \text{cons}.$$

So, the conformable adjoint curve  $\gamma$  of the conformable curve  $x$  is a general helix.

**Theorem 19.** Let  $x$  be a unit speed conformable curve with arc length  $s$  and  $\gamma$  be the conformable adjoint curve of  $x$ . The adjoint curve  $\gamma$  of the curve  $x$  and the curve  $x$  is Bertrand pair.

*Proof.* By Theorem (16), since the conformable principal normal vectors of the curves are same, they are conformable Bertrand-pair.

**Theorem 20.** If the curves  $x(s), \gamma(s)$  are Bertrand pair, then there are following relationship between curvatures  $\kappa^\alpha = s^{1-\alpha}\tau^\alpha$  where  $\kappa^\alpha, \tau^\alpha$  are the curvatures of the conformable curve  $x$ .

*Proof.*

$$\gamma^\alpha(s) = x(s) + \mu n^\alpha(s). \quad (10)$$

If we take  $\alpha$ -conformable derivative of Eq. (10), we get

$$D_\alpha \gamma^\alpha(s) = D_\alpha x(s) + (D_\alpha \mu) n^\alpha(s) + \mu D_\alpha n^\alpha(s) \quad (11)$$

If we arrange Eq. (11) we have

$$b^\alpha(s) = t^\alpha(s)(s^{1-\alpha} - \mu \kappa^\alpha) + \mu \tau^\alpha b^\alpha(s) \quad (12)$$

By this Eq. (12) we have

$$\mu = \frac{1}{\tau^\alpha} = \text{cons}, \quad \mu = \frac{s^{1-\alpha}}{\kappa^\alpha} \quad (13)$$

Rearrange Eq. (13) we get the result.

**Definition 21.** Let  $\chi$  be a unit speed conformable curve with arc length  $s$ .

The conformable Darboux vector of the curve  $\chi$  is defined by

$$W^\alpha = \tau^\alpha t^\alpha + \kappa^\alpha b^\alpha \quad (14)$$

where  $\kappa^\alpha, \tau^\alpha$  are the conformable curvatures of the curve  $\chi$ .

**Theorem 22.** The conformable Darboux vector  $W^\alpha$  of the conformable curve and the Darboux vector  $W$  of a curve have the following relationship:

$$W^\alpha = s^{1-\alpha} W$$

*Proof.* Using the definition of the Darboux vector, we have

$$W^\alpha = \tau^\alpha t^\alpha + \kappa^\alpha b^\alpha. \quad (15)$$

By Corollary (12), we get  $W^\alpha = s^{1-\alpha} W$ .

**Corollary 23.** Let  $\chi$  be a unit speed conformable curve with arc length  $s$  and  $\gamma$  be the conformable adjoint curve of  $\chi$ . If the Darboux vectors of  $\chi$  and  $\gamma$  are  $W_\chi$  and  $W_\gamma$ ; then  $W_\chi = W_\gamma$ .

*Proof.* By the Definition (21); we calculate the Darboux vector of  $W_\chi, W_\gamma$  as;

$$\begin{aligned} W_\chi &= \tau^\alpha t^\alpha + \kappa^\alpha b^\alpha \\ &= \kappa_\alpha^\alpha B^\alpha + \tau_\gamma^\alpha T^\alpha \\ &= W_\gamma \end{aligned}$$

According to Theorem (3), it is accurate to assert that whenever a function  $f$  is differentiable, the conformable derivative simplifies to

$D^\alpha f(t) = t^{1-\alpha} f'(t)$ . Therefore, for classical curves like the helix, the conformable Frenet frame aligns with the traditional one. The innovation of the conformable method emerges in the subsequent characterization of the

adjoint curve. The presence of the additional element  $u^{\alpha-1}$  in the integral

representation causes the conformable adjoint curve to depend on  $\alpha$ . This fractional scaling alters the global geometry of the adjoint, while the underlying Frenet frame remains constant. For example, in the instances of the circle or the helix, the classical adjoint increases linearly, but the

conformable adjoint demonstrates a slower development for  $0 < \alpha < 1$  and

logarithmic behavior as  $\alpha \rightarrow 0$ . These effects offer a new degree for modeling and illustrate the advantages of using conformable derivatives in the analysis of adjoint curves.

**Example 24.** Let  $x(t)$  be a helix such that  $a, b$  are constant and  $t$  is a parameter

$$x(t) = (a \cos t, a \sin t, bt),$$

We obtain the conformable derivative of the helix curve:

$$D^\alpha x(t) = t^{1-\alpha}(-a \sin t, a \cos t, b), \quad \|D^\alpha x(t)\| = t^{1-\alpha} \sqrt{a^2 + b^2}. \quad (16)$$

We find the conformable tangent vector by normalizing Eq. (16),

$$t^\alpha = \left( \frac{-a \sin t}{\sqrt{a^2 + b^2}}, \frac{a \cos t}{\sqrt{a^2 + b^2}}, \frac{b}{\sqrt{a^2 + b^2}} \right)$$

Some basic calculations we can find the conformable normal vector and conformable binormal vector as

$$n^\alpha = (-\cos t, -\sin t, 0), \quad b^\alpha = \left( \frac{b \sin t}{\sqrt{a^2 + b^2}}, \frac{-b \cos t}{\sqrt{a^2 + b^2}}, \frac{a}{\sqrt{a^2 + b^2}} \right)$$

Using Definition (14), the conformable adjoint curve of the curve  $x(t)$  is given by

$$\begin{aligned}\gamma^\alpha(s) &= \int_1^s \frac{b^\alpha(u)}{u^{1-\alpha}} du \\ &= \frac{1}{\sqrt{a^2 + b^2}} \left( b \int_1^s u^{\alpha-1} \sin u \, du, -b \int_1^s u^{\alpha-1} \cos u \, du, a \int_1^s u^{\alpha-1} \, du \right).\end{aligned}$$

where  $b^\alpha$  is a conformable binormal vector of the curve  $x$  and  $a_0 = 1$ . Using the closed-form solution, the conformable adjoint curve for specific values of  $\alpha$  can be plotted. Figure 1v shows the conformable adjoint curve for  $\alpha = 0.3, 0.6, 0.9$ .

It is convenient if we compare the conformable adjoint curve  $\gamma^\alpha$  of the curve  $x$  with the classical adjoint curve  $\gamma$  of a curve graphically. So, the classical adjoint curve a curve is plotted in Figure 1.

Graph of the conformable adjoint curve  $\gamma^\alpha$  of the curve  $x$  such that  $a = 1, b = 0.5$ .

## DISCUSSION

The analysis shows how fractional parameters affect the structure of adjoint curves by introducing fractional scaling effects through the conformable binormal vector. The findings show that the conformable adjoint curve introduces original fractional features, including narrower curves at bigger parameter values, while maintaining the fundamental geometric qualities of its classical counterpart.

The results emphasize the potential of conformable adjoint curves in modeling systems with memory effects and nonlocal dependencies by demonstrating their compatibility with fractional helices and Bertrand pairs. Although theoretical formulations offer a solid basis, additional numerical research and real-world validations would be beneficial for practical applications.

The present paper focused on conformable derivatives because of their computational simplicity and the fact that they preserve many familiar rules of calculus, such as the product rule and chain rule, making them convenient for a first exploration of adjoint curves in a fractional context. However, it must be noted that the conformable derivative has been criticized in literature as not being a true fractional derivative, since it lacks nonlocality and memory effects. Therefore, a natural and important direction for future research is to study adjoint curves using genuine fractional derivatives, such as the Riemann–Liouville or Caputo operators.

In this situation, several challenging questions arise:

- How do memory effects inherent to nonlocal fractional derivatives modify the geometry of the curves?
- Can new geometric invariants emerge in this framework?

Addressing these questions would provide a deeper understanding of the interplay between fractional calculus and geometry and may lead to a genuine fractional theory of curves. The results obtained here with conformable derivatives should be viewed as a preliminary step in this direction, offering intuition and tractable computations that can guide future investigations with more general operators.

## CONCLUSIONS

This paper defines and analyzes conformable adjoint curves, establishing a bridge between classical differential geometry and fractional calculus. Under the control of the parameter  $\alpha$ , the conformable adjoint curve introduces fractional effects while maintaining important characteristics. New understandings of curvature, torsion, and scaling behaviors are made possible by this approach, especially for kinematics, engineering, and physics applications.

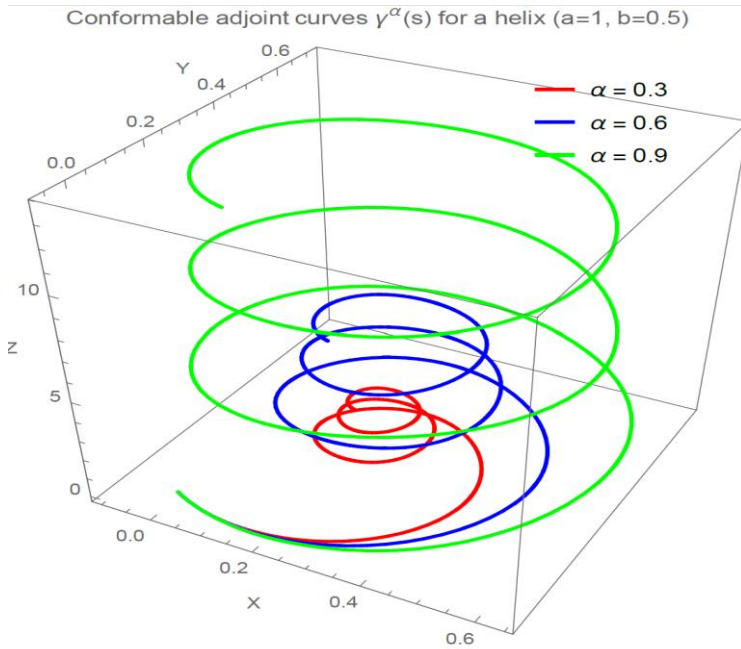


Figure 1: Graph of the conformable adjoint curve  $\gamma^\alpha$  of the curve  $x$  such that  $a = 1, b = 0.5$ .

## REFERENCE

- Abdeljawad, T. (2015). On conformable fractional calculus. *Journal of computational and Applied Mathematics*, 279, 57-66.
- Arıkan, M., and Nurkan, S. K. (2020). Adjoint curve according to modified orthogonal frame with torsion in 3-space. *Uşak Üniversitesi Fen Ve Doğa Bilimleri Dergisi*, 4(2), 54-64.
- Aydin, M. E., and Kaya, S. (2023). Fractional equiaffine curvatures of curves in 3-dimensional affine space. *International Journal of Maps in Mathematics*, 6(1), 67-82.
- Boulaaras, S., Jan, R., and Pham, V. T. (2023). Recent advancement of fractional calculus and its applications in physical systems. *The European Physical Journal Special Topics*, 232(14), 2347-2350.
- Çakmak, A., and Şahin, V. (2022). Characterizations of adjoint curves according to alternative moving frame. *Fundamental Journal of Mathematics and Applications*, 5(1), 42-50.
- Diethelm, K., Garrappa, R., Giusti, A., and Stynes, M. (2020). Why fractional derivatives with nonsingular kernels should not be used. *Fractional Calculus and Applied Analysis*, 23(3), 610-634.



- Gözütok, U., Çoban, H. A., and Sağiroğlu, Y. (2019). Frenet frame with respect to conformable derivative. *Filomat*, 33(6), 1541-1550.
- Has, A., and Yılmaz, B. (2022). Special fractional curve pairs with fractional calculus. *International Electronic Journal of Geometry*, 15(1), 132-144.
- Khalil, R., Al Horani, M., Yousef, A., and Sababheh, M. (2014). A new definition of fractional derivative. *Journal of computational and applied mathematics*, 264, 65-70.
- Martínez, F., Martínez, I., Kaabar, M. K., and Paredes, S. (2020). New results on complex conformable integral. *AIMS Mathematics*, 5(6), 7695-7710.
- Nurkan, S. K., Güven, İ. A., and Karacan, M. K. (2019). Characterizations of adjoint curves in Euclidean 3-space. *Proceedings of the National Academy of Sciences, India Section A: Physical Sciences*, 89(1), 155-161.
- Tarasov, V. E. (2018). No nonlocality. No fractional derivative. *Communications in Nonlinear Science and Numerical Simulation*, 62, 157-163.
- Vivas-Cortez, M., Árciga, M. P., Najera, J. C., and Hernández, J. E. (2023). On some conformable boundary value problems in the setting of a new generalized conformable fractional derivative. *Demonstratio Mathematica*, 56(1), 20220212.
- Yajima, T., Oiwa, S., and Yamasaki, K. (2018). Geometry of curves with fractional-order tangent vector and Frenet-Serret formulas. *Fractional Calculus and Applied Analysis*, 21(6), 1493-1505.
- Ye, Y., Fan, H., Li, Y., Liu, X., and Zhang, H. (2025). Conformable bilinear neural network method: a novel method for time-fractional nonlinear partial differential equations in the sense of conformable derivative. *Nonlinear Dynamics*, 113(7), 7185-7200.
- Yüksel, N., Karacan, M. K., Bükcü, B., İkiz, H., (2017). The Relation Between Base Curve of the Ruled Surface and It's Adjoint Curve. *Hadronic Journal and Algebras, Groups and Geometries*, 34, 203-211.
- Yüksel, N., and Saltık, B. (2023). On inextensible ruled surfaces generated via a curve derived from a curve with constant torsion. *AIMS Mathematics*, 8(5), 11312-11324.



# **Measurement of Clustering Performance in Enzyme Sequence Classification Using a Hybrid Dbscan– Spectral Ensemble**

**Çağın KANDEMİR ÇAVAŞ**

Prof. Dr.; Dokuz Eylül University, Faculty of Sciences, Department of Computer Science,  
cagin.kandemir@deu.edu.tr, ORCID No: 0000-0003-2241-3546

## ABSTRACT

Clustering analysis was performed using biochemical and statistical features extracted from enzyme sequences. A feature matrix was constructed including amino acid frequencies, molecular weight, isoelectric point, hydrophilic/hydrophobic ratio, and entropy values. This matrix was analyzed using DBSCAN and Spectral Clustering algorithms, and the results of both algorithms were integrated through an ensemble clustering method. Evaluation metrics such as the Silhouette Score, Davies-Bouldin Index, and Calinski-Harabasz Score were employed to assess clustering performance. The analysis demonstrated high effectiveness, with a Silhouette Score of 0.8947 and a Calinski-Harabasz Score of 3574.48, indicating that the selected biochemical and statistical features, together with the ensemble approach, provide a robust framework for the functional classification of enzymes.

*Keywords: Protein Sequence Analysis, Unsupervised Clustering, Functional Annotation, Entropy-Based Features.*

---

## INTRODUCTION

Functional classification of enzymes is one of the fundamental building blocks of bioinformatics because it plays a critical role in both understanding biochemical processes and developing biotechnological applications. Enzymes are special proteins that accelerate biochemical reactions and, thanks to this role, they have a central position in the functioning of many physiological processes (Josephs et al., 2019). Classification of enzymes according to their functions is a fundamental step for understanding their behavior in biological systems, improving industrial processes, and designing disease-based drugs. Classification of enzymes is an important approach to predict the potential functions of proteins whose function has not yet been determined, beyond the identification of existing enzymes (Dalkiran et al., 2018).

Traditional enzyme classification methods are generally examined in two main groups: structural and sequence-based approaches. The application of machine learning techniques in enzyme classification has become very widespread due to its success in analyzing complex biological sequences, its ability to easily examine comprehensive datasets, and its ability to accurately predict the functions of enzymes without any prior knowledge (Dalkiran et al., 2018; Kulmanov et al., 2018). Machine learning models, especially those using unsupervised learning algorithms, offer more flexible and scalable solutions in clustering enzymes based on their sequence features, with the

ability to classify enzymes without predefined labels. The main reason for preferring these techniques is that they can improve classification accuracy through processing large and diverse sequence databases, identifying new enzyme families, and better feature representation, as well as overcoming the limitations of traditional methods.

Structural similarity-based methods aim to determine functional similarities based on the three-dimensional structures of enzymes (Chothia and Lesk, 1986). Henrissat and Davies (1997) classified glycoside hydrolase enzymes based on their structure and sequence similarities. Mascotti, Juri Ayub, and Fraaije (2021) developed a comprehensive classification system by dividing F420-coenzyme-dependent oxidoreductase enzymes into five main classes by both sequence- and structure-based analyses. However, these methods have limited application because they require high-resolution structural data, which is not available for many enzymes. On the other hand, approaches based on the comparison of amino acid sequences are widely used, especially in the identification of homologous enzymes. Chou and Elrod (2003) developed a method for the prediction of enzyme family classes based on protein sequences. The study aimed to go beyond traditional sequence features and increase the classification accuracy by using the concept of pseudo amino acid composition. Lee, Lee, Lee, and Ryu (2007) developed a method based on different feature representations to classify enzyme functions from protein sequences. Davies and Sinnott (2008) described how carbohydrate-active enzymes are classified based on sequences. Nasibov and Kandemir-Cavas (2009) compared the effectiveness of K-Nearest Neighbor (KNN) and minimum distance-based classifiers in predicting enzyme families. Ebrahimi and Ebrahimie (2010) used bioinformatics algorithms to predict the thermostability of enzymes based on their amino acid sequences. Choi and Kim (2011) developed a new method based on clustering and information theory to predict catalytic sites from enzyme sequences. Dalkıran et al. (2018) predicted enzyme functions from protein sequences based on the Enzyme Commission classification. Tan et al. (2019) systematically reviewed the existing approaches in this field by compiling and analyzing machine learning methods used in the prediction of enzyme family classes. In addition to evaluating how different techniques affect classification accuracy, recent research has also investigated the impact of how enzymes are encoded on classification performance. Ferdous, Shihab, and Reuel (2022) investigated the effects of sequence features on enzyme classification and demonstrated that enzyme length and amino acid composition, in particular, significantly affect accuracy. Their study found that sequences, especially translocases, with lengths between 300 and 450 amino acids achieved the highest classification accuracy, while the ECpred tool showed the most consistent performance across different conditions. Jemimah, Sekijima, and Gromiha (2020) developed the ProAffiMuSeq method, which estimates the binding free energy change of mutations in protein–protein complexes using only sequence

features and functional classification. Nanni and Brahnam (2020) achieved high accuracy classification by combining different representation methods and SVM models.

The application of machine learning techniques in enzyme classification has become very widespread due to its success in analyzing complex biological sequences, its ability to easily examine comprehensive datasets, and its ability to accurately predict the functions of enzymes without any prior knowledge (Dalkiran et al., 2018; Kulmanov et al., 2018). Machine learning models, especially those using unsupervised learning algorithms, offer more flexible and scalable solutions in clustering enzymes based on their sequence features, with the ability to classify enzymes without predefined labels. The main reason for preferring these techniques is that they can improve classification accuracy through processing large and diverse sequence databases, identifying new enzyme families, and better feature representation, as well as overcoming the limitations of traditional methods.

While machine learning models often require labeled data for training, recent advances in alignment-free methods offer more efficient, scalable, and generalizable approaches. These methods are more computationally efficient as they avoid sequence alignment, making them well-suited for large datasets with many sequences. These methods can accurately detect biochemically and statistically important features of protein sequences without considering the homological relationships of the enzymes. Properties such as amino acid composition, molecular weight, hydrophobicity, and isoelectric point provide important information to understand the structural and functional properties of the sequence. These features are widely used in various fields such as enzyme prediction and functional annotation (Dobson and Doig, 2005; Zhang, Zhang, and Chen, 2005).

In this context, the proposed study emphasizes not only the impact of the chosen classification algorithm but also the value of enriching sequence representations with statistical features to improve model interpretability and performance. To further enhance classification accuracy and generalizability, ensemble learning approaches are adopted, in which multiple models are integrated rather than relying on a single classifier, allowing for more reliable and robust predictions (Mittal, Goyal, Hemanth, and Sethi, 2019).

In this study, a new approach is proposed for the classification of enzyme sequences with numerical features obtained directly from enzyme sequences. These features, which do not depend on sequence alignment and motif inference, offer an alternative approach to traditional methods. This approach significantly reduces computational cost while eliminating problems arising from missing data and sequence misalignments. The aim is to utilize unsupervised learning techniques to enable the identification of functionally related enzyme clusters, even for sequences that are distantly related or whose functions have not yet been characterized.

In addition, this study aims to reveal the hidden relationships among enzyme sequences and determine enzyme classes, especially by using unsupervised learning techniques such as clustering algorithms. Unsupervised learning allows the model to discover hidden patterns and structures in the dataset without the need for labeled data. This is particularly advantageous for enzymes of unknown or uncertain function, as it reduces the dependence on prior knowledge of specific enzyme families or motifs.

As a result, this study presents the use of alignment-free biochemical and statistical features in enzyme classification as an important methodological proposal in the field of bioinformatics. On the other hand, the integration of unsupervised machine learning algorithms overcomes the limitations of traditional alignment-based methods, allowing faster and more efficient analyses on large-scale datasets. This innovative approach provides flexibility in the identification of uncharacterized enzymes, reduces the dependency on pre-existing knowledge, and enables functional predictions for a wider range of enzyme sequences. Therefore, this method helps to obtain more accurate and scalable results in bioinformatics analyses and provides an important methodological step in biotechnological applications such as enzyme function prediction.

## METHODS AND MATERIALS

The Methods and Materials section consists of three main parts. The first part explains the techniques used to convert enzyme data into numerical representations. The second part focuses on the clustering of the encoded data using different clustering algorithms. The third part presents the evaluation of clustering performance. These three components are detailed in the following sections in the given order.

### ***Feature Extraction from Amino Acid Sequences***

In this study, various features are extracted from amino acid sequences to convert alphanumeric protein sequences into numerical form and enable analysis. These features include Amino Acid Composition (AAC), which shows how often each amino acid appears in a sequence, and Shannon Entropy, which reflects the diversity of the sequence. In addition, Hydrophilic/Hydrophobic Ratio (HydroRatio), Average Molecular Weight (MW), and Isoelectric Point (pI) are calculated to describe the physical and chemical properties of the sequences. These features help to provide a clear and informative profile of each amino acid sequence. Because in a

bioinformatics problem, the expression of the data is as important as the algorithmic methods chosen. All these computed metrics are combined into a single feature vector to represent each enzyme sequence comprehensively. Therefore, all metrics used to digitize protein sequences are explained below.

### ***Amino Acid Composition***

Each enzyme sequence was encoded using the following features that is called as Amino Acid Composition (AAC).

The ratio of each amino acid within a sequence is calculated as in Eq. (1)

$$AAC_j = \frac{n_j}{L}, \quad j = 1, 2, \dots, 20 \quad (1)$$

where  $n_j$  is the frequency of the  $j^{\text{th}}$  amino acid and  $L$  is the sequence length.

### ***Shannon Entropy***

Shannon entropy measures the diversity or information content of the sequence can be calculated as in Eq. (2)

$$H = -\sum_{j=1}^{20} p_j \log_2 p_j \quad (2)$$

where  $p_j = AAC_j$ .

### ***Hydrophilic/Hydrophobic Ratio (HydroRatio)***

It is calculated using a binary map of hydrophobic residues.

i. Hydrophobic amino acids: A, V, L, I, M, F, W, Y

Hydrophilic amino acids: R, K, D, E, N, Q, H, S, T

ii. By scanning the protein sequence, a binary mapping is made for each amino acid as follows:

a. If hydrophobic  $\rightarrow 1$

b. If hydrophilic  $\rightarrow 0$

iii. HydroRatio is calculated as follows:

$$HydroRatio = \frac{\text{Number of hydrophobic residues}}{\text{Total number of residues}} \quad (3)$$



### ***Average Molecular Weight (MW) and Isoelectric Point (pI)***

The calculation of Average Molecular Weight (MW) and Isoelectric Point (pI) are given in Eq. (4) and Eq. (5), respectively.

$$\overline{MW} = \frac{1}{L} \sum_{j=1}^{20} n_j \cdot MW_j \quad (4)$$

$$\overline{pI} = \frac{1}{L} \sum_{j=1}^{20} p_j \cdot pI_j \quad (5)$$

where  $L$  is the total number of amino acids in the sequence,  $n_i$  is the count of the  $i^{\text{th}}$  amino acid in the sequence,  $MW_i$  is the molecular weight of the  $i^{\text{th}}$  amino acid (in Daltons),  $pI_i$  is the isoelectric point of the  $i^{\text{th}}$  amino acid as shown in Table 1.

Table 1: Molecular weight and isoelectric point of 20 kind of amino acids.

<b>Amino Acid</b>	<b>One-Letter Code</b>	<b>Molecular Weight (Da)</b>	<b>Isoelectric Point</b>
Alanine	A	89.09	6.01
Cysteine	C	121.15	5.07
Aspartic Acid	D	133.10	2.77
Glutamic Acid	E	147.13	3.22
Phenylalabine	F	165.19	5.48
Glycine	G	75.07	5.97
Histidine	H	155.16	7.59
Isoleucine	I	131.17	6.02
Lysine	K	146.19	9.74
Leucine	L	131.17	5.98
Methionine	M	149.21	5.74
Asparagine	N	132.12	5.41
Proline	P	115.13	6.30
Glutamine	Q	146.15	5.65
Arginine	R	174.20	10.76
Serine	S	105.09	5.68
Threonine	T	119.12	5.60
Valine	V	117.15	5.96
Tryptophan	W	204.23	5.89
Tyrosine	Y	181.19	5.66

### ***Clustering Algorithms***

An ensemble clustering strategy was adopted by aggregating the results of two conceptually different unsupervised learning methods—DBSCAN and Spectral Clustering—via a voting-based consensus framework, as proposed

by Strehl and Ghosh (2002). The methods involved in this approach are described sequentially below.

### ***Density-Based Spatial Clustering of Applications with Noise (DBSCAN)***

A density-based (DBSCAN) algorithm is an unsupervised algorithm that is effective to find arbitrarily shaped clusters and noise. For a given point  $p$ , the  $\epsilon$  –neighborhood includes all points within a radius  $\epsilon$  as shown in Eq. (6)

$$N_{\epsilon}(p) = \{q \in D \mid \text{dist}(p, q) \leq \epsilon\} \quad (6)$$

where  $\text{dist}(p, q)$  denotes the Euclidean distance can be computes using Eq. (7).

$$\text{dist}(p, q) = \sqrt{\sum_{i=1}^n (p_i - q_i)^2} \quad (7)$$

A point  $p$  is a core point if the following condition holds as shown in Eq. (8).

$$|N_{\epsilon}(p)| \geq \text{minPts} \quad (8)$$

where  $N_{\epsilon}(p) = \{q \in D \mid \text{distance}(p, q) \leq \epsilon\}$ ,  $D$  is the protein dataset,  $\epsilon$  is the neighborhood radius and minPts is the minimum number of points required to form a dense region.

Based on these definitions, the DBSCAN algorithm classifies each data point into one of three categories. A core point is one that has at least MinPts neighboring points within a radius  $\epsilon$ , indicating it lies in a dense region. A border point does not meet the density requirement itself (i.e., has fewer than MinPts neighbors within  $\epsilon$ ), but it falls within the  $\epsilon$ -neighborhood of a core point and is therefore included in a cluster. In contrast, a noise point is neither a core point nor a border point; it is isolated from any dense region and does not belong to any cluster.

### ***Spectral Clustering***

Spectral clustering is an unsupervised clustering method that groups data based on the similarity between points, using a similarity matrix and information from its eigenvalues.

The similarity matrix is constructed using Eq. (9).

$$W_{ij} = \exp\left(-\frac{\|x_i - x_j\|^2}{2\sigma^2}\right) \quad (9)$$

where  $x_i$  and  $x_j$  are protein sequences,  $\|x_i - x_j\|$  is the Euclidean distance between the two sequences,  $\sigma$  is a scaling parameter that controls the width of the neighborhood.

Laplacian matrix is identified according to Eq. (10).

$$L = D - W \quad (10)$$

The matrix  $L$  is a diagonal matrix, where each diagonal element  $D(i, i)$  represents the sum of the similarities between protein sequence  $i$  and all other points. Eq. (11) provides the formula for this calculation.

$$D(i, i) = \sum_j W(i, j) \quad (11)$$

Then, to classify the data into  $k$  clusters, the  $k$ -means algorithm is applied to the first  $k$  eigenvectors of  $L$ .

### ***Ensemble Clustering***

Recently, ensemble clustering has been used to obtain a more powerful and reliable clustering by combining the results of different clustering algorithms. It is observed that if only one algorithm is used, its performance may be negatively affected when the structure and type of data sets change. Therefore, ensemble clustering aims to obtain more stable and accurate results by combining the strengths of different methods. By better capturing different features and structures in the dataset, it becomes possible to create more consistent and meaningful clusters (Strehl and Ghosh, 2002).

In this study, ensemble clustering was implemented by integrating the results of two fundamentally different unsupervised learning algorithms—DBSCAN (Density-Based Spatial Clustering of Applications with Noise) and Spectral Clustering—through a simple voting-based consensus mechanism (Strehl and Ghosh, 2002).

This effective method is based on the understanding that different clustering solutions can reveal different characteristics of the data and more effectively. DBSCAN is a density-based algorithm and is quite effective in identifying clusters and outliers with different shapes. However, the performance of the algorithm may decrease when the density differences between clusters are significant. On the other hand, Spectral Clustering models the similarities between the data with a graph and divides this graph into clusters with the eigenvector decomposition of the Laplacian matrix. It is more successful in detecting the global structure of the data, especially in data sets with complex and non-convex geometric structures (Luxburg, 2007).

To benefit from the complementary strengths of these algorithms, a voting strategy was implemented. Accordingly, if both DBSCAN and Spectral

Clustering assign the same cluster label to a data point, this label is assigned in the final ensemble result, if the cluster labels are different, the most common label between the two, i.e. the mode, is assigned.

This simple voting scheme incorporates the “ensemble-vote” paradigm, where each underlying algorithm contributes equally to the final decision (Golalipour et al., 2021). Despite its easy applicability, such ensemble strategies have a negative impact on the quality of clustering, especially in high-dimensional biological data where single algorithms may perform inconsistently in different regions of the feature space (Fred and Jain, 2005).

In this context, ensemble clustering provides advantages at the clustering stage.

- Increased robustness: By reducing the dependency on only one clustering method, ensemble clustering can produce more stable and consistent results across datasets with different densities.

- Improved accuracy: When clustering decisions are combined, errors or biases introduced by individual algorithms can be corrected, especially when the data are based on different assumptions.

- Improved handling of biological complexity: Like many types of biological data, enzyme sequences can exhibit both dense clusters (e.g. enzyme families with highly conserved regions) and scattered groups (e.g. functionally distinct enzymes), and these can be clustered effectively by combining the results of algorithms with different sensitivities.

### ***Clustering Performance Indices***

Silhouette Score (S) is calculated as shown in Eq. (12).

$$S = \frac{b-a}{\max(a,b)} \quad (12)$$

where  $a$  is the average intra-cluster distance and  $b$  is the average nearest-cluster distance.

The calculation of Davies-Bouldin Index (DB) is given in Eq. (13).

$$DB = \frac{1}{k} \sum_{i=1}^k \max_{j \neq i} \left( \frac{S_i + S_j}{M_{ij}} \right) \quad (13)$$

where  $S_i$  is the intra-cluster distance of cluster  $i$ , and  $M_{ij}$  is the inter-centroid distance between clusters  $i$  and  $j$ .

Calinski-Harabasz Score (CH) is is calculated according to Eq. (14)

$$CH = \frac{Tr(B_k)}{Tr(W_k)} \cdot \frac{n-k}{k-1} \quad (14)$$

where  $B_k$  is the between-cluster dispersion matrix, and  $W_k$  is the within-cluster dispersion matrix.

## RESULTS AND DISCUSSION

The clustering analysis was conducted on a sampled dataset of 1000 enzyme sequences, which were represented using a 24-dimensional feature matrix. This feature matrix was constructed by extracting numerical properties from the enzyme sequences, including amino acid composition, molecular weight, isoelectric point, hydrophobicity, entropy, and other statistical features. These features were intended to capture key biochemical and structural characteristics of the enzymes, enabling the identification of functionally relevant clusters through unsupervised learning techniques.

The ensemble clustering method, combining DBSCAN (Density-Based Spatial Clustering of Applications with Noise) and spectral clustering, was applied to this dataset. Ensemble clustering methods are particularly useful in this context as they combine the strengths of multiple clustering algorithms to improve the robustness and accuracy of the results. The ensemble approach helps mitigate the limitations of individual clustering methods and provides a more reliable and consistent clustering structure. The results obtained from this approach are summarized as follows:

The Silhouette Score is a metric used to assess the quality of the clusters formed by a clustering algorithm. It ranges from -1 to +1, with higher values indicating well-separated clusters and better-defined groupings. A Silhouette Score of 0.8947 indicates that the clustering achieved by the ensemble method exhibits strong intra-cluster cohesion and clear separation between the different enzyme groups. This value suggests that the enzymes within each cluster are highly similar to one another, and the boundaries between clusters are distinct, which is highly desirable in classification tasks where accurate grouping is essential. The Silhouette Plot is illustrated in Fig. 1.

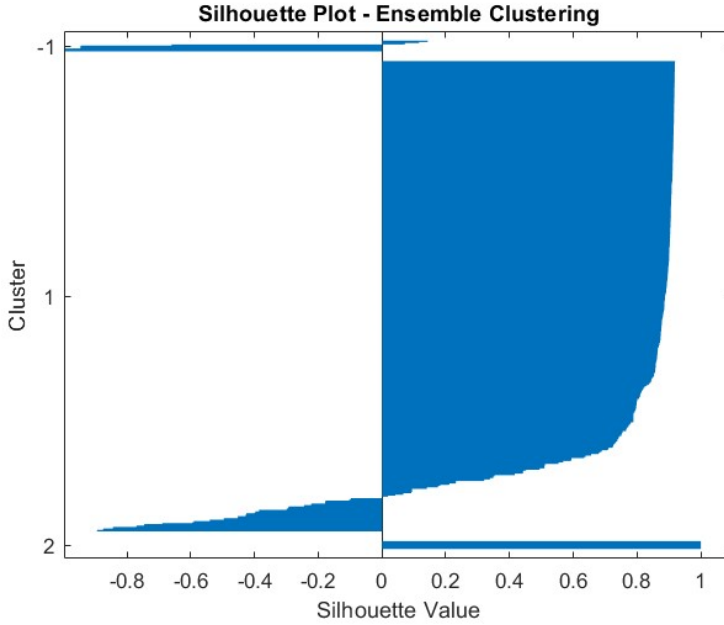


Figure 1: Silhouette Plot of Ensemble Clustering

The Davies-Bouldin Index (DBI) is a commonly used metric for evaluating clustering performance, with lower values indicating better clustering quality. The DBI takes into account both the intra-cluster dispersion (how compact the clusters are) and inter-cluster separation (how distinct the clusters are from each other). A Davies-Bouldin Index of 0.0000 suggests an exceptionally well-separated clustering structure. In this case, the DBI value indicates minimal overlap between the clusters, meaning that each cluster is highly compact and there is very little mixing of data points from different clusters. This is a significant finding, as it suggests that the enzymes are not only correctly grouped but that the clusters are well-defined and distinct from one another, providing a clear differentiation of functional categories.

The Calinski-Harabasz Index measures the ratio of the sum of between-cluster dispersion to within-cluster dispersion, with higher values indicating better-defined and more meaningful clusters. A Calinski-Harabasz Score of 3574.48 signifies that the clustering structure is highly well-separated and dense, with high between-cluster variance and low within-cluster variance. This indicates that the clustering algorithm successfully captured the underlying structure of the data, and the enzyme groups formed are not only compact but also distinct from one another, further supporting the conclusion that the feature matrix used was effective in capturing key information about enzyme functionality.

In the study, in addition to the ensemble method, DBSCAN and Spectral clustering algorithms were applied separately in order to evaluate the effectiveness of the proposed method. The results obtained are given in Table 2.

Table 2: Performance Comparison of DBSCAN, Spectral and Ensemble Clustering Methods

Metrics	DBSCAN	Spectral	Ensemble
Silhouette	0.70807	-0.69496	<b>0.89468</b>
Davies-Bouldin	0.23602	3.1871	<b>0</b>
Calinski-Harabasz	3641.4	3535.9	3591.7

The results show that; in this study, the ensemble clustering method achieved a high Silhouette score of 0.89, indicating that the separation between clusters and the consistency within clusters were at the highest level. Davies-Bouldin index is a measure that measures the similarity between clusters and indicates that lower values indicate a more successful clustering; the ensemble method achieved the lowest value and exhibited superior performance. Calinski-Harabasz index measures the ratio of the distance between clusters and the density within clusters, and higher values indicate more clearly separated and dense clusters. The obtained results show that the ensemble clustering approach both increases the separation between clusters and improves the homogeneity within clusters. In this context, the proposed ensemble method offers superior performance compared to the DBSCAN and Spectral clustering algorithms applied alone.

As a result, the combination of the high Silhouette Score, low Davies-Bouldin Index, and high Calinski-Harabasz Score strongly suggests that the ensemble clustering method was successful in identifying meaningful and distinct functional groups within the enzyme dataset.

This study introduces an innovative and unsupervised approach for clustering enzyme sequences based solely on intrinsic biochemical and statistical features. Unlike conventional methods that depend on sequence alignment or motif recognition, our method bypasses these traditional constraints by directly using features such as amino acid composition, molecular weight, isoelectric point, hydrophobicity, and sequence entropy. This alignment-free approach not only enhances computational efficiency but also enables scalability, making it highly suitable for large-scale datasets.

The originality of this work lies in its ability to integrate both density-based and graph-based clustering methods through an ensemble strategy. By combining DBSCAN and Spectral Clustering, the study effectively leverages the advantages of both techniques, improving the purity and separation of enzyme clusters. This ensemble approach represents a significant step forward

in enzyme classification, offering a robust mechanism for identifying functionally relevant groups in the absence of structural or motif-based data.

Furthermore, the incorporation of entropy as a feature contributes to a deeper understanding of sequence variability, allowing for the detection of subtle yet biologically meaningful patterns that traditional methods may overlook. The method's versatility extends beyond enzyme sequences and could be applied to other biological data types, such as non-coding RNAs or viral sequences, where structural data may be incomplete or unavailable.

Overall, this work provides a novel, alignment-free framework for enzyme functional classification, offering a significant contribution to the fields of bioinformatics, systems biology, and functional genomics. By breaking free from the limitations of sequence alignment, the proposed approach opens new avenues for large-scale, automated sequence analysis and predictive modeling, paving the way for future research and applications in both basic and applied biosciences. The approach also has potential utility in multi-omics integration, where sequence-derived features can be combined with transcriptomic, proteomic, or metabolomic data for more comprehensive biological insights.

## REFERENCE

Choi, K., and Kim, S. (2011). Sequence-based enzyme catalytic domain prediction using clustering and aggregated mutual information content. *Journal of Bioinformatics and Computational Biology*, 9(5), 597–611. <https://doi.org/10.1142/S0219720011005238>

Chothia, C., and Lesk, A. M. (1986). The relation between the divergence of sequence and structure in proteins. *EMBO Journal*, 5(4), 823–826. <https://doi.org/10.1002/j.1460-2075.1986.tb04288.x>

Chou, K. C., and Elrod, D. W. (2003). Prediction of enzyme family classes. *Journal of Proteome Research*, 2(2), 183–190. <https://doi.org/10.1021/pr020060+>

Dalkiran, A., Rifaioglu, A. S., Martin, M. J., Cetin-Atalay, R., Atalay, V., and Doğan, T. (2018). ECPred: A tool for the prediction of the enzymatic functions of protein sequences based on the EC nomenclature. *BMC Bioinformatics*, 19, 1–13. <https://doi.org/10.1186/s12859-018-2126-2>

Davies, G. J., and Sinnott, M. L. (2008). Sorting the diverse: The sequence-based classifications of carbohydrate-active enzymes. *The Biochemist*, 30(4), 26–32.

Dobson, P. D., and Doig, A. J. (2005). Predicting enzyme class from protein structure without alignments. *Journal of Molecular Biology*, 345(1), 187–199. <https://doi.org/10.1016/j.jmb.2004.10.025>



Ebrahimi, M., and Ebrahimie, E. (2010). Sequence-based prediction of enzyme thermostability through bioinformatics algorithms. *Current Bioinformatics*, 5(3), 195–203. <https://doi.org/10.2174/157489310791658755>

Ferdous, S., Shihab, I. F., and Reuel, N. F. (2022). Effects of sequence features on machine-learned enzyme classification fidelity. *Biochemical Engineering Journal*, 187, 108612. <https://doi.org/10.1016/j.bej.2022.108612>

Fred, A. L. N., and Jain, A. K. (2005). Combining multiple clusterings using evidence accumulation. *IEEE Transactions on Pattern Analysis and Machine Intelligence*, 27(6), 835–850. <https://doi.org/10.1109/TPAMI.2005.104>

Golalipour, K., Akbari, E., Hamidi, S. S., Lee, M., and Enayatifar, R. (2021). From clustering to clustering ensemble selection: A review. *Engineering Applications of Artificial Intelligence*, 104, 104388. <https://doi.org/10.1016/j.engappai.2021.104388>

Henrissat, B., and Davies, G. (1997). Structural and sequence-based classification of glycoside hydrolases. *Current Opinion in Structural Biology*, 7(5), 637–644. [https://doi.org/10.1016/S0959-440X\(97\)80072-8](https://doi.org/10.1016/S0959-440X(97)80072-8)

Jemimah, S., Sekijima, M., and Gromiha, M. M. (2020). ProAffiMuSeq: Sequence-based method to predict the binding free energy change of protein–protein complexes upon mutation using functional classification. *Bioinformatics*, 36(6), 1725–1730. <https://doi.org/10.1093/bioinformatics/btz812>

Josephs, R. D., Martos, G., Li, M., Wu, L., Melanson, J. E., Quaglia, M., ... Park, S. R. (2019). Establishment of measurement traceability for peptide and protein quantification through rigorous purity assessment—a review. *Metrologia*, 56(4), 044006. <https://doi.org/10.1088/1681-7575/ab26b0>

Kulmanov, M., et al. (2018). DeepGO: Predicting protein functions from sequence and interactions using a deep ontology-aware classifier. *Bioinformatics*, 34(4), 660–668. <https://doi.org/10.1093/bioinformatics/btx666>

Lee, B. J., Lee, H. G., Lee, J. Y., and Ryu, K. H. (2007, October). Classification of enzyme function from protein sequence based on feature representation. In 2007 IEEE 7th International Symposium on BioInformatics and BioEngineering (pp. 741–747). IEEE. <https://doi.org/10.1109/BIBE.2007.4371920>

Luxburg, U. V. (2007). A tutorial on spectral clustering. *Statistics and Computing*, 17(4), 395–416. <https://doi.org/10.1007/s11222-007-9033-z>

Mascotti, M. L., Juri Ayub, M., and Fraaije, M. W. (2021). On the diversity of F420-dependent oxidoreductases: A sequence- and structure-based classification. *Proteins: Structure, Function, and Bioinformatics*, 89(11), 1497–1507. <https://doi.org/10.1002/prot.26070>

Mittal, M., Goyal, L. M., Hemanth, D. J., and Sethi, J. K. (2019). Clustering approaches for high-dimensional databases: A review. *Wiley Interdisciplinary Reviews: Data Mining and Knowledge Discovery*, 9(3), e1300. <https://doi.org/10.1002/widm.1300>

Nanni, L., and Brahnam, S. (2020). Set of approaches based on position specific scoring matrix and amino acid sequence for primary category enzyme classification. *Journal of Artificial Intelligence and Systems*, 2(1), 38–52.

Nasibov, E., and Kandemir-Cavas, C. (2009). Efficiency analysis of KNN and minimum distance-based classifiers in enzyme family prediction. *Computational Biology and Chemistry*, 33(6), 461–464. <https://doi.org/10.1016/j.compbiolchem.2009.07.003>

Strehl, A., and Ghosh, J. (2002). Cluster ensembles — A knowledge reuse framework for combining multiple partitions. *Journal of Machine Learning Research*, 3, 583–617.

Tan, J. X., Lv, H., Wang, F., Dao, F. Y., Chen, W., and Ding, H. (2019). A survey for predicting enzyme family classes using machine learning methods. *Current Drug Targets*, 20(5), 540–550.  
<https://doi.org/10.2174/1389450120666181119125056>

Zhang, T., Zhang, H., and Chen, L. (2005). Enzyme classification with peptide programs: A comparative study. *BMC Bioinformatics*, 10, 231.  
<https://doi.org/10.1186/1471-2105-10-231>



# **Laser Roughening of Metal Surfaces: An Exemplary Study on the Application of Surface Roughness Parameters**

**Timur CANEL<sup>1</sup>**

1-Prof. Dr.; Kocaeli University, Faculty of Arts and Science, Physics Department. [tcanel@kocaeli.edu.tr](mailto:tcanel@kocaeli.edu.tr).  
ORCID No: 0000-0002-4282-1806

## ABSTRACT

This study examines how the surface morphology and functional characteristics of ST52 steel, a common low-alloy structural material, are affected by laser surface texturing (LST). The study aims to measure the correlation between surface roughness properties, namely the Maximum Peak Height ( $S_p$ ), which has a major impact on tribological behavior, and laser processing parameters. Surface roughness characteristics like  $S_p$ ,  $S_a$ ,  $S_q$ ,  $S_{sk}$ , and  $S_{ku}$  were used to examine the topographies that resulted from laser texturing under various pattern geometries, scan area ratios, and power levels.

Using the "smaller-is-better" criterion, the Taguchi optimization approach was used to determine the ideal processing conditions for producing a surface with a reduced coefficient of friction. The most significant element, according to analysis of variance (ANOVA), was the pattern type (37.52%), which was followed by the scan area ratio (34.03%) and laser power (28.45%). The best combination of square pattern, 60% scan area, and 40 W power produced the lowest  $S_p$  value, which is indicative of better adhesive and frictional performance.

The results show that laser-induced surface modification offers significant benefits over traditional roughening methods by providing precise control over surface topography and functional characteristics. Through regulated microstructural changes, laser texturing not only improves adhesion and wear resistance but also enables surface wettability and hydrophobicity to be tuned. According to these findings, laser roughening offers a highly versatile, industrially scalable, and environmentally friendly method for modifying the performance of metallic surfaces in mechanical, biomedical, and energy applications.

---

*Keywords – ST52 Steel, Surface Roughness, Laser Machining, Taguchi Method.*

---

## INTRODUCTION

Metal, owing to the regularity of its crystal lattice structure and the presence of free electrons, differs from other materials not only in its electrical and optical properties but also in its mechanical and thermal behaviors. The metallic bond in metals is formed through the stabilization of ionized atomic nuclei (a lattice of positive ions) by a cloud of delocalized electrons, often referred to as the "electron sea" (Lang, 2018:1787). The elastic modulus of metals is a direct indicator of the strong metallic bonds between atoms and is generally much higher than that of polymers, yet lower than that of ceramics, thereby providing a balance between strength and workability (Rösler et al., 2007). This structural characteristic enables the highly efficient conduction of both electricity and heat. The coefficient of thermal expansion in metals, which arises from electron–lattice interactions and phonon dynamics, is

typically moderate; this creates a balance between dimensional stability and formability under temperature variations (Jiang, 2015:083001). Furthermore, the crystal lattice of metals is commonly arranged in body-centered cubic (BCC), face-centered cubic (FCC), or hexagonal close-packed (HCP) structures, and such regularity accounts for their high mechanical strength, ductility, and malleability (Baker, 1998:88). Moreover, metals can exhibit phase transformations depending on temperature. For instance, iron undergoes a transition from a BCC structure to an FCC structure at 912 °C; this transformation has a direct impact on strength and magnetic properties (Magomedov, 2021:215).

From the perspective of electronic band theory, the conduction band and valence band in metals either completely overlap or are separated by a very narrow energy gap; therefore, electrons excited by external stimuli can easily transition into the conduction band and move freely (Cox, 2010). This characteristic is the most critical factor distinguishing metals from insulators such as ceramics and polymers, which possess wide band gaps. In addition, conductivity is determined not only by the presence of free electrons but also by scattering mechanisms such as lattice vibrations (phonons), impurities, and grain boundaries (Klemens and Williams, 1986: 197). For this reason, electrical conductivity generally decreases with increasing temperature.

In terms of thermal properties, heat conduction in metals is predominantly explained by the contribution of free electrons, a phenomenon quantitatively described by the Wiedemann–Franz law (Devanathan, 2021:1). Furthermore, the free-electron gas model (Drude model) (Quinn and Yi, 2018:83) and the more advanced quantum-mechanical free-electron model (Sommerfeld model) are employed to explain the specific heat, magnetic behavior, and conductivity mechanisms unique to metals (Solyom, 2009:1). Regarding optical properties, plasmonic oscillations and the interaction of surface free electrons with electromagnetic waves account for the reflectivity and luster characteristic of metals (Zang, 2008:127). Collectively, these parameters render metals indispensable not only as structural materials but also in electronics, optoelectronics, and energy technologies.

### ***The Functional Significance of Surface Roughening in Materials Engineering***

Surfaces of materials are frequently roughened to meet functional and performance requirements (Astakhov, 2010:1). Surface roughening is a critical process that modifies the interaction between a material and its environment, directly influencing properties such as adhesion, friction, wettability, and mechanical interlocking (Onu and Stela, 2024:1). From a physical standpoint, rough surfaces increase the effective contact area, thereby enhancing both mechanical bonding and adhesion during coating or adhesive processes (Croll, 2020:105847). For this reason, roughening is an essential preparatory stage in surface treatments such as painting, coating, bonding, and

welding (Almeida, 2001:3). Moreover, alterations in surface morphology have significant impacts on optical reflectivity, tribological behavior, and fatigue resistance (Orgeldinger, 2023:257).

The industrial and engineering demand for rough surfaces is closely linked to functional expectations. For instance, in the automotive and aerospace sectors, roughened surfaces enhance the mechanical interlocking of coatings or adhesives, thereby improving safety and durability (Parthasarathy, 2025:109). In biomedical applications, the roughening of implant surfaces facilitates biomechanical attachment between the implant and surrounding tissue, improving in vivo compatibility (Thakur et al., 2022:1459). In the energy sector, controlled surface roughening of components such as turbine blades or solar panels is employed to optimize fluid dynamics and light absorption (Zidane et al., 2016:2054). Similarly, in mechanical systems where frictional properties are crucial—such as brake discs, clutch interfaces, or bearing components—rough surfaces are deliberately preferred to enhance performance (Al-Samarai., 2024:1).

Surface roughness has practical advantages, but it also has a significant impact on optical and aesthetic performance (Linke, 2016:064501). Matte surfaces, for example, are achieved through specific roughening processes, while micron-scale surface textures alter light scattering characteristics, thereby controlling reflection and absorption ratios (Osterloo, 2012:404). Micro- and nanoscale roughening has gained prominence in recent years, particularly in materials science and nanotechnology, enabling the design of hydrophobic (water-repellent) or hydrophilic (water-attracting) surfaces through controlled manipulation of surface energy (Garg, 2023). Consequently, rough surfaces represent not merely a structural requirement in modern industry but also a strategic design element that optimizes functional performance.

A variety of techniques are employed in industry to roughen surfaces. Among mechanical methods are sandblasting, shot peening, and milling. These processes create micro- and macro-scale roughness either by applying controlled impacts to the surface or by treating it with abrasive particles. Mechanical roughening methods are widely preferred as a pre-treatment for coating applications, since they not only remove oxide layers and contaminants but also produce a suitable topography for strong bonding (Jena and Swain, 2025: 337).

Chemical methods include acid etching and electrochemical roughening. Acid-based solutions selectively remove material from the surface in a controlled manner, generating an irregular morphology (Zaki, 2022:468). This approach is commonly applied to metals such as aluminum, titanium, and stainless steel to increase surface energy and improve adhesion (Parthasarathy, 2025:109). Electrochemical methods, in contrast, enable more controlled and homogeneous surface roughness.

In recent years, advanced surface modification techniques have emerged. Laser texturing operates by directing high-intensity laser beams onto the surface to generate micro-scale pits and grooves. This method alters both the topography and the microstructural features of the surface, making it particularly advantageous in tribological and biomedical applications. Plasma treatment and ion-beam bombardment are also employed to achieve nanoscale roughening, especially in optoelectronic and biomaterial applications (Sioshansi, 1996:175). Compared to conventional approaches, these advanced techniques offer higher precision and allow for tailored surface design.

### ***Industrial and Engineering Applications of Surface Roughening on Metallic Substrates***

The surfaces of metals are roughened to enhance functional performance and extend service life. Surface roughness is a critical parameter that influences not only the mechanical behavior of metals but also their electrical, optical, and tribological properties. Introducing controlled roughness on metallic surfaces increases the effective surface area, thereby strengthening adhesion and cohesion mechanisms. As a result, bonding strength in industrial processes such as coating, painting, adhesive bonding, and welding is significantly improved (Croll, 2020:105847). Since smooth and slippery surfaces may hinder sufficient adherence of coating layers, controlled surface roughening is often regarded as a mandatory preparatory step in industrial standards (Almeida, 2001:3).

The demand for roughened metal surfaces in industry arises directly from functional requirements. For instance, in the automotive, aerospace, and defense industries, roughening of metallic components enhances the mechanical interlocking of surface coatings, thereby improving corrosion resistance and fatigue strength (Okokpujie, 2024:2). In the biomedical field, surfaces of titanium or stainless-steel implants are roughened to facilitate cell adhesion and tissue integration (Swain, 2020:55). In the energy sector, turbine blades and heat exchanger surfaces are roughened to optimize fluid dynamics and heat transfer efficiency (Abuaf, 1998). Similarly, in friction-based mechanisms such as brake discs and clutch systems, roughened surfaces play a critical role in ensuring safe torque transmission.

Moreover, roughened metallic surfaces provide strategic advantages not only at the macroscopic scale but also at the micro- and nanoscale. Microscale roughening enhances the mechanical interlocking of coatings, whereas nanoscale surface engineering modifies properties such as wettability and surface energy, enabling the design of hydrophobic (water-repellent) or hydrophilic (water-attracting) surfaces (Madhuri, 2025:137). This is particularly significant for improving cell compatibility in biomedical implants or optimizing surface interactions in energy systems. Today, advanced technologies such as laser texturing, plasma processing, and ion



bombardment allow metallic surfaces to be engineered with high precision, offering multifunctional and application-specific performance.

### ***Conventional and Advanced Techniques for the Roughening of Metal Surfaces***

In industry, manufacturing, and scientific research, the roughening of metallic surfaces is performed through various methods to meet different functional requirements. These methods can generally be classified as mechanical, chemical, electrochemical, and advanced surface treatment techniques. The choice of method depends on the type of metal, the intended application, and the desired surface characteristics.

Mechanical methods are among the most widely used surface roughening techniques (Kurup, 2021:84). Processes such as sandblasting, shot peening, milling, and grinding generate surface roughness either by controlled material removal or by creating micro-indentations through impact on the surface (John, 2021:3841). These methods are particularly preferred in surface preparation prior to coating and for enhancing the adhesion strength of bonding agents. Sandblasting and shot peening additionally induce residual compressive stresses on the surface, thereby improving fatigue resistance (Qian, 2023:1210).

Chemical methods, on the other hand, are carried out through acid etching and alkaline solution treatments. In these processes, controlled material removal produces irregular micro-scale topographies. Acid etching, commonly applied to materials such as titanium, aluminum, and stainless steel, increases surface energy and generates biocompatible surfaces for coating and biomedical applications. Electrochemical methods, including specialized treatments following anodization or electropolishing, enable the production of more controlled and homogeneous roughness.

In recent years, advanced surface treatment techniques have gained prominence. Laser texturing operates by generating micro-pits and grooves on the metallic surface through high-intensity laser irradiation; this approach modifies both surface topography and microstructural characteristics, thereby improving tribological performance. Plasma treatment, ion beam bombardment, and electron beam processing provide nanoscale roughening, enabling highly precise surface designs particularly in optoelectronic, biomedical, and energy-related systems.

In scientific studies, the effects of these methods are examined not only in terms of surface topography but also with respect to mechanical properties, corrosion resistance, biocompatibility, and tribological behavior. Consequently, surface roughening has become a strategic process in modern materials engineering, employing both traditional and high-technology-based approaches.

### ***Laser Surface Texturing as a Method for Controlled Surface Modification***

Laser surface texturing is an advanced surface modification technique performed by focusing high-intensity laser beams onto metallic surfaces. In this process, the laser beam interacts with the surface, inducing thermal effects such as localized heating, melting, and vaporization (Kalinowski, 2023:240). By controlling laser parameters—such as wavelength, pulse duration, energy density, repetition frequency, and scanning speed—micro- and nanoscale pits, grooves, or indentations can be generated. As a result, the metallic surface is modified not only in terms of topography but also in its microstructural characteristics.

The fundamental mechanism of laser texturing begins with the absorption of laser energy on the surface. The concentrated energy causes a rapid rise in temperature in the surface layer, leading to short-lived melting. During the cooling stage, rapid solidification occurs, resulting in irregular microstructures, wavy surfaces, or crater-like morphologies. When the laser energy exceeds a threshold value, material is removed from the surface through ablative vaporization, producing more pronounced roughness. Ultrashort laser pulses can induce *laser-induced periodic surface structures* (LIPSS), which generate ordered nanoscale textures (Toyserkani, 2015:441).

One of the key advantages of this method lies in its high precision and controllability. By optimizing laser parameters, the degree of roughness can be tuned at the desired scale, and processing can be restricted to specific regions. Furthermore, as a non-contact technique, laser texturing eliminates tool wear and can be applied effectively to surfaces with complex geometries. In addition, microstructural changes occur during processing; for instance, fine-grained microstructures formed after re-solidification may enhance surface hardness and wear resistance (Ye, 2021:6407).

In industrial and scientific applications, laser surface texturing is utilized in a wide range of fields, including pre-coating preparation, surface modification of biomedical implants, enhancement of tribological performance, and improvement of optical properties (Dong, 2024:847). For example, laser texturing of titanium implant surfaces enhances cell adhesion and biocompatibility, while in the automotive and aerospace sectors, it improves the frictional and wear resistance of metallic components. Consequently, laser texturing has become a high-precision, versatile, and strategically important technology in modern surface engineering.

The type of laser employed in the process directly influences the resulting surface characteristics. CO<sub>2</sub> lasers, operating at a long wavelength (10.6  $\mu\text{m}$ ), are typically preferred for large-area and relatively deep texturing, where thermal effects dominate (Hazzan, 2021:895). Nd:YAG (neodymium-doped yttrium aluminum garnet) lasers, with a shorter wavelength of 1064 nm, enable high-intensity energy focusing and thus provide more precise micro-scale texturing (Roy, 2018). This laser type is widely used in biomedical

applications, particularly for stainless steel and titanium surfaces (Bussoli, 2008:349).

In recent years, fiber lasers have gained prominence in industry due to their high beam quality, low maintenance requirements, and high energy efficiency. Their ability to generate short and ultrashort pulses (picosecond and femtosecond regimes) allows for nanoscale surface structuring (Stoian,2020:4665). Notably, femtosecond laser pulses minimize heat-induced melting and resolidification, enabling the creation of highly precise roughness with minimal thermal damage. This capability provides superior performance in optoelectronic components and precision biomedical devices.

Therefore, different laser types offer a wide range of possibilities for surface texturing across macro-, micro-, and nanoscale levels, providing researchers and industry with diverse options to tailor surface characteristics according to specific functional requirements.

### ***Comparative Advantages of Laser-Based Roughening Methods***

One of the most significant advantages of the laser surface texturing (LST) method is its ability to provide high precision and controllability (Correa, 2017: 8). By adjusting laser parameters—such as power, pulse duration, frequency, and scanning speed—the surface topography can be modified at the desired scale, enabling the degree of roughness to be controlled at both the micro- and nanoscale (Rajab, 2017:688). This precision allows for the fabrication of surface features required in biomedical implants, microelectronic components, and optical systems.

Another advantage is that the process is inherently non-contact. Unlike mechanical texturing techniques, issues such as tool wear or part deformation during processing do not occur in laser-based methods. This makes it possible to texture surfaces with complex geometries or those located in hard-to-reach areas. Furthermore, since the process does not require the use of chemical solutions, laser surface texturing is considered an environmentally friendly technique.

Laser texturing not only alters the surface topography but also induces microstructural transformations in metallic surfaces. Fine-grained structures emerge because of rapid cooling rates, potentially improving surface hardness and wear resistance. (Li, 2021: 2238). In addition, the micro- and nanostructures induced by laser irradiation enable the control of functional properties such as wettability and friction coefficient (Jing, 2022: 130198). This versatility makes laser technology a strategic tool across multiple disciplines, including tribology, biomedical materials engineering, and energy technologies.

Finally, the compatibility of laser systems with automation and their high reproducibility offer significant advantages for efficiency and standardization in industrial applications. The ability to digitally control processing parameters ensures that different parts can be treated with

consistent surface quality. Consequently, laser surface texturing has become not only a method of choice in research laboratories but also an innovative technique increasingly adopted in large-scale manufacturing processes.

### ***Quantitative Characterization of Surface Roughness Parameters***

Surface roughness is a concept that enables the quantitative definition of a material's surface morphology and has a direct effect on functional performance. Roughness parameters characterize the irregularities of the surface at the micro and macro scales using statistical methods (Myshkin, 2003:1001). These parameters are generally classified as mean height-based parameters, statistical distribution parameters, and spatial (geometric) parameters. Techniques including optical interferometry, atomic force microscopy (AFM), and profilometers are typically used for measurement and evaluation (Wang, 2017:164).

Surface roughness parameters on a line are denoted by “R”. By scanning the surface of lines in rows, a three-dimensional surface topography is obtained. Three-dimensional surface roughness parameters are also denoted by “S”. The  $R_a$  (arithmetic mean roughness) value is one of the most often utilized parameters. The most often used criterion in industry for determining surface quality is  $R_a$ , which is the average of the absolute deviations from the surface profile's center line (Sahay, 2018). In addition,  $R_q$  (root mean square roughness, RMS value) provides a more accurate statistical measurement of the surface profile; it is used especially in examining the energy distribution and functional interactions of the surface (McCool, 1987:264). The  $R_z$  parameter, on the other hand, is based on the difference between the highest peak and the deepest valley along the profile and characterizes the maximum irregularities on the surface (Thomas, 1981:97). When these three parameters are used together, they provide comprehensive information about both the overall roughness level and the local irregularities of the surface.

Furthermore, there are factors that provide a more thorough description of the surface's morphological features.  $R_p$  (maximum peak height) and  $R_v$  (maximum valley depth) define the irregularities at the extreme points of the surface. The surface profile's total height between the peak and the valley is expressed by the  $R_t$  parameter. Criteria such as  $S_m$  (average peak spacing) and  $S_{sk}$  (skewness), which are among the spatial parameters, provide information about the degree of regularity and distribution symmetry of the surface profile. In particular, the skewness and kurtosis parameters are critical for predicting the functional behavior of the surface—such as oil film retention capacity, friction characteristics, and wear mechanisms.

In recent years, with the development of three-dimensional (3D) surface measurement techniques, spatial parameters such as  $S_a$  (average surface roughness),  $S_q$  (RMS surface roughness), and  $S_z$  (maximum height) have also begun to be used in addition to two-dimensional profile-based parameters. These parameters provide a more comprehensive assessment covering the

entire surface area, rather than just a single profile. These three-dimensional parameters are essential for comprehending the functional impacts of surface engineering at the micro and nanoscales, especially in scientific research. Below, under headings, are the most frequently used surface parameters along with brief descriptions.

### ***The Arithmetic Mean Height of a Surface***

The surface roughness parameter  $S_a$  is an extension of  $R_a$  (the arithmetic mean height of a line) to the surface.  $S_a$  is the arithmetic mean height of a line across all rows. As an absolute value, it represents the height difference of each point relative to the arithmetic mean of the surface. This parameter is commonly used to evaluate surface roughness. Mathematically, it is expressed as follows (Gadelmawla, 2002:133):

$$S_a = \frac{1}{A} \iint_A |Z(x, y)| dx dy \quad (1)$$

### ***Root Mean Square Deviation Across the Surface***

It shows the ordinate values' root mean square value inside the defined area. It is comparable to the heights' standard deviation. This parameter has the following mathematical definition. (Gadelmawla, 2002:133):

$$S_q = \sqrt{\frac{1}{A} \iint_A \{Z(x, y)\}^2 dx dy} \quad (2)$$

A broad indicator of the surface's texture is provided by the  $S_a$  and  $S_q$  parameters. Identifying peaks, valleys, and ranges of different textural qualities is agnostic to  $S_a$  and  $S_q$ . Because various surfaces with drastically varied spatial and height symmetry features (such as milled and honed surfaces) may have the same  $S_a$  or  $S_q$  value yet function very differently,  $S_a$  or  $S_q$  can therefore be deceptive. The  $S_a$  and  $S_q$  parameters can be utilized to identify notable variations in texture properties after a surface type has been established. Optical surfaces are usually indicated by  $S_q$ , whereas machined surfaces are indicated by  $S_a$ .

### ***Maximum Peak Height in the Defined Area***

The highest peak's elevation within the designated area is symbolizes as  $S_p$ . The mathematical definition of this parameter is as follows (Gadelmawla, 2002:133):

$$S_p = \max_A (Z(x, y)) \quad (3)$$

### ***Maximum Valley Depth in the Defined Area***

It is the absolute value of the height of the deepest pit within the defined area. The mathematical definition of this parameter is as follows (Gadelmawla, 2002:133):

$$S_v = \min_A (Z(x,y)) \quad (4)$$

### ***Maximum Height of the Defined Surface***

It is the total of the maximum values for peak height and valley depth within the designated area (Dong et al., 2024:29).

$S_p$  is the maximum peak height,  $S_v$  is the maximum valley depth, and is expressed as a negative number. These three parameters are related to each other as follows (Blunt et al., 2003:17)).

$$S_z = S_p + S_v \quad (5)$$

$S_p$ ,  $S_v$ , and  $S_z$  tend to result in non-repeatable measurements because they are obtained from single points. Therefore, to produce a statistically significant result when employing these three factors, it is important to carefully modify the spatial filtering bandwidths to remove misleading peaks/valleys and acquire the average of many measurements at random points throughout the sample. Leak-proof surfaces and coating applications are two common uses for  $S_z$ .  $S_p$  might be useful when thinking about surfaces for sliding contact applications. When valley depths associated with liquid retention are present, like in lubrication and coating systems,  $S_v$  may find use (Sudeep et al., 2015:031501).

### ***$S_{sk}$ Skewness Along the Defined Surface***

The roughness values indicate how skewed the roughness profile (asperity) is.  $S_{sk}<0$ : There is a skew in the height distribution above the mean plane. Peaks and troughs in the height distribution are symmetrical around the mean plane when  $S_{sk}=0$ .  $S_{sk}>0$ : The distribution of height is tilted below the mean plane.

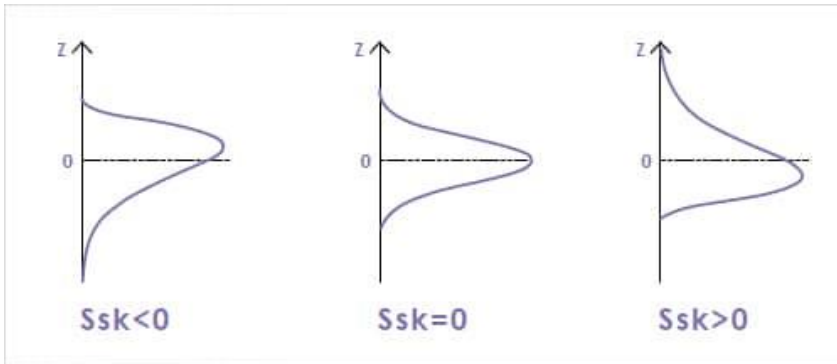


Figure 1: Definition and representation of skewness along the defined surface (Gadelmawla, 2002:133)

The mathematical definition of this parameter is as follows (Gadelmawla, 2002:133).

$$S_{sk} = \frac{1}{S_q^3} \left[ \frac{1}{A} \iint_A Z^3(x, y) dx dy \right] \quad (6)$$

$S_{sk}$  represents the degree of symmetry around the average plane of surface elevations. The sign of  $S_{sk}$  indicates the dominance of the peaks (i.e.,  $S_{sk} > 0$ ) or valleys ( $S_{sk} < 0$ ) that form the surface.

### ***$S_{ku}$ Kurtosis Along the Defined Surface***

The sharpness of abnormalities is gauged by the  $S_{ku}$  value.  
 $S_{ku} < 3$ : The distribution of heights is skewed above the mean.  
 $S_{ku} = 3$ : There is a normal distribution of height. (Indented and sharp portions coexist.)  
 $S_{ku} > 3$ : There is a noticeable variation in height.

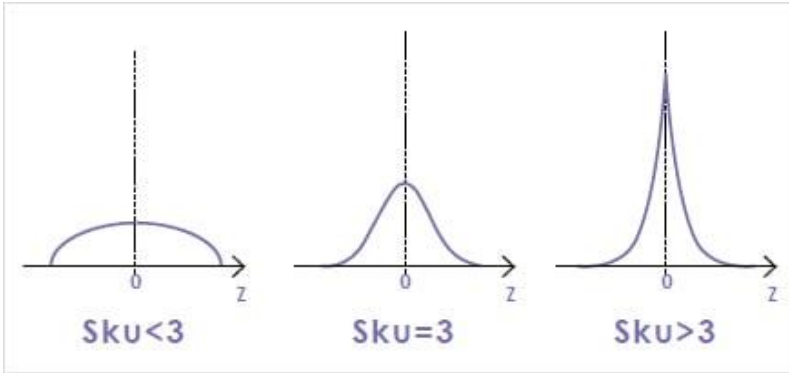


Figure 2: Definition and representation of kurtosis along the defined surface (Gadelmawla, 2002:133)

The mathematical definition of this parameter is as follows (Gadelmawla, 2002:133).

$$S_{ku} = \frac{1}{S_q^4} \left[ \frac{1}{A} \iint_A Z^4(x, y) dx dy \right] \quad (7)$$

$S_{ku}$  shows if the texture's incredibly high peaks and deep valleys are present ( $S_{ku} > 3.00$ ) or absent ( $S_{ku} < 3.00$ ).  $S_{sk}$  is 0.00 and  $S_{ku}$  is 3.00 if surface elevations have a normal distribution, or bell curve.  $S_{ku} < 3.00$  is typically seen on surfaces that shift gently and lack sharp peak or valley features.  $S_{sk}$  is helpful for tracking various wear conditions and recognizing honed surfaces.  $S_{ku}$  may be used to show whether there are any potential surface peak or valley flaws (Pawlus, 2022:163). High-order powers of surface elevations are present in  $S_{sk}$  and  $S_{ku}$ , thus sufficient measurements should be made to get statistically significant values. Additionally, filtering bandwidths should be carefully chosen to remove false peaks or valleys.

## ***The Role of Surface Roughness Parameters in Industrial and Functional Applications***

The selection of surface roughness parameters varies depending on the requirements of the application. For example, in the automotive industry, the  $R_a$  and  $R_q$  parameters are generally emphasized for engine parts and bearing surfaces (Priest, 2000:193). This is because the properties of surfaces, such as friction coefficient, oil film formation, and wear resistance, show a strong correlation with these parameters. Additionally, the  $R_z$  parameter is also considered critical in brake discs or gear systems because the maximum peak-to-valley difference affects the vibration and noise behavior that can occur on the contact surface (Bigerelle et al., 2008:992).

In biomedical applications, the importance of roughness parameters is even more pronounced, especially on implant surfaces. Cell adhesion and biocompatibility of the implant surface are directly related to surface morphology (Bacakova et al., 2011:739). Therefore, three-dimensional parameters such as  $S_a$  and  $S_q$  are more commonly used. For example, micro- and nano-scale roughening of the surface in titanium implants accelerates osseointegration and increases biological compatibility.

In tribology, i.e., the functional impacts of surface characteristics are very important in the research of wear, lubrication, and friction. The  $S_{sk}$  (skewness) value is used to determine the surface's load-carrying capacity and behavior under a lubricant film, while the  $S_{ku}$  (kurtosis) parameter reveals whether sharp protrusions or flattened peaks dominate the surface (Wang et al., 2022:12) (Królczyk et al., 2021:1987). These parameters are preferred, especially in bearing elements and precision moving parts, to ensure long life and low energy loss.

In the optical and electronic industries, roughness parameters take on a different function. For example, atomic-level roughness is critical in laser systems, fiber optics, or semiconductor surfaces. Here, the  $R_q$  and  $S_a$  parameters are used to determine the effect of the surface on light scattering and electron mobility (Jin et al., 2007:8). Furthermore, in the production of high-precision optical lenses, the nanometer-scale roughness of the surface becomes a quality criterion that directly affects product performance.

Consequently, surface roughness parameters must be evaluated not only as measurement values but also as functional performance indicators. Which parameter takes precedence is determined by the specific requirements of the application, such as friction, wear, biocompatibility, optical performance, or structural strength.

The following section presents an example study. According to this study, the surfaces of ST52 steel sheets, which are widely used in industry, were roughened with a laser to reduce their friction coefficients. The optimal laser parameters required to obtain a surface with a lower friction coefficient were determined.



### ***Material Focus: Structural and Functional Characteristics of ST52 Steel***

ST52 steel belongs to the low-alloy structural steel class based on carbon-manganese and is a quality steel defined in particular by DIN (Deutsches Institut für Normung) standards (Schlegel, 2023). This steel has a favorable structure in terms of both mechanical strength and workability thanks to its medium carbon content and well-balanced manganese addition. After normalization annealing, it acquires a homogeneous microstructure, which gives the steel both ductility and sufficient hardness. Furthermore, due to its high weldability, it is one of the preferred steel types in various manufacturing processes.

In terms of mechanical properties, ST52 steel exhibits a tensile strength of approximately 500–700 MPa and a good yield strength (Khalifeh et al., 2018:232). These values create an optimal balance between strength and formability. Its mechanical properties can be further improved through hardening and tempering processes. In addition, its high impact resistance makes it safe to use in structures subject to dynamic loads. Furthermore, its resistance to embrittlement at low temperatures makes this steel suitable for use in different climatic conditions.

Its industrial and manufacturing applications are extremely diverse. ST52 steel is widely preferred in areas such as machine manufacturing, the automotive industry, pressure vessel production, civil engineering applications, load-bearing structural elements, and chassis parts (Khot et al., 2025:136). It can also be used in equipment such as tanks, pipes, and boilers that operate under pressure. This is because the steel's high ductility and toughness allow it to operate safely under pressure.

The main reasons for choosing ST52 steel in these areas are its high weldability and good formability (Roodgari et al., 2020:138775). The low risk of cracking in welded manufacturing processes increases production ease and safety. In load-bearing systems, the high strength-to-weight ratio provides lightness while guaranteeing safety. Its cost-effectiveness makes ST52 steel an economical choice for both small-scale and mass production. Furthermore, the ability to improve the material's properties through surface treatments (roughening, coating, or heat treatment) contributes to the diversification of its applications.

In conclusion, ST52 steel is a strategic material in today's industrial production processes due to its balanced mechanical properties, workability, weldability, and cost-effectiveness. Its reliability in both machine and automotive parts as well as in construction and pressure vessel applications ensures its widespread preference.

### ***Industrial Relevance of Surface Roughening in ST52 Steel Components***

ST52 steel belongs to the group of high-strength, low-alloy structural steels and stands out for its durability, weldability, and ductility properties. Roughening the surfaces of this type of steel in industry and manufacturing is

a critical step in optimizing material performance depending on the intended use. The roughening process creates micro- or nano-scale topographical changes on the steel surface, improving its mechanical, tribological, and chemical properties. Increasing surface roughness, especially in load-bearing and high-load-exposed steels such as ST52, provides stronger bonding in coating and bonding processes.

One of the main purposes of surface roughening in industry is to prepare the surface prior to coating. The surface must be roughened at the micro level to ensure that paint, galvanizing, ceramic coating, or polymer-based protective layers adhere better to the steel (Ulaeto et al., 2023:284). This method minimizes the risk of peeling or cracking of the coating by increasing the adhesion between the surface and the coating. Additionally, controlling the surface roughness of ST52 steel facilitates the retention of lubricating films, thereby reducing the friction coefficient and increasing wear resistance (Morshed-Behbahani et al., 2024:1618). The long-term and reliable operation of moving parts, in particular, depends on such surface modifications.

The applications of rough surfaces are quite extensive. For example, in the automotive industry, surface roughness on chassis elements, connecting parts, and components requiring high impact resistance ensures that paint and anti-corrosion coatings are more effective. In machine manufacturing, roughened ST52 surfaces minimize wear by increasing oil retention capacity in bearing areas. In pressurized vessel and pipe systems, surface roughness both increases durability in welded connection areas and regulates flow characteristics by facilitating the adhesion of liquids on internal surfaces.

Furthermore, the biomedical and energy industries choose rough ST52 surfaces. In wind turbines, the roughness of the load-bearing steel components is crucial for corrosion resistance and coating adherence (Menghani, and Nandedwalia, 2021:115). Similarly, roughened surfaces are used in the metallic substrates of biomedical implants, enabling better integration with biological tissue through surface modification.

Consequently, roughening ST52 steel surfaces is a critical engineering approach not only for aesthetic or surface processing convenience but also for increasing mechanical strength, improving coating and lubrication performance, enhancing corrosion resistance, and improving the functional properties of the surface. Therefore, roughened ST52 steel surfaces have become a strategic choice in industry and manufacturing for both long-term use and reliability.

## RESULTS AND DISCUSSION

### ***Correlation Between Surface Friction and Maximum Peak Height ( $S_p$ ) Parameter***

An important component in the analysis of surface properties and tribological performance is the correlation between friction and the Maximum Peak Height ( $S_p$ ) of a surface (Rudzitis, 2013:149).  $S_p$  provides a measure of extreme roughness characteristics by expressing the height of the highest peak of a surface relative to the surface mean line (Reeves, 1985:429). Prominent peaks on surfaces with high  $S_p$  values can have a large impact on friction behavior. These peaks are the initial contact zones between two surfaces, increasing local pressure and causing mechanical interlocking. Higher frictional forces are the result of this increased interaction because the surfaces resist relative motion more strongly. High peaks can also cause more material deformation and wear, which will further affect the frictional properties. On the other hand, surfaces with low  $S_p$  values exhibit smoother contact interactions with less friction and mechanical interlocking due to less pronounced peaks (Bhushan, 1998:1). Friction can be optimized for a variety of uses by adjusting  $S_p$ , ensuring that surfaces have the appropriate amount of resistance and grip, or effortless, smooth sliding as required. This knowledge is crucial in fields such as materials science, manufacturing and automotive, where accurate surface roughness control can result in longer life, less wear and better performance.

In this study, the smallest  $S_p$  value was chosen as the best value as it was desired to obtain a surface with a smaller coefficient of friction.

### ***Optimization of Laser Processing Parameters Using the Taguchi Method***

The Taguchi Optimization method, a proven reliable method, was used in the study to save on materials, analysis, and time (Canel et al., 2012:2347) (Canel et al., 2019:105714). According to the Taguchi optimization method, optimal parameters can be obtained with fewer trials arranged according to a specific array (Hisam et al., 2024:365). Furthermore, the ANOVA analysis performed can also calculate the extent to which each parameter affects the result (Henson, 2015:477).

The goal of this section of the study was to develop a surface with a reduced coefficient of friction by achieving the smallest  $S_p$  value (Xie and Williams, 1996:21). The "smaller-is-better" principle found in Eqn. 8 was used for this (Sood et al., 2010:135).

$$S/N_i = -10\log_{10} \left[ \frac{1}{n} \sum_{i=1}^n y_{ij}^2 \right] \quad (8)$$

The Maximum Peak Height Along the Surface ( $S_p$ ) values obtained through the examination of the topographies of all laser-treated surfaces, as well as the corresponding Signal-to-Noise (S/N) ratios calculated using these values, are presented in Table 1.

Table 1: Maximum Peak Height along the Surface ( $S_p$ ) and S/N values for all experiments.

	Pattern Type	Scanned Area Rate (%)	Power (W)	$S_p$	S/N
1	Square	80	40	98.90	-39.90
2	Square	60	60	112.00	-40.98
3	Square	40	80	89.30	-39.02
4	Square	20	100	69.10	-36.79
5	Diamond	80	60	184.00	-45.30
6	Diamond	60	40	61.80	-35.82
7	Diamond	40	100	163.00	-44.24
8	Diamond	20	80	155.00	-43.81
9	Hexagon	80	80	855.00	-58.64
10	Hexagon	60	100	351.00	-50.91
11	Hexagon	40	40	121.00	-41.66
12	Hexagon	20	60	161.00	-44.14
13	Circle	80	100	476.00	-53.55
14	Circle	60	80	146.00	-43.29
15	Circle	40	60	61.00	-35.71
16	Circle	20	40	97.80	-39.81

Statistical reliability was tested by calculating the total sum of squares. The ANOVA results are provided in Table 2. The highest levels obtained were "Level 1-(Square)" for pattern type, "Level 4-(20%)" for scan area ratio, and "Level 1-(40 W)" for laser power. The expected S/N and  $S_p$  values for the optimal combination were calculated as "-32.91" and "44.21," respectively.

Table 2: ANOVA table for the Taguchi Method to produce a lower coefficient of friction (higher  $S_p$ ).

Fact.	Levels				Aff. Rate	Opt. Fact.	Opt. Levels
	1.	2.	3.	4.			
Pattern	-39.17	-42.29	-48.83	-43.09	37.52	1	Square
Scanned Area	-49.35	-42.75	-41.64	-41.13	34.03	4	60 %
Power	-39.30	-41.53	-46.19	-46.37	28.45	1	40 W
Average	43.35						
Total					100.0		
Optimum S/N					^		-32.91
Optimum $S_p$							44.21

The most effective parameter for obtaining a surface with a lower coefficient of friction was found to be the pattern type formed on the surface, with a contribution rate of 37.52%. The second most influential parameter was the scanning area, with a contribution rate of 34.43%. Among the parameters examined, the least effective was the laser power, with a contribution rate of 28.45%. The main effect plots for the coefficient of friction are presented in Figure.

### Influence of Laser Processing Parameters on Maximum Peak Height ( $S_p$ )

The impacts of processing factors on the Maximum Peak Height ( $S_p$ ) have been investigated in this phase of the study, as illustrated in Figure 3.

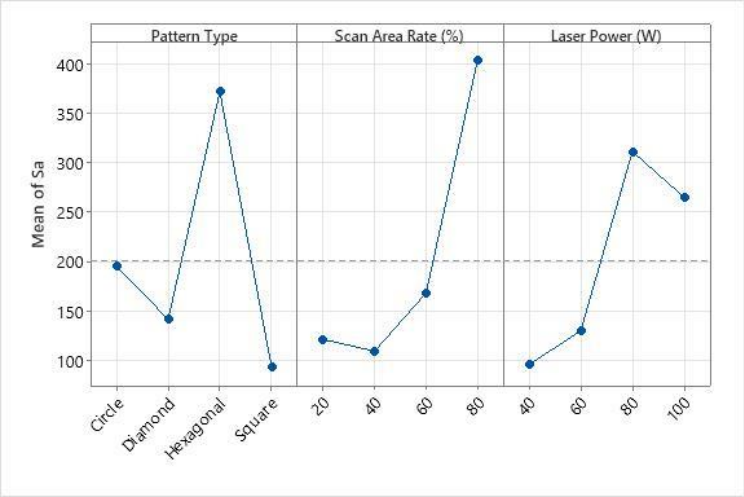


Figure 3: The effects of laser processing parameters on the maximum peak height ( $S_p$ ) are presented in the main effects section.

As shown in Figure 3a, the pattern type with the highest  $S_p$  value is Circular. The lowest  $S_p$  value is obtained in the square pattern type.

In Figure 3b, which examines the effect of scan area on  $S_p$ , a decrease in  $S_p$  value was observed when the scan area was increased from 20% to 40%. When the scan area increased further from 40% to 60%, the  $S_p$  value decreased slightly. However, when the scan area increased from 60% to 80%, the  $S_p$  value increased rapidly and reached its maximum value. The highest  $S_p$  value was obtained at a scan area of 80%, while the lowest  $S_p$  value was obtained at a scan area of 60%.

As can be observed in Figure 3c, which examines how laser power affects  $S_p$ , the  $S_p$  value rose quickly and peaked when the laser power was raised from 40 W to 60 W. The  $S_p$  value dropped almost as much as it had climbed in the preceding range when the laser power was raised from 60 W to 80 W. The  $S_p$  value increased slightly when the laser power was raised from

80 W to 100 W. A laser power of 60 W produced the highest  $S_p$ , whereas a laser power of 40 W produced the lowest  $S_p$  value.

To obtain a more hydrophobic surface, higher  $S_p$  is required. The main effect graph indicates that larger  $S_p$  values, i.e., greater hydrophobicity, were obtained with Circular patterns. It is also observed that a more hydrophobic surface can be achieved when the scan area is 80%. Larger  $S_p$  values were obtained at a laser power of 60 W. Therefore, for a more hydrophobic surface, the Circular pattern type, 80% scan area, and 60 W laser power should be selected.

To obtain a surface with a smaller coefficient of friction, a lower  $S_p$  value is required. The main effect graph shows that smaller  $S_p$  values, i.e., surfaces with lower coefficients of friction, were obtained with square patterns. It is observed that a surface with a smaller coefficient of friction can be achieved when the scan area is 60%. The smallest  $S_p$  values were obtained at a laser power of 40 W. Therefore, for a surface with a smaller coefficient of friction, the square pattern type, 60% scan area, and 40 W laser power should be selected.

To obtain a surface with stronger adhesion, a lower  $S_p$  value is required. The main effect graph shows that smaller  $S_p$  values, i.e., surfaces with stronger adhesion, were obtained with square patterns. It is observed that a surface with stronger adhesion can be achieved when the scan area is 60%. The smallest  $S_p$  values were obtained at a laser power of 40 W. Therefore, to obtain a surface with stronger adhesion, the square pattern type, 60% scan area, and 40 W laser power should be selected.

## REFERENCE

- Abuaf, N., Bunker, R. S., & Lee, C. P. (1998). Effects of surface roughness on heat transfer and aerodynamic performance of turbine airfoils.
- Almeida, E. (2001). Surface treatments and coatings for metals. A general overview. 1. Surface treatments, surface preparation, and the nature of coatings. *Industrial & engineering chemistry research*, 40(1), 3-14.
- Al-Samarai, R. A., & Al-Douri, Y. (2024). The Wear. In *Friction and Wear in Metals* (pp. 1-31). Singapore: Springer Nature Singapore.
- Astakhov, V. P. (2010). Surface integrity—definition and importance in functional performance. In *Surface integrity in machining* (pp. 1-35). London: Springer London.
- Bacakova, L., Filova, E., Parizek, M., Ruml, T., & Svorcik, V. (2011). Modulation of cell adhesion, proliferation and differentiation on materials designed for body implants. *Biotechnology advances*, 29(6), 739-767.

- Baker, H. (1998). Crystal structure of metallic elements. In *Metals Handbook Desk Edition* (pp. 88-95). ASM International.
- Bhushan, B. (1998). Contact mechanics of rough surfaces in tribology: multiple asperity contact. *Tribology letters*, 4(1), 1-35.
- Bigerelle, M., Hagege, B., & El Mansori, M. (2008). Mechanical modelling of micro-scale abrasion in superfinish belt grinding. *Tribology International*, 41(11), 992-1001.
- Blunt, L., & Jiang, X. (2003). Numerical parameters for characterisation of topography. *Advanced Techniques for Assessment Surface Topography*. Oxford, UK: Kogan Page Science, 17-41.
- Bussoli, M., Desai, T., Batani, D., Gakovic, B., & Trtica, M. (2008). Nd: YAG laser interaction with titanium implant surfaces for medical applications. *Radiation Effects & Defects in Solids*, 163(4-6), 349-356.
- Canel, T., Kaya, A. U., & Celik, B. (2012). Parameter optimization of nanosecond laser for microdrilling on PVC by Taguchi method. *Optics & Laser Technology*, 44(8), 2347-2353.
- Canel, T., Zeren, M., & Sinmazçelik, T. (2019). Laser parameters optimization of surface treating of Al 6082-T6 with Taguchi method. *Optics & Laser Technology*, 120, 105714.
- Correa, D. S., Almeida, J. M., Almeida, G. F., Cardoso, M. R., De Boni, L., & Mendonça, C. R. (2017, January). Ultrafast laser pulses for structuring materials at micro/nano scale: From waveguides to superhydrophobic surfaces. In *Photonics* (Vol. 4, No. 1, p. 8). MDPI.
- Cox, P. A. (2010). *Transition metal oxides: an introduction to their electronic structure and properties*. Oxford university press.
- Croll, S. G. (2020). Surface roughness profile and its effect on coating adhesion and corrosion protection: A review. *Progress in organic Coatings*, 148, 105847.
- Devanathan, V. (2021). The Wiedemann-Franz law for electrical and thermal conduction in metals. *Journal of Chennai Academy of Sciences*, 3(1), 1-26.
- Dong, W. P., Sullivan, P. J., & Stout, K. J. (1994). Comprehensive study of parameters for characterising three-dimensional surface topography: III: Parameters for characterising amplitude and some functional properties. *Wear*, 178(1-2), 29-43.
- Dong, Z., Huang, Z., Tang, L., & Lan, H. (2024). Surface modification of biomedical titanium alloy for hard tissue repair and reconstruction. *Surface Engineering*, 40(7-8), 847-862.
- Gadelmawla, E. S., Koura, M. M., Maksoud, T. M., Elewa, I. M., & Soliman, H. H. (2002). Roughness parameters. *Journal of materials processing Technology*, 123(1), 133-145.
- Garg, P. (2023). Urethane-acrylate based Polymeric Superhydrophobic Coatings.
- Hazzan, K. E., Pacella, M., & See, T. L. (2021). Laser processing of hard and ultra-hard materials for micro-machining and surface engineering applications. *Micromachines*, 12(8), 895.
- Henson, R. N. (2015). Analysis of variance (ANOVA). *Brain mapping*, 1, 477-481.
- Hisam, M. W., Dar, A. A., Elrasheed, M. O., Khan, M. S., Gera, R., & Azad, I. (2024). The versatility of the Taguchi method: Optimizing experiments across diverse disciplines. *Journal of Statistical Theory and Applications*, 23(4), 365-389.

- Jena, S., & Swain, B. P. (2025). Surface Passivation and Surface Treatment of Coating Materials. In *Advances in Mechanical Coating: Processing, Properties and Applications* (pp. 337-365). Singapore: Springer Nature Singapore.
- Jin, S., Fischetti, M. V., & Tang, T. W. (2007). Modeling of electron mobility in gated silicon nanowires at room temperature: Surface roughness scattering, dielectric screening, and band nonparabolicity. *Journal of Applied Physics*, 102(8).
- Jing, X., Zhai, Q., Zhang, D., Zheng, S., Jaffery, S. H. I., & Wang, F. (2022). Wettability and frictional properties on zirconia surfaces irradiated by femtosecond laser. *Colloids and Surfaces A: Physicochemical and Engineering Aspects*, 654, 130198.
- Jiang, J. W., Wang, B. S., Wang, J. S., & Park, H. S. (2015). A review on the flexural mode of graphene: lattice dynamics, thermal conduction, thermal expansion, elasticity and nanomechanical resonance. *Journal of Physics: Condensed Matter*, 27(8), 083001.
- John, M., Kalvala, P. R., Misra, M., & Menezes, P. L. (2021). Peening techniques for surface modification: Processes, properties, and applications. *Materials*, 14(14), 3841.
- Kalinowski, A., Radek, N., Orman, Ł., Pietraszek, J., Szczepaniak, M., & Bronček, J. (2023). Laser surface texturing: characteristics and applications. *System Safety: Human-Technical Facility-Environment*, 5(1), 240-248.
- Khalifeh, A. R., Banaraki, A. D., Manesh, H. D., & Banaraki, M. D. (2018). Investigating of the tensile mechanical properties of structural steels at high strain rates. *Materials Science and Engineering: A*, 712, 232-239.
- Khot, M., Chinmya, K. A., Mahesh, S., Suprith, S., & Manish, M. (2025). Selection of Materials, Design and Analysis of FSAE Chassis for Different Engineering Application-A Comprehensive Review. *International Journal of Automotive Science And Technology*, 9(1), 136-157.
- Klemens, P. G., & Williams, R. K. (1986). Thermal conductivity of metals and alloys. *International metals reviews*, 31(1), 197-215.
- Królczyk, G., Kacalak, W., & Wiczorowski, M. (2021). 3D parametric and nonparametric description of surface topography in manufacturing processes. *Materials*, 14(8), 1987.
- Kurup, A., Dhatrak, P., & Khasnis, N. (2021). Surface modification techniques of titanium and titanium alloys for biomedical dental applications: A review. *Materials Today: Proceedings*, 39, 84-90.
- Lang, P. F. (2018). Is a metal “ions in a sea of delocalized electrons?”. *Journal of Chemical Education*, 95(10), 1787-1793.
- Li, H., Zhou, H., Zhang, D., Zhang, P., Zhou, T., & Su, W. (2021). Comparative study of induction quenching and laser surface texturing on anti-wear performance of 40Cr steel. *Journal of Materials Engineering and Performance*, 30(3), 2238-2244.
- Linke, B., & Das, J. (2016). Aesthetics and gloss of ground surfaces: a review on measurement and generation. *Journal of Manufacturing Science and Engineering*, 138(6), 064501.
- Madhuri, A., Parthasarathy, S., & Swain, B. P. (2025). Mechanism of the Wettability of Coating Materials. In *Advances in Mechanical Coating: Processing, Properties and Applications* (pp. 137-163). Singapore: Springer Nature Singapore.



- Magomedov, M. N. (2021). Changes in the properties of iron during BCC–FCC phase transition. *Physics of the Solid State*, 63(2), 215-222.
- McCool, J. I. (1987). Relating profile instrument measurements to the functional performance of rough surfaces. *Journal of tribology*, 109(2), 264-270.
- Menghani, J., & Nandedwalia, P. (2021). Wear and corrosion of wind turbines. In *Tribology and Surface Engineering for Industrial Applications* (pp. 115-140). CRC Press.
- Morshed-Behbahani, K., Farhat, Z., & Nasiri, A. (2024). Effect of surface nanocrystallization on wear behavior of steels: a review. *materials*, 17(7), 1618.
- Myshkin, N. K., Grigoriev, A. Y., Chizhik, S. A., Choi, K. Y., & Petrokovets, M. I. (2003). Surface roughness and texture analysis in microscale. *Wear*, 254(10), 1001-1009.
- Onu, P., & Stella, M. (2024, April). An overview on impact of surface roughness on tribological behaviour. In *2024 International Conference on Science, Engineering and Business for Driving Sustainable Development Goals (SEB4SDG)* (pp. 1-10). IEEE.
- Okokpujie, I. P., Tartibu, L. K., Musa-Basheer, H. O., & Adeoye, A. O. M. (2024). Effect of coatings on mechanical, corrosion and tribological properties of industrial materials: a comprehensive review. *Journal of Bio-and Tribo-Corrosion*, 10(1), 2.
- Orgeldinger, C., Seynstahl, A., Rosnitschek, T., & Tremmel, S. (2023). Surface properties and tribological behavior of additively manufactured components: a systematic review. *Lubricants*, 11(6), 257.
- Osterloo, M. M., Hamilton, V. E., & Anderson, F. S. (2012). A laboratory study of the effects of roughness on the thermal infrared spectra of rock surfaces. *Icarus*, 220(2), 404-426.
- Parthasarathy, S., Madhuri, A., & Swain, B. P. (2025). Adhesion and Surface Modification of Coating Materials. In *Advances in Mechanical Coating: Processing, Properties and Applications* (pp. 109-136). Singapore: Springer Nature Singapore.
- Pawlus, P., Reizer, R., & Wieczorowski, M. (2022). Parametric characterization of machined textured surfaces. *Materials*, 16(1), 163.
- Priest, M., & Taylor, C. M. (2000). Automobile engine tribology—approaching the surface. *Wear*, 241(2), 193-203.
- Qian, W., Wang, Y., Liu, K., Yin, X., He, X., & Xie, L. (2023). Experimental study on the effect of shot peening and re-shot peening on the residual stress distribution and fatigue life of 20CrMnTi. *Coatings*, 13(7), 1210.
- Quinn, J. J., & Yi, K. S. (2018). Free electron theory of metals. In *Solid State Physics: Principles and Modern Applications* (pp. 83-112). Cham: Springer International Publishing.
- Rajab, F. H., Liauw, C. M., Benson, P. S., Li, L., & Whitehead, K. A. (2017). Production of hybrid macro/micro/nano surface structures on Ti6Al4V surfaces by picosecond laser surface texturing and their antifouling characteristics. *Colloids and surfaces B: biointerfaces*, 160, 688-696.
- Reeves, M. J. (1985, December). Rock surface roughness and frictional strength. In *International Journal of Rock Mechanics and Mining Sciences & Geomechanics Abstracts* (Vol. 22, No. 6, pp. 429-442). Pergamon.

- Roodgari, M. R., Jamaati, R., & Aval, H. J. (2020). Microstructure and mechanical properties of IF/St52 steel composite produced by friction stir lap welding. *Materials Science and Engineering: A*, 772, 138775.
- Roy, N. (2018). Study on Laser Beam Micro-Machining with Different Assisted Medium.
- Rösler, J., Harders, H., & Bäker, M. (2007). *Mechanical behaviour of engineering materials: metals, ceramics, polymers, and composites*. Springer Science & Business Media.
- Rudzitis, J., Avisane, A., & Springis, G. (2013). Statistics of roughness peak height of friction surface. *Rigas Tehniskas Universitates Zinatniskie Raksti*, 35, 149.
- Sahay, C., & Ghosh, S. (2018, June). Understanding surface quality: beyond average roughness (Ra). In *2018 ASEE Annual Conference & Exposition*.
- Schlegel, J. (2023). *The World of Steel* (pp. 45-49). Wiesbaden: Springer.
- Sioshansi, P., & Tobin, E. J. (1996). Surface treatment of biomaterials by ion beam processes. *Surface and Coatings Technology*, 83(1-3), 175-182.
- Sólyom, J. (2009). Free-electron model of metals. In *Fundamentals of the Physics of Solids: Volume 2: Electronic Properties* (pp. 1-76). Berlin, Heidelberg: Springer Berlin Heidelberg.
- Sood, A. K., Ohdar, R. K., & Mahapatra, S. S. (2010). Parametric appraisal of fused deposition modelling process using the grey Taguchi method. *Proceedings of the Institution of Mechanical Engineers, Part B: Journal of Engineering Manufacture*, 224(1), 135-145.
- Stoian, R., & Colombier, J. P. (2020). Advances in ultrafast laser structuring of materials at the nanoscale. *Nanophotonics*, 9(16), 4665-4688.
- Sudeep, U., Tandon, N., & Pandey, R. K. (2015). Performance of lubricated rolling/sliding concentrated contacts with surface textures: a review. *Journal of Tribology*, 137(3), 031501.
- Swain, S., & Rautray, T. R. (2020). Effect of surface roughness on titanium medical implants. In *Nanostructured Materials and their applications* (pp. 55-80). Singapore: Springer Singapore.
- Thakur, A., Kumar, A., Kaya, S., Marzouki, R., Zhang, F., & Guo, L. (2022). Recent advancements in surface modification, characterization and functionalization for enhancing the biocompatibility and corrosion resistance of biomedical implants. *Coatings*, 12(10), 1459.
- Thomas, T. R. (1981). Characterization of surface roughness. *Precision Engineering*, 3(2), 97-104.
- Toyserkani, E., & Rasti, N. (2015). Ultrashort pulsed laser surface texturing. *Laser surface engineering*, 441-453.
- Ulaeto, S. B., Ravi, R. P., Udoh, I. I., Mathew, G. M., & Rajan, T. P. D. (2023). Polymer-based coating for steel protection, highlighting metal-organic framework as functional actives: a review. *Corrosion and Materials Degradation*, 4(2), 284-316.
- Wang, Y., Azam, A., Zhang, G., Dorgham, A., Liu, Y., Wilson, M. C., & Neville, A. (2022). Understanding the mechanism of load-carrying capacity between parallel rough surfaces through a deterministic mixed lubrication model. *Lubricants*, 10(1), 12.

- Wang, Y., Xie, F., Ma, S., & Dong, L. (2017). Review of surface profile measurement techniques based on optical interferometry. *Optics and Lasers in Engineering*, 93, 164-170.
- Xie, Y., & Williams, J. A. (1996). The prediction of friction and wear when a soft surface slides against a harder rough surface. *Wear*, 196(1-2), 21-34.
- Ye, C., Zhang, C., Zhao, J., & Dong, Y. (2021). Effects of post-processing on the surface finish, porosity, residual stresses, and fatigue performance of additive manufactured metals: a review. *Journal of Materials Engineering and Performance*, 30(9), 6407-6425.
- Zaki, S., Zhang, N., & Gilchrist, M. D. (2022). Electropolishing and shaping of micro-scale metallic features. *Micromachines*, 13(3), 468.
- Zhang, J. Z., & Noguez, C. (2008). Plasmonic optical properties and applications of metal nanostructures. *Plasmonics*, 3(4), 127-150.
- Zidane, I. F., Saqr, K. M., Swadener, G., Ma, X., & Shehadeh, M. F. (2016). On the role of surface roughness in the aerodynamic performance and energy conversion of horizontal wind turbine blades: a review. *International journal of energy research*, 40(15), 2054-2077.



# **Comparative and Hybrid Application of Ftir and HPLC-Rid For Sugar Analysis in Sugar-Free Products**

**Amırhosein OROUJIEGBAL<sup>1</sup>**  
**Yücel KADIOĞLU<sup>1\*</sup>**

- 1- Amırhosein OROUJIEGBAL; Atatürk Üniversitesi Sağlık Bilimleri Enstitüsü Eczacılık Analitik Kimya Anabilim Dalı Yüksek Lisans Öğrencisi orujiemir@gmail.com ORCID No: 0009-0001-1106-1808
- 2- \* Sorumlu Yazar: Prof. Dr. Yücel KADIOĞLU.;Atatürk Üniversitesi, Eczacılık Fakültesi Temel Eczacılık Bilimleri Bölümü Analitik Kimya Anabilim Dalı. [yucel@atauni.edu.tr](mailto:yucel@atauni.edu.tr) ORCID No 0000-0001-6590-7306

## ABSTRACT

The growing prevalence of diabetes and the rapid expansion of “sugar-free” markets have amplified the importance of reliable sugar analysis. Ensuring accurate determination of mono- and disaccharides, as well as sugar alcohols, is essential for consumer safety and compliance with international standards such as Codex Alimentarius, AOAC methods, and ICH Q2 validation guidelines. Within this framework, two approaches stand out for their complementary strengths: Fourier Transform Infrared (FTIR) spectroscopy and High Performance Liquid Chromatography with Refractive Index Detection (HPLC-RID).

FTIR, particularly in ATR mode, provides rapid, non-destructive screening requiring minimal sample preparation. When combined with multivariate chemometric techniques such as PCA and PLS, it enables discrimination between authentic and adulterated products, as widely demonstrated in honey and other food matrices. In contrast, HPLC-RID remains the regulatory reference method, offering precise quantification and robust validation parameters (LOD, LOQ, accuracy, precision). Although more resource-intensive, it ensures reliable compliance with pharmaceutical and food quality standards.

This chapter critically reviews the role of FTIR and HPLC-RID in sugar and sugar alcohol analysis, summarizing key literature on honey, dairy, beverages, and confectionery. It emphasizes their comparative advantages, discusses existing gaps—particularly the limited quantitative validation of FTIR—and introduces hybrid workflows where rapid FTIR screening is integrated with HPLC confirmation. The future outlook highlights the rise of data fusion, machine learning, and chemometric modeling, positioning hybrid analytical strategies as powerful solutions to bridge scientific, industrial, and regulatory needs in the field of pharmaceutical and food analysis.

*Keywords – Honey, FTIR, HPLC-RID, Chemometrics.*

---

## INTRODUCTION

Diabetes mellitus represents one of the fastest growing chronic diseases worldwide, with global prevalence expected to reach more than 700 million people by 2045 (Kowaltowski & Abdulkader, 2020). Beyond its clinical and economic consequences, diabetes has also reshaped the food and pharmaceutical markets, driving a massive demand for sugar free and reduced sugar products (Tarko et al., 2021; Zhang et al., 2024). These include not only beverages, confectionery, and dairy alternatives but also pharmaceutical formulations such as syrups, lozenges, chewable tablets, and nutraceutical supplements (Piergiovanni et al., 2018). In this context, reliable

assessment of sugar content is vital for two reasons: ensuring consumer and patient safety, and maintaining regulatory compliance with health and trade standards.

Product labels claiming “sugar free” often guide consumer behavior. However, discrepancies between labeling and actual sugar content have been reported in multiple studies, raising concerns about food authenticity and pharmaceutical quality (Piergiovanni et al., 2018; Tarko et al., 2021). Accurate determination of both mono- and disaccharides (glucose, fructose, sucrose) and sugar alcohols (sorbitol, mannitol, xylitol, maltitol) is therefore a critical task for analysts and manufacturers (Piergiovanni et al., 2018; Kowaltowski & Abdulkader, 2020). The analytical challenge is substantial: sugar alcohols share overlapping physicochemical properties with natural sugars (Al-Lafi and Al-Naser, 2022), while food and drug matrices contain excipients and additives that complicate separation or spectral clarity (Zarzo et al., 2023; Saji et al., 2024).

Several international frameworks attempt to address these issues. AOAC methods provide reference procedures for sugar quantification in food (Latimer, 2023), Codex Alimentarius defines minimum standards for honey composition (WHO, 2025), and the ICH Q2 guideline specifies how analytical methods must be validated in terms of accuracy, precision, linearity, detection limits, and quantification limits (ICH, 1995). Nevertheless, a critical gap remains: no single methodology simultaneously fulfils the need for rapid screening, broad sugar/alcohol coverage, and full regulatory validation across complex matrices.

Within this context, two approaches stand out for their complementary strengths: Fourier Transform Infrared (FTIR) spectroscopy and High Performance Liquid Chromatography with Refractive Index Detection (HPL-RID). FTIR, particularly in ATR mode, is valued for minimal sample preparation and rapid spectral acquisition, facilitating multivariate chemometric modeling (Anjos et al., 2015; Basar and Ozdemir, 2018; Antonova et al., 2021; Xagoraris et al., 2021; Bunaciu and Aboul-Enein, 2022; Roberts and Kittredge, 2022; Cardenas-Escudero et al., 2023; Damto et al., 2023; El Hajj and Estephan, 2024; Prata and Da Costa, 2024). HPLC-RID, in contrast, remains the regulatory benchmark, offering validated quantitative accuracy across diverse food and pharmaceutical applications (Kamal and Klein, 2011; Fantoni et al., 2012; Cwikova et al., 2015; Alghamdi et al., 2021; Bhujbal and Pardesi, 2021; Carvalho et al., 2023; Divakar and Vijaykumar, 2023; Egido et al., 2024; Sathianarayanan et al., 2024; Lupu et al., 2025). This chapter therefore aims to critically compare these two approaches, highlight their respective strengths and limitations, and discuss emerging hybrid workflows, including chemometrics and machine learning, as forward looking strategies for sugar analysis (Wu et al., 2013; Rodionova et al., 2024).

## **Chemistry of Sugars and Sugar Alcohols**

Sugars and sugar alcohols form a diverse class of carbohydrates of great importance in both nutritional and pharmaceutical sciences. Structurally, monosaccharides such as glucose and fructose, and disaccharides such as sucrose, are the most common natural sweeteners. Due to their rapid intestinal absorption and direct entry into glycolytic metabolism, they contribute strongly to elevated postprandial glycemia—a concern of particular relevance for diabetic patients ( Kowaltowski & Abdulkader, 2020).

In contrast, sugar alcohols (polyols) such as sorbitol, mannitol, xylitol, maltitol, erythritol, and lactitol are chemically reduced forms of sugars that provide sweetness with lower caloric value and reduced glycemic impact ( Piergiovanni et al., 2018; Kowaltowski & Abdulkader, 2020). Polyols are absorbed slowly or incompletely in the small intestine and may undergo partial fermentation in the colon, resulting in attenuated blood glucose excursions compared to glucose or sucrose (Kowaltowski & Abdulkader, 2020). Clinically, this makes them valuable sugar substitutes for “sugar-free” labeling. However, excessive intake can lead to gastrointestinal adverse effects, highlighting the need for accurate quantification across food and pharmaceutical matrices (Piergiovanni et al., 2018; Tarko et al., 2021).

From an analytical chemistry perspective, both sugars and sugar alcohols present challenges: their structures are highly polar, neutral, and do not contain strong chromophoric groups. Therefore, conventional UV–Vis. Spectroscopy is unsuitable for direct quantification (ICH, 1995). This limitation necessitates the use of methods such as HPLC-RID, which detects refractive index changes in aqueous systems, and FTIR-ATR spectroscopy, which exploits hydroxyl group vibrational modes to discriminate between sugars. As a result, reliable identification and quantification of sugars and polyols has become a central issue in food authenticity, pharmaceutical excipient control, and regulatory compliance (Tarko et al., 2021; Latimer, 2023; WHO, 2025).Major dietary sugars and sugar alcohols are given Table 1.



Table 1. Overview of major dietary sugars and sugar alcohols relevant to “sugar-free” labelling

Compound	Chemical Formula	Class	Approx. Glycemic Index (GI)*	Metabolic/Clinical Relevance	Main Occurrence (Food/Pharmaceutical)
Glucose	C <sub>6</sub> H <sub>12</sub> O <sub>6</sub>	Monosaccharide	100	Rapid absorption; elevates blood sugar quickly; critical in diabetes	Fruits, honey, syrups; IV fluids
Fructose	C <sub>6</sub> H <sub>12</sub> O <sub>6</sub>	Monosaccharide	~19	Low GI; excessive intake → hepatic lipogenesis risk	Fruits, honey, processed foods
Sucrose	C <sub>12</sub> H <sub>22</sub> O <sub>11</sub>	Disaccharide	~65	Hydrolysed to glucose + fructose; high caloric load	Cane sugar, confectionery, syrups
Sorbitol	C <sub>6</sub> H <sub>14</sub> O <sub>6</sub>	Polyol	~9	Slowly absorbed; laxative effect if consumed in excess	Sugar-free gums, syrups, chewable tablets
Mannitol	C <sub>6</sub> H <sub>14</sub> O <sub>6</sub>	Polyol	~2	Minimal glycemic effect; osmotic diuretic in medicine	Pharmaceuticals (IV diuretic), sugar-free confectionery
Xylitol	C <sub>5</sub> H <sub>12</sub> O <sub>5</sub>	Polyol	~7	Anti-cariogenic; promotes dental health	Sugar-free gums, oral care products
Maltitol	C <sub>12</sub> H <sub>24</sub> O <sub>11</sub>	Polyol	~35	Similar sweetness to sucrose; potential laxative effect	Sugar-free chocolates, candies
Erythritol	C <sub>4</sub> H <sub>10</sub> O <sub>4</sub>	Polyol	~0	Non-caloric; absorbed but excreted unchanged; well tolerated	Sugar-free beverages, natural sweeteners, pharmaceutical excipient (4)
Lactitol	C <sub>12</sub> H <sub>24</sub> O <sub>11</sub>	Polyol	~6	Low energy; approved bulk sweetener; mild laxative in high doses	Baked goods, sugar-free ice creams, pharmaceutical formulations

### Analytical Challenges in Sugar-Free Products

Accurate analysis of sugars in products marketed as “sugar free” or “no added sugar” remains highly challenging. Unlike aqueous standards of pure glucose or fructose, real commercial matrices are chemically complex. Foods such as chocolates, dairy desserts, and confectionery often combine

proteins, lipids, polyphenols, and starches that obscure analytical signals (Tarko et al., 2021; Zhang et al., 2024). Similarly, in pharmaceutical products such as syrups and chewable formulations, polyols like sorbitol and mannitol are mixed with flavorants, colorants, and excipients, producing similar interferences (Piergiovanni et al., 2018). These matrix components can suppress or overlap infrared absorption bands in FTIR and, in chromatography, result in co elution or reduced resolution of sugars and sugar alcohols (Al-Lafi and Al-Naser, 2022; Saji et al., 2024).

A second obstacle arises from the structural similarity of sugars and polyols. Monosaccharides (glucose, fructose) and sugar alcohols (sorbitol, mannitol) all share highly polar, hydroxyl rich structures. For example, in sugar free chocolates, maltitol often overlaps with sucrose peaks, and in diet soft drinks mixtures of sorbitol and sucralose complicate spectral interpretation (Zarzo et al., 2023; Saji et al., 2024). Even in pharmaceutical syrups, where sorbitol is a common excipient, differentiating between excipient polyols and active sugar residues remains analytically problematic (Piergiovanni et al., 2018).

Regulatory expectations impose an additional layer of complexity. Frameworks such as ICH Q2 (1995), AOAC Official Methods (Latimer, 2023), and Codex Alimentarius (WHO, 2025) require strict validation of parameters including accuracy, precision, reproducibility, linearity, limit of detection (LOD), and limit of quantification (LOQ). However, while many rapid FTIR based screening methods show promising results, they frequently lack inter laboratory reproducibility and struggle to meet the detection limits required for official compliance (Tarko et al., 2021, Zhang et al., 2024).

Finally, practical limitations cannot be overlooked. HPLC RID provides excellent quantitative precision, but requires costly infrastructure, highly purified solvents, and extended runtime for each sample. FTIR ATR, in contrast, is rapid, non destructive, and allows high throughput, yet cannot independently achieve validated quantitative accuracy without chemometric calibration (Tarko et al., 2021, Zhang et al., 2024). At present, no single method fulfills both rapid screening capacity and full regulatory compliance across diverse food and pharmaceutical matrices—a gap that strongly motivates the hybrid approaches examined later in this chapter.

### **FTIR Spectroscopy for Sugar Analysis**

Fourier Transform Infrared (FTIR) spectroscopy has become a well established approach for sugar analysis, capitalizing on the vibrational transitions of functional groups. Carbohydrates exhibit distinctive absorption bands in the O–H stretching ( $3600\text{--}3000\text{ cm}^{-1}$ ) and C–O stretching region ( $1200\text{--}900\text{ cm}^{-1}$ ), forming unique spectral fingerprints (Basar and Ozdemir, 2018). When operated in Attenuated Total Reflectance (ATR) mode, FTIR offers minimal sample preparation and direct surface measurements, making

it highly suitable for complex matrices where rapid screening is essential (Anjos et al., 2015; Prata and Da Costa, 2024).

The majority of published applications have focused on honey, due to its economic importance and susceptibility to sugar syrup adulteration. FTIR combined with chemometric tools such as PLS and PCR has successfully identified adulteration with beet sugar and corn syrup (Basar and Ozdemir, 2018), and C3 plant syrups (Xagoraris et al., 2021), often at low contamination levels. Other studies have used FTIR to quantify major sugars in honey with HPLC calibration (Anjos et al., 2015), to differentiate floral origins (Bunaciu and Aboul-Enein, 2022; Roberts and Kittredge, 2022; Damto et al., 2023), and to detect heat treatment (Cardenas-Escudero et al., 2023). The high throughput and non destructive nature of FTIR thus make it a powerful first line authentication tool (Antonova et al., 2021; Prata and Da Costa, 2024).

While honey dominates the literature, FTIR applications have also been reported for dairy products (lactose and sweeteners in milk powders) (Saji et al., 2024) and confectionery (maltitol and xylitol profiling in chocolates) (Zarzo et al., 2023). In the pharmaceutical sector, FTIR has occasionally been used for quality control of excipients such as sorbitol and mannitol powders (Piergiovanni et al., 2018), though such applications remain relatively limited. Examples of studies on honey and sugar analysis using the FTIR spectroscopy method in the literature are given in Table 2.

The method's strengths lie in speed, non destructive measurement, and cost effectiveness. However, interpretation faces difficulties due to overlapping absorption bands among sugars and polyols (Antonova et al., 2021). Furthermore, the reliability of FTIR as a quantitative tool is highly dependent on chemometric calibration models. Partial Least Squares (PLS) regression and Principal Component Analysis (PCA) are frequently applied to compensate for signal overlap, but the robustness of these models is often dataset specific and does not always transfer successfully between different instruments or laboratories (Tarko et al., 2021; Zhang et al., 2024). Consequently, FTIR tends to serve best as a screening method, with quantification validated against established chromatographic techniques such as HPLC RID (Anjos et al., 2015).

Table 2. Selected Applications of FTIR Spectroscopy in Sugar and Honey Analysis

Year	Application / Sample	FTIR Mode& Range	Chemometric Tool(s)	Key Findings	Reference
2018	Honey adulteration (beet & corn syrups)	ATR, 4000–600 cm <sup>-1</sup>	Genetic Algorithm + PLS	Detected low-level adulteration with high accuracy	(Basar and Ozdemir, 2018)
2015	Honey (quantification of fructose, glucose, sucrose with HPLC calibration)	ATR, 4000–600 cm <sup>-1</sup>	Calibration vs HPLC	Quantitative sugar measurement achieved with strong correlation	(Anjos et al., 2015)
2021	Honey botanical authentication (88 monofloral samples)	ATR, 4000–600 cm <sup>-1</sup>	PCA, PLS	Successful floral origin discrimination and sugar profiling	(Damto et al., 2023)
2023	Adulteration with C3-plant sugars	ATR, 4000–600 cm <sup>-1</sup>	PCA, PLS	Reliable detection across diverse adulterant sources	(Xagoraris et al., 2021)
2021	Heat-treatment detection in honey	FTIR	Spectral fingerprint monitoring	Identified thermal modification of sugar peaks	(Cardenas -Escudero et al., 2023)
2022	Honey adulteration detection (minimal prep)	ATR, 4000–600 cm <sup>-1</sup>	PCA, PLS	Rapid flagging of adulterated vs authentic honey	(Antonava et al., 2021)
2022	Floral origin discrimination (honey types)	FTIR	PCA, HCA	Clear clustering of honeys by botanical source	(Roberts and Kittredge,

					2022)
2025	Commercial honey profiling	ATR-FTIR direct	PCA, HCA	Differentiated commercial honeys based on sugar spectral patterns	(Bunaciu and Aboul-Enein, 2022)
2024	Review of vibrational spectroscopy (FTIR, NIR, Raman) in honey authentication	ATR and other vibrational modes summarised (general 4000–600 cm <sup>-1</sup> region covered)	PCA, PLS, overview of machine learning approaches	Identified FTIR and related vibrational methods as rapid, non-destructive, first-line tools for honey authenticity; summarised developments, challenges, and future perspectives	(Prata and Da Costa, 2024)
2024	Honey	670-IR spectrometer 375-700 cm <sup>-1</sup>	IR, Chemometric	PCA, PLS-R, SNIP	(El Hajj and Estephan, 2024)

---

### HPLC-RID for Sugar Analysis

High-Performance Liquid Chromatography with Refractive Index Detection (HPLC-RID) is regarded as the gold standard for sugar quantification in both food and pharmaceutical products (Alghamdi et al., 2020). Unlike spectroscopic methods, HPLC provides a true separation of analytes based on interactions with the stationary phase, while RID detects the universal refractive index difference between solute and solvent. This is particularly important because sugars and polyols lack chromophores for UV detection. Ion-exchange columns—especially Ca<sup>2+</sup> and Pb<sup>2+</sup> loaded stationary phases—are widely applied in sugar separations (Carvalho et al., 2023). RID thus enables quantification of glucose, fructose, sucrose, and sugar alcohols in diverse matrices (Alghamdi et al., 2020; Lupu et al., 2025).

A key limitation of RID detection, however, is its sensitivity to temperature changes, flow rate fluctuations, and incompatibility with gradient elution due to refractive index mismatch (Divakar and Vijaykumar,

2023). This restricts flexibility in method development compared to UV or MS detectors, while baseline drift and relatively low sensitivity may affect long-term reproducibility (Egido et al., 2024). Nonetheless, under isocratic conditions, RID offers robust quantification across a wide range of sugars and alcohols.

Although honey has been the dominant model in published literature (Kamal and Klein, 2011; Fantoni et al., 2012; Cwikova et al., 2015; Alghamdi et al., 2021; Bhujbal and Pardesi, 2021; Carvalho et al., 2023; Divakar and Vijaykumar, 2023; Egido et al., 2024; Sathianarayanan et al., 2024; Lupu et al., 2025), HPLC-RID has also been applied to determine the sugar composition of soft drinks, dairy products, and sugar-free confectionery (Al-Lafi and AlNaser, 2022; Zarzo et al., 2023). In pharmaceutical analysis, RID is routinely used for quantification of excipient polyols such as sorbitol and mannitol in syrups, chewable tablets, and intravenous formulations (Piergiovanni et al., 2018). This reflects its broad role in both food authenticity testing and drug quality control.

The main strengths of HPLC-RID lie in its validated accuracy, quantitative reproducibility, suitability for complex sugar mixtures, and acceptance in regulatory frameworks (Latimer, 2023; WHO, 2025). This has made HPLC-RID indispensable for confirmatory analysis, particularly where regulatory compliance is required. Limitations include lengthy runtime per sample, solvent and consumable costs, and the need for stringent control of column temperature. Moreover, while RID offers near-universal detection, it cannot achieve the same detection limits as MS-based detectors. For these reasons, HPLC-RID remains optimal for confirmatory quantification but is less suitable for large-scale rapid screening, supporting the complementary role of FTIR for high-throughput pre-screening. Examples of studies on honey and sugar analysis using the HPLC-RID method in the literature are given in Table 3.

Table 3. Selected Applications of HPLC-RID for Honey and Sugar Analysis

Year	Application / Sample	Column/Detection	Analytes	Key Findings	Reference
2020	Honey sugars + pesticide residues	HPLC-RID + confirmatory MS	Sugar profile + pesticides	Simultaneous sugar analysis and pesticide detection	(Alghamdi et al., 2021)
2025	Comprehensive honey sugar study	HPLC-DAD/RID	Glucose, Fructose, Maltose, Sucrose	Broader validation and expanded sugar profiling accuracy	(Lupu et al., 2025)
2012	Honey compositional analysis by HPLC	Agilent HPLC-RID	Glucose, Fructose, Sucrose + maltose, Melezitose	Provided reliable sugar profile; focused on Agilent instrument performance	(Fantoni et al., 2012)
2010	Honey sugars (fructose, glucose)	Ion-exchange column, RID	Glucose, Fructose	First validated protocol for honey sugar quantification	(Kamal and Klein, 2011)
2024	Honey syrup adulteration	HPLC-UV/RID	Native sugars + syrups	Proved RID efficiency in detecting syrup adulteration	(Egido et al., 2024)
2023	Regional honey sugar study	HPLC-RID	Glucose, Fructose, Maltose	Compared sugar variability among honey types	(Divakar and Vijaykumar, 2023)
2021	Honey adulteration analysis	HPLC-RID	Authentic vs adulterated honeys	Detection of sugar syrup adulteration	(Bhujbal and Pardesi, 2021)
2015	The collected honey from Local beekeepers and regular shopping	HPLC- RID	Glucose, Fructose, Sucrose	Showed reproducibility in commercial honey QC	(Cwikova et al., 2015)
2024	The collected honey from local markets	HPLC-RID	Glucose, Fructose	The ratio of fructose to glucose in these honey samples was in the range of 1.0 to 1.3	(Sathianarayanan et al., 2024)
2023	Screening sugars for adulteration	HPLC-RID	Natural and added sugars	Sugar fingerprints used to detect adulteration	(Carvalho et al., 2023)

### Comparative Analysis: FTIR vs HPLC-RID

The choice between FTIR and HPLC-RID for sugar analysis depends on analytical objectives, available resources, and regulatory context. FTIR spectroscopy offers fast, non-destructive screening with minimal sample

preparation. When combined with chemometric modelling (PCA, PLS), it has demonstrated impressive sensitivity, for example detecting honey adulteration with corn syrup at levels as low as 5–10% w/w (Basar and Ozdemir, 2018). This makes FTIR a practical solution for high-throughput adulteration detection and preliminary fingerprinting (Anjos et al., 2015; Xagoraris et al., 2021). However, its quantification accuracy remains limited, as overlapping sugar absorption bands demand strong model calibration, and FTIR methods alone currently hold no regulatory approval for industry quality control (Latimer, 2023; WHO, 2025).

In contrast, HPLC-RID represents the regulatory “gold standard” for sugar determination. By physically separating individual sugars, it enables robust quantification even in complex matrices, including glucose, fructose, sucrose, maltose, and polyols. Critically, this method is validated according to ICH Q2 guidelines, ensuring reproducibility in inter-laboratory contexts (ICH, 1995). HPLC-RID is routinely employed in food authenticity testing and also in pharmaceutical quality control, for example in the validated quantification of sorbitol and mannitol excipients in syrups and chewables (Piergiovanni et al., 2018). Its drawbacks include relatively long run times (15–40 minutes per sample), strict requirements for temperature stability, inability to accommodate gradient elution due to detector limitations, and higher costs (often \$20–30 per sample when solvents and consumables are considered) (Carvalho et al., 2023; Divakar and Vijaykumar, 2023).

A side-by-side comparison reinforces this complementarity (Table 4). FTIR excels in speed, affordability, and preliminary screening capabilities, while HPLC-RID remains essential for validation and regulatory acceptance. The combined use of both methods—FTIR for screening, HPLC-RID for confirmation—presents an optimised workflow for sugar analysis, aligning speed with precision and regulatory compliance (Wu et al., 2013; Rodionova et al., 2024).

Comparison of FTIR vs HPLC-RID methods used in sugar analysis is given in Table 4.



Table 4. Comparative Performance of FTIR vs HPLC-RID in Sugar Analysis

Parameter	FTIR (ATR-FTIR)	HPLC-RID
<b>Sample Preparation</b>	Minimal (direct spectra, solids/liquids)	Requires dilution, filtration, degassing
<b>Analysis Time</b>	Seconds to minutes	15–40 minutes per run
<b>Throughput</b>	High (hundreds/day possible)	Moderate (dozens/day)
<b>Sensitivity (LOD/LOQ)</b>	Adulteration detectable at 5–10% w/w with chemometrics (Basar and Ozdemir, 2018)	Low mg/L range achievable for individual sugars (Kamal and Klein, 2011; Carvalho et al., 2023)
<b>Quantitative Accuracy</b>	Limited; depends on calibration vs HPLC	High; fully validated accuracy/precision (ICH, 1995; Latimer, 2023; WHO, 2025)
<b>Chemometrics Dependence</b>	Essential (e.g. PCA, PLS models)	Not required
<b>Matrix Tolerance</b>	Susceptible to overlapping peaks	Improved by physical separation
<b>Cost per Sample</b>	<\$5 (minimal consumables)	\$20–30+ (solvents, columns, maintenance)
<b>Regulatory Acceptance</b>	Experimental; no official approval	Regulatory AOAC & Codex accepted method (8, 9)
<b>Pharma Use Case</b>	Rare; exploratory (sorbitol/mannitol powders)	Routine QC for excipient polyols in syrups/tablets

### Hybrid / Combined Strategies for Sugar Analysis

The comparison of FTIR and HPLC-RID indicates that instead of competing, the two methods are best applied as **complementary tools**. Hybrid strategies aim to combine the rapid, low-cost, high-throughput screening capability of FTIR with the robust and regulatory-accepted quantification power of HPLC-RID. In analytical practice and recent literature, four major models of such integration can be identified: Sequential workflows, Data Fusion, Validation Cross-support, and Parallel application (Tarko et al., 2021; Roberts and Kittredge, 2022; Zhang et al., 2024). Hybrid FTIR–HPLC strategies for sugar and sugar alcohol analysis are given in Table 5.

**Sequential Workflow:** This model is straightforward. ATR-FTIR is employed as a prescreening tool to investigate large sets of “sugar-free” products. Only suspect or anomalous samples are then confirmed by HPLC-RID, which ensures validated quantification (Anjos et al., 2015; Carvalho et al., 2023). This workflow is already echoed in food safety labs, and in pharmaceutical contexts it could reduce unnecessary chromatographic testing of excipient batches, saving both time and resources.

**Data Fusion:** In this approach, FTIR spectral fingerprints are mathematically merged with HPLC-RID quantitative datasets, so FTIR learns predictive accuracy from HPLC. Traditionally, multivariate chemometrics such as PCA, PLS, and HCA dominate these models (Basar and Ozdemir, 2018; Antonova et al., 2021). More recently, advanced machine learning frameworks—including random forests, ensemble learning, and deep neural networks—have also been tested, with promising improvements in transferability and prediction accuracy (Wu et al., 2013; Rodionova et al., 2024). Such fusion has the potential to turn FTIR from a semi-qualitative fingerprint method into a quasi-quantitative predictor of sugar content in foods and pharmaceutical excipients.

**Validation Cross-support:** Another model is to develop FTIR as a quantitative method and validate its performance directly against HPLC-RID results using ICH Q2 and AOAC frameworks (Latimer, 2023; WHO, 2025). For example, honey sugar models calibrated by FTIR and checked against HPLC-RID have shown high correlation (Anjos et al., 2015). In pharmaceutical science, this means FTIR-based screening of sorbitol or mannitol excipients could gain regulatory credibility when consistently validated against HPLC data from the same batches.

**Parallel application:** In certain cases, FTIR and HPLC-RID may be applied in parallel on the same or split sample sets. This approach is less efficient in terms of resources but provides a strong dataset where methods can cross validate each other's results (Bhujbal and Pardesi, 2021; Alghamdi et al., 2020). Parallel analysis is particularly relevant in academic research and regulatory submissions, where evidence strength depends on consistency across multiple platforms.

Collectively, these strategies directly address the analytical gap identified earlier: no current single technique is both rapid and fully regulatory compliant across complex food and pharmaceutical matrices. Hybridisation offers a practical solution, enhancing efficiency while protecting regulatory reliability.

Table 5. Hybrid FTIR–HPLC Strategies for Sugar and Sugar Alcohol Analysis

Strategy	Description	Advantages	Limitations	Key References
<b>Sequential Workflow</b>	FTIR prescreening followed by confirmatory HPLC-RID	Cuts down on HPLC load; cost-efficient; reduces runtime in QC	FTIR remains mainly qualitative/semi-quantitative	(Anjos et al., 2015; Carvalho et al., 2023)
<b>Data Fusion (Chemometrics + AI)</b>	Integrates FTIR spectral data with HPLC quantitative results	Transforms FTIR into a semi-quantitative predictor; improves screening precision with AI models	Dataset-specific; inter-lab transferability still weak	(Wu et al., 2013; Basar and Ozdemir, 2018; Antonova et al., 2021; 11, 16, 31, 32)
<b>Validation Cross-Support</b>	FTIR results benchmarked to HPLC under ICH Q2/AOAC guidelines	Provides regulatory credibility; fit-for-purpose QC in food and pharma batches	Requires dual operation; FTIR not yet officially recognized	(Anjos et al., 2015; Latimer, 2023; WHO, 2025)
<b>Parallel Application</b>	Both methods applied independently for comparison	Direct cross-validation between platforms; strong regulatory evidence	Resource-intensive; lower throughput	(Alghamdi et al., 2020; Bhujbal and Padesi, 2021)

### Future Perspectives & Regulatory Impact

The analytical landscape for sugar and sugar alcohol detection is advancing rapidly. While FTIR spectroscopy and HPLC-RID remain central to current workflows, several emerging technologies are poised to reshape the field. Portable FTIR and NIR spectrometers are increasingly compact and user-friendly, enabling on-site inspection of food products and even point-of-care pharmaceutical syrups or excipient powders (Radionova et al., 2024). Meanwhile, microfluidic and chip-based HPLC systems are being developed, offering reduced run times, minimal solvent usage, and potential integration into automated production environments (Wu et al., 2013).

The incorporation of AI and advanced chemometrics has significantly improved data interpretation, surpassing classical PCA and PLS in pattern recognition, classification, and multi-component prediction. Techniques such as ensemble learning, random forests, and neural networks show promise in enhancing FTIR's predictive capabilities. However, their adoption for regulatory decisions remains a challenge; AI-driven models require extensive validation, inter-laboratory reproducibility testing, and harmonization under frameworks like ICH and AOAC before regulatory acceptance can be achieved (Wu et al., 2013; Radionova et al., 2024).

At the policy level, harmonization between global frameworks remains essential. The ICH Q2 guideline specifies how pharmaceutical methods must be validated (ICH, 1995); the AOAC Official Methods provide standardized

approaches to food sugar analysis (Latimer, 2023); and the Codex Alimentarius establishes composition and authenticity standards for honey and related commodities (WHO, 2025). In addition, agencies such as the U.S. FDA and organizations like ISO publish guidelines relevant to sugar-free labeling, excipient control, and analytical good practices, further shaping international expectations (Table 6).

Looking forward, the integration of AI-supported FTIR screening, miniaturized chromatographic platforms, and harmonized validation frameworks may offer practical steps toward faster yet reliable sugar analysis. While no single innovation alone is sufficient, the parallel development of cutting-edge tools and regulatory acceptance pathways may gradually bridge the persistent gap between analytical efficiency and compliance.

Table 6. Key Regulatory and Validation Frameworks Relevant to Sugar Analysis

Framework / Body	Scope	Validation Parameters / Standards	Relevance to Sugars & Polyols	Reference
ICH Q2 (R1)	Pharmaceutical analytical methods	Accuracy, precision, linearity, LOD, LOQ, robustness	Required validation for drug formulations with sugars & excipients	(ICH, 1995)
AOAC Official Methods	Food analytical chemistry	Standardised validated procedures for sugar profiling	Benchmark for regulatory sugar quantification in foods	(Latimer, 2023)
Codex Alimentarius	Food authenticity & global trade	Composition/authenticity standards (e.g. honey)	Reference for sugar-free labelling & product authenticity	(WHO, 2025)
FDA Guidance for Industry / ISO Standards	Food & pharmaceutical regulatory oversight	Industry guidance on sugar-free labelling, excipient controls, good analytical practice	Frame national & international compliance requirements	(Wu et al., 2013)

## CONCLUSION

The reliable determination of sugars and sugar alcohols remains a central challenge for both food authenticity and pharmaceutical quality control. Throughout this chapter, two key analytical platforms were examined: FTIR spectroscopy and HPLC-RID. Each provides unique advantages but also clear limitations.

FTIR-ATR spectroscopy demonstrates strong value as a rapid screening tool. Its ability to deliver results within seconds with minimal sample preparation, and to handle hundreds of spectra per day, makes it ideal for high-throughput preliminary testing. Yet, spectral overlap between structurally similar sugars restricts stand-alone quantification, and critically, no FTIR-based protocols are currently recognised by regulatory frameworks.

HPLC-RID, by contrast, requires 15–40 minutes per run and incurs higher costs due to solvents and consumables—often \$20–30 per sample. However, it offers validated quantitative accuracy, reproducibility, and full acceptance by ICH Q2, AOAC, and Codex frameworks. HPLC-RID is therefore indispensable for confirmatory analysis, and in pharmaceuticals it is the regulatory method of choice for quantifying excipients such as sorbitol and mannitol in syrups, lozenges, and chewable formulations (Piergiovanni et al., 2018).

Comparative analysis across the chapter highlights a fundamental gap: no single method combines rapid throughput with regulatory-level validation. It is here that hybrid strategies—sequential prescreening, data fusion with chemometrics and AI, validation cross-support, and parallel independent application—offer a path forward. These models balance FTIR efficiency with HPLC robustness, tailoring workflows to both industrial constraints and compliance needs.

Looking ahead, the continued development of AI-driven chemometrics, portable FTIR/NIR devices, and microfluidic HPLC systems, together with global harmonisation of regulatory guidelines, is anticipated to contribute to more practical and reliable workflows. While no immediate universal solution exists, the integration of technological innovation and regulatory validation provides a realistic trajectory toward faster, cost-efficient, and globally accepted sugar analysis.

## REFERENCE

- Alghamdi, B.A., Alshumrani, E.S., Saeed, M.S.B., Rawas, G.M., Alharthi, N.T., Baeshen, M.N., and et al. (2020). Analysis of sugar composition and pesticides using HPLC and GC-MS techniques in honey samples collected from Saudi Arabian markets. *Saudi J Biol Sci.* 27(12), 3720-3726.
- Al-Lafi, A.G., and Al-Naser, I. (2022). Application of 2D-COS-FTIR spectroscopic analysis to milk powder adulteration: Detection of melamine. *J Food Compos Anal*, 113, 104720.
- Anjos, O., Campos, M.G., Ruiz, P.C., and Antunes, P. (2015). Application of FTIR-ATR spectroscopy to the quantification of sugar in honey. *Food Chem*, 169, 218-223.
- Antonova, O., Calvo, J., and Seifert, A. (2021). Rapid detection of thermal treatment of honey by chemometrics-assisted FTIR Spectroscopy. *Foods*, 10(11), 2892.
- Basar, B., and Ozdemir, D. (2018). Determination of honey adulteration with beet sugar and corn syrup using infrared spectroscopy and genetic-algorithm-based multivariate calibration. *J Sci Food Agric*, 98(15), 5616-5624.
- Bhujbal, S.R., and Pardesi, V. (2021). Analysis of sugars in honey using the PerkinElmer Altus HPLC System with RI Detection. *Pharm Scien*, 1(2), 18-24.
- Bunaciu, A.A., and Aboul-Enein, H.Y. (2022). Honey discrimination using Fourier Transform-Infrared Spectroscopy. *Chemistry*, 4(3), 848-54.
- Cardenas-Escudero, J., Galan-Madruga, D., and Caceres, J.O. (2023). FTIR-ATR detection method for emerging C3-plants-derived adulterants in honey: Beet, dates, and carob syrups. *Talanta*, 265, 124768.
- Carvalho, M., Köhler, D., Mantani, A., and Acworth, Ian-N. (2023). Simple screening of natural sugars for detecting adulteration in honey. *Food Analysis. ThermoFisher Scientific*. <https://documents.thermofisher.com/TFS-Assets/CMD/Application-Notes/an-000916-hplc-vanquish-core-qc-analysis-honey-an000916-en.pdf>
- Cwikova, O., Pavlíková, H., Ansorgová, A. (2015). Detection of honey adulteration using HPLC method. *Potravinarstvo* 9(1), 388-392.
- Damto, T., Zewdu, A., and Birhanu, T. (2023). Application of Fourier transform infrared (FT-IR) spectroscopy and multivariate analysis for detection of adulteration in honey markets in Ethiopia. *Curr Res Food Sci*, 7, 100565.
- Divakar, S., and Vijaykumar, K. (2023) Determination of sugar content in honey by HPLC Method Kalaburagi, Karnataka, India. *Biol Forum – An Inter J*, 15(6), 864-869.
- Egido, C., Saurina, J., Sentellas, S., and Nunez, O. (2024). Honey fraud detection based on sugar syrup adulterations by HPLC-UV fingerprinting and chemometrics. *Food Chem*, 436,137758.

El Hajj, R., and Estephan, N. (2024). Advances in infrared spectroscopy and chemometrics for honey analysis: a comprehensive review. *Crit Rev Food Sci Nutr*, 12, 1-14. DOI: 10.1080/10408398.2024.2439055.

Fantoni, E., Ball, S., Lyod, L., and Mapp, K. (2012). Honey compositional analysis by HPLC. Agilent Technologies, Inc. . Published in USA. <https://www.agilent.com/cs/library/applications/SI-01920.pdf>

ICH Topic Q2 (R1), Validation of analytical procedures: Text and Methodology. Note For Guidance on Validation of Analytical Procedures: Text And Methodology (CPMP/ICH/381/95) 1995.

Kamal, M.A., and Klein, P. (2011). Determination of sugars in honey by liquid chromatography. *Saudi J Biol Sci*, 18(1), 17-21.

Kowaltowski, A., and Abdulkader, F. (2020). Carbohydrate Metabolism. In: *Where Does All That Food Go?*. Copernicus, Cham. [https://doi.org/10.1007/978-3-030-50968-2\\_3](https://doi.org/10.1007/978-3-030-50968-2_3)

Latimer, G.V. (2023). Official Methods of Analysis of AOAC INTERNATIONAL (22nd edition), <https://doi.org/10.1093/9780197610145.001.0001>

Lupu, D., Sammani, M.S., Palacio, E., Hancu, G., and Ferrer, L. (2025). Comprehensive honey analysis: A novel HPLC-DAD method for hydroxymethyl furfural quantification and quality evaluation via diastase activity and sugar profile determination. *J Food Comp Anal*, 137, 106925.

Piergiorganni, M., Cappiello, A., Famiglini, G., Termopoli, V., and Palma, P. (2018). Determination of benzodiazepines in beverages using green extraction methods and capillary HPLC-UV detection. *J Pharm Biomed Anal*. 154, 492-500.

Prata, J.C., and Da Costa, P.M. (2024). Fourier Transform Infrared Spectroscopy use in honey characterization and authentication: A systematic review. *ACS Food Science & Technology*. 4(8), 1817-1828.

Roberts, D.T., and Kittredge, K. (2022). Using FTIR-ATR and chemometric methods to detect sucrose adulteration in commercial honey samples. *Virginia J Sci*, 73(3), 1-8. <https://doi.org/10.25778/XJDJ-2646>

Rodionova, O.Y., Oliveri, P., Malegori, C., and Pomerantsev, A.L. (2024). Chemometrics as an efficient tool for food authentication: Golden pillars for building reliable models. *Trends Food Sci Technol*, 147, 104429.

Saji, R., Ramani, A., Gandhi, K., Seth, R., and Sharma, R. (2024). Application of FTIR spectroscopy in dairy products: A systematic review. *Food and Humanity*, 2, 100239.

Sathianarayanan, M.P., Hemani, H.K., and Gaonkar, S. (2024). Analysis of sugar composition in honey samples using HPLC separation and RI detection. *BTRA Scan* 53(2), 5-8.

Tarko, T., Januszek, M., Duda-Chodak, A., and Sroka P. (2021). How keeving determines oenological parameters and concentration of volatile compounds in ciders? *J Food Compos Anal*, 100, 103897.

WHO. (2025). Codex Alimentarius International Food Standards: World Health Organization (WHO). <https://www.fao.org/fao-who-codexalimentarius/codex-texts/list-standards/en/>.

Wu, H., Guo, J.B, Du, L.M., Tian, H., Hao, C.X., Wang, Z.F., and et al. (2013). A rapid shaking-based ionic liquid dispersive liquid phase microextraction for the simultaneous determination of six synthetic food colourants in soft drinks, sugar- and gelatin-based confectionery by high-performance liquid chromatography. *Food Chem*, 141(1), 182-186.

Xagoraris, M., Revelou, P-K., Dedegkika, S., Kanakis, C.D., Papadopoulos, G.K., Pappas, C.S., and et al. (2021). SPME-GC-MS and FTIR-ATR Spectroscopic study as a tool for Unifloral Common Greek Honeys' Botanical Origin Identification. *Applied Sciences*, 11(7), 3159.

Zarzo, I., Soler, C., Fernandez-Zamudio, M.A., Pina, T., Barco, H., and Soriano, J.M. (2023). 'Nutritional Footprint' in the food, meals and HoReCa sectors: A Review. *Foods*, 12(2), 409.

Zhang, Z., Li, Y., Zhao, S., Qie, M., Bai, L., Gao, Z., et al. (2024). Rapid analysis technologies with chemometrics for food authenticity field: A review. *Curr Res Food Sci* 8, 100676.





# **Solvothermal Synthesis and Structural Characterization of A Dysprosium-Based Metal–Organic Framework**

**Adem DÖNMEZ<sup>1</sup>**

**Uğur ERKARSLAN<sup>2</sup>**

1. Assoc. Prof. Dr Adem Donmez - Department of Electricity and Energy, Yatagan Vocational School, Mugla Sıtkı Koçman University, Mugla, Turkey. adonmez@mu.edu.tr ORCID No: 0000-0002-9773-0493
2. Assoc. Prof. Dr Ugur Erkarslan - Department of Physics, Molecular Nano-Materials Laboratory, Mugla Sıtkı Kocman University, Mugla, Turkey. eugur@mu.edu.tr ORCID No: 0000-0001-7667-2151

## ABSTRACT

This chapter presents the solvothermal synthesis and structural characterization of a dysprosium (Dy)-based metal–organic framework (MOF) constructed with 2-aminoterephthalic acid (H<sub>2</sub>atpa) as a multifunctional bridging ligand. The synthesized compound, formulated as [Dy<sub>2</sub>(H<sub>2</sub>atpa)<sub>5</sub>(DMF)<sub>2</sub>(H<sub>2</sub>O)], was analyzed using single-crystal X-ray diffraction, revealing a triclinic crystal system with the P-1 space group. Each Dy<sup>3+</sup> ion is coordinated by eight oxygen atoms, forming a distorted square-antiprismatic geometry, while the H<sub>2</sub>atpa ligands link Dy centers through carboxylate and amino coordination modes, generating a two-dimensional polymeric network.

The solvothermal method successfully produced well-defined pure crystalline Dy-based frameworks with high efficiency. The structural analysis showed that the obtained coordination polymer maintains strong metal–ligand bonds and stability through hydrogen bonding and displays typical architectural features of lanthanide-based MOFs. The research results help scientists develop new lanthanide coordination polymers which show promise for use in luminescent and magnetic and catalytic applications.

*Keywords – MOFs; Coordination polymers; Lanthanides; Dysprosium; Solvothermal synthesis; X-ray diffraction*

---

## INTRODUCTION

Metal–organic frameworks (MOFs) consist of hybrid crystalline materials which unite inorganic structural strength with organic linker chemical diversity. The coordination of metal ions or clusters with polyfunctional organic ligands results in the formation of one-dimensional to three-dimensional extended frameworks. The discovery of MOF synthesis in the late 1990s marked the beginning of an exponential growth in the field which connects coordination chemistry with solid-state science and materials engineering (Cui et al., 2014). MOFs demonstrate modularity which enables researchers to precisely control their composition and topology and pore functionality thus making them suitable for creating materials with multiple functions.

MOFs show intrinsic tunability because they contain organic and inorganic components. The rigid framework stability of MOFs arises from transition metal, main-group metal, and lanthanide inorganic nodes, which collaborate with organic linkers to modify structural and electronic properties. The hybrid structure of MOFs enables extensive design flexibility, resulting in materials that exhibit specific chemical, magnetic, optical, and catalytic properties. The adaptable nature of MOFs enables their use in multiple

technological applications, which include gas separation and adsorption, drug delivery, chemical sensing, heterogeneous catalysis, energy storage, and optoelectronic systems (Li et al., 2003). Scientists use MOFs as their primary material system in modern chemistry because they can create framework structures at the molecular level for exact modifications.

The research into lanthanide-based metal–organic frameworks (Ln-MOFs) has seen a surge in interest in recent years. That is mainly due to the distinct electronic behavior of  $\text{Ln}^{3+}$  ions, which differs from that of typical transition metal ions. The 4f orbitals of lanthanides, protected by 5s and 5p orbitals, result in narrow electronic transitions, influential emission bands, and prolonged excited-state lifetimes (Yang et al., 2013). This unique electronic behavior, combined with their high coordination numbers and flexible geometric arrangements, allows lanthanides to form various multidimensional structural frameworks. Ln-MOFs, therefore, have gained significance as multifunctional materials that combine structural integrity with luminescence properties and magnetic behavior.

Dysprosium ( $\text{Dy}^{3+}$ ) stands out among lanthanides due to its exceptional properties. It possesses strong spin–orbit coupling, a high magnetic moment, and an anisotropic electronic structure. These distinctive characteristics enable the construction of single-molecule magnets (SMMs) that maintain bistable magnetic states and exhibit slow molecular-level magnetization relaxation (Oyarzabal et al., 2016). The unique properties of  $\text{Dy}^{3+}$  ions allow for the study of quantum information storage, high-density data recording, and spintronic applications. The intra-4f transitions of  $\text{Dy}^{3+}$  ions create specific optical features, producing narrow luminescent emissions used in display technology, photonic sensors, and anti-counterfeiting systems.

MOFs containing Dy ions achieve expanded potential applications through the use of organic linkers, which provide multiple functional groups. The ligand 2-aminoterephthalic acid ( $\text{H}_2\text{atpa}$ ) demonstrates exceptional versatility because it contains two functional groups, which establish multiple coordination sites and enable hydrogen bonding. These properties of the ligand play a crucial role in achieving the complex coordination networks of the frameworks, which stabilize the structure through  $\pi$ – $\pi$  stacking and hydrogen bonding interactions. The framework achieves better mechanical and thermal stability due to these features, which also allow for precise electronic environment control around the metal center.

The  $\text{Dy}^{3+}$  ion and  $\text{H}_2\text{atpa}$  ligand system demonstrates strong potential to develop hybrid materials that unite magnetic and optical characteristics within one system. The solvothermal method, a key technique in MOF synthesis, allows scientists to create MOFs with perfect crystallinity by using non-aqueous solvents at high pressure and temperature (Kuru, 2019). This method is beneficial as it allows for precise control over the material's structure, particle dimensions, and crystallinity by modifying reaction parameters such as temperature, solvent properties, and precursor amounts.

This chapter presents an extensive explanation of the synthesis protocol and crystal structure evaluation for a newly synthesized Dy-based coordination polymer that utilizes 2-aminoterephthalic acid as its structural component. The single-crystal X-ray diffraction results demonstrate that Dy<sup>3+</sup> ions create a two-dimensional network structure that adopts a square-antiprismatic geometry. The study reveals the structural features of the synthesized compound by connecting it to lanthanide-based MOFs, demonstrating how molecular design influences coordination geometry and functional performance. The research provides a complete understanding of Dy–H<sub>2</sub>atpa systems, which serve as essential building blocks for developing advanced magneto-luminescent hybrid materials of the future.

### ***Background and Significance***

The fundamental principles of coordination chemistry and crystal engineering enable scientists to create metal–organic frameworks (MOFs) through structural design. The basic MOF structure consists of metal clusters or single metal ions which serve as secondary building units (SBUs) that bond with organic molecules containing carboxylates and phosphonates and pyridyls as donor groups. The structural characteristics of the framework including its dimensionality (Xu et al., 2003). Scientists apply reticular chemistry to create materials with desired physical and chemical characteristics through purposeful selection of metal-ligand combinations. and pore connectivity and topology develop from the arrangement of metal centers and ligand donor atoms in space.

MOFs stand apart from other materials because they possess both porous structures and modular design capabilities. The materials exhibit outstanding surface areas exceeding 5000 m<sup>2</sup>/g and adjustable pore sizes which allow precise control of small molecule uptake and transport. The chemical environment of MOF pores becomes accessible for modification through post-synthetic functionalization which enables researchers to control reactivity and selectivity. MOFs show outstanding potential for gas storage of H<sub>2</sub> and CH<sub>4</sub> and CO<sub>2</sub> as well as gas separation and heterogeneous catalysis applications. The catalytic metals Cu<sup>2+</sup> Fe<sup>3+</sup> and Zr<sup>4+</sup> in MOFs achieve efficient catalytic performance for oxidation and hydrogenation and condensation reactions at mild reaction conditions (Li et al., 2003).

Ln-MOFs form a distinct MOF group because their complex electronic structure and wide range of coordination patterns emerge from lanthanide ions. The electrostatic forces between lanthanide ions determine their coordination behavior because their 4f electrons stay protected by 5s and 5p orbitals which leads to flexible network structures with coordination numbers ranging from 8 to 12 (Yang et al., 2013). The flexible nature of these networks creates stable multi-dimensional arrangements which survive heat exposure and polar solvent contact. The 4f electrons of lanthanides show minimal

environmental impact because the filled 5s and 5p orbitals create a protective shield that leads to unique optical transitions. Scientists use Ln-MOFs for developing optical amplifiers and anti-counterfeiting systems and luminescent sensors because these materials exhibit strong emission lines and prolonged luminescence periods and high quantum yields (Cui et al., 2014).

The magnetic behavior of  $\text{Dy}^{3+}$  and  $\text{Tb}^{3+}$  and  $\text{Ho}^{3+}$  ions in lanthanides results from their strong spin-orbit coupling which produces significant single-ion anisotropy. The magnetic behavior of single-molecule magnets (SMMs) depends on their slow magnetization relaxation process which develops from this characteristic (Oyarzabal et al., 2016). The magnetic response of these materials depends on the metal center environment because the surrounding crystal field symmetry affects its behavior. The magnetic ground state of  $\text{Dy}^{3+}$  becomes more stable when the metal center adopts distorted square-antiprismatic or dodecahedral coordination because these structures create strong uniaxial anisotropy that blocks spin-lattice relaxation pathways (Zhenda & Shuang-Quan, 2006). The structural characteristics of Ln-MOFs allow researchers to investigate basic molecular magnetism principles while developing potential applications for quantum computing and spin-based data storage systems.

Ln-MOFs show superior host material properties for energy transfer and photophysical processes because they possess built-in magnetic and luminescent features. The organic linkers in Ln-MOFs serve as antenna ligands which capture light energy before transferring it to lanthanide centers through ligand-to-metal charge transfer (LMCT) processes. The light absorption process enhances overall luminescence output and enables spectral modifications through linker electronic structure modifications (Cui et al., 2014). The photophysical properties of Ln-MOFs reach their best performance when using 2-aminoterephthalic acid ( $\text{H}_2\text{atpa}$ ) as a multifunctional linker because it establishes stable supramolecular networks through its coordination sites and hydrogen-bonding sites.

The production of high-quality Ln-MOFs requires absolute control of the crystallization process. The solvothermal method proves to be the most effective method for creating Ln-MOFs. The sealed autoclave method under high pressure and temperature conditions enables single-crystal growth through controlled nucleation and produces defect-free crystals with uniform morphologies (Kuru, 2019). The reaction media together with DMF and DMSO and ethanol structure-directing properties determine the coordination patterns and framework dimensions of MOFs during synthesis. The solvothermal method produces Dy-based compounds that create two-dimensional polymeric networks through  $\text{Dy}^{3+}$  centers bridged by carboxylates while sometimes incorporating solvent molecules.

The final structure and operational capabilities of lanthanide-based MOFs develop through the interaction between metal ion selection and ligand design and synthesis conditions. Scientists use the structural knowledge

gained from these materials to develop multifunctional frameworks which integrate luminescence with magnetic and catalytic properties into single crystalline structures. The Dy–H<sub>2</sub>atpa system illustrates this approach by showing how a simple yet strategic ligand selection leads to the formation of complex coordination sites which generate multiple material properties. The materials serve dual purposes in scientific research and practical applications because they enable energy-efficient lighting and magneto-optic sensors and information storage and environmental catalysis which makes them vital for contemporary materials science investigations.

## MATERIALS AND METHODS

The research contains two primary sections which involve (i) coordination complex synthesis through solvothermal methods and (ii) structural evaluation of the obtained compound. The researchers achieved the synthesis of a single-crystal metal–organic framework (MOF) which incorporated dysprosium (Dy) as the central atom and 2-aminoterephthalic acid as the ligand through solvothermal synthesis. The researchers used single-crystal X-ray diffraction to achieve the structural refinement of the obtained crystal.

### *Synthesis of the Dy Complex*

All reagents were used as received without further purification. Dysprosium nitrate pentahydrate (Dy(NO<sub>3</sub>)<sub>3</sub>·5H<sub>2</sub>O, 99% purity) and 2-aminoterephthalic acid (H<sub>2</sub>atpa) were purchased from Sigma–Aldrich. For synthesis, 0.1 mmol (0.0449 g) of Dy(NO<sub>3</sub>)<sub>3</sub>·5H<sub>2</sub>O was dissolved in 10 mL of ultrapure water, while 0.1 mmol (0.0249 g) of H<sub>2</sub>atpa was dissolved in 10 mL of N,N-dimethylformamide (DMF). Both solutions were stirred separately for 1 h, then mixed and stirred together for an additional 2 h.

The pH of the mixture was adjusted to approximately 7.0 using NaOH (0.0100 g, 0.25 mmol). The 20 mL solution was then transferred into a 45 mL Teflon-lined stainless-steel autoclave and heated at 140 °C for 3 days in a micro temperature-controlled oven. After being slowly cooled to room temperature over 24 h, colorless block-shaped single crystals were obtained, washed with distilled water, and air-dried. The complete experimental process is shown schematically in Figure 1.

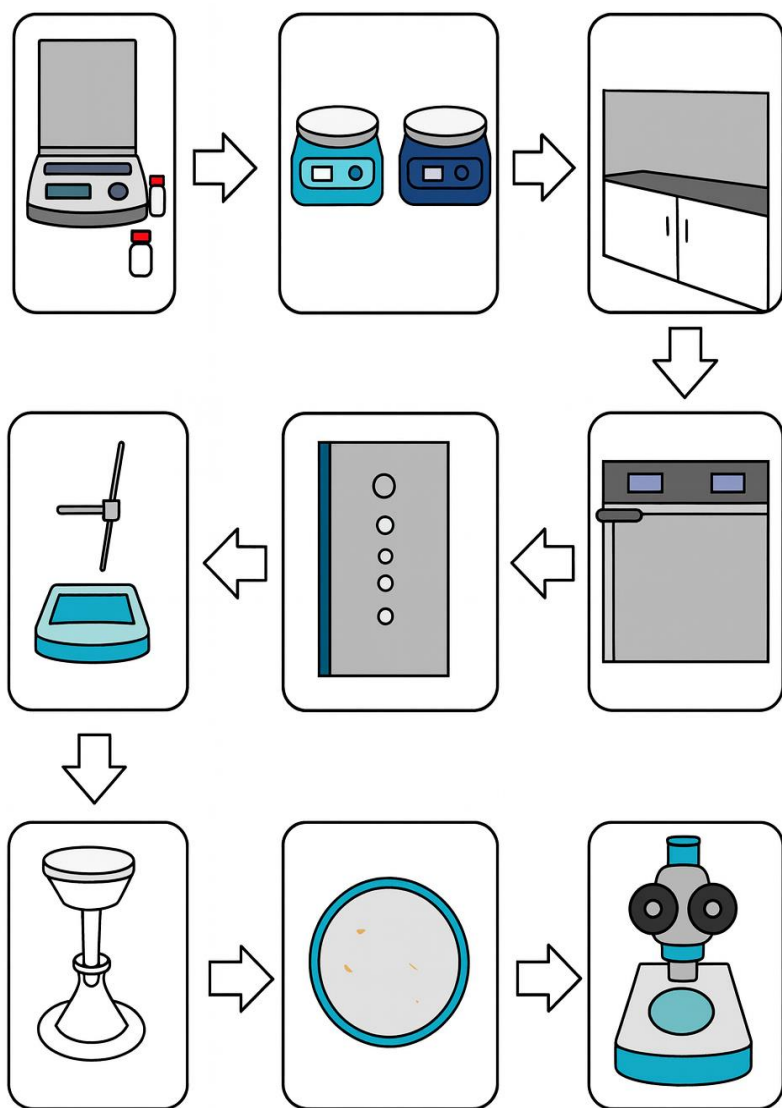


Figure 1. Experimental steps in the solvothermal synthesis of the Dy-based metal–organic framework.

The solvothermal method is one of the most effective approaches for obtaining molecular crystalline materials. Similar to the hydrothermal technique, it employs solvents other than water and requires stainless-steel autoclaves capable of withstanding high pressures and temperatures—typically up to 300 °C. The solvothermal method involves placing precursor solutions into high-pressure autoclaves where controlled heating and cooling cycles occur to stimulate crystal development.



The technique unites elements from sol–gel and hydrothermal synthesis to enable exact control over metal oxide nanostructure dimensions and crystal structure and shape. The experimental parameters of reaction temperature and time and solvent type and surfactant and precursor concentration determine the final properties of the metal oxide nanostructures according to Kuru (2019). The solvothermal method successfully generated high-quality Dy-based MOF crystals which were suitable for structural analysis.

### ***Crystal Structure Determination and Refinement***

The Agilent Xcalibur-Oxford Diffraction diffractometer at Dokuz Eylül University (İzmir, Türkiye) collected single-crystal X-ray diffraction data for the Dy complex at room temperature (293 K). The CrysAlisPro software package performed data reduction and absorption correction operations. The SHELXS program solved the crystal structure through direct methods before SHELXL within OLEX2 software environment performed full-matrix least-squares refinement on  $F^2$ .

The initial atomic positions were located using the Patterson method, and subsequent refinement provided more precise atomic coordinates, bond lengths, bond angles, and thermal displacement parameters. The final refinement converged satisfactorily with acceptable R-factors and goodness-of-fit values.

The solvothermal method employed here offers significant advantages for obtaining crystalline materials with well-defined molecular architectures. Similar to hydrothermal synthesis but typically using non-aqueous solvents, this technique enables control over particle size, morphology, and crystallinity by adjusting reaction temperature, time, solvent type, surfactant, and precursor concentration (Kuru, 2019). In this study, the solvothermal approach proved highly effective for preparing a pure, high-quality Dy-based MOF suitable for structural analysis.

## **RESULTS AND DISCUSSION**

Single-crystal X-ray diffraction analysis revealed that the synthesized complex crystallizes in the triclinic crystal system with the  $P\bar{1}$  space group. The complex exhibits a dimeric structure that extends into a two-dimensional metal–organic framework through polymerization. The asymmetric unit consists of one  $\text{Dy}^{3+}$  cation, one  $\text{H}_2\text{atpa}$  ligand, two coordinated DMF molecules, and one coordinated water molecule.

The molecular structure, shown in Figure 2, illustrates the coordination environment of the dysprosium center with selected atom labeling. Each  $\text{Dy}^{3+}$  ion is coordinated by eight oxygen atoms: four from two symmetry-related  $\text{H}_2\text{atpa}$  ligands and two from coordinated water molecules, forming a distorted square-antiprismatic geometry around the metal center. The Dy–O bond

lengths range from 2.38(2) to 2.47(2) Å, while the O–Dy–O bond angles vary between 53.8(7)° and 155.2(3)°. These structural parameters are consistent with those reported for similar dysprosium coordination polymers (Zhenda, 2006; Rui-Sha, 2008).

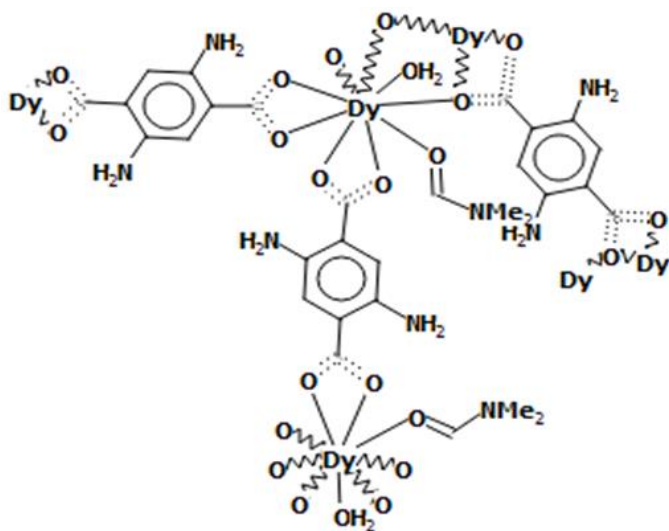


Figure 2. Schematic representation of the coordination modes between the  $\text{Dy}^{3+}$  ion and the H2atpa ligand, showing the distorted square-antiprismatic geometry around the Dy center.

### Structural Characterization

Single-crystal X-ray diffraction analysis confirmed that the synthesized dysprosium complex crystallizes in the triclinic crystal system with the P-1 space group. The complex dimerizes and polymerizes through carboxylate bridges, forming a two-dimensional metal–organic framework. The asymmetric unit consists of one  $\text{Dy}^{3+}$  cation, one H2atpa ligand, two coordinated DMF molecules, and one coordinated water molecule.

The molecular structure is illustrated in Figure 4.1, showing the coordination modes of the H2atpa ligand around the  $\text{Dy}^{3+}$  ions. Each dysprosium atom is coordinated by eight oxygen atoms—four from two symmetry-related carboxylate ligands and two from coordinated water molecules—forming a distorted square-antiprismatic geometry. The Dy–O bond lengths are in the range of 2.326(3)–2.479(3) Å, and the O–Dy–O bond angles vary between 53.8(7)° and 155.2(3)°, consistent with similar Dy-based frameworks reported in the literature (Zhenda, 2006; Rui-Sha, 2008).

A space-filling representation of the Dy coordination environment is presented in Figure 3, while Figure 4 displays the extended two-dimensional network structure, illustrating how Dy centers are connected through H2atpa linkers to form a layered framework stabilized by intermolecular hydrogen bonds.

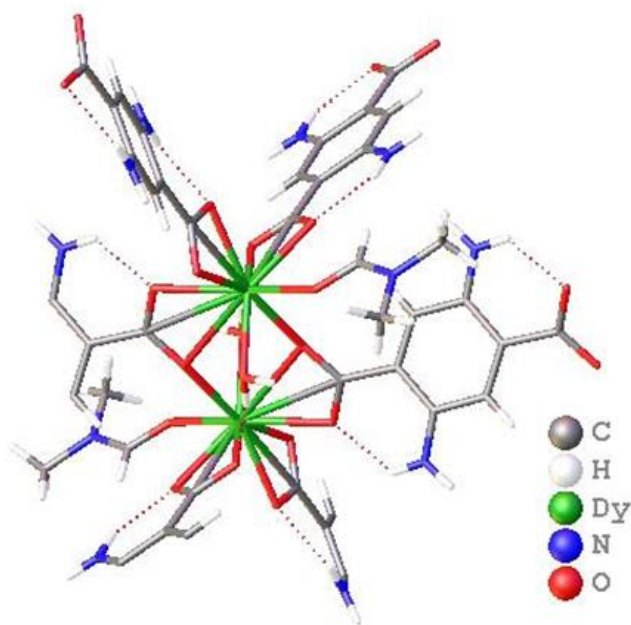


Figure 3. Molecular structure of the Dy-based coordination complex obtained from single-crystal X-ray analysis, showing the coordination geometry around the  $\text{Dy}^{3+}$  center (C: gray, H: white, Dy: green, N: blue, O: red).

The crystallographic refinement and structure validation were carried out using SHELXS and SHELXL programs implemented in the OLEX2 suite. The refinement converged smoothly with satisfactory reliability factors and residual electron densities, confirming the accuracy of the model. The complete crystallographic data and refinement parameters are summarized in Table 1.

The selected bond lengths and angles are listed in Table 2, while the hydrogen-bond geometry and  $\pi$ - $\pi$  stacking interactions between aromatic rings are presented in Table 3. These results clearly indicate the presence of multiple hydrogen bonds ( $\text{O}-\text{H}\cdots\text{O}$ ) that stabilize the 2D coordination polymer through supramolecular interactions.

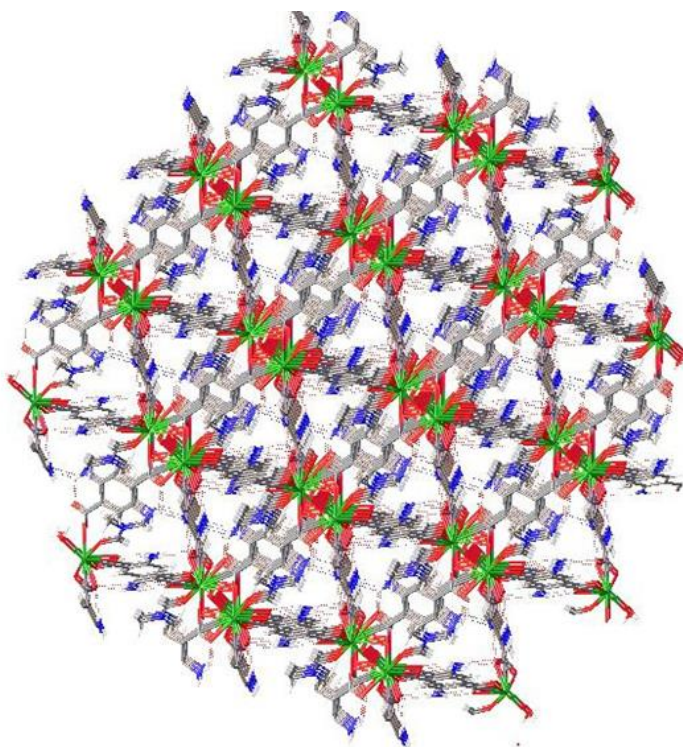


Figure 4. Two-dimensional polymeric framework of the Dy complex viewed along the crystallographic c-axis, showing the extended network constructed through bridging H<sub>2</sub>atpa ligands.

Table 1. Crystallographic data and refinement details for the Dy-based complex (obtained using OLEX2).

Parameter	Description / Value	
Diffractometer	Xcalibur Eos	
X-ray and wavelength (MoK $\alpha$ ), (Å)	1041.59	
Crystal shape	Block	
Crystal dimensions (mm <sup>3</sup> )	0.43 $\times$ 0.32 $\times$ 0.19	
Crystal color	Light pink	
Empirical formula	C <sub>30</sub> H <sub>30</sub> Dy <sub>2</sub> N <sub>5</sub> O <sub>16</sub>	
Formula weight (g $\cdot$ mol <sup>-1</sup> )	436.46	
Crystal system	Triclinic	
Space group	P $\bar{1}$	
Unit cell parameters	a= 8.1742 Å	$\alpha$ = 114.373°
	b=10.218 Å	$\beta$ =98.657°
	c=11.6481 Å	$\gamma$ =99.713°
Unit cell volume (Å <sup>3</sup> )	1041.59	
T <sub>min</sub> , T <sub>max</sub>	0.251, 0.537	

Table 2. Selected bond lengths (Å) and bond angles for the Dy complex.

Dy1—O1	2.381 (3)	Dy1—O6 <sup>i</sup>	2.832 (4)
Dy1—O2	2.479 (3)	Dy1—O6	2.352 (4)
Dy1—O3	2.367 (3)	Dy1—O7 <sup>i</sup>	2.387 (4)
Dy1—O4	2.464 (3)	Dy1—O8	2.326 (3)
Dy1—O5	2.398 (3)		
Symmetry code(s): (i) $-x+1, -y+2, -z+1$ .			

Table 3. Hydrogen-bond geometry (Å, °) and  $\pi$ – $\pi$  interactions between aromatic rings.

D-H $\cdots$ A*	D-H	H $\cdots$ A	D $\cdots$ A	D-H $\cdots$ A	Symmetry
O1-H1A $\cdots$ O7	0.87	2.38	3.04	142	$-1/2+x, 3/2-y, -1/2+z$
O1-H1A $\cdots$ O8	0.87	2.47	2.93	113	$-1/2+x, 3/2-y, -1/2+z$
O1-H1B $\cdots$ O5	0.76	2.39	2.72	110	$-1+x, y, z$
O1-H1B $\cdots$ O6	0.47	2.36	2.85	135	$1-x, 1-y, 1-z$
O2-H2A $\cdots$ O9	0.85	2.45	3.22	151	$3/2-x, 1/2+y, 1/2-z$
O2-H3A $\cdots$ O8	0.59	2.55	2.89	105	$-1/2+x, 3/2-y, -1/2+z$
O2-H2B $\cdots$ O4	0.53	2.54	2.85	103	$1/2-x, -1/2+y, 1/2-z$
O2-H3B $\cdots$ O6	0.58	1.80	2.62	158	$-1/2+x, 1/2-y, -1/2+z$
O9-H4A $\cdots$ O8	0.28	2.19	2.96	151	$x, -1+y, z$
O9-H4B $\cdots$ O1	0.38	2.14	2.80	134	$1/2-x, -1/2+y, 1/2-z$
Cg(I) $\cdots$ Cg(J)			Cg $\cdots$ Cg		
Cg(1) $\cdots$ Cg(1)			3.69	$1-x, 1-y, 1-z$	
Cg(1) $\cdots$ Cg(1)			4.07	$2-x, 1-y, 1-z$	

\* **D**: Donor, **A**: Acceptor, **Cg(I)**: Ring number in parentheses above, **Cg–Cg**: Distance between ring centroids (Å), Cg (1): C2–C3–C4–C5–C6–C7

## DISCUSSION AND CONCLUSIONS

In this study, a novel dysprosium-based metal–organic framework (MOF) was successfully synthesized using the solvothermal method with 2-aminoterephthalic acid as the organic linker. Single-crystal X-ray diffraction analysis confirmed that the complex crystallizes in the triclinic system with the P-1 space group. The asymmetric unit consists of one Dy<sup>3+</sup> ion, one H<sub>2</sub>atpa ligand, two coordinated DMF molecules, and one water molecule. Each Dy<sup>3+</sup> center is coordinated by eight oxygen atoms, forming a distorted square-antiprismatic geometry.

The solvothermal technique proved to be an effective approach for producing high-quality single crystals with well-defined coordination environments. The resulting two-dimensional polymeric network demonstrates that 2-aminoterephthalic acid serves as an efficient bridging

ligand, linking Dy centers through carboxylate and amino coordination modes.

Overall, the structural characterization reveals that the Dy-H<sub>2</sub>atpa framework possesses the essential features typical of lanthanide-based coordination polymers—namely, rich coordination geometry, strong metal–ligand interactions, and structural stability. The findings of this study contribute to the understanding of Dy-containing MOFs and provide a foundation for the development of new lanthanide-based materials with potential applications in luminescence, magnetism, and catalysis.

Dysprosium-based metal–organic frameworks (Dy-MOFs) combine luminescent, magnetic, and catalytic functionalities within a single structural platform, making them promising candidates for advanced technological applications. Their sharp 4f–4f transitions and strong spin–orbit coupling enable potential use in optical sensors, light-emitting devices, and single-molecule magnets for quantum information and magnetic storage systems. The stability and porosity of these frameworks also support catalytic and gas adsorption processes, extending their utility to energy and environmental applications. Future research is expected to focus on hybrid composite design, nanoscale engineering, and device integration, driving the development of multifunctional Dy-based materials for next-generation photonic and magnetic technologies.

## REFERENCES

- Anders, E., et al. (2002). Structural control of metal oxide nanostructures synthesized by solvothermal methods. *Journal of Materials Chemistry*, 12, 283–289.
- Baude, W., et al. (1955). Industrial oxidation of p-xylene for terephthalic acid production. *Industrial and Engineering Chemistry*, 47, 663–669.
- Cui, Y., Yue, Y., Qian, G., & Chen, B. (2014). Luminescent functional metal–organic frameworks. *Chemical Reviews*, 114, 11285–11319.
- Dolomanov, O. V., Bourhis, L. J., Gildea, R. J., Howard, J. A. K., & Puschmann, H. (2009). OLEX2: A complete structure solution, refinement and analysis program. *Journal of Applied Crystallography*, 42, 339–341.
- Kuru, M. (2019). Solvothermal synthesis and structural control of nanocrystalline materials (in Turkish). *Journal of Materials Research and Technology*, 8, 1452–1461.
- Li, J.-R., Kuppler, R. J., & Zhou, H.-C. (2003). Selective gas adsorption and separation in metal–organic frameworks. *Coordination Chemistry Reviews*, 246, 1–21.
- Oliveira, M. A., et al. (2003). Synthesis of nanocrystalline oxides by solvothermal route. *Materials Letters*, 57, 1015–1022.
- Oyarzabal, I., Seco, J. M., Colacio, E., & Mota, A. J. (2016). Slow magnetic relaxation in dysprosium-based coordination polymers. *Inorganic Chemistry*, 55, 11516–11524.

- Rui-Sha, W., & Yong-Zhi, C. (2008). Crystal structures and coordination behavior of lanthanide(III) carboxylates. *Journal of Coordination Chemistry*, 61, 3029–3038.
- Sheldrick, G. M. (2007). SHELXS and SHELXL: Programs for crystal structure determination and refinement. *Acta Crystallographica Section A*, 64, 112–122.
- Xu, H., Wang, X., & Lin, W. (2003). Rational design of coordination polymers with predictable topologies. *Journal of the American Chemical Society*, 125, 12899–12908.
- Yang, J., Ma, J.-F., Liu, Y.-Y., Ma, J.-C., & Ping, G.-J. (2013). Construction of lanthanide coordination polymers with diverse structures and properties. *Dalton Transactions*, 42, 13760–13767.
- Zhenda, L., & Shuang-Quan, Z. (2006). Dysprosium coordination compounds with aminoterephthalate linkers. *Inorganic Chemistry Communications*, 9, 1151–1154.





# Equivalence in Action: Homotopy From Simplicial to Crossed Modules

**Hatice GÜLSÜN AKAY<sup>1</sup>**

**İ.İlker AKÇA<sup>2</sup>**

1. Assoc. Prof. Dr.; Eskişehir Osmangazi University, Faculty of Science, Department of Mathematics and Computer Science. [hgulsun@ogu.edu.tr](mailto:hgulsun@ogu.edu.tr); ORCID No: 0000-0001-7983-6852.
2. Prof. Dr.; Eskişehir Osmangazi University, Faculty of Science, Department of Mathematics and Computer Science. [iakca@ogu.edu.tr](mailto:iakca@ogu.edu.tr); ORCID No: 0000-0003-4269-498X

## ABSTRACT

In this paper, we investigate the homotopy theory of simplicial commutative algebras whose Moore complex is concentrated in degrees zero and one, meaning the complex has length one. This particular class of simplicial algebras is of significant interest because of its categorical equivalence with crossed modules of commutative algebras. Crossed modules, originally arising in algebraic topology, have since found applications in various algebraic settings, particularly in the study of algebraic models of homotopy types and cohomology theories. Our aim is to investigate how homotopical structures arising in the simplicial framework can be translated into the case of crossed modules. More precisely, we examine how a homotopy between simplicial morphisms induces a corresponding homotopy between morphisms in the category of crossed modules.

*Keywords – Algebra, category, crossed module, homotopy, simplicial*

---

## INTRODUCTION

Homotopy theory provides a rich and flexible framework for studying topological spaces up to continuous deformation. In recent years, higher-dimensional algebraic structures have emerged as powerful tools for encoding and analyzing such homotopical phenomena. Among these structures, simplicial sets and crossed modules play particularly important roles in modeling homotopy types, especially in low-dimensional cases. Two maps  $\rho, \tau: P \rightarrow T$  are said to be homotopic if there exists a continuous deformation from one to the other through a family of maps, reflecting the idea that they are "essentially the same" from a homotopical perspective.

Let  $\mathfrak{C}$  be an algebraic category (e.g., **Grp**, **Ab**, **Mod<sub>R</sub>**, **Ring**), a simplicial object in  $\mathfrak{C}$  is a functor  $\Omega: \Delta^{op} \rightarrow \mathfrak{C}$  where  $\Delta$  is a simplex category. This means:

- For each  $n \geq 0$ , there is an object  $\Omega_n \in \mathfrak{C}$ ,
- There are morphisms in  $\mathfrak{C}$  called face maps  $d_n^i: \Omega_n \rightarrow \Omega_{n-1}$  and degeneracy maps  $s_n^i: \Omega_n \rightarrow \Omega_{n+1}$  satisfying the simplicial identities given in (André, 1974:206) or (Illusie, 1972:239).

The development of simplicial commutative algebras has established deep connections among homotopy theory, algebra, and geometry. Arvasi and Porter (1996:428, 1997:7) investigated the  $n$ -types of simplicial algebras, contributing to the understanding of their higher-dimensional behavior. Also

Akça and Pak (2010:481) explored pseudo-simplicial groups and examined equivalence of pseudo 2-crossed modules and pseudo-simplicial groups.

Crossed modules of groups arise naturally in algebraic topology, group cohomology, and higher-dimensional algebra as algebraic models of homotopy-theoretic structures. In (1941:420), Whitehead introduced the concept of crossed modules to capture the algebraic structure underlying homotopy 2-types, that is, spaces whose higher homotopy groups (above dimension two) are trivial. This concept was later extended to the setting of commutative algebras by (Ellis, 1984:11). Boyacı and Avcioğlu (2014:414) established that crossed modules are equivalent to certain simplicial objects with Moore complexes of length one in modified categories of interest. Afterwards, the notion of homotopy for 2-algebras given in (Akça and Ege Arslan, 2022:173) and for quadratic modules over Lie algebras studied in (Ege Arslan and Özel, 2022:161). More recently, an equivalence relation between simplicial morphisms was introduced by Gülsün Akay (2025:573), contributing to the categorical understanding of simplicial structures.

This paper begins with a review of the necessary background on simplicial algebra, simplicial homotopy and crossed modules. Then, we analyze the correspondence between simplicial homotopies and crossed module homotopies.

## SIMPLICIAL ALGEBRAS

Let  $\mathfrak{R}$  be a commutative ring, and let  $Alg_{\mathfrak{R}}$  denote the category of (or associative)  $\mathfrak{R}$ -algebras.

A simplicial  $\mathfrak{R}$ -algebra is a functor

$$\mathcal{F}: \Delta^{op} \rightarrow Alg_{\mathfrak{R}}$$

from the opposite of the simplex category  $\Delta$  to  $Alg_{\mathfrak{R}}$ . Concretely, this means:

- There is a family  $\{\mathcal{F}_m\}_{m \geq 0}$  of  $\mathfrak{R}$ -algebras, called the algebras of  $m$ -simplices.
- For each  $m \geq 1$ , there are face morphisms

$$\partial_m^r: \mathcal{F}_m \rightarrow \mathcal{F}_{m-1}$$

and for each  $m \geq 0$ , there are degeneracy morphisms

$$\epsilon_m^r: \mathcal{F}_m \rightarrow \mathcal{F}_{m+1}$$

all of which are morphisms of  $\mathfrak{R}$ -algebras. These morphisms are required to satisfy the following simplicial identities:

$$\begin{aligned}
\partial_r \partial_s &= \partial_{s-1} \partial_r & \text{for } r < s \\
\partial_r \epsilon_s &= \begin{cases} \epsilon_{s-1} \partial_r & \text{for } r < s \\ id & \text{for } r = s, s+1 \\ \epsilon_s \partial_{r-1} & \text{for } r > s+1 \end{cases} \\
\epsilon_r \epsilon_s &= \epsilon_s \partial_{r-1} & \text{for } r \leq s
\end{aligned}$$

A simplicial map  $f: \mathcal{F}_\bullet \rightarrow \mathcal{F}'_\bullet$  is a family of morphisms  $f_m: \mathcal{F}_m \rightarrow \mathcal{F}'_m$  commuting with the  $\partial_r$  and  $\epsilon_r$ :

$$\begin{array}{ccccccc}
\mathcal{F}_\bullet & \xrightarrow{\quad \quad \quad} & \mathcal{F}_2 & \begin{array}{c} \xrightarrow{\partial_0} \\ \xrightarrow{\partial_1} \\ \xrightarrow{\partial_2} \\ \xleftarrow{\epsilon_0} \\ \xleftarrow{\epsilon_1} \end{array} & \mathcal{F}_1 & \begin{array}{c} \xrightarrow{\partial_0} \\ \xrightarrow{\partial_1} \\ \xleftarrow{\epsilon_0} \end{array} & \mathcal{F}_0 \\
\downarrow f & & \downarrow f_2 & & \downarrow f_1 & & \downarrow f_0 \\
\mathcal{F}'_\bullet & \xrightarrow{\quad \quad \quad} & \mathcal{F}'_2 & \begin{array}{c} \xrightarrow{\delta_0} \\ \xrightarrow{\delta_1} \\ \xrightarrow{\delta_2} \\ \xleftarrow{\beta_0} \\ \xleftarrow{\beta_1} \end{array} & \mathcal{F}'_1 & \begin{array}{c} \xrightarrow{\delta_0} \\ \xrightarrow{\delta_1} \\ \xleftarrow{\beta_0} \end{array} & \mathcal{F}'_0
\end{array}$$

We get the category of simplicial algebras, **SimpAlg**.

Given a simplicial  $\mathfrak{R}$ -algebra  $\mathcal{F}_\bullet$ , we define its  $t$ -truncation, denoted  $\mathcal{F}_{\leq t}$  as the structure obtained by restricting  $\mathcal{F}_\bullet$  to degrees  $\leq t$ , together with the induced face and degeneracy maps between them. This truncation preserves the lower-dimensional homotopical structure but discards information about homotopies occurring above dimension  $t$ . The result behaves like a simplicial algebra “with only  $t$  layers of homotopy.” We denote the category whose objects are such  $t$ -truncated simplicial algebras by **Tr SimpAlg**.

Let  $\mathcal{F}_\bullet$  simplicial  $\mathfrak{R}$ -algebra, and let  $M(\mathcal{F}_\bullet)$  denote its associated Moore complex. We say that  $M_m(\mathcal{F}_\bullet)$  is of length  $t$  if  $M_m(\mathcal{F}_\bullet) = 0$  for all  $m \geq t+1$ . In this case, since the complex vanishes in all degrees  $m > t$ , it is also said to be of length  $s$  for any integer  $s \geq t$ ; that is, the length condition is preserved under any greater bound.

A simplicial algebra  $\mathcal{F}_\bullet$  is said to be free (Mutlu and Uslu, 2009:1491), if the following conditions are satisfied:

- i) For each  $m \geq 0$ , the algebra  $\mathcal{F}_m$  is a free algebra generated by a specified set  $\mathcal{B}_m \subseteq \mathcal{F}_m$ ;
- ii) The generating sets  $\{\mathcal{B}_m\}$  are preserved under the action of degeneracy maps. That is, for all integers  $m \geq 0$  and  $0 \leq r \leq m$ , and for every generator  $b \in \mathcal{B}_m$ , the image  $\epsilon_r(b) \in \mathcal{F}_{m+1}$  lies in  $\mathcal{B}_{m+1}$ .

### Simplicial Homotopy

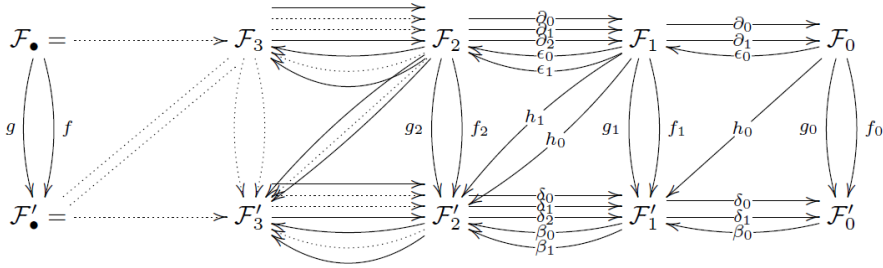
Let  $f, g: \mathcal{F}_\bullet \rightarrow \mathcal{F}'_\bullet$  are two simplicial maps, a homotopy  $\mathbf{h}$  of  $f$  and  $g$  is a family of morphisms

$$h_r: \mathcal{F}_{\bullet, m} \rightarrow \mathcal{F}'_{\bullet, m}, \quad 0 \leq r \leq m$$

for each  $m \geq 0$  which satisfies the following identities;

- i)  $\partial_0 h_0 = f$   
 $\partial_{m+1} h_m = g$
- ii)  $\partial_r h_s = h_{s-1} \partial_r, \quad r < s$   
 $\partial_{s+1} h_{s+1} = \partial_{s+1} h_{js}$   
 $\partial_r h_s = h_s \partial_{r-1}, \quad r > s + 1$
- iii)  $\epsilon_r h_s = h_{s+1} \epsilon_r, \quad r \leq s$   
 $\epsilon_r h_s = h_s \epsilon_{r-1}, \quad r > s.$

We denote a homotopy  $f$  onto  $g$  by  $\mathbf{h}: f \simeq g$ . For the homotopy  $\mathbf{h}$ , source of  $\mathbf{h}$  is  $f$  and target of  $\mathbf{h}$  is  $g$ , we denote by  $s_r(\mathbf{h}) = f_r$  and  $t_r(\mathbf{h}) = g_r$ . All fits in the following diagram:



### Crossed Modules

Let  $\kappa$  be a fixed commutative base ring and and let  $\mathcal{F}$  be a unital commutative  $\kappa$ -algebra. A crossed module of commutative  $\kappa$ -algebras over  $\mathcal{F}$  consists of:

- a commutative  $\mathcal{F}$ -algebra  $\mathcal{E}$ ,
  - a morphism of  $\mathcal{F}$ -algebras  $\rho: \mathcal{E} \rightarrow \mathcal{F}$ ,
  - together with an  $\mathcal{F}$ -action on  $\mathcal{E}$ , written  $f \bullet e$  for  $f \in \mathcal{F}$  and  $e \in \mathcal{E}$
- such that the following conditions hold for all  $f, f' \in \mathcal{F}$  and  $e, e' \in \mathcal{E}$ ;

$$\text{CM1} \quad \rho(f \bullet e) = f \rho(e)$$

$$\text{CM2} \quad \rho(e) \cdot e' = ee'$$

We denote such a crossed module by the triple  $(\mathcal{E}, \mathcal{F}, \rho)$ .

A morphism of crossed modules

$$(\gamma, \delta): (\mathcal{E}, \mathcal{F}, \rho) \rightarrow (\mathcal{E}', \mathcal{F}', \rho')$$

consists of a pair of  $\kappa$ -algebra morphisms  $\gamma: \mathcal{E} \rightarrow \mathcal{E}'$  and  $\delta: \mathcal{F} \rightarrow \mathcal{F}'$  such that the following two conditions are satisfied:

- $\delta \rho = \rho' \gamma$ , i.e. the diagram

$$\begin{array}{ccc}
\mathcal{E} & \xrightarrow{\gamma} & \mathcal{E}' \\
\rho \downarrow & & \downarrow \rho' \\
\mathcal{F} & \xrightarrow{\delta} & \mathcal{F}'
\end{array}$$

commutes;

- $\gamma(f \bullet e) = \delta(f) \bullet \gamma(e)$  for all  $f \in \mathcal{F}$  and  $e \in \mathcal{E}$ ;

Therefore we get the category of crossed module, denoted by **XMod**.

The following theorem is well known from (Arvasi and Porter, 1997:16) for algebra case:

**Theorem:** The category of crossed modules is equivalent to the category of simplicial algebras whose Moore complex is concentrated in degrees zero and one.

Proof: Let  $\mathcal{F}_\bullet$  be a simplicial (commutative) algebra with Moore complex of length one:

$$\mathcal{F}_\bullet = \cdots \rightarrow \mathcal{F}_2 \begin{array}{c} \xrightarrow{\partial_0} \\ \xrightarrow{\partial_1} \\ \xrightarrow{\partial_2} \end{array} \mathcal{F}_1 \begin{array}{c} \xrightarrow{\partial_0} \\ \xrightarrow{\partial_1} \\ \xrightarrow{\partial_2} \end{array} \mathcal{F}_0$$

$\xleftarrow{\epsilon_0}$        $\xleftarrow{\epsilon_1}$

Put

$$\begin{aligned}
\wp &= \mathcal{F}_0 \\
\mathfrak{I} &= \ker(\partial_0: \mathcal{F}_1 \rightarrow \mathcal{F}_0)
\end{aligned}$$

and

$$\begin{aligned}
\chi &= \partial_1 \\
(\text{restricted to } \mathfrak{I}). \text{ Then } p \in \wp \text{ acts on } \ell \in \mathfrak{I} \text{ by } p \bullet \ell &= s_0(p)\ell \text{ and} \\
\chi(p \bullet \ell) &= \partial_1(\epsilon_0(p)\ell) \\
&= \partial_1 \epsilon_0(p) \partial_1(\ell) \\
&= p(\ell) \\
&= p\chi(\ell).
\end{aligned}$$

Since the Moore complex  $\cdots \rightarrow 0 \rightarrow \mathfrak{I} \rightarrow \wp \rightarrow 0$  is length one we have

$$\begin{aligned}
(p \bullet \ell) &= \epsilon_0 \partial_1(\ell) \ell' \\
&= \epsilon_0 \partial_1(\ell) \ell - \ell \ell' + \ell \ell' \\
&= \partial_2 \epsilon_0(\ell) \partial_2 \epsilon_1(\ell') - \partial_2 \epsilon_1(\ell) \partial_2 \epsilon_1(\ell') + \ell \ell' \\
&= \partial_2(\epsilon_0(\ell) \epsilon_1(\ell') - \epsilon_1(\ell) \epsilon_1(\ell')) + \ell \ell' \\
&= \ell \ell'
\end{aligned}$$

for  $\ell, \ell' \in \mathfrak{I}$ , because  $\epsilon_0(\ell) \epsilon_1(\ell') - \epsilon_1(\ell) \epsilon_1(\ell')$  lies in  $\ker(\partial_0) \cap \ker(\partial_1) = 0$ . Then

$$\chi: \mathfrak{I} \rightarrow \wp$$

is a crossed module. Thus we get a functor:

$$\mathfrak{A}: \mathbf{SimpAlg}_{\leq 1} \rightarrow \mathbf{XMod}$$

defined by  $\mathfrak{A}(\mathcal{A}) = (\chi: \mathfrak{T} \rightarrow \wp)$  for simplicial algebra  $\mathcal{F}_\bullet$  and by  $\mathfrak{A}(f) = (f_1/\mathfrak{T}, f_0)$  for a simplicial morphism  $f = (f_1, f_0)$ .

Now we give the following theorems from (Gülsün Akay, 2025:573):

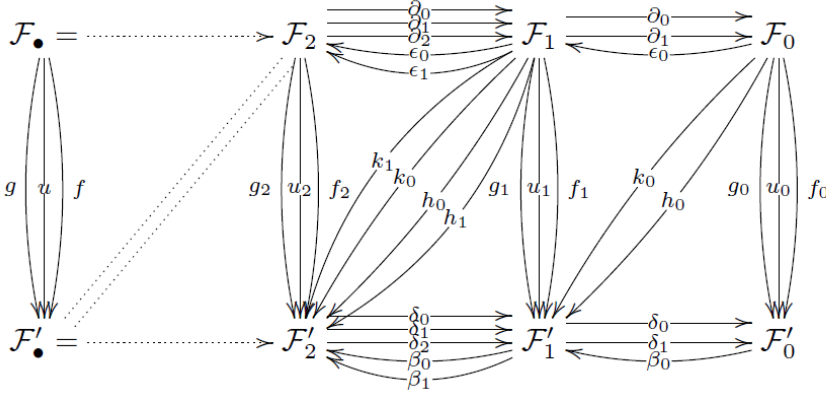
**Theorem:** Let  $\mathcal{F}_\bullet$  and  $\mathcal{F}'_\bullet$  be two arbitrary but fixed simplicial (commutative) algebras, where  $\mathcal{F}_\bullet$  is a free simplicial algebra. The relation below between simplicial morphisms  $f, g: \mathcal{F}_\bullet \rightarrow \mathcal{F}'_\bullet$  is an equivalence relation:

“ $f \simeq g \Leftrightarrow$  there exists a simplicial homotopy  $\mathbf{h}$  of  $f$  onto  $g$ ”

**Theorem:** Let  $\mathcal{F}_\bullet$  and  $\mathcal{F}'_\bullet$  be simplicial algebras with Moore complexes of length one. Suppose that  $\mathcal{F}_\bullet$  is free simplicial algebra. We have a groupoid  $(\mathbf{Simp.Gr}(\mathcal{F}_\bullet, \mathcal{F}'_\bullet))$  whose objects are the simplicial morphisms  $\mathcal{F}_\bullet \rightarrow \mathcal{F}'_\bullet$ , the morphisms being the simplicial homotopies between them.

### Relating Simplicial Homotopies to Crossed Module Homotopies

Let  $\mathcal{F}_\bullet$  and  $\mathcal{F}'_\bullet$  be simplicial algebras with Moore complexes of length one. Let  $f, g, u: \mathcal{F}_\bullet \rightarrow \mathcal{F}'_\bullet$  be simplicial algebra morphisms and  $\mathbf{h}$  be a simplicial homotopy  $f$  onto  $g$  and  $\mathbf{k}$  be a simplicial homotopy  $g$  onto  $u$ .



If the functor

$$\mathfrak{A}: \mathbf{SimpAlg}_{\leq 1} \rightarrow \mathbf{XMod}$$

is applied to a simplicial algebra  $\mathcal{F}_\bullet$ , we obtain crossed modules

$$\mathfrak{A}(\mathcal{F}_\bullet) = \chi: \mathfrak{T} \rightarrow \wp$$

and

$$\mathfrak{A}(\mathcal{F}'_\bullet) = \chi': \mathfrak{T}' \rightarrow \wp'$$

and crossed module morphism

$$\mathfrak{A}(f) = (f_1/\mathfrak{T}, f_0).$$

Here

$$\begin{aligned} \wp &= \mathcal{F}_0 \\ \mathfrak{T} &= \ker \partial_0^1 \\ \chi &= \partial_1^1 / \mathfrak{T} \end{aligned}$$

and the action  $\wp$  on  $\mathfrak{T}$  is

$$p \bullet \ell = \epsilon_0(p)\ell$$

for all  $p \in \wp$  and  $\ell \in \mathfrak{T}$ . Moreover,

$$\begin{aligned}\wp' &= \mathcal{F}'_0 \\ \mathfrak{T}' &= \ker \delta_0^1 \\ \chi' &= \delta_1^1 / \mathfrak{T}'\end{aligned}$$

and the action  $\wp'$  on  $\mathfrak{T}'$  is

$$p' \bullet \ell' = \beta_0^0(p')\ell'$$

for all  $p' \in \wp'$  and  $\ell' \in \mathfrak{T}'$ .

**Lemma:** For all  $p \in \wp$ ;

$$k(p) = h_0^0(p) - \partial_0^0 f_0(p) \in \ker \delta_0^1 = \mathcal{NF}'_1.$$

Proof:

$$\begin{aligned}\delta_0^1(k(p)) &= \delta_0^1(h_0^0(p) - \beta_0^0 f_0(p)) \\ &= \delta_0^1 h_0^0(p) - \delta_0^1 \beta_0^0 f_0(p) \\ &= f_0(p) - f_0(p) \\ &= 0\end{aligned}$$

Then we get  $k(p) \in \ker \delta_0^1$ . Thus we can define;

$$k: \wp \rightarrow \mathfrak{T}'$$

by  $k(p) = h_0^0(p) - \beta_0^0 f_0(p)$ .

**Lemma:** For  $k: \wp \rightarrow \mathfrak{T}'$ ,

$$\begin{aligned}\delta_1^1 k &= g_0 - f_0 \\ k \partial_1^1 &= g_1 - f_1.\end{aligned}$$

Proof: For all  $p \in \wp$ ;

$$\begin{aligned}\delta_1^1 k(p) &= \delta_1^1(h_0^0(p) - \beta_0^0 f_0(p)) \\ &= \delta_1^1 h_0^0(p) - \delta_1^1 \beta_0^0 f_0(p) \\ &= g_0(p) - f_0(p)\end{aligned}$$

For all  $f \in \mathcal{F}_1$ ,



$$\begin{aligned}
k\partial_1^1(\mathfrak{f}) &= h_0^0\partial_1^1(\mathfrak{f}) - \beta_0^0f_0\partial_1^1(\mathfrak{f}) \\
&= h_0^0\partial_1^1(\mathfrak{f}) - \beta_0^0\delta_0^1h_0^0\partial_1^1(\mathfrak{f}) \\
&= \delta_2^2h_0^1(\mathfrak{f}) - \beta_0^0\delta_0^1\delta_2^2h_0^1(\mathfrak{f}) \\
&= \delta_2^2h_0^1(\mathfrak{f}) - \beta_0^0\delta_1^1\delta_0^2h_0^1(\mathfrak{f}) \\
&= \delta_2^2h_0^1(\mathfrak{f}) - \delta_2^2\partial_0^1\delta_0^2h_0^1(\mathfrak{f}) \\
&= \delta_2^2h_0^1(\mathfrak{f}) - \delta_2^2\beta_0^1\delta_0^2h_0^1(\mathfrak{f}) + \delta_2^2h_1^1(\mathfrak{f}) - \delta_2^2h_1^1(\mathfrak{f}) \\
&\quad + \delta_0^2h_0^1(\mathfrak{f}) - \delta_0^2h_0^1(\mathfrak{f}) \\
&= (\delta_2^2h_0^1(\mathfrak{f}) - \delta_2^2\beta_0^1\delta_0^2h_0^1(\mathfrak{f}) - \delta_2^2h_1^1(\mathfrak{f}) + \delta_0^2h_0^1(\mathfrak{f}) \\
&\quad + \delta_2^2h_1^1(\mathfrak{f}) - \delta_0^2h_0^1(\mathfrak{f})) \\
&= \delta_2^2(h_0^1(\mathfrak{f}) - \beta_0^1\delta_0^2h_0^1(\mathfrak{f}) - h_1^1(\mathfrak{f}) + \partial_1^1\delta_0^2h_0^1(\mathfrak{f})) \\
&\quad + \delta_2^2h_1^1(\mathfrak{f}) - \delta_0^2h_0^1(\mathfrak{f}).
\end{aligned}$$

Let  $e \in \ker\partial_0^1$ , then we get

$$\begin{aligned}
\delta_0^2(h_0^1 - \beta_0^1\delta_0^2h_0^1 - h_1^1 + \beta_1^1\delta_0^2h_0^1)(e) &= \delta_0^2h_0^1(e) - \delta_0^2\beta_0^1\delta_0^2h_0^1(e) - \delta_0^2h_1^1(e) \\
&\quad + \delta_0^2\partial_1^1\delta_0^2h_0^1(e) \\
&= \delta_0^2h_0^1(e) - \delta_0^2h_0^1(e) - h_0^0\partial_0^1(e) \\
&\quad + \beta_0^0\delta_0^1\delta_1^2h_0^1(e) \\
&= -h_0^0\partial_0^1(e) + \partial_0^0\delta_0^1\delta_1^2h_0^1(e) \\
&= -h_0^0\partial_0^1(e) + \delta_0^2\beta_1^1\delta_0^2h_1^1(e) \\
&= h_0^0\partial_0^1(e) + \delta_0^2\beta_1^1h_0^0\partial_0^1(e).
\end{aligned}$$

If  $e \in \ker\partial_0^1$ , then  $\partial_0^1(e) = 0$ . Thus we get

$$\delta_0^2(h_0^1 - \beta_0^1\delta_0^2h_0^1 - h_1^1 + \beta_1^1\delta_0^2h_0^1)(e) = 0.$$

Similarly,

$$\begin{aligned}
\delta_1^2(h_0^1 - \beta_0^1\delta_0^2h_0^1 - h_1^1 + \beta_1^1\delta_0^2h_0^1)(e) &= \delta_1^2h_0^1(e) - \delta_1^2\beta_0^1\delta_0^2h_0^1(e) - \delta_1^2h_1^1(e) \\
&\quad + \delta_1^2\beta_1^1\delta_0^2h_0^1(e) \\
&= \delta_1^2h_0^1(e) - \delta_1^2h_0^1(e) - \delta_1^2h_1^1(e) + \delta_0^2h_0^1(e) \\
&= \delta_1^2h_1^1(e) - \delta_1^2h_0^1(e) - \delta_1^2h_1^1(e) + \delta_0^2h_0^1(e) \\
&= 0
\end{aligned}$$

Thus, if  $e \in \ker\partial_0^1$  then we get

$$(h_0^1 - \beta_0^1\delta_0^2h_0^1 - h_1^1 + \beta_1^1\delta_0^2h_0^1) \in \ker\delta_0^2 \cap \ker\delta_1^2 = \mathcal{NF}'_2 = 0$$

and that means

$$\delta_1^2(h_0^1 - \beta_0^1\delta_0^2h_0^1 - h_1^1 + \beta_1^1\delta_0^2h_0^1)(e) = 0.$$

Through this,

$$\begin{aligned}
k\partial_1^1(\mathfrak{f}) &= \delta_2^2h_1^1(\mathfrak{f}) - \delta_0^2h_0^1(\mathfrak{f}) \\
&= g_1(\mathfrak{f}) - f_1(\mathfrak{f}).
\end{aligned}$$

Hence, for the map  $k: \wp \rightarrow \mathfrak{T}'$ , the following equations hold:

$$\begin{aligned} g_0 &= f_0 + \epsilon k \\ g_1 &= f_1 + k\partial_1^1 \end{aligned}$$

so;

$$\begin{aligned} g_0 &= f_0 + \beta' k \\ g_1 &= f_1 + k\chi. \end{aligned}$$

**Lemma:** For  $p, p' \in \wp$ ,

$$k(pp') = f_0(p) \cdot k(p') + f_0(p') \cdot k(p) + k(p)k(p')$$

and equality is achieved, that is,  $k$  is a  $f_0$ -derivation.

Proof: For  $p, p' \in \wp$ ,

$$\begin{aligned} k(p, p') &= (h_0^0 - \beta_0^0 f_0)(pp') \\ &= h_0^0(p)h_0^0(p') - \beta_0^0 f_0(p)\beta_0^0 f_0(p') \end{aligned}$$

and

$$\begin{aligned} &f_0(p) \cdot k(p') + f_0(p') \cdot k(p) + k(p)k(p') \\ &= \beta_0^0 f_0(p)k(p') + \beta_0^0 f_0(p')k(p) + k(p)k(p') \\ &= \beta_0^0 f_0(p) \left( h_0^0(p') - \beta_0^0 f_0(p') \right) + \beta_0^0 f_0(p') \left( h_0^0(p) - \beta_0^0 f_0(p) \right) \\ &\quad + \left( h_0^0(p) - \beta_0^0 f_0(p) \right) \left( h_0^0(p') - \beta_0^0 f_0(p') \right) \\ &= \beta_0^0 f_0(p)h_0^0(p') - \beta_0^0 f_0(p)\beta_0^0 f_0(p') + \beta_0^0 f_0(p')h_0^0(p) - \beta_0^0 f_0(p')\beta_0^0 f_0(p) \\ &\quad + h_0^0(p)h_0^0(p') - h_0^0(p)\beta_0^0 f_0(p') - \beta_0^0 f_0(p)h_0^0(p') + \beta_0^0 f_0(p)\beta_0^0 f_0(p') \\ &= h_0^0(p)h_0^0(p') - \beta_0^0 f_0(p)\beta_0^0 f_0(p') \end{aligned}$$

so we get  $k(pp') = f_0(p) \cdot k(p') + f_0(p') \cdot k(p) + k(p)k(p')$ .

**Corollary:**  $\mathfrak{U}(\mathbf{h}) = k: \wp \rightarrow \mathfrak{T}'$ ,

$$\mathfrak{U}(\mathbf{h})(p) = k(p) = h_0^0(p) - \beta_0^0 \delta_0 \mathbf{h}(p)$$

is a crossed module homotopy of  $\mathfrak{U}(f): \mathfrak{U}(\mathcal{F}_\bullet) \rightarrow \mathfrak{U}(\mathcal{F}_\bullet')$  onto  $\mathfrak{U}(g): \mathfrak{U}(\mathcal{F}_\bullet) \rightarrow \mathfrak{U}(\mathcal{F}_\bullet')$ .

**Lemma:** Let  $\mathbf{h}: f \simeq g$  and  $\mathbf{l}: g \simeq u$ . If  $\mathfrak{U}(\mathbf{h}) = k$  and  $\mathfrak{U}(\mathbf{l}) = k'$ , then

$$\mathfrak{U}(\mathbf{h} \odot \mathbf{l}) = k + k'.$$

Proof: For the map  $w_0^{2(h,l)}: \mathcal{F}_0 \rightarrow \mathcal{F}_2'$ ,  $\delta_0^2 w_0^{2(h,l)}(p) = 0$  and  $\delta_1^2 w_0^{2(h,l)}(p) = 0$ , then we get;

$$w_0^{2(h,l)} \in \ker \delta_0^2 \cap \ker \delta_1^2 = \mathcal{NF}_2'$$

for each  $p \in \wp$ . Therefore  $\delta_2^2 w_0^{2(h,l)}(p) = 0$ , since  $\mathcal{F}_2'$  is a simplicial algebra with Moore complex of length one and  $\mathcal{NF}_2' = 0$ . Thus;

$$\begin{aligned} (h_0^0 \odot l_0^0)(p) &= h_0^0(p) + l_0^0(p) - \beta_0^0 g_0(p) + \delta_2^2 w_0^{2(h,l)}(p) \\ &= h_0^0(p) + l_0^0(p) - \beta_0^0 g_0(p). \end{aligned}$$

For each  $p \in \wp = \mathcal{F}_0$ ,

$$\begin{aligned}
\mathfrak{A}(\mathbf{h} \odot \mathbf{l})(p) &= h_0^0(p) + l_0^0(p) - \beta_0^0 g_0(p) - \beta_0^0 f_0(p) \\
&= h_0^0(p) - \beta_0^0 f_0(p) + l_0^0(p) - \beta_0^0 g_0(p) \\
&= h_0^0(p) - \beta_0^0 \delta_0 \mathbf{h}(p) + l_0^0(p) - \beta_0^0 \delta_0 \mathbf{l}(p) \\
&= \mathfrak{A}(\mathbf{h})(p) + \mathfrak{A}(\mathbf{l})(p).
\end{aligned}$$

**Lemma:** For  $\beta_0^0 f_0: f \simeq f$ ,  $\mathfrak{A}(\beta_0^0 f_0) = 0$ .

Proof:  $\mathfrak{A}(\beta_0^0 f_0) = \beta_0^0 f_0 - \beta_0^0 f_0 = 0$ .

**Lemma:** Let be  $\mathbf{h}: f \simeq g$ . For  $\bar{\mathbf{h}}: g \simeq f$ ,  $\mathfrak{A}(\mathbf{h}) = -\mathfrak{A}(\bar{\mathbf{h}})$ .

**Theorem:** Let  $\mathcal{F}_\bullet$  and  $\mathcal{F}'_\bullet$  be simplicial algebras with Moore complexes of length one and  $\mathcal{F}_\bullet$  be a free simplicial algebra. The functor

$$\mathfrak{A}: \mathbf{SimpAlg}_{\leq 1} \rightarrow \mathbf{XMod}$$

preserve the equivalence relation

“ $f \simeq g \Leftrightarrow$  there exists a simplicial homotopy  $\mathbf{h}$  of  $f$  onto  $g$ ”.

## RESULTS AND DISCUSSION

Simplicial commutative algebras play a significant role in various areas of mathematics, including homological algebra, homotopy theory, algebraic  $t$ -theory, and algebraic geometry. It is well-established that simplicial commutative algebras whose Moore complexes are concentrated in degrees zero and one are categorically equivalent to crossed modules of commutative algebras. This equivalence allows us to induce a homotopy between morphisms of crossed modules from a simplicial homotopy.

## REFERENCE

- André, M. (1974). *Homologies des algebres commutatives*. Die Grundlehren der mathematischen Wissenschaften, Band 206, Springer- Verlag, Berlin- New York.
- Akça, İ.İ. and Ege Arslan, U. (2022). Homotopies of 2-Algebra Morphisms. *Communications in Advanced Mathematical Sciences*, 5(4), 170-179
- Akça, İ.İ. and Pak, S. (2010). Pseudosimplicial groups and crossed modules. *Turkish Journal of Mathematics*, 34, 475-487.
- Arvasi, Z. and Porter, T. (1996). Simplicial and crossed resolutions of commutative algebras. *J. Algebras*, 181, 426-448.
- Arvasi, Z. and Porter, T. (1997). Higher dimensional Peiffer elements in simplicial commutative algebras. *Theory and Applications of Categories*, 3(1), 1-23.
- Boyacı, Y. and Avcioğlu, O. (2014). Some relations between crossed modules and simplicial objects in categories of interest. *European Journal of Pure and Applied Mathematics*, 7(4), 412-418.
- Ege Arslan, U. and Özel, E. (2022). On Homotopy Theory of Quadratic Modules of Lie Algebras. *Konuralp Journal of Mathematics*, 10(1), 159-165.
- Ellis, G.J. (1984). *Crossed modules and their higher dimensional analogue*. Doctoral dissertation, University of Wales, Bangor.
- Gülsün Akay, H. (2025). An Equivalence Relation and Groupoid on Simplicial Morphisms. *FILOMAT*, 39(2), 565-574.

- Illusie, L. (1971). *Complex cotangent et deformations I,II*. Springer Lecture Notes in Math. 239, II:283.
- Mutlu, A. and Uslu, E. (2009). To Construction of Free Simplicial Algebras with Given CW-Basis. International Mathematical Forum, 4, 1489-1495.
- Whitehead, J.H.C. (1941). On adding relation to homotopy groups. Annals of Mathematics. 42(2), 409-428.



# **Eco-Friendly Tri-Layer Electrospun Nanofiber Filters: PVA–CS/Cellulose Architecture for High-Efficiency PM2.5 Removal**

**Kenan ISAZADE<sup>1</sup>**

**Hülya KARA SUBAŞAT<sup>2</sup>**

1. Kenan Isazade - Department of Energy, Molecular Nano-Materials Laboratory, Muğla Sıtkı Koçman University, Muğla, Turkey. [orcid.org/0000-0003-0435-6146](https://orcid.org/0000-0003-0435-6146); email: [kananisazade@posta.mu.edu.tr](mailto:kananisazade@posta.mu.edu.tr)
2. Prof. Dr Hülya Kara Subaşat - Department of Energy, Molecular Nano-Materials Laboratory, Muğla Sıtkı Koçman University, Muğla, Turkey. [orcid.org/0000-0002-2032-8930](https://orcid.org/0000-0002-2032-8930); email: [hulyasubasat@mu.edu.tr](mailto:hulyasubasat@mu.edu.tr)

## ABSTRACT

Air pollution, particularly from fine particulate matter (PM<sub>2.5</sub>), poses a major threat to public health worldwide. In this work, a recyclable tri-layer nanofibrous air filter was fabricated via electrospinning using PVA–chitosan (outer layers) and PVA–cellulose (middle layer). The resulting membrane exhibited a uniform fiber morphology with diameters ranging from 270 to 360 nm, and porometry confirmed a smallest pore size of 0.512  $\mu\text{m}$  with a mean flow pore size of 0.843  $\mu\text{m}$ . Filtration tests (TSI 8130, 2% NaCl aerosol, 32 L/min airflow) revealed a removal efficiency of 99.95–99.97% with penetration below 0.05%, while the associated pressure drop was approximately 1504 Pa. Mechanical evaluation showed a tensile strength of 8.60 MPa and a tear resistance of 8.11 MPa, confirming structural stability under operational conditions. To the best of our knowledge, this is the first report of a recyclable tri-layer PVA–chitosan / PVA–cellulose / PVA–chitosan air filter that combines high filtration efficiency, controlled pore structure, and strong mechanical performance without relying on electret charging. This scalable and environmentally friendly approach offers a promising solution for reducing PM<sub>2.5</sub> exposure and improving indoor air quality.

*Keywords – nanofiber air filter, PM<sub>2.5</sub>, electrospinning, poly(vinyl alcohol), cellulose, recyclable membranes, filtration efficiency*

---

## INTRODUCTION

Nanotechnology has emerged as one of the most transformative fields in modern materials science, offering innovative solutions to persistent environmental and industrial challenges. Among its many applications, the development of nanofibers represents a particularly dynamic research area due to their unique combination of high surface-to-volume ratio, controllable porosity, and exceptional functionality. These characteristics make nanofibers highly attractive for next-generation air filtration technologies, where the efficient removal of fine particulate matter (PM) is crucial for both human health and environmental protection.

### ***Air Pollution and the Need for High-Performance Filters***

Air pollution, especially from PM<sub>2.5</sub> (particles with an aerodynamic diameter below 2.5  $\mu\text{m}$ ), remains a major global concern. Prolonged exposure to PM<sub>2.5</sub> has been directly linked to cardiovascular, respiratory, and neurological disorders. Conventional filtration media such as nonwoven polypropylene mats or electret filters often struggle to maintain both high

capture efficiency and low pressure drop while also facing limitations in recyclability. Therefore, the search for sustainable, bio-based, and recyclable filtration materials has intensified in recent years, aligning with global sustainability goals

### ***Electrospinning as a Versatile Fabrication Technique***

Electrospinning has become the most reliable and scalable technique for fabricating nanofibers with diameters typically below one micron. The process, first introduced in the early 20th century and later popularized in the 1990s, uses electrostatic forces to draw polymer solutions into fine fibers. This approach allows precise control of morphology and thickness by adjusting parameters such as polymer concentration, applied voltage, tip-to-collector distance, and flow rate. Compared with other fabrication methods, electrospinning offers superior uniformity, tunability, and the possibility of combining multiple polymeric or inorganic phases within a single continuous fiber network (Bhardwaj and Kundu, 2010; Liu et al., 2017; Kuru et al., 2023, Erkarslan et al, 2024). These attributes make it ideal for air filtration, where submicron fiber diameters enhance particle capture efficiency while maintaining adequate permeability.

### ***Advancements and Limitations in Nanofiber-Based Filters***

Recent studies have demonstrated a wide range of electrospun nanofiber membranes engineered for air filtration. Wang et al. (2017) reported multilayer PA6/PTT nanofiber membranes exhibiting reduced pressure drops compared with single-layer systems, while Li et al. (2020) showed that incorporating zein into PVA nanofibers improved capture efficiency due to smaller fiber diameters. Functional modifications, such as the inclusion of reduced graphene oxide (Zhang et al., 2018) or metal oxide nanoparticles (Lv et al., 2019), have further expanded the versatility of these systems. However, many existing membranes still depend on synthetic polymers, non-biodegradable components, or electret charging, which limits their sustainability and long-term performance

### ***Motivation for Bio-Based Tri-Layer Design***

To address these challenges, bio-based polymers such as chitosan and cellulose have drawn significant interest due to their abundance, biodegradability, and favorable mechanical properties. Chitosan, a derivative of chitin, offers antimicrobial activity and surface functionality, whereas cellulose provides structural stability and chemical resistance. Combining these biopolymers within a tri-layer configuration—with PVA–chitosan outer layers and a PVA–cellulose middle layer—enables the creation of a recyclable, high-performance nanofibrous air filter. Such architecture harmonizes mechanical integrity with efficient PM2.5 capture and balanced airflow resistance, eliminating the need for electret charging



### ***Objective of the Present Work***

This chapter introduces a novel tri-layer PVA–chitosan / PVA–cellulose / PVA–chitosan electrospun air filter designed to achieve both environmental compatibility and superior filtration performance. The study explores how multilayer structuring and material synergy influence morphological uniformity, pore distribution, mechanical strength, and filtration efficiency. The approach aligns with contemporary green manufacturing trends, offering a potential pathway toward scalable, recyclable, and high-efficiency air filtration materials suitable for real-world applications.

## **MATERIALS AND METHODS**

### ***Materials***

All materials used in this study were selected to ensure environmental compatibility, high purity, and reproducibility. Poly(vinyl alcohol) (PVA, average molecular weight 85,000–124,000 g·mol<sup>-1</sup>, degree of hydrolysis 87–89%), chitosan (degree of deacetylation 75–85%), and cellulose (molecular weight ~30,000 g·mol<sup>-1</sup>, degree of substitution 2.36) were obtained from Sigma-Aldrich (Germany). Analytical-grade acetic acid, ethanol, and deionized (DI) water were used as solvents and diluents without further purification.

PVA was selected as the matrix polymer due to its excellent fiber-forming ability, water solubility, and mechanical strength. Chitosan was incorporated to provide surface functionality and biodegradability, whereas cellulose was employed for structural reinforcement and chemical stability. Together, these materials ensured mechanical robustness, environmental friendliness, and recyclability—key requirements for sustainable air filtration systems.

### ***Preparation of Polymer Solutions***

Two polymer blends were prepared for the tri-layer membrane: PVA–chitosan (8:2 w/w) for the outer layers and PVA–cellulose (9:1 w/w) for the middle layer.

Chitosan was dissolved in 2 wt.% acetic acid under magnetic stirring at 50 °C for 12 h. In parallel, PVA was dissolved in a water/ethanol mixture (80/20 v/v) at 80 °C for 2 h. The two solutions were combined and stirred for 6 h, followed by ultrasonic homogenization for 1 h to remove air bubbles and ensure homogeneity.

The cellulose-based solution was prepared by dispersing cellulose powder in DI water at 60 °C until uniform, then blending it with a 10 wt.% PVA solution (9:1 ratio) and ultrasonicated for 30 min. Both solutions were

aged for 12 h at room temperature ( $\sim 25\text{ }^{\circ}\text{C}$ ) before electrospinning to stabilize viscosity ( $350\text{--}450\text{ mPa}\cdot\text{s}$ ).

**Electrospinning Process**

Electrospinning was carried out using an Inovenso S1 system under controlled ambient conditions ( $25 \pm 2\text{ }^{\circ}\text{C}$ ; 15–20% RH). The polymer solutions were loaded into 10 mL syringes equipped with stainless-steel needles (0.8 mm inner diameter). A high-voltage DC supply provided the electric field, while a precision syringe pump regulated the polymer flow (see Figure 1 and Table 1).

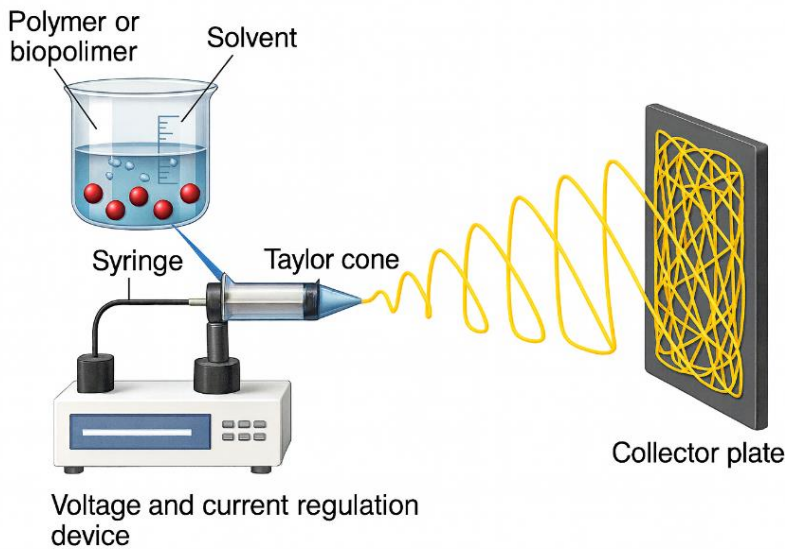


Figure 1. Schematic representation of the electrospinning setup showing the formation of the Taylor cone and fiber jet deposition on the collector plate. A high voltage applied between the syringe tip and collector induces the jet, forming continuous nanofibers.

**Table 1.** Electrospinning parameters used for the fabrication of PVA–Chitosan and PVA–Cellulose nanofiber layers.

Parameter	PVA–Chitosan	PVA–Cellulose
Applied Voltage (kV)	20.4 ± 0.5	22.0 ± 0.5
Flow Rate (mL·h <sup>-1</sup> )	0.01	0.018
Tip-to-Collector Distance (cm)	22	22
Deposition Time per Layer (h)	4	4

Sequential deposition was carried out to form a tri-layer structure (PVA–CS / PVA–Cellulose / PVA–CS) on a polypropylene (PP) spunbond substrate (Figure 2). The total spinning time was 12 h. A drum collector

rotating at 500 rpm promoted random fiber orientation. After fabrication, the membranes were vacuum-dried at 60 °C for 12 h to remove residual solvents and enhance interlayer adhesion.

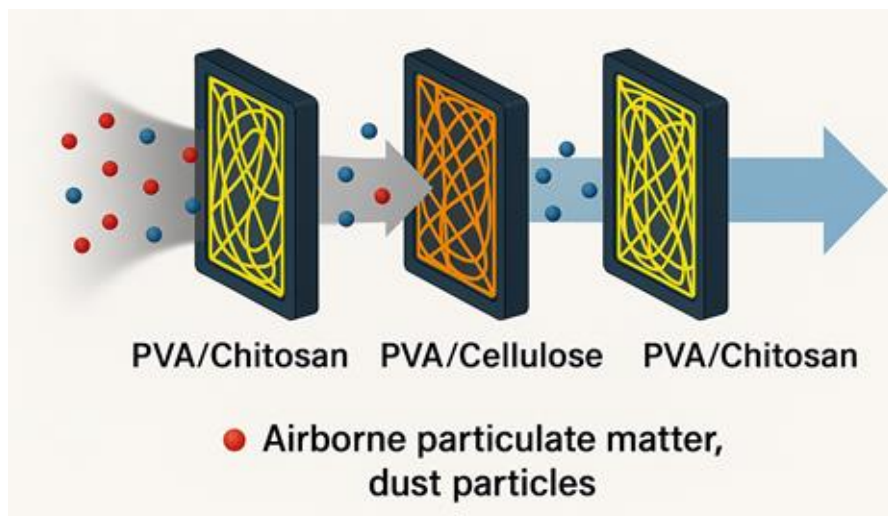


Figure 2. Schematic of the tri-layer membrane structure fabricated by sequential electrospinning: outer PVA–chitosan layers and a middle PVA–cellulose layer on PP substrate.

## STRUCTURAL CHARACTERIZATION

### *Morphology and Fiber Diameter*

The surface morphology of the nanofibers was examined by Scanning Electron Microscopy (SEM). The images revealed a uniform and bead-free morphology with fiber diameters ranging from 270 to 360 nm, depending on polymer composition and spinning parameters (see Figure 3). The corresponding diameter distribution histogram confirmed a narrow and symmetric size distribution, indicating stable electrospinning conditions.

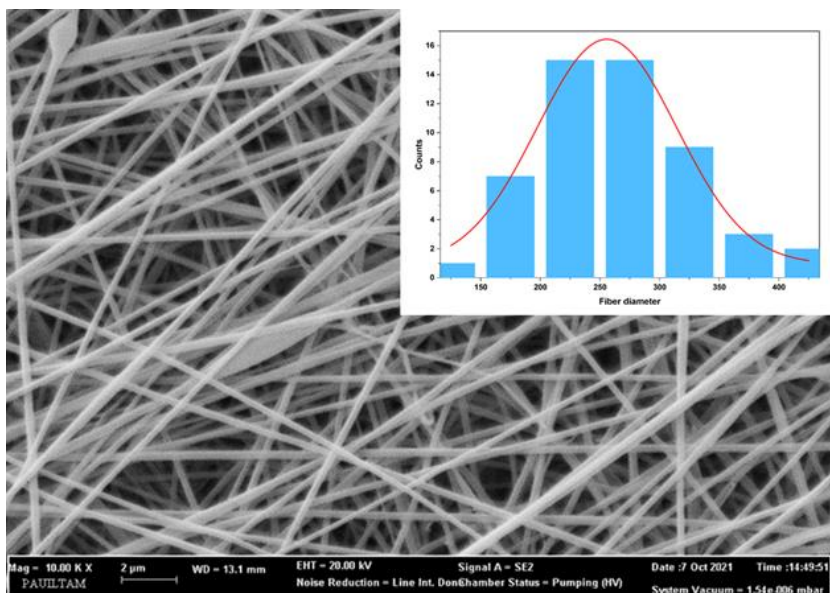


Figure 3. SEM micrograph of the electrospun tri-layer nanofiber membrane showing uniform, bead-free morphology. The inset histogram represents the fiber diameter distribution fitted with a Gaussian curve (mean diameter  $\approx$  270–360 nm).

### ***Porometry and Pore Size Distribution***

Pore-structure analysis was carried out using a Porolux 1000 capillary-flow porometer in accordance with ASTM F316-03. Measurement parameter settings value used for porosity analysis is given in Table 2. A wetting fluid with surface tension of  $16 \text{ dyn}\cdot\text{cm}^{-1}$  was employed to determine the smallest pore, mean-flow pore, and bubble-point diameters.

Table 2. Measurement settings used for porosity analysis.

Parameter	Value
Initial pressure (bar)	0.000
Final pressure (bar)	2.000
Wet measurement	40
Dry measurement	50
Bubble point flow rate (mL/min)	30.00
Bubble point deviation (%)	30.00
Pressure gradient (s/bar)	120.0

Table 3. Results of porosity measurements for the nanofiber filter.

Parameter	Value
Smallest pore size ( $\mu\text{m}$ )	0.5121
Mean flow pore (MFP) size ( $\mu\text{m}$ )	0.8430
Bubble point pore size ( $\mu\text{m}$ )	1.395
Pressure at smallest pore (bar)	1.250
Pressure at MFP (bar)	0.7592
Pressure at bubble point (bar)	0.4588
Bubble point flow rate (L/min)	0.01807

The flow–pressure behavior of the wet and dry curves is presented in Figure 4, while the pore-size distribution derived from these data is shown in Figure 5.

The smallest pore size, mean-flow pore, and bubble-point values were calculated as 0.512  $\mu\text{m}$ , 0.843  $\mu\text{m}$ , and 1.395  $\mu\text{m}$ , respectively (Table 3). The cumulative and differential flow curves confirmed a narrow distribution centered around  $\approx 0.8 \mu\text{m}$ , demonstrating a well-defined porous network that ensures high air permeability and effective particle capture.

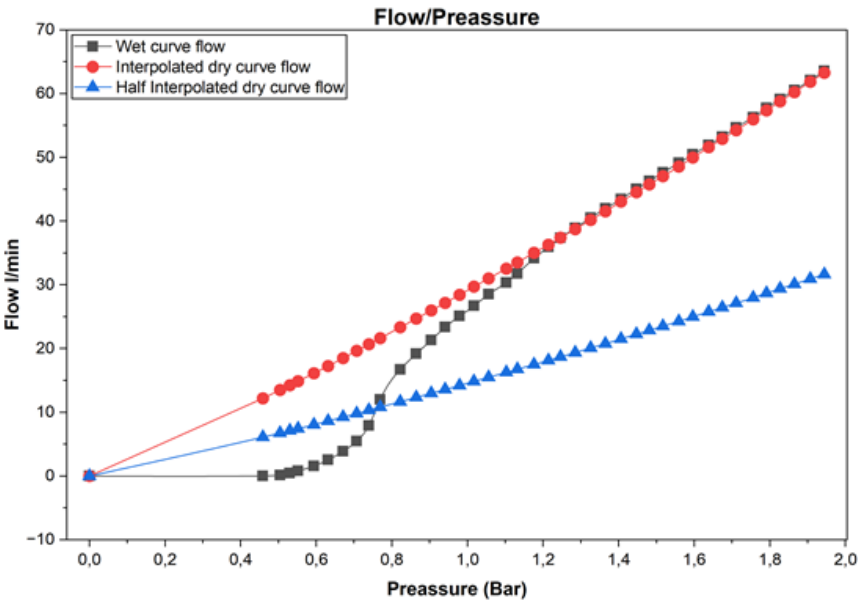


Figure 4. Flow–pressure characteristics obtained from capillary-flow porometry for the tri-layer nanofiber membrane. The wet-curve, interpolated dry-curve, and half-dry-curve data were used to determine pore-size parameters.

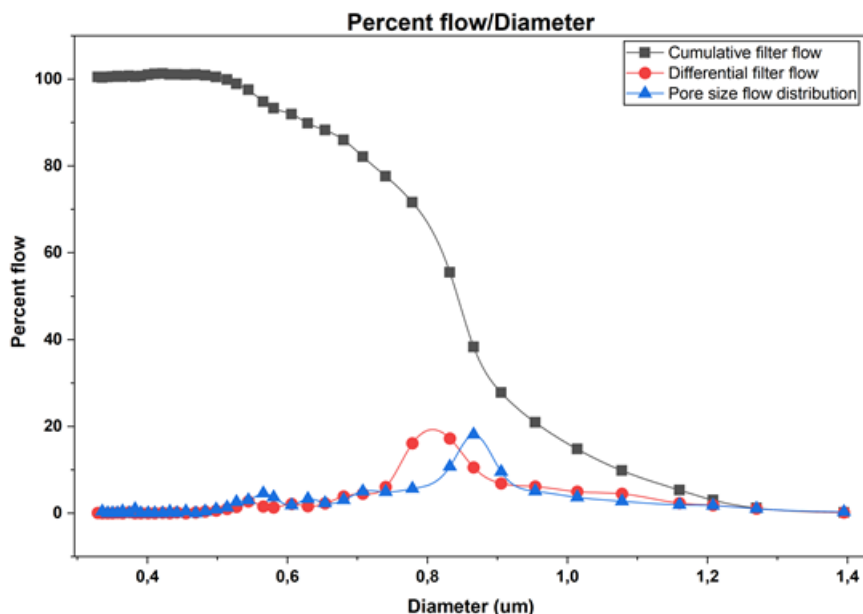


Figure 5. Pore-size distribution of the tri-layer membrane obtained from porometry analysis. Cumulative, differential, and normalized flow curves indicate a narrow pore-diameter range centered near 0.8  $\mu\text{m}$ .

### ***Filtration Performance***

Filtration efficiency was evaluated using a TSI 8130 automated filter tester with a 2 wt.% NaCl aerosol at a flow rate of  $32 \text{ L} \cdot \text{min}^{-1}$  (face velocity  $5.33 \text{ cm} \cdot \text{s}^{-1}$ ), in accordance with EN 1822-3:2009. The tri-layer membrane achieved a filtration efficiency of 99.95–99.97%, penetration below 0.05%, and a pressure drop around 1504 Pa. The detailed air permeability and filtration performance parameters for both samples are summarized in Table 4.

Table 4. Air permeability and filtration performance of the fabricated nanofiber filters.

Sample	Resistance (Pa)	Penetration (%)	Filtration efficiency (%)
Sample 1	1504.0	0.029	99.97
Sample 2	1504.2	0.044	99.95

### ***Mechanical Testing***

Mechanical properties were evaluated to ensure that the tri-layer nanofiber system could withstand handling and operational stresses. Tensile strength and tear resistance tests were performed using an SDL Testometric M350–10 CT universal testing machine following ISO 527-1/-3 and ISO 6383-1 standards, respectively.

- Tensile strength: 8.60 MPa
- Tear resistance: 8.11 MPa

These results indicated that the combination of cellulose and chitosan layers significantly enhanced the membrane's mechanical robustness, enabling reuse and structural stability during prolonged filtration cycles.

## DISCUSSION

### *Correlation Between Morphology and Filtration Performance*

The morphology of electrospun fibers plays a decisive role in determining both airflow resistance and particle-capture efficiency. The SEM observations (Figure 2.2) showed a continuous and bead-free fiber network with diameters between 270–360 nm, which lies within the optimum range for PM<sub>2.5</sub> interception and diffusion-based capture mechanisms. Fibers thinner than 400 nm enhance interception and Brownian diffusion effects, improving fine-particle removal efficiency, while maintaining sufficient mechanical cohesion.

The narrow fiber diameter distribution and homogeneously packed tri-layer structure led to uniform pore formation, as confirmed by porometry (Figures 4 and 5). Such microstructural uniformity ensures consistent air permeability, preventing localized air bypass or excessive pressure drop. Consequently, the tri-layer membrane achieved a stable filtration efficiency of 99.95–99.97%, demonstrating that fiber uniformity and pore-size control are key factors governing high-performance filtration.

### *Role of Tri-Layer Configuration*

The designed PVA–CS / PVA–Cellulose / PVA–CS configuration successfully combined the advantages of each biopolymer layer. The outer chitosan-based layers provided surface functionality and particle adhesion sites, while the cellulose-rich middle layer served as a structural backbone, contributing to porosity and mechanical support. This sandwich-like arrangement improved filtration stability and mechanical endurance during continuous operation.

The porometric data (Table 2) indicate that the membrane's mean-flow pore size (MFP) was 0.843  $\mu\text{m}$ , which is particularly effective for trapping particles smaller than 2.5  $\mu\text{m}$  without generating excessive pressure loss. The symmetrical pore distribution centered near this MFP value further suggests that the layer interfaces did not introduce dead zones or irregular permeability regions—an issue commonly observed in non-uniform multilayer filters.

This tri-layer design thus achieves a balance rarely found in single-layer electrospun membranes:

- High filtration efficiency from the outer functionalized layers,
- Structural reinforcement and uniform permeability from the middle layer,

- Recyclable, all-bio-based composition enhancing environmental sustainability.

### ***Influence of Material Composition***

Each polymer component contributed synergistically to the overall performance. Poly(vinyl alcohol) acted as a stabilizing matrix with excellent electrospinnability and adhesion between layers. Chitosan, with its amino and hydroxyl groups, introduced polar surface sites, improving particle adsorption through dipole–dipole and hydrogen-bonding interactions. Cellulose imparted stiffness, enhancing mechanical robustness and reducing fiber shrinkage during drying.

This compositional synergy explains the observed combination of high tensile strength (8.60 MPa) and tear resistance (8.11 MPa) with low structural deformation. Similar trends have been reported in hybrid PVA–biopolymer nanofibers (Wang et al., 2017; Li et al., 2020), where reinforcement through hydrogen bonding improves both morphology and strength. However, in contrast to these studies, the present tri-layer design achieves comparable or superior efficiency without requiring electret treatment or synthetic additives, emphasizing its sustainable and recyclable nature.

### ***Comparison with Literature***

The obtained filtration efficiencies ( $\approx 99.9\%$ ) are competitive with or superior to values reported for conventional electrospun membranes. For instance, Wang et al. (2017) achieved 99.8% efficiency at 1300 Pa using PA6/PTT multilayers, while Zhang et al. (2018) reported 99.9% with rGO-doped PVDF membranes but required corona charging to maintain stability. In comparison, the PVA–CS/cellulose system reached 99.97% efficiency at 1504 Pa under neutral electrostatic conditions, validating its intrinsic structural performance.

Furthermore, the mean-flow pore size ( $0.843\ \mu\text{m}$ ) measured here is narrower and better controlled than in most single-layer PVA or PAN membranes (typically  $1.0\text{--}1.5\ \mu\text{m}$ ). This tight control translates directly to reduced aerosol penetration and more predictable air permeability, offering an attractive route toward low-pressure-drop, bio-based HEPA alternatives.

### ***Practical Implications and Recyclability***

From an application perspective, the membrane's combination of mechanical durability, filtration stability, and biodegradability positions it as a strong candidate for next-generation indoor air filtration, HVAC pre-filters, and personal protective systems. Unlike conventional polypropylene-based electret filters, which lose charge over time and are not recyclable, the present PVA–chitosan/cellulose composite can be regenerated by mild washing and drying cycles due to its aqueous compatibility and chemical stability.



This recyclability provides both economic and environmental advantages by reducing solid waste and minimizing the carbon footprint associated with filter replacement. The fully aqueous-based fabrication route also avoids toxic solvents such as DMF or HFIP, further reinforcing the green-chemistry principle embedded in the membrane design.

## CONCLUSION

In this study, an eco-friendly tri-layer electrospun nanofiber membrane composed of PVA–chitosan / PVA–cellulose / PVA–chitosan was successfully fabricated and evaluated for high-efficiency air filtration applications. The multilayer configuration, prepared entirely through aqueous-based electrospinning, enabled a sustainable manufacturing approach free of toxic solvents or synthetic additives.

The resulting membrane exhibited a uniform and bead-free morphology, with nanofiber diameters ranging from 270 to 360 nm and a mean-flow pore size of 0.843  $\mu\text{m}$ . Porometry confirmed a well-defined, narrow pore-size distribution (0.5–1.4  $\mu\text{m}$ ), while filtration tests demonstrated PM<sub>2.5</sub> removal efficiencies exceeding 99.95% at a pressure drop of approximately 1504 Pa. Mechanical characterization revealed excellent integrity, with tensile strength of 8.60 MPa and tear resistance of 8.11 MPa, ensuring durability and reusability under practical operation.

The synergistic combination of PVA's mechanical stability, cellulose's structural rigidity, and chitosan's surface functionality produced a filter medium that is not only high-performing but also biodegradable and recyclable. The design successfully eliminates the need for electret charging while achieving filtration metrics comparable to or superior to commercial HEPA materials.

From a broader perspective, this research highlights the potential of bio-derived and green-manufactured nanofibers as viable alternatives to petroleum-based filter media. The presented tri-layer system can be adapted for diverse applications—including indoor air purification, HVAC systems, respiratory masks, and biomedical clean environments—while supporting circular-economy principles through washable and compostable filter design.

Future work should focus on scaling the process through multi-nozzle or needleless electrospinning, integrating functional additives such as antimicrobial or photocatalytic agents, and performing long-term reusability and environmental exposure tests. Such advancements will further establish the proposed material as a cornerstone in the development of next-generation sustainable air-filtration technologies.

## REFERENCES

- Bhardwaj, N., & Kundu, S. C. (2010). *Electrospinning: A fascinating fiber fabrication technique*. *Biotechnology Advances*, 28(3), 325–347.
- Cui, Y., Li, B., He, H., Zhou, W., Chen, B., & Qian, G. (2014). *Metal–organic frameworks as platforms for functional materials*. *Accounts of Chemical Research*, 47(9), 3050–3060.
- Erkarslan, U., Oylumluoglu, Eroğlu, Ö., Coban, M. B., Subasat, H. K. (2024). *Synthesis and photoluminescence study of two new complexes  $Er^{3+}$  and  $Yb^{3+}$  and their PMMA based composite fibers*. *Journal of Molecular Structure*, 1312, 138633
- Li, Y., Zhang, X., & Liu, J. (2020). *Zein/poly(vinyl alcohol) nanofibrous membranes for particulate filtration*. *Journal of Applied Polymer Science*, 137(8), 48532.
- Lv, D., Zhu, M., Jiang, Z., Jiang, S., Zhang, Q., & Zhang, T. (2019). *Preparation and characterization of  $TiO_2$ –PVDF nanofibers for air filtration applications*. *Separation and Purification Technology*, 214, 1–8.
- Kuru, F., Coban, M. B., Erkarslan, U., Donmez, A., Oylumluoglu, G., Aygun, M., Subasat, H. K. (2023). *Improved photoluminescence properties of one-dimensional (1D) composite fibers of  $Ho@PVP$  and  $Yb@PVP$  prepared by electrospinning*. *Polyhedron*, 242, 116492
- Wang, C., Wu, S., Jian, M., Xie, J., Xu, Z., Li, Y., & Zhang, Y. (2017). *Multilayer PA6/PTT nanofiber membranes with improved mechanical strength and filtration performance*. *ACS Applied Materials & Interfaces*, 9(5), 4325–4333.
- Yang, J., Zhang, L., Ma, J., & Xu, R. (2013). *Luminescent lanthanide metal–organic frameworks and their applications*. *Chemical Society Reviews*, 42(2), 849–885.
- Zhang, R., Liu, C., Hsu, P.-C., Zhang, C., Liu, N., Zhang, J., Lee, H. R., Lu, Y., Qiu, Y., Chu, S., & Cui, Y. (2018). *Nanofiber air filters with high-temperature stability for efficient  $PM_{2.5}$  removal from the pollution sources*. *Nano Letters*, 16(6), 3642–3649.



# **Fabrication of 3D PCL/GEL/NHA Scaffolds for Bone Tissue Engineering Applications**

**Özay EROĞLU<sup>1</sup>**

**Hülya KARA SUBAŞAT<sup>2</sup>**

1. Özay Eroğlu - Department of Energy, Molecular Nano-Materials Laboratory, Mugla Sıtkı Koçman University, Muğla, Turkey. [orcid.org/0000-0001-6268-9155](https://orcid.org/0000-0001-6268-9155); email: [ozayeroglu2@posta.mu.edu.tr](mailto:ozayeroglu2@posta.mu.edu.tr)
2. Prof. Dr Hülya Kara Subaşat - Department of Energy, Molecular Nano-Materials Laboratory, Mugla Sıtkı Koçman University, Muğla, Turkey. [orcid.org/0000-0002-2032-8930](https://orcid.org/0000-0002-2032-8930); email: [hulyasubasat@mu.edu.tr](mailto:hulyasubasat@mu.edu.tr)

## ABSTRACT

Each year, more than 2.2 million bone graft procedures are performed worldwide to promote adequate bone healing in various skeletal conditions, including nonunion fractures, cervical and lumbar spine fusions, joint arthrodeses, and revision arthroplasties. Bone is currently considered the second most frequently implanted tissue after blood. Bone tissue engineering aims to address these challenges by developing systems that provide alternative bone graft sources and designing three-dimensional, porous scaffolds that facilitate both cell migration and angiogenesis. In this context, the materials used must possess properties similar to those of natural bone tissue. In this study, new compressible and easily moldable composite fibrous materials were fabricated and optimized by electrospinning to model the extracellular matrix (ECM) of bone. These materials were prepared by blending polycaprolactone (PCL), gelatin(GEL), and nano-hydroxyapatite (nHA) in specific ratios to form three-dimensional structures containing a large number of pores of appropriate size for the repair of complex bone fractures. Scanning Electron Microscopy (SEM) analysis revealed the formation of highly porous and interconnected three-dimensional nanofiber structures. Water vapor transmission rate (WVTR), swelling behavior, and biodegradation tests demonstrated that the developed scaffolds possess suitable moisture permeability, water absorption capacity, and a controlled degradation profile. These results indicate that the produced three-dimensional PCL/GEL/nHA scaffolds have strong potential for application in bone tissue engineering.

*Keywords – Bone Tissue Engineering, Nanofiber Scaffolds, Biodegradability, Electrospinning*

---

## INTRODUCTION

Bone can self-renew and self-repair, thus allowing it to heal minor defects. However, aging, malnutrition, infections, inflammation, underlying conditions, drug use, anemia, and smoking can impair its capacity for self-healing. In addition, the size, shape, and location of bone defects often make natural healing more difficult and prolonged (Horner et al., 2010; Correia et al., 2014; Swetha et al., 2010). More than 2.2 million bone grafting procedures (including autografts and allografts) are performed worldwide each year to address these complications.

However, the challenges in the current methodology have led to the development of a field known as bone tissue engineering. Such approaches can be categorized under the field of biomimetics, wherein biomimetic scaffolds are formulated that mimic the extracellular matrix (ECM) of bone.

These scaffolds aim to support cellular processes, including adhesion, proliferation, and differentiation, while promoting angiogenesis and bone regeneration. Among these, electrospinning is one of the most recognized techniques for preparing nanofiber-based scaffolds due to its simplicity, versatility, and the natural bone ECM-like porous structures it yields (Chang et al., 2017). Such scaffolds comprise both organic elements, such as synthetic and natural polymers, and inorganic materials like hydroxyapatite (HA), to achieve desirable attributes of bioactivity, osteoinductivity, and mechanical properties (Pramanik et al., 2023; Liu et al., 2022).

Several biodegradable polymers, including PCL and GEL, offer good prospects in tissue engineering applications owing to their biocompatibility, degradability, and ease of processing (Nair et al., 2007). GEL is a polymer formed by the degradation of collagen, in which RGD sequences enhance cell adhesion and growth; however, it has low mechanical strength and a high degradation rate. These shortcomings are addressed using PCL, a polymer known for its higher mechanical properties and slower degradation rates. PCL resists internal degradation for a long time, making it a suitable component in scaffold design. Research has shown that utilizing PCL and GEL independently or together can produce biomedical materials with enhanced mechanical strength and cell compatibility. This approach shows significant potential for applications in bone tissue engineering (Yao et al., 2016). Incorporating these materials into composite scaffolds enables the creation of structures that accurately mimic the bone extracellular matrix in terms of its microporous nature, mechanical characteristics, and biological functionality. This strategy has considerable potential in solving problems related to bone regeneration, particularly for critical-sized bone defects and those with complex shapes.

Recently, the electrospinning method has gained popularity for creating nanofibers and their scaffolds due to its user-friendly nature, operational flexibility, and ability to produce porous structures (Kuru et al., 2023). However, currently known electrospinning techniques are limited to fabricating two-dimensional structures with small pore sizes, which are rigid, tightly stacked, and challenging to shape. Such restrictions limit the clinical use of these materials, especially in critical-sized bone defects with irregular shapes (Betz et al., 2002; Liu et al., 2022). To address these limitations, advanced techniques have been developed for creating three-dimensional nanofibrous scaffolds. These methods utilize innovative collectors that enable a broader distribution of the electrical field, resulting in structures with enhanced flexibility and porosity (Blakeney et al., 2011).

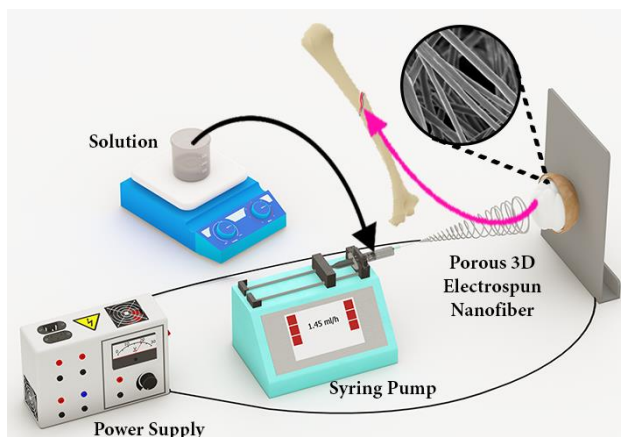


Figure 1. Schematic representation of the electrospinning process for fabricating 3D PCL/GEL/nHA nanofiber scaffolds.

This chapter builds upon previous research by developing innovative, three-dimensional scaffolds that are cotton-like and easily moldable. These scaffolds were created using a flexible electrospinning technique and a custom-designed spherical collector, as illustrated in Figure 1. The structural supports were fabricated using PCL and GEL polymers, which have previously demonstrated their suitability for bone tissue engineering applications due to their compatibility with biological systems and ability to promote tissue growth. These innovative composite scaffolds possess attributes that closely mimic the extracellular matrix (ECM) of bone, addressing the limitations associated with traditional two-dimensional materials in bone regeneration and the treatment of difficult-to-heal bone fractures.

## MATERIALS AND METHODS

### *Materials*

The materials used in this study were obtained from commercial sources, and the chemical solvents were of analytical grade and used as received without further purification. Sigma-Aldrich supplied the following materials: PCL with an approximate molecular weight of 80,000, GEL derived from bovine skin (Type B), trifluoroethanol (TFE), and phosphate-buffered saline (PBS). Nanohydroxyapatite with a particle size of 200 nm was acquired from Nanografi.

### *Preparation of PCL/GEL/nHA solution*

The PCL/GEL mixture was formulated according to the method outlined in the study by Anjum et al. (2017). A 10% (w/v) PCL solution and a 12% (w/v) GEL solution were separately prepared in TFE at room temperature. The two solutions were then combined in equal proportions (PCL: GEL at 50:50) and agitated at ambient temperature for a full day to

create a uniform mixture. nHA was then added to the prepared solution in varying proportions (5–15%), and the mixtures were homogenized first using a magnetic stirrer and then with an ultrasonic bath.

### ***Production of 3D Nanofibers by Electrospinning***

Nanofibers were produced using Spingenix SG100 electrospinning equipment (Figure 2). The prepared polymer solutions were transferred into five cc syringes equipped with 22-gauge blunt needles and placed into the syringe pump integrated with the electrospinning device (Ciftci et al., 2015). During the electrospinning process, the solutions were deposited onto a pre-designed spherical collector under an applied voltage of 15–20 kV and at a flow rate of 0.4–1.2 mL/h. The nanofibers collected on the spherical collector exhibited a three-dimensional, low-density, uncompressed structure resembling a cotton ball (Figures 3 and 4) (Blakeney et al., 2011).

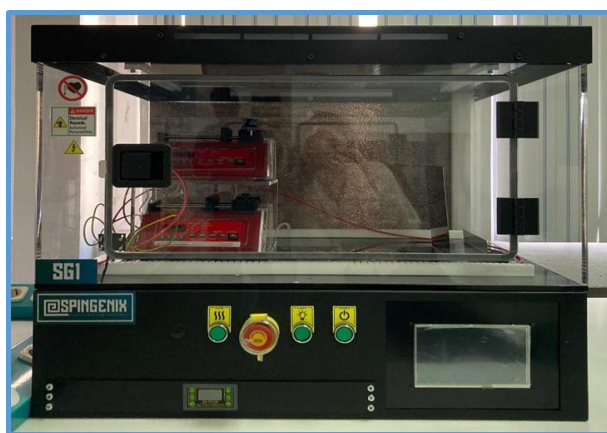


Figure 2. Illustration of the Electrospinning Device.

### ***Morphological study***

The surface morphology and fiber architecture of the electrospun scaffolds were examined using ZEISS GEMINI-500 FESEM. Before imaging, samples were sputter-coated with a thin layer of gold to enhance electrical conductivity. SEM micrographs were obtained at various magnifications to evaluate fiber uniformity, porosity, and structural integrity. Fiber diameter distributions were determined by analyzing at least 100 fibers per sample using ImageJ software (NIH, USA). The average fiber diameter and standard deviation were calculated and reported. Morphological differences between scaffolds with and without HA incorporation were comparatively assessed to observe potential changes in fiber continuity and porosity.

### ***Fourier Transform Infrared spectroscopy***



Fourier transform infrared (FTIR) spectroscopy was employed to determine the chemical structure and confirm the presence of specific functional groups in the produced scaffolds. Spectra were obtained in the 4000–400  $\text{cm}^{-1}$  range with a Perkin-Elmer Spectrum 65-FTIR spectrophotometer.

### ***Water Vapor Transmission Rate (WVTR) study***

The water vapor transmission rate (WVTR) of the scaffolds was measured to evaluate the moisture permeability, which is critical for maintaining a suitable environment for tissue regeneration. The gravimetric method for PCL/GEL/nHA nanofiber scaffolds was carried out using the cup method. The thickness of the scaffold samples used was 5 mm. In the setup used for the tests, glass containers were filled with 10 mL of distilled water and the initial weights ( $W_0$ ) were recorded. Then, the 3D scaffolds were fixed by placing them in the open mouths of the glass containers. The final weights of the assemblies, which were kept at controlled room temperature ( $25 \pm 2^\circ\text{C}$ ) for 24 hours, were measured again after the scaffolds were removed and recorded ( $W_t$ ). The measurements were carried out in triplicate ( $n=3$ ). Using the obtained data, the water vapor permeability rate of the scaffolds ( $\text{mg/m}^2\text{h}$ ) was calculated using equation 1 (Lima et al., 2019).  $\text{WVTR} = (W_0 - W_t) / (A \times t)$  Equation 1 (Lima et al., 2019).

Where ( $W_0 - W_t$ ) is the weight loss of water in milligrams,  $A$  is the mouth area of the container ( $\text{m}^2$ ), and  $t$  is the time in hours (h).

$$\text{WVTR} = \frac{W_0 - W_t}{A \times t} \quad (1)$$

### ***Swelling Study***

Swelling tests were performed for PCL/GEL/nHA nanofiber scaffolds. For the tests, each sample was cut into 6  $\text{cm}^2$  pieces in sets of three, and the weights of the dry scaffolds were first measured. The samples were then incubated in 15 mL of phosphate-buffered saline (PBS) solution (pH: 7.4) in an oven at  $37 \pm 0.5^\circ\text{C}$ . The samples were monitored at specific time points to analyze both initial rapid water retention and long-term behavior: The first 24 hours were used to assess rapid water retention. The scaffolds in PBS were then removed from the buffer, and excess liquid was removed from the scaffold using an air pump. The wet weights of the samples were then weighed to determine their water retention percentages. Measurements were performed in triplicate ( $n=3$ ). Using the dry and wet weights of the scaffolds, time-

dependent water retention rates were calculated using Equation 2 (Shimojo et al., 2016).

Weight: The wet weight of the scaffold measured at the end of a specific incubation period. W<sub>0</sub>: Dry weight of the scaffold measured at the beginning of the test.

$$\text{Swelling Ratio}(\%) = \frac{W_t - W_0}{W_0} \times 100 \quad (2)$$

### ***Biodegradation Study***

In vitro biodegradability tests of PCL/GEL/nHA scaffolds were carried out. Each sample was prepared in sets of triplicates by cutting into 6 cm<sup>2</sup> pieces. To determine the biodegradability properties, the initial dry weights of the samples were recorded; then, each set was incubated in 15 mL of phosphate-buffered saline (PBS, pH 7.4) in an oven at 37 ± 0.5 °C. On days 1, 7, and 14 of incubation, the kept scaffolds were taken out of the buffer and excess liquid was removed from the scaffolds with the help of an air pump. The scaffolds were dried at 37 ± 0.5 °C and weighed again. The percent mass losses of the scaffolds with time in the initial (W<sub>0</sub>) and final (W<sub>t</sub>) weights were determined with the help of the following equation 3 (Ghorbani et al., 2015). Time points of 1, 7, and 14 days were selected to assess initial weight loss, which is primarily associated with the degradation of the more soluble gelatin component and provides information about the early-stage stability of the scaffold. Measurements were performed in triplicate (n=3).

W<sub>t</sub>: The wet weight of the scaffold measured at the end of a specified incubation period (day 1, 7 or 14). W<sub>0</sub>: The dry weight of the scaffold measured at the beginning of the test.

$$\text{Degradation Rate} (\%) = \frac{W_t - W_0}{W_0} \times 100 \quad (3)$$

## **RESULTS AND DISCUSSIONS**

### ***Electrospinning Optimization and Scaffold Morphology***

Ideal nanofibers should exhibit uniform distribution, smooth morphology, and be free of bead structures. For the experiments, mixture ratios of PCL, GEL, and nHA solutions that demonstrated promising potential in bone tissue engineering applications were chosen, based on an evaluation of the nanofiber porosity produced by various proportions of these components. In cases where nanofibers with appropriate morphology could not be obtained, the concentrations and mixture ratios were adjusted, and the system was optimized following the methodology described in the literature (Yılmaz et al., 2017).

Critical variables, including electrical potential, liquid movement rate, and the gap between the needle and collector, were methodically fine-tuned to produce flawless nanofibers with the intended structural properties (Süpüren et al., 2017). The optimization process focused on ensuring uniform fiber formation, minimizing bead structures, and producing a cotton-like, low-density structure suitable for 3D scaffolds. The PCL/GEL solution, prepared at a 50:50 (PCL:GEL) ratio, was supplemented with 5%, 10%, and 15% nHA, respectively. The system was then optimized using the electrospinning parameters provided in Table 2.

Table 2. Optimized Electrospinning Parameters

PCL: GEL Ratio (v/v)	nHA Concentration (%)	Distance (cm)	Voltage (kV)	Flow Rate (mL/min)
50: 50	5%	21	20	0,08
50: 50	10%	17	20	0,14
50 : 50	15%	19	22	0,17

### Morphology of the Scaffolds

Figure 3 shows the morphological properties of PCL/GEL/nHA (%5%, 10%, 15%) nanofiber scaffolds produced via electrospinning, as analyzed through scanning electron microscopy (SEM). The SEM images reveal that the nanofibers exhibit a randomly arranged, three-dimensional structure, providing a suitable microenvironment for cell adhesion, proliferation, and differentiation.

The diameter distribution graphs in Figure 4 provide quantitative confirmation of the morphological observations made using SEM. The addition of nHA results in a statistically significant decrease in average fiber diameter:  $790 \pm 100$  nm for 5% nHA,  $750 \pm 45$  nm for 10%, and  $650 \pm 77$  nm for 15%. This trend aligns with previous reports, where the inclusion of ceramic nanoparticles led to increased conductivity and more efficient fiber elongation during electrospinning (Pramanik et al., 2023; Blakeney et al., 2011).

Correspondingly, porosity values decreased from 84% to 73%, indicating a denser fiber network with higher nHA loading. However, all values remain within the optimal range (>70%) for tissue engineering scaffolds, ensuring sufficient nutrient and oxygen diffusion as well as space for neovascularization (Holzwarth & Ma, 2011).

Significantly, the combination of reduced fiber diameter and retained porosity enhances both the surface interaction area and scaffold permeability—key factors for promoting osteoconduction and supporting new tissue ingrowth. These results affirm that the fabricated scaffolds not only replicate bone ECM topography but also possess tunable properties that can be modulated via nHA concentration to suit various regenerative needs.

Generally, smaller fiber diameters lead to a decrease in the pore size of nanofiber scaffolds (Garcia et al., 2021). Increasing the nHA concentration resulted in a reduction in fiber diameter, enabling cells to establish greater contact with the scaffold surface. This, as noted in the literature, enhances cellular behaviors such as adhesion and growth (Yao et al., 2016; Pramanik et al., 2023). The three-dimensional nanofiber structure, combined with the osteoinductive properties of nHA, offers a supportive platform for cell migration and growth, particularly for bone regeneration.

Figure 5 illustrates the physical characteristics of the produced PCL/GEL/nHA nanofiber scaffolds, particularly highlighting their *compressibility*, *reshaping capability*, and *three-dimensional moldability*. In subfigures (a–d), the scaffolds were manually compressed using light hand pressure to visually demonstrate their elastic deformation capacity without structural disintegration. This simple mechanical demonstration was intended to simulate clinical handling conditions where materials must conform to irregular bone defect geometries. Subfigures (e.g.) present the identical scaffold specimens after being reshaped by hand into new configurations, showing their recoverable and adaptable structure. This moldable nature is a critical property for scaffolds intended for in vivo bone tissue engineering, where patient-specific defect shapes require materials that can adapt while maintaining mechanical integrity and porosity.

The compressibility and reshaping evaluations were qualitative and performed manually without instrumentation, based on methods reported in similar studies that aimed to assess the formability of fibrous scaffolds for orthopedic use (Blakeney et al., 2011). These visual tests emphasize the practical applicability of the fabricated 3D nanofiber scaffolds in clinical environments.

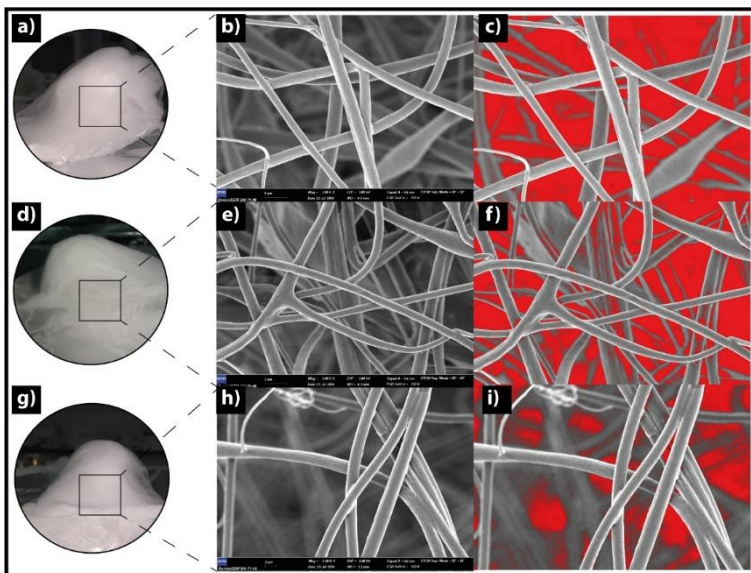


Figure 3. (a) 3D Nanofiber (b) SEM Image (c) Porosity for PCL/GEL/nHA (%5) scaffolds, (d) 3D Nanofiber (e) SEM Image, (f) Porosity for PCL/GEL/nHA (%10) scaffolds, (g) 3D Nanofiber (h) SEM Image, (i) Porosity for PCL/GEL/nHA (%15) scaffolds.

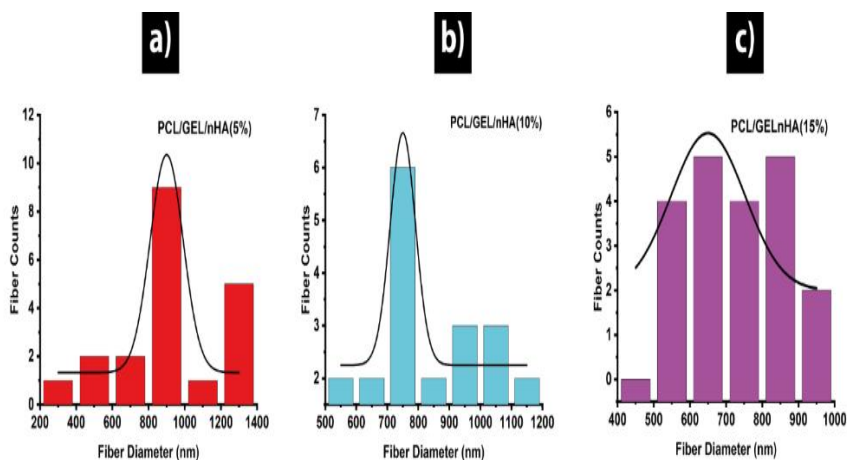


Figure 4. Fiber diameter distributions of PCL/GEL/nHA; (a) 5%, (b) 10%, (c) 15%

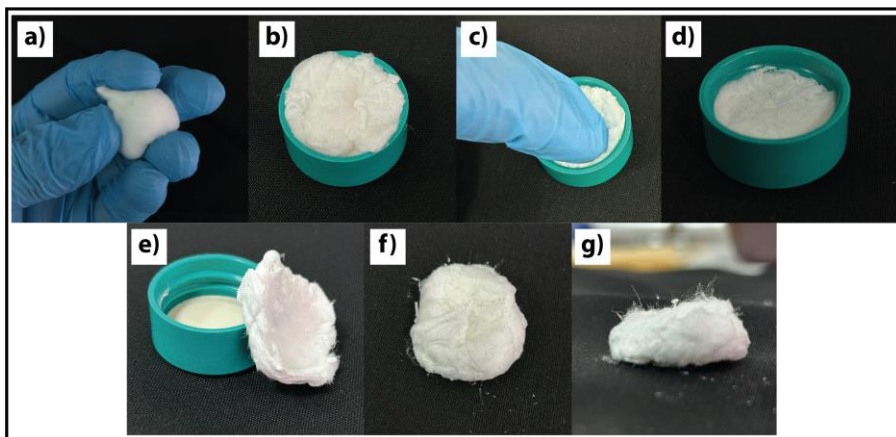


Figure 5. Physical properties of the PCL/GEL/nHA nanofiber scaffolds: a), b), c) and d) compressibility of the scaffold, e) and f) reshaped scaffold from the side view, and g) side profile showing three-dimensional moldability.

### ***FTIR Spectroscopy***

The FTIR analysis, performed to identify the functional groups in the PCL/GEL scaffold and the PCL/GEL/nHA nanocomposite scaffold, is shown in Figure 5. In the FTIR spectrum of PCL/GEL, the bands at 2933 and 2864  $\text{cm}^{-1}$  of PCL correspond to the asymmetric and symmetric stretching of  $\text{CH}_2$ , respectively. A sharp band at 1727  $\text{cm}^{-1}$  belongs to the carbonyl ( $\text{C}=\text{O}$ ) stretching, while the band at 1238  $\text{cm}^{-1}$  is associated with the asymmetric  $\text{C}-\text{O}-\text{C}$  stretching (Dönmez, A., 2020). Furthermore, the bands at 1240  $\text{cm}^{-1}$  and 1170  $\text{cm}^{-1}$  are associated with the asymmetric and symmetric  $\text{C}-\text{O}-\text{C}$  stretching vibrations, respectively, which is consistent with previous studies (Laleh et al., 2010; Lim et al., 2011). The characteristic bands of gelatin were observed at 1638, 1532, and 1240  $\text{cm}^{-1}$ , which correspond to  $\text{C}-\text{O}$  stretching vibrations,  $\text{N}-\text{H}$  bending vibrations, and  $\text{N}-\text{H}$  stretching vibrations, respectively. These bands were also identified by Lim et al. (Lim et al., 2011). In the FTIR spectrum of nHA, the characteristic band at 1028  $\text{cm}^{-1}$  was observed due to the functional group ( $\text{PO}_4^{3-}$ ) in nHA. Furthermore, the slight shifts observed in the positions of amide I and II peaks (e.g., 1532.01  $\rightarrow$  1532.57  $\text{cm}^{-1}$ ) and the decrease in their intensities suggested that HA interacted with the polymer matrix and probably formed hydrogen bonds. Similar results were found in the FTIR spectrum of nHA (Poinern et al., 2011). PCL/GEL/nHA nanocomposite scaffold showed all the characteristic bands of PCL, gelatin, and nHA. In the FTIR spectrum of the PCL/GEL/nHA nanocomposite scaffold, small shifts in these bands and the presence of characteristic bands of low intensity nHA indicated that nHA was deposited onto the PCL/GEL scaffold (Gautam et al., 2021).

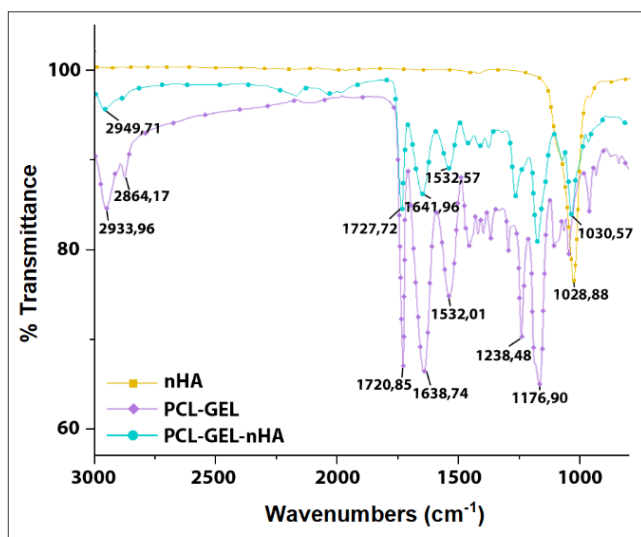


Figure 6. FTIR spectra of nHA, PCL/GEL, and PCL/GEL/nHA scaffolds show each component's characteristic absorption bands.

### ***WVTR, Swelling, and Biodegradation of the Scaffolds***

The moisture vapor permeability (WVTR) and moisture balance of scaffolds used in bone tissue engineering are critical for cell viability and tissue integration. However, excessively high WVTR can cause excessive moisture in the scaffold, while too low can lead to dryness. Therefore, the moisture permeability properties of scaffolds should be optimized to provide a suitable microenvironment for cell survival and proliferation. The functional properties of the scaffolds, including WVTR, swelling, and biodegradation, were evaluated using the 15% nHA formulation, as this group exhibited the most uniform and bead-free fiber morphology, identifying it as the most promising candidate for tissue engineering applications. The PCL/GEL/nHA scaffold's WVTR was measured as approximately 290.2 mg/m<sup>2</sup> h, indicating moderate moisture permeability. This level of water vapor transmission is beneficial for maintaining appropriate moisture at the scaffold-tissue interface, supporting cellular viability and tissue integration, and is consistent with previously reported values in biomedical applications (Zhang et al., 2021).

The 1-day swelling and biodegradation profiles of the scaffold are presented in Figure 7. The scaffold exhibited rapid hydrophilic behavior, absorbing a significant amount of water within the first 24 hours and reaching a maximum swelling ratio of  $89.53 \pm 5.2\%$  at the end of 24 hours (Figure 7). This high water retention capacity is critical for creating a humid environment conducive to cell attachment and nutrient transport.

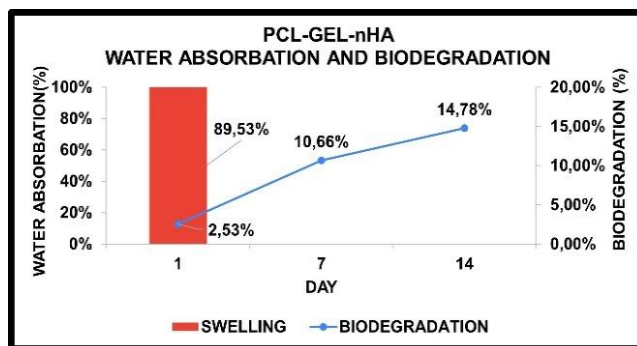


Figure 7. Swelling ratio and biodegradation behavior of the PCL/GEL/nHA scaffold over 14 days.

In terms of biodegradability, the scaffold exhibited a gradual weight loss of approximately 14.78% over 14 days, indicating a controlled degradation profile suitable for tissue engineering applications. This behavior is consistent with the degradation kinetics typically observed in composite systems that combine a slow-degrading synthetic polymer (PCL) with a faster-degrading natural polymer (gelatin). In the early stages, gelatin components are preferentially resorbed, while PCL ensures long-term structural integrity. Moreover, the incorporation of nano-hydroxyapatite (nHA) may further influence the degradation behavior by altering the surface hydrophilicity and porosity of the scaffold, as reported in similar nanocomposite systems (Ghorbani et al., 2015; Rashid Mad Jin et al., 2015). This finely tuned degradation process is particularly advantageous in bone tissue engineering, where initial mechanical support must be followed by gradual replacement with regenerating tissue.

Similarly, the scaffold exhibited a swelling ratio of approximately 89.53% after 14 days, which can be attributed to the hydrophilic nature of gelatin and the highly porous nanofiber structure. Gelatin's amino acid residues and RGD sequences readily bind water molecules, while nHA contributes by introducing functional groups that promote capillary-driven absorption. Previous studies have reported comparable swelling behavior in gelatin-based electrospun scaffolds, highlighting its role in enhancing nutrient transport, waste exchange, and cell adhesion (Yao et al., 2016; Liu et al., 2020). Such high water uptake capacity creates a hydrated microenvironment, which is critical for maintaining cell viability and proliferation.

Taken together, the observed swelling and biodegradation characteristics are in agreement with prior studies on PCL/gelatin-based scaffolds incorporating bioactive ceramics, such as HA, where a balance between mechanical stability and bioresorption is essential (Liu et al., 2022; Rashid et al., 2015). These findings support the conclusion that the developed PCL/GEL/nHA scaffolds exhibit a favorable combination of moisture



permeability, hydrophilicity, and controlled degradation, underscoring their potential as promising candidates for bone tissue regeneration.

## CONCLUSIONS

In this study, three-dimensional (3D) nanofiber scaffolds composed of PCL, GEL, and nHA were successfully fabricated using a customized electrospinning method. Optimization of electrospinning parameters, including solution composition, applied voltage, flow rate, and needle-to-collector distance, enabled the production of uniform, bead-free nanofibers with controlled fiber diameters and high porosity, as confirmed by scanning electron microscopy (SEM) analysis.

FTIR spectroscopy confirmed the chemical integration of PCL, GEL, and nHA components, with characteristic absorption bands corresponding to each material and indicating successful composite formation. SEM imaging revealed randomly oriented, highly porous three-dimensional fiber networks, favorable for facilitating cell migration, nutrient diffusion, and vascularization.

Physical evaluations demonstrated that the scaffolds exhibited desirable water vapor permeability ( $\sim 290.2 \text{ mg/m}^2\cdot\text{h}$ ), swelling behavior ( $\sim 89.53\%$  water uptake), and a controlled biodegradation profile ( $\sim 14.78\%$  weight loss over 14 days), aligning well with the requirements for bone tissue engineering applications. These properties, combined with the compressibility and moldability of the scaffolds, suggest their suitability for conforming to irregularly shaped bone defects.

Overall, the developed 3D PCL/GEL/nHA scaffolds demonstrate a promising combination of physicochemical properties, biodegradability, and osteoconductivity. Their structure closely mimics the native extracellular matrix of bone, offering significant potential for use in regenerative therapies targeting critical-sized and complex bone defects.

## REFERENCES

- Akgüner, Z. P. ve Bal Öztürk, A. (2021). Development of tissue scaffolds with nanoparticles for bone tissue engineering applications. *Pamukkale University Journal of Engineering Sciences*, 27(7), 842–850. doi:10.5505/pajes.2020.63933
- Anjum, F., Agabalyan, N. A., Sparks, H. D., Rosin, N. L., Kallos, M. S. ve Biernaskie, J. (2017). Biocomposite nanofiber matrices to support ECM remodeling by human dermal progenitors and enhanced wound closure. *Scientific Reports*, 7(1), 1–17. doi:10.1038/s41598-017-10735-x
- Betz, R. ve R., M. D. (2002). Limitations of autograft and allograft: New synthetic solutions., S561–S570.
- Blakeney, B. A., Tambralli, A., Anderson, J. M., Andukuri, A., Lim, D. J., Dean, D. R. ve Jun, H. W. (2011). Cell infiltration and growth in a low-density,

- uncompressed three-dimensional electrospun nanofibrous scaffold. *Biomaterials*, 32(6), 1583–1590. doi:10.1016/j.biomaterials.2010.10.056
- Campana, V., Milano, G., Pagano, E., Barba, M., Cicione, C., Salonna, G., ... Logroscino, G. (2014). Bone substitutes in orthopaedic surgery: from basic science to clinical practice. *Journal of Materials Science: Materials in Medicine*, 25(10), 2445–2461. doi:10.1007/s10856-014-5240-2
- Cestari, F., Petretta, M., Yang, Y., Motta, A., Grigolo, B. ve Sglavo, V. M. (2021). 3D printing of PCL/nano-hydroxyapatite scaffolds derived from biogenic sources for bone tissue engineering. *Sustainable Materials and Technologies*, 29(July), e00318. doi:10.1016/j.susmat.2021.e00318
- Chang, B., Ahuja, N., Ma, C. ve Liu, X. (2017). Injectable scaffolds: Preparation and application in dental and craniofacial regeneration. *Materials Science and Engineering R: Reports*, 111, 1–26. doi:10.1016/j.mser.2016.11.001
- Çiftci, Ş., Özek, S., Aksoy, S. A., Aksoy, K. ve Göde, F. (2015). Nanokil Katkılı PVA/Kitosan Nanolif Sentezi ve Karakterizasyonu Synthesis and Characterization of PVA/Chitosan Nanofiber Added Nanoclay. *SDU Journal of Science (E-Journal)*, 10(1), 118–128.
- Correia, S. I., Pereira, H., Silva-Correia, J., Van Dijk, C. N., Espregueira-Mendes, J., Oliveira, J. M. ve Reis, R. L. (2014). Current concepts: Tissue engineering and regenerative medicine applications in the ankle joint. *Journal of the Royal Society Interface*, 11(92). doi:10.1098/rsif.2013.0784
- Dönmez, A. (2020) Synthesis, Structure and Photoluminescence Analysis of a Ho<sup>3+</sup>-cluster-based 3D coordination polymer: {Ho<sub>2</sub>(H<sub>2</sub>O)<sub>2</sub>(DMF)<sub>2</sub>(ATPA)<sub>3</sub>}<sub>n</sub>. *Journal of Cluster Science*, 31, 887-896
- Ebrahimi, Z., Irani, S., Ardeshirylajimi, A., & Seyedjafari, E. (2022). Enhanced osteogenic differentiation of stem cells by 3D printed PCL scaffolds coated with collagen and hydroxyapatite. *Scientific Reports*, 12, 12359. <https://doi.org/10.1038/s41598-022-15602-y>
- Gautam, S., Sharma, C., Purohit, S. D., Singh, H., Dinda, A. K., Potdar, P. D., Chou, C.-F., & Mishra, N. C. (2021). Gelatin-polycaprolactone-nanohydroxyapatite electrospun nanocomposite scaffold for bone tissue engineering. *Materials Science and Engineering C*, 119, 111588. <https://doi.org/10.1016/j.msec.2020.111588>
- Gautam, S., Purohit, S. D., Singh, H., Dinda, A. K., Potdar, P. D., Sharma, C., Chou, C.-F., & Mishra, N. C. (2023). Surface modification of PCL-gelatin-chitosan electrospun scaffold by nano-hydroxyapatite for bone tissue engineering. *Materials Today Communications*, 34, 105237. <https://doi.org/10.1016/j.mtcomm.2022.105237>
- Garcia, R. A., Stevanovic, T., Berthier, J., Njamen, G., Tolnai, B., & Achim, A. (2021). A review of cellulose, nanocellulose, and antimicrobial materials for manufacturing disposable face masks. *BioResources*, 16(2), 4321.
- Gentzkow, G., Iwasaki, S., Kenneth, H., Mengel, M., Prendergast, J., Ricotta, J. ve Lipkin, S. (1996). Dermis, to Treat Diabetic Foot Ulcers. *Diabetes Care*, 19(4), 350–354.
- Giuntoli, G., Muzio, G., Actis, C., Ganora, A., Calzone, S., Bruno, M., ... Tonda-Turo, C. (2021). In-vitro Characterization of a Hernia Mesh Featuring a Nanostructured Coating. *Frontiers in Bioengineering and Biotechnology*, 8(January), 1–17. doi:10.3389/fbioe.2020.589223

- Ghorbani, F. M., Kaffashi, B., Shokrollahi, P., Seyedjafari, E., & Ardeshtyrlajimi, A. (2015). PCL/chitosan/Zn-doped nHA electrospun nanocomposite scaffold promotes adipose-derived stem cells adhesion and proliferation. *Carbohydrate polymers*, 118, 133-142.
- He, M., Ichinose, T., Yoshida, Y., Arashidani, K., Yoshida, S., Takano, H., ... Shibamoto, T. (2017). Urban PM2.5 exacerbates allergic inflammation in the murine lung via a TLR2. *Scientific Reports*, 7(1), 1–9. doi:10.1038/s41598-017-11471-y
- Holzwarth, J. M. ve Ma, P. X. (2011). Biomimetic nanofibrous scaffolds for bone tissue engineering. *Biomaterials*, 32(36), 9622–9629. doi:10.1016/j.biomaterials.2011.09.009
- Horner, E. A., Kirkham, J., Wood, D., Curran, S., Smith, M., Thomson, B. ve Yang, X. B. (2010). Long bone defect models for tissue engineering applications: criteria for choice. *Tissue engineering. Part B, Reviews*, 16(2), 263–271. doi:10.1089/ten.teb.2009.0224
- Kuru, F., Coban, M. B., Erkarlan, U., Donmez, A., Oylumluoglu, G., Aygun, M., Subasat, H. K. (2023). *Improved photoluminescence properties of one-dimensional (1D) composite fibers of Ho@ PVP and Yb@ PVP prepared by electrospinning*. *Polyhedron*, 242, 116492
- Laleh, G. M., Molamma, P. P., Mohammad, M., Mohammad, H. N., & Ramakrishna, S. (2010). Bio-functionalized PCL nanofibrous scaffolds for nerve tissue engineering. *Mater Sci Eng C*, 30, 1129-1136.
- Lim, Y. C., Johnson, J., Fei, Z., Wu, Y., Farson, D. F., Lannutti, J. J., ... & Lee, L. J. (2011). Micropatterning and characterization of electrospun poly ( $\epsilon$ -caprolactone)/gelatin nanofiber tissue scaffolds by femtosecond laser ablation for tissue engineering applications. *Biotechnology and bioengineering*, 108(1), 116-126.
- Lima, L. L., Taketa, T. B., Beppu, M. M., de Oliveira Sousa, I. M., Foglio, M. A., & Moraes, A. M. (2019). Coated electrospun bioactive wound dressings: mechanical properties and ability to control lesion microenvironment. *Materials Science and Engineering: C*, 100, 493-504.
- Liu, J., Wu, S., Ma, J., Liu, C., Dai, T., Wu, X., ... Zhou, D. (2022). Polycaprolactone/Gelatin/Hydroxyapatite Electrospun Nanomembrane Materials Incorporated with Different Proportions of Attapulgit Synergistically Promote Bone Formation. *International Journal of Nanomedicine*, 17(August), 4087–4103. doi:10.2147/IJN.S372247
- Liu, Y., Weng, R., Wang, W., Wei, X., Li, J., Chen, X., ... Li, Y. (2020). Tunable physical and mechanical properties of gelatin hydrogel after transglutaminase crosslinking on two gelatin types. *International Journal of Biological Macromolecules*, 162, 405–413. doi:10.1016/j.ijbiomac.2020.06.185
- Nair, L. S. ve Laurencin, C. T. (2007). Biodegradable polymers as biomaterials. *Progress in Polymer Science (Oxford)*, 32(8–9), 762–798. doi:10.1016/j.progpolymsci.2007.05.017
- Pezeshki-Modaress, M., Zandi, M. ve Rajabi, S. (2018). Tailoring the gelatin/chitosan electrospun scaffold for application in skin tissue engineering: an in vitro study. *Progress in Biomaterials*, 7(3), 207–218. doi:10.1007/s40204-018-0094-1
- Poinern, G. J. E., Brundavanam, R. L. X. T., Le, X. T., Djordjevic, S., Prokic, M., & Fawcett, D. (2011). Thermal and ultrasonic influence in the formation of

- nanometer scale hydroxyapatite bio-ceramic. *International journal of nanomedicine*, 2083-2095.
- Pramanik, S., Kharche, S., More, N., Ranglani, D., Singh, G. ve Kapusetti, G. (2023). Natural Biopolymers for Bone Tissue Engineering: A Brief Review. *Engineered Regeneration*, 4(2), 193–204. doi:10.1016/j.engreg.2022.12.002
- Rashid Mad Jin, R., Sultana, N., Baba, S., Hamdan, S., & Ismail, A. F. (2015). Porous PCL/Chitosan and nHA/PCL/Chitosan scaffolds for tissue engineering applications: Fabrication and evaluation. *Journal of Nanomaterials*, 2015, Article ID 357372. <https://doi.org/10.1155/2015/357372>
- Samorezov, J. E. ve Alsberg, E. (2015). Spatial regulation of controlled bioactive factor delivery for bone tissue engineering. *Advanced Drug Delivery Reviews*, 84, 45–67. doi:10.1016/j.addr.2014.11.018
- Semnani, D., Naghashzargar, E., Hadjianfar, M., Dehghan Manshadi, F., Mohammadi, S., Karbasi, S. ve Effaty, F. (2017). Evaluation of PCL/chitosan electrospun nanofibers for liver tissue engineering. *International Journal of Polymeric Materials and Polymeric Biomaterials*, 66(3), 149–157. doi:10.1080/00914037.2016.1190931
- Shimojo, A. A. M., Perez, A. G. M., Galdames, S. E. M., Brissac, I. C. S., & Santana, M. H. A. (2016). Stabilization of porous chitosan improves the performance of its association with platelet-rich plasma as a composite scaffold. *Materials Science and Engineering: C*, 60, 538-546.
- Süpüren, G., Kanat, E., Çay, A., Kırıcı, T., Gülümser, T. ve Tarakçıoğlu, I. (2007). Nano lifler (Bölüm 2). *Tekstil ve Konfeksiyon*, 17(2), 83–89.
- Swetha, M., Sahithi, K., Moorthi, A., Srinivasan, N., Ramasamy, K. ve Selvamurugan, N. (2010). Biocomposites containing natural polymers and hydroxyapatite for bone tissue engineering. *International Journal of Biological Macromolecules*, 47(1), 1–4. doi:10.1016/j.ijbiomac.2010.03.015
- Thomson, R. C., Yaszemski, M. J., Powers, J. M. ve Mikos, A. G. (1996). Fabrication of biodegradable polymer scaffolds to engineer trabecular bone. *Journal of Biomaterials Science, Polymer Edition*, 7(1), 23–38. doi:10.1163/156856295X00805
- Tiğli, R. S., Kazaroglu, N. M., Maviş, B. ve Gumusderelioglu, M. (2011). Cellular behavior on epidermal growth factor (EGF)-immobilized PCL/gelatin nanofibrous scaffolds. *Journal of Biomaterials Science, Polymer Edition*, 22(1–3), 207–223. doi:10.1163/092050609X12591500475424
- Wang, T., Yang, X., Qi, X. ve Jiang, C. (2015). Osteoinduction and proliferation of bone-marrow stromal cells in three-dimensional poly ( $\epsilon$ -caprolactone)/hydroxyapatite/collagen scaffolds. *Journal of Translational Medicine*, 13(1), 1–11. doi:10.1186/s12967-015-0499-8
- Yao, R., He, J., Meng, G., Jiang, B. ve Wu, F. (2016). Electrospun PCL/Gelatin composite fibrous scaffolds: Mechanical properties and cellular responses. *Journal of Biomaterials Science, Polymer Edition*, 27(9), 824–838. doi:10.1080/09205063.2016.1160560
- Yılmaz, M. ve Altan, A. (2017). ELEKTROEĞİRME Yöntemine Dayalı Nanosensörlerin Gıda Alanındaki Uygulamaları. *Gıda / the Journal of Food*, 42(6), 708–725. doi:10.15237/gida.gd17057
- Zhang, M., Qiao, X., Han, W., Jiang, T., Liu, F., & Zhao, X. (2021). Alginate-chitosan oligosaccharide-ZnO composite hydrogel for accelerating wound healing. *Carbohydrate polymers*, 266, 118100.



# **Numerical solutions of the Caudrey-Dodd-Gibbon Equation**

**Melis ZORŞAHİN<sup>1</sup>**

**Dursun IRK<sup>2</sup>**

- 1- Assoc.Prof.Dr.; Department of Mathematics and Computer Science, Eskişehir Osmangazi University.  
mzorsahin@ogu.edu.tr ORCID No: [0000-0001-7506-4162](https://orcid.org/0000-0001-7506-4162)
- 2- Prof. Dr.; Department of Mathematics and Computer Science, Eskişehir Osmangazi University.  
dirk@ogu.edu.tr ORCID No: [0000-0002-3340-1578](https://orcid.org/0000-0002-3340-1578)

## ABSTRACT

In this paper, two different collocation methods based on the octic (8th degree) and the nonic (9th degree) B-spline functions are used to get the numerical solutions of the Caudrey-Dodd-Gibbon equation (CDGE). The single soliton solution of the CDGE is examined by both of the B-splines algorithms and the comparison of the numerical results with the exact solution of the CDGE are given by the tables and the figures.

*Keywords – Collocation method, Octic B-spline, Nonic B-spline, Caudrey-Dodd-Gibbon equation*

---

## INTRODUCTION

The CDGE is given in (Caudrey et al., 1976) as

$$u_t + u_{xxxxx} + 30uu_{xxx} + 30u_x u_{xx} + 180u^2u_x = 0. \quad (1)$$

with the initial and boundary conditions

$$u(x, 0) = f(x), x \in [-a, a], \quad (2)$$

$$u(-a, t) = \alpha_1, u(a, t) = \alpha_2, t > 0,$$

$$u_x(-a, t) = \alpha_3, u_x(a, t) = \alpha_4,$$

$$u_{xx}(-a, t) = \alpha_5, u_{xx}(a, t) = \alpha_6, \quad (3)$$

$$u_{xxx}(-a, t) = \alpha_7, u_{xxx}(a, t) = \alpha_8,$$

$$u_{xxxx}(-a, t) = \alpha_9, u_{xxxx}(a, t) = \alpha_{10}.$$

The Eq. (1) is a class of fifth order Korteweg-de Vries equation which is used to model the well known wave phenomena in the quantum mechanics and the nonlinear optics. The numerical solutions for the CDGE are studied by some researchers before. The modified Adomian decomposition method to solve numerically the CDGE is used by Bakodah (2013). The Haar wavelet collocation method is presented to solve the CDGE by Saleem and Hussain (2020). The CDGE is solved by using the dual-Petrov-Galerkin method in (Yuan and Wu, 2010). The numerical solution of the CDGE using the collocation method with the help of the quintic B-spline basis is obtained by Karaagac (2019). The modified variational iteration algorithm-I and II are proposed to obtain the numerical solution of the CDGE in (Ahmad et al., 2020(a); 2020(b)). In this paper, two simple numerical B-spline algorithms are proposed, taking into account the difficulties of getting the exact solution of the equation due to its non-linearity and having a fifth order derivative. The proposed numerical methods including the collocation methods based on the octic and nonic B-spline functions are presented in section 2 and 3, respectively. The numerical results obtained by both of the methods and the comparisons with the analytical solution are given in section 4.

## NUMERICAL METHODS

To construct the numerical methods, let us consider a uniform mesh  $\Omega$  with the knots  $x_r$  on  $[-a, a]$  such that  $\Omega: -a = x_0 < x_1 < \dots < x_N = a$  where by denoting  $h = \frac{2a}{N}$  as the space step,  $x_r = x_x + rh; r = 0, \dots, N$ .

The exact solutions of the unknown functions and the numerical solution of its at the knots represent respectively by  $u(x_r, t_s) = u_r^s$  and  $U_r^s = U(x_r, t_s)$  where  $t_s = s\Delta t; s = 0, 1, 2, \dots$  and  $\Delta t$  denotes the time step.

To get the Crank-Nicolson time discretization of the Eq. (1), using the approximations

$$\begin{aligned} u &= \frac{u^{s+1} + u^s}{2}, u_t = \frac{u^{s+1} - u^s}{\Delta t}, \\ u_x &= \frac{u_x^{s+1} + u_x^s}{2}, u_{xx} = \frac{u_{xx}^{s+1} + u_{xx}^s}{2} \\ u_{xxx} &= \frac{u_{xxx}^{s+1} + u_{xxx}^s}{2}, u_{xxxx} = \frac{u_{xxxx}^{s+1} + u_{xxxx}^s}{2} \end{aligned}$$

in Eq. (1),

$$\begin{aligned} u^{s+1} + \frac{\Delta t}{2} (u_{xxxxx}^{s+1} + 30u^{s+1}u_{xxx}^{s+1} + 30u_x^{s+1}u_{xx}^{s+1} \\ + 180(u^{s+1})^2u_x^{s+1}) = u^s - \frac{\Delta t}{2} (u_{xxxxx}^s + 30u^s u_{xxx}^s \\ + 30u_x^s u_{xx}^s + 180(u^s)^2u_x^s) \end{aligned} \quad (4)$$

is obtained.

Using the following resursive formula mentioned by DeBoor (1978)

$$B_i^k = \frac{x - x_i}{x_{i+k} - x_i} B_i^{k-1}(x) + \frac{x_{i+k+1} - x}{x_{i+k+1} - x_{i+1}} B_{i+1}^{k-1}(x) \quad (5)$$

where the B-spline functions of order  $k$  denoted by  $B_i^k$  and

$$B_i^k = \begin{cases} 1, & x_i \leq x < x_{i+1}, \\ 0, & \text{otherwise,} \end{cases} \quad (6)$$

$k \geq 0$  and  $i = 0, \pm 1, \pm 2, \dots$ , the octic and the nonic B-spline functions are obtained.

### OCTIC B-SPLINE COLLOCATION METHOD (OBSCM)

The octic B-spline functions at the knots  $x_r; r = 0, \dots, N$  in the domain  $[-a, a]$  can be obtained using recurrence relation (5) as in (Koyulmus, 2021)



$$B_r^8 = \begin{cases} \varphi_1, x_{r-4} \leq x < x_{r-3}, \\ \varphi_2, x_{r-3} \leq x < x_{r-2}, \\ \varphi_3, x_{r-2} \leq x < x_{r-1}, \\ \varphi_4, x_{r-1} \leq x < x_r, \\ \varphi_5, x_r \leq x < x_{r+1}, \\ \varphi_6, x_{r+1} \leq x < x_{r+2}, \\ \varphi_7, x_{r+2} \leq x < x_{r+3}, \\ \varphi_8, x_{r+3} \leq x < x_{r+4}, \\ \varphi_9, x_{r+4} \leq x < x_{r+5}, \\ 0, & \text{otherwise} \end{cases} \quad (7)$$

where

$$\varphi_1 = (x - x_{r-4})^8,$$

$$\begin{aligned} \varphi_2 = & h^8 + 8h^7(x - x_{r-3}) + 28h^6(x - x_{r-3})^2 + 56h^5(x - x_{r-3})^3 \\ & + 70h^4(x - x_{r-3})^4 + 56h^3(x - x_{r-3})^5 + 28h^2(x - x_{r-3})^6 \\ & + 8h(x - x_{r-3})^7 - 8(x - x_{r-3})^8, \end{aligned}$$

$$\begin{aligned} \varphi_3 = & 247h^8 + 952h^7(x - x_{r-2}) + 1540h^6(x - x_{r-2})^2 \\ & + 1288h^5(x - x_{r-2})^3 + 490h^4(x - x_{r-2})^4 \\ & - 56h^3(x - x_{r-2})^5 - 140h^2(x - x_{r-2})^6 \\ & - 56h(x - x_{r-2})^7 + 28(x - x_{r-2})^8, \end{aligned}$$

$$\begin{aligned} \varphi_4 = & 4293h^8 + 8568h^7(x - x_{r-1}) + 5292h^6(x - x_{r-1})^2 \\ & - 504h^5(x - x_{r-1})^3 - 1890h^4(x - x_{r-1})^4 \\ & - 504h^3(x - x_{r-1})^5 + 252h^2(x - x_{r-1})^6 \\ & + 168h(x - x_{r-1})^7 - 56(x - x_{r-1})^8, \end{aligned}$$

$$\begin{aligned} \varphi_5 = & 15619h^8 + 9800h^7(x - x_r) - 6860h^6(x - x_r)^2 \\ & - 5320h^5(x - x_r)^3 + 1330h^4(x - x_r)^4 \\ & + 1400h^3(x - x_r)^5 - 140h^2(x - x_r)^6 - 280h(x - x_r)^7 \\ & + 70(x - x_r)^8, \end{aligned}$$

$$\begin{aligned} \varphi_6 = & 15619h^8 - 9800h^7(x - x_{r+1}) - 6860h^6(x - x_{r+1})^2 \\ & + 5320h^5(x - x_{r+1})^3 + 1330h^4(x - x_{r+1})^4 \\ & - 1400h^3(x - x_{r+1})^5 - 140h^2(x - x_{r+1})^6 \\ & + 280h(x - x_{r+1})^7 - 56(x - x_{r+1})^8, \end{aligned}$$

$$\begin{aligned} \varphi_7 = & 4293h^8 - 8568h^7(x - x_{r+2}) + 5292h^6(x - x_{r+2})^2 \\ & + 504h^5(x - x_{r+2})^3 - 1890h^4(x - x_{r+2})^4 \\ & + 504h^3(x - x_{r+2})^5 + 252h^2(x - x_{r+2})^6 \\ & - 168h(x - x_{r+2})^7 + 28(x - x_{r+2})^8, \end{aligned}$$

$$\begin{aligned} \varphi_8 = & 247h^8 - 952h^7(x - x_{r+3}) + 1540h^6(x - x_{r+3})^2 \\ & - 1288h^5(x - x_{r+3})^3 + 490h^4(x - x_{r+3})^4 \\ & + 56h^3(x - x_{r+3})^5 - 140h^2(x - x_{r+3})^6 \\ & + 56h(x - x_{r+3})^7 - 8(x - x_{r+3})^8, \end{aligned}$$

$$\varphi_9 = (h - (x - x_{r+4}))^8.$$

The set of octic B-spline functions  $\{B_{-4}^8(x), B_{-3}^8(x), B_{-2}^8(x), \dots, B_{N+2}^8(x), B_{N+3}^8(x)\}$  generates a basis over the solution domain  $[-a, a]$ .

For the spce discretization of the Eq. (4), let take the approximation solution  $U$  as

$$U(x, t) = \sum_{l=-4}^{N+3} TB_l^8(x)\delta_l(t) \quad (8)$$

where  $B^8$  is the octic B-splines and  $\delta_l$  are time dependent unknowns which will be calculated. The approximate solution and its first seventh order derivatives over the element  $[x_r, x_{r+1}]$  can obtains by using the Eq. (7) in the Eq. (8) as

$$\begin{aligned} U_r &= \delta_{r-4} + 247\delta_{r-3} + 4293\delta_{r-2} + 15619\delta_{r-1} + 15619\delta_r \\ &\quad + 4293\delta_{r+1} + 247\delta_{r+2} + \delta_{r+3}; \\ U'_r &= \frac{8}{h}(-\delta_{r-4} - 119\delta_{r-3} - 1071\delta_{r-2} - 1225\delta_{r-1} + 1225\delta_r \\ &\quad + 1071\delta_{r+1} + 119\delta_{r+2} + \delta_{r+3}); \\ U''_r &= \frac{56}{h^2}(\delta_{r-4} + 55\delta_{r-3} + 189\delta_{r-2} - 245\delta_{r-1} - 245\delta_r \\ &\quad + 189\delta_{r+1} + 55\delta_{r+2} + \delta_{r+3}); \\ U'''_r &= \frac{336}{h^3}(-\delta_{r-4} - 23\delta_{r-3} + 9\delta_{r-2} + 95\delta_{r-1} - 95\delta_r - 9\delta_{r+1} \\ &\quad + 23\delta_{r+2} + \delta_{r+3}); \\ U_r^{(4)} &= \frac{1680}{h^4}(\delta_{r-4} + 7\delta_{r-3} - 27\delta_{r-2} + 19\delta_{r-1} + 19\delta_r \\ &\quad - 27\delta_{r+1} + 7\delta_{r+2} + \delta_{r+3}); \\ U_r^{(5)} &= \frac{6720}{h^5}(-\delta_{r-4} + \delta_{r-3} + 9\delta_{r-2} - 25\delta_{r-1} + 25\delta_r - 9\delta_{r+1} \\ &\quad - \delta_{r+2} + \delta_{r+3}); \\ U_r^{(6)} &= \frac{20160}{h^6}(\delta_{r-4} - 5\delta_{r-3} + 9\delta_{r-2} - 5\delta_{r-1} - 5\delta_r + 9\delta_{r+1} \\ &\quad - 5\delta_{r+2} + \delta_{r+3}); \\ U_r^{(7)} &= \frac{40320}{h^7}(-\delta_{r-4} + 7\delta_{r-3} - 21\delta_{r-2} + 35\delta_{r-1} - 35\delta_r \\ &\quad + 21\delta_{r+1} - 7\delta_{r+2} + \delta_{r+3}). \end{aligned} \quad (9)$$

The fully discretized form of the Eq. (1) is obtained by using the Eq. (9) in Eq. (4) as

$$\begin{aligned} &(1 + \gamma_1^{s+1})\delta_{r-4}^{s+1} + (247 + \gamma_2^{s+1})\delta_{r-3}^{s+1} + (4293 + \gamma_3^{s+1})\delta_{r-2}^{s+1} \\ &\quad + (15619 + \gamma_4^{s+1})\delta_{r-1}^{s+1} + (15619 + \gamma_5^{s+1})\delta_r^{s+1} \\ &\quad + (4293 + \gamma_6^{s+1})\delta_{r+1}^{s+1} + (247 + \gamma_7^{s+1})\delta_{r+2}^{s+1} \\ &\quad + (1 + \gamma_8^{s+1})\delta_{r+3}^{s+1} \\ &= (1 - \gamma_1^s)\delta_{r-4}^s + (247 - \gamma_2^s)\delta_{r-3}^s \\ &\quad + (4293 - \gamma_3^s)\delta_{r-2}^s + (15619 - \gamma_4^s)\delta_{r-1}^s \\ &\quad + (15619 - \gamma_5^s)\delta_r^s + (4293 - \gamma_6^s)\delta_{r+1}^s \\ &\quad + (247 - \gamma_7^s)\delta_{r+2}^s + (1 - \gamma_8^s)\delta_{r+3}^s \end{aligned} \quad (10)$$

where

$$\begin{aligned}
\beta_1 &= \frac{3360\Delta t}{h^5}, \beta_2^j = \frac{5040\Delta t}{h^3} \eta^j, \\
\beta_3^j &= \frac{840\Delta t}{h^2} \eta_x^j, \beta_4^j = \frac{720\Delta t}{h} (\eta^j)^2, \\
\gamma_1^j &= -\beta_1 - \beta_2^j + \beta_3^j - \beta_4^j, \\
\gamma_2^j &= \beta_1 - 23\beta_2^j + 55\beta_3^j - 119\beta_4^j, \\
\gamma_3^j &= 9\beta_1 + 9\beta_2^j + 189\beta_3^j - 1071\beta_4^j, \\
\gamma_4^j &= -25\beta_1 + 95\beta_2^j - 245\beta_3^j - 1225\beta_4^j, \\
\gamma_5^j &= 25\beta_1 - 95\beta_2^j + 245\beta_3^j + 1225\beta_4^j, \\
\gamma_6^j &= -9\beta_1 - 9\beta_2^j + 189\beta_3^j + 1071\beta_4^j, \\
\gamma_7^j &= -\beta_1 + 23\beta_2^j + 55\beta_3^j + 119\beta_4^j, \\
\gamma_8^j &= \beta_1 + \beta_2^j + \beta_3^j + \beta_4^j, \\
\eta^j &= \delta_{r-4}^j + 247\delta_{r-3}^j + 4293\delta_{r-2}^j + 15619\delta_{r-1}^j + 15619\delta_r^j \\
&\quad + 4293\delta_{r+1}^j + 247\delta_{r+2}^j + \delta_{r+3}^j; \\
\eta_x^j &= \frac{8}{h} (-\delta_{r-4}^j - 119\delta_{r-3}^j - 1071\delta_{r-2}^j - 1225\delta_{r-1}^j + 1225\delta_r^j \\
&\quad + 1071\delta_{r+1}^j + 119\delta_{r+2}^j + \delta_{r+3}^j); \\
j &= s + 1, s.
\end{aligned}$$

Consequently, a system comprising  $N + 1$  equations and  $N + 8$  unknowns is derived. By incorporating the boundary conditions defined in Eq. (3), the parameters  $\delta_{-4}, \delta_{-3}, \delta_{-2}, \delta_{-1}, \delta_{N+1}, \delta_{N+2}$  and  $\delta_{N+3}$  are eliminated, reducing the system to a solvable  $(N + 1) \times (N + 1)$  matrix. This reduced linear system is efficiently solved using MATLAB. The initial vector  $\delta^0$  is determined using the initial condition (2) in conjunction with the boundary conditions (3). Subsequently, the solution vector  $\delta^s$  at time level  $t^s = s \Delta t$  is computed iteratively. As Eq. (10) leads to an implicit formulation in terms of  $\delta$ , an inner iteration scheme is employed at each time step to obtain the numerical solution before progressing to the next time level.

### NONIC B-SPLINE COLLOCATION METHOD (NBSCM)

The nonic B-spline functions at the knots  $x_r$ ;  $r = 0, \dots, N$  in the domain  $[-a, a]$  can be obtained using recurrence relation (5) as in (Koyulmus, 2021)

$$B_r^9 = \begin{cases} \psi_1, x_{r-5} \leq x < x_{r-4}, \\ \psi_2, x_{r-4} \leq x < x_{r-3}, \\ \psi_3, x_{r-3} \leq x < x_{r-2}, \\ \psi_4, x_{r-2} \leq x < x_{r-1}, \\ \psi_5, x_{r-1} \leq x < x_r, \\ \psi_6, x_r \leq x < x_{r+1}, \\ \psi_7, x_{r+1} \leq x < x_{r+2}, \\ \psi_8, x_{r+2} \leq x < x_{r+3}, \\ \psi_9, x_{r+3} \leq x < x_{r+4}, \\ \psi_{10}, x_{r+4} \leq x < x_{r+5}, \\ 0, & \text{otherwise} \end{cases} \quad (11)$$

where

$$\psi_1 = (x - x_{r-5})^9,$$

$$\begin{aligned} \psi_2 = & h^9 + 9h^8(x - x_{r-4}) + 36h^7(x - x_{r-4})^2 + 84h^6(x - x_{r-4})^3 \\ & + 126h^5(x - x_{r-4})^4 + 126h^4(x - x_{r-4})^5 \\ & + 84h^3(x - x_{r-4})^6 + 36h^2(x - x_{r-4})^7 + 9h(x - x_{r-4})^8 \\ & - 9(x - x_{r-4})^9, \end{aligned}$$

$$\begin{aligned} \psi_3 = & 502h^9 + 2214h^8(x - x_{r-3}) + 4248h^7(x - x_{r-3})^2 \\ & + 4536h^6(x - x_{r-3})^3 + 2772h^5(x - x_{r-3})^4 \\ & + 756h^4(x - x_{r-3})^5 - 168h^3(x - x_{r-3})^6 \\ & - 216h^2(x - x_{r-3})^7 - 72h(x - x_{r-3})^8 + 36(x - x_{r-3})^9, \end{aligned}$$

$$\begin{aligned} \psi_4 = & 14608h^9 + 36414h^8(x - x_{r-2}) + 34272h^7(x - x_{r-2})^2 \\ & + 11256h^6(x - x_{r-2})^3 - 4032h^5(x - x_{r-2})^4 \\ & - 4284h^4(x - x_{r-2})^5 - 672h^3(x - x_{r-2})^6 \\ & + 504h^2(x - x_{r-2})^7 + 252h(x - x_{r-2})^8 \\ & - 84(x - x_{r-2})^9, \end{aligned}$$

$$\begin{aligned} \psi_5 = & 88234h^9 + 101934h^8(x - x_{r-1}) + 5544h^7(x - x_{r-1})^2 \\ & - 36456h^6(x - x_{r-1})^3 - 10836h^5(x - x_{r-1})^4 \\ & + 5796h^4(x - x_{r-1})^5 + 2856h^3(x - x_{r-1})^6 \\ & - 504h^2(x - x_{r-1})^7 - 504h(x - x_{r-1})^8 \\ & + 126(x - x_{r-1})^9, \end{aligned}$$

$$\begin{aligned} \psi_6 = & 156190h^9 - 88200h^7(x - x_r)^2 + 23940h^5(x - x_r)^4 \\ & - 4200h^3(x - x_r)^6 + 630h(x - x_r)^8 - 126(x - x_r)^9, \end{aligned}$$

$$\begin{aligned} \psi_7 = & 88234h^9 - 101934h^8(x - x_{r+1}) + 5544h^7(x - x_{r+1})^2 \\ & - 36456h^6(x - x_{r+1})^3 - 10836h^5(x - x_{r+1})^4 \\ & - 5796h^4(x - x_{r+1})^5 + 2856h^3(x - x_{r+1})^6 \\ & + 504h^2(x - x_{r+1})^7 - 504h(x - x_{r+1})^8 \\ & + 84(x - x_{r+1})^9, \end{aligned}$$

$$\begin{aligned} \psi_8 = & 14608h^9 - 36414h^8(x - x_{r+2}) + 34272h^7(x - x_{r+2})^2 \\ & - 11256h^6(x - x_{r+2})^3 - 4032h^5(x - x_{r+2})^4 \\ & + 4284h^4(x - x_{r+2})^5 - 672h^3(x - x_{r+2})^6 \\ & - 504h^2(x - x_{r+2})^7 + 252h(x - x_{r+2})^8 \\ & - 36(x - x_{r+2})^9, \end{aligned}$$

$$\begin{aligned}\psi_9 = & 502h^9 - 2214h^8(x - x_{r+3}) + 4248h^7(x - x_{r+3})^2 \\ & - 4536h^6(x - x_{r+3})^3 + 2772h^5(x - x_{r+3})^4 \\ & - 756h^4(x - x_{r+3})^5 - 168h^3(x - x_{r+3})^6 \\ & + 216h^2(x - x_{r+3})^7 - 72h(x - x_{r+3})^8 + 9(x - x_{r+3})^9 \\ \psi_{10} = & (h - (x - x_{r+4}))^9.\end{aligned}$$

The set of notic B-spline functions  $\{B_{-4}^9(x), B_{-3}^9(x), B_{-2}^9(x), \dots, B_{N+2}^9(x), B_{N+3}^9(x), B_{N+4}^9(x)\}$  generates a basis over the solution domain  $[-a, a]$ .

For the spce discretization of the Eq. (4) by the NBSCM, let we take the approximation solution  $U$  in terms fort he nonic B-splines  $B^9$  as

$$U(x, t) = \sum_{l=-4}^{N+4} TB_l^9(x)\delta_l(t) \quad (12)$$

where  $\delta_l$  are time dependent unknowns which will be calculated. By using the Eq. (11) in the Eq. (12), the approximate solution and its first eighth order derivatives over the element  $[x_r, x_{r+1}]$  can written as

$$\begin{aligned}U_r = & \delta_{r-4} + 502\delta_{r-3} + 14608\delta_{r-2} + 88234\delta_{r-1} + 156190\delta_r \\ & + 88234\delta_{r+1} + 14608\delta_{r+2} + 502\delta_{r+3} + \delta_{r+4}; \\ U'_r = & \frac{9}{h}(-\delta_{r-4} - 246\delta_{r-3} - 4046\delta_{r-2} - 11326\delta_{r-1} \\ & + 11326\delta_{r+1} + 404\delta_{r+2} + 246\delta_{r+3} + \delta_{r+4}); \\ U''_r = & \frac{72}{h^2}(\delta_{r-4} + 118\delta_{r-3} + 952\delta_{r-2} + 154\delta_{r-1} - 2450\delta_r \\ & + 154\delta_{r+1} + 952\delta_{r+2} + 118\delta_{r+3} + \delta_{r+4}); \\ U'''_r = & \frac{504}{h^3}(-\delta_{r-4} - 54\delta_{r-3} - 134\delta_{r-2} + 434\delta_{r-1} - 434\delta_{r+1} \\ & + 134\delta_{r+2} + 54\delta_{r+3} + \delta_{r+4}); \\ U_r^{(4)} = & \frac{3024}{h^4}(\delta_{r-4} + 22\delta_{r-3} - 32\delta_{r-2} - 86\delta_{r-1} + 190\delta_r \\ & - 86\delta_{r+1} - 32\delta_{r+2} + 22\delta_{r+3} + \delta_{r+4}); \\ U_r^{(5)} = & \frac{15120}{h^5}(-\delta_{r-4} - 6\delta_{r-3} + 34\delta_{r-2} - 46\delta_{r-1} + 46\delta_{r+1} \\ & - 34\delta_{r+2} + 6\delta_{r+3} + \delta_{r+4}); \\ U_r^{(6)} = & \frac{60480}{h^6}(\delta_{r-4} - 2\delta_{r-3} - 8\delta_{r-2} + 34\delta_{r-1} - 50\delta_r \\ & + 34\delta_{r+1} - 8\delta_{r+2} - 2\delta_{r+3} + \delta_{r+4}); \\ U_r^{(7)} = & \frac{181440}{h^7}(-\delta_{r-4} + 6\delta_{r-3} - 14\delta_{r-2} + 14\delta_{r-1} - 14\delta_{r+1} \\ & + 14\delta_{r+2} - 6\delta_{r+3} + \delta_{r+4}). \\ U_r^{(8)} = & \frac{362880}{h^8}(\delta_{r-4} - 8\delta_{r-3} + 28\delta_{r-2} - 56\delta_{r-1} + 70\delta_r \\ & - 56\delta_{r+1} + 28\delta_{r+2} - 8\delta_{r+3} + \delta_{r+4}).\end{aligned} \quad (13)$$

The fully discretized form of the Eq. (1) is obtained by using the Eq. (13) in Eq. (4) as

$$\begin{aligned}
& (1 + \gamma_1^{s+1})\delta_{r-4}^{s+1} + (502 + \gamma_2^{s+1})\delta_{r-3}^{s+1} + (14608 + \gamma_3^{s+1})\delta_{r-2}^{s+1} \\
& + (88234 + \gamma_4^{s+1})\delta_{r-1}^{s+1} + (156190 + \gamma_5^{s+1})\delta_r^{s+1} \\
& + (88234 + \gamma_6^{s+1})\delta_{r+1}^{s+1} + (14608 + \gamma_7^{s+1})\delta_{r+2}^{s+1} \\
& + (502 + \gamma_8^{s+1})\delta_{r+3}^{s+1} + (1 + \gamma_9^{s+1})\delta_{r+4}^{s+1} \\
& = (1 - \gamma_1^s)\delta_{r-4}^s + (502 - \gamma_2^s)\delta_{r-3}^s \\
& + (14608 - \gamma_3^s)\delta_{r-2}^s + (88234 - \gamma_4^s)\delta_{r-1}^s \\
& + (156190 - \gamma_5^s)\delta_r^s + (88234 - \gamma_6^s)\delta_{r+1}^s \\
& + (14608 - \gamma_7^s)\delta_{r+2}^s + (502 - \gamma_8^s)\delta_{r+3}^s \\
& + (1 - \gamma_9^s)\delta_{r+4}^s
\end{aligned} \tag{10}$$

where

$$\begin{aligned}
\beta_1 &= \frac{7560\Delta t}{h^5}, \beta_2^j = \frac{7560\Delta t}{h^3}\eta^j, \\
\beta_3^j &= \frac{1080\Delta t}{h^2}\eta_x^j, \beta_4^j = \frac{810\Delta t}{h}(\eta^j)^2, \\
\gamma_1^j &= -\beta_1 - \beta_2^j + \beta_3^j - \beta_4^j, \\
\gamma_2^j &= -6\beta_1 - 54\beta_2^j + 118\beta_3^j - 246\beta_4^j, \\
\gamma_3^j &= 34\beta_1 - 134\beta_2^j + 952\beta_3^j - 4046\beta_4^j, \\
\gamma_4^j &= -46\beta_1 + 434\beta_2^j + 154\beta_3^j - 11326\beta_4^j, \\
\gamma_5^j &= -2450\beta_3^j, \\
\gamma_6^j &= 46\beta_1 - 434\beta_2^j + 154\beta_3^j + 11326\beta_4^j, \\
\gamma_7^j &= -34\beta_1 + 134\beta_2^j + 952\beta_3^j + 4046\beta_4^j, \\
\gamma_8^j &= 6\beta_1 + 54\beta_2^j + 118\beta_3^j + 246\beta_4^j, \\
\gamma_9^j &= 6\beta_1 + 54\beta_2^j + 118\beta_3^j + 246\beta_4^j, \\
\gamma_9^j &= \beta_1 + \beta_2^j + \beta_3^j + \beta_4^j, \\
\eta^j &= \delta_{r-4}^j + 502\delta_{r-3}^j + 14608\delta_{r-2}^j + 88234\delta_{r-1}^j + 156190\delta_r^j \\
& + 88234\delta_{r+1}^j + 14608\delta_{r+2}^j + 502\delta_{r+3}^j + \delta_{r+4}^j, \\
\eta_x^j &= \frac{9}{h}(-\delta_{r-4}^j - 246\delta_{r-3}^j - 4046\delta_{r-2}^j - 11326\delta_{r-1}^j + 11326\delta_{r+1}^j \\
& + 4046\delta_{r+2}^j + 246\delta_{r+3}^j + \delta_{r+4}^j), \\
j &= s + 1, s.
\end{aligned}$$

As a result, the system yields  $N + 1$  equations involving  $N + 9$  unknowns. By applying the boundary conditions given in Eq. (3), the parameters  $\delta_{-4}, \delta_{-3}, \delta_{-2}, \delta_{-1}, \delta_{N+1}, \delta_{N+2}, \delta_{N+3}$  and  $\delta_{N+4}$  are eliminated, reducing the system to a solvable  $(N + 1) \times (N + 1)$  matrix. This reduced system is efficiently solved using MATLAB. The initial condition (2) along with the boundary conditions (3) are employed to compute the initial vector  $\delta^0$ , which serves as the starting point for the iterative time-stepping procedure. Subsequently, for each time level  $t^s = s \Delta t$ , the solution vector  $\delta^s$  is computed iteratively. As in the previous approach, the discretization leads to

an implicit system with respect to  $\delta$ , necessitating an inner iteration process at each time step.

## PROPAGATION OF SINGLE SOLITON WAVE

In this section, the propagation of the single soliton wave is examined for both of the methods. The accuracy of the methods is calculated by using the following error norm

$$L_\infty = \max_r |u_r - U_r|, \quad (15)$$

and the time and space discretizations order of convergence are computed by the following formula

$$\text{order} = \frac{\log \left| \frac{(L_\infty)_{k_r}}{(L_\infty)_{k_{r+1}}} \right|}{\log \left| \frac{k_r}{k_{r+1}} \right|}, k_r = \Delta t_r, h_r, \quad (16)$$

where  $(L_\infty)_{k_r}$  is the error norm  $L_\infty$  for the steps  $k_r$ .

The single soliton wave solution of the CDGE is given as

$$u(x, t) = \frac{\exp(x - t)}{(1 + \exp(x - t))^2}. \quad (17)$$

The computation domain is fixed in the intervals  $-50 \leq x \leq 50$  and  $0 \leq t \leq 0.04$ . By taking  $t = 0$  in the exact solution (17), the initial condition can be obtained as

$$u(x, 0) = \frac{\exp(x)}{(1 + \exp(x))^2}. \quad (18)$$

The boundary conditions are taken as zero. The simulation of the wave during the time interval  $[0, 0.04]$  is shown in Figure 1 for the OBSCM and NBSCM and the error norms are given in Table 1 for the various time and space steps. From the Figure 1, it is seen that the obtained wave remains its initial shape during the running time for the both of the methods. Looking at the change in the error norms over time from Table 1, it can be said that it supports this situation and the methods successfully simulate this wave.

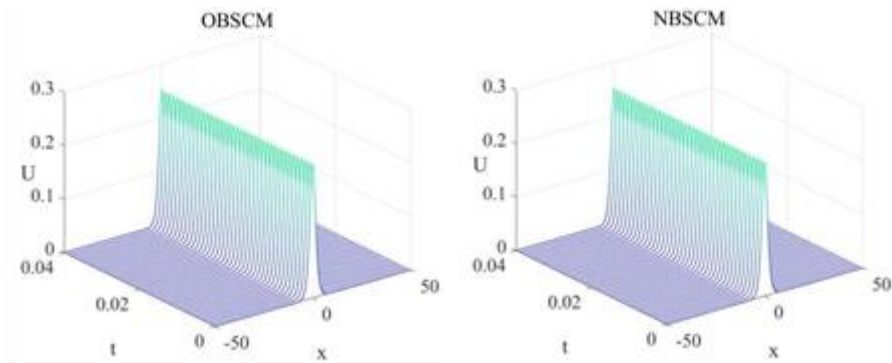


Figure 1:  $U(x, t)$  at various times with  $h = 0.1$  and  $\Delta t = 0.001$ .

Table 1: Error norms  $L_\infty$  for  $\Delta t = 0.001$ .

OBSCM		
$h$	$t$	$L_\infty$
0.25	0.01	$8.97124 \times 10^{-7}$
	0.02	$1.40517 \times 10^{-6}$
	0.03	$1.79479 \times 10^{-6}$
	0.04	$2.19988 \times 10^{-6}$
0.1	0.01	$2.05991 \times 10^{-8}$
	0.02	$3.34160 \times 10^{-8}$
	0.03	$4.38311 \times 10^{-8}$
	0.04	$5.35373 \times 10^{-8}$
0.05	0.01	$1.17923 \times 10^{-9}$
	0.02	$1.85740 \times 10^{-9}$
	0.03	$2.42016 \times 10^{-9}$
	0.04	$2.94193 \times 10^{-9}$
0.025	0.01	$1.09783 \times 10^{-10}$
	0.02	$1.95161 \times 10^{-10}$
	0.03	$2.70487 \times 10^{-10}$
	0.04	$3.43455 \times 10^{-10}$
NBSCM		
$h$	$t$	$L_\infty$
0.25	0.01	$5.66884 \times 10^{-8}$
	0.02	$7.92532 \times 10^{-8}$
	0.03	$9.53754 \times 10^{-8}$
	0.04	$1.13422 \times 10^{-7}$
0.1	0.01	$3.20468 \times 10^{-10}$
	0.02	$5.25457 \times 10^{-10}$
	0.03	$7.15481 \times 10^{-10}$
	0.04	$8.93902 \times 10^{-10}$
0.05	0.01	$1.12971 \times 10^{-10}$
	0.02	$2.26083 \times 10^{-10}$
	0.03	$3.38661 \times 10^{-10}$
	0.04	$4.51518 \times 10^{-10}$
0.025	0.01	$1.11331 \times 10^{-10}$
	0.02	$2.23158 \times 10^{-10}$
	0.03	$3.32768 \times 10^{-10}$
	0.04	$4.44877 \times 10^{-10}$

The comparison of the obtained error norm  $L_\infty$  values for each of the proposed methods and the quintic B-spline collocation method (QBSCM) in



[5] are given in Table 2. According to the table, while space step is decreased from 0.25 to 0.025, all of the error norms  $L_\infty$  decrease for the proposed methods. It is seen clearly from the Table 2, the OBSCM and NBSCM have lesser error norm values than the QBSCM and the NBSCM has the less errors for the various values of  $h$ .

Table 2: Error norms  $L_\infty$  for  $\Delta t = 0.001$  at  $t = 0.04$ .

$h$	OBSCM	NBSCM	QBSCM (Karaagac, 2019)
0.25	$2.1999 \times 10^{-6}$	$1.1343 \times 10^{-7}$	$3.6541 \times 10^{-6}$
0.1	$5.3537 \times 10^{-8}$	$8.9390 \times 10^{-10}$	$9.4868 \times 10^{-8}$
0.05	$2.9419 \times 10^{-9}$	$4.5152 \times 10^{-10}$	$1.0079 \times 10^{-7}$
0.025	$3.4346 \times 10^{-10}$	$4.4488 \times 10^{-10}$	$1.2773 \times 10^{-8}$

Tablo 3 and Tablo 4 are given to see the conservation invariants for the proposed methods. From Table 3, when the time step  $\Delta t$  is fixed as 0.001, the space discretization order of the convergence of the OBSCM is around 5 and the space discretization order of the convergence of the NBSCM is around 6. From Table 4, when the space step  $h$  is fixed as 0.025, the time discretization order of the convergence of the OBSCM and NBSCM is around 2.

Table 3: Error norms  $L_\infty$  and rate of convergence for  $\Delta t = 0.001$  at  $t = 0.04$ .

OBSCM		
$h$	$L_\infty$	order
1	$1.40962 \times 10^{-3}$	5.002
0.5	$4.39963 \times 10^{-5}$	4.329
0.25	$2.19988 \times 10^{-6}$	4.055
0.1	$5.35373 \times 10^{-8}$	4.186
0.05	$2.94193 \times 10^{-9}$	3.099
0.025	$3.43455 \times 10^{-10}$	
NBSCM		
$h$	$L_\infty$	order
1	$5.57213 \times 10^{-4}$	5.998
0.5	$8.72011 \times 10^{-6}$	6.265
0.25	$1.13422 \times 10^{-7}$	5.286
0.1	$8.93902 \times 10^{-10}$	0.985
0.05	$4.51518 \times 10^{-10}$	0.021
0.025	$4.44877 \times 10^{-10}$	

Table 4: Error norms  $L_\infty$  and rate of convergence for  $h = 0.025$  at  $t = 0.04$ .

OBSCM		
$t$	$L_\infty$	order
0.04	$1.43257 \times 10^{-6}$	2.517
0.02	$2.50341 \times 10^{-7}$	2.291
0.01	$5.11516 \times 10^{-8}$	2.137
0.005	$1.16329 \times 10^{-8}$	2.142
0.002	$1.63362 \times 10^{-9}$	2.250
0.001	$3.43455 \times 10^{-10}$	
NBSCM		
$t$	$L_\infty$	order
0.04	$7.09949 \times 10^{-7}$	1.995
0.02	$1.78118 \times 10^{-7}$	2.002
0.01	$4.44598 \times 10^{-8}$	2.001
0.005	$1.11038 \times 10^{-8}$	2.003
0.002	$1.77183 \times 10^{-9}$	1.994
0.001	$4.44877 \times 10^{-10}$	

Figure 2 illustrates the distribution of the absolute error - defined as the difference between the analytical and numerical solutions - at time  $t = 0.04$  for both the OBSCM and NBSCM methods. A detailed examination of the figure reveals that the maximum error occurs near the center of the spatial domain. This observation is consistent with the results presented in Table 1, further validating the numerical behavior of the methods.

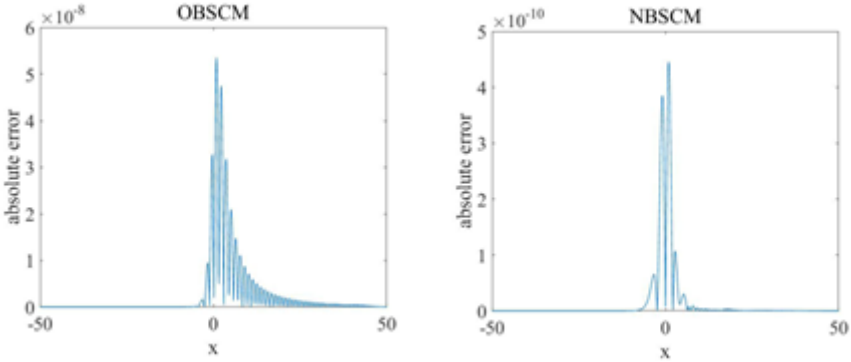


Figure 2: The distribution of the absolute errors for  $h = 0.1$  and  $\Delta t = 0.001$ .

## RESULTS AND DISCUSSION

This study presents the numerical solution of the CDGE using two finite element approaches: collocation methods based on octic and nonic B-spline functions. For spatial discretization, high-degree B-spline functions - specifically octic and nonic- are employed as trial functions, while the Crank-Nicolson scheme is utilized for temporal integration. A noteworthy aspect of

this work is the application of high-degree B-splines, which are not commonly adopted in the numerical treatment of higher-order partial differential equations. The soliton wave solution of the CDGE is effectively simulated, demonstrating the robustness and accuracy of the proposed methods. The results show that the error norm  $L_\infty$  remains significantly low for both approaches, indicating high computational accuracy

## REFERENCES

- Ahmad, H., Khan, T. A., Stanimirovic, P. S. and Ahmad, I. (2020). Modified variational iteration technique for the numerical solution of fifth order KdV-type equations. *Journal of Applied and Computational Mechanics*, 6(Special Issue), 1220-1227.
- Ahmad, H., Khan, T. A. and Yao, S. W. (2020). An efficient approach for the numerical solution of fifth-order KdV equations. *Open Mathematics*, 18(1), 738-748.
- Bakodah, H. O. (2013). Modified Adomain Decomposition Method for the Generalized Fifth Order KdV Equations. *American Journal of Computational Mathematics*, 3, 53-58.
- Caudrey, P. J., Dodd, R. K. and Gibbon, J. D. (1976). A new hierarchy of Korteweg–de Vries equations. *Proceedings of the Royal Society of London. A. Mathematical and Physical Sciences*, 351(1666), 407-422.
- De Boor, C., & De Boor, C. (1978). *A practical guide to splines* (Vol. 27, p. 325). New York: springer.
- Karaagac, B. (2019). A numerical approach to Caudrey Dodd Gibbon equation via collocation method using quintic B-spline basis. *TWMS Journal of Applied and Engineering Mathematics*, 9(1), 1-8.
- Koyulmus, B. On high degree B-spline functions, Master thesis, Eskişehir Osmangazi University, Eskişehir, Türkiye, 2021 (in Turkish).
- Saleem, S. and Hussain, M. Z. (2020). Numerical solution of nonlinear fifth-order KdV-type partial differential equations via Haar wavelet. *International Journal of Applied and Computational Mathematics*, 6(6), 164.
- Yuan, J. M. and Wu, J. (2010). A dual-Petrov-Galerkin method for two integrable fifth-order KdV type equations. *Discrete and Continuous Dynamical Systems A*, 26(4), 1525-1536.



# **Geometry of Canal Surfaces Via Darboux Frame**

**Prof. Dr. Nural YÜKSEL<sup>1</sup>**

**Nurdan OĞRAŞ<sup>2</sup>**

- 1- Department of Mathematics, Erciyes University, Kayseri, Turkey, e-mail:yukseln@erciyes.edu.tr; ORCIDiDs: <https://orcid.org/0000-0003-3360-5148>.
- 2- Graduate School of Natural and Applied Sciences, Erciyes University, Kayseri, Turkey, e-mail:nurdanogras@gmail.com, ORCIDiDs: <https://orcid.org/0000-0002-5539-4890>

## ABSTRACT

In this study, we investigate the geometric characteristics of canal-type surfaces defined in the Euclidean three-dimensional space using the Darboux frame. Surfaces formed by the motion of a sphere along a spine curve, commonly known as canal surfaces, possess rich differential geometric structures. The Darboux frame is a fundamental tool in differential geometry used to analyze the local geometry of curves lying on the surface. As a surface-adapted version of the Frenet frame, it takes into account the tangent direction of the curve together with the surface-tangent and surface-normal components. This framework enables a detailed study of geodesic, asymptotic, and curvature lines, offering deeper insight into the intrinsic geometry of surfaces. First, the fundamental forms (from the first to the third) of the canal surface expressed in the Darboux frame are obtained, along with the corresponding curvature quantities. And, we focus on Weingarten surfaces, including linear Weingarten canal surfaces, and analyze their characteristics in terms of curvature relations. Additionally, we examine developable and minimal canal surfaces, determining the conditions that characterize their existence. To validate our theoretical findings, we present a concrete example constructed with specific parametric equations. This example illustrates how the derived conditions manifest in practice and confirms the applicability of our approach. The results contribute to the broader study of surface theory and may be useful in fields such as computer-aided geometric design and theoretical physics.

*Keywords – Euclidean 3-space, Canal surfaces, Darboux frame, Weingarten surfaces, Linear Weingarten surfaces*

---

## INTRODUCTION

The theory of surfaces in differential geometry has long been central to both pure mathematics and numerous applied fields, including architecture, mechanical engineering, computer-aided geometric design (CAGD), and scientific visualization. Since Monge's 18th-century work on surface envelopes, and Gauss's foundational investigations in the 19th century, geometers have sought effective tools to describe how curves and surfaces interact in space.

Among the many special classes of surfaces, canal surfaces stand out for their intuitive construction and widespread utility. In geometric terms, canal surfaces are produced by the motion of a sphere whose center travels along a

space curve known as the spine curve. Equivalently, one may view a canal surface as sweeping a sphere of varying radius along a guiding curve, or as sweeping a circle orthogonal to that curve. When the radius remains constant, the resulting geometry reduces to a tube or pipe surface, familiar in both theoretical and engineering contexts.

A canal surface  $M$  can be described as the envelope generated by a one-parameter family of spheres. Its general parametrization reads

$$\Psi(s, \theta) = \nu(s) + r(s) \left( -r'(s)T(s) + \sqrt{1 - r'(s)^2} (\cos \theta N(s) + \sin \theta B(s)) \right), \quad (1)$$

where  $\nu(s)$  is a unit-speed center curve,  $r(s)$  is the radius function, and  $\{T(s), N(s), B(s)\}$  denotes the Frenet frame of  $\nu(s)$ .

In CAGD, canal surfaces are indispensable for modeling tubular structures such as pipes, cables, blood vessels, and hoses, thanks to their smooth transitions and easy control of cross-sectional shape. In computer graphics and animation, they serve for rapid prototyping of complex organic forms; in robotics, they guide collision-free path planning around slender obstacles; and in architectural design, they underpin freeform shell structures and fluid façade elements.

From a theoretical perspective, canal surfaces exhibit rich curvature behavior. Classical studies by Xu, Feng and Sun (2006:220) explored the Gaussian and mean curvatures of canal surfaces in Euclidean space, while Kim, Liu and Qian (2016:463) obtained characterizations using a different approach. Recent studies have extended these analyses to different spaces and frames, as well as to special Weingarten and linear Weingarten subclasses. (Doğan and Yaylı, 2012:752; Uçum and İlarslan, 2016:449; Soliman et al., 2019:67; Yüksel, Tunçer and Karacan, 2011:41; Elashiry et al., 2025:212; Damar et al., 2025:206).

A particularly natural and powerful tool for studying curve–surface interactions is the Darboux frame. Unlike the Frenet–Serret frame, which depends solely on the curve's curvature and torsion, the Darboux frame incorporates the surface normal and thus captures how the curve sits in the surface. Its characteristic quantities, including the geodesic curvature, the normal curvature, and the geodesic torsion, offer direct insight into both intrinsic and extrinsic bending. By combining these with the sphere-

envelope conditions of a canal surface, one obtains compact and geometrically transparent characterizations of when a canal surface is minimal, developable, or of Weingarten type. The Darboux frame is often used to investigate the characteristic properties of curves and surfaces (Saçlı, 2013:45; Bektaş and Yüce, 2012:3; Ouarab, 2021:9912624; Ünlütürk, Çimdiker and Ekici, 2016:28).

The aim of this study is to investigate canal-type surfaces within 3D Euclidean space using the Darboux frame, and to demonstrate some of their geometric characteristics through examples. As a first step, we derive the first three fundamental forms of the canal-type surface defined via the Darboux frame and compute its Gaussian, mean, and principal curvatures. Next, we investigate the conditions under which the surface is developable, minimal, or flat. Finally, we establish the specific conditions under which a canal surface exhibits Weingarten or linear-Weingarten properties, and we provide a graphical illustration of a canal surface defined via the Darboux frame.

## MATERIALS AND METHODS

Let  $\gamma(s)$  an arc-length parametrized regular curve lying on a smooth surface  $M \subset E^3$ , parametrized by arc-length  $s$ . At each point of  $\gamma$ , the Darboux frame  $\{\mathbf{T}, \mathbf{b}, \mathbf{n}\}$  is defined as follows:

- $\mathbf{T}$  : the vector tangent to  $\gamma(s)$ , normalized to unit magnitude,
- $\mathbf{n}$  : the perpendicular unit vector to the surface at  $\gamma(s)$ ,
- $\mathbf{b} = \mathbf{n} \times \mathbf{T}$  : The perpendicular vector obtained from the cross product of the surface normal and  $\mathbf{T}$ .

With respect to arc length, the rate of change of the Darboux frame vectors is described by the following system of equations:

$$\frac{d\mathbf{T}}{ds} = \kappa_g \mathbf{b} + \kappa_n \mathbf{n},$$

$$\frac{d\mathbf{b}}{ds} = -\kappa_g \mathbf{T} + \tau_g \mathbf{n},$$

$$\frac{d\mathbf{n}}{ds} = -\kappa_n \mathbf{T} - \tau_g \mathbf{b},$$



where;

- $(\kappa_g)$ : *geodesic curvature*,
- $(\kappa_n)$ : *normal curvature*,
- $(\tau_g)$ : *geodesic torsion*.

This moving frame captures both the intrinsic and extrinsic geometry of the curve as it lies on the surface. The values  $(\kappa_g, \kappa_n, \tau_g)$  provide geometric interpretations:

- *If  $(\kappa_g = 0)$ , the curve is geodesic.*
- *If  $(\kappa_n = 0)$ , the curve is asymptotic.*
- *If  $(\tau_g = 0)$ , the curve follows a principal direction.*

Let  $M \subset E^3$  be a smooth regular surface parameterized by

$$\Psi(u, \theta): D \subset E^2 \rightarrow E^3,$$

where  $\Psi(u, \theta) \in C^\infty$ , and the partial derivatives  $\Psi_u$  and  $\Psi_\theta$  are linearly independent for all  $(u, \theta) \in D$ .

The first fundamental form  $I$  is given by:

$$I = Edu^2 + 2Fdud\theta + Gd\theta^2,$$

where

$$E = \langle \Psi_u, \Psi_u \rangle, \quad F = \langle \Psi_u, \Psi_\theta \rangle, \quad G = \langle \Psi_\theta, \Psi_\theta \rangle.$$

The unit normal vector to the surface is:

$$U = \frac{\Psi_u \times \Psi_\theta}{\|\Psi_u \times \Psi_\theta\|}.$$

The second fundamental form, denoted by  $II$ , can be expressed as:

$$II = Ldu^2 + 2Mdu d\theta + Nd\theta^2,$$

with coefficients:

$$L = -\langle \Psi_s, U_s \rangle, \quad M = -\langle \Psi_\theta, U_s \rangle, \quad N = -\langle \Psi_\theta, U_\theta \rangle.$$

The third fundamental form  $III$  is given by:

$$III = edu^2 + 2f dud\theta + gd\theta^2,$$

with coefficients:

$$e = \langle \mathbf{U}_s, \mathbf{U}_s \rangle, \quad f = \langle \mathbf{U}_\theta, \mathbf{U}_s \rangle, \quad g = \langle \mathbf{U}_\theta, \mathbf{U}_\theta \rangle.$$

The Gaussian curvature  $K$  and mean curvature  $H$  are computed as:

$$K = \frac{LN - M^2}{EG - F^2},$$

$$H = \frac{EN + GL - 2FM}{2(EG - F^2)}.$$

## RESULTS AND CONCLUSION

The canal surface, described using the Darboux frame, can be parametrized as follows:

$$\Psi(s, \theta) = c(s) - rr'\mathbf{T} + r\sqrt{1-r'^2} (\cos \theta \mathbf{b} + \sin \theta \mathbf{n}) \quad (2)$$

(Doğan and Yaylı, 2012:752).

From Eq. (1) we can assume that  $-r'(s) = \cos \varphi$  for some smooth function  $\varphi = \varphi(s)$ . Then, the canal surface  $\Psi(s, \theta)$  can be written as:

$$\Psi(s, \theta) = c(s) + r \cos \varphi \mathbf{T} + r \sin \varphi (\cos \theta \mathbf{b} + \sin \theta \mathbf{n}).$$

Through differentiation with respect to  $s$ , we get,

$$\Psi_s(s, \theta) = \Psi_s^1(s, \theta)\mathbf{T} + \Psi_s^2(s, \theta)\mathbf{b} + \Psi_s^3(s, \theta)\mathbf{n},$$

where,

$$\Psi_s^1(s, \theta) = \sin^2 \varphi - rr'' + r \sin \varphi w_1,$$

$$\Psi_s^2(s, \theta) = r' \sin \varphi \cos \theta - r' r \kappa_g - r' r \varphi' \cos \theta - r \tau_g \sin \theta,$$

$$\Psi_s^3(s, \theta) = r' \sin \varphi \sin \theta - r' r \kappa_n - r' r \varphi' \sin \theta + r \tau_g \cos \theta,$$

$$w_1 = \kappa_g \cos \theta + \kappa_n \sin \theta.$$

Also,

$$\Psi_\theta(s, \theta) = \Psi_\theta^1(s, \theta)\mathbf{T} + \Psi_\theta^2(s, \theta)\mathbf{b} + \Psi_\theta^3(s, \theta)\mathbf{n},$$

where,

$$\Psi_\theta^1(s, \theta) = 0,$$

$$\Psi_\theta^2(s, \theta) = -r \sin \varphi \sin \theta,$$

$$\Psi_\theta^3(s, \theta) = r \sin \varphi \cos \theta.$$

The component functions of the first fundamental form can be expressed as:

$$E = \langle \Psi_s, \Psi_s \rangle = r^2 \left( \sin^2 \varphi w_1^2 + r'^2 (\kappa_g^2 + \kappa_n^2) + \varphi'^2 + 2\varphi' w_1 + \tau_g^2 \sin^2 \varphi \right. \\ \left. + 2r' \tau_g \sin \varphi w_2 \right)$$

$$-2r(r'' - \sin \varphi w_1) + \sin^2 \varphi,$$

$$F = \langle \Psi_s, \Psi_\theta \rangle = r(r' \sin \varphi w_2 + r \tau_g \sin^2 \varphi),$$

$$w_2 = \kappa_g \sin \theta - \kappa_n \cos \theta,$$

$$G = \langle \Psi_\theta, \Psi_\theta \rangle = r^2 \sin^2 \varphi.$$

The vector field  $\mathbf{U}$ , defining the unit normal of  $\Psi(s, \theta)$  is represented as:

$$\mathbf{U}(s, \theta) = \frac{\Psi_s \times \Psi_\theta}{\| \Psi_s \times \Psi_\theta \|} \\ = \cos \varphi \mathbf{T} + \sin \varphi \cos \theta \mathbf{b} + \sin \varphi \sin \theta \mathbf{n}.$$

$$\mathbf{U}_s = \mathbf{U}_s^1 \mathbf{T}(s) + \mathbf{U}_s^2 \mathbf{b}(s) + \mathbf{U}_s^3 \mathbf{n}(s),$$

where,

$$\mathbf{U}_s^1 = -r'' - \sin \varphi w_1,$$

$$\mathbf{U}_s^2 = -r' \kappa_g - r' \varphi' \cos \theta - \tau_g \sin \varphi \sin \theta,$$

$$\mathbf{U}_s^3 = -r' \kappa_n - r' \varphi' \sin \theta + \tau_g \sin \varphi \cos \theta$$

And,

$$\mathbf{U}_\theta(s, \theta) = \mathbf{U}_\theta^2(s, \theta)\mathbf{b} + \mathbf{U}_\theta^3(s, \theta)\mathbf{n},$$

where,

$$\mathbf{U}_\theta^1(s, \theta) = 0,$$

$$\mathbf{U}_\theta^2(s, \theta) = -\sin \varphi \sin \theta,$$

$$\mathbf{U}_\theta^3(s, \theta) = \sin \varphi \cos \theta.$$

The component expressions that define the second fundamental form are given below:

$$L = -\langle \Psi_s, \mathbf{U}_s \rangle = -r \left( \varphi'^2 + r'^2 (\kappa_g^2 + \kappa_n^2) + 2\varphi' w_1 + \sin^2 \varphi w_1^2 \right) + (r'' + \sin \varphi w_1),$$

$$M = -\langle \Psi_\theta, \mathbf{U}_s \rangle = -r (\tau_g \sin^2 \varphi + r' \sin \varphi w_2),$$

$$N = -\langle \Psi_\theta, \mathbf{U}_\theta \rangle = -r \sin^2 \varphi.$$

Consequently, the third fundamental form can be described in terms of the following functional components:

$$e = \langle \mathbf{U}_s, \mathbf{U}_s \rangle = \varphi'^2 + r'^2 (\kappa_n^2 + \kappa_g^2) + 2\varphi' w_1 + \sin^2 \varphi w_1^2 + \tau_g^2 \sin^2 \varphi + 2r' \tau_g \sin \varphi w_2,$$

$$f = \langle \mathbf{U}_\theta, \mathbf{U}_s \rangle = r' \sin \varphi w_2 + \tau_g \sin^2 \varphi,$$

$$g = \langle \mathbf{U}_\theta, \mathbf{U}_\theta \rangle = \sin^2 \varphi.$$

**Lemma 1.** The Darboux canal surface  $\Psi(s, \theta)$  fulfills the conditions imposed by its first, second, and third fundamental forms

$$L = \frac{E + \rho}{-r}, \quad M = \frac{F}{-r}, \quad N = \frac{G}{-r},$$

$$e = \frac{L - Q}{-r}, \quad f = \frac{M}{-r}, \quad g = \frac{N}{-r},$$

where,

$$Q = r'' + \sin \varphi w_1, \quad \rho = rQ - \sin^2 \varphi.$$

Based on Lemma 1, the Gaussian and mean curvatures of  $\Psi(s, \theta)$  are respectively obtained as follows:

$$K = \frac{LN - M^2}{EG - F^2} = \frac{Q}{r\rho},$$

$$H = \frac{EN - 2FM + GL}{2(EG - F^2)} = \frac{2\rho + \sin^2 \varphi}{-2r\rho}.$$

**Proposition 2.** The Gaussian and mean curvatures associated with  $\Psi(s, \theta)$  are written as:

$$H = -\frac{1}{2} \left( Kr + \frac{1}{r} \right).$$

**Definition 3.** When the curvatures  $(K, H)$  of a canal surface  $M$  satisfy  $\Phi(x, y) = 0$ , the surface is classified as a Weingarten canal surface, where  $\Phi$  represents the Jacobi function  $\Phi = xy - yx$  (Kim, Liu and Qian, 2016:463).

**Definition 4.** When the curvatures  $(K, H)$  of a canal surface  $M$  satisfy  $ax + by = c$  the surface is classified as a linear Weingarten canal surface, where  $(a, b, c) \in \mathbb{R}$  and  $(a, b, c) \neq (0, 0, 0)$  (López, 2009:3).

**Lemma 5.** For the canal surface  $\Psi(s, \theta)$ , the partial derivatives of  $K$  and  $H$  can be written as:

$$K_s = \frac{\sin^2 \varphi (-2rr'w_1^2 - rr''' - r \sin \varphi w_1' + r' \sin \varphi w_1 + r' r'')}{r^2 \rho^2},$$

$$K_\theta = -\frac{\sin^3 \varphi w_2}{r \rho^2},$$

$$H_s = \frac{\sin^2 \varphi (2r^2 r' w_1^2 + r^2 r''' + r^2 \sin \varphi w_1' - 2rr' \sin \varphi w_1 - 2rr' r'' + r' \sin^2 \varphi) + 4r^2 r' r''^2 + 5r^2 r' r'' \sin^2 \varphi w_1}{2r^2 \rho^2},$$

$$H_\theta = \frac{\sin^3 \varphi w_2}{2\rho^2}.$$

**Theorem 6.** Let

$$\Psi(s, \theta) = c(s) + r(s) \left( \cos \varphi(s) T(s) + \sin \varphi(s) \cos \theta b(s) + \sin \varphi(s) \sin \theta n(s) \right)$$

be a canal surface parametrized via the Darboux frame  $\{T, b, n\}$ . Then  $X$  is a  $(K, H)$ –Weingarten surface if and only if it is either

- tube surface, i.e.  $r'(s) = 0$  (constant radius), or
- The surface qualifies as a surface of revolution if the spine curve has curvature  $(\kappa(s) = 0)$  (zero curvature).

**Proof:**  $\Rightarrow$ : A canal surface  $\Psi(s, \theta)$  is  $(K, H)$ –Weingarten precisely when its Gaussian and mean curvatures satisfy the Jacobi equation

$$H_s K_\theta - H_\theta K_s = 0.$$

Using the explicit formulas from Proposition 2. one shows that this condition factorizes as

$$\left( K r' - \frac{r'}{r^2} \right) K_\theta = 0.$$

Hence either

$$r'(s) = 0,$$

in which case  $r$  is constant and  $\Psi$  is a tube surface, or

$$K_\theta = 0.$$

A direct computation of  $K_\theta$  in Darboux coordinates yields

$$K_\theta = \sin^2 \varphi \left( \kappa_n \cos \theta - \kappa_g \sin \theta \right),$$

so  $K_\theta = 0$  implies  $\kappa_n \cos \theta = \kappa_g \sin \theta$  for all  $\theta$ . This forces  $\kappa_g = \kappa_n = 0$ , i.e. the spine curve has zero curvature and  $\Psi$  corresponds to a surface generated by revolution.

$\Leftarrow$ : *Case I*: Tube surface ( $r' = 0$ ). Then

$$\cos \phi = -r' = 0, \quad \sin \phi = 1,$$

From Lemma 1. we get;

$$\begin{aligned}
\rho &= -rw_1 - 1, & Q &= -w_1, \\
K &= \frac{w_1}{r(rw_1 + 1)}, & H &= \frac{2rw_1 + 1}{2r(rw_1 + 1)}, \\
K_s &= \frac{-w_1'}{r(rw_1 + 1)^2}, & K_\theta &= \frac{-w_2'}{r(rw_1 + 1)^2}, \\
H_s &= \frac{-w_1'}{2(rw_1 + 1)^2}, & H_\theta &= \frac{-w_2'}{2(rw_1 + 1)^2}.
\end{aligned} \tag{3}$$

From Eq. (3) the Jacobi equation is satisfied everywhere.

*Case 2:* Surface of revolution ( $\kappa = 0$ ). If the spine  $c(s)$  is a straight line, then in suitable Cartesian coordinates  $\Psi(s, \theta)$  can be written as

$$\Psi(s, \theta) = (f(s) \cos \theta, f(s) \sin \theta, s)$$

for some function  $f(s)$ . It is well known that for such a surface of revolution both  $K$  and  $H$  depend solely on  $s$ , so again

$$K_\theta = 0, \quad H_\theta = 0,$$

and thus, the Jacobi equation ( $H_s K_\theta - H_\theta K_s = 0$ ) holds identically. In both cases the Jacobi equation is satisfied, completing the converse proof.

**Theorem 7.** Let  $\Psi(s, \theta)$  be a Darboux canal surface in  $E^3$ . Then  $\Psi$  is developable if and only if one of the following holds:

- The canal surface is a surface of revolution (i.e., the spine curve  $c(s)$  is a straight line, so  $(\kappa(s) = 0)$ , or
- The canal surface is a cone, that is, the radius function is linear:  $(r(s) = as + b)$ , and the spine lies in a plane.

**Proof:** Darboux canal surface  $\Psi(s, \theta)$  is developable if and only if its Gaussian curvature  $K = 0$ ,

$$K = 0 \Leftrightarrow r''(s) + \sin \varphi(s) w_1$$

where  $(w_1 = \kappa_g \cos \theta + \kappa_n \sin \theta)$ .

This expression vanishes identically if one of the following holds:

- If the spine is a straight line ( $\kappa(s) = 0 \Rightarrow \kappa_g = \kappa_n = 0$ ), then

$$(w_1 = 0) \text{ and } (K = 0),$$

- If  $r(s)$  is linear and the spine lies in a plane, then the surface becomes a cone, which is known to be developable.

Therefore,  $\Psi(s, \theta)$  is developable if and only if it is a surface of revolution or a cone.

**Theorem 8.** Let  $\Psi(s, \theta)$  be a Darboux canal surface in  $E^3$ . Then  $\Psi(s, \theta)$  is a minimal surface if and only if it is part of a catenoid, i.e., the spine curve is a straight line, and the radius function satisfies

$$r(s) = \sqrt{a^2 + (s + b)^2}$$

for constants  $(a, b \in \mathbb{R})$ .

**Proof:** A Darboux canal surface  $\Psi(s, \theta)$  is classified as minimal precisely when  $H = 0$ ; according to Lemma 1:

$$H = 0 \Leftrightarrow 2rr'' + \sin^2 \varphi = 0 \quad \text{and} \quad 2r \sin \varphi w_1 = 0.$$

Since  $(\sin \varphi = \sqrt{1 - (r')^2} \neq 0)$ , otherwise parametrization degenerates to a curve and fails to describe a surface, we must have:

$$w_1 = \kappa_g \cos \theta + \kappa_n \sin \theta = 0 \quad \text{for all } \theta.$$

$$(\sin \varphi \neq 0 \Rightarrow w_1 = 0), \text{ so:}$$

$$\kappa_g \cos \theta + \kappa_n \sin \theta = 0.$$

This must hold for all  $\theta$ , which is only possible if:

$$\kappa_g = 0 \quad \text{and} \quad \kappa_n = 0 \Rightarrow \kappa = 0.$$

Therefore, the spine curve forms a straight line. Substituting this into the first condition gives:

$2rr'' + 1 - r'^2 = 0 \Rightarrow$  (using  $\cos \varphi = -r'$  and  $\sin^2 \varphi = 1 - r'^2$ ). Solving this ODE gives:

$r(s) = \sqrt{a^2 + (s + b)^2}$ , which defines a catenoid. Hence the only regular minimal canal surfaces are catenoids.

**Theorem 9.** Consider the canal surface  $\Psi(s, \theta)$  in  $E^3$  defined with respect to the Darboux frame. It constitutes a linear Weingarten surface obeying the

$$aK + bH = c$$

for constants  $(a, b, c \in \mathbb{R})$ , if and only if either:



- The surface can be described as generated by revolution, where the spine curve is a straight line ( $\kappa = 0$ ), and the radius function fulfills:

$$r(s) = \sqrt{a_0^2 + (s + b_0)^2}$$

for some constants ( $a_0, b_0 \in \mathbb{R}$ ), or

- The radius function  $r(s)$  satisfies the differential identity

$$\left( ar + \frac{b}{2} \right) (2r'' + \sin^2 \varphi) + br \sin \varphi w_1 = cr^2.$$

**Proof:** From Proposition 2. the Gaussian and mean curvature of the Darboux canal surface is expressed in terms of  $r(s)$ ,  $r'(s)$ ,  $\varphi(s)$ , and  $w_1$ . A linear relation ( $aK + bH = c$ ) yields:

$$aK + bH - c = 0.$$

Substituting the explicit formulas of  $K$  and  $H$ , and simplifying (see Lemma 1.) one arrives at:

$$\left( ar + \frac{b}{2} \right) (2r'' + \sin^2 \varphi) + br \sin \varphi w_1 = cr^2.$$

Now, for the case ( $\kappa = 0$ ), i.e., the spine curve is a straight line, we have ( $\kappa_g = \kappa_n = 0 \Rightarrow w_1 = 0$ ), and from minimal surface analysis we know:

$$2r'' + \sin^2 \varphi = 0.$$

Substituting into the above identity, we get:

$$\left( ar + \frac{b}{2} \right) (0) + 0 = cr^2 \Rightarrow c = 0.$$

Thus, the equation is satisfied for a specific choice of constants, and the surface is both minimal and linear Weingarten.

Conversely, if the differential identity holds for arbitrary  $r(s)$ , then  $\Psi(s, \theta)$  is a linear Weingarten surface by definition.

**Example 10.** The standard parameterization of a cylinder:

$$\Psi(u, v) = (\cos u, \sin u, v), \quad u \in [0, 2\pi], v \in \mathbb{R}$$

Unit normal vector:

$$\mathbf{U}(u, v) = \frac{\Psi_u \times \Psi_v}{\|\Psi_u \times \Psi_v\|} = (\cos u, \sin u, 0)$$

For the unit-speed helix curve on the cylinder:

$$c(s) = (\cos s, \sin s, s), \quad s \in \mathbb{R}$$

Tangent vector:

$$\mathbf{T}(s) = \frac{dc}{ds} = (-\sin s, \cos s, 1)$$

Normal vector (surface normal):

$$\mathbf{n}(s) = \mathbf{U}(s, s) = (\cos s, \sin s, 0)$$

Binormal vector:

$$\mathbf{b}(s) = \mathbf{T}(s) \times \mathbf{n}(s) = (-\sin s, \cos s, -1)$$

Given:

$$\text{Radius function: } r(s) = 0.3 + 0.1 \sin(2s)$$

$$\text{Its derivative: } r'(s) = 0.2 \cos(2s)$$

Angle function satisfying:

$$\cos \phi(s) = -r'(s) = -0.2 \cos(2s), \quad \sin \phi(s) = \sqrt{1 - 0.04 \cos^2(2s)}$$

The Darboux canal surface is then:

$$\begin{aligned} \Psi(s, \theta) = & c(s) + r(s) \left[ -0.2 \cos(2s) \mathbf{T}(s) \right. \\ & \left. + \sqrt{1 - 0.04 \cos^2(2s)} (\cos \theta \mathbf{n}(s) + \sin \theta \mathbf{b}(s)) \right] \end{aligned}$$

which expands to:

$$\Psi(s, \theta) = (\cos s, \sin s, s) + (0.3 + 0.1 \sin 2s) \left[ 0.2 \cos(2s)(\sin s, -\cos s, -1) + \sqrt{1 - 0.04 \cos^2(2s)} (\cos \theta(\cos s, \sin s, 0) + \sin \theta(-\sin s, \cos s, -1)) \right]$$

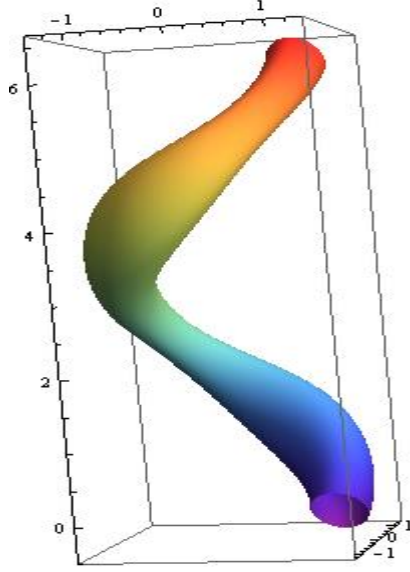


Figure 1:  $\Psi(s, \theta)$  Darboux Canal Surface

## Conclusions

In this study, we analysed canal surfaces in three-dimensional Euclidean space using the Darboux frame. By parametrizing the canal surface via a unit-speed spine curve together with a variable radius function, we derived the first, second, and third fundamental forms, along with the Gaussian and mean curvatures and the principal curvatures. The geometric conditions under which a Darboux canal surface becomes developable, minimal were also investigated. In addition, we established the necessary and sufficient criteria for such surfaces to be of Weingarten or linear Weingarten type. A graphical example was provided to illustrate and support the analytical findings.

One of the key contributions of this study is showing that under specific conditions, the Darboux canal surface reduces to a surface of revolution or a tubular surface. These results generalize and complement earlier works in the literature, especially those formulated in the Frenet or Bishop frames.

For future work, one may consider extending this framework to other ambient spaces such as Minkowski or isotropic spaces. Additionally, a similar analysis could be carried out for canal surfaces according to the different frames or using more general parameterizations.

## REFERENCE

- Bektaş, Ö., and Yüce, S. (2012). Special Smarandache curves according to Darboux frame in  $E^3$ . *arXiv preprint*, arXiv:1203.4830.
- Damar, E., Saltık Baek, B., Yüksel, N., and Oğraş, N. (2025). Tubular surfaces of adjoint curves according to the modified orthogonal frame. *Black Sea Journal of Engineering and Science*, 8(1), 206–213.
- Doğan, F., and Yaylı, Y. (2012). Tubes with Darboux frame. *International Journal of Contemporary Mathematical Sciences*, 7(16), 751–758.
- Elashiry, M. I., Saad, M. K., Yüksel, N., Oğraş, N., and Abdel-Salam, A. A. (2025). Non-null canal surfaces with Bishop frame in Minkowski 3-space. *International Journal of Analysis and Applications*, 23, 212–212.
- Gray, A., Abbena, E., and Salamon, S. (2017). *Modern differential geometry of curves and surfaces with Mathematica* (3rd ed.). CRC Press.
- Karacan, M. K., and Tunçer, Y. (2013). Tubular surfaces of Weingarten types in Galilean and pseudo-Galilean. *Bulletin of Mathematical Analysis and Applications*, 5(2), 87–100.
- Kim, Y. H., Liu, H., and Qian, J. (2016). Some characterizations of canal surfaces. *Bulletin of the Korean Mathematical Society*, 53(2), 461–477.
- Ouarab, S. (2021). Smarandache ruled surfaces according to Darboux frame in  $E^3$ . *Journal of Mathematics*, 2021(1), Article ID 9912624.
- Saçlı, Y. G. (2013). *Darboux çatılı regle yüzeylerin karakteristik özellikleri* (Master's thesis). Yıldız Technical University, İstanbul.
- Soliman, M. A., Mahmoud, W. M., Solouma, E. M., and Bary, M. (2019). The new study of some characterization of canal surfaces with Weingarten and linear Weingarten types according to Bishop frame. *Journal of the Egyptian Mathematical Society*, 27(1), 26.
- Uçum, A., and İlarslan, K. (2016). New types of canal surfaces in Minkowski 3-space. *Advances in Applied Clifford Algebras*, 26(1), 449–468.
- Ünlütürk, Y., Cimdiker, M., and Ekici, C. (2016). Characteristic properties of the parallel ruled surfaces with Darboux frame in Euclidean 3-space. *Communication in Mathematical Modeling and Applications*, 1(1), 26–43.
- Xu, Z. Q., Feng, R. Z., and Sun, J. G. (2006). Analytic and algebraic properties of canal surfaces. *Journal of Computational and Applied Mathematics*, 195(1–2), 220–228.
- Yüksel, N., Tunçer, Y., and Karacan, M. K. (2011). Tabular surfaces with Bishop frame of Weingarten types in Euclidean 3-space. *Acta Universitatis Apulensis*, 27, 39–50.



# **A Study on TB-Smarandache Tube Surfaces in Three-Dimensional Euclidean Space**

**Prof. Dr. Nural YÜKSEL<sup>1</sup>**

**Nurdan OĞRAŞ<sup>2</sup>**

- 1- Department of Mathematics, Erciyes University, Kayseri, Turkey, e-mail:yukseln@erciyes.edu.tr; ORCIDiDs: <https://orcid.org/0000-0003-3360-5148>.
- 2- Graduate School of Natural and Applied Sciences, Erciyes University, Kayseri, Turkey, e-mail:nurdanogras@gmail.com, ORCIDiDs: <https://orcid.org/0000-0002-5539-4890>

## ABSTRACT

In the present work, a novel tube surface is generated by considering the **TB**–Smarandache curve as the central curve in the Euclidean three-dimensional space. The study provides explicit computations for the fundamental forms associated with the **TB**–Smarandache tube surface. From these results, the corresponding mean and Gaussian curvatures are obtained. Using these findings, detailed analyses are carried out to determine when the surface is flat or minimal. Furthermore, the asymptotic and geodesic curvatures of the surface are investigated, and the nature of its curvature lines is discussed. Special attention is given to the characterization of the surface under Weingarten and linear Weingarten conditions. These classifications provide insight into the intrinsic and extrinsic geometry of the surface and help identify special cases with simplified curvature behaviour. An illustrative example is presented to demonstrate the theoretical results, and the corresponding surface is visualized graphically. The obtained results expand knowledge of Smarandache-type geometrical constructions and indicate prospective implementations in shape modeling, CAD environments, and the examination of space curves influenced by moving frames.

*Keywords – Euclidean 3-space, Tube surfaces, Frenet frame, Smarandache curves, Weingarten surfaces*

---

## INTRODUCTION

Defined as the envelope of a sphere whose center curve is  $\alpha(s)$  and radius is  $r(s)$ , a canal surface appears frequently in computational geometry, CAD/CAM modeling, tool-path computation, and the graphical representation of tubular or filamentary forms. A standard parameterization is

$$\Psi(s, \theta) = \alpha(s) - r'(s)r(s)\mathbf{T}(s) \pm r(s)\sqrt{1-(r'(s))^2}(\cos \theta \mathbf{N}(s) + \sin \theta \mathbf{B}(s)), \quad (1)$$

where  $\alpha(s)$  is unit-speed,  $\{\mathbf{T}, \mathbf{N}, \mathbf{B}\}$  its Frenet frame and  $r'(s) = \frac{dr}{ds}$ .

When  $r(s) = r > 0$  is constant, Eq. (1) reduces to the classical tubular surface

$$\Psi(s, \theta) = \alpha(s) + r(\cos \theta \mathbf{N}(s) + \sin \theta \mathbf{B}(s)), \quad s \in I, \theta \in [0, 2\pi),$$

which has been extensively studied in Frenet frame for its stability, fundamental forms, curvature behavior and rendering algorithms (Fu et al., 2019; Kim et al., 2016).

Beyond their theoretical significance, tube surfaces contribute to various practical fields—ranging from geometric recovery and robotic movement design to smooth surface blending and visual analysis of fine geometrical shapes. Recent investigations have broadened the scope of these analyses to include various geometric spaces, alternative frame structures, and specialized subclasses such as Weingarten and linear Weingarten surfaces (Damar et al., 2025:210; Saad et al., 2024:12485; Yüksel et al., 2011:45; Nurkan et al., 2019:158).

A Smarandache curve in  $E^3$  is obtained by normalizing a constant-linear combination of the Frenet frame of a base space curve  $\alpha(s)$ . Precisely, for fixed coefficients  $(a, b, c \in \mathbb{R})$ ,

$$\rho_{(a,b,c)}(s) = \frac{a\mathbf{T}(s) + b\mathbf{N}(s) + c\mathbf{B}(s)}{\|a\mathbf{T}(s) + b\mathbf{N}(s) + c\mathbf{B}(s)\|}$$

where  $\{\mathbf{T}, \mathbf{N}, \mathbf{B}\}$  is the Frenet–Serret frame along the unit-speed curve  $\alpha(s)$ . Important special cases are the

$\mathbf{TN}$ –Smarandache curve, obtained by normalizing  $(\mathbf{T} + \mathbf{N})$ ; the  $\mathbf{NB}$ –Smarandache curve, obtained by normalizing  $(\mathbf{N} + \mathbf{B})$ ; and the  $\mathbf{TB}$ –Smarandache curve, obtained by normalizing  $(\mathbf{T} + \mathbf{B})$ . In formulas:

$$\begin{aligned} \rho_{\mathbf{T}+\mathbf{N}}(s) &= \frac{\mathbf{T}(s) + \mathbf{N}(s)}{\sqrt{2}}, \\ \rho_{\mathbf{N}+\mathbf{B}}(s) &= \frac{\mathbf{N}(s) + \mathbf{B}(s)}{\sqrt{2}}, \\ \rho_{\mathbf{T}+\mathbf{B}}(s) &= \frac{\mathbf{T}(s) + \mathbf{B}(s)}{\sqrt{2}}. \end{aligned}$$

These definitions yield novel center-curves with distinct curvature–torsion behaviors (Ali, 2010:30; Turgut and Yılmaz, 2008:51).



Smarandache curves have found diverse applications across several disciplines. In Computer-Aided Geometric Design (CAGD) and CAD/CAM systems, they enable smooth blending between structural elements along twisted centerlines. In the field of robot motion planning, these curves assist in generating end-effector trajectories with prescribed torsion profiles. Scientific visualization benefits from their ability to model helical biostructures such as DNA strands, protein chains, and engineered springs. Additionally, architectural geometry utilizes Smarandache curves for designing free-form shells and sculptural surfaces via modified offset techniques.

These general Smarandache curves enrich classical curve theory by embedding frame-dependent offsets, yielding new families of space curves with distinctive geometric invariants. Numerous studies have explored their properties and applications in various frame contexts (Baek, 2025:396; Ouarab, 2021:9912624; Bektaş and Yüce, 2012:5; Şenyurt, Ayvaci and Canlı, 2023:18).

In this study, the centre curve of the tubular surface in Euclidean 3 space is based on **TB**–Smarandache curve and investigated in the Frenet-Serret frame. For the constructed Smarandache tube surface, both fundamental forms as well as the mean and Gaussian curvatures are computed, and the cases where the surface becomes flat or minimal are examined. Some results are found for asymptotic curvature, geodesic curvature and curvature line states. Weingarten and linear Weingarten conditions of **TB**–Smarandache tube surface are also researched. Finally, an example is given for the examined surface and its graph is plotted.

## METARIALS AND METHODS

Let  $\Psi(s, \theta)$  a surface in  $E^3$  and  $U(s, \theta)$  be the standard unit normal vector field on  $\Psi(s, \theta)$  defined by

$$U = \frac{\Psi_s \times \Psi_\theta}{\|\Psi_s \times \Psi_\theta\|}, \text{ where, } \Psi_s = \frac{\partial \Psi}{\partial s}, \Psi_\theta = \frac{\partial \Psi}{\partial \theta}$$

are the tangent vectors of  $\Psi(s, \theta)$ . We define on  $\Psi(s, \theta)$  a metric, representing its first fundamental form, in the following manner:

$$I = g_{11}ds^2 + 2g_{12}dsd\theta + g_{22}d\theta^2,$$

where,

$$g_{11} = \langle \Psi_s, \Psi_s \rangle, g_{12} = \langle \Psi_s, \Psi_\theta \rangle \text{ and } g_{22} = \langle \Psi_\theta, \Psi_\theta \rangle.$$

In addition, the second fundamental form associated with  $\Psi(s, \theta)$  is introduced in the following way:

$$II = h_{11}ds^2 + 2h_{12}dsd\theta + h_{22}d\theta^2,$$

where,

$h_{11} = \langle \Psi_{ss}, \mathbf{U} \rangle$ ,  $h_{12} = \langle \Psi_{s\theta}, \mathbf{U} \rangle$  and  $h_{22} = \langle \Psi_{\theta\theta}, \mathbf{U} \rangle$ . For the surface, the Gaussian curvature  $K$  and mean curvature  $H$  are expressed through the following formulas:

$$K = \frac{h_{11}h_{22} - h_{12}^2}{g_{11}g_{22} - g_{12}^2},$$

$$H = \frac{h_{11}g_{22} - 2g_{12}h_{12} + g_{11}h_{22}}{2(g_{11}g_{22} - g_{12}^2)}.$$

We define a unit-speed curve  $\alpha(s)$  along with its Frenet frame  $\{\mathbf{T}, \mathbf{N}, \mathbf{B}\}$  and denote its curvature and torsion by  $\kappa(s)$  and  $\tau(s)$ , respectively. The  $\mathbf{TB}$  – Smarandache curve,

$$\beta_{TB}(s) = \frac{\mathbf{T}(s) + \mathbf{B}(s)}{\|\mathbf{T}(s) + \mathbf{B}(s)\|} = \frac{\mathbf{T}(s) + \mathbf{B}(s)}{\sqrt{2}}$$

has the following Frenet elements (see e.g. Turgut and Yılmaz, 2008:51),

$$\mathbf{T}_{TB}(s) = \mathbf{N}(s),$$

$$\mathbf{N}_{TB}(s) = \frac{-\kappa(s)\mathbf{T}(s) + \tau(s)\mathbf{B}(s)}{\sqrt{\kappa(s)^2 + \tau(s)^2}},$$

$$\mathbf{B}_{TB}(s) = \frac{\tau(s)\mathbf{T}(s) + \kappa(s)\mathbf{B}(s)}{\sqrt{\kappa(s)^2 + \tau(s)^2}},$$

$$\begin{aligned}\kappa_{TB}(s) &= \sqrt{2} \frac{\sqrt{\kappa(s)^2 + \tau(s)^2}}{|\kappa(s) - \tau(s)|}, \\ \tau_{TB}(s) &= \sqrt{2} \frac{1}{|\kappa(s) - \tau(s)| (\kappa(s)^2 + \tau(s)^2)} \left( \frac{\tau(s)}{\kappa(s)} \right)'.\end{aligned}\tag{2}$$

**Definition 1.** A Weingarten canal surface is defined as a canal surface  $M$  whose Gaussian and mean curvatures satisfy  $\Phi(x, y) = 0$ ; here,  $\Phi$  is the Jacobi function  $\Phi = xy - yx$ . (Kim, Liu and Qian, 2016:463).

**Definition 2.** If a canal surface  $M$  has curvatures  $(K, H)$  that satisfy the equation  $ax + by = c$ , it is recognized as a linear Weingarten surface, with the parameters set as  $(a, b, c) \in \mathbb{R}$  and  $(a, b, c) \neq (0, 0, 0)$  (López, 2009:3).

## RESULTS AND CONCLUSION

The tubular surface with radius  $r(s)$  centered at  $\beta(s)$  is given by:

$$\Psi(s, \theta) = \beta(s) + r(s) [\cos \theta N_\beta(s) + \sin \theta B_\beta(s)]$$

Using the Frenet frame components from Eq. (2):

$$\Psi(s, \theta) = \frac{\mathbf{T} + \mathbf{B}}{\sqrt{2}} + r \left[ \frac{-\kappa \mathbf{T} + \tau \mathbf{B}}{\sqrt{\kappa^2 + \tau^2}} \cos \theta + \frac{\tau \mathbf{T} + \kappa \mathbf{B}}{\sqrt{\kappa^2 + \tau^2}} \sin \theta \right]$$

Let  $\sin \phi = \tau / \sqrt{\kappa^2 + \tau^2}$  and  $\cos \phi = \kappa / \sqrt{\kappa^2 + \tau^2}$ . The surface simplifies to:

$$\Psi(s, \theta) = \frac{\mathbf{T} + \mathbf{B}}{\sqrt{2}} + r [-\cos \psi \mathbf{T} + \sin \psi \mathbf{B}]$$

where,  $\psi = \phi + \theta$ .

Derivative with respect to  $s$ ,

$$\Psi_s = \left( \frac{\kappa - \tau}{\sqrt{2}} - r\kappa \cos \psi - r\tau \sin \psi \right) \mathbf{N} + r\phi' \sin \psi \mathbf{T} + r\phi' \cos \psi \mathbf{B}$$

where,

$$\phi' = \frac{d}{ds}(\arctan(\tau / \kappa)) = \frac{\kappa\tau' - \tau\kappa'}{\kappa^2 + \tau^2}.$$

The second derivative  $\Psi_{ss}$  describes the curvature of the coordinate curves:

$$\begin{aligned} \Psi_{ss} = & \left[ -\kappa \left( \frac{\kappa - \tau}{\sqrt{2}} - r\kappa \cos \psi - r\tau \sin \psi \right) + r\phi'' \sin \psi + r(\phi')^2 \cos \psi \right] \mathbf{T} \\ & + \left[ \frac{\kappa' - \tau'}{\sqrt{2}} - r\kappa' \cos \psi - r\tau' \sin \psi \right] \mathbf{N} \\ & + \left[ \tau \left( \frac{\kappa - \tau}{\sqrt{2}} - r\kappa \cos \psi - r\tau \sin \psi \right) - r\phi'' \cos \psi + r(\phi')^2 \sin \psi \right] \mathbf{B} \end{aligned}$$

Derivative with respect to  $\theta$ ,

$$\Psi_\theta = r[\sin \psi \mathbf{T} + \cos \psi \mathbf{B}].$$

The second derivative  $\Psi_{\theta\theta}$  describes the curvature of the coordinate curves:

$$\Psi_{\theta\theta} = r[\cos \psi \mathbf{T} - \sin \psi \mathbf{B}],$$

The cross product  $\Psi_s \times \Psi_\theta$  yields:

$$\Psi_s \times \Psi_\theta = Ar[-\cos \psi \mathbf{T} + \sin \psi \mathbf{B}],$$

where,

$$A = \frac{\kappa - \tau}{\sqrt{2}} - r\kappa \cos \psi - r\tau \sin \psi$$

The unit normal vector is:

$$\mathbf{U}(s, \theta) = \frac{A}{|A|} [-\cos(\phi + \theta) \mathbf{T} + \sin(\phi + \theta) \mathbf{B}]$$

The unit normal vector becomes:

$$\mathbf{U}(s, \theta) = -\cos \psi \mathbf{T} + \sin \psi \mathbf{B},$$

$$\mathbf{U}_s = \phi'(\sin \psi \mathbf{T} + \cos \psi \mathbf{B}) - (\kappa \cos \psi + \tau \sin \psi) \mathbf{N}$$

$$\mathbf{U}_\theta = \sin \psi \mathbf{T} + \cos \psi \mathbf{B}$$

For the first fundamental form, its component functions are represented in the following manner:

$$I = g_{11} ds^2 + 2g_{12} ds d\theta + g_{22} d\theta^2$$

$$g_{11} = \langle \Psi_s, \Psi_s \rangle = A^2 + r^2 (\phi')^2,$$

$$g_{12} = \langle \Psi_s, \Psi_\theta \rangle = r^2 \phi', \quad g_{22} = \langle \Psi_\theta, \Psi_\theta \rangle = r^2$$

For the second fundamental form, its component expressions are formulated in the following manner:

$$II = h_{11} ds^2 + 2h_{12} ds d\theta + h_{22} d\theta^2$$

$$h_{11} = -\langle \Psi_s, \mathbf{U}_s \rangle = A(\kappa \cos \psi + \tau \sin \psi) - r(\phi')^2$$

$$h_{12} = -\langle \Psi_s, \mathbf{U}_\theta \rangle = -r\phi' \quad h_{22} = -\langle \Psi_\theta, \mathbf{U}_\theta \rangle = -r$$

Gaussian and mean curvatures are, respectively given by;

$$K = \frac{h_{11}h_{22} - h_{12}^2}{g_{11}g_{22}} = -\frac{A(\kappa \cos \psi + \tau \sin \psi)}{(A^2 + r^2 (\phi')^2)r} \quad (3)$$

$$H = \frac{h_{11}g_{22} + h_{22}g_{11}}{2g_{11}g_{22}} = \frac{Ar(\kappa \cos \psi + \tau \sin \psi) - A^2 - 2r^2 (\phi')^2}{2r(A^2 + r^2 (\phi')^2)}$$

**Theorem 3.** Let  $\Psi(s, \theta)$  be a tubular surface in  $E^3$  with constant radius  $r$ . Then:

- i. Provided that the  $s$ -parameter curves are asymptotic, the following relation becomes valid.

$$r = \frac{\left( \frac{\kappa - \tau}{\sqrt{2}} \right) (\kappa \cos \psi + \tau \sin \psi)}{(\kappa \cos \psi + \tau \sin \psi)^2 + \phi'^2} \quad (4)$$

- ii. The  $\theta$ -parameter curves cannot be asymptotic curves for any  $r > 0$ .

**Proof:**

- i. For asymptotic  $s$  curves, the condition  $h_{11} = 0$  must hold. From our exact calculations:

$$h_{11} = \left( \frac{\kappa - \tau}{\sqrt{2}} \right) (\kappa \cos \psi + \tau \sin \psi) - r \left( (\kappa \cos \psi + \tau \sin \psi)^2 + \phi'^2 \right) = 0$$

Hence the  $s$  – parameter curves are asymptotic precisely when Eq.(4) holds.

- ii. For  $\theta$  – curves the asymptotic condition requires  $h_{22} = 0$ . However, our exact computation shows:  $h_{22} = r > 0 \quad \forall r > 0$ . Thus, no asymptotic  $\theta$  – curves exist.

**Theorem 4.** Let  $\Psi(s, \theta)$  be a tubular surface in  $E^3$ . Then:

- i. The  $s$  – parameter curves are never geodesics in general.
- ii. The  $\theta$  -parameter curves are geodesics for any  $r > 0$ .

**Proof:**

- i. Let the second derivative and the unit normal vector be:

$$\Psi_{ss} = C_T \mathbf{T} + C_N \mathbf{N} + C_B \mathbf{B}, \quad \mathbf{U} = -\cos \psi \mathbf{T} + \sin \psi \mathbf{B} \text{ where,}$$

$$C_T = -\kappa A + r\phi'' \sin \psi + r(\phi')^2 \cos \psi$$

$$C_N = \frac{\kappa' - \tau'}{\sqrt{2}} - r\kappa' \cos \psi - r\tau' \sin \psi$$

$$C_B = \tau A - r\phi'' \cos \psi + r(\phi')^2 \sin \psi$$

Then the cross product becomes:

$$\Psi_{ss} \times \mathbf{U} = C_N \sin \psi \mathbf{T} - (C_T \sin \psi + C_B \cos \psi) \mathbf{N} - C_N \cos \psi \mathbf{B}$$

For the  $s$  – parameter curve to be geodesic:

$$\Psi_{ss} \times \mathbf{U} = \mathbf{0} \Rightarrow \text{Each component must vanish:}$$

$$C_N \sin \psi = 0,$$

$$C_T \sin \psi + C_B \cos \psi = 0,$$

$$C_N \cos \psi = 0 \Rightarrow C_N = 0, \quad C_T \sin \psi + C_B \cos \psi = 0$$

These conditions cannot generally be satisfied simultaneously for nontrivial  $\kappa(s)$  and  $\tau(s)$ , hence  $s$  – curves are not geodesics in general.

- ii. For  $\theta$  - parameter curve we have,  $\Psi_{\theta\theta} = -rU$  showing that the acceleration is normal to the surface. Therefore, every  $\theta$  - parameter curve is always geodesics.

**Theorem 5.** Let  $\Psi(s, \theta)$  be a tubular surface in  $E^3$  with constant radius  $r > 0$ , constructed along a space curve  $\beta(s)$  having curvature  $\kappa(s)$  and torsion  $\tau(s)$ . Provided that the parameter curves are lines of curvature, the surface satisfies the condition below.

$$\frac{\tau(s)}{\kappa(s)} = \text{constant} \quad - \quad \phi'(s) = 0,$$

where  $\phi(s) = \arctan \frac{\tau(s)}{\kappa(s)}$ .

**Proof:** For the tubular parametrization (with  $\psi = \phi + \theta$ ) the mixed coefficients are

$$\begin{aligned} g_{12} &= \langle \Psi_s, \Psi_\theta \rangle = r^2 \phi', \\ h_{12} &= -\langle \Psi_s, U_\theta \rangle = -r \phi'. \end{aligned}$$

The first and second fundamental forms become simultaneously diagonal, so that the coordinate curves align with the lines of curvature, precisely when  $\phi' = 0$ . But

$\phi' = \frac{d}{ds} \arctan \frac{\tau}{\kappa} = 0 \quad - \quad \frac{\tau}{\kappa} = \text{constant}$ , which means that the central curve  $\beta(s)$  is a general helix.

**Theorem 6.** Let  $\Psi(s, \theta)$  be a tubular surface in  $E^3$  with constant radius  $r > 0$ , constructed around a general helix whose curvature and torsion satisfy

$\frac{\tau}{\kappa} = c = \text{constant}$ . If the surface  $\Psi$  is minimal then,

$$r = \frac{\kappa - \tau}{2\sqrt{2(\kappa^2 + \tau^2)}} \sec \theta.$$

**Proof:** For a general helix,  $\frac{\tau}{\kappa} = c$  implies  $\phi'(s) = 0$ , and hence  $\psi = \phi + \theta$  is constant with respect to  $s$ .

The corrected coefficients of the fundamental forms reduce to

$$\begin{aligned} g_{11} &= A^2, & g_{22} &= r^2, \\ h_{11} &= A(\kappa \cos \psi + \tau \sin \psi), & h_{22} &= -r, \end{aligned}$$

where  $(A = \frac{\kappa - \tau}{\sqrt{2}} - r(\kappa \cos \psi + \tau \sin \psi))$ .

Then the mean curvature becomes

$$H = \frac{rB - A}{2rA}, \quad \text{where } B = \kappa \cos \psi + \tau \sin \psi. \quad \text{For minimality, } H = 0$$

gives  $rB = A$ . Substituting  $A = \frac{\kappa - \tau}{\sqrt{2}} - rB$  and solving for  $r$  yields

$$2rB = \frac{\kappa - \tau}{\sqrt{2}} \Rightarrow r = \frac{\kappa - \tau}{2\sqrt{2}B}.$$

Using  $B = \sqrt{\kappa^2 + \tau^2} \cos \theta$ , we obtain

$$r = \frac{\kappa - \tau}{2\sqrt{2(\kappa^2 + \tau^2)}} \sec \theta.$$

**Theorem 7.** Let  $\Psi(s, \theta)$  be a tubular surface in  $E^3$  with constant radius  $r > 0$ , constructed about a general helix whose curvature and torsion satisfy a given condition. Assume the parametrization is nondegenerate (in particular  $A \neq 0$ ). If the tubular surface  $\Psi$  is flat then,



$$B = 0 \quad - \quad \cos \theta = 0,$$

i.e. precisely for the angular parameters  $\theta = \frac{\pi}{2} + k\pi$ ,  $k \in \mathbb{Z}$ .

**Proof:** Under the helix assumption we have  $\phi'(s) = 0$ , hence the corrected fundamental form coefficients reduce to

$$\begin{aligned} g_{11} &= A^2, & g_{22} &= r^2, \\ h_{11} &= AB, & h_{22} &= -r, & h_{12} &= 0, \end{aligned}$$

with  $A = \frac{\kappa - \tau}{\sqrt{2}} - rB$  and  $B = \kappa \cos \psi + \tau \sin \psi$ . The Gaussian curvature is

$$K = \frac{h_{11}h_{22} - h_{12}^2}{g_{11}g_{22}} = \frac{(AB)(-r)}{A^2r^2} = -\frac{B}{rA}, \text{ provided } A \neq 0. \text{ Hence, under the}$$

nondegeneracy hypothesis  $A \neq 0$ , we have  $K = 0$  if and only if  $B = 0$ .

Finally, using the trigonometrical reduction

$$B = \kappa \cos \psi + \tau \sin \psi = \sqrt{\kappa^2 + \tau^2} \cos \theta,$$

the condition  $B = 0$  is equivalent to  $\cos \theta = 0$ , i.e.  $\theta = \frac{\pi}{2} + k\pi$ .

**Lemma 8.** Let  $\Psi(s, \theta)$  be a tubular surface in  $E^3$  with constant radius  $r > 0$ . The Gaussian and mean curvatures satisfy the identity

$$K = 2H - \frac{(r+1)A(\kappa \cos \psi + \tau \sin \psi) - A^2 - 2r^2(\psi')^2}{r(A^2 + r^2(\psi')^2)}.$$

**Proposition 9.** Let  $\Psi(s, \theta)$  be the tubular surface as above. If  $\psi' \equiv 0$  (equivalently the generating curve is a general helix) and  $A \neq 0$ , then  $\Psi$  is  $(K, H)$ -Weingarten surface.

**Proof:** With  $\psi' \equiv 0$  we have the simplified formulas

$$K = -\frac{B}{rA}, \quad H = \frac{rB - A}{2rA},$$

so  $K$  is an affine function of  $H$ :

$$K = -\frac{2}{r}H - \frac{1}{r^2}.$$

Hence  $(K = F(H))$  with  $(F'(H) = -2/r)$  and therefore  $(K_s = F'(H)H_s, K_\theta = F'(H)H_\theta)$ . This implies  $(H_s K_\theta - H_\theta K_s = 0)$ .

**Proposition 10.** Let  $\Psi(s, \theta)$  be the tubular surface as above. Then necessarily  $\psi' \equiv 0$  (the generating curve is a general helix). For a surface  $\Psi$  that is linear Weingarten, the associated relation is formulated as:

$$a = -r^2, \quad b = -2r,$$

must satisfy.

**Proof:** Taking Eq. (3) into account and setting  $\psi' \equiv 0$ , we find the following,

$$a\left(-\frac{B}{rA}\right) + b\left(\frac{rB - A}{2rA}\right) = 1,$$

$$-2Ba + rbB - bA = 2rA$$

and

$$B(rb - 2a) - A(2r + b) = 0.$$

Since  $A \neq 0, b = -2r$ ; therefore,  $a = -r^2$ .

**Example 11.** To exemplify the earlier analysis, consider a computational instance in which the center curve  $\alpha$  is given by:

$$\alpha(s) = \left( \cos\left(\frac{\sqrt{5}}{3}s\right), \sin\left(\frac{\sqrt{5}}{3}s\right), \frac{2s}{3} \right),$$

Following this, the Frenet frame of the curve is computed in the following manner:

$$\mathbf{T}(s) = \left( -\frac{\sqrt{5}}{3} \sin\left(\frac{\sqrt{5}}{3}s\right), \frac{\sqrt{5}}{3} \cos\left(\frac{\sqrt{5}}{3}s\right), \frac{2}{3} \right),$$

$$\mathbf{N}(s) = \left( -\cos\left(\frac{\sqrt{5}}{3}s\right), -\sin\left(\frac{\sqrt{5}}{3}s\right), 0 \right),$$

$$\mathbf{B}(s) = \left( \frac{2}{3} \sin\left(\frac{\sqrt{5}}{3}s\right), -\frac{2}{3} \cos\left(\frac{\sqrt{5}}{3}s\right), \frac{\sqrt{5}}{3} \right)$$

when the radius function  $r(s) = 1$ , we obtain the tubular surface:

$$\Psi_1(s, \theta) = \begin{pmatrix} \cos\left(\frac{\sqrt{5}}{3}s\right) - \cos\theta \cos\left(\frac{\sqrt{5}}{3}s\right) + \frac{2}{3} \sin\theta \sin\left(\frac{\sqrt{5}}{3}s\right), \\ \sin\left(\frac{\sqrt{5}}{3}s\right) - \cos\theta \sin\left(\frac{\sqrt{5}}{3}s\right) - \frac{2}{3} \sin\theta \cos\left(\frac{\sqrt{5}}{3}s\right), \\ \frac{2s}{3} + \frac{\sqrt{5}}{3} \sin\theta. \end{pmatrix}$$

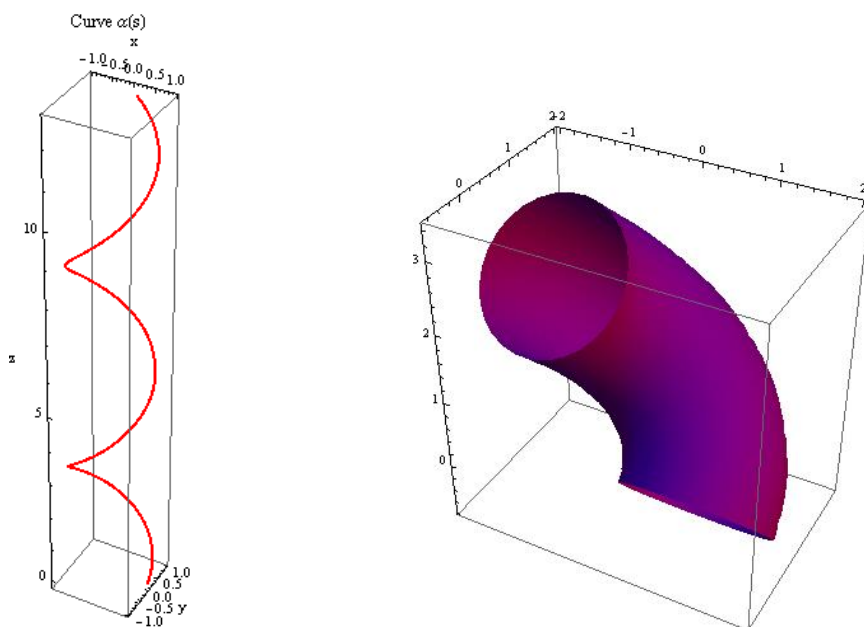


Figure 1: The curve  $\alpha(s)$  and its tube surface  $\Psi_1(s, \theta)$ ,

Now we obtain the **TB** – smarandache curve as follows.

$$\rho_{T+B}(s) = \left( \frac{-\sqrt{5}+2}{3\sqrt{2}} \sin\left(\frac{\sqrt{5}}{3}s\right), \frac{\sqrt{5}-2}{3\sqrt{2}} \cos\left(\frac{\sqrt{5}}{3}s\right), \frac{2+\sqrt{5}}{3\sqrt{2}} \right)$$

Let the center curve be taken as the curve  $(\rho_{T+B}(s))$ , defined by:

$$\rho_{T+B}(s) = \left( \frac{-\sqrt{5}+2}{3\sqrt{2}} \sin\left(\frac{\sqrt{5}}{3}s\right), \frac{\sqrt{5}-2}{3\sqrt{2}} \cos\left(\frac{\sqrt{5}}{3}s\right), \frac{2+\sqrt{5}}{3\sqrt{2}} \right)$$

Substituting the expressions of  $(\rho_{T+B}(s))$ ,  $(N(s))$ , and  $(B(s))$ , we obtain:

$$\Psi_2(s, \theta) = \begin{pmatrix} \frac{-\sqrt{5}+2}{3\sqrt{2}} \sin\left(\frac{\sqrt{5}}{3}s\right) - \cos\theta \cos\left(\frac{\sqrt{5}}{3}s\right) + \frac{2}{3} \sin\theta \sin\left(\frac{\sqrt{5}}{3}s\right) \\ \frac{\sqrt{5}-2}{3\sqrt{2}} \cos\left(\frac{\sqrt{5}}{3}s\right) - \cos\theta \sin\left(\frac{\sqrt{5}}{3}s\right) - \frac{2}{3} \sin\theta \cos\left(\frac{\sqrt{5}}{3}s\right) \\ \frac{2+\sqrt{5}}{3\sqrt{2}} + \frac{\sqrt{5}}{3} \sin\theta \end{pmatrix}$$

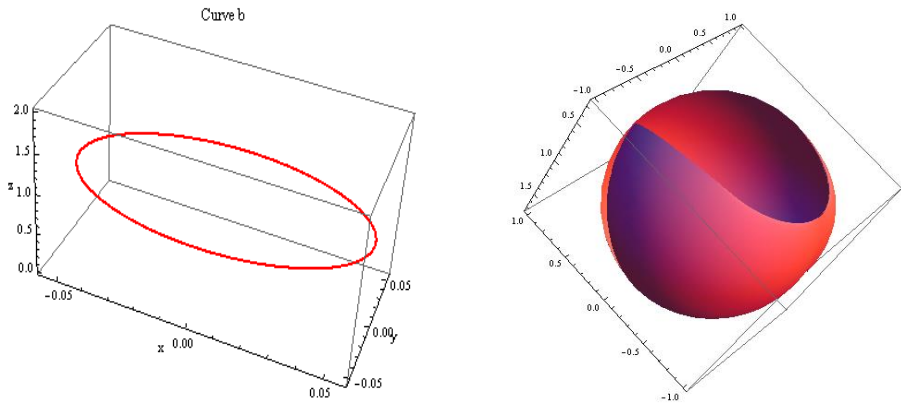


Figure 2: The curve  $\rho(s)$  and its tube surface  $\Psi_2(s, \theta)$ ,

This representation describes a tube surface constructed by translating a unit circle along the curve  $(\rho_{T+B}(s))$  with the normal and binormal vectors inherited from the original center curve  $(\alpha(s))$ .

## Conclusions

In the present study, we construct a novel tube surface by using the **TB** – Smarandache curve as the center curve in  $E^3$ . The geometric attributes of the surface were investigated via the Frenet–Serret frame, with explicit derivations provided for both the fundamental forms and the Gaussian and mean curvatures. The study identifies, from these results, the specific conditions under which the surface exhibits flatness or minimality.

Additionally, the asymptotic and geodesic curvatures, as well as the behavior of curvature lines, were analyzed to provide a deeper understanding of the surface geometry. The investigation of Weingarten and linear Weingarten conditions revealed further classifications and special cases within the surface family.

The example presented confirmed the theoretical findings and illustrated the geometric structure of the **TB** -Smarandache tube surface. The present results advance the understanding of Smarandache-type constructions and may act as a stepping stone for future work in differential geometry, including applications in geometric modeling and design.

## REFERENCE

- Ali, A. T. (2010). Special Smarandache curves in the Euclidean space. *International Journal of Mathematical Combinatorics*, 2(1), 30–36.
- Baek, B. S. (2025). Smarandache ruled surfaces according to the modified orthogonal frame. *Honam Mathematical Journal*, 47(3), 396–413.
- Bektaş, Ö., and Yüce, S. (2012). Special Smarandache curves according to Darboux frame in  $E^3$ . *arXiv preprint*, arXiv:1203.4830.
- Damar, E., Saltık Baek, B., Yüksel, N., and Oğraş, N. (2025). Tubular surfaces of adjoint curves according to the modified orthogonal frame. *Black Sea Journal of Engineering and Science*, 8(1), 206–213
- Fu, X., Jung, S. D., Qian, J., and Su, M. (2019). Geometric characterizations of canal surfaces in Minkowski 3-space I. *Bulletin of the Korean Mathematical Society*, 56(4), 867–883.

- Kim, Y. H., Liu, H., and Qian, J. (2016). Some characterizations of canal surfaces. *Bulletin of the Korean Mathematical Society*, 53(2), 461–477. <http://dx.doi.org/10.4134/BKMS.2016.53.2.461>
- Lopez, R. (2009). Linear Weingarten surfaces in Euclidean and hyperbolic space. *arXiv preprint* arXiv:0906.3302.
- Nurkan, S. K., Güven, İ. A., and Karacan, M. K. (2019). Characterizations of adjoint curves in Euclidean 3-space. *Proceedings of the National Academy of Sciences, India Section A: Physical Sciences*, 89(1), 155–161.
- O'Neill, B. (2006). *Elementary Differential Geometry*. Elsevier.
- Ouarab, S. (2021). Smarandache ruled surfaces according to Darboux frame in  $E^3$ . *Journal of Mathematics*, 2021(1), Article ID 9912624.
- Saad, M. K., Yüksel, N., Oğraş, N., Alghamdi, F., & Abdel-Salam, A. A. (2024). Geometry of tubular surfaces and their focal surfaces in Euclidean 3-space. *AIMS Mathematics*, 9(5), 12479–12493.
- Şenyurt, S., Ayvaci, K. H., and Canlı, D. (2023). Special Smarandache ruled surfaces according to FLC frame in  $E^3$ . *Applications and Applied Mathematics*, 18(1).
- Turgut, M., and Yılmaz, S. (2008). Smarandache curves in Minkowski space-time. *International Journal of Mathematical Combinatorics*, 3(1), 51–55.
- Yüksel, N., Tuncer, Y., and Karacan, M. K. (2011). Tabular surfaces with Bishop frame of Weingarten types in Euclidean 3-space. *Acta Universitatis Apulensis*, 27(1), 39–50.



# **Double fractional integral inequalities including for functions whose higher-order partial derivatives are elements of the $L_1$ space**

**Samet ERDEN<sup>1</sup>**

**Neslihan UYANIK<sup>2</sup>**

- 1- Assoc. Prof.; Department of Mathematics, Faculty of Science, Bartın University, Bartın, Türkiye.  
erdensmt@gmail.com ORCID No: 0000-0001-8430-7533
- 2- Assoc. Prof.; Department of Mathematics and Science Education, Faculty of Education, Anadolu University,  
Eskişehir, Türkiye. nuyanik@anadolu.edu.tr ORCID No: 0000-0003-1037-8843



## ABSTRACT

The primary aim of this study is to establish new inequalities involving the Riemann--Liouville fractional integrals for functions in two variables. Two identities concerning the Riemann--Liouville fractional integrals for higher-order partial derivatives of functions, which were established in previous studies, are presented here. In the following, new double integral inequalities are derived for functions whose higher-order partial derivatives belong to the  $L_1$  spaces. In addition to the main results, several special cases derived from the present findings are discussed, and their connections with previously established results are highlighted.

*Keywords* –The space of integrable functions, Fractional integrals, Ostrowski type inequalities. MSC 2020-26B30, 26A33, 26D15, 26D10

---

## INTRODUCTION

Over the past few decades, integral inequalities have evolved into indispensable analytical instruments within various domains of mathematical analysis, owing to their extensive applicability in numerical integration, approximation theory, and differential equations. Beyond furnishing accurate estimations, these inequalities offer profound insights into the structural behavior of functions under the operation of integration. Among the classical results in this field, the inequality formulated by A. M. Ostrowski has received particular attention for its effectiveness in assessing the deviation of a function from its integral mean.

**Theorem 1.** (Ostrowski, 1938) Assume that  $\psi: [a_1, \sigma_2] \rightarrow R$  is a differentiable mapping on  $(\sigma_1, \sigma_2)$  whose derivative  $\psi': (\sigma_1, \sigma_2) \rightarrow R$  is bounded on  $(\sigma_1, \sigma_2)$ , i.e.  $\|\psi'\|_\infty := \sup_{\tau \in (\sigma_1, \sigma_2)} |\psi'(\tau)| < \infty$ . Then, one has the integral inequality

$$\left| \psi(\zeta) - \frac{1}{\sigma_2 - \sigma_1} \int_{\sigma_1}^{\sigma_2} \psi(\tau) d\tau \right| \leq \left[ \frac{1}{4} + \frac{\left( \zeta - \frac{\sigma_1 + \sigma_2}{2} \right)^2}{(\sigma_2 - \sigma_1)^2} \right] (\sigma_2 - \sigma_1) \|\psi'\|_\infty,$$

for all  $\zeta \in [\sigma_1, \sigma_2]$ . The constant  $\frac{1}{4}$  is the best possible.

Due to its precision in estimating the deviation of a function from its integral mean, the Ostrowski inequality has become a focal point in both

classical and modern analysis. Its wide applicability has inspired numerous extensions and generalizations, particularly for functions defined on various functional spaces or exhibiting specific structural properties. For example, Dragomir and Wang established refined Ostrowski-type inequalities for functions whose first derivatives are integrable within various Lebesgue spaces in the references (Dragomir and Wang, 1997) and (Dragomir and Wang, 1998). An important extension to functions of two variables, together with applications in numerical analysis, was later provided by Barnett and Dragomir in (Barnett, 2001). Beyond these fundamental results, numerous studies devoted to Ostrowski-type inequalities have been published in the literature (for example, (Dragomir et al., 2003)).

In various branches of analysis and applied mathematics, there arise problems that require not only first- and second-order derivatives but also derivatives of arbitrary order. This naturally motivates the investigation of Ostrowski-type inequalities for functions possessing higher-order differentiability. As a result, considerable attention has been directed toward the development of such inequalities involving higher-order derivatives, owing to their relevance in both theoretical studies and practical applications. Driven by the motivation to generalize classical inequalities to wider classes of functions, the pioneering works of (Fink, 1992) and (Anastassiou, 1995) established fundamental Ostrowski-type inequalities for functions with bounded higher-order derivatives, forming the cornerstone for further studies in this area. Subsequent studies, such as (Cerone et al., 1999), expanded this framework through additional integral inequalities involving similar function classes. Continuing this progression, (Sofo, 2002) and (Wang and Zhao, 2009) derived generalized Ostrowski-type inequalities applicable to functions whose derivatives of arbitrary order are either bounded or  $L_p$ -integrable. The theoretical basis of this paper lies in the double integral inequalities derived for functions with higher-order partial derivatives, the key foundational works on which are documented in the cited references (Changjian and Cheung, 2010), (Hanna et al., 2002), (Erden et al., 2024) and (Ujevi, 2003).

The theory of Riemann-Liouville fractional integrals represents another key subject examined in this study, and it is therefore pertinent to recall the essential definitions related to this concept.

**Definition 1.** (Podlubni, 1999) Assume that  $\psi \in L_1[\sigma_1, \sigma_2]$  and  $\alpha > 0$ . The left-sided Riemann-Liouville fractional integral of order  $\alpha$  is defined by

$$I_{\sigma_1+}^{\alpha} \psi(\zeta) = \frac{1}{\Gamma(\alpha)} \int_{\sigma_1}^{\zeta} (\zeta - \tau)^{\alpha-1} \psi(\tau) d\tau, \quad \zeta > \sigma_1$$

while the right-sided Riemann-Liouville fractional integral is given by

$$I_{\sigma_2-}^{\alpha} \psi(\zeta) = \frac{1}{\Gamma(\alpha)} \int_{\zeta}^{\sigma_2} (\tau - \zeta)^{\alpha-1} \psi(\tau) d\tau, \quad \zeta < \sigma_2.$$

Here,  $\Gamma(\alpha)$  denotes the classical Euler gamma function. These operators reduce to the standard integral when  $\alpha = 1$ , and serve as the foundation for various fractional analogues of classical integral inequalities.

In addition, definitions of the Riemann-Liouville fractional integrals have been formulated for functions involving two independent variables, thereby providing a natural extension of the classical one-dimensional framework to a bivariate context.

**Definition 2.** (Sarikaya, 2014) Let  $\psi \in L_1([\sigma_1, \sigma_2] \times [\rho_1, \rho_2])$ . The Riemann-Liouville fractional integrals  $I_{\sigma_1+, \rho_1+}^{\alpha, \beta}$ ,  $I_{\sigma_1+, \rho_2-}^{\alpha, \beta}$ ,  $I_{\sigma_2-, \rho_1+}^{\alpha, \beta}$  and  $I_{\sigma_2-, \rho_2-}^{\alpha, \beta}$  are defined by

$$I_{\sigma_1+, \rho_1+}^{\alpha, \beta} \psi(\zeta, \vartheta) = \frac{1}{\Gamma(\alpha)\Gamma(\beta)} \int_{\sigma_1}^{\zeta} \int_{\rho_1}^{\vartheta} (\zeta - \tau)^{\alpha-1} (\vartheta - \varsigma)^{\beta-1} \psi(\tau, \varsigma) d\varsigma d\tau,$$

$$\zeta > \sigma_1, \quad \vartheta > \rho_1,$$

$$I_{\sigma_1+, d-}^{\alpha, \beta} \psi(\zeta, \vartheta) = \frac{1}{\Gamma(\alpha)\Gamma(\beta)} \int_{\sigma_1}^{\zeta} \int_{\vartheta}^{\rho_2} (\zeta - \tau)^{\alpha-1} (\varsigma - \vartheta)^{\beta-1} \psi(\tau, \varsigma) d\varsigma d\tau,$$

$$\zeta > \sigma_1, \quad \vartheta < d,$$

$$I_{\sigma_2-, \rho_1+}^{\alpha, \beta} \psi(\zeta, \vartheta) = \frac{1}{\Gamma(\alpha)\Gamma(\beta)} \int_{\zeta}^{\sigma_2} \int_{\rho_1}^{\vartheta} (\tau - \zeta)^{\alpha-1} (\vartheta - \varsigma)^{\beta-1} \psi(\tau, \varsigma) d\varsigma d\tau,$$

$$\zeta < \sigma_2, \quad \vartheta > \rho_1,$$

$$I_{\sigma_2-, d-}^{\alpha, \beta} \psi(\zeta, \vartheta) = \frac{1}{\Gamma(\alpha)\Gamma(\beta)} \int_{\zeta}^{\sigma_2} \int_{\vartheta}^{\rho_2} (\tau - \zeta)^{\alpha-1} (\varsigma - \vartheta)^{\beta-1} \psi(\tau, \varsigma) d\varsigma d\tau,$$

$$\zeta < \sigma_2, \quad \vartheta < d.$$

Here,  $\Gamma(\cdot)$  denotes the classical Euler gamma function.

Extensive research has been devoted to the Riemann-Liouville fractional integrals, emphasizing their fundamental role in fractional calculus. Comprehensive treatments of this topic are provided in the monographs by (Gorenflo and Mainardi, 1997) and (Podlubni, 1999). In addition, one of the earliest contributions to Hermite-Hadamard type inequalities involving Riemann-Liouville fractional integrals was introduced by Sarikaya et al. in (Sarikaya et al., 2013). Furthermore, Sarikaya (Sarikaya, 2014) extended this line of research by establishing Hermite-Hadamard type inequalities for fractional integrals defined on functions of two variables, particularly within the framework of coordinated convexity. Some fundamental studies on Ostrowski-type inequalities involving Riemann-Liouville fractional integrals for functions with one independent variable are provided in references (Aglic Aljinovic, 2014), (Dragomir, 2017a), (Dragomir, 2017b), (Lakoud and Aissaoui, 2013), (Qayyum et al., 2019), and (Sarikaya et al., 2015). As this paper mainly deals with functions of two variables, it is important to note the inequalities involving their Riemann-Liouville fractional integrals. In this context, Latif and Hussain (2012) developed fractional integral inequalities of Ostrowski type for functions with two independent variables. Some notable works that provide Ostrowski-type results including double fractional integrals for various classes of functions of two variables are listed in the references (Erden et al., 2024), (Erden et al., 2020a), (Erden et al., 2020b), and (Sarikaya, 2023).

This section is devoted to the analysis of recent fractional integral inequalities that can be derived for functions with higher-order partial derivatives, in the light of the aforementioned studies. In the second section, two previously established double integral identities involving the Riemann-Liouville fractional integrals of functions with higher-order partial derivatives are presented. In the final section, new double integral inequalities are obtained for functions whose higher-order partial derivatives are assumed to belong to the space of integrable functions.

## **SOME IDENTITIES FOR DOUBLE INTEGRALS**

This section provides the fundamental identities essential for deriving the main results. As the integrals involving higher-order partial derivatives

are often difficult to compute and express explicitly, certain notations are introduced to clarify and simplify the forthcoming identities.

$$I_1(\psi; \zeta, \vartheta) = J_{\sigma_1+, \rho_1+}^{\alpha, \beta} \psi(\zeta, \vartheta) + (-1)^m J_{\sigma_1+, \rho_2-}^{\alpha, \beta} \psi(\zeta, \vartheta) \\ + (-1)^n J_{\sigma_2-, \rho_1+}^{\alpha, \beta} \psi(\zeta, \vartheta) + (-1)^{n+m} J_{\sigma_2-, \rho_2-}^{\alpha, \beta} \psi(\zeta, \vartheta), \quad (1)$$

$$\Phi_1(\psi; \zeta, \vartheta; n, m) \quad (2)$$

$$= \sum_{k=0}^{n-1} \sum_{j=0}^{m-1} \frac{(\zeta - \sigma_1)^{\alpha+k} \left[ (\vartheta - \rho_1)^{\beta+j} \frac{\partial^{k+j} \psi(\sigma_1, \rho_1)}{\partial \tau^k \partial \varsigma^j} \right. \\ \left. + (-1)^{m+j} (\rho_2 - \vartheta)^{\beta+j} \frac{\partial^{k+j} \psi(\sigma_1, \rho_2)}{\partial \tau^k \partial \varsigma^j} \right]}{\Gamma(\alpha + k + 1) \Gamma(\beta + j + 1)} \\ + \sum_{k=0}^{n-1} \sum_{j=0}^{m-1} \frac{(-1)^{n+k} (\sigma_2 - \zeta)^{\alpha+k} \left[ (\vartheta - \rho_1)^{\beta+j} \frac{\partial^{k+j} \psi(\sigma_2, \rho_1)}{\partial \tau^k \partial \varsigma^j} \right. \\ \left. + (-1)^{m+j} (\rho_2 - \vartheta)^{\beta+j} \frac{\partial^{k+j} \psi(\sigma_2, \rho_2)}{\partial \tau^k \partial \varsigma^j} \right]}{\Gamma(\alpha + k + 1) \Gamma(\beta + j + 1)}$$

$$\Phi_2(\psi; \zeta, \vartheta; n, m) \quad (3)$$

$$= \sum_{k=0}^{n-1} \frac{(\zeta - \sigma_1)^{\alpha+k}}{\Gamma(\alpha + k + 1)} \left[ J_{\rho_1+}^{\beta} \frac{\partial^k \psi(\sigma_1, \vartheta)}{\partial \tau^k} + (-1)^m J_{d-}^{\beta} \frac{\partial^k \psi(\sigma_1, \vartheta)}{\partial \tau^k} \right] \\ + \sum_{k=0}^{n-1} \frac{(-1)^{n+k} (\sigma_2 - \zeta)^{\alpha+k}}{\Gamma(\alpha + k + 1)} \left[ J_{\rho_1+}^{\beta} \frac{\partial^k \psi(\sigma_2, \vartheta)}{\partial \tau^k} + (-1)^m J_{d-}^{\beta} \frac{\partial^k \psi(\sigma_2, \vartheta)}{\partial \tau^k} \right] \\ + \sum_{j=0}^{m-1} \frac{(\vartheta - \rho_1)^{\beta+j}}{\Gamma(\beta + j + 1)} \left[ J_{\sigma_1+}^{\alpha} \frac{\partial^j \psi(\zeta, \rho_1)}{\partial \varsigma^j} + (-1)^n J_{\sigma_2-}^{\alpha} \frac{\partial^j \psi(\zeta, \rho_1)}{\partial \varsigma^j} \right] \\ + \sum_{j=0}^{m-1} \frac{(-1)^{m+j} (d - \vartheta)^{\beta+j}}{\Gamma(\beta + j + 1)} \left[ J_{\sigma_1+}^{\alpha} \frac{\partial^j \psi(\zeta, d)}{\partial \varsigma^j} + (-1)^n J_{\sigma_2-}^{\alpha} \frac{\partial^j \psi(\zeta, d)}{\partial \varsigma^j} \right],$$

$$\Phi_3(\psi; \zeta, \vartheta; n, m) \quad (4)$$

$$\begin{aligned}
&= \left( \frac{(\vartheta - \rho_1)^{m+\beta} + (d - \vartheta)^{m+\beta}}{\Gamma(m + \beta + 1)} \right) \\
&\times \sum_{k=0}^{n-1} \frac{(\zeta - \sigma_1)^{\alpha+k} \frac{\partial^{k+m} \psi(\sigma_1, \vartheta)}{\partial \tau^k \partial \vartheta^m} + (-1)^{n+k} (\sigma_2 - \zeta)^{\alpha+k} \frac{\partial^{k+m} \psi(\sigma_2, \vartheta)}{\partial \tau^k \partial \vartheta^m}}{\Gamma(\alpha + k + 1)} \\
&+ \left( \frac{(\zeta - \sigma_1)^{n+\alpha} + (\sigma_2 - \zeta)^{n+\alpha}}{\Gamma(n + \alpha + 1)} \right) \\
&\times \sum_{j=0}^{m-1} \frac{(\vartheta - \rho_1)^{\beta+j} \frac{\partial^{n+j} \psi(\zeta, \rho_1)}{\partial \zeta^n \partial \zeta^j} + (-1)^{m+j} (\rho_2 - \vartheta)^{\beta+j} \frac{\partial^{n+j} \psi(\zeta, d)}{\partial \zeta^n \partial \zeta^j}}{\Gamma(m + \beta + 1)},
\end{aligned}$$

$$F_1(\psi; \zeta, \vartheta; n, m) = \left( \frac{(\vartheta - \rho_1)^{m+\beta} + (\rho_2 - \vartheta)^{m+\beta}}{\Gamma(m + \beta + 1)} \right) \quad (5)$$

$$\begin{aligned}
&\times \left[ J_{\sigma_1+}^{\alpha} \frac{\partial^m \psi(\zeta, \vartheta)}{\partial \vartheta^m} + (-1)^n J_{\sigma_2-}^{\alpha} \frac{\partial^m \psi(\zeta, \vartheta)}{\partial \vartheta^m} \right] \\
&+ \left( \frac{(\zeta - \sigma_1)^{n+\alpha} + (\sigma_2 - \zeta)^{n+\alpha}}{\Gamma(n + \alpha + 1)} \right) \left[ J_{\rho_1+}^{\beta} \frac{\partial^n \psi(\zeta, \vartheta)}{\partial \zeta^n} + (-1)^m J_{\rho_2-}^{\beta} \frac{\partial^n \psi(\zeta, \vartheta)}{\partial \zeta^n} \right],
\end{aligned}$$

$$F_2(\psi; \zeta, \vartheta; n, m) \quad (6)$$

$$= \frac{[(\zeta - \sigma_1)^{n+\alpha} + (\sigma_2 - \zeta)^{n+\alpha}][(\vartheta - \rho_1)^{m+\beta} + (\rho_2 - \vartheta)^{m+\beta}]}{\Gamma(n + \alpha + 1)\Gamma(m + \beta + 1)} \frac{\partial^{n+m} \psi(\zeta, \vartheta)}{\partial \zeta^n \partial \vartheta^m},$$

$$F_3(\psi; \zeta, \vartheta; n, m) = \left( \frac{(\zeta - \sigma_1)^{n+\alpha} + (\sigma_2 - \zeta)^{n+\alpha}}{\Gamma(n + \alpha + 1)} \right) \quad (7)$$

$$\begin{aligned}
&\times \left[ (-1)^m J_{\vartheta-}^{\beta} \frac{\partial^n \psi(\zeta, \rho_1)}{\partial \zeta^n} + J_{\vartheta+}^{\beta} \frac{\partial^n \psi(\zeta, \vartheta \rho_2)}{\partial \zeta^n} \right] \\
&+ \left( \frac{(\vartheta - \rho_1)^{m+\beta} + (\rho_2 - \vartheta)^{m+\beta}}{\Gamma(m + \beta + 1)} \right) \\
&\times \left[ (-1)^n J_{\zeta-}^{\alpha} \frac{\partial^m \psi(\sigma_1, \vartheta)}{\partial \vartheta^m} + J_{\zeta+}^{\alpha} \frac{\partial^m \psi(\sigma_2, \vartheta)}{\partial \vartheta^m} \right],
\end{aligned}$$

$$I_2(\psi; \zeta, \vartheta) = (-1)^{n+m} J_{\zeta-, \vartheta-}^{\alpha, \beta} \psi(\sigma_1, \rho_1) + (-1)^n J_{\zeta-, \vartheta+}^{\alpha, \beta} \psi(\sigma_1, \rho_2) \quad (8)$$

$$+(-1)^m J_{\zeta+, \vartheta-}^{\alpha, \beta} \psi(\sigma_2, \rho_1) + J_{\zeta+, \vartheta+}^{\alpha, \beta} \psi(\sigma_2, \rho_2),$$

$$\begin{aligned} & \Phi_4(\psi; \zeta, \vartheta; n, m) \\ &= \sum_{k=0}^{n-1} \sum_{j=0}^{m-1} \frac{[(-1)^{n+k}(\zeta - \sigma_1)^{\alpha+k} + (\sigma_2 - \zeta)^{\alpha+k}]}{\Gamma(\alpha + k + 1)} \\ & \times \frac{[(-1)^{m+j}(\vartheta - \rho_1)^{\beta+j} + (\rho_2 - \vartheta)^{\beta+j}]}{\Gamma(\beta + j + 1)} \frac{\partial^{k+j} \psi(\zeta, \vartheta)}{\partial \zeta^k \partial \vartheta^j} \\ & - \sum_{k=0}^{n-1} \frac{(-1)^{n+k}(\zeta - \sigma_1)^{\alpha+k} + (\sigma_2 - \zeta)^{\alpha+k}}{\Gamma(\alpha + k + 1)} \\ & \times \left[ (-1)^m J_{\vartheta-}^{\beta} \frac{\partial^k \psi(\zeta, \rho_1)}{\partial \zeta^k} + J_{\vartheta+}^{\beta} \frac{\partial^k \psi(\zeta, \rho_2)}{\partial \zeta^k} \right] \\ & - \sum_{j=0}^{m-1} \frac{(-1)^{m+j}(\vartheta - \rho_1)^{\beta+j} + (\rho_2 - \vartheta)^{\beta+j}}{\Gamma(\beta + j + 1)} \\ & \times \left[ (-1)^n J_{\zeta-}^{\alpha} \frac{\partial^j \psi(\sigma_1, \vartheta)}{\partial \vartheta^j} + J_{\zeta+}^{\alpha} \frac{\partial^j \psi(\sigma_2, \vartheta)}{\partial \vartheta^j} \right], \end{aligned} \tag{9}$$

$$\begin{aligned} & \Phi_5(\psi; \zeta, \vartheta; n, m) = \frac{(\zeta - \sigma_1)^{n+\alpha} + (\sigma_2 - \zeta)^{n+\alpha}}{\Gamma(n + \alpha + 1)} \\ & \times \sum_{j=0}^{m-1} \frac{[(-1)^{m+j}(\vartheta - \rho_1)^{\beta+j} + (\rho_2 - \vartheta)^{\beta+j}]}{\Gamma(\beta + j + 1)} \frac{\partial^{n+j} \psi(\zeta, \vartheta)}{\partial \zeta^n \partial \vartheta^j} \\ & + \frac{(\vartheta - \rho_1)^{m+\beta} + (\rho_2 - \vartheta)^{m+\beta}}{\Gamma(m + \beta + 1)} \\ & \times \sum_{k=0}^{n-1} \frac{[(-1)^{n+k}(\zeta - \sigma_1)^{\alpha+k} + (\sigma_2 - \zeta)^{\alpha+k}]}{\Gamma(\alpha + k + 1)} \frac{\partial^{k+m} \psi(\zeta, \vartheta)}{\partial \zeta^k \partial \vartheta^m}, \end{aligned} \tag{10}$$

By applying integration by parts and elementary analytical techniques, the identities involving Riemann-Liouville fractional integrals of functions of two variables, whose higher-order partial derivatives are continuous, were previously obtained by Erden and Uyanık (2025) and are recalled here for

reference. The identities that play a crucial role in obtaining our main results are stated in the following lemmas.

**Lemma 1.** (Erden and Uyanik, 2025) Assume that  $\psi: [\sigma_1, \sigma_2] \times [\rho_1, \rho_2] =: \Delta \subset R^2 \rightarrow R$  is an absolutely continuous mapping such that the partial derivatives  $\frac{\partial^{k+j}\psi(\tau, \varsigma)}{\partial \tau^k \partial \varsigma^j}$  exists and are continuous on  $\Delta$  for  $k = 0, 1, 2, \dots, n$ ,  $j = 0, 1, 2, \dots, m$  with  $n, m \in N^+$ . Then, for any  $(\zeta, \vartheta) \in \Delta$ , one possesses

$$\begin{aligned} & \frac{1}{\Gamma(n+\alpha)\Gamma(m+\beta)} \\ & \times \int_{\sigma_1}^{\sigma_2} \int_{\rho_1}^{\rho_2} Q(\zeta, \tau, \vartheta, \varsigma) \left( \int_{\zeta}^{\tau} \int_{\vartheta}^{\varsigma} \frac{\partial^{n+m+2}\psi(u, v)}{\partial u^{n+1} \partial v^{m+1}} dv du \right) d\varsigma d\tau \\ & = J_1(\psi; \zeta, \vartheta) + \Phi_1(\psi; \zeta, \vartheta; n, m) - \Phi_2(\psi; \zeta, \vartheta; n, m) \\ & + \Phi_3(\psi; \zeta, \vartheta; n, m) - F_1(\psi; \zeta, \vartheta; n, m) + F_2(\psi; \zeta, \vartheta; n, m) \end{aligned} \quad (11)$$

where  $Q(\zeta, \tau, \vartheta, \varsigma)$  are defined by

$$\begin{aligned} & Q(\zeta, \tau, \vartheta, \varsigma) \\ & := \begin{cases} (\zeta - \tau)^{n+\alpha-1}(\vartheta - \varsigma)^{m+\beta-1}, & \sigma_1 \leq \tau < \zeta \text{ and } \rho_1 \leq \varsigma < \vartheta \\ (\zeta - \tau)^{n+\alpha-1}(\varsigma - \vartheta)^{m+\beta-1}, & \sigma_1 \leq \tau < \zeta \text{ and } \vartheta \leq \varsigma \leq \rho_2 \\ (\tau - \zeta)^{n+\alpha-1}(\vartheta - \varsigma)^{m+\beta-1}, & \zeta \leq \tau \leq \sigma_2 \text{ and } \rho_1 \leq \varsigma < \vartheta \\ (\tau - \zeta)^{n+\alpha-1}(\varsigma - \vartheta)^{m+\beta-1}, & \zeta \leq \tau \leq \sigma_2 \text{ and } \vartheta \leq \varsigma \leq \rho_2. \end{cases} \end{aligned}$$

Here, the expressions  $J_1(\psi; \zeta, \vartheta)$ ,  $\Phi_1(\psi; \zeta, \vartheta; n, m)$ ,  $\Phi_2(\psi; \zeta, \vartheta; n, m)$ ,  $\Phi_3(\psi; \zeta, \vartheta; n, m)$ ,  $F_1(\psi; \zeta, \vartheta; n, m)$  and  $F_2(\psi; \zeta, \vartheta; n, m)$  are also as given in (1)-(6), respectively.

**Lemma 2.** (Erden and Uyanik, 2025) Assume that  $\psi: [\sigma_1, \sigma_2] \times [\rho_1, \rho_2] =: \Delta \subset R^2 \rightarrow R$  is an absolutely continuous mapping such that the partial derivatives  $\frac{\partial^{k+j}\psi(\tau, \varsigma)}{\partial \tau^k \partial \varsigma^j}$  exists and are continuous on  $\Delta$  for  $k = 0, 1, 2, \dots, n$ ,  $j = 0, 1, 2, \dots, m$  with  $n, m \in N^+$ . Then, for any  $(\zeta, \vartheta) \in \Delta$ , one possesses



$$\begin{aligned}
& \frac{1}{\Gamma(n+\alpha)\Gamma(m+\beta)} \\
& \times \int_{\sigma_1}^{\sigma_2} \int_{\rho_1}^{\rho_2} \Omega(\tau, \varsigma) \left( \int_{\zeta}^{\tau} \int_{\vartheta}^{\varsigma} \frac{\partial^{n+m+2} \psi(u, v)}{\partial u^{n+1} \partial v^{m+1}} dv du \right) d\varsigma d\tau \\
& = J_2(\psi; \zeta, \vartheta) + \Phi_4(\psi; \zeta, \vartheta; n, m) + \Phi_5(\psi; \zeta, \vartheta; n, m)
\end{aligned} \tag{12}$$

where  $\Omega(\tau, \varsigma)$  is defined by

$$\begin{aligned}
& \Omega(\tau, \varsigma) \\
& := \begin{cases} (\tau - \sigma_1)^{n+\alpha-1} (\varsigma - \rho_1)^{m+\beta-1}, & \sigma_1 \leq \tau < \zeta \text{ and } \rho_1 \leq \varsigma < \vartheta \\ (\tau - \sigma_1)^{n+\alpha-1} (\rho_2 - \varsigma)^{m+\beta-1}, & \sigma_1 \leq \tau < \zeta \text{ and } \vartheta \leq \varsigma \leq \rho_2 \\ (\sigma_2 - \tau)^{n+\alpha-1} (\varsigma - \rho_1)^{m+\beta-1}, & \zeta \leq \tau \leq \sigma_2 \text{ and } \rho_1 \leq \varsigma < \vartheta \\ (\sigma_2 - \tau)^{n+\alpha-1} (\rho_2 - \varsigma)^{m+\beta-1}, & \zeta \leq \tau \leq \sigma_2 \text{ and } \vartheta \leq \varsigma \leq \rho_2, \end{cases}
\end{aligned}$$

and the expressions  $F_2(\psi; \zeta, \vartheta; n, m)$ ,  $F_3(\psi; \zeta, \vartheta; n, m)$ ,  $J_2(\psi; \zeta, \vartheta)$ ,  $\Phi_4(\psi; \zeta, \vartheta; n, m)$  and  $\Phi_5(\psi; \zeta, \vartheta; n, m)$  are defined as in (6)-(10), respectively.

## DOUBLE INTEGRAL INEQUALITIES FOR $L_1$ - NORM

This section presents several results involving fractional integrals for functions whose higher-order derivatives belong to the  $L_1$  -norm space.

**Theorem 2.** Suppose that all the assumptions of Lemma 1 hold. If the partial derivative of order  $n + m + 2$  of  $\psi$  exists and is element of  $L_1[\Delta]$ , i.e.,

$$\|\psi^{(n+m+2)}\|_1 = \int_{\sigma_1}^{\sigma_2} \int_{\rho_1}^{\rho_2} \left| \frac{\partial^{n+m+2} \psi(u, v)}{\partial u^{n+1} \partial v^{m+1}} \right| dv du < \infty$$

then, for any  $(\zeta, \vartheta) \in \Delta$ , one has the inequalities

$$|J_1(\psi; \zeta, \vartheta) + \Phi_1(\psi; \zeta, \vartheta; n, m) - \Phi_2(\psi; \zeta, \vartheta; n, m)| \tag{13}$$

$$\begin{aligned}
& +\Phi_3(\psi; \zeta, \vartheta; n, m) - F_1(\psi; \zeta, \vartheta; n, m) + F_2(\psi; \zeta, \vartheta; n, m)| \\
& \leq \frac{[(\zeta - \sigma_1)^{n+\alpha} + (\sigma_2 - \zeta)^{n+\alpha}][(\vartheta - \rho_1)^{m+\beta} + (\rho_2 - \vartheta)^{m+\beta}]}{\Gamma(n + \alpha + 1)\Gamma(m + \beta + 1)} \|\psi^{(n+m+2)}\|_1
\end{aligned}$$

where the expressions  $J_1(\psi; \zeta, \vartheta)$ ,  $\Phi_1(\psi; \zeta, \vartheta; n, m)$ ,  $\Phi_2(\psi; \zeta, \vartheta; n, m)$ ,  $\Phi_3(\psi; \zeta, \vartheta; n, m)$ ,  $F_1(\psi; \zeta, \vartheta; n, m)$  and  $F_2(\psi; \zeta, \vartheta; n, m)$  are also as given in (1)-(6), respectively.

**Proof.** Taking the absolute value of both sides of the identity (11), due to the condition of the function  $\frac{\partial^{n+m+2}\psi(u,v)}{\partial u^{n+1}\partial v^{m+1}}$ , it follows that

$$\begin{aligned}
& |J_1(\psi; \zeta, \vartheta) + \Phi_1(\psi; \zeta, \vartheta; n, m) - \Phi_2(\psi; \zeta, \vartheta; n, m) \\
& + \Phi_3(\psi; \zeta, \vartheta; n, m) - F_1(\psi; \zeta, \vartheta; n, m) + F_2(\psi; \zeta, \vartheta; n, m)| \\
& \leq \frac{1}{\Gamma(n + \alpha)\Gamma(m + \beta)} \\
& \times \int_{\sigma_1}^{\sigma_2} \int_{\rho_1}^{\rho_2} |Q(\zeta, \tau, \vartheta, \varsigma)| \left| \int_{\zeta}^{\tau} \int_{\vartheta}^{\varsigma} \frac{\partial^{n+m+2}\psi(u, v)}{\partial u^{n+1}\partial v^{m+1}} dv du \right| d\varsigma d\tau \\
& \leq \frac{\|\psi^{(n+m+2)}\|_{[\sigma_1, \sigma_2] \times [\rho_1, \rho_2], 1}}{\Gamma(n + \alpha)\Gamma(m + \beta)} \int_{\sigma_1}^{\sigma_2} \int_{\rho_1}^{\rho_2} |Q(\zeta, \tau, \vartheta, \varsigma)| d\varsigma d\tau.
\end{aligned}$$

If the definition of  $Q(\zeta, \tau, \vartheta, \varsigma)$  is used to calculate the integral on the right-hand side of the above expression, it is easy to see that

$$\begin{aligned}
& \int_{\sigma_1}^{\sigma_2} \int_{\rho_1}^{\rho_2} |Q(\zeta, \tau, \vartheta, \varsigma)| d\varsigma d\tau \\
& = \int_{\sigma_1}^{\zeta} \int_{\rho_1}^{\vartheta} (\zeta - \tau)^{n+\alpha-1} (\vartheta - \varsigma)^{m+\beta-1} d\varsigma d\tau \\
& + \int_{\sigma_1}^{\zeta} \int_{\vartheta}^{\rho_2} (\zeta - \tau)^{n+\alpha-1} (\varsigma - \vartheta)^{m+\beta-1} d\varsigma d\tau \\
& + \int_{\zeta}^{\sigma_2} \int_{\rho_1}^{\vartheta} (\tau - \zeta)^{n+\alpha-1} (\vartheta - \varsigma)^{m+\beta-1} d\varsigma d\tau
\end{aligned}$$

$$+ \int_{\zeta}^{\sigma_2} \int_{\vartheta}^{\rho_2} (\tau - \zeta)^{n+\alpha-1} (\varsigma - \vartheta)^{m+\beta-1} d\varsigma d\tau.$$

We can now proceed to compute the four integrals presented above. It is celar that

$$\int_{\sigma_1}^{\zeta} \int_{\rho_1}^{\vartheta} (\zeta - \tau)^{n+\alpha-1} (\vartheta - \varsigma)^{m+\beta-1} d\varsigma d\tau = \frac{(\zeta - \sigma_1)^{n+\alpha} (\vartheta - \rho_1)^{m+\beta}}{(n + \alpha)(m + \beta)},$$

$$\int_{\sigma_1}^{\zeta} \int_{\vartheta}^{\rho_2} (\zeta - \tau)^{n+\alpha-1} (\varsigma - \vartheta)^{m+\beta-1} d\varsigma d\tau = \frac{(\zeta - \sigma_1)^{n+\alpha} (\rho_2 - \vartheta)^{m+\beta}}{(n + \alpha)(m + \beta)},$$

$$\int_{\zeta}^{\sigma_2} \int_{\rho_1}^{\vartheta} (\tau - \zeta)^{n+\alpha-1} (\vartheta - \varsigma)^{m+\beta-1} d\varsigma d\tau = \frac{(\sigma_2 - \zeta)^{n+\alpha} (\vartheta - \rho_1)^{m+\beta}}{(n + \alpha)(m + \beta)}$$

and

$$\int_{\zeta}^{\sigma_2} \int_{\vartheta}^{\rho_2} (\tau - \zeta)^{n+\alpha-1} (\varsigma - \vartheta)^{m+\beta-1} d\varsigma d\tau = \frac{(\sigma_2 - \zeta)^{n+\alpha} (\rho_2 - \vartheta)^{m+\beta}}{(n + \alpha)(m + \beta)}.$$

So, we can write the expression

$$\begin{aligned} & \frac{\|\psi^{(n+m+2)}\|_{[\sigma_1, \sigma_2] \times [\rho_1, \rho_2], 1}}{\Gamma(n + \alpha)\Gamma(m + \beta)} \int_{\sigma_1}^{\sigma_2} \int_{\rho_1}^{\rho_2} |Q(\zeta, \tau, \vartheta, \varsigma)| d\varsigma d\tau \\ &= \frac{[(\zeta - \sigma_1)^{n+\alpha} + (\sigma_2 - \zeta)^{n+\alpha}][(\vartheta - \rho_1)^{m+\beta} + (\rho_2 - \vartheta)^{m+\beta}]}{\Gamma(n + \alpha + 1)\Gamma(m + \beta + 1)} \|\psi^{(n+m+2)}\|_1. \end{aligned}$$

This completes the proof and establishes the desired inequality (13).

**Remark 1.** With  $n = m = 0$  and the same assumption of Teorem t3, the sum symbols disappear and 0 is substituted insted of  $n$  and  $m$  in the remaining expressions, one possesses the inequalities

$$\begin{aligned} & |J_{\sigma_1+, \rho_1+}^{\alpha, \beta} \psi(\zeta, \vartheta) + J_{\sigma_1+, \rho_2-}^{\alpha, \beta} \psi(\zeta, \vartheta) + J_{\sigma_2-, \rho_1+}^{\alpha, \beta} \psi(\zeta, \vartheta) + J_{\sigma_2-, \rho_2-}^{\alpha, \beta} \psi(\zeta, \vartheta) \\ & - \frac{(\vartheta - \rho_1)^\beta + (\rho_2 - \vartheta)^\beta}{\Gamma(\beta + 1)} [J_{\sigma_1+}^\alpha \psi(\zeta, \vartheta) + J_{\sigma_2-}^\alpha \psi(\zeta, \vartheta)] \end{aligned}$$

$$\begin{aligned}
& - \frac{(\zeta - \sigma_1)^\alpha + (\sigma_2 - \zeta)^\alpha}{\Gamma(\alpha + 1)} \left[ J_{\rho_1+}^\beta \psi(\zeta, \vartheta) + J_{\rho_2-}^\beta \psi(\zeta, \vartheta) \right] \\
& + \frac{[(\sigma_2 - \zeta)^\alpha + (\zeta - \sigma_1)^\alpha][(\rho_2 - \vartheta)^\beta + (\vartheta - \rho_1)^\beta]}{\Gamma(\alpha + 1)\Gamma(\beta + 1)} \psi(\zeta, \vartheta) \Big| \\
& \leq \frac{[(\zeta - \sigma_1)^\alpha + (\sigma_2 - \zeta)^\alpha][(\vartheta - \rho_1)^\beta + (\rho_2 - \vartheta)^\beta]}{\Gamma(\alpha + 1)\Gamma(\beta + 1)} \|\psi_{uv}^{(2)}\|_1
\end{aligned}$$

which was proved Erden et al. in the reference (Erden et al., 2020b).

In the following theorem, we investigate a new fractional inequality derived from the application of the second identity (12).

**Theorem 3.** Suppose that all the assumptions of Lemma 2 hold. If the partial derivative of order  $n + m + 2$  of  $\psi$  exists and is element of  $L_1[\Delta]$ , i.e.,

$$\|\psi^{(n+m+2)}\|_1 = \int_{\sigma_1}^{\sigma_2} \int_{\rho_1}^{\rho_2} \left| \frac{\partial^{n+m+2} \psi(u, v)}{\partial u^{n+1} \partial v^{m+1}} \right| dv du < \infty$$

then, for any  $(\zeta, \vartheta) \in \Delta$ , one has the inequalities

$$\begin{aligned}
& |J_2(\psi; \zeta, \vartheta) + \Phi_4(\psi; \zeta, \vartheta; n, m) + \Phi_5(\psi; \zeta, \vartheta; n, m) \\
& - F_3(\psi; \zeta, \vartheta; n, m) + F_2(\psi; \zeta, \vartheta; n, m)| \\
& \leq \frac{[(\zeta - \sigma_1)^{n+\alpha} + (\sigma_2 - \zeta)^{n+\alpha}][(\vartheta - \rho_1)^{m+\beta} + (\rho_2 - \vartheta)^{m+\beta}]}{\Gamma(n + \alpha + 1)\Gamma(m + \beta + 1)} \|\psi^{(n+m+2)}\|_1
\end{aligned} \tag{14}$$

where the expressions  $F_2(\psi; \zeta, \vartheta; n, m)$ ,  $F_3(\psi; \zeta, \vartheta; n, m)$ ,  $J_2(\psi; \zeta, \vartheta)$ ,  $\Phi_4(\psi; \zeta, \vartheta; n, m)$  and  $\Phi_5(\psi; \zeta, \vartheta; n, m)$  are defined as in (6)-(10), respectively.

**Proof.** Taking modulus both sides of the identity (12), owing to the condition of the function  $\frac{\partial^{n+m+2} \psi(u, v)}{\partial u^{n+1} \partial v^{m+1}}$ , it is found that

$$\begin{aligned}
& |J_2(\psi; \zeta, \vartheta) + \Phi_4(\psi; \zeta, \vartheta; n, m) + \Phi_5(\psi; \zeta, \vartheta; n, m) \\
& - F_3(\psi; \zeta, \vartheta; n, m) + F_2(\psi; \zeta, \vartheta; n, m)|
\end{aligned}$$

$$\leq \frac{1}{\Gamma(n+\alpha)\Gamma(m+\beta)} \int_{\sigma_1}^{\sigma_2} \int_{\rho_1}^{\rho_2} |\Omega(\tau, \varsigma)| \left| \int_{\zeta}^{\tau} \int_{\vartheta}^{\varsigma} \frac{\partial^{n+m+2} \psi(u, v)}{\partial u^{n+1} \partial v^{m+1}} dv du \right| d\varsigma d\tau$$

$$\leq \frac{\|\psi^{(n+m+2)}\|_{[\sigma_1, \sigma_2] \times [\rho_1, \rho_2], 1}}{\Gamma(n+\alpha)\Gamma(m+\beta)} \int_{\sigma_1}^{\sigma_2} \int_{\rho_1}^{\rho_2} |\Omega(\tau, \varsigma)| d\varsigma d\tau$$

If the procedure employed in the proof of Theorem 2 is followed in a similar manner, taking into account the definition of the kernel  $\Omega(\tau, \varsigma)$ , the required result (14) is obtained.

**Remark 2.** If  $n = m = 0$  is chosen specifically under the conditions of the Theorem 3, since the sum symbols are vanished, one has the inequalities

$$\begin{aligned} & \left| J_{\zeta+, \vartheta+}^{\alpha, \beta} \psi(\sigma_2, \rho_2) + J_{\zeta+, \vartheta-}^{\alpha, \beta} \psi(\sigma_2, \rho_1) + J_{\zeta-, \vartheta+}^{\alpha, \beta} \psi(\sigma_1, \rho_2) + J_{\zeta-, \vartheta-}^{\alpha, \beta} \psi(\sigma_1, \rho_1) \right. \\ & - \frac{(\rho_2 - \vartheta)^\beta + (\vartheta - \rho_1)^\beta}{\Gamma(\beta + 1)} [J_{\zeta+}^{\alpha} \psi(\sigma_2, \vartheta) + J_{\zeta-}^{\alpha} \psi(\sigma_1, \vartheta)] \\ & - \frac{(\sigma_2 - \zeta)^\alpha + (\zeta - \sigma_1)^\alpha}{\Gamma(\alpha + 1)} [J_{\vartheta+}^{\beta} \psi(\zeta, \rho_2) + J_{\vartheta-}^{\beta} \psi(\zeta, \rho_1)] \\ & \left. + \frac{[(\sigma_2 - \zeta)^\alpha + (\zeta - \sigma_1)^\alpha][(\rho_2 - \vartheta)^\beta + (\vartheta - \rho_1)^\beta]}{\Gamma(\alpha + 1)\Gamma(\beta + 1)} \psi(\zeta, \vartheta) \right| \\ & \leq \frac{[(\zeta - \sigma_1)^\alpha + (\sigma_2 - \zeta)^\alpha][(\vartheta - \rho_1)^\beta + (\rho_2 - \vartheta)^\beta]}{\Gamma(\alpha + 1)\Gamma(\beta + 1)} \|\psi_{uv}^{(2)}\|_1 \end{aligned}$$

which was proved Erden et al. in the reference (Erden et al., 2020b).

## REFERENCE

- Aglić Aljinović, A. (2014). Montgomery identity and Ostrowski type inequalities for Riemann-Liouville fractional integral, Journal of Mathematics, Article ID 503195, pp. 1-6
- Anastassiou, G. (1995). Ostrowski type inequalities, Proc. of the American Math. Soc., 123(12), pp. 3775-378.
- Barnett, N. S., and Dragomir, S. S. (2001). An Ostrowski type inequality for double integrals and applications for cubature formulae, Soochow J. Math., 27(1), pp. 1-10.

- Cerone, P., Dragomir, S. S., and Roumeliotis, J. (1999) Some Ostrowski type inequalities for  $n$ -time differentiable mappings and applications, *Demonstratio Math.*, 32(4), pp. 697-712.
- Changjian, Z., and Cheung, W. S. (2010). On Ostrowski-type inequalities for heigher-order partial derivatives, *Journal of Ineqaulities and Applications*, Article ID 960672, pp. 1-8.
- Dragomir, S. S. (2017a). Ostrowski Type inequalities for riemann-Liouville fractional integrals of absolutely continuous functions in terms of  $\infty$  - norms, *RGMIA Research Report Collection*, 20, Article 49, pp. 1-14.
- Dragomir, S. S. (2017b). Ostrowski Type inequalities for riemann-Liouville fractional integrals of absolutely continuous functions in terms of  $p$  - norms, *RGMIA Research Report Collection*, 20, Article 50.
- Dragomir, S. S., and Wang, S. (1997). A new inequality of Ostrowski's type in  $L_1$  - norm and applications to some special means and to some numerical quadrature rules., *Tamkang J. of Math.*, 28(3), pp. 239-244.
- Dragomir, S. S., and Wang, A. (1998). A new inequality of Ostrowski's type in  $L_p$  - norm and applications to some special means and to some numerical quadrature rules, *Indian Journal of Mathematics*, 40(3), pp. 299-304.
- Dragomir, S. S., Barnett, N. S., and Cerone, P. (2003). An Ostrowski type inequality for double integrals in terms of  $L_p$ -norms and applications in numerical integration, *Anal. Num. Theor. Approx.*, 32(2), pp. 161-169.
- Erden, S., Özdemir, B. G., Kılıçer, S., and Demir, C. (2024). Ostrowski Type Inequalities Including Riemann-Liouville Fractional Integrals for Two Variable Functions., *Konuralp Journal of Mathematics*, 12(1), pp. 62-73.
- Erden, S., Budak, H., and Sarıkaya, M. Z. (2020)a. Fractional Ostrowski type inequalities for functions of bounded variaton with two variables, *Miskolc Mathematical Notes*, 21(1), pp. 171-188.
- Erden, S., Budak, H., Zeki Sarıkaya, M., Iftikhar, S., and Kumam, P. (2020b). Fractional Ostrowski type inequalities for bounded functions, *Journal of Inequalities and Applications*, 123, pp. 1-11.
- Erden, S., and Uyanik, N. (2025). Fractional inequalities involving double integrals of Riemann-Liouville for higher-order partial differential functions. *Thermal Science*, 29(4 Part B), 3013-3022.
- Erden, S., and Sarıkaya, M. Z. (2024). New weighted inequalities for functions whose higher-order partial derivatives are co-ordinated convex. *Fundamental Journal of Mathematics and Applications*, 7(2), 77-86.
- Fink, M. A. (1992). Bounds on the deviation of a function from its averages, *Czechoslovak Mathematical Journal*, 42(117), pp. 289-310.
- Gorenflo, R., and Mainardi, F. (1997). *Fractional calculus: integral and differential equations of fractional order*, Springer Verlag, Wien, pp. 223-276, 1997.
- Hanna, G., Dragomir, S. S., and Cerone, P. (2002). A general Ostrowski type inequality for double integrals, *Tamkang Journal of Mathematics*, 33(4), pp. 319-333.
- Lakoud, A. G. and Aissaoui, F. (2013) New fractional inequalities of Ostrowski type, *Transylv. J. Math. Mech.*, 5(2), pp. 103-106.
- Latif M. A. and Hussain, S. (2012) New inequalities of Ostrowski type for co-ordinated convex functions via fractional integrals, *J Fractional Calc Appl.*, 2(9), pp. 1-15.

- Ostrowski, A. M. (1938). Über die absolutabweichung einer differentiebaren funktion von ihrem integralmittelwert, *Comment. Math. Helv.* 10, pp. 226-227.
- Podlubni, I. (1999). *Fractional Differential Equations*, Academic Press, San Diego, 1999.
- Qayyum, A., Shoaib, M., and Erden, S. (2019). Generalized fractional Ostrowski type inequality for higher order derivatives, *New Trends in Mathematical Sciences (NTMSCI)*, 4(2), pp. 111-124.
- Sarkaya, M. Z. (2014). On the Hermite--Hadamard-type inequalities for co-ordinated convex function via fractional integrals, *Integral Transforms and Special Functions*, 25(2), pp. 134-147.
- Sarikaya, M. Z., Set, E., Yaldiz, H., and Başak, N. (2013). Hermite--Hadamard's inequalities for fractional integrals and related fractional inequalities, *Mathematical and Computer Modelling*, 57, (9-10), pp. 2403-2407.
- Sarikaya, M. Z., Filiz, H., and Kiris, M. E. (2015). On some generalized integral inequalities for Riemann-Liouville fractional integrals, *Filomat* 29(6), 1307--1314, Doi:10.2298/FIL1506307S.
- Sarkaya, M. Z. (2023). On the generalized Ostrowski type inequalities for co-ordinated convex functions, *Filomat*, 37(22), pp. 7351-7366.
- Sofo, A. (2002). Integral inequalities for  $n$ - times differentiable mappings, with multiple branches, on the  $L_p$  norm, *Soochow Journal of Mathematics*, 28(2), pp. 179-221.
- Ujević, N. (2003). Ostrowski-Grüss type inequalities in two dimensional, *J. of Ineq. in Pure and Appl. Math.*, 4(5), article 101.
- Wang M., and Zhao, X. (2009). Ostrowski type inequalities for higher-order derivatives, *J. of Inequalities and App.*, Vol. 2009, Article ID 162689, pp. 1-8.





# **DFT and Topological Insights into the Structural and Reactive Features of a Pyridine Based Hydrazone**

**Sevgi KANSIZ<sup>1</sup>**

**Okan ŞİMŞEK<sup>2</sup>**

- 1- Asst. Prof.; Samsun University, Faculty of Engineering and Natural Sciences, Department of Fundamental Sciences. sevgi.kansiz@samsun.edu.tr ORCID No: 0000-0002-8433-7975.
- 2- Res. Asst.; Ondokuz Mayıs University, Faculty of Science, Department of Physics. okan.simsek@omu.edu.tr ORCID No: 0000-0003-1157-4088.

## ABSTRACT

A detailed density functional theory (DFT) investigation was performed on the hydrazone derivative  $C_{14}H_{12}FN_3O$  to elucidate its structural, electronic, and non-covalent interaction features. The optimized geometry shows a nearly planar structure that supports  $\pi$ -electron delocalization along the hydrazone chain. Frontier molecular orbital (FMO) analysis reveals a HOMO–LUMO energy gap of 3.48 eV, indicating moderate stability and reactivity. The calculated global descriptors ( $\chi = 7.28$  eV,  $\eta = 1.74$  eV) confirm the molecule's electrophilic nature. Molecular electrostatic potential (MEP) maps identify the carbonyl oxygen and azomethine nitrogen as preferred electrophilic centers. The ELF and LOL analyses highlight strong electron localization along the conjugated C–C and C–N bonds, consistent with a predominantly covalent character. Reduced Density Gradient (RDG) and Non-Covalent Interaction (NCI) analyses reveal a balance of weak van der Waals and electrostatic interactions (red–green regions), with localized steric repulsion (red zones) near the fluorophenyl group. These findings demonstrate that the compound's overall stability arises from the interplay between covalent bonding and weak dispersive forces, providing a comprehensive understanding of its electronic and reactive characteristics.

*Keywords – Pyridine, hydrazone, DFT, MEP, HOMO-LUMO, NCI-RDG*

---

## INTRODUCTION

Pyridine was first synthesized by Ramsay in 1877 through the reaction of acetylene and hydrogen cyanide in a tube furnace. Pyridine nuclei are present in numerous natural products, including vitamins, alkaloids, coenzymes, and various drugs and pesticides (Al-thamili et al., 2020; Ling et al., 2021; Xia et al., 2023). As polar and ionizable aromatic compounds, pyridine and its derivatives enhance solubility and bioavailability, making them valuable heterocyclic scaffolds in biomedical research (Ebenezer et al., 2020; Qadir et al., 2019a; Tber et al., 2019). Their chemical versatility, including basicity, hydrogen-bonding capacity, and solubility, renders pyridine an important building block in pharmaceutical and agrochemical design (Jiang et al., 2022; Kansız et al., 2020; Tighadouini et al., 2020). These features have contributed to the widespread exploration of pyridine derivatives for various biological activities, including antitumor, antibacterial, antifungal, antiviral, analgesic, anti-inflammatory, antiproliferative, and antidiabetic effects, as well as applications in bioimaging and drug delivery (Ali et al., 2021; Kamat et al., 2020).

Hydrazine and its derivatives, including hydrazones, are another important class of nitrogen-containing compounds with significant chemical and biological relevance (Dietl et al., 2015; Kansız, 2023;). Hydrazine is a

highly reactive molecule that serves as a precursor for various heterocyclic compounds and pharmaceuticals. Hydrazones, formed through the condensation of hydrazine with carbonyl compounds, possess unique structural and electronic features that enable diverse chemical reactivity (Kucukoglu et al., 2019; Murugappan et al., 2024; Verma et al., 2014). These compounds have been extensively studied for their biological activities, including antimicrobial, anticancer, and anti-inflammatory effects, and are also employed in drug design and molecular recognition. The combination of pyridine and hydrazone motifs in a single molecule can therefore provide synergistic properties, enhancing both reactivity and potential biological activity.

In this study, a detailed theoretical investigation was performed on a pyridine-based hydrazone derivative to examine its structural, electronic, and supramolecular properties. Density Functional Theory (DFT) calculations were employed for geometry optimization and to analyze the electronic distribution. Frontier molecular orbital (HOMO–LUMO) analysis provided insights into the energy gap, chemical reactivity, and stability of the molecule. Molecular electrostatic potential (MEP) mapping was used to locate electrophilic and nucleophilic regions, identifying potential reactive sites. Additionally, electron localization function (ELF) and localized orbital locator (LOL) analyses were carried out to characterize electron-pair distribution and bonding patterns. Noncovalent Interaction–Reduced Density Gradient (NCI-RDG) analysis allowed visualization of weak interactions, including van der Waals forces, hydrogen bonds, and  $\pi$ – $\pi$  stacking, thus highlighting the compound's supramolecular features.

### ***Materials and Method***

Density Functional Theory (DFT) computations were conducted using the Gaussian 09W program (Frisch et al., 2016), and molecular structures were visualized with GaussView 6.0 (Dennington et al., 2016). Geometry optimization and electronic structure analyses were performed at the B3LYP/6-31G(d,p) level of theory (Becke, 1993; Lee et al., 1988), providing a reliable balance between computational cost and accuracy. The obtained results were used to determine the HOMO–LUMO energy gap and to construct the Molecular Electrostatic Potential (MEP) map, which highlights electrophilic and nucleophilic sites of the molecule. Topological analyses, including ELF, LOL, and RDG, were carried out using Multiwfn 3.7 (Lu and Chen, 2012) and visualized with VMD software (Humphrey et al., 1996).

## **RESULTS AND DISCUSSION**

### ***Optimized geometry of $C_{14}H_{12}FN_3O$***

The optimized geometry of  $C_{14}H_{12}FN_3O$  reveals an extended conjugated system across the pyridine ring, the hydrazone linkage and the ortho-fluoro substituted phenyl ring (Figure 1). The aromatic C–C bond lengths

adopt the expected averaged value for aromatic rings ( $\approx 1.39$  Å), while selected bond lengths and angles in the hydrazone/acetyl core and at the linker atoms indicate significant  $\pi$ -conjugation and partial double-bond character in the C–N / N–N framework (Gümüş et al., 2025; Kansız et al., 2025; Simsek et al., 2022; Yeşilbağ et al., 2024). Aromatic C–C bond distances are in good agreement with reported values (Cakmak et al., 2022; Chkirate et al., 2019; Gumus et al., 2018; Gümüş et al., 2020; Ilmi et al., 2023; Kansız, 2023). Selected bond lengths and bond angles used to describe the optimized geometry are given in Table 1. The carbonyl C19–O20 distance (1.184 Å) is characteristic of a C=O double bond and confirms the presence of the acetyl carbonyl functionality. The hydrazone/azomethine region shows shortened C–N distances consistent with C=N character: C11–N16 = 1.304 Å and C1–N10 / C2–N10 = 1.327 Å and 1.331 Å, respectively. These values support delocalization of electron density into the imine/hydrazone linkage. The N16–N17 distance (1.365 Å) is shorter than a typical single N–N bond, indicating partial double-bond character and conjugation across the N–N unit. Several C–C single bonds connecting aromatic fragments are noticeably longer than the aromatic average (e.g., C11–C12 = 1.527 Å, C2–C11 = 1.475 Å, C19–C21 = 1.492 Å). The C22–F31 bond (1.355 Å) is consistent with a typical C–F single bond; the relatively large C21–C22–F31 angle ( $123^\circ$ ) indicates the steric/electronic influence of the ortho-fluoro substituent on the local geometry. The combination of shortened C–N and N–N distances together with near-planar bond angles around the hydrazone/acetyl core indicates effective  $\pi$ -conjugation across the linkage connecting the pyridine and phenyl rings. The carbonyl geometry (O20–C19–N17  $\approx 119^\circ$ ) and the short C=O bond corroborates a classical acetyl carbonyl. Longer inter-ring C–C linkages ( $\approx 1.48$ – $1.53$  Å) reflect single-bond character that partially localizes the aromatic systems while still permitting conjugation through the hydrazone bridge. Overall, the optimized geometry is consistent with a resonance-stabilized hydrazone structure where electronic delocalization is distributed over the C=N–N–C=O fragment and the adjacent aromatic rings.

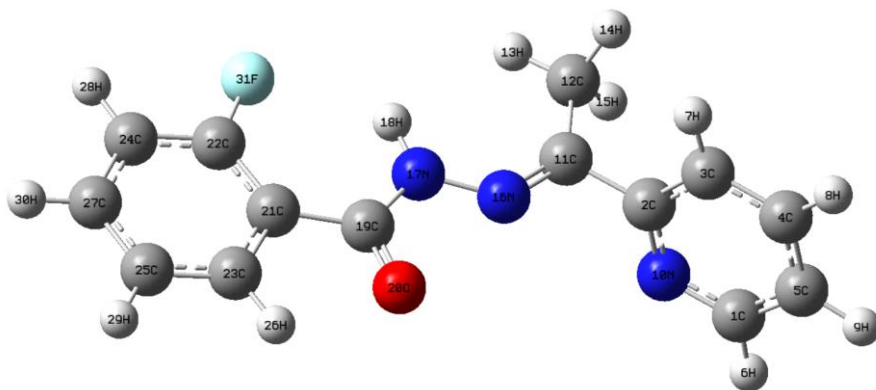


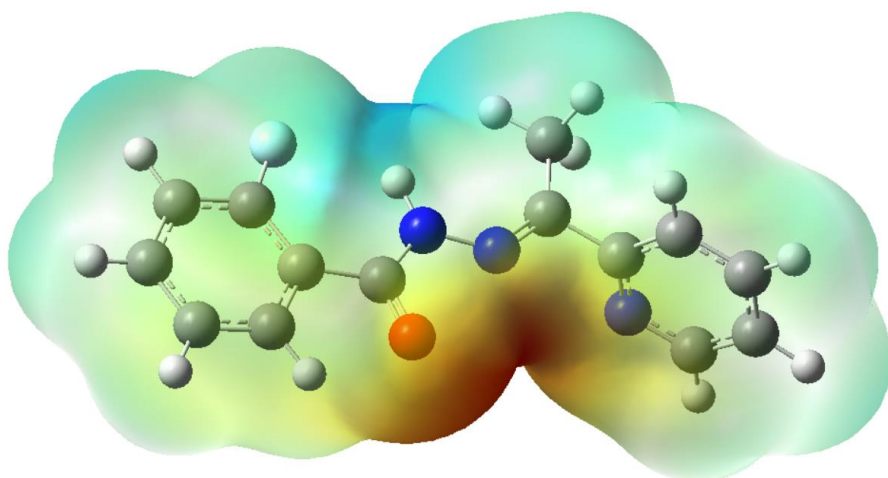
Figure 1: The optimized structure of  $C_{14}H_{12}FN_3O$ .

Table 1: Selected bond lengths of C<sub>14</sub>H<sub>12</sub>FN<sub>3</sub>O.

Bond length	Distance, Å	Bond angle	Value, deg
C1–N10	1.327	C1–N10–C2	116
C2–N10	1.331	C2–C11–C12	114
C11–N16	1.304	C2–C11–N16	110
C19–N17	1.351	C11–N16–N17	129
C19–O20	1.184	C19–N17–N16	117
N16–N17	1.365	O20–C19–N17	119
C22–F31	1.355	C21–C19–O20	117
C11–C12	1.527	C21–C22–F31	123
C2–C11	1.475	C24–C22–F31	115
C19–C21	1.492	C19–C21–C23	113

### MEP surface analysis of C<sub>14</sub>H<sub>12</sub>FN<sub>3</sub>O

The molecular electrostatic potential (MEP) map of the compound C<sub>14</sub>H<sub>12</sub>FN<sub>3</sub>O, shown in Figure 2, provides valuable insight into its charge distribution and reactive regions. In line with our previous computational investigations, the Molecular Electrostatic Potential (MEP) analysis was performed to examine the charge distribution and reactive sites of the molecule (Adhikari et al., 2023; 2024; Arumugam et al., 2021; El Bakri et al., 2024; El Kalai et al., 2023). The map reveals that the carbonyl oxygen and azomethine nitrogen atoms are the most electron-rich sites, indicating their potential as preferred centers for electrophilic interactions. In contrast, the hydrogen atoms attached to the aromatic and azomethine moieties exhibit positive potential regions, suggesting their susceptibility to nucleophilic attack. This charge separation highlights the molecule's polarized electronic structure and supports its capability to engage in intermolecular interactions through both electrophilic and nucleophilic sites.

Figure 2: MEP surface of C<sub>14</sub>H<sub>12</sub>FN<sub>3</sub>O.

### **Frontier molecular orbital analysis of $C_{14}H_{12}FN_3O$**

Figure 3 presents the computed HOMO and LUMO surfaces of  $C_{14}H_{12}FN_3O$ . Table 2 represents the computed energies and global descriptors. From these values, we further obtain the chemical potential and electrophilicity:  $\mu = -\chi = -7.28$  eV and electrophilicity index  $\omega = \mu^2 / (2\eta) = (7.28^2)/(2 \times 1.74) \approx 15.24$  eV. The HOMO–LUMO gap ( $\Delta E = 3.48$  eV) indicates a balance between kinetic stability and chemical reactivity. It is large enough to imply the molecules are not highly reactive (i.e., not a very soft, easily oxidized species), yet small enough to allow participation in electronic transitions and charge-transfer interactions under appropriate conditions (Kargar et al., 2025; OmarAli et al., 2020; 2023; Qadir et al., 2019b). Practically, this gap is consistent with a conjugated hydrazone system with moderate electronic delocalization. The relatively deep HOMO ( $-9.02$  eV) shows the molecule is a poor electron donor (low tendency to lose electrons). The LUMO energy ( $-5.54$  eV) is also relatively low, indicating reasonable electron-accepting capability. The large electronegativity ( $\chi = 7.28$  eV) and high electrophilicity ( $\omega \approx 15.24$  eV) together point to an overall electron-deficient character: the molecule is more prone to act as an electrophile/accept electron density than as a strong nucleophile. The hardness value  $\eta = 1.74$  eV signals moderate resistance to change in electron density (i.e., not very polarizable). Consequently, the molecule is not extremely "soft" and will preferentially undergo interactions governed by hard–soft complementarity, it will react more readily with relatively "soft" nucleophiles only if local orbital match and energetics allow (Ozsanlı et al., 2024; Simsek et al., 2023). The low softness ( $S = 0.29$ ) supports the interpretation of moderate chemical reactivity.

As shown in Figure 3, the HOMO is primarily localized on the conjugated aromatic/hydrazone framework (pyridine ring and phenyl/hydrazone linkage). This localization indicates these regions are the most electron-rich parts of the molecule and, while overall poor donors, they are the likeliest sites to participate in electron donation in intermolecular contacts ( $\pi$ – $\pi$  interactions, H-bonding where electron density is required). The LUMO surface is concentrated on the azomethine/carbonyl-containing fragment ( $C=N-N-C=O$  moiety) and adjacent pyridine ring, suggesting that these atoms will accept incoming electron density. Therefore, nucleophilic attack or coordination (e.g., metal complexation) is more likely to involve the hydrazone/carbonyl region and the pyridine nitrogen. These features suggest that (i) electronic excitations and charge-transfer processes will involve the conjugated hydrazone–pyridine system and (ii) nucleophilic interactions or coordination are most likely to occur at the hydrazone/carbonyl moiety. The Fourier molecular orbital picture supports the assignment of the hydrazone fragment as an electron-accepting site and rationalizes observed or expected reactivity patterns for this class of compounds.

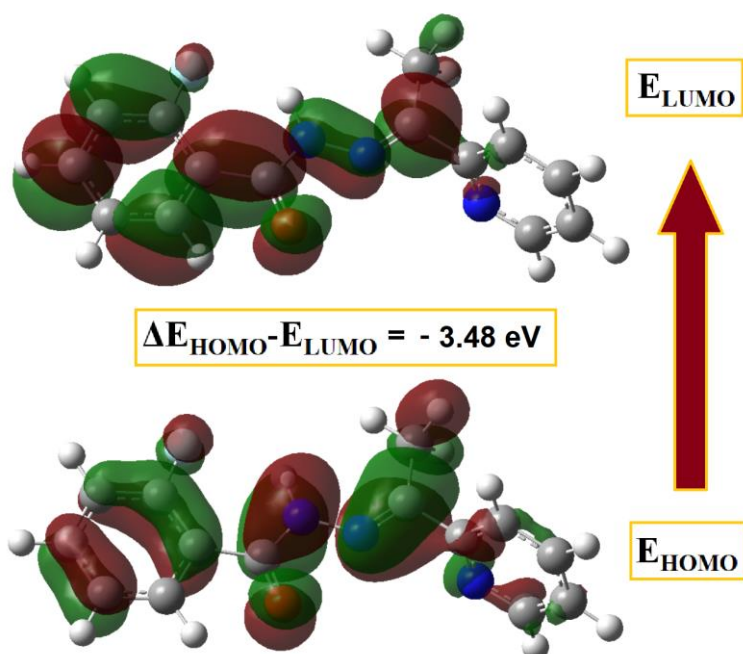


Figure 3: HOMO-LUMO surface of  $C_{14}H_{12}FN_3O$ .

Table 2: The energy values of the global reactivity parameters of  $C_{14}H_{12}FN_3O$ .

Parameters	
$E_{HOMO}$ (eV)	-9.02
$E_{LUMO}$ (eV)	-5.54
Energy gap (eV)	3.48
Ionization potential ( $I=-E_{HOMO}$ )	9.02
Electron affinity ( $A=-E_{LUMO}$ )	5.54
Electronegativity ( $\chi=(I + A)/2$ )	7.28
Hardness ( $\eta=(I - A)/2$ )	1.74
Softness ( $S=1/2\eta$ )	0.29

### ***ELF and LOL analysis of $C_{14}H_{12}FN_3O$***

The ELF map (Figure 4a) shows pronounced red regions ( $ELF \approx 0.8$ ) around the bonding zones between carbon and nitrogen, as well as within aromatic C–C bonds. This indicates strong electron localization corresponding to covalent bonding and  $\pi$ -delocalization within the conjugated aromatic systems. The nearly circular high-ELF basins in the pyridine and phenyl rings suggest typical  $\pi$ -bonding delocalization patterns, confirming the aromatic character. Moderate ELF values (0.5–0.7) near the hydrazone (C=N–N–C=O) linkage and the carbonyl oxygen correspond to partially localized lone-pair electrons and resonance interactions within the C=N–N–C=O conjugated segment. The fluor atom attached to the phenyl

ring also exhibits a localized high-ELF region, representing the nonbonding electron pairs on fluorine and the polarization of the C–F bond.

The LOL distribution (Figure 4b) exhibits high values along the C–C and C–N bonds, particularly in the aromatic and hydrazone regions, confirming a high degree of covalent character and effective orbital overlap. The continuous LOL density through the  $\pi$ -system indicates conjugation across the molecule. Regions of lower LOL values (blue/green areas) appear near heteroatoms and inter-ring connections, suggesting reduced electron sharing and localized lone-pair density. In the vicinity of the carbonyl oxygen, LOL minima correspond to the localization of nonbonding electron pairs, consistent with the electrophilic nature of the C=O center inferred from the FMO analysis. The combined ELF–LOL analysis highlights that the electron density is strongly localized within the aromatic and hydrazone frameworks, with significant delocalization across the  $\pi$ -conjugated pathway (C<sub>6</sub>–C<sub>5</sub>–N–N–C=O). The C=O and C–F bonds exhibit partial charge separation due to strong electronegativity differences, which aligns with the molecule's electrophilic behavior predicted from the HOMO–LUMO results. These topological features confirm that the molecule possesses both localized and delocalized electronic regions, supporting its moderate stability and reactive potential toward non-covalent interactions (such as hydrogen bonding and  $\pi$ – $\pi$  stacking) that stabilize its crystal structure.

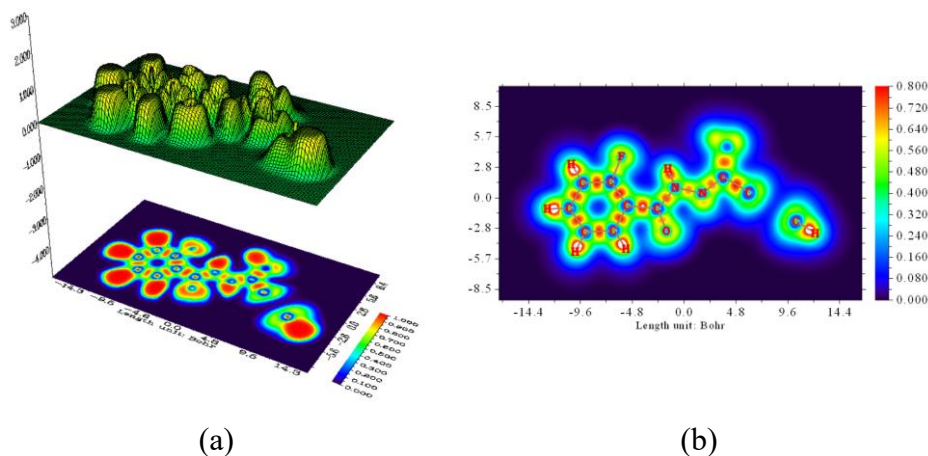


Figure 4: ELF (a) and LOL (b) maps of C<sub>14</sub>H<sub>12</sub>FN<sub>3</sub>O.

### NCI-RDG analysis of C<sub>14</sub>H<sub>12</sub>FN<sub>3</sub>O

The Reduced Density Gradient (RDG) analysis was employed to visualize and characterize the weak non-covalent interactions (NCIs) and the overall molecular stability of C<sub>14</sub>H<sub>12</sub>FN<sub>3</sub>O. This topological approach enables a clear distinction between different types of intra- and intermolecular interactions through the relationship between the electron density ( $\rho$ ) and the second eigenvalue ( $\lambda_2$ ) of the Hessian matrix of the electron density. The RDG scatter graph of C<sub>14</sub>H<sub>12</sub>FN<sub>3</sub>O (Figure 5) plots the



$\text{sign}(\lambda_2)\rho$  function ranging from  $-0.05$  to  $+0.05$  a.u. against the reduced density gradient, enabling interpretation of various interaction regions. In this representation:

Blue regions ( $\lambda_2 < 0, \rho > 0$ ) correspond to strong attractive interactions, such as hydrogen bonding and other electrostatic attractions. Green regions ( $\lambda_2 \approx 0$ ) indicate weak van der Waals interactions and dipole–dipole forces, characteristic of non-covalent stabilization between closely packed aromatic fragments or heteroatoms. Red regions ( $\lambda_2 > 0$ ) are associated with steric repulsion arising from atomic proximity and electron cloud overlap in crowded molecular environments.

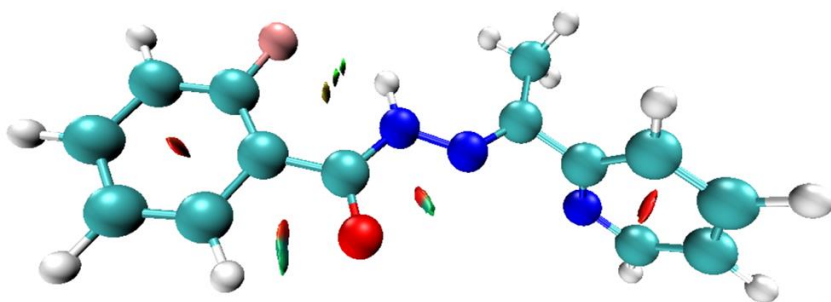
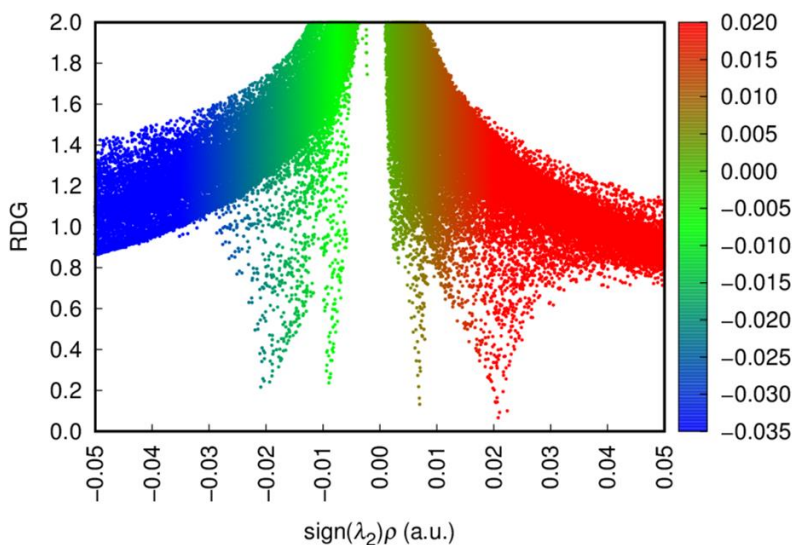


Figure 5: RDG scatter plot and RDG isosurface of  $\text{C}_{14}\text{H}_{12}\text{FN}_3\text{O}$ .

For the  $\text{C}_{14}\text{H}_{12}\text{FN}_3\text{O}$  molecule, the RDG isosurface analysis revealed. Distinct red-green patches localized mainly near the N–N, C=O, and C=N segments, which correspond to attractive intramolecular electrostatic interactions stabilizing the hydrazone framework. Green isosurfaces between  $-0.02$  and  $0.01$  a.u., spread over the aromatic rings and between adjacent  $\pi$ -systems, suggesting  $\pi \cdots \pi$  stacking and van der Waals contacts that

contribute to the overall molecular cohesion and possible crystal packing stabilization. Red isosurfaces in the range of 0.01–0.05 a.u., particularly near the ortho-fluorophenyl and pyridine region, highlight areas of steric congestion due to the close spatial arrangement of fluorine and neighboring hydrogen atoms.

These results indicate that both intra- and intermolecular non-covalent interactions coexist and synergistically stabilize the structure. The presence of multiple interaction zones—electrostatic, dispersive, and steric—confirms the dynamic electronic environment of the molecule. The NCI isosurface mapping further validates that the molecule's stability is governed by a delicate balance between electrostatic attraction within the hydrazone core and dispersion interactions among the aromatic systems, consistent with the moderate HOMO–LUMO gap and delocalized electron distribution inferred from FMO and ELF/LOL analyses.

In summary, the RDG analysis clearly visualizes the interplay of attractive (blue), neutral (green), and repulsive (red) regions within the molecule, confirming that weak van der Waals and  $\pi\cdots\pi$  interactions significantly enhance the structural integrity of  $C_{14}H_{12}FN_3O$ , while localized steric effects remain confined to specific substituent-rich zones.

## CONCLUSION

Theoretical studies conducted on  $C_{14}H_{12}FN_3O$  demonstrate that the compound possesses a conjugated framework exhibiting moderate electronic delocalization and a balanced donor–acceptor character. The HOMO–LUMO energy gap (3.48 eV) and associated global descriptors indicate that the molecule is chemically stable yet reactive enough to engage in non-covalent and charge-transfer interactions. The MEP and ELF/LOL analyses collectively reveal that the hydrazone linkage ( $C=N-N-C=O$ ) serves as the primary reactive center due to localized electron density and polarization effects, while the aromatic fragments provide additional  $\pi$ -electron stabilization. The RDG and NCI analyses further confirm the coexistence of weak electrostatic and van der Waals interactions, which play a crucial role in maintaining molecular integrity and potentially influencing crystal packing behavior. The predominance of blue and green isosurfaces in the RDG plots underscores the significance of attractive non-covalent interactions within the molecular system. In summary, the integration of multiple theoretical approaches confirms that  $C_{14}H_{12}FN_3O$  exhibits a stable yet electronically responsive architecture, capable of engaging in both covalent and non-covalent interactions—an important consideration for its

potential use in coordination chemistry, supramolecular assembly, or optoelectronic applications.

## REFERENCES

- Ali, E. M., Abdel-Maksoud, M. S., Hassan, R. M., Mersal, K. I., Ammar, U. M., Se-In, C., He-Soo, H., Kim, H.-K., Lee, A., and Lee, K.-T. (2021). Design, synthesis and anti-inflammatory activity of imidazole-5-yl pyridine derivatives as p38 $\alpha$ /MAPK14 inhibitor. *Bioorganic & Medicinal Chemistry*, 31, Article 115969.
- Al-thamili, D. M., Almansour, A. I., Arumugam, N., Kansız, S., Dege, N., Soliman, S. M., Azam, M., and Kumar, R. S. (2020). Highly functionalized N-1-(2-pyridinylmethyl)-3,5-bis[(E)-arylmethylidene]tetrahydro-4(1H)-pyridinones: Synthesis, characterization, crystal structure and DFT studies. *Journal of Molecular Structure*, 1222, 128940.
- Arumugam, N., Almansour, A. I., Kumar, R. S., Yeswanthkumar, S., Padmanaban, R., Arun, Y., Kansız, S., Dege, N., Manohar, T. S., and Venketesh, S. (2021). Design, stereoselective synthesis, computational studies and cholinesterase inhibitory activity of novel spiropyrrolidinoquinoxaline tethered indole hybrid heterocycle. *Journal of Molecular Structure*, 1225, 129165.
- Becke, A. D. (1993). Density-functional thermochemistry. III. The role of exact exchange. *The Journal of Chemical Physics*, 98(7), 5648–5652.
- Chkirate, K., Kansiz, S., Karrouchi, K., Mague, J. T., Dege, N., and Essassi, E. M. (2019). Crystal structure and Hirshfeld surface analysis of N-{2-[(E)-(4-methylbenzylidene) amino] phenyl}-2-(5-methyl-1-H-pyrazol-3-yl) acetamide hemihydrate. *Acta Crystallographica Section E, Crystallographic Communications*, 75(2), 154–158.
- Cakmak, S., Kansiz, S., Azam, M., Ersanlı, C. C., Idil, O., Veyisoglu, A., Yakan, H., Kütük, H., and Chutia, A. (2022). Synthesis, structural investigation, Hirshfeld surface analysis, and biological evaluation of N-(3-Cyanothiophen-2-yl)-2-(thiophen-2-yl) acetamide. *ACS omega*, 7(13), 11320–11329.
- Dennington, R., Keith, T. A., and Millam, J. M. (2016). GaussView 6.0.16. *Semichem Inc., Shawnee Mission*.
- Dietl, A., Ferousi, C., Maalcke, W. J., Menzel, A., de Vries, S., Keltjens, J. T., Jetten, M. S. M., Kartal, B., and Barends, T. R. (2015). The inner workings of the hydrazine synthase multiprotein complex. *Nature*, 527(7578), 394–397.
- Ebenezer, O., Awolade, P., Koorbanally, N., and Singh, P. (2020). New library of pyrazole–imidazo[1,2- $\alpha$ ]pyridine molecular conjugates: Synthesis, antibacterial activity and molecular docking studies. *Chemistry & Biology Drug Design*, 95, 162–173.
- El Kalai, F., Abraham, C. S., Kansiz, S., Oulmidi, A., Muthu, S., Prasana, J. C., Dege, N., Abuelizz, H. A., Al-Salahi, R., Benchat, N., and Karrouchi, K. (2023). Synthesis, crystal structure, and computational investigations of 2-(2-(4-fluorophenyl)-2-oxoethyl)-6-methyl-5-(4-methylbenzyl)pyridazin-3(2H)-one as antiviral agent. *Crystals*, 13(7), 1098.
- Frisch, M. J., Trucks, G. W., Schlegel, H. B., Scuseria, G. E., Robb, M. A., Cheeseman, J. R., Montgomery Jr., J. A., Vreven, T., Kudin, K. N., Burant, J. C., Millam, J. M., Iyengar, S. S., Tomasi, J., Barone, V., Mennucci, B., Cossi, M., Scalmani, G., Rega, N., Petersson, G. A., Nakatsuji, H., Hada, M.,

- Ehara, M., Toyota, K., Fukuda, R., Hasegawa, J., Ishida, M., Nakajima, T., Honda, Y., Kitao, O., Nakai, H., Klene, M., Li, X., Knox, J. E., Hratchian, H. P., Cross, J. B., Bakken, V., Adamo, C., Jaramillo, J., Gomperts, R., Stratmann, R. E., Yazyev, O., Austin, A. J., Cammi, R., Pomelli, C., Ochterski, J. W., Ayala, P. Y., Morokuma, K., Voth, G. A., Salvador, P., Dannenberg, J. J., Zakrzewski, V. G., Dapprich, S., Daniels, A. D., Strain, M. C., Farkas, O., Malick, D. K., Rabuck, A. D., Raghavachari, K., Foresman, J. B., Ortiz, J. V., Cui, Q., Baboul, A. G., Clifford, S., Cioslowski, J., Stefanov, B. B., Liu, G., Liashenko, A., Piskorz, P., Komaromi, I., Martin, R. L., Fox, D. J., Keith, T., Al-Laham, M. A., Peng, C. Y., Nanayakkara, A., Challacombe, M., Gill, P. M. W., Johnson, B., Chen, W., Wong, M. W., Gonzalez, C., and Pople, J. A. (2016). Gaussian 09, Revision A.02. *Gaussian, Inc., Wallingford CT*.
- Gumus, M. K., Kansiz, S., Dege, N., and Kalibabchuk, V. A. (2018). Hirshfeld surface analysis and crystal structure of 7-methoxy-5-methyl-2-phenyl-11, 12-dihydro-5,11-methano-1,2,4-triazolo [1,5-c][1,3,5] benzoxadiazocine. *Acta Crystallographica Section E, Crystallographic Communications*, 74(9), 1211-1214.
- Gümüş, M. K., Kansiz, S., Tulemisova, G. B., Dege, N. and Saif, E. (2022). Crystal structure and Hirshfeld surface analysis of 3-(hydroxymethyl)-3-methyl-2, 6-diphenylpiperidin-4-one. *Acta Crystallographica Section E, Crystallographic Communications*, 78(1), 29-32.
- Gümüş, M. K., Kansiz, S., Tulemisova, G. B., and Dege, N. (2025). Synthesis, Crystal Structure, and Hirshfeld Surface Analysis of 4, 4A, 5, 6, 7, 8-Hexahydro-4A-Methyl-2, 5, 7-Triphenyl-2 H-Pyrido [4, 3-d][1, 3] Oxazine. *Journal of Structural Chemistry*, 66(1), 201-213.
- Humphrey, W., Dalke, A., and Schulten, K. (1996). VMD: visual molecular dynamics. *Journal of Molecular Graphics*, 14(1), 33–38.
- Ilmi, R., Kansiz, S., Al Rasbi, N. K., Husband, J., Dege, N., and Khan, M. S. (2023). Synthesis, X-ray crystal structure and determination of non-covalent interactions through Hirshfeld surface analysis of a pure red emitting asymmetrical octacoordinated Sm (III) complex. *Polyhedron*, 246, 116673.
- Jiang, W., Cheng, W., Zhang, T., Lu, T., Wang, J., Yan, Y., Tang, X., and Wang, X. (2022). Synthesis and antifungal activity evaluation of novel pyridine derivatives as potential succinate dehydrogenase inhibitors. *Journal of Molecular Structure*, 1270, 133901.
- Kamat, V., Santosh, R., Poojary, B., Nayak, S. P., Kumar, B. K., Sankaranarayanan, M., Faheem, Khanapure, S., Barretto, D. A., and Vootla, S. K. (2020). Pyridine- and thiazole-based hydrazides with promising anti-inflammatory and antimicrobial activities along with their in silico studies. *ACS Omega*, 5, 25228–25239.
- Kansiz, S. (2023). Synthesis and Structural Investigations of 1, 2-bis (2-ethoxybenzylidene) hydrazine. *Sakarya University Journal of Science*, 27(4), 768-780.
- Kansiz, S. (2023). Investigating the structural and surface properties of copper and nickel complexes fluorine-based salen type Schiff bases. *Journal of Structural Chemistry*, 64(12), 2295-2310.
- Kansiz, S., Faizi, M. S. H., Aydin, T. M., Dege, N., Icbudak, H., and Golenya, I. A. (2020). Crystal structure and Hirshfeld surface analysis of 2-amino-3-

- hydroxypyridin-1-ium 6-methyl-2, 2, 4-trioxo-2H, 4H-1, 2, 3-oxathiazin-3-ide. *Acta Crystallographica Section E, Crystallographic Communications*, 76(4), 572-575.
- Kansız, S., Kaştaş, G., Gümüş, M. K., Dege, N., and Aydın, R. (2025). Synthesis, Structural Characterization, and Supramolecular Assembly of a One-Dimensional Cobalt (II) Coordination Polymer with Succinato and Isonicotinamide Ligands. *Journal of Structural Chemistry*, 66(4), 722-732.
- Kargar, H., Fallah-Mehrjardi, M., Munawar, K. S., Acar, E., Dege, N., and Kansız, S. (2025). Structural dynamics of a phenoxy-bridged heteronuclear Cu (II)/Hg (II)-Salen complex: synthesis, characterization, DFT insights, and Hirshfeld surface analysis. *Journal of the Iranian Chemical Society*, 22(4), 769-780.
- Kucukoglu, K., Gul, H. I., Taslimi, P., Gulcin, I., and Supuran, C. T. (2019). Investigation of inhibitory properties of some hydrazone compounds on hCA I, hCA II and AChE enzymes. *Bioorganic Chemistry*, 86, 316-321.
- Lee, C., Yang, W., and Parr, R. G. (1988). Development of the Colle-Salvetti correlation-energy formula into a functional of the electron density. *Physical Review B*, 37(2), 785-789.
- Ling, Y., Hao, Z.-Y., Liang, D., Zhang, C.-L., Liu, Y.-F., and Wang, Y. (2021). The expanding role of pyridine and dihydropyridine scaffolds in drug design. *Drug Design, Development and Therapy*, 2021, 4289-4338.
- Lu, T., and Chen, F. (2012). Multiwfn: A multifunctional wavefunction analyzer. *Journal of Computational Chemistry*, 33(5), 580-592.
- Murugappan, S., Dastari, S., Jungare, K., Barve, N. M., and Shankaraiah, N. (2024). Hydrazone-hydrazone/hydrazone as enabling linkers in anti-cancer drug discovery: A comprehensive review. *Journal of Molecular Structure*, 1307, 138012.
- OmarAli, A. A. B., Ahmed, R. K., Al-Karawi, A. J. M., Marah, S., Kansız, S., Sert, Y., Jaafar, M. I., Dege, N., Poyraz, E. B., Ahmed, A. M. A., Ozen, T., Loukil, M., and Jwad, R. S. (2023). Designing of two new cadmium (II) complexes as bio-active materials: Synthesis, X-ray crystal structures, spectroscopic, DFT, and molecular docking studies. *Journal of Molecular Structure*, 1290, 135974.
- OmarAli, A. A. B., Al-Karawi, A. J. M., Dege, N., Kansız, S., and Ithawi, H. A. D. (2020). Synthesis and X-ray crystal structures of two different zinc (II) complexes of N,N'-cyclohexane-1,2-diylidene-bis(4-fluorobenzoylhydrazide) based on zinc salt effect. *Journal of Molecular Structure*, 1217, 128387.
- Ozsanlı, H., Simsek, O., Yılmaz, O. R., Cicek, C., Agar, E., Coruh, U., and Vazquez-Lopez, E. M. (2024). Synthesis, crystal structure, Hirshfeld surface analysis, supramolecular and computational investigation of the (E)-4-methoxy-2-(((2-methoxy-5-(trifluoromethyl)phenyl)imino)methyl) phenol compound. *Journal of Structural Chemistry*, 65(5), 946-957.
- Qadir, A. M., Kansiz, S., Rosair, G. M., Dege, N., and Safyanova, I. S. (2019a). Crystal structure and Hirshfeld surface analysis of a zinc xanthate complex containing the 2, 2'-bipyridine ligand. *Acta Crystallographica Section E, Crystallographic Communications*, 75(12), 1857-1860.
- Qadir, A. M., Kansiz, S., Dege, N., Rosair, G. M., and Fritsky, I. O. (2019b). Crystal structure and DFT study of a zinc xanthate complex. *Acta Crystallographica Section E, Crystallographic Communications*, 75(11), 1582-1585.

- Simsek, O., Ashfaq, M., Tahir, M. N., Ozturk, S., and Agar, E. (2023). Synthesis and characterizations of the Schiff base derived from 2-hydroxy-5-nitrobenzaldehyde along with Hirshfeld surface analysis and computational study. *Journal of Structural Chemistry*, 64(5), 942–953.
- Simsek, O., Dincer, M., Dege, N., Saif, E., Yilmaz, I., and Cukurovali, A. (2022). Crystal structure and Hirshfeld surface analysis of (Z)-4-{[4-(3-methyl-3-phenylcyclobutyl) thiazol-2-yl] amino}-4-oxobut-2-enoic acid. *Acta Crystallographica Section E: Crystallographic Communications*, 78(2), 120–124.
- Tber, Z., Kansiz, S., El Hafi, M., Loubidi, M., Jouha, J., Dege, N., Essassic, E. M., and Mague, J. T. (2019). Crystal structure and Hirshfeld surface analysis of N-(tert-butyl)-2-(phenylethynyl) imidazo [1, 2-a] pyridin-3-amine. *Acta Crystallographica Section E, Crystallographic Communications*, 75(10), 1564-1567.
- Tighadouini, S., Radi, S., Benabbes, R., Youssoufi, M. H., Shityakov, S., El Massaoudi, M., and Garcia, Y. (2020). Synthesis, biochemical characterization, and theoretical studies of novel  $\beta$ -keto-enol pyridine and furan derivatives as potent antifungal agents. *ACS Omega*, 5, 17743–17752.
- Verma, G., Marella, A., Shaquiquzzaman, M., Akhtar, M., Ali, M. R., and Alam, M. M. (2014). A review exploring biological activities of hydrazones. *Journal of Pharmacy and Bioallied Sciences*, 6(2), 69–80.
- Xia, J., Xin, L., Li, J., Tian, L., Wu, K., Zhang, S., Yan, W., Li, H., Zhao, Q., and Liang, C. (2023). Discovery of quaternized pyridine-thiazole-pleuromutilin derivatives with broad-spectrum antibacterial and potent anti-MRSA activity. *Journal of Medicinal Chemistry*, 66, 5061–5078.
- Yeşilbağ, S., Kansız, S., Dege, N., and Açar, E. (2024). Structural investigation and Hirshfeld surface analysis of two [ONO]-type Schiff bases. *Journal of Structural Chemistry*, 65(3), 464-477.



# **On Desargues Theorem in The Smallest Cartesian Group Plane**

**Sümeyye Büşra YAMAN<sup>1</sup>**

**Ziya AKÇA<sup>2</sup>**

- 1- PhD student ; Eskişehir Osmangazi University, Faculty of Science, Department of Mathematics and Computer Science, 26480 Eskişehir, Türkiye. [kbsumeyye@gmail.com](mailto:kbsumeyye@gmail.com) ORCID No: 0000-0002-5148-0767
- 2- Prof. Dr.; Eskişehir Osmangazi University, Faculty of Science, Department of Mathematics and Computer Science, 26480 Eskişehir, Türkiye. [zakca@ogu.edu.tr](mailto:zakca@ogu.edu.tr) ORCID No: 0000-0001-6379-0546



## ABSTRACT

This document contains codes for the calculation of Desargues theorem in the projective plane of order 25, which is the smallest Cartesian group with algebraic structure. In other words, we present examples showing that Desargues Theorem is valid in this projective plane.

*Keywords – Euclidean geometry, Cartesian group, Projective plane, Desargues Theorem, Incidence geometry.*

---

## INTRODUCTION

Akça [1] introduced the construction of the Cartesian group plane of order 25, providing the foundation for further studies on finite projective geometries based on Cartesian groups.

In a later study, Akça and Güneltili [2] investigated the  $(k,3)$ -arcs of the Cartesian projective plane  $CPG(2,25,5)$ , contributing to the classification of arcs in finite geometries.

Bayar, Akça, and Ekmekçi [3] examined the embedding of the projective plane  $PG(2,4)$  into the projective space  $P(4,4)$ , offering new insights into the relationships between lower- and higher-dimensional projective spaces.

Ekmekçi, Bayar, and Akça [4] extended this line of research by analysing the structure of projective planes within the projective space  $PG(4,4)$ , further enriching the understanding of incidence relations in such spaces.

Ekmekçi et al. [5] studied the complete  $(k,2)$ -arcs of the Hall plane of order 9, presenting detailed results relevant to combinatorial configurations in finite geometries.

Panella [7] laid the theoretical groundwork for Cartesian systems by defining and analysing a class of Cartesian coordinate systems, which later became a cornerstone in the study of Cartesian group planes.

The definitions and theorems given in the study are taken from [6].

Drawing on Felix Klein's definition of transformation-based geometry, this study explains in detail how various geometries arise by restricting or expanding the set of symmetries acting on a set of points. Specifically, it defines a geometric structure as a triple consisting of points, lines, and the one-to-one relation  $(\mathcal{N}, \mathcal{D}, \circ)$  and introduces the classical axioms P1, P2, P3 characterising a projective plane. Fundamental results are stated, such as the fact that any two lines intersect at exactly one point and that any finite projective plane of order  $n$  has  $n^2 + n + 1$  points and lines. This study then turns to the coordinates of projective planes: given a suitable "quadrilateral" of four noncollinear points and a set  $S$  (with distinguishing elements 0 and 1), coordinates can be assigned to the points and lines to reduce the occurrence rate, subject to algebraic conditions. As a prime example, the smallest Cartesian group is constructed on the plane  $GF(5)$  and the structure of a Cartesian group is obtained by defining a binary operation  $(S, \oplus, \otimes)$  with a specially chosen rule. This involves creating a subplane of order 5 and verifying Desargues Theorem using a central perspective Python code. The code calculates the intersection of corresponding sides of two triangles and checks whether these intersections lie on a line, thus verifying that perspective from a point implies direct perspective.

## **EUCLIDEAN GEOMETRY AND OTHER GEOMETRIES**

The general definition of geometry was given by the German mathematician Felix Klein as follows: Geometry is the study of properties of a set  $S$  that remain invariant under transformations that are elements of  $G$ , where  $S$  is a set and  $G$  is a group of transformations that transform the set  $S$  into itself.

### ***1.1. Euclidean Geometry***

It is the geometry that studies lines, circles, parallel lines, angles, similar triangles, planes, and so on. Topology is the most general geometry. All other geometries can be thought of as sub-geometries derived from projective geometry through various specialisations.

### ***1.2. Various Geometric Structures***

**Primitive Concepts 1.2.1:** Each fundamental proposition without proof is called an axiom. The set or collection of points is denoted by  $\mathcal{N}$ , and the set or collection of lines is denoted by  $\mathcal{D}$ . Here,  $\mathcal{N}$  and  $\mathcal{D}$  are disjoint. That is, a point cannot be considered a line, nor can a line be considered a point. Points that are elements of  $\mathcal{N}$  are denoted by capital letters such as  $A, B, C, \dots, K, L, M, \dots$ . Lines that are elements of  $\mathcal{D}$  are denoted by  $d1, d2, d3, \dots$ .

**Incidence Relation 1.2.2:** For  $N \in \mathcal{N}$  and  $d \in \mathcal{D}$ ,  $(N, d)$  implies that  $N$  lies on the line  $d$  or the line  $d$  passing through the point  $N$ . We must consider a subset of  $\mathcal{N} \times \mathcal{D}$ . This subset or incidence relation is denoted by  $\circ$ . That is,  $(N, d) \in \circ \Rightarrow N \circ d$  or  $d \circ N$ . The triple  $(\mathcal{N}, \mathcal{D}, \circ)$  is called a *geometric structure*.

### 1.3. *The* *Projective* *Plane*

Let  $\mathcal{N}$  be a set of points and  $\mathcal{D}$  a set of lines, with  $\mathcal{N} \cap \mathcal{D} \neq \emptyset$ . Let  $\circ$  denote the incidence relation on  $\mathcal{N} \times \mathcal{D}$ . If the geometric structure  $\mathbb{P} = (\mathcal{N}, \mathcal{D}, \circ)$  satisfies the following axioms, then the system is called a *projective plane*:

- **P1.** For  $\forall M, N \in \mathcal{N}$ ,  $M \neq N$ , there exists a unique line  $d \in \mathcal{D} \ni d \circ N$  and  $d \circ M$ . In other words: *Through any two points, there passes exactly one line.*
- **P2.** For  $\forall c, d \in \mathcal{D}$ , there exists a point  $N \in \mathcal{N} \ni N \circ c$  and  $N \circ d$ . In other words: *Any two lines intersect at a point.*
- **P3.** There exist  $M, N, P, Q \in \mathcal{N}$  such that no three of them are collinear.  
(That is, in  $\mathcal{N}$  there exist four points, no three of which lie on the same line.)

**Theorem 1.3.1.** In a projective plane  $\mathbb{P} = (\mathcal{N}, \mathcal{D}, \circ)$ , any two distinct lines intersect in exactly one point. That is, for  $\forall c, d \in \mathcal{D}$ ,  $c \neq d$ , there exists a unique point  $N \in \mathcal{N} \ni N \circ c$  and  $N \circ d$ .

**Theorem 1.3.2.** In a projective plane  $\mathbb{P} = (\mathcal{N}, \mathcal{D}, \circ)$ , for any two distinct lines there exists at least one point not lying on either of them.

**Theorem 1.3.3.** For any finite projective plane  $\mathbb{P} = (\mathcal{N}, \mathcal{D}, \circ)$ , there exists an integer  $n \in \mathbb{N}$  such that:

1. Each line of  $\mathbb{P}$  contains exactly  $n+1$  points.
2. Exactly  $(n+1)$  lines pass through any point of  $\mathbb{P}$ .  
The total number of points and the total number of lines are equal to each other and
3. The total number of points and the total number of lines are equal to each other and  
 $|\mathcal{N}| = |\mathcal{D}| = n^2 + n + 1$ .

The number  $n$  is called the order of the projective plane  $\mathbb{P}$ .

**Corollary 1.3.1.** Every line contains the same number of points.

**Example 1.3.1.** The smallest projective plane has 7 points and 7 lines. This projective plane with seven points is called the *Fano Plane*.

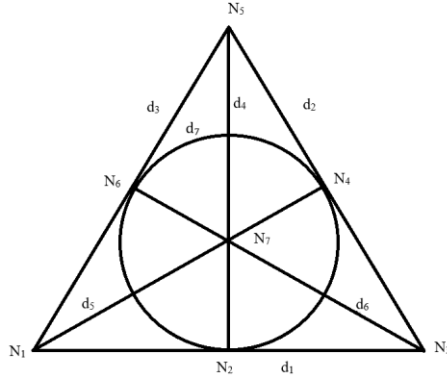


Figure 1.3.1

$\mathcal{N} = \{N_1, N_2, N_3, N_4, N_5, N_6, N_7\}$ ,  $\mathcal{D} = \{d_1, d_2, d_3, d_4, d_5, d_6, d_7\}$ ,  
 $d_1 = \{N_1, N_2, N_3\}$ ,  $d_2 = \{N_3, N_4, N_5\}$ ,  $d_3 = \{N_1, N_5, N_6\}$ ,  $d_4 = \{N_2, N_5, N_7\}$ ,  
 $d_5 = \{N_1, N_4, N_7\}$ ,  $d_6 = \{N_3, N_6, N_7\}$ ,  $d_7 = \{N_2, N_4, N_6\}$ .

**Example 1.3.2.** Consider a point origin  $O$  in  $\mathbb{R}^3$ .

$\mathcal{N} = \{X : X \text{ is a Euclidean line through } O\}$ ,

$\mathcal{D} = \{d : d \text{ is a Euclidean plane through } O\}$ ,

$\circ : X \text{ lies in } d$ .

The system  $(\mathcal{N}, \mathcal{D}, \circ)$  is a projective plane.

**Theorem 1.3.4.** For any given field  $F$ , there exists a projective plane whose points and lines can be described algebraically using the elements of this field.

**Example 1.3.3.** The projective plane  $\mathbb{P}_2 F$  whose points and lines are coordinated with the Galois field  $F = GF(2)$  is as follows.

$\mathcal{N} = \{(x_1, x_2, x_3) : x_i \in F, (x_1, x_2, x_3) \neq (0, 0, 0), \lambda \in F, \lambda \neq 0,$

$(x_1, x_2, x_3) \equiv \lambda(x_1, x_2, x_3)\}$ ,

$\mathcal{D} = \{[a_1, a_2, a_3] : a_i \in F, [a_1, a_2, a_3] \neq [0, 0, 0], \lambda \in F, \lambda \neq 0, [a_1, a_2, a_3] \equiv \lambda [a_1,$

$a_2, a_3]\}$ ,  
 $\circ : (x_1, x_2, x_3) \circ [a_1, a_2, a_3] \Leftrightarrow a_1x_1 + a_2x_2 + a_3x_3 = 0$ .

That is, the points:

$\mathcal{N} = \{(1, 0, 0), (0, 1, 0), (0, 0, 1), (1, 1, 0), (1, 0, 1), (0, 1, 1), (1, 1, 1)\}$ .

The lines:

$\mathcal{D} = \{[1, 0, 0], [0, 1, 0], [0, 0, 1], [1, 1, 0], [1, 0, 1], [0, 1, 1], [1, 1, 1]\}$ .

For example, for the line  $[0, 0, 1]$  the points

$$(x_1, x_2, x_3) \circ [0, 0, 1] \Leftrightarrow 0x_1 + 0x_2 + 1x_3 = 0 \Rightarrow x_3 = 0 \\ \Rightarrow x_1, x_2 \in F, x_3 = 0$$

Points on other lines can be obtained in a similar manner. Considering all lines, it is seen that axioms P1, P2, P3 are satisfied for this field.

#### 1.4. Coordinatization of Projective Planes

Every projective plane can be coordinatized using the elements of a suitable set  $S$ .

**Definition 1.4.1.** Let  $\mathbb{P}$  be a projective plane of order  $n$ , and let  $S$  be a set with cardinality  $n \geq 2$  that contains two distinguished elements denoted by 0 and 1. In  $\mathbb{P}$ , select four points  $\{O, E, U, V\}$  such that no three of them are collinear. This quadrilateral, together with the set  $S$ , is called a *coordinatizing quadrangle*. Using it, the points, lines, and incidence relation of  $\mathbb{P}$  can be determined.

##### 1.4.1. Coordinatization of Points

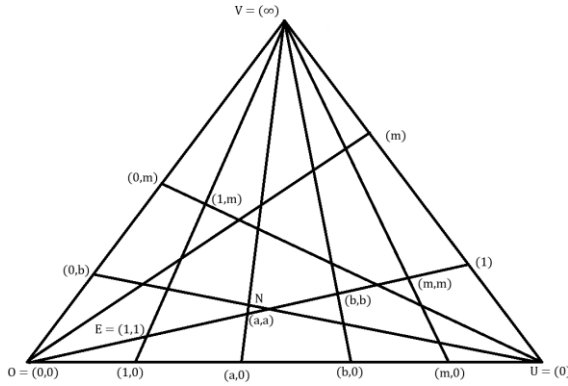


Figure 1.4.1.1

Let us map a unique element of  $S^2$  of the form  $(a, a)$  to every point on the line  $OE$  other than  $OE \wedge UV$ . In particular, let  $O = (0, 0)$ ,  $E = (1, 1)$ . For any optional point  $N$  not on the line  $UV$ , let  $N = (a, b)$  if  $NU \wedge OE = (b, b)$  and  $NV \wedge OE = (a, a)$ . In particular, points on the line  $OU$  have coordinates of the form  $(a, 0)$  and points on the line  $OV$  have coordinates of the form  $(0, b)$ . Since  $[(0, 0) \vee (1, m)] \wedge UV$  of  $UV$ ,  $U = (0)$ .  $OE \wedge UV = [(0, 0) \vee (1, 1)] \wedge UV$ , and  $OE \wedge UV = (1)$ . Let  $V = (\infty)$  for point  $V$  of  $UV$ , such that  $\infty \notin S$ .

### 1.4.2. Coordinatization of Lines

Let us assign the coordinate  $[m, k]$  to the line that does not pass through the point  $V = (\infty)$  and therefore has a common point  $(m)$  with  $UV$  and a common point  $(0, k)$  with  $OV$ ; let us assign the coordinate  $[k]$  to the line that passes through  $V = (\infty)$  and has a common point  $(k, 0)$  with the line  $OU = [0, 0]$ , and the coordinate  $[\infty]$  to the  $UV$  line.

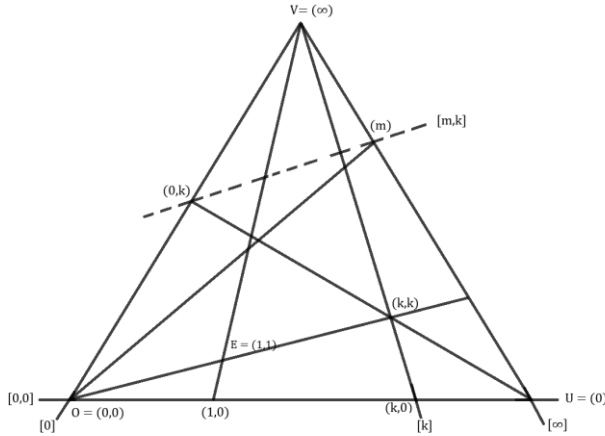


Figure 1.4.2.1

It is important to note that this coordinatization depends on the chosen quadrangle  $\{O, E, U, V\}$ .

### 1.4.3. Incidence Relation

For all  $m, k, x, y \in S$ :

$$(\infty) \circ [\infty], (\infty) \circ [k], (\infty) \circ [\infty], (\infty) \not\circ [m, k]$$

$$(x) \circ [\infty], (x) \not\circ [k], (x) \circ [m, k] \Leftrightarrow x = m$$

$$(x, y) \not\circ [\infty], (x, y) \circ [k] \Leftrightarrow x = k, (x, y) \circ [m, k] \Leftrightarrow y = T(m, x, k)$$

Considering the set  $S$  together with the ternary operation

$$T: S^3 \rightarrow S \ni T(m, x, k) = y \Leftrightarrow (x, y) \circ [m, k],$$

new concepts can be defined.

### 1.4.4 The Smallest Cartesian Group

Let  $F_5 = \{0, 1, 2, 3, 4\}$  be the set of residues modulo 5. With the operations  $+$  and  $\cdot$  defined as addition and multiplication modulo 5, respectively,  $(F_5, +, \cdot)$  forms a field.

Define  $S = F_5 \times F_5 = \{(x, y) \mid x, y \in F_5\}$  and introduce two binary operations  $\oplus$  and  $\otimes$  as follows:

$$(a, b) \oplus (c, d) = (a + c, b + d)$$

$$(a, b) \otimes (c, d) = \begin{cases} (a, b) * (c, d), & b = 0 \text{ or } (bc - ad)^2 - 2d^2 = 0, 1, 4 \\ - (a, b) * (c, d), & \text{otherwise} \end{cases}$$

$$(a, b) * (c, d) = \begin{cases} (ac, ad), & b = 0 \\ (ac - b^{-1}d(a^2 - 2), bc - ad) & b \neq 0 \end{cases}.$$

Thus, the system  $(S, \oplus, \otimes)$  forms a Cartesian group.

The multiplication table of the second operation can be easily calculated as follows:

$\otimes$	00	01	02	03	04	10	11	12	13	14	20	21	22	23	24	30	31	32	33	34	40	41	42	43	44
00	00	00	00	00	00	00	00	00	00	00	00	00	00	00	00	00	00	00	00	00	00	00	00	00	00
01	00	30	10	40	20	01	21	14	44	31	02	33	42	12	23	03	32	43	13	22	04	24	11	41	34
02	00	40	30	20	10	02	43	22	32	13	04	14	31	21	44	01	11	34	24	41	03	42	23	33	12
03	00	10	20	30	40	03	12	33	23	42	01	41	24	34	11	04	44	21	31	14	02	13	32	22	43
04	00	20	40	10	30	04	34	41	11	24	03	22	13	43	32	02	23	12	42	33	01	31	44	14	21
10	00	01	02	03	04	10	11	12	13	14	20	21	22	23	24	30	31	32	33	34	40	41	42	43	44
11	00	14	23	32	41	11	30	21	43	03	22	31	10	01	42	33	13	04	40	24	44	02	12	34	20
12	00	34	13	42	21	12	41	30	01	22	24	02	32	44	10	31	40	11	23	03	43	33	04	20	14
13	00	24	43	12	31	13	23	04	30	44	21	10	41	33	03	34	02	22	14	40	42	11	20	01	32

14	00 44 33 22 11 14 02 42 24 30 23 43 04 10 34 32 21 40 01 12 41 20 31 13 03
20	00 02 04 01 03 20 22 24 21 23 40 42 44 41 43 10 12 14 11 13 30 32 34 31 33
21	00 22 44 11 33 21 04 32 40 12 42 30 03 24 14 13 41 31 02 20 34 43 10 23 01
22	00 12 24 31 43 22 40 03 14 34 44 23 30 13 01 11 04 42 20 32 33 21 41 02 10
23	00 42 34 21 13 23 31 11 02 40 41 04 12 30 22 14 33 20 43 01 32 10 03 44 24
24	00 32 14 41 23 24 13 40 33 01 43 11 21 02 30 12 20 03 34 44 31 04 22 10 42
30	00 03 01 04 02 30 33 31 34 32 10 13 11 14 12 40 43 41 44 42 20 23 21 24 22
31	00 23 41 14 32 31 42 10 22 04 12 44 34 03 20 43 30 02 21 11 24 01 33 40 13
32	00 13 21 34 42 32 24 44 03 10 14 01 43 20 33 41 22 30 12 04 23 40 02 11 31
33	00 43 31 24 12 33 10 02 41 21 11 32 20 42 04 44 01 13 30 23 22 34 14 03 40
34	00 33 11 44 22 34 01 23 10 43 13 20 02 31 41 42 14 24 03 30 21 12 40 32 04
40	00 04 03 02 01 40 44 43 42 41 30 34 33 32 31 20 24 23 22 21 10 14 13 12 11
41	00 11 22 33 44 41 03 13 31 20 32 12 01 40 21 23 34 10 04 43 14 30 24 42 02
42	00 31 12 43 24 42 32 01 20 11 34 40 14 22 02 21 03 33 41 10 13 44 30 04 23
43	00 21 42 13 34 43 14 20 04 33 31 03 23 11 40 24 10 44 32 02 12 22 01 30 41
44	00 41 32 23 14 44 20 34 12 02 33 24 40 04 13 22 42 01 10 31 11 03 43 21 30

### ***1.5. Construction of a Subplane of order 5 of Cartesian Group Plane $P_2S$ :***

A subplane order of 5 of the Cartesian group plane order of 25, whose points and lines are coordinated with the elements of S, was obtained as follows [1].

#### **I) Points of the Plane**

$((0, 0), (0, 0)), ((0, 0), (1, 0)), ((0, 0), (2, 0)), ((0, 0), (3, 0)), ((0, 0), (4, 0)),$   
 $((0, 0))$   
 $((1, 0), (0, 0)), ((1, 0), (1, 0)), ((1, 0), (2, 0)), ((1, 0), (3, 0)), ((1, 0), (4, 0)),$   
 $((1, 0))$   
 $((2, 0), (0, 0)), ((2, 0), (1, 0)), ((2, 0), (2, 0)), ((2, 0), (3, 0)), ((2, 0), (4, 0)),$   
 $((2, 0))$   
 $((3, 0), (0, 0)), ((3, 0), (1, 0)), ((3, 0), (2, 0)), ((3, 0), (3, 0)), ((3, 0), (4, 0)),$   
 $((3, 0))$   
 $((4, 0), (0, 0)), ((4, 0), (1, 0)), ((4, 0), (2, 0)), ((4, 0), (3, 0)), ((4, 0), (4, 0)),$   
 $((4, 0))$

$(\infty)$



## II) Lines of the Plane

$[(0, 0), (0, 0)], [(0, 0), (1, 0)], [(0, 0), (2, 0)], [(0, 0), (3, 0)], [(0, 0), (4, 0)],$   
 $[(0, 0)]$   
 $[(1, 0), (0, 0)], [(1, 0), (1, 0)], [(1, 0), (2, 0)], [(1, 0), (3, 0)], [(1, 0), (4, 0)],$   
 $[(1, 0)]$   
 $[(2, 0), (0, 0)], [(2, 0), (1, 0)], [(2, 0), (2, 0)], [(2, 0), (3, 0)], [(2, 0), (4, 0)],$   
 $[(2, 0)]$   
 $[(3, 0), (0, 0)], [(3, 0), (1, 0)], [(3, 0), (2, 0)], [(3, 0), (3, 0)], [(3, 0), (4, 0)],$   
 $[(3, 0)]$   
 $[(4, 0), (0, 0)], [(4, 0), (1, 0)], [(4, 0), (2, 0)], [(4, 0), (3, 0)], [(4, 0), (4, 0)],$   
 $[(4, 0)]$

$[(\infty)]$

## III) Which Points Lie on Which Lines

$[(0, 0), (0, 0)]:$	$((0, 0), (0, 0)), ((1, 0), (0, 0)), ((2, 0), (0, 0)), ((3, 0), (0, 0)), ((4, 0), (0, 0)), ((0, 0))$
$[(0, 0), (1, 0)]:$	$((0, 0), (1, 0)), ((1, 0), (1, 0)), ((2, 0), (1, 0)), ((3, 0), (1, 0)), ((4, 0), (1, 0)), ((0, 0))$
$[(0, 0), (2, 0)]:$	$((0, 0), (2, 0)), ((1, 0), (2, 0)), ((2, 0), (2, 0)), ((3, 0), (2, 0)), ((4, 0), (2, 0)), ((0, 0))$
$[(0, 0), (3, 0)]:$	$((0, 0), (3, 0)), ((1, 0), (3, 0)), ((2, 0), (3, 0)), ((3, 0), (3, 0)), ((4, 0), (3, 0)), ((0, 0))$
$[(0, 0), (4, 0)]:$	$((0, 0), (4, 0)), ((1, 0), (4, 0)), ((2, 0), (4, 0)), ((3, 0), (4, 0)), ((4, 0), (4, 0)), ((0, 0))$
$[(1, 0), (0, 0)]:$	$((0, 0), (0, 0)), ((1, 0), (1, 0)), ((2, 0), (2, 0)), ((3, 0), (3, 0)), ((4, 0), (4, 0)), ((1, 0))$
$[(1, 0), (1, 0)]:$	$((0, 0), (1, 0)), ((1, 0), (2, 0)), ((2, 0), (3, 0)), ((3, 0), (4, 0)), ((4, 0), (0, 0)), ((1, 0))$
$[(1, 0), (2, 0)]:$	$((0, 0), (2, 0)), ((1, 0), (3, 0)), ((2, 0), (4, 0)), ((3, 0), (0, 0)), ((4, 0), (1, 0)), ((1, 0))$
$[(1, 0), (3, 0)]:$	$((0, 0), (3, 0)), ((1, 0), (4, 0)), ((2, 0), (0, 0)), ((3, 0), (1, 0)), ((4, 0), (2, 0)), ((1, 0))$
$[(1, 0), (4, 0)]:$	$((0, 0), (4, 0)), ((1, 0), (0, 0)), ((2, 0), (1, 0)), ((3, 0), (2, 0)), ((4, 0), (3, 0)), ((1, 0))$
$[(2, 0), (0, 0)]:$	$((0, 0), (0, 0)), ((1, 0), (2, 0)), ((3, 0), (1, 0)), ((2, 0), (4, 0)), ((4, 0), (3, 0)), ((2, 0))$
$[(2, 0), (1, 0)]:$	$((0, 0), (1, 0)), ((1, 0), (3, 0)), ((2, 0), (0, 0)), ((3, 0), (2, 0)), ((4, 0), (4, 0)), ((2, 0))$
$[(2, 0), (2, 0)]:$	$((0, 0), (2, 0)), ((1, 0), (4, 0)), ((2, 0), (1, 0)), ((3, 0), (3, 0)), ((4, 0), (0, 0)), ((2, 0))$
$[(2, 0), (3, 0)]:$	$((0, 0), (3, 0)), ((1, 0), (0, 0)), ((2, 0), (2, 0)), ((3, 0), (4, 0)), ((4, 0), (1, 0)), ((2, 0))$
$[(2, 0), (4, 0)]:$	$((0, 0), (4, 0)), ((1, 0), (1, 0)), ((2, 0), (3, 0)), ((3, 0), (0, 0)), ((4, 0), (2, 0)), ((2, 0))$
$[(3, 0), (0, 0)]:$	$((0, 0), (0, 0)), ((3, 0), (4, 0)), ((2, 0), (1, 0)), ((4, 0), (2, 0)), ((4, 0), (3, 0)), ((3, 0))$
$[(3, 0), (1, 0)]:$	$((0, 0), (1, 0)), ((1, 0), (4, 0)), ((2, 0), (2, 0)), ((3, 0), (0, 0)), ((4, 0), (3, 0)), ((3, 0))$
$[(3, 0), (2, 0)]:$	$((0, 0), (2, 0)), ((1, 0), (0, 0)), ((2, 0), (3, 0)), ((3, 0), (1, 0)), ((4, 0), (4, 0)), ((3, 0))$
$[(3, 0), (3, 0)]:$	$((0, 0), (3, 0)), ((1, 0), (1, 0)), ((2, 0), (4, 0)), ((3, 0), (2, 0)), ((4, 0), (0, 0)), ((3, 0))$
$[(3, 0), (4, 0)]:$	$((0, 0), (4, 0)), ((1, 0), (2, 0)), ((2, 0), (0, 0)), ((3, 0), (3, 0)), ((4, 0), (1, 0)), ((3, 0))$
$[(4, 0), (0, 0)]:$	$((0, 0), (0, 0)), ((1, 0), (4, 0)), ((2, 0), (3, 0)), ((3, 0), (2, 0)), ((4, 0), (1, 0)), ((4, 0))$
$[(4, 0), (1, 0)]:$	$((0, 0), (1, 0)), ((1, 0), (0, 0)), ((2, 0), (4, 0)), ((3, 0), (3, 0)), ((4, 0), (2, 0)), ((4, 0))$
$[(4, 0), (2, 0)]:$	$((0, 0), (2, 0)), ((1, 0), (1, 0)), ((2, 0), (0, 0)), ((3, 0), (4, 0)), ((4, 0), (3, 0)), ((4, 0))$
$[(4, 0), (3, 0)]:$	$((0, 0), (3, 0)), ((1, 0), (2, 0)), ((2, 0), (1, 0)), ((3, 0), (0, 0)), ((4, 0), (4, 0)), ((4, 0))$
$[(4, 0), (4, 0)]:$	$((0, 0), (4, 0)), ((1, 0), (3, 0)), ((2, 0), (2, 0)), ((3, 0), (1, 0)), ((4, 0), (0, 0)), ((4, 0))$
$[(0, 0)]:$	$((0, 0), (0, 0)), ((0, 0), (1, 0)), ((0, 0), (2, 0)), ((0, 0), (3, 0)), ((0, 0), (4, 0)), (\infty)$
$[(1, 0)]:$	$((1, 0), (0, 0)), ((1, 0), (1, 0)), ((1, 0), (2, 0)), ((1, 0), (3, 0)), ((1, 0), (4, 0)), (\infty)$
$[(2, 0)]:$	$((2, 0), (0, 0)), ((2, 0), (1, 0)), ((2, 0), (2, 0)), ((2, 0), (3, 0)), ((2, 0), (4, 0)), (\infty)$
$[(3, 0)]:$	$((3, 0), (0, 0)), ((3, 0), (1, 0)), ((3, 0), (2, 0)), ((3, 0), (3, 0)), ((3, 0), (4, 0)), (\infty)$
$[(4, 0)]:$	$((4, 0), (0, 0)), ((4, 0), (1, 0)), ((4, 0), (2, 0)), ((4, 0), (3, 0)), ((4, 0), (4, 0)), (\infty)$
$[\infty]:$	$((0, 0)), ((1, 0)), ((2, 0)), ((3, 0)), ((4, 0)), (\infty)$

## 1.6. Desargues Theorem

In this section, some Desargues configurations provided by the subplane given above will be given.

**Definition 1.6.1:** Let  $A, B, C, A', B', C'$  be any six points of a geometric structure. If  $A, B, C$  are not collinear, the set  $\{A, B, C\}$  is called a triangle. Let  $\{A, B, C\}$  and  $\{A', B', C'\}$  be two triangles. Denote  $A$  and  $A', B$  and  $B', C$  and  $C'$  as corresponding vertices of the triangles. If there exists a point  $M$  such that the triples  $M, A, A'; M, B, B';$  and  $M, C, C'$  are collinear, the triangles are said to be perspective from  $M$ . Furthermore, the point  $M$  is called the *center of perspectivity*, and the pairs of lines  $AB$  and  $A'B', AC$  and  $A'C', BC$  and  $B'C'$  are called corresponding sides of the triangles. If the intersection points  $P = AB \cap A'B', Q = AC \cap A'C', R = BC \cap B'C'$  of the corresponding sides are collinear, the line on which they lie is called the *axis of perspectivity*. Two triangles that have an axis of perspectivity  $e$  are said to be *perspective from the axis  $e$* .

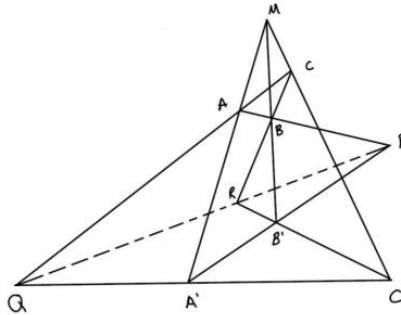


Figure 1.6.1

Now, let us give a theorem showing that Desargues Theorem cannot be derived from the axioms P1, P2, P3 ; in other words, it is independent of these axioms and can therefore hold in any projective plane.

### SOME EXAPLES OF DESARGUES THEOREM IN THE SMALLEST CARTESIAN GROUP PLANE

**Theorem 1.6.1:** Let  $F$  be any field. Then all projective planes  $\mathbb{P}_2F$  are Desarguesian.

In this section, we give codes for the calculation of Desargues theorem in the projective plane of order 25, which is the smallest Cartesian group with

algebraic structure. In other words, we present examples showing that Desargues theorem is valid in this projective plane.

## 2.1 Python Code to Find Desargues Configurations in $P_2S$

```

from ast import literal_eval
# Table
table = {
    "[ (0,0),(0,0) ]": [ ((0,0),(0,0)), ((1,0),(0,0)), ((2,0),(0,0)), ((3,0),(0,0)),
    ((4,0),(0,0)), ((0,0)) ],
    "[ (0,0),(1,0) ]": [ ((0,0),(1,0)), ((1,0),(1,0)), ((2,0),(1,0)), ((3,0),(1,0)),
    ((4,0),(1,0)), ((0,0)) ],
    "[ (0,0),(2,0) ]": [ ((0,0),(2,0)), ((1,0),(2,0)), ((2,0),(2,0)), ((3,0),(2,0)),
    ((4,0),(2,0)), ((0,0)) ],
    "[ (0,0),(3,0) ]": [ ((0,0),(3,0)), ((1,0),(3,0)), ((2,0),(3,0)), ((3,0),(3,0)),
    ((4,0),(3,0)), ((0,0)) ],
    "[ (0,0),(4,0) ]": [ ((0,0),(4,0)), ((1,0),(4,0)), ((2,0),(4,0)), ((3,0),(4,0)),
    ((4,0),(4,0)), ((0,0)) ],
    "[ (1,0),(0,0) ]": [ ((0,0),(0,0)), ((1,0),(1,0)), ((2,0),(2,0)), ((3,0),(3,0)),
    ((4,0),(4,0)), ((1,0)) ],
    "[ (1,0),(1,0) ]": [ ((0,0),(1,0)), ((1,0),(2,0)), ((2,0),(3,0)), ((3,0),(4,0)),
    ((4,0),(0,0)), ((1,0)) ],
    "[ (1,0),(2,0) ]": [ ((0,0),(2,0)), ((1,0),(3,0)), ((2,0),(4,0)), ((3,0),(0,0)),
    ((4,0),(1,0)), ((1,0)) ],
    "[ (1,0),(3,0) ]": [ ((0,0),(3,0)), ((1,0),(4,0)), ((2,0),(0,0)), ((3,0),(1,0)),
    ((4,0),(2,0)), ((1,0)) ],
    "[ (1,0),(4,0) ]": [ ((0,0),(4,0)), ((1,0),(0,0)), ((2,0),(1,0)), ((3,0),(2,0)),
    ((4,0),(3,0)), ((1,0)) ],
    "[ (2,0),(0,0) ]": [ ((0,0),(0,0)), ((1,0),(2,0)), ((3,0),(1,0)), ((2,0),(4,0)),
    ((4,0),(3,0)), ((2,0)) ],
    "[ (2,0),(1,0) ]": [ ((0,0),(1,0)), ((1,0),(3,0)), ((2,0),(0,0)), ((3,0),(2,0)),
    ((4,0),(4,0)), ((2,0)) ],
    "[ (2,0),(2,0) ]": [ ((0,0),(2,0)), ((1,0),(4,0)), ((2,0),(1,0)), ((3,0),(3,0)),
    ((4,0),(0,0)), ((2,0)) ],
    "[ (2,0),(3,0) ]": [ ((0,0),(3,0)), ((1,0),(0,0)), ((2,0),(2,0)), ((3,0),(4,0)),
    ((4,0),(1,0)), ((2,0)) ],
    "[ (2,0),(4,0) ]": [ ((0,0),(4,0)), ((1,0),(1,0)), ((2,0),(3,0)), ((3,0),(0,0)),
    ((4,0),(2,0)), ((2,0)) ],
    "[ (3,0),(0,0) ]": [ ((0,0),(0,0)), ((3,0),(4,0)), ((2,0),(1,0)), ((4,0),(2,0)),
    ((4,0),(3,0)), ((3,0)) ],
    "[ (3,0),(1,0) ]": [ ((0,0),(1,0)), ((1,0),(4,0)), ((2,0),(2,0)), ((3,0),(0,0)),
    ((4,0),(3,0)), ((3,0)) ],
    "[ (3,0),(2,0) ]": [ ((0,0),(2,0)), ((1,0),(0,0)), ((2,0),(3,0)), ((3,0),(1,0)),
    ((4,0),(4,0)), ((3,0)) ],

```

```

    "[ (3,0),(3,0) ]": [ ((0,0),(3,0)), ((1,0),(1,0)), ((2,0),(4,0)), ((3,0),(2,0)),
    ((4,0),(0,0)), ((3,0)) ],
    "[ (3,0),(4,0) ]": [ ((0,0),(4,0)), ((1,0),(2,0)), ((2,0),(0,0)), ((3,0),(3,0)),
    ((4,0),(1,0)), ((3,0)) ],
    "[ (4,0),(0,0) ]": [ ((0,0),(0,0)), ((1,0),(4,0)), ((2,0),(3,0)), ((3,0),(2,0)),
    ((4,0),(1,0)), ((4,0)) ],
    "[ (4,0),(1,0) ]": [ ((0,0),(1,0)), ((1,0),(0,0)), ((2,0),(4,0)), ((3,0),(3,0)),
    ((4,0),(2,0)), ((4,0)) ],
    "[ (4,0),(2,0) ]": [ ((0,0),(2,0)), ((1,0),(1,0)), ((2,0),(0,0)), ((3,0),(4,0)),
    ((4,0),(3,0)), ((4,0)) ],
    "[ (4,0),(3,0) ]": [ ((0,0),(3,0)), ((1,0),(2,0)), ((2,0),(1,0)), ((3,0),(0,0)),
    ((4,0),(4,0)), ((4,0)) ],
    "[ (4,0),(4,0) ]": [ ((0,0),(4,0)), ((1,0),(3,0)), ((2,0),(2,0)), ((3,0),(1,0)),
    ((4,0),(0,0)), ((4,0)) ],
    "[ (0,0) ]": [ ((0,0),(0,0)), ((0,0),(1,0)), ((0,0),(2,0)), ((0,0),(3,0)),
    ((0,0),(4,0)), float('inf') ],
    "[ (1,0) ]": [ ((1,0),(0,0)), ((1,0),(1,0)), ((1,0),(2,0)), ((1,0),(3,0)),
    ((1,0),(4,0)), float('inf') ],
    "[ (2,0) ]": [ ((2,0),(0,0)), ((2,0),(1,0)), ((2,0),(2,0)), ((2,0),(3,0)),
    ((2,0),(4,0)), float('inf') ],
    "[ (3,0) ]": [ ((3,0),(0,0)), ((3,0),(1,0)), ((3,0),(2,0)), ((3,0),(3,0)),
    ((3,0),(4,0)), float('inf') ],
    "[ (4,0) ]": [ ((4,0),(0,0)), ((4,0),(1,0)), ((4,0),(2,0)), ((4,0),(3,0)),
    ((4,0),(4,0)), float('inf') ],
    "[ ∞ ]": [ ((0,0)), ((1,0)), ((2,0)), ((3,0)), ((4,0)), float('inf') ]
}

```

# Safe function for parsing point input

```

def parse_input(point_str):
    point_str = point_str.replace(" ", "")
    return literal_eval(point_str)

```

# Check if a point exists in a table row

```

def point_exists(point, row_points):
    for n in row_points:
        if n != float('inf') and n == point:
            return True
    return False

```

# Get points from user

```

A = parse_input(input("Point A: "))
B = parse_input(input("Point B: "))
C = parse_input(input("Point C: "))
A_ = parse_input(input("Point A': "))

```

```

B_ = parse_input(input("Point B: "))
C_ = parse_input(input("Point C: "))

# Find line pairs
line_pairs = [("AB", A, B), ("A'B'", A_, B_), ("AC", A, C), ("A'C'", A_, C_),
("B'C", B, C), ("B'C'", B_, C_)]
rows = {}

for name, point1, point2 in line_pairs:
    found = False
    for row, points in table.items():
        if point_exists(point1, points) and point_exists(point2, points):
            rows[name] = row
            print(f"Line {name}: {row}")
            found = True
            break
    if not found:
        print(f"Line {name} not found.")

# Find common points
def all_common_points(points1, points2):
    return tuple(point for point in points1 if point_exists(point, points2))

P_list = all_common_points(table[rows["AB"]], table[rows["A'B'"]])
Q_list = all_common_points(table[rows["AC"]], table[rows["A'C'"]])
R_list = all_common_points(table[rows["BC"]], table[rows["B'C'"]])

# Find intersection rows of P, Q, R
def intersection_rows(P_list, Q_list, R_list):
    result_rows = []

    if P_list == Q_list and P_list != R_list:
        for row, points in table.items():
            if any(point_exists(n, points) for n in P_list) and any(point_exists(n,
points) for n in R_list):
                result_rows.append(row)
    elif P_list == R_list and P_list != Q_list:
        for row, points in table.items():
            if any(point_exists(n, points) for n in P_list) and any(point_exists(n,
points) for n in Q_list):
                result_rows.append(row)
    elif Q_list == R_list and Q_list != P_list:
        for row, points in table.items():

```

```

        if any(point_exists(n, points) for n in Q_list) and any(point_exists(n,
points) for n in P_list):
            result_rows.append(row)
        elif P_list == Q_list == R_list:
            for row, points in table.items():
                if all(point_exists(n, points) for n in P_list):
                    result_rows.append(row)
        else:
            for row, points in table.items():
                if (any(point_exists(n, points) for n in P_list) and
                    any(point_exists(n, points) for n in Q_list) and
                    any(point_exists(n, points) for n in R_list)):
                    result_rows.append(row)
    return result_rows

common_rows = intersection_rows(P_list, Q_list, R_list)

# Print common points
def print_commons(label, commons):
    if len(commons) == 1:
        print(f'{label} common points: {commons[0]}')
    else:
        print(f'{label} common points: {commons}')

print_commons("P", P_list)
print_commons("Q", Q_list)
print_commons("R", R_list)

if common_rows:
    print(f'Intersection rows of P, Q, R: {common_rows}')
else:
    print("No intersection of P, Q, R")

```

This code assigns single points in sequence to three lines passing through the center. Each of these three lines contains two points. A, A' are the points on the first line, B, B' are the points on the second line, and C, C' are the points on the third line. The code assigns these points in order according to the names of the lines. It then determines the lines AB, AC, BC, A'B', A'C', B'C'. Next, the intersection of AB and A'B' gives us point P. The intersection of AC and A'C' gives us point Q. The intersection of BC and B'C' gives us point R. After obtaining these, the code provides the line on which points P, Q, R intersect. As a result, it is found that the configuration is perspective from the center.

**Example 2.1.1:** A: ((0, 0), (0, 0)) A': ((0, 0), (1, 0)) B: ((1, 0), (0, 0)) B': ((1, 0), (1, 0)) C: ((2, 0), (2, 0)) C': ((2, 0), (3, 0))  
 AB: [(0,0), (0,0)]  
 A'B': [(0,0), (1,0)]  
 AC: [(1,0), (0,0)]  
 A'C': [(1,0), (1,0)]  
 BC: [(2,0), (3,0)]  
 B'C': [(2,0), (4,0)]  
 P (AB  $\cap$  A'B'): ((0,0))  
 Q (AC  $\cap$  A'C'): ((1,0))  
 R (BC  $\cap$  B'C'): ((2,0))  
 P, Q, R common rows: [ $\infty$ ]

**Example 2.1.2:** A: ((0, 0), (0, 0)) A': ((0, 0), (1, 0)) B: ((1, 0), (0, 0)) B': ((1, 0), (1, 0)) C: ((2, 0), (3, 0)) C': ((2, 0), (4, 0))  
 AB: [(0,0), (0,0)]  
 A'B': [(0,0), (1,0)]  
 AC: [(4,0), (0,0)]  
 A'C': [(4,0), (1,0)]  
 BC: [(3,0), (2,0)]  
 B'C': [(3,0), (3,0)]  
 P (AB  $\cap$  A'B'): ((0,0))  
 Q (AC  $\cap$  A'C'): ((4,0))  
 R (BC  $\cap$  B'C'): ((3,0))  
 P, Q, R common rows: [ $\infty$ ]

**Example 2.1.3:** A: ((2, 0), (4, 0)) A': ((2, 0), (3, 0)) B: ((3, 0), (4, 0)) B': ((3, 0), (3, 0)) C: ((4, 0), (1, 0)) C': ((4, 0), (0, 0))  
 AB: [(0,0), (4,0)]  
 A'B': [(0,0), (3,0)]  
 AC: [(1,0), (2,0)]  
 A'C': [(1,0), (1,0)]  
 BC: [(2,0), (3,0)]  
 B'C': [(2,0), (2,0)]  
 P (AB  $\cap$  A'B'): ((0,0))  
 Q (AC  $\cap$  A'C'): ((1,0))  
 R (BC  $\cap$  B'C'): ((2,0))  
 P, Q, R common rows: [ $\infty$ ]

**Example 2.1.4:** A: ((2, 0), (4, 0)) A': ((2, 0), (3, 0)) B: ((3, 0), (4, 0)) B': ((3, 0), (3, 0)) C: ((4, 0), (2, 0)) C': ((4, 0), (1, 0))  
 AB: [(0,0), (4,0)]  
 A'B': [(0,0), (3,0)]  
 AC: [(4,0), (1,0)]

$A'C': [(4,0), (0,0)]$   
 $BC: [(3,0), (0,0)]$   
 $B'C': [(3,0), (4,0)]$   
 $P(AB \cap A'B'): ((0,0))$   
 $Q(AC \cap A'C'): ((4,0))$   
 $R(BC \cap B'C'): ((3,0))$   
 $P, Q, R \text{ common rows: } [\infty]$

## RESULTS

In this study, the validity of Desargues Theorem in the Cartesian group plane of order 25 was examined in detail, and verifications were made using various examples and Python code. The analyses demonstrated that the algebraic structure of Cartesian group planes is compatible with projective geometry and that classical geometric theorems are also valid in these structures.

The concept of central perspective, which forms the basis of Desargues's Theorem, is of particular importance in this study. Analyses based on this principle have shown that if triangles are in perspective from a single point, their corresponding sides are also in perspective on a line. Applications demonstrated that this property holds for the Cartesian group plane of order 25, thus proving that the plane is Desarguesian.

This result demonstrates that the Cartesian group plane in question presents a consistent structure not only algebraically but also geometrically, satisfying the axioms of classical projective geometry. In addition, this study sheds light on the relationship between algebraic structures and geometric concepts and provides a basis for more comprehensive research on finite geometries.

So Python Code was written for examples that show that this projective plane is a-a transitive.

## REFERENCES

- [1] Akça Z. (1991). The construction of the cartesian group plane of order 25. MSc, University of Anadolu, Eskişehir, Turkey.
- [2] Akça Z, Günlü İ. (2012). On the  $(k,3)$ -arcs of  $CPG(2,25,5)$ . Anadolu University Journal of Science and-B Theoretical Sciences, 2 - 1 : 21-27.
- [3] Bayar A, Akça Z, Ekmekçi S. (2022). On Embedding the Projective Plane  $PG(2,4)$  to the Projective Space  $P(4,4)$ . New Trends in Mathematical Sciences, 10- 4: 142–150.



[4] Ekmekçi S, Bayar A, Akça Z. (2022). On The Projective Planes in Projective Space  $PG(4,4)$ . Erciyes Üniversitesi Fen Bilimleri Enstitüsü Fen Bilimleri Dergisi, 38- 3: 519–524.

[5] Ekmekçi S, Bayar A, Altıntaş Kahrıman E, Akça Z. (2016). On the Complete  $(k,2)$ -arcs of the Hall plane of order 9. International Journal of Advanced Research in Computer Science and Software Engineering, 6-10: 282–288.

[6] Kaya, R. (2005). *Projektif Geometri*, ESOGU Yayını

[7] Panella, G. (1965). Una Classe Di Sistemi Cartesiani. Atti Della Accademia Nazionale Lincei Rendiconti, 38; 480-485.



# **A Quick Overview on Electronic Structure, Solvatochromic Behavior and Optoelectronic Applications of Schiff Bases**

**Yadigar GÜLSEVEN SIDIR**

Prof. Dr.; Bitlis Eren University, Faculty of Arts and Science, Department of Physics,  
[yadigar.gulseven@gmail.com](mailto:yadigar.gulseven@gmail.com), ygsidir@beu.edu.tr ORCID No: 0000-0002-5329-2815

## ABSTRACT

Schiff bases, containing the characteristic azomethine ( $-\text{C}=\text{N}-$ ) linkage, represent a versatile class of compounds with significant importance in coordination chemistry, spectroscopy, and optoelectronic materials. Their structural flexibility, ease of synthesis, and strong affinity for metal ions make them excellent candidates for exploring relationships between molecular structure, electronic configuration, and photophysical behavior. The chapter discusses the fundamental aspects of Schiff bases, including tautomerism between phenol-imine and keto-amine forms, and the influence of chelation and solvent environment on their optical properties. Quantum chemical approaches based on Density Functional Theory (DFT) are used to elucidate electronic structures, frontier molecular orbitals (HOMO-LUMO), chemical reactivity parameters, and molecular electrostatic potential (MEP) surfaces. The solvatochromic and fluorescence behaviors are analyzed through UV-Vis spectra and linear solvation energy relationships, highlighting the role of solvent polarity in modulating ground- and excited-state dipole moments. Photophysical processes such as Intramolecular Charge Transfer (ICT), Excited-State Intramolecular Proton Transfer (ESIPT), and Photo-Induced Electron Transfer (PET) are emphasized as key mechanisms determining emission characteristics. Furthermore, the potential applications of Schiff bases and their metal complexes in nonlinear optical (NLO) devices, organic light-emitting diodes (OLEDs), organic solar cells (OSCs), and fluorescent metal-ion sensors are explored.

*Keywords – Schiff bases; DFT; tautomerism; solvatochromism; ICT; ESIPT; PET; optoelectronic applications*

---

## INTRODUCTION- Basic Chemistry and Importance of Schiff Bases

Schiff bases, first synthesized in 1864 by German chemist Hugo Schiff, are compounds containing an imine or azomethine functional group at their core (Schiff, 1864; Adesina, 2022). The imine group confers unique chemical and physicochemical versatility to the structure. Schiff bases have a wide range of applications, from organic synthesis to medicinal chemistry, due to their ease of synthesis, high thermal stability, and ability to coordinate with metal ions as ligands (Uddin et al., 2025; Madaboina and Kamala, 2025; Kagatkar and Sunil, 2021). This review examines the unique properties of the imine nucleus, particularly those relevant to optical, electronic, and optoelectronic device applications.

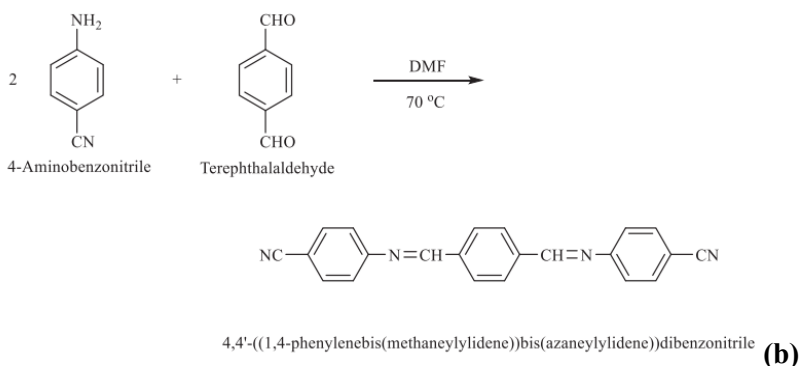
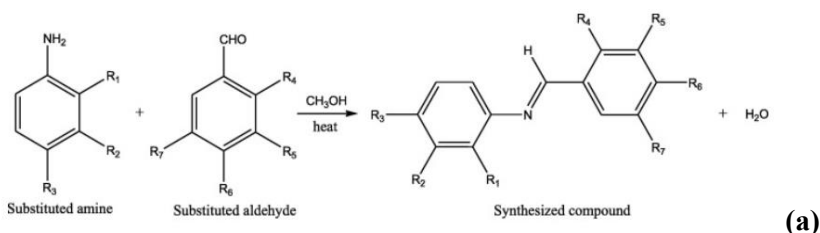


Figure 1. Synthesis Scheme of Schiff bases. (a) Gülseven Sıdır, 2022- (b) Udin, 2025.

### ***Tautomerism and Chelate Formation***

One of the most important structural features affecting the photophysical properties of Schiff bases is the keto-amine phenol-imine tautomeric equilibrium observed when the compound contains a hydroxyl group (Schiff, 1864; Kırca, Kaştaş, and Ersanlı, 2021; Užarević et al., 2010; Sıdır, Sıdır, and Berber, 2022).

The enol-imine form generally exhibits aromatic stability and involves intramolecular hydrogen bonding (Bhat et al., 2024).

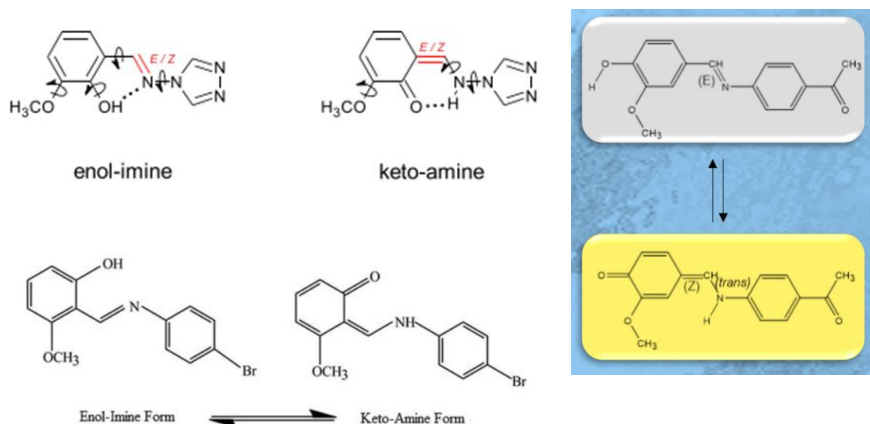


Figure 2. Enol-Imine and Keto-Amine Tautomeric Forms. (Sıdır, 2022; Sıdır, 2024; Bhat, 2024)

The keto-amine form, on the other hand, is characterized by intramolecular hydrogen bonding and can generally exhibit greater aromaticity (Flores-Leonar et al., 2011).

This tautomeric equilibrium is sensitive to environmental conditions such as solvent polarity and temperature (Atzin-Macedo et al., 2020). Additionally, Schiff bases can readily complex with metal ions. Coordination depends on the presence of heteroatoms such as oxygen, sulfur, and nitrogen, as well as the imine group. Due to the weak basic character of the group, the presence of a hydroxyl group that can readily donate a hydrogen atom is preferred for the formation of stable chelate rings in metal-Schiff base complexes (Flores-Leonar et al., 2011). These chelate complexes play important roles in optical, catalytic, and biological functions (Madaboina and Kamala, 2025).

## 2. ELECTRONIC STRUCTURE AND QUANTUM CHEMICAL ANALYSIS

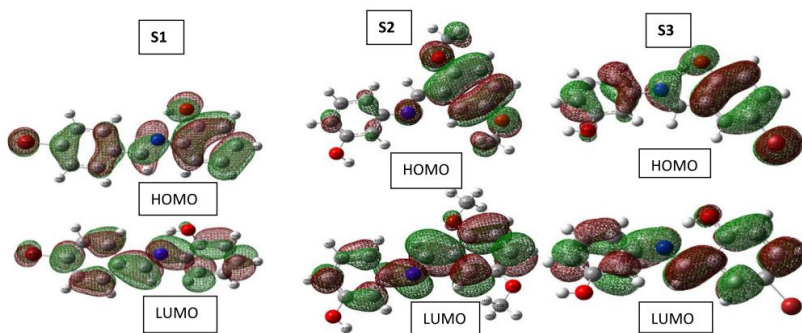
Understanding molecular optoelectronic properties relies on electronic structure analysis supported by quantum chemical methods such as Density Functional Theory (DFT) (Sıdır et al., 2019).

## 2.1. Frontier Molecular Orbitals (HOMO and LUMO)

The energy levels of the Highest Occupied Molecular Orbital (HOMO) and the Lowest Unoccupied Molecular Orbital (LUMO) determine the optoelectronic and chemical reactivity of a molecule (Delgado-Montiel et al., 2019).

The HOMO characterizes the molecule's ability to donate electrons (oxidation potential), while the LUMO characterizes its ability to accept electrons (reduction potential) (Adindu et al., 2023; Kourat et al., 2025).

**The HOMO-LUMO Gap:** This energy difference represents the lowest-energy electronic excitation, which determines the wavelengths at which the molecule absorbs light. In Schiff bases, narrow values indicate high chemical reactivity and easy polarizability (Mohamed et al., 2025; Al-Farraj and Mohammed, 2025; Shafieyoon, Mehdipour, and Mary, 2019).



S1:2-((4-bromobenzylidene)amino)phenol,

S2:3-((2, 5-dimethoxybenzylidene)amino)phenol,

S3:3-(5-bromo-2-hydro xybenzylideneamino)phenol

Figure 3: Frontier Molecular Orbital Distribution in a Typical Schiff Bases  
(Gülseven Sıdır, 2022)

DFT calculations show that the HOMO is generally located on electron-donating groups or conjugated nuclei, while the LUMO is located on electron-withdrawing groups (e.g., imine bonds (Mohamed et al., 2025) and This spatial separation facilitates the intramolecular charge transfer (ICT) process (Shafieyoon, Mehdipour, and Mary, 2019). Various theoretical studies have shown that basis sets such as DFT/B3LYP produce reliable results in the electronic structure analysis of Schiff bases. However, it has also been reported that functionals such as PBE0 can provide better mean absolute errors (MAE) in experimental correlations.

## **2.2. Chemical Reactivity and Molecular Electrostatic Potential (MEP)**

Chemical hardness, softness, and electrophilicity/nucleophilicity indices derived from frontier orbitals illuminate the reactivity profile of Schiff bases. Molecular Electrostatic Potential (MEP) maps visualize the electrophilic (positive potential, usually around atoms) and nucleophilic (negative potential, usually around electronegative atoms) regions of the molecule, which supports the binding ability and stability of the molecule (Ramasamy, 2022; Akbari, 2025).

## **3. OPTICAL PROPERTIES AND PHOTOPHYSICAL MECHANISMS**

The optical properties of Schiff bases can be easily tuned through their conjugated systems and heteroatom content, making them attractive for sensors and optoelectronic devices (Afrin et al., 2023).

### **3.1. UV-Vis Absorption and Emission**

The ultraviolet-visible (UV-Vis) spectra of Schiff bases typically exhibit four main bands (Afrin et al., 2023):

**High-Energy Bands:** Electronic transitions resulting from delocalization or transitions in the phenyl rings (Aroua et al., 2023).



**Low-Energy Bands:** Transitions resulting from conjugation between the imine system and aromatic rings (Santos et al., 2021).

**Transitions:** Weaker transitions resulting from bonded electrons in the azomethine group and are usually observed in certain solvents (Abdel Aziz and Abdel-Aziz, n.d.; Sıdır et al., 2017). Similar transitions are observed in the fluorescence spectrum, but the emission is affected by changes in the geometry and polarity of the molecule in the excited state (Santos et al., 2021).

### 3.2. Internal Photophysical Processes: ICT, ESIPT, and PET

Schiff bases can exhibit a variety of mechanisms underlying their optical response, making them vital for biosensing and light-emitting devices (Afrin et al., 2023).

**Intramolecular Charge Transfer (ICT):** In the excited state, electron density shifts from the donor to the acceptor. This process causes the excited-state dipole moment to be higher than the ground-state dipole moment, resulting in a large Stokes shift (Sıdır et al., 2022).

**Excited-State Intramolecular Proton Transfer (ESIPT):** This process is seen in Schiff bases containing hydrogen-bonded donor and acceptor groups, such as salicylimine (Joshi and Antonov, 2021). ESIPT prevents self-absorption by causing a large Stokes shift, improving fluorescence analysis (Joshi and Antonov, 2021).

**Photo-Induced Electron Transfer (PET):** This is a mechanism in which emission is quenched by the transfer of an electron from an excited state to an electron-donor group. Complexation with metal ions can block the PET process, causing a "turn-on" fluorescence response (Goshisht, Patra, and Tripathi, 2022). Complexation with copper ions can cause a quenching due to ICT (Goshisht, Patra, and Tripathi, 2022).

## 4. SOLVATOCHROMISM AND EXCITED STATE STRUCTURE

The color and emission of Schiff bases are highly dependent on the polarity of the solvent environment. This phenomenon, known as solvatochromism, results from the ground and excited states of molecules being stabilized to varying degrees by the solvent (Sıdır et al., 2022).

### *4.1. Solvatochromic Analysis Models*

Linear solvation energy relationship (LSER) methods are used for the quantitative analysis of solvatochromic shifts. The most commonly used models are (Sıdır, Sıdır, and Berber, 2022):

**Lippert-Mataga, Bakhshiev, and Reichardt Equations:** These equations are used to predict changes in the ground-state and excited-state dipole moments of a molecule using the relationship between the Stokes shift and the solvent polarity function (Sıdır et al., 2019).

**Kamlet-Abboud-Taft and Catalan Parameters:** These models are used to quantitatively investigate solvent-solute interactions, allowing, for example, to separate the relative effects of specific and nonspecific interactions such as hydrogen bonding, receptivity, and polarization (Sıdır et al., 2021).

These analyses confirm that the dipole moments of Schiff bases in the excited state are generally higher than in the ground state (Sıdır et al., 2022). For example, a large bathochromic shift in the emission spectrum from n-hexane to acetone indicates positive solvatochromism and a more polar excited state. This is attributed to the intramolecular charge transfer (ICT) process causing a change in the geometry and polarity of the molecule in the excited state (Santos et al., 2021). Chemical hardness, softness, and electrophilicity/nucleophilicity indices derived from frontier orbitals illuminate the reactivity profile of Schiff bases (Sıdır et al., 2017; Sıdır et al., 2022). Molecular Electrostatic Potential (MEP) maps visualize the

electrophilic (positive potential, usually around atoms) and nucleophilic (negative potential, usually around electronegative atoms such as and) regions of the molecule, which supports the binding ability and stability of the molecule.

## 5. OPTOELECTRONIC APPLICATIONS

Schiff bases and their metal complexes are being explored in a wide range of optoelectronic devices due to their excellent optical, thermal, and coordination properties (Goshisht, Patra, and Tripathi, 2022).

### 5.1. *Nonlinear Optical (NLO) Materials*

Schiff bases are promising candidates for nonlinear optical (NLO) devices; These devices are used in applications such as optical switching, frequency conversion, and optical computers (Arumugam et al., 2023).

**Push-Pull Structure:** High NLO properties are typically achieved through molecular engineering approaches by combining an electron-donating and an electron-withdrawing functional group along the conjugated backbone. This push-pull effect leads to high hyperpolarizability values.

**Theoretical Validation:** DFT calculations are used to predict the values of **22** with high accuracy, particularly with functionals such as CAM-B3LYP and M06-2X. This helps optimize the molecular design of optical switches and frequency converters, which are experimentally expensive (Arumugam et al., 2023).

### 5.2. *Organic Light Emitting Diodes (OLED) and Solar Cells (OSC)*

Schiff bases have potential applications as emitters, dopants, or hole-transporting materials in Organic Light Emitting Diodes (OLEDs) and as active layer components for Organic Solar Cells (OSCs) (Nowsherwan et al., 2024).

**OLED Eliminators:** Metal complexes such as Schiff bases have been shown to be promising emission materials in optoelectronic systems (Arumugam et al., 2023; Gusev et al., 2021). Fluorescent Schiff bases and their complexes have been used in blue-emitting OLED applications, and some devices have achieved high quantum efficiency and brightness. For high-efficiency OLEDs, materials with Thermally Activated Delayed Fluorescence or Phosphorescence mechanisms that can utilize triplet excitons are required (Adachi et al., 2001).

**OSC Applications:** For Organic Solar Cells, Schiff bases and their complexes can be used as active layer materials (Pan, 2024) or as hole-transporting layers (Anrango-Camacho et al., 2022). HTL materials should provide high hole-transport rates and close to the energy level of the donor . must have a specific energy level (Anrango-Camacho et al., 2022). Efficiency in OSCs depends on nanometer-scale morphology control of the donor-acceptor interface for exciton dissociation and charge transport efficiency (Peng et al., 2022).

### ***5.3. Fluorescent Sensors and Logic Gates***

Schiff bases have widespread applications as fluorescent chemical sensors for metal ion detection (Afrin et al., 2023).

**Selectivity and Sensitivity:** Due to their simple synthesis and ability to coordinate with metal ions, Schiff bases exhibit excellent selectivity, sensitivity, and fast response time toward metal ions. For example, some Schiff bases can detect ions such as and with low detection limits, which are essential for biological cell imaging and environmental monitoring (Afrin et al., 2023).

**Molecular Logic Devices:** The optical switching properties of Schiff bases have also been applied to the construction of molecular-level logic gates and molecular keypads using chemical inputs (Goshisht, Patra, and Tripathi, 2022).

## 6. CONCLUSION AND FUTURE PERSPECTIVES

Schiff bases play a critical role in optoelectronic materials and sensors due to the versatility and flexibility of the azomethine group as a ligand. Precise tuning of their electronic structures (HOMO/LUMO) and photophysical mechanisms (ICT, ESIPT, PET) through structural modification has led to the development of optical and It allows optoelectronic properties to be optimized. Future studies should focus on the use of Schiff bases and their complexes as donors for highly efficient and stable blue OLEDs, or as internal stabilizers or materials in perovskite solar cells. The use of artificial intelligence tools, such as structural deep learning, is important for exploring the chemical space and predicting new Schiff bases with desired properties, which will accelerate the discovery process. Schiff bases continue to attract considerable attention due to their structural diversity, tunable electronic configurations, and remarkable optical and coordination properties. Their ability to undergo tautomeric transformations and to form stable metal complexes provides a flexible platform for modulating photophysical behavior and optoelectronic performance. The interplay between molecular structure, solvent environment, and electronic distribution governs their solvatochromic and emission characteristics, which can be finely adjusted through rational molecular design. Advances in Density Functional Theory (DFT) and related computational methods have provided deep insights into the frontier molecular orbitals, charge-transfer processes, and excited-state mechanisms such as ICT, ESIPT, and PET. These theoretical approaches have become indispensable for predicting and optimizing the properties of new Schiff base systems prior to experimental validation. In the context of materials science, Schiff bases and their metal complexes offer great promise for nonlinear optical (NLO) applications, organic light-emitting diodes (OLEDs), organic solar cells (OSCs), and fluorescent chemical sensors. The design of donor–acceptor frameworks and push–pull architectures can further enhance their hyperpolarizability and charge-transport efficiency. Future research should focus on developing highly efficient and stable Schiff base derivatives for blue-emitting OLEDs, perovskite solar cells, and molecular sensing platforms. The integration of artificial intelligence and machine learning approaches will be crucial for accelerating molecular design, enabling the prediction of new Schiff base structures with tailored electronic

and optoelectronic functionalities. Such interdisciplinary strategies will open pathways toward next-generation smart materials based on Schiff base chemistry.

## REFERENCE

Adindu, E. A., Godfrey, O. C., Agwupuye, E. I., Ekpong, B. O., Agurokpon, D. C., Ogbodo, S. E., Benjamin, I., and Louis, H. (2023). Structural analysis, reactivity descriptors (HOMO-LUMO, ELF, NBO), effect of polar (DMSO, EtOH, H<sub>2</sub>O) solvation, and libido-enhancing potential of resveratrol by molecular docking. *Chemical Physics Impact*, 7, 100296.

Adesina, A. D. (2022). Synthesis of Schiff Bases by Non-Conventional Methods. In *Schiff Base in Organic, Inorganic and Physical Chemistry*. In tech Open.

Afrin, A., Jayaraj, A., Gayathri, M. S., and Swamy P., C. A. (2023). An overview of Schiff base-based fluorescent turn-on probes: a potential candidate for tracking live cell imaging of biologically active metal ions. *Sensors and Diagnostics*, 2, 988-1076.

Adachi, C., Baldo, M. A., Thompson, M. E., and Forrest, S. R. (2001). Nearly 100% internal phosphorescence efficiency in an organic light-emitting device. *Journal of Applied Physics*, 90(10), 5048–5051.

Al-Farraj, E. S., and Mohammed, M. A. (2025). Comprehensive Exploration of Water-Soluble Schiff Base Complexes of Ni (II), Cu (II), Mn (II), and Ce (III): Electrochemical, Computational, and Biological Studies. Volume 39, Issue 4, e70122.

Anrango-Camacho, C., Pavón-Ipiales, K., Frontana-Uribe, B. A., and Palma-Cando, A. (2022). Recent Advances in Hole-Transporting Layers for Organic Solar Cells. *Nanomaterials*, 12(3), 443.

Akbari, Z., Stagno, C., Iraci, N., Efferth, T., Omer, E.A., Piperno, A., Montazerozohori, M., Feizi-Dehneyebi, M., Micale, N. Micale Biological evaluation, DFT, MEP, HOMO-LUMO analysis and ensemble docking studies of Zn(II) complexes of bidentate and tetradentate Schiff base ligands as antileukemia agents. *Journal of Molecular Structure*, 1301, 137400.

Aroua, L. M., Ali, R., Albadri, A. E. A. E., Messaoudi, S., Alminderej, F. M., and Saleh, S. M. (2023). A New, Extremely Sensitive, Turn-Off Optical Sensor Utilizing Schiff Base for Fast Detection of Cu(II). *Biosensors*, 13(3), 359.

Arumugam, A., Shanmugam, R., Munusamy, S., Muhammad, S., Algarni, H., and Sekar, M. (2023). Schiff Base Zinc(II) Complexes as Promising Emitters for Blue Organic Light-Emitting Diodes. *ACS Omega*, 8(17), 15168–15180.

Atzin-Macedo, C. M., Pastor-Ramírez, C., González-Peláez, R., Pérez-Flores, F. J., Hernández-Anzaldo, S., Vazquez-Lima, H., and Reyes-Ortega, Y. (2020). Tautomeric Study of Schiff Bases Derived from o-Dihydroxybenzaldehyde by UV-Vis, IR, <sup>1</sup>H NMR, <sup>13</sup>C NMR Spectroscopy and Computational Modeling. Volume 5, Issue 36, 11120-11126.

Bhat, M. A., Alabada, R., Ajaj, Y., Kaur, M., Kaur, H., Abduldayeva, A., Sinha, A., Saraswat, V., Sood, G., Almarhoon, Z. M., and Butcher, R. J. (2024). Structure directing interactions in the crystals of o-hydroxyaryl/naphthyl derived aldimines: X-ray structure, Hirshfeld surface analysis, DFT and Molecular docking studies. *Journal of Molecular Structure*, 1309, 138211.

Delgado-Montiel, T., Soto-Rajo, R., Baldenebro-López, J., and Glossman-Mitnik, D. (2019). Theoretical Study of the Effect of Different  $\pi$  Bridges Including an Azomethine Group in Triphenylamine-Based Dye for Dye-Sensitized Solar Cells. *Molecules*, 24(21), 3897. <https://doi.org/10.3390/molecules24213897>

Demircioğlu, Z., Kaştaş, Ç. A., and Büyükgüngör, O. (2017). X-ray structural, spectroscopic and computational approach (NBO, MEP, NLO, NPA, fukui function analyses) of (E)-2-((4-bromophenylimino)methyl)-3-methoxyphenol. *Molecular Crystals and Liquid Crystals*, 656(1).

Flores-Leonar, M., Esturau-Escofet, N., Méndez-Stivalet, J. M., Marín-Becerra, A., and Amador-Bedolla, C. (2011). Factors determining tautomeric equilibria in Schiff bases. *Journal of Molecular Structure*, 1006(1-3), 600-605.

Goshisht, M. K., Patra, G. K., and Tripathi, N. (2022). Fluorescent Schiff base sensors as a versatile tool for metal ion detection: strategies, mechanistic insights, and applications. *Materials Advances*, 3, 2612–2669.

Gusev, A. N., Kiskin, M. A., Braga, E. V., Kryukova, M. A., Baryshnikov, G. V., Karaush-Karmazin, N. N., Minaeva, V. A., Minaev, B. F., Ivaniuk, K., Stakhira, P., Ågren, H., and Linert, W. (2021). Schiff Base Zinc(II) Complexes as Promising Emitters for Blue Organic Light-Emitting Diodes. *ACS Applied Electronic Materials*, 3(8), 3436–3444.

Gülseven Sıdır, Y., Aslan, C., Berber, H., and Sıdır, İ. (2019). The electronic structure, solvatochromism and electric dipole moments of new Schiff base derivatives using absorbance and fluorescence spectra. *Structural Chemistry*, 30, 835–851.

Gülseven Sıdır, Y., Pirbudak, G., Berber, H., and Sıdır, İ. (2017). Study on electronic and photophysical properties of substitute ((2-phenoxybenzylidene)amino)phenol derivatives: Synthesis, Solvatochromism, Electric Dipole Moments and DFT calculations. *Journal of Molecular Liquids*, 242, 1096–1110.

Gülseven Sıdır, Y., Sıdır, İ., and Berber, H. (2022). Optoelectronic properties by solution technique and comprehensive solvatochromism of novel fluorescent Schiff base derivatives. *Journal of Molecular Liquids*, 357, 119110.

Joshi, H. C., and Antonov, L. (2021). Excited-State Intramolecular Proton Transfer: A Short Introductory Review. *Molecules*, 26(5), 1475. <https://doi.org/10.3390/molecules26051475>

Kagatıkar, S., and Sunil, D. (2021). Schiff Bases and Their Complexes in Organic Light Emitting Diode Application. *Journal of Electronic Materials*, 50, 6708–6723. <https://doi.org/10.1007/s11664-021-09197-9>

Kırca, B. K., Kaştas, Ç. A., and Ersanlı, C. C. (2021). Molecular and electronic structures of two new Schiff base compounds: (E)-2-bromo-6-[(2-bromo-4-methylphenylimino) methyl]-4-chlorophenol and (E)-2-bromo-6-[(4-bromo-3-methylphenylimino) methyl]-4-chlorophenol. *Journal of Molecular Structure*, 1241, 130643.

Kourat, O., Benhalima, N., Al-Dies, A. A. M., Ardjouni, A., Cherouana, A., Jilani, A., and Djedidi, D. (2025). Structural, nonlinear optical, and molecular docking studies of schiff base compounds as multi-target inhibitors of AChE, BChE, and carbonic anhydrases. *Scientific Reports*, 15, 34818.



Madaboina, S. D., and Kamala, G. R. (2025). Structure, Biological Activities and Synthesis of Schiff Bases: Review Article. *Journal of Pharma Insights and Research*, 3(4), 094-101.

Mohamed, A., Visco, D. P., Jr., Breimaier, K., and Bastidas, D. M. (2025). Effect of Molecular Structure on the B3LYP-Computed HOMO–LUMO Gap: A Structure –Property Relationship Using Atomic Signatures. *ACS Omega*, 10(3), 2799–2808.

Nowsherwan, G. A., Ali, Q., Ali, U. F., Ahmad, M., Khan, M., and Hussain, S. S. (2024). Advances in Organic Materials for Next-Generation Optoelectronics: Potential and Challenges. *Organics*, 5(4), 520-560. <https://doi.org/10.3390/org5040028>

Pan, C. (2024). Solar Active Layer Materials and Research Progress. 5th International Conference on Mechanical Engineering, Civil Engineering and Material Engineering (MECEME 2024).

Peng, W. T., Brey, D., Giannini, S., Dell’Angelo, D., Burghardt, I., and Blumberger, J. (2022). Exciton Dissociation in a Model Organic Interface: Excitonic State-Based Surface Hopping versus Multiconfigurational Time-Dependent Hartree. *Journal of Physical Chemistry Letters*, 13(31), 7105–7112.

Ramasamy, S., Rajan, A.T. (2022) Unraveling the Pharmaceutical Benefits of Freshly Prepared Amino Acid-Based Schiff Bases Via DFT, In Silico Molecular Docking and ADMET. *Journal of Fluorescence*, (32), 1873-1888.

Santos, E. M., Sheng, W., Salmani, R. E., Tahmasebi, S., Ghanbarpour, A., Gholami, H., Vasileiou, C., Geiger, J. H., and Borhan, B. (2021). Design of Large Stokes Shift Fluorescent Proteins Based on Excited State Proton Transfer of an Engineered Photobase. *Journal of the American Chemical Society*, 143(37), 15091–15102.

Schiff, H. (1864). Mittheilungen aus dem Universitätslaboratorium in Pisa: eine neue Reihe organischer Basen. *Justus Liebigs Annalen der Chemie*, 131(1), 118.

Shafieyoon, P., Mehdipour, E., and Mary, Y. S. (2019). Synthesis, characterization and biological investigation of glycine-based sulfonamide derivative

and its complex: Vibration assignment, HOMO – LUMO analysis, MEP and molecular docking. *Journal of Molecular Structure*, 1181, 244-252.

Sıdır, İ., Sıdır, Y. G., and Berber, H. (2022). Solvato-, thermo- and photochromism in a new diazo diaromatic dye: 2-(p-tolyldiazenyl)naphthalen-1-amine. *Journal of Molecular Structure*, 1267, 133595.

Sıdır, İ., Sıdır, Y. G., Berber, H., Ramos, M. L., Justino, L. L. G., and Fausto, R. (2025). Reversal in Solvatochromism, enol-imine/keto-amine Tautomerism and (E)-(Z) Photoisomerizations in a Benzylidene Aniline Schiff Base Derivative in Different Solvents. *Molecules*, 30(3), 745.

Sıdır, İ., Sıdır, Y. G., Khan, N., and Berber, H. (2021). Optoelectronic and photonic properties of  $\pi$ -conjugated benzonitrile derivative bis-Schiff base by solution technique. *Optik*, 241, 166825.

Sıdır, İ., Sıdır, Y. G., Berber, H., and Demiray, F. (2019). Electronic structure and optical properties of Schiff base hydrazone derivatives by solution technique for optoelectronic devices: Synthesis, experiment and quantum chemical investigation. *Journal of Molecular Structure*, 1176, 31-46.

Sıdır, İ., Sarı, T., Sıdır, Y. G., and Berber, H. (2022). Synthesis, solvatochromism and dipole moment in the ground and excited states of substitute phenol derivative fluorescent Schiff base compounds. *Journal of Molecular Liquids*, 346, 117075.

Uddin, E., Sardar, M. N., Reza, M. S., Al-Otaibi, N. H., Al-Harbi, T. H., and Hossain, M. K. (2025). Emerging pharmaceutically active drugs: synthesis and pharmacology of Schiff base ligands with their metal complexes. *Discovery Chemistry*, 2, 153. <https://doi.org/10.1007/s44371-025-00228-6>

Užarević, K., Rubčić, M., Stilinović, V., Kaitner, B., and Cindrić, M. (2010). Keto–enol tautomerism in asymmetric Schiff bases derived from p-phenylenediamine. *Journal of Molecular Structure*, 984(1-3), 232-239. <https://doi.org/10.1016/j.molstruc.2010.09.034>



# **Toxicological Effects of Hexythiazox (Yoksorrun-5EC) on Ovarian Folliculogenesis in Zebrafish: A Histopathological Perspective**

**Yücel BAŞIMOĞLU KOCA<sup>1</sup>**

1- Prof. Dr., Aydın Adnan Menderes Üniversitesi, Fen Fakültesi, Biyoloji Bölümü, [ykoca@adu.edu.tr](mailto:ykoca@adu.edu.tr),  
ORCID: 0000-0002-1031-923X.

## ABSTRACT

This study aimed to investigate the histopathological and morphometric effects of the acaricide Yoksorrün (hexythiazox) on the ovary of zebrafish (*Danio rerio*), a critical reproductive organ. Fish from experimental and control groups were euthanised via hypothermic shock using an ice-water mixture and subsequently fixed in Bouin's solution. Tissue sections were stained with standard histological techniques and examined under a microscope. Results revealed a dose-dependent increase in degenerative alterations and structural disruptions within the ovarian tissue. The low-dose group exhibited disrupted nuclear morphology and reduced nucleoli in primary oocytes; cortical alveolus-stage oocytes showed zona radiata irregularities and morphological deformities; vitellogenic oocytes presented disorganized vitelline granules and compromised membrane integrity. In the moderate-dose group, a decrease in primary oocyte numbers was accompanied by pronounced nuclear and nucleolar abnormalities, nuclear condensation, and eccentric nuclear positioning. Vacuolisation within cortical granules and separations between the zona radiata and granules were also observed. Vitellogenic oocytes demonstrated zona radiata loss and accumulation of eosinophilic granules. The highest dose group displayed intensified and widespread degenerative changes, confirming a clear dose-dependent toxicity. In conclusion, Yoksorrün-5EC exerts significant dose-dependent toxic effects on zebrafish ovarian folliculogenesis, with potential impairment of reproductive function.

*Keywords: Zebrafish, hexythiazox (yoksorrün-5EC), ovarian folliculogenesis, histopathology, morphometry*

---

## INTRODUCTION

Pesticides, widely employed in chemical pest control to enhance agricultural productivity by eliminating harmful organisms, are linked to numerous issues, including adverse effects on human health and the environment. Growing evidence underscores the impact of pesticides on endocrine, immune, and nervous systems, contributing to various disorders (FAO/WHO Joint Meeting On Pesticide Specifications, 2010; Munoz Quezada et al., 2013:407; Mostafalou & Abdollahi, 2013:157; Blair et al., 2015:81; Food And Agriculture Organization Of The United Nations [FAO], 2021; U.S. Environmental Protection Agency [EPA], (2025).

Beyond systemic toxicity, pesticides pose risks to ovarian tissues and other organs. Exposure of *Brachydanio rerio* ovaries to varying concentrations of malathion, an organophosphorus pesticide, resulted in significant reductions in nucleic acids (DNA and RNA), protein content, and alkaline phosphatase activity. At the same time, total free amino acids and acid

phosphatase activity increased. Histopathological analyses revealed developmental arrest from oogonia to tertiary-stage oocytes (Ansari & Kumar, 1987:489). Another study reported proliferation of atretic vitellogenic oocytes, follicular cells, and inflammatory infiltration in the ovaries of fish exposed to the herbicide thiobencarb, indicating toxic effects that impair physiological functions in African catfish (Elias et al., 2020:1589).

Sex-specific differences have been observed in fish treated with the atrazine herbicide, with females exhibiting greater tolerance than males. Histopathological alterations included testicular architecture deterioration, disrupted spermatogonia distribution, vacuolation, and hyperplasia. In ovaries, epithelial separation and lysis were also noted (Nassar, Mohamed, & Said, 2022:1095).

Recent research on *Mastacembelus cavasius* exposed to cypermethrin revealed multiple histopathological changes, such as wrinkled oocytes, cytoplasmic clumping, atretic follicles, degenerated granulosa layers, oocyte wall degeneration, increased inter-follicular spaces, adhesions, cyst formation, and necrosis, which intensified with higher pesticide concentrations and longer exposure times (Uddin et al., 2022).

Acaricides are extensively used against mites in agriculture. Yoksorrün 5EC (50 g/L), a carboxamide-class acaricide containing hexythiazox, targets red spider mites (*Tetranychus urticae*, *T. cinnabarinus*, *Panonychus ulmi*), which damage fruits, vegetables, and cotton crops. Yoksorrün exhibits contact and stomach activity with translaminar properties, primarily affecting eggs, larvae, and nymphs (Anon 2019a, 2019b, 2020; U.S. Environmental Protection Agency [EPA], 2007a).

Zebrafish (*Danio rerio*) serve as an ideal model organism not only for vertebrate toxicity assessments but also for ecotoxicological studies evaluating chemical effects on survival, growth, and reproduction (Hill et al., 2005:6; Noelia et al., 2014:55). Its asynchronous ovulation and ovarian follicles at multiple developmental stages provide valuable advantages for assessing environmental toxicity (Maack, 1964:467; Garg, 1998:1).

While most acaricide research has focused on mite species' sensitivity and resistance (Yamamoto et al., 1996:23; Na et al., 2009:123), limited studies have addressed their histopathological impact on fish tissues. Aside from our recent investigations into Yoksorrün's effects on various zebrafish tissues (Başımoğlu Koca & Kara, 2021:1; Başımoğlu Koca et al., 2022:1808), there is a paucity of data. Therefore, the present study aims to elucidate the histopathological and morphometric effects of Yoksorrün on the zebrafish ovary, a critical organ for fish reproduction.

## MATERIAL METHOD

### *Fish Care and Grouping*

All fish care and experimental procedures described in this study were conducted with the approval of the Local Animal Ethics Committee of Adnan Menderes University (Ethics Approval Number: FEF-2015/098) and in compliance with institutional guidelines for the ethical use of animals in experimentation.

A total of 120 adult zebrafish (*Danio rerio*) were obtained from a local supplier. Upon arrival, the fish were acclimated under appropriate laboratory conditions and housed in glass aquaria measuring 30 × 80 × 40 cm. During both the acclimation period and the experimental phase, the fish were maintained in continuously aerated and filtered sterile water at a temperature of 26 ± 1 °C, under a 14-hour light/10-hour dark photoperiod. The acclimation period lasted two weeks, during which the fish were fed a commercial diet.

Yoksorrun 5EC is an acaricide belonging to the carboxamide group, containing 5% hexythiazox (C<sub>17</sub>H<sub>21</sub>ClN<sub>2</sub>O<sub>2</sub>S), and is commonly used in agriculture for the control of harmful mite species. The pesticide was obtained from a local commercial supplier (Agrobrest Group, İzmir, Turkey). The concentrations used in this study were determined based on reports published by the European Chemicals Agency (ECHA, 2017) and the United States Environmental Protection Agency (EPA, 2007a, b). To maintain stable pesticide concentrations throughout the exposure period, aquarium water was renewed every 24 hours in accordance with OECD guidelines (1992).

Each experimental condition was replicated three times. The zebrafish were randomly assigned to control and treatment groups, with 10 individuals per group. The experimental design was structured as follows: Control Group (C) with no chemical exposure; Group 1 (G1) exposed to 0.01 mL/L hexythiazox; Group 2 (G2) exposed to 0.02 mL/L hexythiazox; and Group 3 (G3) exposed to 0.03 mL/L hexythiazox. After 96 hours of exposure, all fish from the control and treatment groups were subjected to histological processing in their entirety for subsequent microscopic analysis.

### *Tissue collection and histological analysis*

Fish from both the experimental and control groups were euthanised by hypothermic shock using an ice-water mixture (Zhang et al., 2020:341). The fins and tail were removed using a lancet.

For histological analysis, Bouin's fixative was administered through the mouth, gills, and abdominal cavity, after which the fish were immersed in the same fixative at +4 °C for 24 hours. After fixation at +4 °C for 24 hours, the fish were dehydrated using a graded ethanol series and then cleared with xylene before being embedded in paraffin. Paraffin blocks were sectioned at

5–7  $\mu\text{m}$  using a rotary microtome (Leica RM 2145) and mounted on slides for Mayer's hematoxylin and eosin (H&E), Gomori trichrome (GT), and periodic acid–Schiff (PAS) staining procedures (Bancroft & Cook, 1994). The stained sections were evaluated and imaged using an Olympus BX51 brightfield microscope equipped with an Olympus E-330 digital camera (Shinjuku, Tokyo, Japan).

## RESULTS

### *Histological results*

#### *Control group*

In the control group, ovarian tissues exhibited a healthy histological architecture, with all stages of oogenesis distinguishable under the microscope. During the primary growth phase, oocytes displayed multiple nucleoli within the germinal vesicle. At the cortical alveolus stage, oocytes became prominent due to the accumulation and expansion of cortical alveoli surrounding the nucleus, accompanied by a notable increase in oocyte diameter. The onset of zona radiata formation was visible, with the zona radiata and surrounding follicular epithelial layers well-defined microscopically. During the vitellogenic phase, oocytes underwent further enlargement as yolk (vitellus) accumulated within the cytoplasm, accompanied by a marked thickening of the zona radiata. In mature oocytes, the nucleus became indistinguishable, and the ooplasm was densely filled with yolk granules, indicating the completion of maturation.



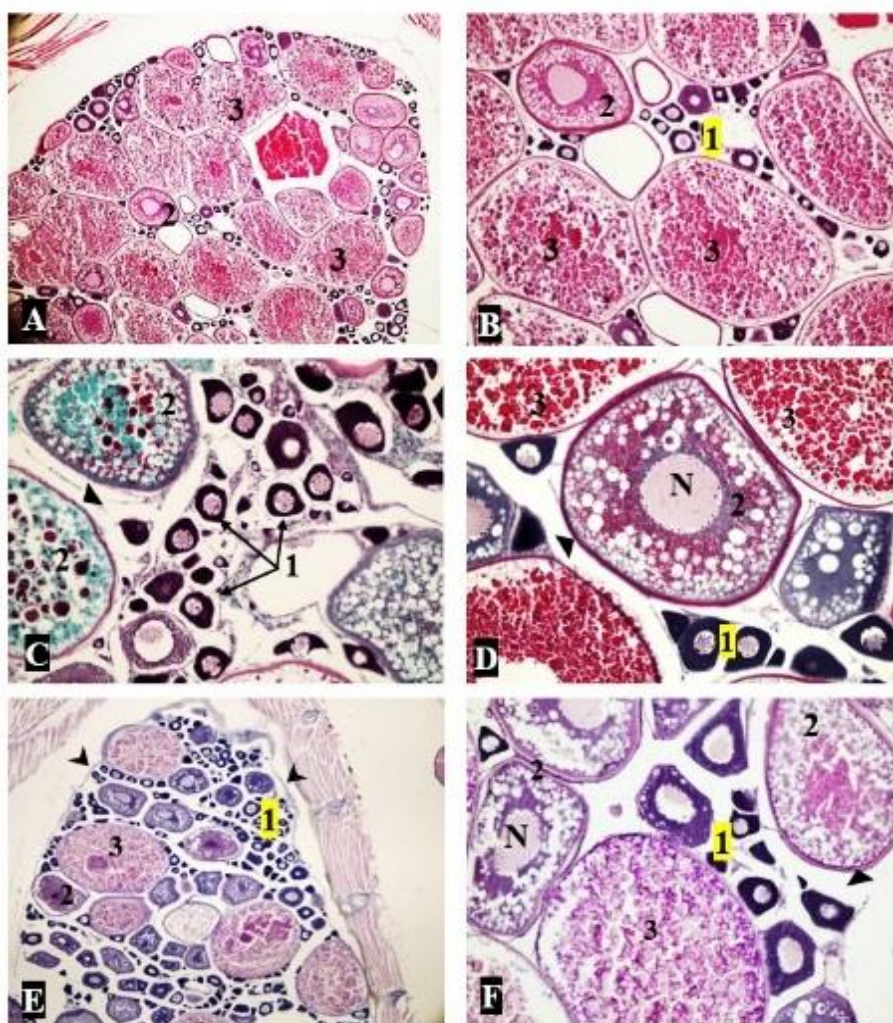


Fig. 1. Control group ovarian sections. 1. primary oocytes; 2. oocytes at the cortical alveoli stage; 3. vitellogenic oocytes; > tunica albuginea. Staining: A, B; H&E, C, D; Gomori trichrome, E, F; PAS+H. Magnification; A, D; 4X - B,C; 10X - D,F; 20X

### ***Experimental groups***

**Group 1:** Although the alterations in group 1 (G1) were less severe than those observed in the high-dose groups, distinct degenerative changes were observed compared to the control group. The primary oocytes showed disrupted nuclear architecture and a noticeable reduction in the number of nucleoli. Oocytes at the cortical alveolus stage exhibited irregularities in the zona radiata, morphological deformities, and significant disorganisation of the granular structure. In some follicles, cortical alveolus formation was reduced. Vitellogenic stage oocytes displayed structural disorganisation of vitelline granules, with evident damage to the integrity of the vitelline membrane and zona radiata; in some specimens, these structures were completely lost.

**Group 2:** In group 2 (G2), a reduction in the number of primary oocytes was observed in some individuals. Additionally, pronounced abnormalities in nuclear and nucleolar structures were detected, most notably the loss of nucleoli. Some primary oocytes also exhibited shrinkage in the nucleoplasm. At the cortical alveolus stage, many oocytes presented similar nuclear and nucleolar anomalies, with some displaying eccentrically located nuclei devoid of nucleoli. Separations were noted between the zona radiata and cortical granules. In cortical oocytes, primarily in the vitellogenic stage, marked losses in the zona radiata were accompanied by structural disintegration and a decrease in the vitelline content. During the cortical granule phase, cytoplasmic vacuolisation and fusion of cortical alveoli were observed.

**Group 3:** In the highest dose group (G3), the degenerative changes previously observed in Groups 1 and 2 were markedly more severe, widespread, and histopathologically advanced. Prominent cellular and structural damages, such as pronounced cytoplasmic vacuolisation, nucleolar loss, and disruption of tissue architecture, were evident. Additionally, thickening, folding, and even complete loss of the zona radiata were observed in some vitellogenic oocytes. These pathological alterations demonstrate a significant dose-dependent progression in both the severity and extent of damage. The findings strongly indicate that prolonged or high-dose exposure leads to irreversible cellular degeneration and compromised tissue integrity.

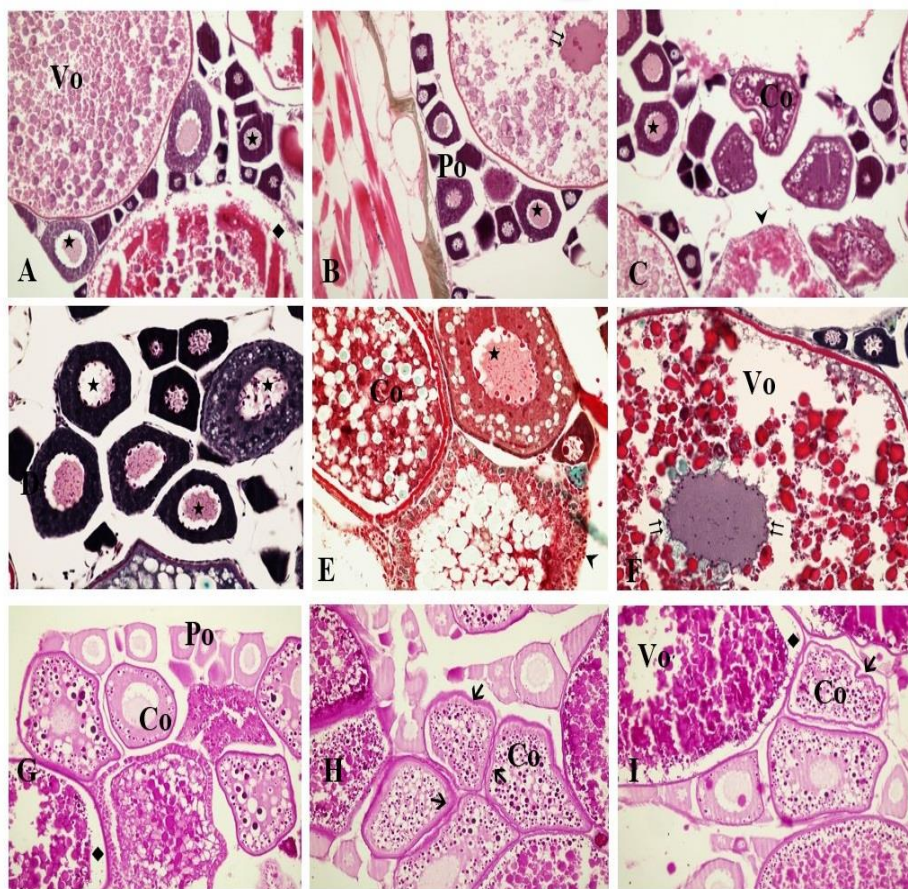


**Fig. 2.** Histological structure of the ovary in Group 1. Loss of nucleolus organization and nucleoplasm structure in degenerated the primary follicles oocyte (★), morphological alterations and degeneration of the follicular epithelium at the cortical alveolus stage (➤), detachment of the zona radiata from the vitelline envelope during the early-late cortical alveolus and vitellogenic follicle stages (◆) and thickening and undulation of the zona radiata (➡), deformation of the nuclear membrane and nucleoplasm in the vitellogenic oocyte (➢). Po: primary oocyte stage, Co: cortical alveolus stage, Vo: vitellogenic oocyte. Staining: A, B; H&E, C, D; Gomori trichrome, E, F; PAS+H. Magnification; A,D; 4X - B,C; 10X - D,F; 20X



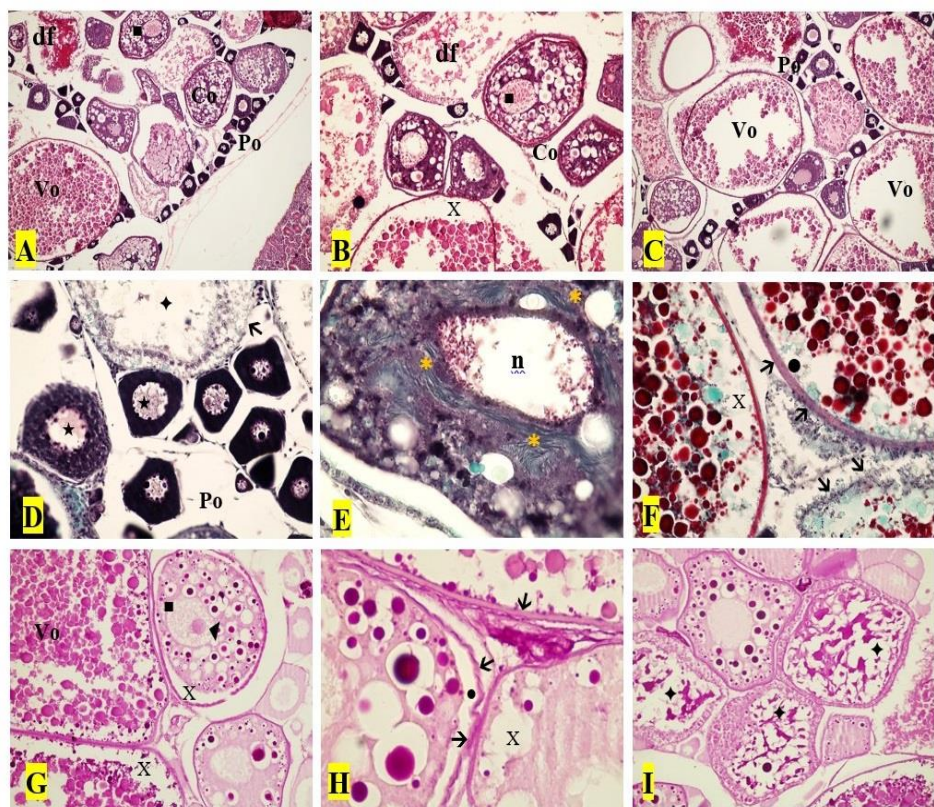


**Fig. 3.** Histological alterations in Group 2 ovaries: loss of nucleolus and nucleoplasm shrinkage in primary oocytes (★); structural degeneration of the nuclear degeneration with eccentric and nucleolus-lacking nuclei at the cortical alveolus stage (■), nuclear dissolution in some cortical alveolus stage oocytes (n), separation between zona radiata and cortical granules at the cortical granule stage (X), thickening and loss of the zona radiata in cortical and vitellogenic oocytes (→), cytoplasmic vacuolization (♦) in some cortical alveoli stage and dense filamentous bodies in early cortical follicles (★), a giant nucleolus in the oocyte at the cortical granule stage (◆) and reduced vitelline content with structural deterioration. **Po:** primary oocyte stage, **Co:** cortical alveolus stage, **Vo:** vitellogenic oocyte, **df:** degenerated follicle, **Staining:** A, B, C, H&E; D, E, F, Gomori trichrome; G, H, I, PAS. **Magnification:** A, B, C:10X - D, F, G, I: 20× - E, H: 40X.

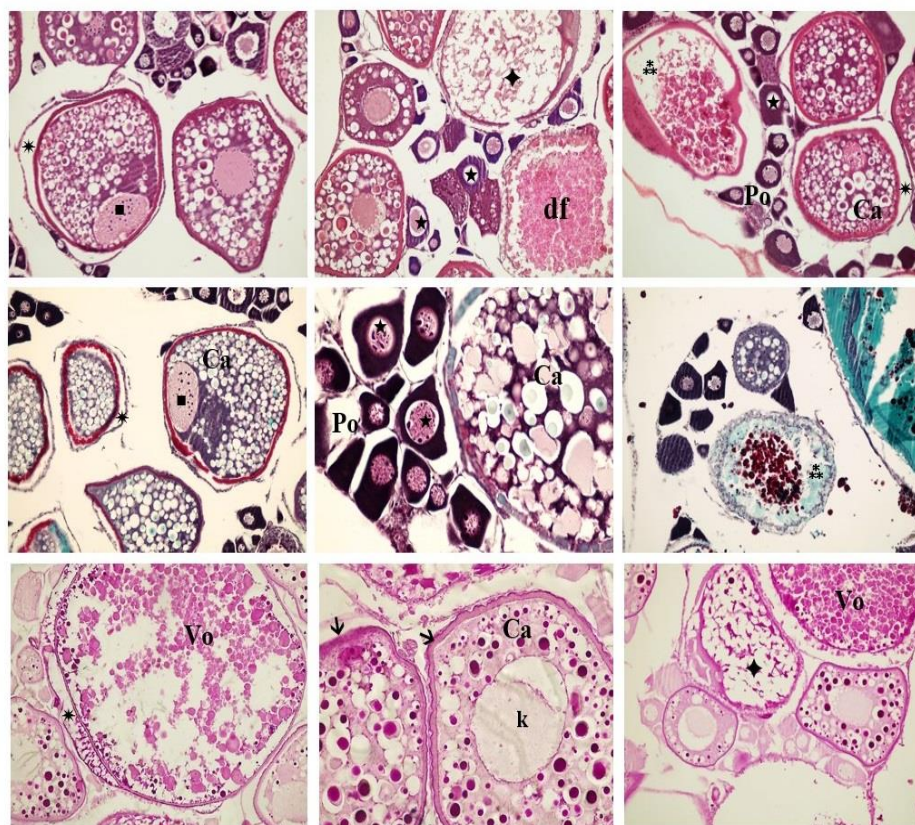


**Fig. 4.** Histopathological alterations observed in the zebrafish ovary of Group 3. Loss of the nucleolus in primary oocytes and shrinkage of the nucleoplasm (★), morphological deformities in follicles at the cortical alveolus stage (✱✱), eccentrically located nucleus (■) and nuclear karyolysis in oocytes at the cortical alveolar stage (k), separation of the follicular epithelium from the zona radiata due to edema (✱), thickening and undulation of the zona radiata in cortical alveolar oocytes (➔), cytoplasmic vacuolization with fusion of cortical alveoli (✦). **Po:** primary oocyte stage, **Co:** cortical alveolus stage, **Vo:** vitellogenic oocyte and degenerated follicle (df). **Staining:** A, B; H&E, C, D; Gomori trichrome, E, F; PAS+H. **Magnification;** A,D; 4X - B,C; 10X - D,F; 20X

## DISCUSSION

In our previous studies (Başımoğlu Koca et al., 2021:1; Başımoğlu Koca & Kara, 2022:1808), exposure to Yoksorrün-5EC (hexythiazox) was shown to induce significant histopathological and molecular alterations in zebrafish muscle, gill, and intestinal tissues. The observed changes in myoglobin and periostin expression, along with structural disruptions in these organs, indicate the systemic toxicity of the pesticide. The dose-dependent histopathological damage and structural abnormalities observed at various stages of oogenesis in the present study further corroborate the toxic effects of Yoksorrün-5EC on the reproductive system, supporting our previous findings. This comprehensive approach highlights the extensive toxic impact of pesticide exposure across multiple tissues and systems in aquatic organisms.

The histopathological findings obtained from this study clearly demonstrate that pesticide exposure induces dose-dependent structural abnormalities in the zebrafish ovarian tissue and triggers a progressive degeneration process across different stages of oogenesis. These damages indicate potentially critical functional implications for reproductive health. The intact histoarchitecture in the control group provided a solid baseline to evaluate pesticide-induced toxicity. In Group 1, the presence of mild structural deformities and nuclear abnormalities indicates early-stage cytological damage. These observations parallel the findings of Suzuki et al. (2019:545), who reported nuclear and cytoplasmic damage in ovarian cells caused by aquatic pollutants. Their study emphasised early toxic stress markers, including zona radiata and follicular epithelium alterations, which may directly compromise oocyte integrity. The disorganised zona radiata they identified is consistent with the anomalies detected in our Group 1 specimens.

Observed in group 2, the manifestation of nuclear shrinkage, nucleolar disintegration, and severe structural impairments in both the zona radiata and vitelline granules is aligned with the mechanisms discussed by Miyazaki et al. (2021:20548). They showed that such structural injuries disrupt cellular homeostasis and compromise oocyte development and fertilisation. The fusion between the nuclear envelope and cytoplasmic vacuoles, along with disrupted granule morphology in our samples, aligns closely with their molecular findings. Moreover, our data corroborate the work of Patel et al. (2023:418), who reported reproductive toxicity associated with pesticide-induced damage, highlighting the broader ecological implications through potential effects on population dynamics.

In Group 3, extensive degeneration correlated with increasing pesticide concentrations, paralleling findings by Zhang et al. (2018:606), who observed widespread necrosis and impaired function in ovarian tissues under high-dose toxin exposure. They reported severe deterioration in the zona radiata and

vitelline granules, interfering with key reproductive processes such as maturation and fertilisation. The extensive tissue degeneration and oocyte dysfunction we documented support this dose-response relationship. Similarly, Gomez et al. (2020:228) identified a negative correlation between pesticide concentration and reproductive success in zebrafish, further reinforcing our results.

This study provides compelling evidence of dose-dependent histopathological alterations in zebrafish ovarian tissue following pesticide exposure, and identifies key structural targets, such as the zona radiata, vitelline granules, and nuclear components, that are critically involved in the proper progression of oogenesis. The observed morphological disruptions not only delineate the extent of tissue damage but also emphasise the urgent need for advanced biochemical and molecular investigations to elucidate the underlying mechanisms of pesticide-induced reproductive toxicity. By establishing a solid scientific foundation, this research supports multidisciplinary efforts aimed at understanding the broader reproductive and ecological consequences of environmental contaminants.

Moreover, the growing use of zebrafish as a model organism presents valuable opportunities to elucidate the molecular pathways underlying pesticide toxicity and associated reproductive disorders. These insights are instrumental in shaping evidence-based mitigation strategies aimed at reducing ecological and public health risks. Given the widespread and frequently unregulated use of pesticides, implementing stringent preventive policies and reinforcing environmental regulations through effective monitoring and risk assessment frameworks are imperative to safeguard both ecosystem integrity and human well-being.

### ***Acknowledgements***

The authors thank Mrs. Nazlı Kara for her assistance with animal care and tissue processing.

### ***Disclosure statement***

The authors declare no conflict of interest.

### ***Funding***

This study was funded by Adnan Menderes University Scientific Researcher Project Unit [Number: ADU/FEF 16020].

## REFERENCES

- Anon. (2019a). Hexythiazox. PubChem. Retrieved from <http://pubchem.ncbi.nlm.nih.gov/compound/Hexythiazox>
- Anon. (2019b). Ilac information. Agrobest Grup. Retrieved from <http://www.agrobestgrup.com/ilac.php>
- Anon. (2020). PPDB: Pesticide properties database. Retrieved from <http://sitem.herts.ac.uk/aeru/ppdb/en/Reports/385.htm>
- Ansari, B. A., & Kumar, K. (1987). Malathion toxicity: Effect on the ovary of the zebra fish *Brachydanio rerio* (Cyprinidae). *International Review of Hydrobiology*, 72(4), 489–495. <https://doi.org/10.1002/iroh.19870720408>
- Bancroft, J. D., & Cook, H. C. (1994). *Manual of histological techniques and their diagnostic application*. Churchill Livingstone.
- Başımoğlu Koca, Y., Koca, S., Öztel, Z., & Balcan, E. (2021). Determination of histopathological effects and myoglobin, periostin gene-protein expression levels in *Danio rerio* muscle tissue after acaricide Yoksorrün-5EC (hexythiazox) application. *Drug and Chemical Toxicology*, 1–9. <https://doi.org/10.1080/01480545.2021.2007945>
- Başımoğlu Koca, Y., & Kara, N. (2022). Alterations in gills and intestine of *Danio rerio* after exposure to acaricide Yoksorrün-5EC (hexythiazox): Histopathologic and morphometric evaluation. *Drug and Chemical Toxicology*, 45(4), 1808–1817. <https://doi.org/10.1080/01480545.2021.1880428>
- Blair, A., Ritz, B., Wesseling, C., & Freeman, L. B. (2015). Pesticides and human health. *Occupational and Environmental Medicine*, 72(2), 81–82. <https://doi.org/10.1136/oemed-2014-102591>
- Elias, N. S., Abouelghar, G. E., Sobhy, H. M., El Meniawy, H. M., & Elsaiedy, E. G. (2020). Sublethal effects of the herbicide thiobencarb on fecundity, histopathological and biochemical changes in the African catfish (*Clarias gariepinus*). *Iranian Journal of Fisheries Sciences*, 19(3), 1589–1614. <https://doi.org/10.22092/jifro.2020.1234567>
- European Chemicals Agency (ECHA). (2017). CLH report: Proposal for harmonised classification and labelling based on Regulation (EC) No 1272/2008 (CLP Regulation), Annex VI, Part 2. Retrieved from <https://echa.europa.eu/documents/10162/ab41a759-e051-5f5e-1a3e-4cfcbfc75d2b>
- FAO/WHO Joint Meeting on Pesticide Specifications. (2010). *Manual on development and use of FAO and WHO specifications for pesticides* (1st rev. ed.). Food and Agriculture Organization of the United Nations & World Health Organization.
- Food and Agriculture Organization of the United Nations. (2021). *Q&A on pests and pesticide management*. <https://www.fao.org/pest-management/en>



- Garg, S. K. (1998). Reproductive biology of the zebrafish (*Danio rerio*): A review. *Aquaculture Research*, 29(1), 1–7. <https://doi.org/10.1046/j.1365-2109.1998.00217.x>
- Gomez, L., Rivera, A., & Alvarez, M. (2020). Dose-dependent reproductive toxicity of common pesticides in zebrafish (*Danio rerio*): Histological and behavioural perspectives. *Aquatic Toxicology*, 228, 105642. <https://doi.org/10.1016/j.aquatox.2020.105642>
- Hill, A. J., Teraoka, H., Heideman, W., & Peterson, R. E. (2005). Zebrafish as a model vertebrate for investigating chemical toxicity. *Toxicological Sciences*, 86(1), 6–19. <https://doi.org/10.1093/toxsci/kfi110>
- Maack, G. (1964). Estrogen-related alterations of gonad development and reproduction in the zebrafish, *Danio rerio*. *Zeitschrift für Zellforschung und Mikroskopische Anatomie*, 62(3), 467–481. <https://doi.org/10.1007/BF00336616>
- Miyazaki, H., Okano, K., Sato, T., & Yamada, N. (2021). Mechanisms of oocyte developmental disruption induced by pesticide exposure in teleost fish. *Environmental Science and Pollution Research*, 28(16), 20548–20560. <https://doi.org/10.1007/s11356-021-12436-z>
- Mostafalou, S., & Abdollahi, M. (2013). Pesticides and human chronic diseases: Evidence, mechanisms, and perspectives. *Toxicology and Applied Pharmacology*, 268(2), 157–177. <https://doi.org/10.1016/j.taap.2013.01.025>
- Munoz Quezada, M. T., Lucero, B. A., Barr, D. B., Steenland, K., Levy, K., Ryan, P. B., & Calafat, A. M. (2013). Organophosphate pesticide exposure and neurodevelopment in young Mexican-American children. *Environmental Health Perspectives*, 121(3), 407–412. <https://doi.org/10.1289/ehp.1206187>
- Na, C. I., Lee, S. H., & Park, J. S. (2009). Sensitivity and resistance of various mite species to acaricides in agricultural fields. *Journal of Asia-Pacific Entomology*, 12(2), 123–128. <https://doi.org/10.1016/j.aspen.2009.03.004>
- Nassar, S. E., Mohamed, A. A., & Said, R. M. (2022). Effects of herbicide atrazine on reproductive hormonal levels, cytochrome P450, and gonadal structure of adult male and female crayfish (*Procambarus clarkii*). *Egyptian Journal of Aquatic Biology and Fisheries*, 26(6), 1095–1114. <https://doi.org/10.21608/ejabf.2022.279076>
- Noelia, P., Ana, M., Alfonso, B., María, A., & Rosario, M. S. (2014). Structural and ultrastructural evaluations of zebrafish ovaries after exposure to 2,3,7,8-tetrachlorodibenzo-p-dioxin. *Acta Adriat*, 55–57.
- Organisation for Economic Co-operation and Development (OECD). (1992). OECD guideline for testing of chemicals. Section 2: Effects on biotic systems. Test No. 203: Fish, acute toxicity test. Retrieved from [https://www.oecd-ilibrary.org/environment/test-no-203-fish-acute-toxicity-test\\_9789264069961-en](https://www.oecd-ilibrary.org/environment/test-no-203-fish-acute-toxicity-test_9789264069961-en)

- Patel, R., Singh, A., & Verma, P. (2023). Pesticide-induced reproductive toxicity in fish: A review of histopathological and molecular insights. *Toxicology Reports*, 10, 418–430. <https://doi.org/10.1016/j.toxrep.2023.01.034>
- Suzuki, Y., Nakamura, T., Fujimoto, H., & Takahashi, T. (2019). Structural damage to ovarian follicles in zebrafish exposed to environmental contaminants. *Ecotoxicology and Environmental Safety*, 172, 545–553. <https://doi.org/10.1016/j.ecoenv.2019.01.014>
- Uddin, M. H., Ali, M. H., Sumon, K. A., Shahjahan, M., & Rashid, H. (2022). Effects of pyrethroid pesticide cypermethrin on the gonad and hematobiochemical parameters of female Gangetic Mystus (*Mystus cavasius*). *Aquaculture Studies*, 22(3), AQUAST819. <http://doi.org/10.4194/AQUAST819>
- United States Environmental Protection Agency. (2007a). Reregistration eligibility decision for hexythiazox (EPA 738-R-07-004). Retrieved from <https://nepis.epa.gov/Exe/ZyPDF.cgi/P1000KS4.PDF>
- United States Environmental Protection Agency. (2007b). Ecological effects test guidelines: OCSPP 850.4100 fish early-life stage toxicity test (EPA 712-C-07-009). Retrieved from <https://www.epa.gov/sites/default/files/2015-06/documents/850-4100.pdf>
- United States Environmental Protection Agency. (2025). What is a pesticide? Retrieved from <https://www.epa.gov/minimum-risk-pesticides/what-pesticide>
- Yamamoto, I., Kitagawa, S., & Saito, H. (1996). Mechanisms of acaricide resistance in *Tetranychus urticae* Koch. *Pesticide Biochemistry and Physiology*, 56(1), 23–33. <https://doi.org/10.1006/pest.1996.0029>
- Zhang, X., Li, Y., Huang, J., & Chen, G. (2018). High-dose pesticide exposure leads to ovarian necrosis and dysfunction in zebrafish: Evidence from histopathology and reproductive endpoints. *Chemosphere*, 210, 606–613. <https://doi.org/10.1016/j.chemosphere.2018.07.051>
- Zhang, Z., et al., 2020. Complete genome analysis of a virulent *Vibrio scophthalmi* strain VSc190401 isolated from diseased marine fish half-smooth tongue sole, *Cynoglossus semilaevis*. *BMC Microbiology*, 20(1), 341.



# **Sectoral Analysis of Greenhouse Gas Emissions in Türkiye: Trends, Breakpoints, and Policy Recommendations (1990–2023)**

**Ece ÖZGÖREN ÜNLÜ\***

<sup>1</sup>Department of Statistics, Süleyman Demirel University, Türkiye \* (eceeozgoren@sdu.edu.tr)

## ABSTRACT

This study examines Türkiye's greenhouse gas emissions at the sectoral level for the period 1990–2023. Emissions from the energy, industry, agriculture, and waste sectors were analyzed using official statistics published by the Turkish Statistical Institute (TURKSTAT). The study includes descriptive statistics, calculation of sectoral shares, time series trends, and breakpoint analyses. The findings demonstrate that Türkiye's greenhouse gas emissions rose from approximately 230 MtCO<sub>2</sub>-eq in 1990 to 550 MtCO<sub>2</sub>-eq in 2023. The energy sector is the dominant sector, accounting for over 70% of total emissions. The industrial sector has increased significantly, especially since the 2000s, while the agriculture and emissions sectors have remained relatively stable. Additionally, developments such as economic crises (2001, 2008), global financial fluctuations, and the COVID-19 pandemic (2020) have been found to cause temporary breakpoints in emission trends. However, these effects have not altered the long-term upward trend. The study emphasizes that Türkiye's climate policies should focus on transforming the energy sector, increasing renewable energy investments, promoting energy efficiency measures, and developing clean production technologies.

*Keywords – Greenhouse gas emissions, Energy sector, Time series analysis, Breakpoint, Climate change, Türkiye*

---

### I. INTRODUCTION

Climate change is one of the most significant environmental issues facing the world today, primarily caused by the increase in greenhouse gas emissions released into the atmosphere [1]. Since the Industrial Revolution, the intensive consumption of fossil fuels, particularly for energy production and industrial activities, has accelerated the accumulation of greenhouse gases such as carbon dioxide (CO<sub>2</sub>), methane (CH<sub>4</sub>), and nitrous oxide (N<sub>2</sub>O) in the atmosphere [2], [3]. This process has caused global temperatures to rise by approximately 1.1°C compared to pre-industrial levels and has brought with it more serious environmental, economic, and social risks depending on future emission scenarios [4], [5].

The increase in greenhouse gas emissions not only affects the global climate system; it also plays a decisive role in countries' development policies, energy strategies, and sustainability goals [6]. Increased environmental awareness and education levels facilitate the adoption of these policies by society; studies show that individuals with high environmental awareness embrace sustainable production and consumption habits more effectively [7]. In this context, international agreements including United Nations Framework Convention on Climate Change (UNFCCC) and Kyoto Protocol have regulated countries' obligations to monitor, report, and reduce greenhouse gas emissions [8].

Through the Paris Agreement adopted in 2015, countries have committed to limiting global temperature increase to 1.5–2°C [9], [10].

Türkiye acceded to the UNFCCC in 2004 and the Kyoto Protocol in 2009 and ratified the Paris Agreement in 2021 [11], [12]. Türkiye's greenhouse gas emissions rose from 230 MtCO<sub>2</sub>-eq in 1990 to 550 MtCO<sub>2</sub>-eq in 2023 [11]. This increase is evaluated as one of the rapid increases among The Organisation for Economic Co-operation and Development (OECD) countries [6]. The energy sector, in particular, is the dominant source, accounting for more than 70% of total emissions [2], [13]. The industrial sector also substantially contributes to emissions with its increasing production capacity, while the agriculture and waste sectors follow a more stable trajectory [4], [14].

Studies in the literature on Türkiye's greenhouse gas emissions generally emphasize the dominance of energy-intensive sectors, the role of structural factors in industry and agriculture, and the importance of emissions from waste management [14], [15]. Furthermore, studies conducted using breakpoint analysis show that economic crises (2001, 2008), the COVID-19 pandemic (2020), and energy price fluctuations (2022) have caused temporary interruptions in emission trends [2], [16]. However, these interruptions apparently remained temporary and have not changed the long-term upward trend [1]. In Türkiye's case, examining the historical development and sectoral distribution of greenhouse gas emissions is crucial for developing sustainable development policies. National and international obligations, energy efficiency, increased use of renewable energy sources, and widespread adoption of clean production technologies are emerging as priority strategies for reducing emissions [4], [6], [10].

## II. MATERIALS AND METHOD

### A. Data Source

The greenhouse gas emission data used in this study were obtained from official statistics published by TURKSTAT. The data were calculated based on the 2006 Intergovernmental Panel on Climate Change (IPCC) Guidelines and are consistent with the National Inventory Reports submitted to the United Nations Framework Convention on Climate Change (UNFCCC) Secretariat [17], [18].

### B. Aim and Scope

The analysis covers direct greenhouse gas emissions from energy, Industrial Processes and Product usage (IPPU), agriculture, and waste sectors. These emissions include:

- Carbon dioxide (CO<sub>2</sub>),

- Methane (CH<sub>4</sub>),
- Nitrous oxide (N<sub>2</sub>O), and
- Fluorinated gases (F-gases).

By contrast, indirect greenhouse gas emissions such as nitrogen oxides (NO<sub>x</sub>), non-methane volatile organic compounds (NMVOC), carbon monoxide (CO), and sulfur dioxide (SO<sub>2</sub>) have not been included in the calculations. Besides, land use, land-use change, and forestry emissions (LULUCF) are also excluded from the scope.

### *C. Geographical and Temporal Scopes*

The data has been calculated for Türkiye as a country and is available on an annual basis starting from 1990. The greenhouse gas emission statistics published by TURKSTAT are made available to the public approximately two years after the end of the reference year.

### *D. Method*

The IPCC (2006) methodology is used in calculations by TURKSTAT. Within this scope, emission data for the energy, industry, agriculture, and waste sectors are estimated using activity data collected in the national statistical system and multiplier (emission factor) methods [17]. The data are reported in carbon dioxide equivalent (CO<sub>2</sub>-eq) to maintain international comparability.

### *E. Statistical Processing and Analysis*

The analysis described below was performed using the data series on greenhouse gas emissions published by TURKSTAT.

Descriptive statistics: Calculation of average, minimum, and maximum emission values.

Time series analysis: Examination of annual trends in emissions between 1990 and 2023.

Sectoral distribution: Calculation of each sector's share of total emissions.

Inflection point analysis: Determination of changes in emission trends during periods such as economic crises (2001, 2008), the pandemic (2020), and energy crises (2022) using statistical methods.

### *F. Legal Framework and Data Quality*

Data is collected in accordance with the Turkish Statistics Law No. 5429 dated November 10, 2005, and the Presidential Decree dated July 15, 2018. In line with data privacy principles, it has been published in a way that prevents individual identification. TURKSTAT also makes information on methodology publicly available through the annual National Inventory Report.

III. RESULTS

The results section focuses on describing the temporal evolution and sectoral distribution of Türkiye’s greenhouse gas emissions, highlighting key breakpoints and structural changes within the 1990–2023 period.

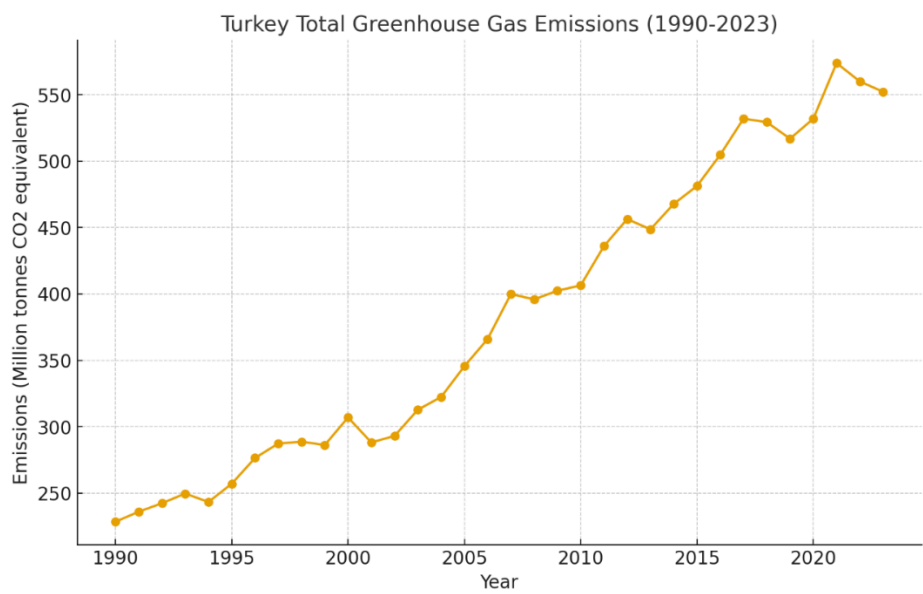


Fig. 1 Türkiye’s Total Greenhouse Gas Emissions

Figure 1 illustrates Türkiye's total greenhouse gas emissions on an annual basis between 1990 and 2023. Emissions, which stood at approximately 230 MtCO<sub>2</sub>-eq in 1990, showed an upward trend over the years and approached the 300 MtCO<sub>2</sub>-eq threshold by the 2000s. A brief decline was observed in 2001, after which emissions began to rise again starting in 2002. A steady increase was recorded until 2008, with a slowdown in the rate of increase during the 2008–2009 period due to the global crisis. An upward trend began again in 2010, reaching 530 MtCO<sub>2</sub>-eq levels in 2017. Emissions temporarily decreased in 2020 due to the impact of the COVID-19 pandemic but increased in subsequent years. Approximately 550 MtCO<sub>2</sub>-eq total emissions have been reached as of 2023. The chart generally shows a steady long-term increase, despite fluctuations.



### Greenhouse Gas Emissions by Sectors in 2023

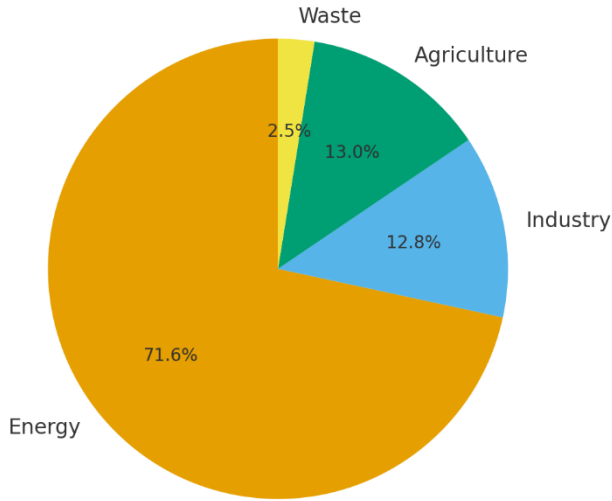


Fig. 2 Greenhose Gas Emissions by Sectors

Figure 2 plots the sectoral distribution of Türkiye's greenhouse gas emissions in 2023. The energy sector accounts for 71.6% of total emissions and is the dominant sector. This ratio implies that approximately three-quarters of total emissions are energy-related. The agriculture sector ranks second with 13.0%, while the industrial sector ranks third with 12.8%. The waste sector has the lowest contribution at 2.5%, making a relatively limited contribution compared to other sectors. This distribution clearly demonstrates that greenhouse gas emissions in Türkiye are largely energy-related, followed by agriculture and industry, while the waste sector has a low impact on the total.

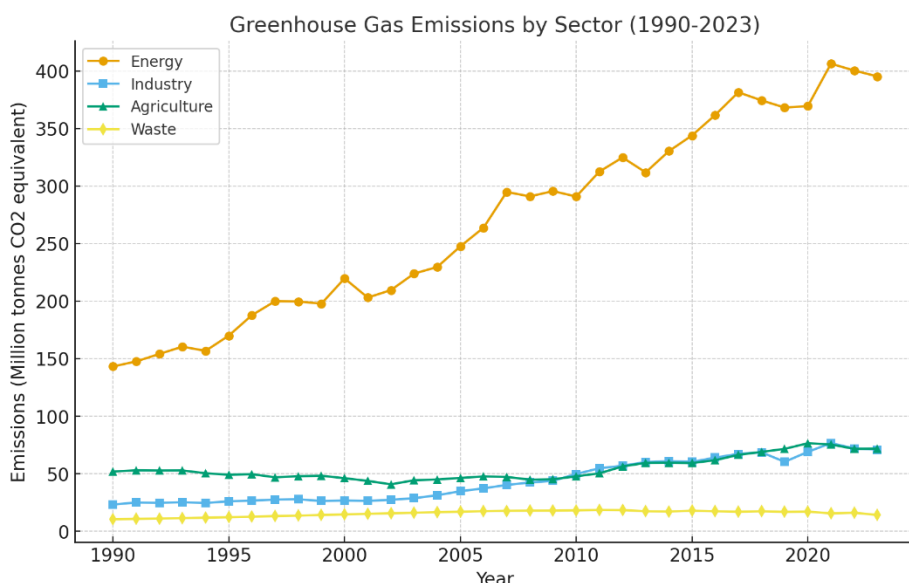


Fig. 3 Greenhouse Gas Emissions by Sector (1990-2023)

Figure 3 provides an overview of the year-to-year variation in greenhouse gas emissions across sectors from 1990 to 2023. The energy sector started at 145 MtCO<sub>2</sub>-eq in 1990 and has shown a steady increase over the years. It exceeded 250 MtCO<sub>2</sub>-eq in the mid-2000s, rose to between 300 and 400 MtCO<sub>2</sub>-eq in the 2010s, and reached 400 MtCO<sub>2</sub>-eq in 2023. Furthermore, while the industrial sector was at approximately 20 MtCO<sub>2</sub>-eq in 1990, it remained flat until 2000, showed a marked increase after 2005, and reached 70 MtCO<sub>2</sub>-eq by 2023.

In contrast, the agriculture sector remained within the range of approximately 50–70 MtCO<sub>2</sub>-eq and did not show significant fluctuations during the period. The waste sector, on the other hand, was at 10 MtCO<sub>2</sub>-eq in the 1990s, gradually rising to around 20 MtCO<sub>2</sub>-eq, but showed a downward trend again by the 2020s. This graph provides a detailed comparative overview of the long-term trends of the sectors.

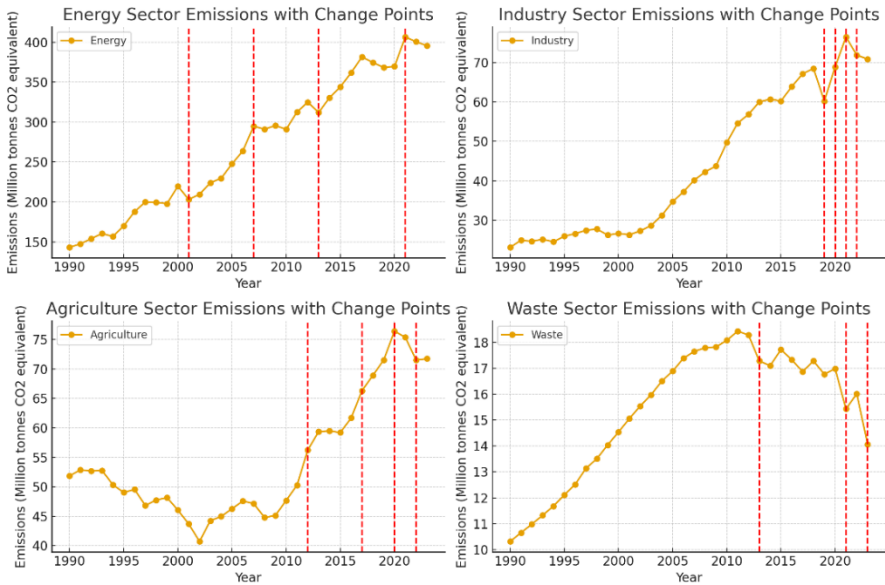


Fig. 4 Waste Sector Emissions with Change Points

Figure 4 depicts the breakpoints observed in emission trends for each sector. In the Energy sector, breakpoints were recorded in 2001, 2007, 2013, and 2021. Significant changes in the rate of increase occurred during these years. In the Industry sector, breakpoints were observed in 2019, 2020, 2021, and 2022, with dramatic shifts in direction occurring during these periods. For the Agriculture sector, breakpoints were identified in 2012, 2017, 2020, and 2022. The graph specifically shows that the curve changed direction in these years. On the last dimension, the waste sector recorded breakpoints in 2013, 2021, and 2023. In this sense, the graph indicates that each sector experienced breakpoints in different periods according to its own dynamics.

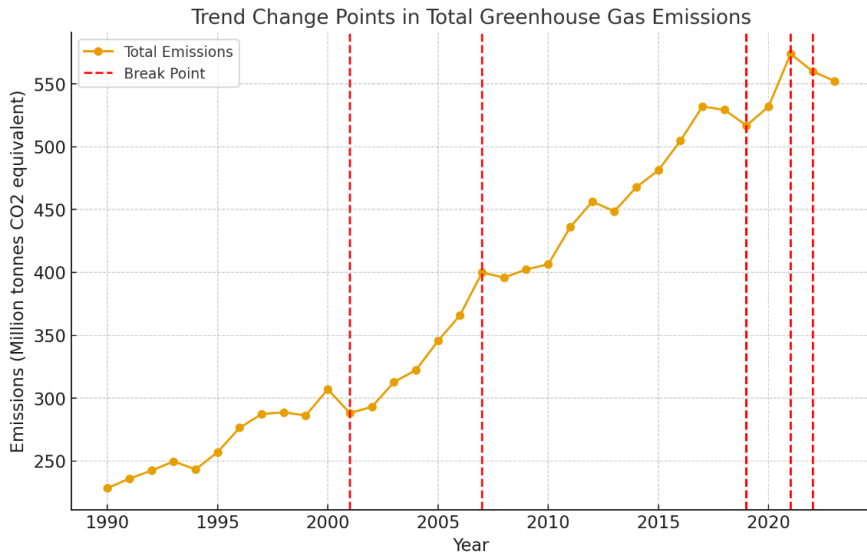
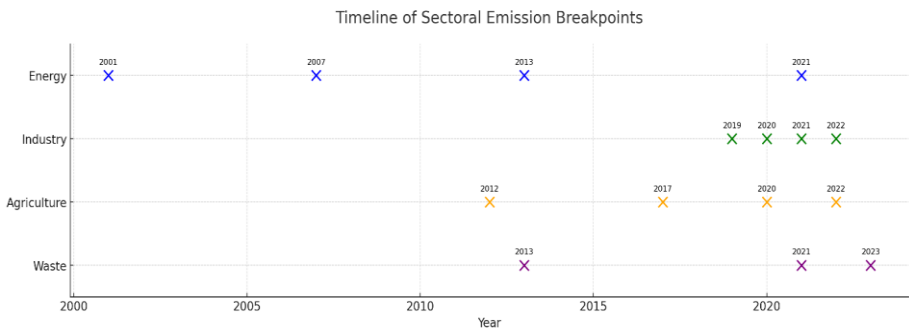


Fig. 5 Trend Change Points in Total Greenhouse Gas Emissions

Figure 5 shows the breakpoints in Türkiye's total greenhouse gas emissions. The years indicated by the red dotted lines are 2001, 2007, 2019, 2021, and 2022. Indicating points where the rate of increase in total emissions changed or reversed direction. The graph highlights these breakpoints within the overall trend of total emissions.



Sector	Year	Associated Global/National Event
Energy	2001	Turkey Economic Crisis
Energy	2007	Global Financial Crisis (2008)
Energy	2013	EU Climate Policy Updates
Energy	2021	Post-pandemic Recovery
Industry	2019	Turkey Economic Contraction
Industry	2020	COVID-19 Pandemic
Industry	2021	Post-pandemic Recovery
Industry	2022	Global Energy Crisis
Agriculture	2012	Post-Kyoto Transition
Agriculture	2017	US withdrawal from Paris Agreement
Agriculture	2020	COVID-19 Pandemic
Agriculture	2022	Global Energy Crisis
Waste	2013	EU Climate Policy Updates
Waste	2021	Post-pandemic Recovery
Waste	2023	Post-Crisis Adjustments

Fig. 6 Timeline of Sectoral Emission Breakpoints

Figure 6 presents the key sectoral breakpoints through a combined timeline and table representation. In the timeline at the top, the breakpoints for the energy, industry, agriculture, and waste sectors are marked in different colors.

Energy sector: 2001, 2007, 2013, 2021  
Industrial sector: 2019, 2020, 2021, 2022  
Agricultural sector: 2012, 2017, 2020, 2022  
Waste sector: 2013, 2021, 2023

The table on the bottom matches the specified years with national and global developments. For exemplary purposes, 2001 is associated with the Türkiye’s economic crisis, 2007 with the global financial crisis, 2012 with the transition to the post-Kyoto era, and 2020 with the COVID-19 pandemic. This figure illustrates the timing of sectoral breakpoints and their alignment with particular global or national events.

IV. DISCUSSION

Emissions data for the period 1990–2023 reveal a long-term upward trend in Türkiye's greenhouse gas emissions. Total emissions started at approximately 230 MtCO<sub>2</sub>-eq in 1990 and reached 550 MtCO<sub>2</sub>-eq in 2023 [11]. This is parallel to the emission increase trends observed in developing countries [2].

The energy sector dominates, accounting for over 70% of total emissions in the sectoral distribution. IPCC (2023) reports emphasize that the energy sector is the most significant source of emission increases in countries dependent on fossil fuel-based energy production [5]. Studies conducted specifically on Türkiye also show that the high share of coal and natural gas in electricity production has led to this result [13], [19]. Additionally, strategic applications aimed at increasing energy and resource efficiency in production sectors not only strengthen economic performance but also environmental sustainability, thus becoming an effective policy tool for reducing greenhouse gas emissions [20].

The industrial sector has shown an upward trend in emissions, particularly since the mid-2000s. The rise in production in energy-intensive sectors such as cement, iron and steel, and chemicals has been a key driver of this trend [6]. In contrast, the agriculture sector has followed a relatively stable trajectory between 1990 and 2023. However, a significant portion of agriculture-related emissions consist of methane (CH<sub>4</sub>) and nitrous oxide (N<sub>2</sub>O) gases, which have a high global warming potential [14]. Although the waste sector has the lowest share, it is important in terms of reduction policies, particularly due to methane emissions [4].

An analysis of trend breakpoints reveals that economic crises and global events have short-term effects. During the 2001 economic crisis, the 2008 global financial crisis, and the 2020 COVID-19 pandemic, there were temporary declines in total emissions. However, these interruptions did not change the long-term upward trend [16]. This situation highlights that Türkiye's emissions are strongly linked to economic growth and energy demand.

As a result, Türkiye's emissions profile is consistent with international observations in the literature. As a result, Türkiye's emissions profile is consistent with international observations in the literature. The energy sector is the leading contributor, while industrial emissions continue to increase, and the agriculture and waste sectors have a more stable structure. Türkiye's emission growth rate is above the OECD average, making it imperative to transform the energy and industrial sectors in particular in climate policies [6]. In this context, strengthening leadership, communication, and awareness-raising processes is crucial to achieving sustainability goals [21].

## V. CONCLUSION

In this study, Türkiye's greenhouse gas emissions for the period 1990–2023 were examined by sector and time series analyses were performed. According to the findings, total greenhouse gas emissions rose from approximately 230 MtCO<sub>2</sub>-eq in 1990 to 550 MtCO<sub>2</sub>-eq in 2023 [11]. The energy sector has maintained its position as the primary source, accounting for over 70% of total emissions. The industrial sector has shown a marked upward trend, particularly since the 2000s, while the agriculture and waste sectors have followed a relatively more stable trajectory. Trend breaks observed in 2001, 2008, 2019, 2020, and 2022 have been associated with economic crises, global financial fluctuations, and the pandemic process; however, these periodic effects did not lead to a permanent decline, and the long-term upward trend has continued. Overall, Türkiye's emissions profile is consistent with the trends indicated for developing countries in international reports [1], [2].

In conclusion, the success of Türkiye's greenhouse gas emission reduction policies depends on increasing renewable energy sources and promoting energy efficiency practices, particularly in the energy sector. Furthermore, developing clean production technologies in the industrial sector, reducing methane and N<sub>2</sub>O emissions in agriculture, and implementing modern waste management methods are critical to controlling the rate of emission growth. However, the success of environmental strategies is directly linked not only to technological measures but also to society's perception of justice and level of participation. In this context, the impact of perceived justice on organizational commitment and voluntary participation highlights the importance of fair and inclusive governance in climate policies [22].

## ACKNOWLEDGMENT

Artificial intelligence programs have been partially utilized to enhance the language accuracy and correct the writing errors in this study.

## REFERENCES

- [1] Intergovernmental Panel on Climate Change (IPCC), *Climate Change 2023: Synthesis Report. Contribution of Working Groups I, II and III to the Sixth Assessment Report*, Geneva, Switzerland: IPCC, 2023. [Online]. Available: [https://www.ipcc.ch/report/ar6/syr/downloads/report/IPCC\\_AR6\\_SYR\\_Longer\\_Report.pdf](https://www.ipcc.ch/report/ar6/syr/downloads/report/IPCC_AR6_SYR_Longer_Report.pdf)
- [2] International Energy Agency (IEA), *CO<sub>2</sub> Emissions in 2023*, Paris, France: IEA, 2024. [Online]. Available: <https://www.iea.org/reports/co2-emissions-in-2023>
- [3] World Meteorological Organization (WMO), *State of the Global Climate 2022*, Geneva, Switzerland: WMO, 2022.
- [4] United Nations Environment Programme (UNEP) and Climate and Clean Air Coalition (CCAC), *Global Methane Assessment: Benefits and Costs of Mitigating Methane Emissions*, Nairobi, Kenya: UNEP, 2021. [Online]. Available: [https://www.ccacoalition.org/sites/default/files/resources/2021\\_Global-Methane\\_Assessment\\_full\\_0.pdf](https://www.ccacoalition.org/sites/default/files/resources/2021_Global-Methane_Assessment_full_0.pdf)
- [5] Intergovernmental Panel on Climate Change (IPCC), *Climate Change 2021: The Physical Science Basis*, Geneva, Switzerland: IPCC, 2021. [Online]. Available: <https://www.ipcc.ch/report/ar6/wg1/>
- [6] Organisation for Economic Co-operation and Development (OECD), *OECD Environmental Performance Reviews: Turkey 2021*, Paris, France: OECD, 2021. [Online]. Available: <https://sdg.eydk.org/wp-content/uploads/2021/12/OECD-Environmental-Performance-Reviews-Turkey.pdf>
- [7] M. Shell. (2002) IEEEtran homepage on CTAN. [Online]. Available: <http://www.ctan.org/tex-archive/macros/latex/contrib/supported/IEEEtran/>
- [8] S. Saraçlı, İ. Kılıç, A. H. Türkan, P. Dursun, İ. Doğan, Ş. Özdemir, and C. Gazeloğlu, “Analysis of university students’ environmental knowledge and behaviors using structural equation modeling,” *IAAOJ Scientific Science*, vol. 2, no. 1, pp. 1–11, 2014.
- [9] United Nations Framework Convention on Climate Change (UNFCCC), *National Inventory Submissions 2022*, 2022.
- [10] United Nations Framework Convention on Climate Change (UNFCCC), *Paris Agreement*, 2015. [Online]. Available: [https://unfccc.int/sites/default/files/english\\_paris\\_agreement.pdf](https://unfccc.int/sites/default/files/english_paris_agreement.pdf)
- [11] C. F. Schleussner, J. Rogelj, M. Schaeffer, T. Lissner, R. Licker, E. M. Fischer, R. Knutti, A. Levermann, K. Frieler, and W. Hare, “Science and policy characteristics of the Paris Agreement temperature goal,” *Nature Climate Change*, vol. 6, pp. 827–835, 2016.
- [12] Turkish Statistical Institute (TURKSTAT), *Greenhouse Gas Emission Statistics, 1990–2023*, Ankara, Turkey: TURKSTAT, 2024.
- [13] M. C. Sezgin, “Paris Climate Agreement, European Green Deal and Turkey’s Position,” *IKV Brief*, Istanbul: Economic Development Foundation (İKV), June

2022. [Online]. Available: [https://www.ikv.org.tr/images/files/IKV\\_Brief\\_Paris\\_Agreement.pdf](https://www.ikv.org.tr/images/files/IKV_Brief_Paris_Agreement.pdf)
- [13] U. Soytaş and R. Sarı, “Energy consumption, economic growth, and carbon emissions: Challenges faced by an EU candidate member,” *Ecological Economics*, vol. 68, no. 6, pp. 1667–1675, 2009.
- [14] M. Isik, I. Ari, and K. Sarica, “Challenges in the CO<sub>2</sub> emissions of the Turkish power sector: Evidence from a two-level decomposition approach,” *Utilities Policy*, vol. 70, p. 101227, 2021.
- [15] S. A. Miçoogulları, “The nexus between carbon emissions and economic growth in Türkiye at the 100th anniversary of the Republic: Rolling window causality analysis with historical data,” *Kent Akademisi Dergisi*, vol. 16, Special Issue, pp. 175–188, 2023.
- [16] E. Akbostancı, G. İ. Tunç, and S. Türüt-Aşık, “CO<sub>2</sub> emissions of Turkish manufacturing industry: A decomposition analysis,” *Applied Energy*, vol. 88, no. 6, pp. 2273–2278, 2011.
- [17] World Bank, World Development Indicators: Environment and Climate, Washington, DC: The World Bank, 2022.
- [18] Intergovernmental Panel on Climate Change (IPCC), *2006 IPCC Guidelines for National Greenhouse Gas Inventories*, 2006. [Online]. Available: <https://www.ipcc-nggip.iges.or.jp/public/2006gl/index.html>
- [19] United Nations Framework Convention on Climate Change (UNFCCC), *National Inventory Submissions 2022*, 2022. [Online]. Available: <https://unfccc.int/process-and-meetings/transparency-and-reporting/reporting-and-review/reporting-and-review-under-the-convention/greenhouse-gas-inventories-annex-i-parties/submissions/national-inventory-submissions-2022>
- [20] S. Saraçlı, İ. Kılıç, İ. Doğan, and C. Gazeloğlu, “An application of data envelopment analysis on marble factories,” *Journal of Inequalities and Applications*, vol. 2013, no. 139, pp. 1–8, 2013.
- [21] Ö. Çelikkol, H. Mertol, and C. Gazeloğlu, “A scale development study: Successful university academicians perceived by students,” *Turkish Studies – Educational Sciences*, vol. 13, no. 19, pp. 473–499, 2018.
- [22] E. Kılıç, C. Gazeloğlu, and E. Aytekin, “Organizational justice perceptions of hospitality business employees in the scope of demographic characteristics: A study in Rize,” in *Issues in Tourism, Human Rights & Sustainable Environment*, pp. 19–33, 2018.





# **Ionic Liquids in the Extraction of Flavonoids from Plants**

**Murat YILDIZ**

Lecturer; Uşak University, Ulubey Vocational School, Department of Design [murat.yildiz@usak.edu.tr](mailto:murat.yildiz@usak.edu.tr)  
ORCID No: 0000-0002-9577-9840

## ABSTRACT

Flavonoids are polyphenolic compounds widely found in plants, notable for their broad spectrum of biological activities, including antioxidant, anti-inflammatory, and antimicrobial effects. The efficient, environmentally friendly, and high-purity extraction of these compounds from plant sources is one of the primary objectives of modern green chemistry approaches. Traditional solvent-based extraction methods are environmentally unsustainable due to their high organic solvent consumption, long processing times, and elevated temperature requirements. Consequently, in recent years, ionic liquids (ILs) have emerged as an alternative class of solvents compatible with the principles of green chemistry for flavonoid extraction.

Unlike conventional solvents, ionic liquids consist entirely of ionic components, enabling them to exhibit both polar and nonpolar characteristics. By modifying the chemical structure of their cations and anions, properties such as viscosity, polarity, and solvation capacity can be precisely tuned. This “designer solvent” feature allows for the selective extraction of flavonoids with different structural characteristics. Moreover, the high thermal and chemical stability of ILs prevents the degradation of heat-sensitive flavonoids, while their ability to form hydrogen bonds and  $\pi$ - $\pi$  interactions significantly enhances solubility.

From an environmental perspective, the low vapor pressure and recyclability of ILs minimize solvent loss, waste generation, and toxic emissions. Furthermore, ILs can function not only as solvents but also as catalysts, enzyme stabilizers, or phase-transfer agents, expanding their utility in extraction processes.

In conclusion, ionic liquid-assisted extraction systems offer a powerful alternative for the environmentally friendly, energy-efficient, and high-yield production of flavonoids. The future of this technology lies in the development of biodegradable ILs and the optimization of large-scale processes, which will further strengthen the integration of green chemistry principles into sustainable production practices.

*Keywords – Ionic liquids, Flavonoid extraction, Green chemistry, Modern extraction techniques, Sustainability*

---

# 1 INTRODUCTION

Flavonoids are polyphenolic compounds synthesized as secondary metabolites in plants, possessing multi-ring structures and representing one of the most important classes of natural compounds in terms of both biological activity and industrial applications. In plants, they play crucial roles in pigmentation, UV protection, and defense mechanisms, while in human health, they exhibit antioxidant, anti-inflammatory, antimicrobial, and cardioprotective properties. Consequently, the efficient and environmentally friendly extraction of flavonoids from natural sources has become an increasingly significant research area in the food, pharmaceutical, cosmetic, and textile industries. However, the extraction of flavonoids is challenging due to their sensitivity to oxidation, heat, and pH fluctuations. Traditional solvent-based methods often require high temperatures, long extraction times, and toxic organic solvents, leading to compound degradation and environmental pollution (Rodríguez De Luna et al., 2020).

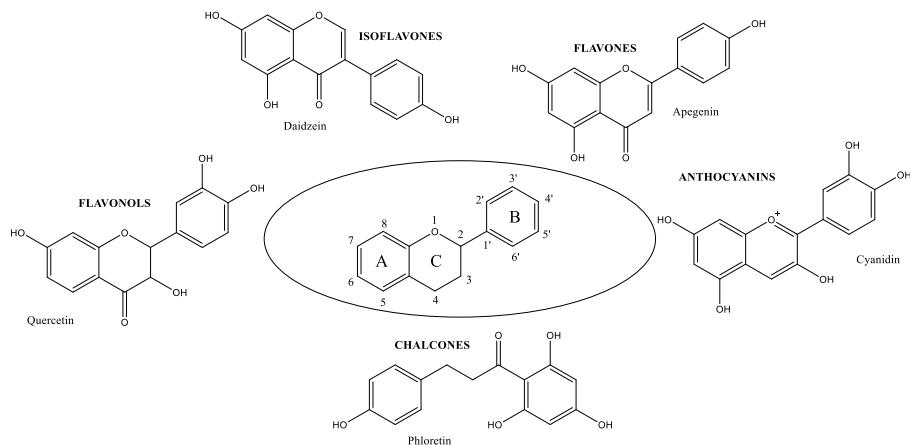


Figure 1 Basic skeleton structure of flavonoids and their classes

To address these challenges, green extraction strategies have been developed, with particular emphasis on the use of ionic liquids (ILs). ILs are liquid salts composed of organic cations and organic or inorganic anions that typically melt below 100 °C. Their low vapor pressure, high thermal stability, tunable chemical structure, and broad solvation range offer several advantages over conventional organic solvents. The use of ILs in flavonoid extraction is especially valuable because these compounds possess both aromatic and hydroxyl functional groups, which can form strong complexes with IL components through hydrogen bonding,  $\pi$ - $\pi$  interactions, and ion-dipole forces (Zhang et al., 2020).

This property makes ILs significantly more selective than conventional solvents. Imidazolium-based ionic liquids ([C<sub>4</sub>mim][Cl], [C<sub>4</sub>mim][BF<sub>4</sub>],

[C<sub>6</sub>mim][PF<sub>6</sub>]) and choline-based biocompatible ILs enhance flavonoid solubility and extraction efficiency by forming strong hydrogen-bond interactions with hydroxyl groups (Ventura et al., 2017). For example, the use of ILs in the extraction of model flavonoids such as rutin, quercetin, and catechin provides not only improved solubility but also greater selectivity in separation (Zhao et al., 2014).

The structural diversity of flavonoids—including flavones, flavanones, flavonols, and isoflavones—results in distinct extraction behaviors due to differences in polarity, hydroxylation degree, and conjugation patterns. Thus, a “single-solvent” approach is often insufficient. The greatest advantage of ILs lies in their ability to be modularly designed to accommodate this structural diversity. By selecting appropriate cations and anions, properties such as viscosity, polarity, hydrophobicity, and solvation capacity can be tuned according to the target flavonoid (Greer, 2020). Hence, ILs are recognized as “designer solvents.”

Because flavonoids are often bound within cellular compartments or cell walls, extraction efficiency is limited. Therefore, ILs are frequently combined with modern assisted techniques such as ultrasound, microwave, and pressurized liquid extraction. Ultrasound-assisted IL extraction (IL-UAE) facilitates cell wall disruption via cavitation, enhancing flavonoid release and significantly reducing extraction time (Jiang et al., 2018). Ji et al. (2018) reported that IL-UAE systems provided significantly higher flavonoid yields in shorter extraction times relative to conventional ultrasound extraction methods. Similarly, microwave-assisted IL extraction (IL-MAE) enables efficient energy absorption due to the high dielectric constant of ILs, resulting in rapid extraction and high yield (Cao et al., 2024).

Some studies have also demonstrated that ILs can function not only as solvents but also as phase-transfer catalysts or reactive media. Protonic ionic liquids and Lewis acidic ILs, for instance, can act as both solvents and reaction media in the conversion of glycosylated flavonoids (e.g., rutin, naringin) to their aglycone forms (Katsoura et al., 2006), enabling a “one-step” process that integrates extraction and pretreatment.

The environmental advantages of ILs stem from their low volatility and recyclability. Since they do not evaporate, ILs produce no atmospheric emissions and can often be recovered after extraction by distillation, membrane separation, or salt precipitation methods. In some systems, ILs have been reused up to five times without significant loss of extraction efficiency (Zhou et al., 2018). However, not all ILs are entirely benign; fluorine-containing anions such as [PF<sub>6</sub>]<sup>−</sup> and [BF<sub>4</sub>]<sup>−</sup> can hydrolyze in the presence of water to produce toxic fluorinated species (Shukla & Mikkola, 2020). Therefore, recent research has focused on developing biodegradable ILs (bio-ILs) based on amino acids, choline, or natural organic acids, which are increasingly preferred for flavonoid extraction (Gómez et al., 2019).

The selection of an IL for flavonoid extraction is generally determined by the target compound's polarity, degree of hydroxylation, and glycosylation. According to Guo et al. (2007) and follow-up COSMO-RS studies, the solubilities of flavonoids in ILs depend strongly on anion–cation combinations, which implies that more hydrophilic ILs (e.g. those with  $\text{Cl}^-$ ) tend to better solubilize polar flavonoids, whereas ILs with more hydrophobic anions (e.g.  $\text{PF}_6^-$ ,  $\text{NTf}_2^-$ ) favor less polar compounds. Thus, ILs can function as dual-purpose solvents: serving as both extraction media and molecular recognition agents that promote selective solvation.

The success of IL-based systems in flavonoid extraction extends beyond yield enhancement. These systems also offer shorter processing times, lower energy consumption, and reduced waste generation. When combined with ultrasound or microwave irradiation, ILs support the key principles of green chemistry—waste prevention, energy efficiency, and safer solvent use (Ventura et al., 2017).

In conclusion, ionic liquids have emerged as high-performance, selective, and environmentally compatible solvents capable of replacing conventional organic solvents in flavonoid extraction. Nevertheless, to achieve full sustainability, further research on the biodegradability, toxicological safety, and economic recovery of ILs remains essential. In the future, with the widespread adoption of bio-ILs, the eco-friendly and high-yield extraction of flavonoids at industrial scale is expected to become a practical reality.

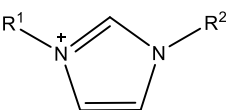
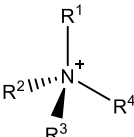
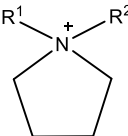
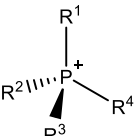
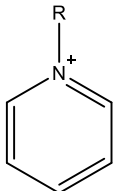
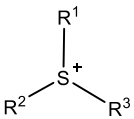
Cations		Anions
		$\text{Cl}^-/\text{AlCl}_4^-$
		$\text{Cl}^-, \text{Br}^-, \text{I}^-$
		$\text{NO}_3^-, \text{SO}_4^{2-}, \text{EtSO}_4^-$
		$\text{CF}_3\text{COO}^-, \text{CH}_3\text{COO}^-, \text{CF}_3\text{COO}^-$
		$\text{BF}_4^-, \text{PF}_6^-$
		$(\text{CF}_3\text{SO}_2)_2\text{N}^-, (\text{CN})_2\text{N}^-$

Figure 2 Anions and cations of Ionic liquids

## 2 ADVANTAGES OF IONIC LIQUIDS IN EXTRACTION

Ionic liquids (ILs) offer a wide range of advantages in the extraction of flavonoids compared to conventional organic solvents. These benefits can be comprehensively evaluated under several key aspects, including solvent efficiency, environmental safety, energy efficiency, and process flexibility.

### 2.1 *High Solubility, Selectivity, and Thermal Stability*

In the efficient extraction of flavonoids from plant materials, solubility and selectivity are among the most critical parameters. Most flavonoids are polyphenolic compounds composed of aromatic rings bearing one or more hydroxyl groups, making them capable of forming hydrogen bonds and engaging in  $\pi$ - $\pi$  interactions. However, conventional organic solvents (such as ethanol, methanol, and acetone) can interact with these complex structures only to a limited extent, often resulting in low solubility and poor selectivity (Chaves et al., 2020). Consequently, the use of ionic liquids (ILs) over the past decade has brought about a major transformation in improving solubility and thermal stability in flavonoid extraction.

Ionic liquids, owing to their fully ionic nature, can form strong molecular interactions with flavonoids. The cations typically consist of imidazolium, choline, or pyridinium derivatives, while the anionic components may include acetate, chloride, tetrafluoroborate, or phosphate ions. This configuration enables ILs to act as either hydrogen bond donors or acceptors. Zhao et al. (2014) demonstrated that ionic liquid-based ultrasonic-microwave-assisted extraction (IL-UMAE) significantly increased the yields of rutin and quercetin—by approximately 2.0- to 2.3-fold compared with conventional ethanol reflux extraction—due to enhanced hydrogen-bond and electrostatic interactions between the flavonoid hydroxyl groups and IL anions. Similarly, Liu et al. (2013) investigated the extraction of quercetin and kaempferol using imidazolium-based ionic liquids and confirmed that  $\pi$ - $\pi$  stacking and hydrogen-bonding interactions between  $[C_4mim]^+$  cations and flavonoid aromatic rings were responsible for the marked improvement in solubility and extraction efficiency.

This selectivity is significant not only in terms of solubility but also for molecular separation. ILs can discriminate between phenolic and flavonoid subgroups based on their polarity differences. For instance, glycosylated flavonoids such as rutin dissolve more effectively in hydrophilic ILs like  $[C_2mim][Br]$  or choline-based  $[Ch][DHP]$ , whereas aglycone forms such as naringenin and hesperetin exhibit higher solubility in hydrophobic ILs with longer alkyl chains such as  $[C_6mim][PF_6]$  and  $[C_8mim][NTf_2]$  (Liu et al., 2013). Thus, IL systems provide designer selectivity, enabling the targeted extraction of specific flavonoid subclasses.

Another notable advantage of ILs is their ability to provide thermal stability. Flavonoids are heat-sensitive compounds, and prolonged exposure to elevated temperatures can cause oxidative degradation of phenolic rings and

lead to discoloration. The high heat capacity and low vapor pressure of ionic liquids help regulate thermal transfer within the extraction medium, thereby minimizing degradation of heat-sensitive flavonoids (Zeng et al., 2010). In a comparative study, Zhao et al. (2014) reported that microwave-assisted extraction in ionic liquid media preserved anthocyanin and flavonoid stability by approximately 25–30% compared with ethanol systems, while significantly enhancing total antioxidant capacity. Consequently, ILs act as both physical and chemical protectants.

In summary, the high solubility, selectivity, and thermal stability provided by ionic liquids represent key advancements in the efficiency of flavonoid extraction. These properties position ILs as superior alternatives to conventional solvents, offering safer, more sustainable, and higher-yielding solutions for natural product isolation.

## **2.2 Environmental Safety, Recoverability, and Waste Reduction**

One of the core principles of the green chemistry approach is to minimize the use of hazardous solvents and reduce the environmental impact of chemical processes. The extraction of flavonoids from plant materials has traditionally relied on organic solvents, which often involve the use of large amounts of volatile compounds such as methanol, acetone, and ethyl acetate, leading to significant solvent waste. This not only increases production costs but also poses substantial environmental risks (Chave et al., 2020). Ionic liquids (ILs), with their low volatility, recoverability, and reusability, offer a sustainable and long-term solution to these challenges.

A defining feature of ILs is their extremely low vapor pressure. As a result, they do not evaporate into the atmosphere during extraction, do not generate volatile organic compound (VOC) emissions, and eliminate solvent loss. Ventura et al. (2017) described ILs as “non-toxic volatile alternatives,” noting that imidazolium-based ILs such as [C<sub>4</sub>mim][Cl] have evaporation tendencies up to 1000 times lower than those of conventional volatile solvents. This characteristic not only enhances laboratory safety but also contributes to a significant reduction in the carbon footprint.

Beyond their environmental advantages, ILs are highly valued for their recoverability. Most ionic liquids can be reused after extraction through distillation, liquid–liquid separation, adsorption, or membrane filtration techniques (Zuo & Guo, 2020). This reusability not only minimizes waste generation but also reduces overall process costs. Additionally, due to their chemical stability, ILs do not degrade during extraction, and the resulting waste does not contain toxic residues.

The environmental safety of ILs is also linked to their biodegradability. Fluorine-containing anions such as [BF<sub>4</sub>]<sup>−</sup> and [PF<sub>6</sub>]<sup>−</sup> can hydrolyze under high-temperature conditions to produce toxic fluoride species. Consequently, recent research has focused on developing biodegradable ionic liquids (Bio-ILs) based on amino acids, choline, or natural organic acids. These ILs are



environmentally compatible, low in toxicity, and especially suitable for applications in the food and cosmetic industries, where the safety of flavonoid extracts is paramount.

Another ecological advantage of ILs lies in their ability to minimize solvent consumption and waste generation. While conventional extraction systems typically require large volumes of organic solvents, IL-assisted processes operate efficiently with small amounts. Their strong solvation capacity and tunable polarity enhance extraction efficiency and selectivity, thereby reducing the need for repeated extraction cycles (Zhao et al., 2014; Zeng et al., 2010; Liu et al., 2013).

In conclusion, owing to their chemical stability, reusability, and low environmental impact, ionic liquids stand out as eco-friendly solvents that generate minimal waste in flavonoid extraction. These characteristics align ILs perfectly with the green chemistry principles of waste prevention, safer solvent use, and resource efficiency.

### **2.3 Energy Efficiency and Process Intensification**

Flavonoid extraction is typically a multi-step and time-consuming process. In conventional solvent systems, long extraction durations, high temperature requirements, and limited mass transfer increase energy consumption and reduce overall economic efficiency. The integration of ionic liquids (ILs) into these systems enhances both energy efficiency and extraction kinetics. Due to their high dielectric constant, ionic conductivity, and tunable viscosity, ILs optimize energy transfer, offering significant advantages—particularly in microwave-assisted extraction (MAE) and ultrasound-assisted extraction (UAE) systems (El Maabiche et al., 2025). In microwave-assisted systems, ionic liquids efficiently absorb microwave energy because of their high dielectric loss factor ( $\epsilon''$ ), resulting in rapid and uniform heat transfer throughout the medium. This property dramatically reduces extraction time compared to conventional solvents (Zhao et al., 2023) al. (2021).

The heat capacity and viscosity of ionic liquids play a critical role in determining energy efficiency. Owing to their high thermal conductivity, ILs distribute heat evenly, eliminating local temperature gradients. This is especially beneficial for heat-sensitive flavonoids such as anthocyanins, rutin, and morin, where degradation risks are significantly reduced (Zhao et al., 2020). Furthermore, the high solvation capability of ILs facilitates the rapid disintegration of cell wall barriers during extraction, accelerating mass transfer.

From an energy-saving perspective, another advantage of IL-based systems is their compatibility with multiple energy sources. They can be efficiently integrated into microwave, ultrasonic, thermal, and pressure-driven extraction methods. In pressurized liquid extraction (PLE) and supercritical fluid extraction (SFE), the excellent thermal stability of ILs allows them to remain chemically intact under high temperature and pressure, enabling faster equilibrium and higher mass-transfer efficiency (Wu et al., 2012).

Furthermore, the use of IL media enhances the mass transfer coefficient by weakening cell-wall integrity and reducing interfacial resistance, thereby accelerating the diffusion of intracellular flavonoids (Zhao et al., 2014).

In conclusion, ionic liquids serve not only as environmentally friendly solvent alternatives but also as energy-efficient process accelerators in flavonoid extraction. IL-based systems can reduce energy consumption by up to 40% in microwave and ultrasonic extractions while shortening total process time to just a few minutes. As a result, these systems provide significant improvements in both yield and sustainability, establishing energy-efficient extraction processes that are fully aligned with the core principles of green chemistry.

#### **2.4 Designability and Multifunctionality**

The most significant and distinctive feature of ionic liquids (ILs) is their ability to be tailored to the target molecule—a property that has earned them the title of *designer solvents*. While traditional solvents possess fixed polarity and solubility characteristics within narrow ranges, ILs can be precisely tuned by altering their cation and anion components. This tunability provides a major advantage, particularly for the selective extraction of flavonoids with different polarities such as quercetin, naringenin, rutin, and morin. By modifying the cation's alkyl chain length, the anion's hydrogen-bonding capacity, or the degree of basicity, the polarity, viscosity, and solvation capacity of the IL can be optimized for a specific target compound (Rahman et al, 2017).

Wu et al. (2012) compared 3 different alkyl length ionic liquids and found that increasing the alkyl chain length enhanced the solubility of hydrophobic flavonoids, whereas shorter-chained and more hydrophilic ILs performed better for glycosylated flavonoids. This finding demonstrates that the molecular level designability of ILs directly determines flavonoid selectivity. The designability of ILs extends beyond solvation properties—it also encompasses multifunctionality. ILs can act as phase-transfer catalysts, reactive media, enzyme stabilizers, or co-solvents in the extraction process.

Protonic ionic liquids (PILs) and Brønsted-acidic ILs can act simultaneously as solvents and catalysts in the hydrolysis of flavonoid glycosides into their corresponding aglycone forms, enabling an integrated *reactive extraction* process. For example, Yao et al. (2012) demonstrated that the Brønsted-acidic ionic liquid  $[\text{HO}_3\text{S}(\text{CH}_2)_4\text{mim}]\text{HSO}_4$  facilitated both the extraction and hydrolysis of flavonol glycosides from *Ginkgo biloba* foliage within a single step under microwave-assisted conditions. Similarly, Xu et al. (2012) showed that imidazolium-based ionic liquids can promote both solubilization and catalytic activity during microwave-assisted extraction of flavonoids from *Bauhinia championii*. In enzyme-assisted systems, ILs have been found to enhance enzymatic stability and activity by maintaining the hydrogen-bonding network and preventing protein denaturation, as demonstrated by Katsoura et al. (2006) during biocatalytic modification of flavonoids in ionic

liquid media. Furthermore, ILs facilitate interfacial interactions in biphasic systems, increasing the selectivity of flavonoid recovery by promoting the separation between phenolic and lipophilic compounds due to their amphiphilic nature and tunable polarity.

The multifunctional nature of ILs also supports process scalability. Employing a single IL system as both solvent and catalytic medium eliminates the need for solvent exchange and reduces waste generation. Consequently, IL-based extraction systems become economically and environmentally viable for scaling up from laboratory to industrial applications.

In summary, the designable structure and multifunctionality of ionic liquids provide unique advantages in flavonoid extraction, including high selectivity, single-step process integration, and strong alignment with green chemistry principles. These qualities make ILs not only efficient solvents but also active participants in chemical processes—establishing a new paradigm for sustainable and high-performance extraction technologies.

### **3 IONIC LIQUIDS IN MODERN EXTRACTION TECHNIQUES**

Modern extraction techniques developed for the environmentally friendly and high-efficiency recovery of flavonoids from plant matrices are grounded in the fundamental principles of green chemistry. Methods such as ultrasound-assisted extraction (UAE), microwave-assisted extraction (MAE), pressurized liquid extraction (PLE), supercritical fluid extraction (SFE), and enzyme-assisted extraction (EAE) have gained prominence due to their low energy consumption, short processing time, and minimal solvent use.

In these systems, the incorporation of ionic liquids (ILs) as solvents or co-solvent phases enhances selectivity, facilitates solvent recovery, and minimizes environmental impact. ILs improve mass transfer, stabilize thermolabile flavonoids, and reduce the need for hazardous organic solvents. As a result, the integration of ILs into modern extraction technologies has introduced a new dimension to flavonoid recovery—combining high efficiency with environmental sustainability in full alignment with the goals of green chemistry.

#### **3.1 *Ultrasound-Assisted Extraction (UAE)***

Ultrasound-assisted extraction (UAE) is among the most efficient modern techniques for obtaining flavonoids from plant matrices, combining mechanical disruption and enhanced mass transfer under relatively mild conditions. The cavitation effect generated by ultrasonic waves produces microbubbles that collapse violently, causing localized high temperatures and pressure differentials that rupture plant cell walls and facilitate the release of intracellular compounds (Rodríguez De Luna et al., 2020). This mechanism significantly accelerates solvent penetration and shortens

extraction time while maintaining the structural integrity of heat-sensitive flavonoids.

The integration of ionic liquids (ILs) into UAE systems has further improved extraction efficiency, selectivity, and sustainability. ILs act not only as solvents but also as phase-transfer enhancers, improving the solubility of both hydrophilic and hydrophobic flavonoids through hydrogen bonding,  $\pi$ - $\pi$  stacking, and electrostatic interactions (Ventura et al., 2017; Zuo et al., 2020). Ji et al. (2018) demonstrated that an IL-UAE system using [C<sub>4</sub>mim][Cl] achieved a 45% higher total flavonoid yield from *Glycyrrhiza uralensis* compared to ethanol under optimized conditions (50 °C, 25 min, 200 W). Similarly, Jiang et al. (2018) reported that ultrasound-assisted extraction with imidazolium-based ILs enhanced the recovery of biflavonoids from *Selaginella helvetica* by improving antioxidant activity and reducing extraction time by nearly two-thirds relative to conventional solvents.

The physicochemical properties of ILs—especially viscosity, polarity, and cation-anion structure—play a critical role in UAE performance. Zhao et al. (2014) and Wang et al. (2016) showed that moderate-viscosity ILs, particularly choline and imidazolium derivatives, produce optimal cavitation effects by balancing bubble formation and collapse dynamics. Excessively viscous ILs can inhibit cavitation and lower mass transfer efficiency; therefore, binary solvent systems (e.g., IL-ethanol or IL-water mixtures) are often employed to optimize viscosity and facilitate solvent recovery (Zhou et al., 2018).

Zuo et al. (2020) further demonstrated that dual-chain imidazolium ILs improve cavitation intensity and stabilize the resulting emulsions, achieving superior extraction yields and selectivity for flavonoids. The strong solvation capability of ILs also helps minimize co-extraction of undesired pigments or tannins, leading to higher purity of extracts (El Maabiche et al., 2025). Importantly, UAE with ILs aligns with green chemistry principles by reducing solvent consumption and energy requirements. Compared to traditional maceration, IL-UAE systems typically use five to ten times less solvent and consume up to 40% less energy while providing higher extraction efficiency (Chaves et al., 2020; Cao et al., 2024).

From an environmental perspective, the use of biodegradable ILs—particularly choline-based and amino-acid-derived types—further minimizes toxicity and enhances process sustainability (Gómez et al., 2019). ILs can be effectively recovered and reused up to five times without significant efficiency loss, contributing to circular solvent utilization (Zhou et al., 2018; Ventura et al., 2017).

Overall, IL-assisted UAE represents a sustainable, high-yield, and energy-efficient technique for flavonoid extraction. The synergy between ultrasound-induced cavitation and IL solvation properties enhances both the rate and selectivity of extraction, while also reducing environmental impact.

This technology thus offers a viable industrial pathway for eco-friendly flavonoid recovery under the framework of green chemistry.

### 3.2 **Microwave-Assisted Extraction (MAE)**

Microwave-assisted extraction (MAE) is an advanced, energy-efficient technique that utilizes electromagnetic radiation to rapidly heat both the solvent and plant matrix through dipole rotation and ionic conduction. The oscillating microwave field induces localized pressure and temperature gradients within the plant tissues, leading to cell wall rupture and enhanced release of flavonoids into the extraction medium (Rodríguez De Luna et al., 2020). This method minimizes processing time and solvent usage compared to conventional heating, aligning well with green chemistry principles.

The incorporation of ionic liquids (ILs) into MAE systems has significantly improved extraction efficiency, selectivity, and process sustainability. ILs possess high dielectric constants and strong microwave absorption capacities, allowing for rapid and uniform heating. Xu et al. (2012) demonstrated that imidazolium-based ILs such as [C<sub>4</sub>mim][BF<sub>4</sub>] enabled highly efficient extraction of flavonoids from *Bauhinia championii* under microwave irradiation, achieving over 50% yield improvement compared with ethanol-based systems. Similarly, Yao et al. (2012) reported that a Brønsted-acidic IL, [HO<sub>3</sub>S(CH<sub>2</sub>)<sub>4</sub>mim]HSO<sub>4</sub>, simultaneously facilitated extraction and hydrolysis of flavonol glycosides from *Ginkgo biloba* foliage, exemplifying the dual solvent–catalyst role of certain ILs.

Recent investigations confirm that IL–MAE systems can enhance extraction efficiency not only by improved dielectric heating but also by promoting stronger solute–solvent interactions such as hydrogen bonding,  $\pi$ – $\pi$  stacking, and electrostatic attraction (Zhao et al., 2023; Zhang et al., 2020). Cao et al. (2024) showed that microwave-assisted extraction using choline-based ILs from *Carica papaya* leaves yielded higher total polyphenol content and antioxidant activity than other green solvents, including ethanol and deep eutectic mixtures. Likewise, Zeng et al. (2010) demonstrated that IL-based MAE significantly increased rutin recovery from traditional Chinese medicinal plants while maintaining structural integrity of the molecule.

IL physicochemical properties—especially viscosity, polarity, and cation–anion combination—are key factors influencing extraction efficiency. Liu et al. (2013) highlighted that medium-viscosity imidazolium ILs provided optimal microwave penetration and heat transfer during simultaneous extraction of kaempferol and quercetin, resulting in higher purity and reduced degradation. However, excessively viscous ILs may hinder diffusion and microwave energy dispersion; therefore, binary solvent systems (e.g., IL–ethanol or IL–water mixtures) are often employed to achieve an optimal balance (Zhou et al., 2018).

From an environmental standpoint, IL–MAE systems are advantageous because they minimize solvent waste, reduce energy consumption, and allow solvent recovery and reuse. Ventura et al. (2017) and Zhou et al. (2018)

emphasized that many ILs can be recycled multiple times without significant loss of extraction performance, substantially lowering process costs and emissions. Moreover, bio-based and biodegradable ILs—such as choline and amino-acid-derived variants—further reduce toxicity and align the MAE process with sustainable production goals (Gómez et al., 2019).

Overall, IL-assisted MAE represents one of the most promising green extraction strategies for flavonoids. The synergy between microwave irradiation and ionic liquid media enhances heating uniformity, selectivity, and catalytic potential while dramatically reducing extraction time and energy use. These advantages make IL–MAE systems an efficient and environmentally responsible technology for large-scale production of high-value flavonoids.

### **3.3 Pressurized Liquid Extraction (PLE)**

Pressurized Liquid Extraction (PLE), also known as accelerated solvent extraction, is a modern green technology that enables rapid recovery of flavonoids and other polyphenolic compounds using moderate temperatures and high pressures while maintaining the solvent in a liquid state. By operating typically between 50–200 °C and 10–20 MPa, PLE combines the diffusivity of gases with the solvation strength of liquids, resulting in improved penetration of the solvent into plant tissues and faster mass transfer of intracellular compounds (Dobroslavić et al., 2022). This method significantly reduces solvent usage and extraction time compared to conventional techniques, aligning closely with green chemistry principles.

The integration of ionic liquids (ILs) into PLE systems has opened new avenues for sustainable and selective flavonoid extraction. ILs provide enhanced thermal stability, high solvation capacity, and tunable polarity, enabling them to withstand elevated temperatures and pressures without degradation (Ventura et al., 2017; Pérez-Vázquez et al., 2023). For example, imidazolium-based ILs such as [C<sub>4</sub>mim][BF<sub>4</sub>] and [C<sub>4</sub>mim][Cl] have demonstrated improved extraction efficiency for flavonoids like quercetin and rutin compared to ethanol and acetone systems (Zuo et al., 2020). These ILs promote stronger hydrogen-bonding and  $\pi$ – $\pi$  interactions with hydroxylated aromatic rings, resulting in higher selectivity toward target compounds (Zhang et al., 2020).

Chaves et al. (2020) and Rodríguez De Luna et al. (2020) highlighted that IL-assisted PLE achieves up to 40–60% higher flavonoid recovery than conventional organic solvents under equivalent operating conditions. This enhancement is primarily attributed to the synergistic effect of high-pressure mass transfer and the adjustable physicochemical properties of ILs. In addition, the reduced viscosity of ILs at elevated temperatures improves diffusion coefficients, allowing the solvent to penetrate the plant matrix more efficiently (Cao et al., 2024).

From an environmental and operational perspective, IL–PLE systems are particularly advantageous due to their recyclability and low volatility. Zhou

et al. (2018) reported that ILs can be recovered and reused multiple times without significant performance loss, minimizing both waste generation and process costs. Moreover, the use of biodegradable ILs—especially those derived from choline or amino acids—reduces the ecological footprint associated with traditional fluorinated ILs (Gómez et al., 2019; Ventura et al., 2017).

Recent studies also demonstrate that IL-assisted PLE systems enhance antioxidant activity and total phenolic content in extracts, confirming that high temperature and pressure do not compromise the bioactivity of thermally sensitive compounds (Pérez-Vázquez et al., 2023). The combination of ILs' thermal resistance and selective solvation mechanisms makes PLE particularly suitable for the large-scale valorization of agro-industrial by-products as sources of natural antioxidants.

Overall, IL-based PLE systems combine the benefits of rapid extraction, solvent reduction, and process sustainability. Through precise adjustment of IL composition and extraction parameters, it is possible to achieve high yields of structurally intact flavonoids with minimal environmental impact. Thus, IL-PLE represents one of the most powerful and environmentally responsible strategies within modern green extraction technologies.

### **3.4 Supercritical Fluid Extraction (SFE)**

Supercritical Fluid Extraction (SFE) is a highly efficient and environmentally benign technique for isolating bioactive compounds such as flavonoids from plant matrices. It typically employs supercritical carbon dioxide (scCO<sub>2</sub>) as the extraction solvent, owing to its low toxicity, non-flammability, and ease of recyclability. Above its critical point (31.1 °C and 7.38 MPa), CO<sub>2</sub> exhibits dual characteristics of gases and liquids—high diffusivity and adjustable solvating power—which allow it to penetrate plant cells and solubilize target compounds effectively (Rodríguez De Luna et al., 2020). This makes SFE an excellent choice for the recovery of thermolabile flavonoids while minimizing solvent residues and environmental burden.

However, because CO<sub>2</sub> is a relatively nonpolar solvent, its application for polar flavonoids is limited. To overcome this challenge, ionic liquids (ILs) have been introduced as co-solvents or modifiers in SFE systems. ILs possess tunable polarity and high thermal stability, which enable them to act as mediators between nonpolar CO<sub>2</sub> and polar solutes, thereby enhancing mass transfer and solubility (Ventura et al., 2017; Pérez-Vázquez et al., 2023). In particular, choline-based and imidazolium-based ILs have shown strong affinity for hydroxylated aromatic systems, facilitating hydrogen bonding and  $\pi$ - $\pi$  interactions with flavonoid molecules (Zuo et al., 2020; Wang et al., 2016).

Pérez-Vázquez et al. (2023) demonstrated that introducing [C<sub>4</sub>mim][BF<sub>4</sub>] and [Ch][DHP] into scCO<sub>2</sub> significantly improved the extraction yield of quercetin and naringenin from citrus peels by 50–65% compared to conventional CO<sub>2</sub> systems. This enhancement results from the formation of

transient IL–CO<sub>2</sub> complexes that increase solvent polarity without compromising gas-like diffusivity. Similarly, Zuo et al. (2020) reported that dual-chain imidazolium ILs enhanced CO<sub>2</sub> solubility and mass transfer, leading to superior extraction efficiency for plant-derived flavonoids.

From a green chemistry perspective, the IL–SFE combination offers several sustainability benefits. The low volatility and recyclability of ILs prevent solvent losses and volatile organic compound emissions, while the use of CO<sub>2</sub> as a primary solvent ensures complete recovery and reuse (Zhou et al., 2018). Gómez et al. (2019) demonstrated that choline amino-acid-based ILs could be recovered for multiple extraction cycles with negligible performance loss, underscoring their circular solvent potential. Additionally, these bio-derived ILs reduce the toxicity associated with fluorinated anions such as [PF<sub>6</sub>]<sup>−</sup> and [BF<sub>4</sub>]<sup>−</sup>, which are known to hydrolyze under moisture and produce hazardous species (Ventura et al., 2017).

The coupling of ILs with SFE not only enhances extraction yields but also preserves the bioactivity of flavonoids. The mild operating conditions and inert nature of CO<sub>2</sub> protect phenolic hydroxyl groups from oxidation, while ILs provide additional stabilization through noncovalent interactions (El Maabiche et al., 2025). Moreover, ILs reduce energy consumption by allowing the system to reach thermodynamic equilibrium faster and at lower pressures (Chaves et al., 2020).

Overall, IL-assisted SFE represents one of the most advanced and environmentally responsible extraction strategies available for high-value flavonoids. By integrating the tunable solvating capacity of ILs with the clean and recyclable nature of supercritical CO<sub>2</sub>, this hybrid technique combines high selectivity, short processing time, and minimal waste generation. It therefore aligns perfectly with the green chemistry principles of safer solvents, waste prevention, and energy efficiency, providing a viable industrial pathway for sustainable flavonoid production.

### 3.5 *Enzyme-Assisted Extraction (EAE)*

Enzyme-Assisted Extraction (EAE) is a biocatalytic approach that employs cell-wall-degrading enzymes to release flavonoids and other phenolic compounds from plant matrices under mild conditions. Plant cell walls are composed primarily of cellulose, hemicellulose, lignin, and pectin, which form a complex network that limits solvent penetration and the release of intracellular metabolites. Enzymes such as cellulase, pectinase, and  $\beta$ -glucosidase selectively hydrolyze these components, weakening structural barriers and facilitating the diffusion of bioactives into the solvent phase (Rodríguez De Luna et al., 2020). Compared to conventional extraction, EAE offers higher selectivity, lower energy consumption, and improved preservation of thermolabile compounds.

The integration of ionic liquids (ILs) with EAE systems has emerged as an innovative strategy to enhance enzymatic efficiency and process



sustainability. ILs provide a tunable environment that stabilizes enzyme conformation and maintains catalytic activity by modulating polarity, viscosity, and hydrogen-bonding capacity (Ventura et al., 2017). Katsoura et al. (2006) demonstrated that certain imidazolium- and ammonium-based ILs can serve as effective biocatalytic media for flavonoid modification reactions, preserving enzyme activity and improving reaction selectivity. This stabilization effect is attributed to the ability of ILs to create microenvironments that strengthen intramolecular hydrogen bonds and prevent protein denaturation.

Furthermore, biocompatible ILs—especially those derived from choline or amino acids—can function synergistically with enzymes by increasing substrate accessibility and reducing enzyme inhibition (Gómez et al., 2019; El Maabiche et al., 2025). These ILs partially solubilize plant cell wall components, enhancing enzyme–substrate interactions and accelerating flavonoid release. Zuo et al. (2020) also reported that dual-chain ILs improve mass transfer in biphasic systems, promoting selective solubilization of flavonoids over nonpolar impurities.

From a sustainability standpoint, IL–EAE systems align strongly with green chemistry principles. The use of recyclable and biodegradable ILs minimizes solvent waste and toxicity, while the enzymatic process itself reduces thermal and chemical degradation risks. Zhou et al. (2018) emphasized that ILs can be efficiently recovered and reused without substantial loss in enzymatic efficiency, enabling circular process operation. Chaves et al. (2020) and Ventura et al. (2017) further noted that coupling ILs with enzyme catalysis not only enhances extraction yield but also maintains the structural and antioxidant integrity of the flavonoids extracted.

The mild operating conditions of IL-assisted EAE—typically between 35–55 °C—prevent oxidation or hydrolysis of sensitive phenolic structures, resulting in extracts with high bioactivity. Additionally, enzyme specificity allows for the targeted hydrolysis of glycosidic bonds, yielding aglycones with greater biological potency. These combined effects render IL–EAE a powerful alternative to conventional solvent-based extraction for the sustainable recovery of high-value flavonoids.

Overall, the combination of enzymatic catalysis and ionic liquid systems provides a highly selective, low-energy, and environmentally friendly platform for flavonoid extraction. By merging biological and chemical green technologies, IL-assisted EAE exemplifies a next-generation approach to sustainable bioprocessing within the framework of circular and green chemistry.

Table 1 Extraction of Flavonoids Using IL-Based Processes

Extracted Flavonoid(s)	Extraction Technique	Key Findings	Reference
<b>Rutin and Quercetin</b>	Ionic liquid–microwave-assisted extraction (IL–MAE)	Imidazolium IL [C <sub>4</sub> mim][BF <sub>4</sub> ] achieved ~50% higher extraction yield than ethanol; improved microwave heating efficiency and reduced degradation.	Xu at al., 2012
<b>Flavonol glycosides (<i>Ginkgo biloba</i>)</b>	Brønsted-acidic IL–MAE	Brønsted-acidic IL [HO <sub>3</sub> S(CH <sub>2</sub> ) <sub>4</sub> mim]HSO <sub>4</sub> enabled simultaneous extraction and hydrolysis of glycosides in a single step under microwave conditions.	Yao at al., 2012
<b>Rutin (velvetleaf leaves)</b>	Simultaneous ultrasonic- and microwave-assisted IL extraction	IL [C <sub>4</sub> mim][Cl] increased rutin yield by 60% compared to ethanol; total time reduced to 20 min.	Zhao at al., 2014
<b>Kaempferol and Quercetin</b>	IL–MAE (simultaneous extraction)	Medium-viscosity imidazolium ILs provided optimal dielectric heating and high-purity flavonoid recovery.	Liu at al., 2013
<b>Biflavonoids (<i>Selaginella helvetica</i>)</b>	IL–UAE (ultrasound-assisted extraction)	Imidazolium ILs doubled extraction yield and enhanced antioxidant activity compared with conventional solvents.	Jiang at al., 2018
<b>Flavonoid glycosides and saponins (<i>Glycyrrhiza uralensis</i>)</b>	IL–UAE	[C <sub>4</sub> mim][Cl] yielded 45% higher total flavonoid content than ethanol under optimized ultrasonic conditions (50 °C, 25 min).	Ji at al., 2018
<b>Flavonoids (Chinese medicinal plants)</b>	IL–MAE	Ionic-liquid media improved rutin recovery and preserved molecular integrity; efficient dielectric heating.	Zeng at al., 2010
<b>Flavonoids (<i>Carica papaya</i> leaves)</b>	IL–MAE	Choline-based ILs provided the highest total polyphenol yield and antioxidant activity; reduced energy consumption.	Cao at al., 2024

Extracted Flavonoid(s)	Extraction Technique	Key Findings	Reference
<b>Plant-derived Flavonoids</b>	Dual-chain IL-assisted extraction	Dual-chain imidazolium ILs enhanced mass transfer and selectivity for flavonoids, yielding higher recovery efficiency.	Zuo at al., 2020
<b>Flavonoids (Citrus peels)</b>	IL–SFE (supercritical CO <sub>2</sub> + IL)	[C <sub>4</sub> mim][BF <sub>4</sub> ] and [Ch][DHP] increased quercetin and naringenin yields by 50–65% vs. pure CO <sub>2</sub> ; improved solvent polarity and diffusion.	Pérez-Vázquez at al., 2023
<b>Flavonoid derivatives</b>	Enzyme-assisted biocatalysis in IL media	IL systems preserved enzyme activity and enhanced synthesis of antioxidant flavonoid derivatives.	Katsoura at al., 2006

## 4 IONIC LIQUIDS IN TRADITIONAL EXTRACTION TECHNIQUES

Traditional extraction methods used for isolating flavonoids from plant materials have long formed the foundation of research and industrial production. Classical approaches such as maceration and Soxhlet extraction are known for their operational simplicity and well-established experimental history. However, these techniques involve significant disadvantages, including the extensive use of organic solvents, long extraction durations, and high energy consumption—all of which conflict with the principles of green chemistry. In recent years, the integration of ionic liquids (ILs) into such traditional systems has been recognized as a promising step toward reducing solvent consumption, enhancing selectivity, and transforming conventional extraction methods into more sustainable and environmentally friendly processes.

### 4.1 *Maceration*

Maceration is one of the oldest solvent-based extraction techniques used for isolating flavonoids from plant materials. In this method, the plant matrix is immersed in a solvent for a specific duration at ambient or slightly elevated temperature, allowing solute diffusion into the liquid phase. Although simple and inexpensive, conventional maceration often suffers from long extraction times, high solvent consumption, and limited efficiency in recovering intracellular flavonoids due to diffusion barriers and thermal degradation risks (Rodríguez De Luna et al., 2020).

The introduction of ionic liquids (ILs) into maceration systems has considerably improved extraction selectivity and sustainability. ILs provide

tunable polarity, strong hydrogen-bonding capacity, and the ability to disrupt plant cell walls, thereby facilitating the solubilization of hydroxylated aromatic compounds such as quercetin, rutin, and luteolin (Ventura et al., 2017; Chaves et al., 2020). Wang et al. (2016) demonstrated that choline amino-acid-based ILs enhanced the dissolution of flavonoids from *Citrus reticulata* peels while simultaneously aiding pectin removal, increasing extraction efficiency by nearly 40 % compared with ethanol. This synergistic dissolution of polysaccharides and phenolics creates a more permeable plant matrix and accelerates diffusion.

Moreover, Gómez et al. (2019) reported that biodegradable choline amino-acid ILs form aqueous biphasic systems capable of selectively partitioning flavonoids, reducing solvent toxicity and improving recovery. These IL systems can be reused several times with minimal performance loss, highlighting their economic and ecological advantages (Zhou et al., 2018). In another study, Zuo et al. (2020) synthesized dual-chain imidazolium ILs that enhanced flavonoid solubility and mass transfer even under mild maceration conditions, confirming the importance of structural tunability for optimizing solvation behavior.

From a green chemistry perspective, IL-assisted maceration offers a significant improvement over traditional organic solvents. The low volatility and high recyclability of ILs minimize environmental emissions, while their tunable polarity enables selective extraction of target flavonoids using lower solvent volumes (Cao et al., 2024). Additionally, biodegradable ILs derived from choline or amino acids eliminate the hazards associated with fluorinated anions, improving compatibility with food and cosmetic applications (Gómez et al., 2019).

Overall, IL-based maceration combines the simplicity of a conventional technique with the advanced selectivity and environmental safety of modern green solvents. By replacing volatile organic solvents with recyclable, bio-based ILs, this approach achieves higher yields, shorter extraction times, and reduced ecological impact—representing an important step toward fully sustainable flavonoid recovery.

#### **4.2 Soxhlet Extraction**

Soxhlet extraction is a classical and well-established method for recovering flavonoids and other phenolic compounds from plant materials through continuous solvent reflux. In this technique, a condensed solvent repeatedly passes through the plant matrix, ensuring exhaustive extraction of target compounds. Despite its efficiency in mass transfer, conventional Soxhlet extraction requires prolonged heating, large solvent volumes, and significant energy input, which often leads to degradation of thermolabile flavonoids and conflicts with the principles of green chemistry (Rodríguez De Luna et al., 2020).

The application of ionic liquids (ILs) within Soxhlet systems has recently been proposed as a means of increasing extraction selectivity while reducing

environmental impact. ILs, owing to their negligible vapor pressure and tunable polarity, can replace or modify conventional organic solvents to enhance solubility and stability of hydroxylated flavonoids such as quercetin, rutin, and naringenin (Ventura et al., 2017). Wang et al. (2016) reported that choline amino-acid-based ILs used under Soxhlet-like reflux conditions extracted higher levels of flavonoids from *Citrus reticulata* peels than ethanol, while simultaneously removing pectin and other polysaccharides that hinder diffusion.

The structural design of ILs—particularly the balance between hydrophobic alkyl chains and hydrogen-bond-accepting anions—determines their dissolution capacity in Soxhlet environments. Zuo et al. (2020) synthesized dual-chain imidazolium ILs with improved solvating power, resulting in greater mass transfer and higher selectivity for flavonoids under continuous reflux. These ILs enhanced solute–solvent interactions through  $\pi$ – $\pi$  stacking and hydrogen bonding, which stabilized the extracted molecules and minimized degradation. From a green chemistry standpoint, IL-based Soxhlet extraction reduces both solvent waste and emissions. ILs’ low volatility prevents solvent loss through evaporation, while their recyclability allows repeated use without significant efficiency loss (Zhou et al., 2018; Gómez et al., 2019). Additionally, replacing toxic halogenated ILs with biodegradable choline or amino-acid-derived ILs eliminates hydrolysis by-products such as fluorinated species, thereby improving environmental compatibility (Cao et al., 2024).

Although the combination of ILs and Soxhlet extraction retains the process’s high efficiency, it also addresses its major ecological and safety limitations. The integration of recyclable and low-toxicity ILs decreases energy consumption and solvent usage by more than 50%, while maintaining or enhancing extraction yields (Chaves et al., 2020). Consequently, IL-assisted Soxhlet extraction represents a sustainable modernization of a traditional technique—preserving the benefits of exhaustive extraction while achieving compliance with green chemistry principles such as waste prevention, safer solvent use, and energy efficiency.

## 5 CONCLUSION

The extraction of flavonoids using ionic liquid (IL)-based systems represents a major advancement in aligning natural product recovery with the principles of green chemistry. Conventional solvent-based methods such as maceration and Soxhlet extraction, while effective, typically require large volumes of volatile organic solvents, high temperatures, and long processing times that can lead to degradation of thermolabile compounds and environmental burdens (Rodríguez De Luna et al., 2020). The incorporation of ILs into both traditional and modern extraction techniques has transformed these limitations into opportunities for sustainable optimization, offering higher

yields, lower solvent consumption, and enhanced selectivity toward target flavonoids.

Modern extraction techniques—particularly ultrasound-assisted extraction (UAE), microwave-assisted extraction (MAE), pressurized liquid extraction (PLE), supercritical fluid extraction (SFE), and enzyme-assisted extraction (EAE)—have demonstrated substantial synergy with ILs. Studies by Xu et al. (2012), Yao et al. (2012), and Ji et al. (2018) revealed that imidazolium- and Brønsted-acidic ILs facilitate efficient cell wall disruption and dielectric heating, leading to up to 60% higher extraction yields and significant reductions in processing time. Similarly, IL–SFE and IL–PLE systems (Pérez-Vázquez et al., 2023; Zuo et al., 2020) exhibit enhanced solubility and mass transfer through  $\pi$ – $\pi$  stacking and hydrogen-bonding mechanisms, maintaining the structural integrity and bioactivity of flavonoids even under elevated temperature and pressure.

From an environmental and operational standpoint, IL-assisted systems greatly reduce solvent waste and emissions due to their negligible vapor pressure and recyclability (Zhou et al., 2018; Gómez et al., 2019). Biodegradable ILs derived from choline or amino acids have emerged as promising alternatives to fluorinated ILs, offering comparable solvation capacity while mitigating ecological risks (Wang et al., 2016; Ventura et al., 2017). These systems not only decrease environmental toxicity but also enable circular solvent recovery, allowing repeated reuse without significant performance loss.

In addition, the tunable physicochemical properties of ILs—such as polarity, viscosity, and hydrogen-bonding ability—provide molecular-level control over extraction selectivity and kinetics (Zuo et al., 2020; Zhang et al., 2020). Chaves et al. (2020) and Cao et al. (2024) emphasized that integrating ILs into energy-efficient processes such as MAE or UAE reduces energy consumption by up to 40%, while enhancing total flavonoid recovery and antioxidant activity. Collectively, these findings confirm that ILs can function not merely as solvents but as multifunctional components—serving as catalysts, stabilizers, and co-solvents—to improve extraction performance and sustainability.

Overall, ionic liquids have redefined the paradigm of flavonoid extraction by combining high efficiency, selectivity, and environmental responsibility. Their integration into both modern and traditional extraction technologies has enabled the development of low-impact, high-yield, and recyclable processes that comply with the key principles of green chemistry: waste prevention, safer solvent design, energy efficiency, and renewable feedstock utilization. As ongoing research continues to refine biodegradable IL formulations and scale up recovery systems, IL-assisted extraction is poised to become the benchmark for sustainable flavonoid production in food, pharmaceutical, and cosmetic industries.

## REFERENCES

- Cao, D., Qiao, X., Guo, Y., & Liu, P. (2024). Valorization of pawpaw (*Carica papaya* L.) leaves as a source of polyphenols by ionic liquid-based microwave-assisted extraction: Comparison with other extraction methods and bioactivity evaluation. *Food Chemistry: X*, 22, 101500.
- Chaves, J. O., De Souza, M. C., Da Silva, L. C., Lachos-Perez, D., Torres-Mayanga, P. C., Machado, A. P. D. F., ... & Rostagno, M. A. (2020). Extraction of flavonoids from natural sources using modern techniques. *Frontiers in chemistry*, 8, 507887.
- El Maabiche, O., Benkirane, C., Abid, M., Serghini-Caid, H., Elamrani, A., & Mansouri, F. (2025). Sustainable Extraction of Bioactive Compounds From Plant Materials: Advances in Green Technologies and Solvent Systems. In *Green Chemistry, Sustainable Processes, and Technologies* (pp. 433-464). IGI Global Scientific Publishing.
- Gómez, E., Requejo, P. F., Tojo, E., & Macedo, E. A. (2019). Recovery of flavonoids using novel biodegradable choline amino acids ionic liquids based ATPS. *Fluid Phase Equilibria*, 493, 1-9.
- Greer, A. J., Jacquemin, J., & Hardacre, C. (2020). Industrial applications of ionic liquids. *Molecules*, 25(21), 5207.
- Guo, Z., Lue, B. M., Thomasen, K., Meyer, A. S., & Xu, X. (2007). Predictions of flavonoid solubility in ionic liquids by COSMO-RS: experimental verification, structural elucidation, and solvation characterization. *Green Chemistry*, 9(12), 1362-1373.
- Ji, S., Wang, Y., Su, Z., He, D., Du, Y., Guo, M., ... & Tang, D. (2018). Ionic liquids-ultrasound based efficient extraction of flavonoid glycosides and triterpenoid saponins from licorice. *RSC advances*, 8(25), 13989-13996.
- Jiang, Y., Li, D., Ma, X., Jiang, F., He, Q., Qiu, S., ... & Wang, G. (2018). Ionic liquid-ultrasound-based extraction of biflavonoids from *Selaginella helvetica* and investigation of their antioxidant activity. *Molecules*, 23(12), 3284.
- Katsoura, M. H., Polydera, A. C., Tsironis, L., Tselepis, A. D., & Stamatis, H. (2006). Use of ionic liquids as media for the biocatalytic preparation of flavonoid derivatives with antioxidant potency. *Journal of Biotechnology*, 123(4), 491-503.
- Liu, X., Huang, X., Wang, Y., Huang, S., & Lin, X. (2013). Design and performance evaluation of ionic liquid-based microwave-assisted simultaneous extraction of kaempferol and quercetin from Chinese medicinal plants. *Analytical Methods*, 5(10), 2591-2601.
- Rahman, N. R. A., Yunus, N. A., & Mustaffa, A. A. (2017, June). Selection of optimum ionic liquid solvents for flavonoid and phenolic acids extraction. In *IOP Conference Series: Materials Science and Engineering* (Vol. 206, No. 1, p. 012061). IOP Publishing.
- Rodríguez De Luna, S. L., Ramírez-Garza, R. E., & Serna Saldivar, S. O. (2020). Environmentally friendly methods for flavonoid extraction from plant material: Impact of their operating conditions on yield and antioxidant properties. *The Scientific World Journal*, 2020(1), 6792069.
- Shukla, S. K., & Mikkola, J. P. (2020). Use of ionic liquids in protein and DNA chemistry. *Frontiers in Chemistry*, 8, 598662.

- Ventura, S. P. M., Silva, F. A., & Coutinho, J. A. P. (2017). *Ionic-Liquid-Mediated Extraction and Separation Processes for bioactive compounds: Past, present, and future. Chemical Reviews, 117*(10), 6984–7052.
- Wang, R., Chang, Y., Tan, Z., & Li, F. (2016). Applications of choline amino acid ionic liquid in extraction and separation of flavonoids and pectin from ponkan peels. *Separation Science and Technology, 51*(7), 1093-1102.
- Xu, W., Chu, K., Li, H., Zhang, Y., Zheng, H., Chen, R., & Chen, L. (2012). Ionic liquid-based microwave-assisted extraction of flavonoids from *Bauhinia championii* (Benth.) Benth. *Molecules, 17*(12), 14323-14335.
- Yao, H., Du, X., Yang, L., Wang, W., Yang, F., Zhao, C., ... & Zu, Y. (2012). Microwave-assisted method for simultaneous extraction and hydrolysis for determination of flavonol glycosides in Ginkgo foliage using Brønsted acidic ionic-liquid [HO3S (CH<sub>2</sub>)<sub>4</sub>mim] HSO<sub>4</sub> aqueous solutions. *International Journal of Molecular Sciences, 13*(7), 8775-8788.
- Zeng, H., Wang, Y., Kong, J., Nie, C., & Yuan, Y. (2010). Ionic liquid-based microwave-assisted extraction of rutin from Chinese medicinal plants. *Talanta, 83*(2), 582-590.
- Zhang, Y., Cao, Y., & Wang, H. (2020). Multi-interactions in ionic liquids for natural product extraction. *Molecules, 26*(1), 98.
- Zhao, Z., Li, H., & Gao, X. (2023). Microwave encounters ionic liquid: synergistic mechanism, synthesis and emerging applications. *Chemical Reviews, 124*(5), 2651-2698.
- Zhao, C., Lu, Z., Li, C., He, X., Li, Z., Shi, K., ... & Zu, Y. (2014). Optimization of ionic liquid based simultaneous ultrasonic-and microwave-assisted extraction of rutin and quercetin from leaves of velvetleaf (*Abutilon theophrasti*) by response surface methodology. *The Scientific World Journal, 2014*(1), 283024.
- Zhou, J., Sui, H., Jia, Z., Yang, Z., He, L., & Li, X. (2018). Recovery and purification of ionic liquids from solutions: a review. *Rsc Advances, 8*(57), 32832-32864.
- Zuo, L., Ao, X., & Guo, Y. (2020). Study on the synthesis of dual-chain ionic liquids and their application in the extraction of flavonoids. *Journal of Chromatography A, 1628*, 461446.





# **On the Apollonian Sets in the Chinese Checkers Plane**

**Süheyla EKMEKÇİ<sup>1</sup>**

1- Prof. Dr.; Eskişehir Osmangazi University, Department of Mathematics and Computer Science, Faculty of Science, [sekmekci@ogu.edu.tr](mailto:sekmekci@ogu.edu.tr) ORCID No: 0000-0003-2820-2096

## ABSTRACT

This study presents a comprehensive investigation of the Apollonian sets in the Chinese Checkers plane ( $R_C^2$ ) defined by the Chinese Checkers distance. The research systematically classifies and analyzes the Apollonian sets for two distinct points and a positive real number  $\lambda$ . The geometric structures of these sets have been examined according to the type of the line passing through the given points. The general equations of the Apollonian sets are provided and interpreted according to the values of  $\lambda$ . It has been established that the Apollonian sets consist of simple polygons formed by line segments. Depending on the positions of the points and the value of  $\lambda$ , it was observed that the number of line segments composing the set varies. When the points lie on the coordinate axes, lines parallel to the axes, or on separator lines, the set is a simple polygon composed of eight line segments and is convex. In particular, when the points lie on a gradual line, the study identifies critical thresholds of the parameter  $\lambda$  that determine changes in the Apollonian sets and their convexity. The results extend the concept and properties of classical Apollonian circles to the Chinese Checkers plane, a non-Euclidean geometry, and provide a geometric classification under the Chinese Checkers distance.

*Keywords – Chinese Checkers distance; Apollonian sets.*

---

## INTRODUCTION

The distance between two or more things, points, persons, or concepts can be measured numerically or sometimes qualitatively. There are many ways of measuring. Unusual definitions of distance can be helpful to model certain physical situations, but are also used in theoretical mathematics. The taxicab, and maximum, Chinese Checker distances are well-known non-Euclidean distances. Numerous studies have examined non-Euclidean planes and spaces, which are defined by these metrics. A few noteworthy additions to (Akça and Kaya, 1997:151), (Özcan et al, 2002: 381), (Akça and Kaya, 2004:521), (Akça and Kaya, 2004:491), (Akça and Çalış, 2021:175), (Kaya et al, 2000:135).

The Chinese Checkers distance (or CC-metric) is an alternative distance definition used instead of the classical Euclidean distance. This metric takes its name from the move rules in the game of Chinese Checkers because the pieces can move both horizontally/vertically and diagonally (at a  $45^\circ$  angle) — which gives the concept of distance a different geometry. The studies (Bayar and Ekmekçi, 2006: 249), (Gelişgen and Kaya, 2015:82), (Gelişgen and Kaya, 2006:179), (Gelişgen et al, 2006: 35), (Kaya et al, 2006:221), (Pekzorlu and Bayar, 2022: 28), (Pekzorlu and Bayar, 2020: 1498), (Turan and Özcan, 2006:393), (Turan and Özcan, 2004:119) and

(Turan and Özcan, 2004) in the Chinese Checkers plane and space have made important contributions to an alternative geometric system.

An Apollonian set is defined as the collection of all points whose distances from two fixed points maintain a constant ratio, denoted as  $\lambda$ . In the Euclidean plane, this set forms a circle, with the exception of the degenerate cases that occur when  $\lambda = 0$  or  $\lambda = 1$ . Investigating how the definition of the Apollonian set behave under Chinese checkers metrics has become a fruitful research area. In this work, the Apollonian sets are examined in the Chinese checkers plane. It is determined that the Apollonian set is not a Chinese checkers circle, but a simple polygon.

## PRELIMINARIES

In this section, some definitions, concepts and theorems used throughout this work are mentioned.

**Definition 2.1.** Let  $A = (a_1, a_2)$  and  $B = (b_1, b_2)$  be any two points in the analytic plane. The function

$$d_C(A, B) = \max\{|a_1 - b_1|, |a_2 - b_2|\} + (\sqrt{2} - 1) \min\{|a_1 - b_1|, |a_2 - b_2|\}.$$

is defined  $d_C : \mathbf{R}^2 \times \mathbf{R}^2 \rightarrow [0, \infty)$  is called *the Chinese Checker distance function* between the points  $A$  and  $B$  in the analytic plane.

As is evident from the Definition 2.1, the Chinese Checker distance between the points  $A$  and  $B$  is equal to the sum of the maximum and  $(\sqrt{2} - 1)$  times the minimum of the Euclidean lengths of the sides parallel to the coordinates axes in the right triangle with the hypotenuse  $AB$ , respectively. The shortest path between the points  $A$  and  $B$  is the union of a vertical or a horizontal line segment and a separator line segment. Thus, the shortest distance from the point  $A$  to the point  $B$  is the sum of the Euclidean lengths of these two line segment.

. The Chinese Checkers plane  $\mathbf{R}_C^2 = (\mathbf{R}^2, d_C)$  is the Euclidean plane equipped with the Chinese Checkers distance  $d_C$ . The plane  $\mathbf{R}_C^2$  closely resembles the Euclidean plane, geometric properties and concepts that depend on the notion of distance may vary considerably from those in Euclidean geometry.

Krause classified lines depending on their slope as the following definition:

**Definition 2.2.** Let  $m$  be the slope of the line  $l$ . The line  $l$  is referred to as *the steep line*, *the gradual line* and *the separator line* in the cases where  $|m| > 1$ ,  $|m| < 1$  and  $|m| = 1$ , respectively. In the special cases that the line  $l$  is parallel to x-axis or y-axis, it is called *the horizontal line* or *the vertical line*, respectively, (Krause, 1975:31).

The geometric features of the plane  $\mathbf{R}_C^2$  are systematically studied using Krause's classification as a primary analytical tool in this study.

**Theorem 2.3.** All translations of the Euclidean plane are isometries in the plane  $\mathbf{R}_C^2$ , (Kaya et al, 2006:221).

**Theorem 2.4.** In the plane  $\mathbf{R}_C^2$ , the reflections about the line  $y = mx$  is an isometry if and only if  $m \in \left\{0, \pm 1, \pm(\sqrt{2}-1), \pm(\sqrt{2}+1)\right\}$ , (Kaya et al, 2006:221).

**Theorem 2.5.** The set of isometric rotations in the plane  $\mathbf{R}_C^2$  is  $\left\{r_\theta \mid \theta = k\frac{\pi}{4}, k = 0, 1, \dots, 7\right\}$ , (Kaya et al, 2006:221).

**Definition 2.6.** Let  $A$  and  $B$  be any two points in the plane  $\mathbf{R}_C^2$ . The minimum distance set of the points  $A$  and  $B$  is defined by the set

$$\left\{X \in \mathbf{R}_C^2 \mid d_C(X, A) + d_C(X, B) = d_C(A, B)\right\},$$

(Kaya et al, 2006:221).

When the points  $A$  and  $B$  are on a coordinate axis, on a line parallel to a coordinate axis, or on a separator line, the minimum distance set of these points is the line segment  $AB$ . If the points  $A$  and  $B$  are on a gradual (respectively, steep) line, the minimum distance set is the region bounded by the parallelogram formed by the separator lines and the horizontal (respectively, vertical) lines passing through these points.

**Definition 2.7.** Let  $A$  and  $B$  be any two points in the plane  $\mathbf{R}_C^2$ . The midset of the points  $A$  and  $B$  is defined by the set

$$\left\{X \in \mathbf{R}_C^2 \mid d_C(X, A) = d_C(X, B)\right\}.$$

When the midset is examined according to the class of the line passing through the points  $A$  and  $B$ , it is obtained as follows:

- 1) If the points  $A$  and  $B$  are on a horizontal (respectively, vertical) line, the midset is the vertical (respectively, horizontal) line passing through the midpoint of them.
- 2) If the points  $A$  and  $B$  are on a separator line, the midset is the other separator line passing through the midpoint of them.
- 3) If the points  $A$  and  $B$  are on a gradual line, the midset of these points consists of five line segments and two vertical rays such that three steep line segments are parallel and have a slope of  $\text{sgn}(-m)(\sqrt{2}+1)$ , while two remaining segments are also parallel and vertical where  $m$  is the slope of the line  $AB$ .
- 4) If the points  $A$  and  $B$  are on a gradual line with a slope of  $\pm(\sqrt{2}-1)$ , the midset of these points consists of one line segment and two regions. The steep line segment passes through the midpoint of the points  $A$  and  $B$  and

has a slope of  $\operatorname{sgn}(-m)(\sqrt{2}+1)$ . Each region is formed by the vertical line passing through one of the points and the separator line with slope  $\operatorname{sgn}(-m)$ .1 passing through the other point.

5) If the points  $A$  and  $B$  are on a steep line, the midset of these points consists of five line segments and two horizontal rays such that three gradual line segments are parallel and have a slope of  $\operatorname{sgn}(-m)(\sqrt{2}-1)$ , while two remaining segments are also parallel and horizontal.

6) If the points  $A$  and  $B$  are on a steep line with a slope of  $\pm(\sqrt{2}+1)$ , the midset of these points consists of one line segment and two regions. The gradual line segment passes through the midpoint of the points  $A$  and  $B$  and has a slope of  $\operatorname{sgn}(-m)(\sqrt{2}-1)$ . Each region is formed by the horizontal line passing through one of the points and the separator line with slope  $\operatorname{sgn}(-m)$ .1 passing through the other point.

### THE APOLLONIAN SETS IN THE CHINESE CHECKERS PLANE

In the Euclidean plane, for two distinct points  $A$  and  $B$  and a positive real number  $\lambda$ , the Apollonian set  $A(A,B;\lambda)$  is defined as the locus of all points  $X$  satisfying the equality

$$\frac{d(X,A)}{d(X,B)}=\lambda.$$

For  $\lambda \neq 1$ , the Apollonian set  $A(A,B;\lambda)$  forms a circle except for  $\lambda \in \{0,1,\infty\}$ . When  $\lambda = 1$ , this set corresponds to the set of points that are equidistant from the points  $A$  and  $B$ , namely, the perpendicular bisector of the line segment  $AB$ . This concept can be extended to various metric spaces. For instance, the studies in (Bahuaud,2020:25), (Ekmekçi and Yıldırım,2022:151) and (Ekmekçi,2024:1) have characterized Apollonian sets in the taxicab, the maximum plane and the generalized taxicab]. A key finding from these researches is that in these non-Euclidean geometries, the Apollonian sets do not form standard (generalized) taxicab or maximum circles

In this section, it is introduced the basic definition of the Apollonian set in the Chinese Checkers plane  $\mathbb{R}_C^2$  and discussed its essential properties. Then, Apollonian sets are examined in terms of two distinct points and a positive real value, through which they are characterized.

**Definition 3.1.** Let  $A$  and  $B$  be any two distinct points in the plane  $\mathbb{R}_C^2$  and let  $\lambda$  be a positive real number. The set

$$\left\{X \in \mathbb{R}_C^2 \mid \frac{d(X,A)}{d(X,B)}=\lambda\right\}.$$

is called the Apollonian set in the plane  $R_C^2$  and denoted by  $A_C(A, B; \lambda)$ .

In the cases of  $\lambda = 0$  and  $\lambda \rightarrow \infty$ , it is clear from the definition that  $A_C(A, B; 0) = \{A\}$  and  $A_C(A, B; \infty) = \{B\}$ , respectively. When  $\lambda = 1$ ,  $A_C(A, B; 1)$  is the midset of the points  $A$  and  $B$ .

**Theorem 3.2.** Let any two distinct points be  $A$  and  $B$  in  $R_C^2$  and let  $\lambda$  be a positive real number. Then  $A_C(A, B; \lambda) = A_C(B, A; \frac{1}{\lambda})$ .

Under the conventions  $\frac{1}{\infty} = 0$  and  $\frac{1}{0} = \infty$  for  $\lambda$ , it is clear that  $A_C(A, B; 0) = A_C(B, A; \infty)$  and  $A_C(A, B; \infty) = A_C(B, A; 0)$ . This theorem allows us to restrict our attention to values of the parameter  $\lambda$  in the interval  $[1, \infty)$  in the further study of the Apollonian set.

Now, it is investigated how isometries of the Chinese Checkers plane act upon Apollonian sets.

**Theorem 3.3.** Let  $A$  and  $B$  be two distinct points in  $R_C^2$  and let  $\lambda > 1$ . If  $\varphi$  is an isometry of the plane  $R_C^2$ , then the following equality holds:

$$\varphi(A_C(A, B; \lambda)) = A_C(\varphi(A), \varphi(B); \lambda).$$

The proofs of Theorem 3.2 and Theorem 3.3 are analogous to those presented for Apollonian sets in the taxicab plane (Bahuaud, 2020:25), the maximum plane (Ekmekçi and Yıldırım, 2022:151), and the generalized taxicab plane (Ekmekçi, 2024:1). Therefore, the detailed verification is omitted here.

**Theorem 3.4.** Let  $A$  and  $B$  be two distinct points in  $R_C^2$  and let  $\lambda > 1$ . If  $\varphi$  is the rotation by  $\pi$ -angle at the midpoint  $M$  of the points  $A$  and  $B$ , then

$$\varphi(A_C(A, B; \lambda)) = A_C\left(A, B; \frac{1}{\lambda}\right).$$

**Proof.** Let  $\varphi$  be the rotation by  $\pi$ -angle at the midpoint  $M$  of the points  $A$  and  $B$ . Then, it is clear that  $\varphi(A) = B$  and  $\varphi(B) = A$ . From Theorem 3.3 and Theorem 3.2,

$$\varphi(A_C(A, B; \lambda)) = A_C(\varphi(A), \varphi(B); \lambda) = A_C(B, A; \lambda) = A_C\left(A, B; \frac{1}{\lambda}\right).$$

Thus, the proof is complete.

Since isometries in the plane  $R_C^2$  preserve the properties of Apollonian sets, it is not necessary to take two fixed points in the general position. Throughout this study, choosing one point at the origin and the other in the first quadrant of the coordinate plane will simplify the analysis and will not affect the generality.

**Theorem 3.5.** Let two distinct points  $A$  and  $B$  be on the same coordinate axis in  $\mathbb{R}_C^2$  and let  $\lambda > 1$ . Then the Apollonian set  $A_C(A, B; \lambda)$  satisfies the following properties:

- i) It consists of eight line segments whose slopes are  $\pm(\sqrt{2}+1)(\frac{\lambda+1}{\lambda-1}), \pm(\sqrt{2}-1),$   
 $\pm(\frac{(\sqrt{2}-1)\lambda+1}{\lambda-(\sqrt{2}-1)}).$
- ii) All vertices are on the horizontal line, the vertical line, and the two separator lines through the point  $B$ .
- iii) The set is symmetric with respect to the line  $AB$  and is convex.
- iv) If pairs of opposite sides are extended to lines, their intersection points lie on the other axis passing through point  $A$ .
- v) The point  $B$  divides the diagonals internally in the ratios  $\frac{|1-\lambda|}{(\sqrt{2}-1)+\lambda}, \frac{\lambda-1}{\lambda+1}$

and 1.

**Proof.** Assume without loss of generality that two distinct points are  $A = O$  and  $B = (b_1, 0)$  on the  $x$ -axis where  $b_1 > 0$ . For  $\lambda > 1$ , the Apollonian set  $A_C(A, B; \lambda)$  is defined by the equality

$$\frac{\max\{|x|, |y|\} + (\sqrt{2}-1)\min\{|x|, |y|\}}{\max\{|x-b_1|, |y|\} + (\sqrt{2}-1)\min\{|x-b_1|, |y|\}} = \lambda. \quad (1)$$

Considering all possible cases in equation (10) and correctly solving the absolute values demonstrates that  $A_C(A, B; \lambda)$  is the union of these line segments: The equation

$$(1+\lambda)x + (\sqrt{2}-1)(\lambda-1)y = \lambda b_1 \quad (2)$$

is line segment with the endpoints  $K_1 = (\frac{\lambda}{\lambda+1}b_1, 0)$  and

$$K_8 = (\frac{\sqrt{2}\lambda - (\sqrt{2}-1)}{(2-\sqrt{2}) + \sqrt{2}\lambda}b_1, \frac{-1}{(2-\sqrt{2}) + \sqrt{2}\lambda}b_1), \text{ the equation} \quad (3)$$

is line segment with the endpoints  $K_1$  and  $K_2 = (\frac{\sqrt{2}\lambda - (\sqrt{2}-1)}{(2-\sqrt{2}) + \sqrt{2}\lambda}b_1, \frac{1}{(2-\sqrt{2}) + \sqrt{2}\lambda}b_1),$

the equation

$$x - (\sqrt{2}-1)y = \frac{\lambda}{\lambda-1}b_1 \quad (4)$$

is line segment with the endpoints  $K_5 = (\frac{\lambda}{\lambda-1}b_1, 0)$  and

$$K_6 = (\frac{-\sqrt{2}\lambda + (\sqrt{2}-1)}{\sqrt{2}(\lambda-1)}b_1, \frac{1}{\sqrt{2}(\lambda-1)}b_1), \text{ the equation}$$

$$x + (\sqrt{2}-1)y = \frac{\lambda}{\lambda-1}b_1 \quad (5)$$



is line segment with the endpoints  $K_5$  and  $K_4 = (\frac{-\sqrt{2}\lambda + (\sqrt{2}-1)}{\sqrt{2}(1-\lambda)}b_1, \frac{-1}{\sqrt{2}(1-\lambda)}b_1)$ , the equation

$$(1 + (\sqrt{2}-1)\lambda)x + (\lambda - (\sqrt{2}-1))y = (\sqrt{2}-1)\lambda b_1 \quad (6)$$

is line segment with the endpoints  $K_7 = (b_1, -\frac{1}{\lambda - (\sqrt{2}-1)}b_1)$  and  $K_8$ , the equation

$$(1 + (\sqrt{2}-1)\lambda)x - (\lambda - (\sqrt{2}-1))y = (\sqrt{2}-1)\lambda b_1 \quad (7)$$

is line segment with the endpoints  $K_3 = (b_1, \frac{1}{\lambda - (\sqrt{2}-1)}b_1)$  and  $K_2$ , the equation

$$(1 - (\sqrt{2}-1)\lambda)x + (\lambda - (\sqrt{2}-1))y = -(\sqrt{2}-1)\lambda b_1 \quad (8)$$

is line segment with the endpoints  $K_6$  and  $K_7$ , the equation

$$(1 - (\sqrt{2}-1)\lambda)x - (\lambda - (\sqrt{2}-1))y = -(\sqrt{2}-1)\lambda b_1 \quad (9)$$

is line segment with the endpoints  $K_2$  and  $K_3$ . Thus, the set  $A_C(A, B; \lambda)$  corresponding to the equation (1) consists of the line segments  $K_i K_{i+1}$ ,  $i = 1, \dots, 8$ . The opposite side of a side  $K_i K_{i+1}$  in  $A_C(A, B; \lambda)$  is formed by the other endpoints of the diagonals  $K_i B$  and  $K_{i+1} B$ . The opposite side of the side  $K_1 K_8$  is  $K_4 K_5$ , and when these sides are extended to lines, they intersect at the point  $(0, \frac{\lambda b_1}{(\sqrt{2}-1)(\lambda-1)})$  on the  $y$ -axis. Similarly, when the pairs

of the opposite sides  $K_1 K_2$  and  $K_5 K_6$ ;  $K_2 K_3$  and  $K_6 K_7$ ;  $K_3 K_4$  and  $K_7 K_8$  are completed to lines, they intersect on the  $y$ -axis.

The reflection in the line  $AB$  leaves the vertices  $K_1$  and  $K_5$  fixed while mapping the vertices  $K_2$ ,  $K_3$  and  $K_4$  to the vertices  $K_8$ ,  $K_7$  and  $K_6$ , respectively. Also, the sides  $K_1 K_2$ ,  $K_2 K_3$ ,  $K_3 K_4$  and  $K_4 K_5$  are mapped to the sides  $K_1 K_8$ ,  $K_7 K_8$ ,  $K_6 K_7$  and  $K_5 K_6$  under this reflection. Thus,  $A_C(A, B; \lambda)$  is symmetric about the line  $AB$  ( $x$ -axis).

It is easily to see that the point  $B$  divides the diagonals  $K_4 K_8$  and  $K_2 K_6$  in the ratio  $\frac{|K_4 B|}{|BK_8|} = \frac{|K_2 B|}{|BK_6|} = \frac{|1-\lambda|}{(\sqrt{2}-1)+\lambda}$ , the diagonal  $K_3 K_7$  in the ratio  $\frac{|K_3 B|}{|BK_7|} = 1$ , the diagonal  $K_1 K_5$  in the ratio  $\frac{|K_1 B|}{|BK_5|} = \frac{\lambda-1}{\lambda+1}$ . Thus, the proof is completed. The

sets  $A_C(A, B; \lambda)$  and  $A_C(A, B; \frac{1}{\lambda})$  are shown on the right and left of Figure 1(a), respectively. In the case that the points  $A$  and  $B$  are on the  $y$ -axis, it is

immediately seen that  $A_C(A, B; \lambda)$  has the same properties by using the reflection in the separator line  $y = x$  and Theorem 3.3. When the points  $A$  and  $B$  are on either a horizontal or a vertical line, similar results follow directly by applying a suitable translation.

Now, the properties of the Apollonian set are analyzed for the case where the two distinct points are on a same separator line.

**Theorem 3.6.** Let two distinct points  $A$  and  $B$  be on the same separator line in  $R_C^2$  and let  $\lambda > 1$ . Then the Apollonian set  $A_C(A, B; \lambda)$  satisfies the following properties:

- i) It consists of eight line segments whose slopes are  $\text{sgn}(-m).m'$  and  $\text{sgn}(-m).\frac{1}{m'}$  where  $m' \in \left\{ \sqrt{2}-1, (\sqrt{2}-1)\frac{1-\lambda}{1+\lambda}, \frac{\lambda+\sqrt{2}-1}{1-(\sqrt{2}-1)\lambda}, \frac{\lambda+\sqrt{2}-1}{1+(\sqrt{2}-1)\lambda} \right\}$  and  $m$  is the slope of the line  $AB$ .
- ii) All vertices are on the horizontal line, the vertical line, and the two separator lines through the point  $B$ .
- iii) The set is symmetric with respect to the line  $AB$ .
- iv) If pairs of opposite sides are extended to lines, their intersection points lie on the other separator line passing through point  $A$ .
- v) The point  $B$  divides the diagonals internally in the ratios  $\frac{\lambda+\sqrt{2}-1}{|1-\lambda|}$ ,

$$\frac{|1-\lambda|}{(\sqrt{2}-1)+\lambda}, \frac{\lambda-1}{\lambda+1} \text{ and } 1.$$

**Proof.** Assume without loss of generality that two distinct points are  $A = O$  and  $B = (b_1, b_1)$  on the separator line  $y = x$  where  $b_1 > 0$ . For  $\lambda > 1$ , the Apollonian set  $A_C(A, B; \lambda)$  is defined by the equality

$$\frac{\max\{|x|, |y|\} + (\sqrt{2}-1)\min\{|x|, |y|\}}{\max\{|x-b_1|, |y-b_1|\} + (\sqrt{2}-1)\min\{|x-b_1|, |y-b_1|\}} = \lambda \quad (10)$$

where  $\lambda > 1$ . Focusing on all possible cases in the equality (10) and solving for the absolute values appropriately,  $A_C(A, B; \lambda)$  is determined as the union of the following line segments: The equation

$$(1-\lambda)x + (\sqrt{2}-1)(\lambda+1)y = (\sqrt{2}-2)\lambda b_1 \quad (11)$$

is line segment with the endpoints  $K_5 = \left(\frac{\lambda+(\sqrt{2}-1)}{\lambda-1}b_1, b_1\right)$  and

$K_6 = \left(-\frac{\lambda+(2-\sqrt{2})}{\sqrt{2}-1-\lambda}b_1, \frac{\sqrt{2}-\lambda}{\sqrt{2}-1-\lambda}b_1\right)$ , the equation

$$x + (\sqrt{2}-1)y = \frac{\sqrt{2}\lambda}{\lambda-1}b_1 \quad (12)$$

is line segment with the endpoints  $K_4 = \left(\frac{\lambda}{\lambda-1}b_1, \frac{\lambda}{\lambda-1}b_1\right)$  and  $K_5$ , the equation

$$(1+(\sqrt{2}-1)\lambda)x + (\lambda+(\sqrt{2}-1))y = \sqrt{2}\lambda b_1 \quad (13)$$

is line segment with the endpoints  $K_7 = (b_1, \frac{\lambda-1}{\lambda+\sqrt{2}-1}b_1)$  and  $K_8 = (-\frac{\lambda}{\lambda+1}b_1, -\frac{\lambda}{\lambda+1}b_1)$ , the equation

$$(1-(\sqrt{2}-1)\lambda)x + (\lambda+\sqrt{2}-1)y = (2-\sqrt{2})\lambda b_1 \quad (14)$$

is line segment with the endpoints  $K_6$  and  $K_7$ , the equation

$$(\lambda+(\sqrt{2}-1))x + (1+(\sqrt{2}-1)\lambda)y = \sqrt{2}\lambda b_1 \quad (15)$$

is line segment with the endpoints  $K_1 = (\frac{\lambda-1}{\lambda+\sqrt{2}-1}b_1, b_1)$  and  $K_8$ , the equation

$$(\lambda+(\sqrt{2}-1))x + (1-(\sqrt{2}-1)\lambda)y = (2-\sqrt{2})\lambda b_1 \quad (16)$$

is line segment with the endpoints  $K_1$  and  $K_2 = (\frac{\sqrt{2}-\lambda}{\sqrt{2}-1-\lambda}b_1, -\frac{\lambda+2-\sqrt{2}}{\sqrt{2}-1-\lambda}b_1)$ , the equation

$$(\sqrt{2}-1)(1+\lambda)x + (1-\lambda)y = (\sqrt{2}-2)\lambda b_1 \quad (17)$$

is line segment with the endpoints  $K_3 = (b_1, \frac{\lambda+\sqrt{2}-1}{\lambda-1}b_1)$  and  $K_2$ , the equation

$$(\sqrt{2}-1)x + y = \frac{\sqrt{2}\lambda}{\lambda-1}b_1 \quad (18)$$

is line segment with the endpoints  $K_3$  and  $K_4$ . It is seen that all the vertices of  $A_C(A, B; \lambda)$  are on the horizontal, vertical, two separator lines through  $B$ . Since the images of the points satisfying the equality (10) the reflection with respect to the line  $AB$  also satisfy the equality (10), the set  $A_C(A, B; \lambda)$  is symmetric about the separator line  $AB$ . The opposite sides  $K_1K_8$  and  $K_4K_5$  are extended to lines, they intersect at the point  $(\frac{\sqrt{2}\lambda b_1}{(2-\sqrt{2})(\lambda-1)}, -\frac{\sqrt{2}\lambda b_1}{(2-\sqrt{2})(\lambda-1)})$  on

the other separator line ( $y = -x$ ) passing through  $A$ . Similarly, when the pairs of the opposite sides  $K_1K_2$  and  $K_5K_6$ ;  $K_2K_3$  and  $K_6K_7$ ;  $K_3K_4$  and  $K_7K_8$  are completed to lines, the intersection points are collinear. It is easily to see that the point  $B$  divides the diagonals  $K_4K_8$  and  $K_2K_6$  in the ratio  $\frac{|K_4B|}{|BK_8|} = \frac{\lambda+1}{\lambda-1}$  and  $\frac{|K_2B|}{|BK_6|} = 1$ , the diagonal  $K_3K_7$  in the ratio  $\frac{|K_3B|}{|BK_7|} = \frac{\lambda+\sqrt{2}-1}{|1-\lambda|}$ , the diagonal  $K_1K_5$  in the ratio  $\frac{|K_1B|}{|BK_5|} = \frac{\lambda-1}{\lambda+\sqrt{2}-1}$ . Thus, the proof is completed. The

sets  $A_C(A, B; \lambda)$  and  $A_C(A, B; \frac{1}{\lambda})$  are shown on the right and left of Figure 1(b), respectively.

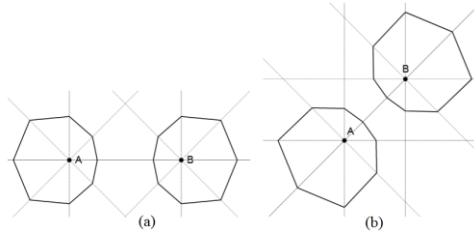


**Figure 1.**  $A_c(A, B; \lambda)$  and  $A_c\left(A, B; \frac{1}{\lambda}\right)$

In the case that the points  $A$  and  $B$  are on the separator line  $y = -x$ , it is immediately seen that  $A_c(A, B; \lambda)$  can be shown to have the same properties by applying a suitable isometry.

In the study, it was observed that when two distinct points lie on a gradual line, the geometric structure of the Apollonian set changes depending on the values taken by the parameter  $\lambda$ . During the analysis, the general equations of the set were first derived, and then a classification is made according to the values of  $\lambda$ , revealing the geometric shapes and properties for each case. Then, the findings obtained as a result of this classification are presented below.

Now, suppose that two distinct points are  $A = O$  and  $B = (b_1, b_2)$  on a gradual line where  $b_1 > b_2 > 0$ . For  $\lambda > 1$ , the Apollonian set  $A_c(A, B; \lambda)$  is defined by the equality

$$\frac{\max\{|x|, |y|\} + (\sqrt{2} - 1)\min\{|x|, |y|\}}{\max\{|x - b_1|, |y - b_2|\} + (\sqrt{2} - 1)\min\{|x - b_1|, |y - b_2|\}} = \lambda \quad (19)$$

where  $\lambda > 1$ . Focusing on all possible cases in the equality (19) and solving for the absolute values appropriately,  $A_c(A, B; \lambda)$  is determined.

The region defined by the inequalities  $|x| \geq |y|$  and  $|x - b_1| \geq |y - b_2|$  is analyzed according to the subregions in terms of equation (19) as follows. Consider the regions where  $0 \leq x \leq b_1$ . When  $y < 0$ , the equality (19) reduces the equation

$$(1 + \lambda)x + (\sqrt{2} - 1)(\lambda - 1)y = \lambda(b_1 + (\sqrt{2} - 1)b_2). \quad (20)$$

If  $1 < \lambda < \frac{1}{\sqrt{2} - 1}$ , the equality (20) is the line segment joining the points  $\left(\frac{\lambda(b_1 + (\sqrt{2} - 1)b_2)}{\lambda + 1}, 0\right)$  and  $\left(\frac{-(\sqrt{2} - 1)(b_1 - b_2) + \sqrt{2}\lambda b_1}{2 - \sqrt{2} + \sqrt{2}\lambda}, \frac{-(b_1 - b_2) + \sqrt{2}\lambda b_2}{2 - \sqrt{2} + \sqrt{2}\lambda}\right)$ . When  $\lambda = \frac{1}{\sqrt{2} - 1}$ , these points coincide. When  $\lambda > \frac{1}{\sqrt{2} - 1}$ , the line (20) does not pass through the region

formed. When  $0 \leq y \leq b_2$ , the equality (19) reduces the equation

$$x + (\sqrt{2} - 1)y = \frac{\lambda}{1 + \lambda}(b_1 + (\sqrt{2} - 1)b_2). \quad (21)$$

If  $1 < \lambda \leq \frac{1}{\sqrt{2}}$ , the equality (21) is the line segment joining the points

$(\frac{\lambda(b_1 + (\sqrt{2}-1)b_2)}{\lambda+1}, 0)$  and  $(\frac{\lambda b_1 - (\sqrt{2}-1)b_2}{\lambda+1}, b_2)$ . When  $\lambda > \frac{1}{\sqrt{2}}$ , the equality (21) is the line segment joining the points  $(\frac{(\sqrt{2}-1)(b_1 - b_2) + \sqrt{2}\lambda b_1}{\sqrt{2}(\lambda+1)}, \frac{-(b_1 - b_2) + \sqrt{2}\lambda b_2}{\sqrt{2}(\lambda+1)})$  and  $(\frac{\lambda b_1 - (\sqrt{2}-1)b_2}{\lambda+1}, b_2)$ . When  $y \geq b_2$ , the equality (19) reduces the equation

$$(1 + \lambda)x + (\sqrt{2} - 1)(1 - \lambda)y = \lambda(b_1 - (\sqrt{2} - 1)b_2). \quad (22)$$

The equality (22) is the line segment joining the points  $(\frac{\lambda b_1 - (\sqrt{2}-1)b_2}{\lambda+1}, b_2)$  and  $(\frac{-(\sqrt{2}-1)(b_1 + b_2) + \sqrt{2}\lambda b_1}{2 - \sqrt{2} + \sqrt{2}\lambda}, \frac{(b_1 + b_2) + \sqrt{2}\lambda b_2}{2 - \sqrt{2} + \sqrt{2}\lambda})$  where  $1 < \lambda \leq \frac{a_1 + a_2}{a_1 - a_2}$ . If  $\lambda > \frac{a_1 + a_2}{a_1 - a_2}$ , (22) is the line segment joining the points  $(\frac{\lambda b_1 - (\sqrt{2}-1)b_2}{\lambda+1}, b_2)$  and  $(\frac{\lambda(b_1 - (\sqrt{2}-1)b_2)}{\sqrt{2} + (2 - \sqrt{2})\lambda}, \frac{\lambda(b_1 - (\sqrt{2}-1)b_2)}{\sqrt{2} + (2 - \sqrt{2})\lambda})$ .

Take into account the regions where  $x \geq b_1$ . When  $y$  is negative, the equality (19) becomes the equation

$$x - (\sqrt{2} - 1)y = \frac{\lambda}{\lambda - 1}(b_1 - (\sqrt{2} - 1)b_2). \quad (23)$$

(23) states the line segment joining the points  $(\frac{\lambda(-b_1 + (\sqrt{2}-1)b_2)}{1 - \lambda}, 0)$  and  $(\frac{(\sqrt{2}-1)(b_1 + b_2) - \sqrt{2}\lambda b_1}{\sqrt{2}(1 - \lambda)}, \frac{(b_1 + b_2) - \sqrt{2}\lambda b_2}{\sqrt{2}(1 - \lambda)})$  where  $\lambda < \frac{1}{\sqrt{2}}$ . When  $\lambda = \frac{1}{\sqrt{2}}$ , these points coincide. When  $\lambda > \frac{1}{\sqrt{2}}$ , the line specified by (23) does not pass through the region formed. When  $0 \leq y \leq b_2$ , the equality (19) becomes the equation

$$(1 - \lambda)x + (\sqrt{2} - 1)(1 + \lambda)y = \lambda(-b_1 + (\sqrt{2} - 1)b_2). \quad (24)$$

(24) states the line segment joining the points  $(\frac{\lambda(-b_1 + (\sqrt{2}-1)b_2)}{1 - \lambda}, 0)$  and  $(\frac{\lambda b_1 + (\sqrt{2}-1)b_2}{\lambda - 1}, b_2)$  where  $\lambda \leq \frac{1}{\sqrt{2}}$ . If  $\lambda > \frac{1}{\sqrt{2}}$ , then it specifies the line segment joining the points  $(\frac{\lambda b_1 + (\sqrt{2}-1)b_2}{\lambda - 1}, b_2)$  and  $(\frac{(\sqrt{2}-1)(b_1 + b_2) + \sqrt{2}\lambda b_1}{\sqrt{2} - 2 + \sqrt{2}\lambda}, \frac{-(b_1 + b_2) + \sqrt{2}\lambda b_2}{\sqrt{2} - 2 + \sqrt{2}\lambda})$ .

Considering the case of  $y \geq b_2$ . From (19), one gets that

$$x + (\sqrt{2} - 1)y = \frac{\lambda}{\lambda - 1}(b_1 + (\sqrt{2} - 1)b_2). \quad (25)$$

(25) gives the line segment joining the points  $(\frac{\lambda b_1 + (\sqrt{2}-1)b_2}{\lambda - 1}, b_2)$  and  $(\frac{(\sqrt{2}-1)(b_1 - b_2) - \sqrt{2}\lambda b_1}{\sqrt{2}(1 - \lambda)}, \frac{-(b_1 - b_2) - \sqrt{2}\lambda b_2}{\sqrt{2}(1 - \lambda)})$ . In the region determined by the inequalities  $|x| \geq |y|$  and  $|x - b_1| \leq |y - b_2|$ , (19) is examined according to the subregions as follows. Consider the regions where  $0 \leq x \leq b_1$ . When  $y < 0$ , the equality (19) reduces the equation

$$(1 + (\sqrt{2} - 1)\lambda)x + (\lambda - (\sqrt{2} - 1))y = \lambda(b_2 + (\sqrt{2} - 1)b_1). \quad (26)$$

(26) states the line segment joining the points  $(\frac{-(\sqrt{2}-1)(b_1-b_2)+\sqrt{2}\lambda b_1}{2-\sqrt{2}+\sqrt{2}\lambda}, \frac{-(b_1-b_2)+\sqrt{2}\lambda b_2}{2-\sqrt{2}+\sqrt{2}\lambda})$  and  $(b_1, \frac{-b_1+\lambda b_2}{\lambda-(\sqrt{2}-1)})$  where  $\lambda \leq \frac{1}{\sqrt{2}-1}$ . If  $\frac{1}{\sqrt{2}-1} \leq \lambda < \frac{1}{m}$ , then (26) gives the line segment joining the points  $(b_1, \frac{-b_1+\lambda b_2}{\lambda-(\sqrt{2}-1)})$  and  $(\frac{\lambda((\sqrt{2}-1)b_1+b_2)}{1+(\sqrt{2}-1)\lambda}, 0)$ . When  $\lambda > \frac{1}{m}$ , the line specified by (26) does not pass

through the region formed. If  $0 \leq y \leq b_2$ , the equality (19) means

$$(1 + (\sqrt{2} - 1)\lambda)x + (\lambda + (\sqrt{2} - 1))y = \lambda(b_2 + (\sqrt{2} - 1)b_1). \quad (27)$$

(27) states the line segment joining the points  $(\frac{(\sqrt{2}-1)(b_1-b_2)+\sqrt{2}\lambda b_1}{\sqrt{2}(\lambda+1)}, \frac{-(b_1-b_2)+\sqrt{2}\lambda b_2}{\sqrt{2}(\lambda+1)})$  and  $(\frac{\lambda((\sqrt{2}-1)b_1+b_2)}{1+(\sqrt{2}-1)\lambda}, 0)$  where  $\frac{1}{\sqrt{2}} \leq \lambda \leq \frac{1}{m}$ . If  $\lambda > \frac{1}{m}$ , then it gives the line segment joining the points  $(b_1, \frac{-b_1+\lambda b_2}{\lambda-(\sqrt{2}-1)})$  and  $(\frac{(\sqrt{2}-1)(b_1-b_2)+\sqrt{2}\lambda b_1}{\sqrt{2}(\lambda+1)}, \frac{-(b_1-b_2)+\sqrt{2}\lambda b_2}{\sqrt{2}(\lambda+1)})$ .

Considering the case of  $y \geq b_2$ . From (19), one gets that

$$(1 + (\sqrt{2} - 1)\lambda)x + (-\lambda + (\sqrt{2} - 1))y = \lambda(-b_2 + (\sqrt{2} - 1)b_1). \quad (28)$$

(28) is the equation of the line segment joining the points  $(\frac{-(\sqrt{2}-1)(b_1+b_2)+\sqrt{2}\lambda b_1}{2-\sqrt{2}+\sqrt{2}\lambda}, \frac{(b_1+b_2)+\sqrt{2}\lambda b_2}{2-\sqrt{2}+\sqrt{2}\lambda})$  and  $(b_1, \frac{b_1+\lambda b_2}{\lambda-(\sqrt{2}-1)})$  where  $\lambda > \frac{\sqrt{2}}{1-m}$ . If  $\frac{1+m}{1-m} \leq \lambda \leq \frac{\sqrt{2}}{1-m}$ , then it gives the line segment joining the points  $(\frac{-(\sqrt{2}-1)(b_1+b_2)+\sqrt{2}\lambda b_1}{2-\sqrt{2}+\sqrt{2}\lambda}, \frac{(b_1+b_2)+\sqrt{2}\lambda b_2}{2-\sqrt{2}+\sqrt{2}\lambda})$  and  $(\frac{\lambda((\sqrt{2}-1)b_1-b_2)}{\sqrt{2}+(\sqrt{2}-2)\lambda}, \frac{\lambda((\sqrt{2}-1)b_1-b_2)}{\sqrt{2}+(\sqrt{2}-2)\lambda})$ . Take into account the regions where  $x \geq b_1$ . When  $y < 0$ , the equality (19) reduces the equation

$$(1 - (\sqrt{2} - 1)\lambda)x + (\lambda - (\sqrt{2} - 1))y = \lambda(b_2 - (\sqrt{2} - 1)b_1). \quad (29)$$

(29) states the line segment joining the points  $(\frac{(\sqrt{2}-1)(b_1+b_2)-\sqrt{2}\lambda b_1}{\sqrt{2}(1-\lambda)}, \frac{(b_1+b_2)-\sqrt{2}\lambda b_2}{\sqrt{2}(1-\lambda)})$  and  $(b_1, \frac{-b_1+\lambda b_2}{\lambda-(\sqrt{2}-1)})$  where  $\lambda \leq \frac{1}{\sqrt{2}}$ . If  $\frac{1}{\sqrt{2}} \leq \lambda < \frac{1}{m}$ , then (29) gives the line segment joining the points  $(b_1, \frac{-b_1+\lambda b_2}{\lambda-(\sqrt{2}-1)})$  and  $(\frac{\lambda(-(\sqrt{2}-1)b_1+b_2)}{1-(\sqrt{2}-1)\lambda}, 0)$ . When  $\lambda > \frac{1}{m}$ , the line specified by (29) does not pass

through the region formed. When  $0 \leq y \leq b_2$ , the equality (19) reduces the equation

$$(1 - (\sqrt{2} - 1)\lambda)x + (\lambda + (\sqrt{2} - 1))y = \lambda(b_2 - (\sqrt{2} - 1)b_1). \quad (29')$$

(29') states the line segment joining the points  $(\frac{(\sqrt{2}-1)(b_1+b_2)+\sqrt{2}\lambda b_1}{\sqrt{2}-2+\sqrt{2}\lambda}, \frac{-(b_1+b_2)+\sqrt{2}\lambda b_2}{\sqrt{2}-2+\sqrt{2}\lambda})$  and  $(\frac{\lambda(-(\sqrt{2}-1)b_1+b_2)}{1-(\sqrt{2}-1)\lambda}, 0)$  where  $\frac{1}{m}+1 < \lambda < \frac{1}{m}$ . If  $\lambda > \frac{1}{m}$ , then it is the equation of the line segment joining the points  $(\frac{(\sqrt{2}-1)(b_1+b_2)+\sqrt{2}\lambda b_1}{\sqrt{2}-2+\sqrt{2}\lambda}, \frac{-(b_1+b_2)+\sqrt{2}\lambda b_2}{\sqrt{2}-2+\sqrt{2}\lambda})$  and  $(b_1, \frac{-b_1+\lambda b_2}{\lambda+(\sqrt{2}-1)})$ . In the case of  $\lambda = \frac{1}{m}$ , the points  $(\frac{\lambda(-(\sqrt{2}-1)b_1+b_2)}{1-(\sqrt{2}-1)\lambda}, 0)$  and  $(b_1, \frac{-b_1+\lambda b_2}{\lambda+(\sqrt{2}-1)})$  are coincide. If  $y \geq b_2$ , the equality (19) means

$$(1-(\sqrt{2}-1)\lambda)x + (-\lambda+(\sqrt{2}-1))y = \lambda(-b_2-(\sqrt{2}-1)b_1). \quad (30)$$

(30) states the line segment joining the points

$(\frac{(\sqrt{2}-1)(b_1-b_2)-\sqrt{2}\lambda b_1}{\sqrt{2}(1-\lambda)}, \frac{-(b_1-b_2)-\sqrt{2}\lambda b_2}{\sqrt{2}(1-\lambda)})$  and  $(b_1, \frac{b_1+\lambda b_2}{\lambda-(\sqrt{2}-1)})$  where  $\frac{\sqrt{2}}{1-m} \leq \lambda$ . If  $\frac{\sqrt{2}}{1-m} \geq \lambda$ , then it gives the line segment joining the points

$(\frac{(\sqrt{2}-1)(b_1-b_2)-\sqrt{2}\lambda b_1}{\sqrt{2}(1-\lambda)}, \frac{-(b_1-b_2)-\sqrt{2}\lambda b_2}{\sqrt{2}(1-\lambda)})$  and  $(\frac{\lambda((\sqrt{2}-1)b_1+b_2)}{\sqrt{2}(\lambda-1)}, \frac{\lambda((\sqrt{2}-1)b_1+b_2)}{\sqrt{2}(\lambda-1)})$ . In

the region determined by the inequalities  $|x| \leq |y|$  and  $|x-b_1| \geq |y-b_2|$ , (19) is examined according to the subregions as follows. Consider the regions where  $0 \leq x \leq b_1$ . When  $y \geq b_2$ , the equality (19) reduces the equation

$$(1-(\sqrt{2}-1)\lambda)y + (\lambda+(\sqrt{2}-1))x = \lambda(b_1-(\sqrt{2}-1)b_2). \quad (31)$$

(31) states the line segment joining the points  $(\frac{-(b_1+b_2)+\sqrt{2}\lambda b_1}{\sqrt{2}-2+\sqrt{2}\lambda}, \frac{(\sqrt{2}-1)(b_1+b_2)+\sqrt{2}\lambda b_2}{\sqrt{2}-2+\sqrt{2}\lambda})$  and  $(\frac{\lambda(b_1-(\sqrt{2}-1)b_2)}{\sqrt{2}+(2-\sqrt{2})\lambda}, \frac{\lambda(b_1-(\sqrt{2}-1)b_2)}{\sqrt{2}+(2-\sqrt{2})\lambda})$  where  $\lambda < \frac{1+m}{1-m}$ . the line specified by (29) does not pass through the region

formed. For other values of  $\lambda$ , the equation (31) yields the line that is not contained in the described region. In the region determined by the inequalities  $|x| \leq |y|$  and  $|x-b_1| \leq |y-b_2|$ , (19) is examined according to the subregions as follows. Consider the regions where  $0 \leq x \leq b_1$ . When  $y < 0$ , the equality (19) reduces the equation

$$(-1+\lambda)y + (\sqrt{2}-1)(\lambda+1)x = \lambda(b_2+(\sqrt{2}-1)b_1). \quad (32)$$

(32) states the line segment joining the points  $(b_1, \frac{(\sqrt{2}-1)b_1-\lambda b_2}{1-\lambda})$  and  $(\frac{\lambda(b_2+(\sqrt{2}-1)b_1)}{\sqrt{2}+(\sqrt{2}-2)\lambda}, \frac{-\lambda(b_2+(\sqrt{2}-1)b_1)}{\sqrt{2}+(\sqrt{2}-2)\lambda})$  where  $\lambda \leq \frac{\sqrt{2}}{1+m}$ . In the remaining cases, no

solution to (32) exists in the designated domain. When  $y \geq b_2$ , the equality (19) means that the line segment with the equation

$$(1-\lambda)y + (\sqrt{2}-1)(\lambda+1)x = \lambda(-b_2+(\sqrt{2}-1)b_1). \quad (33)$$

(33) gives the equation of the line segment joining points  $(b_1, \frac{(\sqrt{2}-1)b_1 + \lambda b_2}{\lambda-1})$  and  $(\frac{-(b_1+b_2) + \sqrt{2}\lambda b_1}{\sqrt{2}-2+\sqrt{2}\lambda}, \frac{(\sqrt{2}-1)(b_1+b_2) + \sqrt{2}\lambda b_2}{\sqrt{2}-2+\sqrt{2}\lambda})$  where  $\lambda \leq \frac{1+m}{1-m}$ . If  $\frac{1+m}{1-m} < \lambda < \frac{\sqrt{2}}{1-m}$ , then it is the equation of the line segment joining points  $(b_1, \frac{(\sqrt{2}-1)b_1 + \lambda b_2}{\lambda-1})$  and  $(\frac{\lambda((\sqrt{2}-1)b_1 - b_2)}{\sqrt{2} + (\sqrt{2}-2)\lambda}, \frac{\lambda((\sqrt{2}-1)b_1 - b_2)}{\sqrt{2} + (\sqrt{2}-2)\lambda})$ . For other values of  $\lambda$ , the equation (33) yields the line that is not contained in the described region. Consider the regions where  $x \geq b_1$ . When  $y < 0$ , the equality (19) reduces the equation

$$(-1+\lambda)y + (\sqrt{2}-1)(1-\lambda)x = \lambda(b_2 - (\sqrt{2}-1)b_1). \quad (34)$$

(34) states the line segment joining the points  $(b_1, \frac{(\sqrt{2}-1)b_1 - \lambda b_2}{1-\lambda})$  and  $(\frac{\lambda(b_2 - (\sqrt{2}-1)b_1)}{\sqrt{2}(1-\lambda)}, \frac{\lambda(b_2 - (\sqrt{2}-1)b_1)}{\sqrt{2}(1-\lambda)})$  where  $\lambda \leq \frac{\sqrt{2}}{1+m}$ . In the remaining cases, no solution to (34) exists in the designated domain. When  $y \geq b_2$ , the equality (19) reduces the equation

$$y + (\sqrt{2}-1)x = \frac{\lambda}{\lambda-1}(b_2 + (\sqrt{2}-1)b_1). \quad (35)$$

(35) states the line segment joining the points  $(b_1, \frac{(\sqrt{2}-1)b_1 + \lambda b_2}{\lambda-1})$  and  $(\frac{\lambda((\sqrt{2}-1)b_1 + b_2)}{\sqrt{2}(\lambda-1)}, \frac{\lambda((\sqrt{2}-1)b_1 + b_2)}{\sqrt{2}(\lambda-1)})$  where  $\lambda \leq \frac{\sqrt{2}}{1-m}$ . In the remaining cases, no solution to (35) exists in the designated domain.

Now, after these general assessment, the classifications of the Apollonian sets for the points  $A$  and  $B$  on a gradual line, according to the value of  $\lambda$ , are presented below.

**Corollary 3.7.** Let two distinct points  $A$  and  $B$  be on the same gradual line in  $R_C^2$  and let  $\lambda < \frac{\sqrt{2}}{1+m}$  where  $m$  is the slope of the line  $AB$ . Then the

Apollonian set  $A_C(A, B; \lambda)$  satisfies the following properties:

i) It constitutes a non-convex polygon composed of fourteen line segments whose slopes are  $\pm \frac{\lambda+1}{(\sqrt{2}-1)(\lambda-1)}$ ,  $\pm \frac{1}{\sqrt{2}-1}$ ,  $\pm(\sqrt{2}-1)$ ,  $\frac{\lambda-1}{(\sqrt{2}-1)(\lambda+1)}$ ,  $-\frac{1+(\sqrt{2}-1)\lambda}{\lambda-(\sqrt{2}-1)}$ ,  $\pm \frac{1-(\sqrt{2}-1)\lambda}{\lambda-(\sqrt{2}-1)}$ ,  $-\frac{\lambda+\sqrt{2}-1}{1-(\sqrt{2}-1)\lambda}$ ,  $\pm \frac{(\sqrt{2}-1)(\lambda+1)}{\lambda-1}$ .

ii) Eight vertices are on the horizontal line, the vertical line, and the two separator lines through the point  $B$  and the remaining six vertices are on the horizontal line, the separator lines through the point  $A$ .

**Proof.** From the general analysis given above, the following results are immediately observed for the values of  $\lambda$  satisfying the inequality  $\lambda < \frac{\sqrt{2}}{1+m}$



and the Apollonian set  $A_C(A, B; \lambda)$  is formed by the union of line segments given below: The equality (20) is the line segment joining the points  $(\frac{\lambda(b_1 + (\sqrt{2}-1)b_2)}{\lambda+1}, 0)$  and  $(\frac{-(\sqrt{2}-1)(b_1 - b_2) + \sqrt{2}\lambda b_1}{2 - \sqrt{2} + \sqrt{2}\lambda}, \frac{-(b_1 - b_2) + \sqrt{2}\lambda b_2}{2 - \sqrt{2} + \sqrt{2}\lambda})$ . (21) is the line segment joining the points  $(\frac{\lambda(b_1 + (\sqrt{2}-1)b_2)}{\lambda+1}, 0)$  and  $(\frac{\lambda b_1 - (\sqrt{2}-1)b_2}{\lambda+1}, b_2)$ . The equality (22) is the line segment joining the points  $(\frac{\lambda b_1 - (\sqrt{2}-1)b_2}{\lambda+1}, b_2)$  and  $(\frac{\lambda(b_1 - (\sqrt{2}-1)b_2)}{\sqrt{2} + (2 - \sqrt{2})\lambda}, \frac{\lambda(b_1 - (\sqrt{2}-1)b_2)}{\sqrt{2} + (2 - \sqrt{2})\lambda})$ . (23) states the line segment joining the points  $(\frac{\lambda(-b_1 + (\sqrt{2}-1)b_2)}{1-\lambda}, 0)$  and  $(\frac{(\sqrt{2}-1)(b_1 + b_2) - \sqrt{2}\lambda b_1}{\sqrt{2}(1-\lambda)}, \frac{(b_1 + b_2) - \sqrt{2}\lambda b_2}{\sqrt{2}(1-\lambda)})$ . (24) states the line segment joining the points  $(\frac{\lambda(-b_1 + (\sqrt{2}-1)b_2)}{1-\lambda}, 0)$  and  $(\frac{\lambda b_1 + (\sqrt{2}-1)b_2}{\lambda-1}, b_2)$ . (25) gives the line segment joining the points  $(\frac{\lambda b_1 + (\sqrt{2}-1)b_2}{\lambda-1}, b_2)$  and  $(\frac{(\sqrt{2}-1)(b_1 - b_2) - \sqrt{2}\lambda b_1}{\sqrt{2}(1-\lambda)}, \frac{-(b_1 - b_2) - \sqrt{2}\lambda b_2}{\sqrt{2}(1-\lambda)})$ . (26) states the line segment joining the points  $(\frac{-(\sqrt{2}-1)(b_1 - b_2) + \sqrt{2}\lambda b_1}{2 - \sqrt{2} + \sqrt{2}\lambda}, \frac{-(b_1 - b_2) + \sqrt{2}\lambda b_2}{2 - \sqrt{2} + \sqrt{2}\lambda})$  and  $(\frac{\lambda(b_2 + (\sqrt{2}-1)b_1)}{\sqrt{2} + (\sqrt{2}-2)\lambda}, \frac{-\lambda(b_2 + (\sqrt{2}-1)b_1)}{\sqrt{2} + (\sqrt{2}-2)\lambda})$ . (29) states the line segment joining the points  $(\frac{\lambda(b_2 - (\sqrt{2}-1)b_1)}{\sqrt{2} + (1-\lambda)}, \frac{-\lambda(b_2 - (\sqrt{2}-1)b_1)}{\sqrt{2} + (1-\lambda)})$  and  $(\frac{(\sqrt{2}-1)(b_1 + b_2) - \sqrt{2}\lambda b_1}{\sqrt{2}(1-\lambda)}, \frac{(b_1 + b_2) - \sqrt{2}\lambda b_2}{\sqrt{2}(1-\lambda)})$ . (30) states the line segment joining the points  $(\frac{(\sqrt{2}-1)(b_1 - b_2) - \sqrt{2}\lambda b_1}{\sqrt{2}(1-\lambda)}, \frac{-(b_1 - b_2) - \sqrt{2}\lambda b_2}{\sqrt{2}(1-\lambda)})$  and  $(\frac{\lambda((\sqrt{2}-1)b_1 + b_2)}{\sqrt{2}(\lambda-1)}, \frac{\lambda((\sqrt{2}-1)b_1 + b_2)}{\sqrt{2}(\lambda-1)})$ . (31) states the line segment joining the points  $(\frac{-(b_1 + b_2) + \sqrt{2}\lambda b_1}{\sqrt{2} - 2 + \sqrt{2}\lambda}, \frac{(\sqrt{2}-1)(b_1 + b_2) + \sqrt{2}\lambda b_2}{\sqrt{2} - 2 + \sqrt{2}\lambda})$  and  $(\frac{\lambda(b_1 - (\sqrt{2}-1)b_2)}{\sqrt{2} + (2 - \sqrt{2})\lambda}, \frac{\lambda(b_1 - (\sqrt{2}-1)b_2)}{\sqrt{2} + (2 - \sqrt{2})\lambda})$ . (32) states the line segment joining the points  $(b_1, \frac{(\sqrt{2}-1)b_1 - \lambda b_2}{1-\lambda})$  and  $(\frac{\lambda(b_2 + (\sqrt{2}-1)b_1)}{\sqrt{2} + (\sqrt{2}-2)\lambda}, \frac{-\lambda(b_2 + (\sqrt{2}-1)b_1)}{\sqrt{2} + (\sqrt{2}-2)\lambda})$ . (33) gives the equation of the line segment joining points  $(b_1, \frac{(\sqrt{2}-1)b_1 + \lambda b_2}{\lambda-1})$  and  $(\frac{-(b_1 + b_2) + \sqrt{2}\lambda b_1}{\sqrt{2} - 2 + \sqrt{2}\lambda}, \frac{(\sqrt{2}-1)(b_1 + b_2) + \sqrt{2}\lambda b_2}{\sqrt{2} - 2 + \sqrt{2}\lambda})$ . (34) states the line segment joining the points  $(b_1, \frac{(\sqrt{2}-1)b_1 - \lambda b_2}{1-\lambda})$  and  $(\frac{\lambda(b_2 - (\sqrt{2}-1)b_1)}{\sqrt{2}(1-\lambda)}, \frac{-\lambda(b_2 - (\sqrt{2}-1)b_1)}{\sqrt{2}(1-\lambda)})$ . (35) states the line segment joining the points  $(b_1, \frac{(\sqrt{2}-1)b_1 + \lambda b_2}{\lambda-1})$  and  $(\frac{\lambda((\sqrt{2}-1)b_1 + b_2)}{\sqrt{2}(\lambda-1)}, \frac{\lambda((\sqrt{2}-1)b_1 + b_2)}{\sqrt{2}(\lambda-1)})$ . Also, the line segment connecting any two points on the line segments in (30) and (35) is outside  $A_C(A, B; \lambda)$ . Therefore, the set  $A_C(A, B; \lambda)$  fails to be convex. The set  $A_C(A, B; \lambda)$  for this case is shown on Figure 2(a).

When  $\lambda = \frac{\sqrt{2}}{1+m}$ , the endpoints of the line segment in (32) are coincide.

Similarly, the endpoints of the line segment in (34) are coincide. So, the line segments and vertices, except for the line segments specified in (32) and in (34) in the proof of Corollary 3.7, remain the same and the Apollonian set  $A_C(A, B; \lambda)$  consists of twelve line segments.

**Corollary 3.8.** Let two distinct points  $A$  and  $B$  be on the same gradual line in  $R_C^2$  and let  $\frac{\sqrt{2}}{1+m} \leq \lambda < \frac{1+m}{1-m}$  where  $m$  is the slope of the line  $AB$ . Then the

Apollonian set  $A_C(A, B; \lambda)$  satisfies the following properties:

i) It constitutes a non-convex polygon composed of twelve line segments whose slopes are  $\pm \frac{\lambda+1}{(\sqrt{2}-1)(\lambda-1)}$ ,  $\pm \frac{1}{\sqrt{2}-1}$ ,  $-(\sqrt{2}-1)$ ,  $\frac{\lambda-1}{(\sqrt{2}-1)(\lambda+1)}$ ,  $-\frac{1+(\sqrt{2}-1)\lambda}{\lambda-(\sqrt{2}-1)}$ ,  $\pm \frac{1-(\sqrt{2}-1)\lambda}{\lambda-(\sqrt{2}-1)}$ ,  $-\frac{\lambda+\sqrt{2}-1}{1-(\sqrt{2}-1)\lambda}$ ,  $\frac{(\sqrt{2}-1)(\lambda+1)}{\lambda-1}$ .

ii) Eight vertices are on the horizontal line, the vertical line, and the two separator lines through the point  $B$  and the remaining four vertices are on the horizontal line and the separator line through the point  $A$ .

**Proof.** From the general analysis given above, the following results are immediately observed for the values of  $\lambda$  satisfying the inequality  $1 < \frac{\sqrt{2}}{1+m} \leq \lambda < \frac{1+m}{1-m}$  and the Apollonian set  $A_C(A, B; \lambda)$  is formed by the union of

line segments given below:

The equality (20) is the line segment joining the points  $(\frac{\lambda(b_1+(\sqrt{2}-1)b_2)}{\lambda+1}, 0)$  and

$(\frac{-(\sqrt{2}-1)(b_1-b_2)+\sqrt{2}\lambda b_1}{2-\sqrt{2}+\sqrt{2}\lambda}, \frac{-(b_1-b_2)+\sqrt{2}\lambda b_2}{2-\sqrt{2}+\sqrt{2}\lambda})$ . (21) is the line segment joining the points

$(\frac{\lambda(b_1+(\sqrt{2}-1)b_2)}{\lambda+1}, 0)$  and  $(\frac{\lambda b_1-(\sqrt{2}-1)b_2}{\lambda+1}, b_2)$ . The equality (22) is the line segment

joining the points  $(\frac{\lambda b_1-(\sqrt{2}-1)b_2}{\lambda+1}, b_2)$  and  $(\frac{\lambda(b_1-(\sqrt{2}-1)b_2)}{\sqrt{2}+(2-\sqrt{2})\lambda}, \frac{\lambda(b_1-(\sqrt{2}-1)b_2)}{\sqrt{2}+(2-\sqrt{2})\lambda})$ . (23)

states the line segment joining the points  $(\frac{\lambda(-b_1+(\sqrt{2}-1)b_2)}{1-\lambda}, 0)$  and

$(\frac{(\sqrt{2}-1)(b_1+b_2)-\sqrt{2}\lambda b_1}{\sqrt{2}(1-\lambda)}, \frac{(b_1+b_2)-\sqrt{2}\lambda b_2}{\sqrt{2}(1-\lambda)})$  (24) states the line segment joining the

points  $(\frac{\lambda(-b_1+(\sqrt{2}-1)b_2)}{1-\lambda}, 0)$  and  $(\frac{\lambda b_1+(\sqrt{2}-1)b_2}{\lambda-1}, b_2)$ . (25) gives the line segment

joining the points  $(\frac{\lambda b_1+(\sqrt{2}-1)b_2}{\lambda-1}, b_2)$  and  $(\frac{(\sqrt{2}-1)(b_1-b_2)-\sqrt{2}\lambda b_1}{\sqrt{2}(1-\lambda)}, \frac{-(b_1-b_2)-\sqrt{2}\lambda b_2}{\sqrt{2}(1-\lambda)})$ . (26)

states the line segment joining the points  $(\frac{-(\sqrt{2}-1)(b_1-b_2)+\sqrt{2}\lambda b_1}{2-\sqrt{2}+\sqrt{2}\lambda}, \frac{-(b_1-b_2)+\sqrt{2}\lambda b_2}{2-\sqrt{2}+\sqrt{2}\lambda})$

and  $(b_1, \frac{-b_1+\lambda b_2}{\lambda-(\sqrt{2}-1)})$ . (29) states the line segment joining the points

$(\frac{(\sqrt{2}-1)(b_1+b_2)-\sqrt{2}\lambda b_1}{\sqrt{2}(1-\lambda)}, \frac{(b_1+b_2)-\sqrt{2}\lambda b_2}{\sqrt{2}(1-\lambda)})$  and  $(b_1, \frac{-b_1+\lambda b_2}{\lambda-(\sqrt{2}-1)})$ . (30) states the line segment

joining the points  $(\frac{(\sqrt{2}-1)(b_1-b_2)-\sqrt{2}\lambda b_1}{\sqrt{2}(1-\lambda)}, \frac{(b_1-b_2)-\sqrt{2}\lambda b_2}{\sqrt{2}(1-\lambda)})$  and  $(\frac{\lambda((\sqrt{2}-1)b_1+b_2)}{\sqrt{2}(\lambda-1)}, \frac{\lambda((\sqrt{2}-1)b_1+b_2)}{\sqrt{2}(\lambda-1)})$ .

(31) states the line segment joining the points  $(\frac{-(b_1+b_2)+\sqrt{2}\lambda b_1}{\sqrt{2}-2+\sqrt{2}\lambda}, \frac{(\sqrt{2}-1)(b_1+b_2)+\sqrt{2}\lambda b_2}{\sqrt{2}-2+\sqrt{2}\lambda})$  and  $(\frac{\lambda(b_1-(\sqrt{2}-1)b_2)}{\sqrt{2}+(2-\sqrt{2})\lambda}, \frac{\lambda(b_1-(\sqrt{2}-1)b_2)}{\sqrt{2}+(2-\sqrt{2})\lambda})$ . (33) gives

the equation of the line segment joining points  $(b_1, \frac{(\sqrt{2}-1)b_1+\lambda b_2}{\lambda-1})$  and

$(\frac{-(b_1+b_2)+\sqrt{2}\lambda b_1}{\sqrt{2}-2+\sqrt{2}\lambda}, \frac{(\sqrt{2}-1)(b_1+b_2)+\sqrt{2}\lambda b_2}{\sqrt{2}-2+\sqrt{2}\lambda})$ . (35) states the line segment joining the points

$(b_1, \frac{(\sqrt{2}-1)b_1+\lambda b_2}{\lambda-1})$  and  $(\frac{\lambda((\sqrt{2}-1)b_1+b_2)}{\sqrt{2}(\lambda-1)}, \frac{\lambda((\sqrt{2}-1)b_1+b_2)}{\sqrt{2}(\lambda-1)})$ . Also, the line segment

connecting any two points on the line segments in (30) and (35) is outside  $A_C(A, B; \lambda)$ . Therefore, the set  $A_C(A, B; \lambda)$  fails to be convex. The set  $A_C(A, B; \lambda)$  for this case is shown on Figure 2(b).

When  $\lambda = \frac{1+m}{1-m}$ , the endpoints of the line segment in (31) are coincide.

So, the line segments and vertices, except for the line segment specified in (31) in the proof of Corollary 3.8, remain the same and the Apollonian set  $A_C(A, B; \lambda)$  consists of eleven line segments.

**Corollary 3.9.** Let two distinct points  $A$  and  $B$  be on the same gradual line in  $R_C^2$  and let  $\frac{1+m}{1-m} < \lambda < \frac{\sqrt{2}}{1-m}$  where  $m$  is the slope of the line  $AB$ . Then the

Apollonian set  $A_C(A, B; \lambda)$  satisfies the following properties:

i) It constitutes a non-convex polygon composed of twelve line segments whose slopes are  $\pm \frac{\lambda+1}{(\sqrt{2}-1)(\lambda-1)}$ ,  $\pm \frac{1}{\sqrt{2}-1}$ ,  $-(\sqrt{2}-1)$ ,  $\frac{\lambda-1}{(\sqrt{2}-1)(\lambda+1)}$ ,  $\pm \frac{1+(\sqrt{2}-1)\lambda}{\lambda-(\sqrt{2}-1)}$ ,  $\pm \frac{1-(\sqrt{2}-1)\lambda}{\lambda-(\sqrt{2}-1)}$ ,  $\frac{(\sqrt{2}-1)(\lambda+1)}{\lambda-1}$ .

ii) Eight vertices are on the horizontal line, the vertical line, and the two separator lines through the point  $B$  and the remaining four vertices are on the horizontal line and the separator line through the point  $A$ .

**Proof.** From the general analysis given above, the following results are immediately observed for the values of  $\lambda$  satisfying the inequality  $\frac{1+m}{1-m} < \lambda < \frac{\sqrt{2}}{1-m}$  and the Apollonian set  $A_C(A, B; \lambda)$  is formed by the union of line

segments given below:

The equality (20) is the line segment joining the points  $(\frac{\lambda(b_1+(\sqrt{2}-1)b_2)}{\lambda+1}, 0)$  and

$(\frac{-(\sqrt{2}-1)(b_1-b_2)+\sqrt{2}\lambda b_1}{2-\sqrt{2}+\sqrt{2}\lambda}, \frac{-(b_1-b_2)+\sqrt{2}\lambda b_2}{2-\sqrt{2}+\sqrt{2}\lambda})$ . (21) is the line segment joining the points

$(\frac{\lambda(b_1+(\sqrt{2}-1)b_2)}{\lambda+1}, 0)$  and  $(\frac{\lambda b_1-(\sqrt{2}-1)b_2}{\lambda+1}, b_2)$ . The equality (22) is the line segment

joining the points  $(\frac{\lambda b_1 - (\sqrt{2}-1)b_2}{\lambda+1}, \frac{b_2}{\lambda+1})$  and  $(\frac{-(\sqrt{2}-1)(b_1+b_2) + \sqrt{2}\lambda b_1}{2-\sqrt{2}+\sqrt{2}\lambda}, \frac{(b_1+b_2) + \sqrt{2}\lambda b_2}{2-\sqrt{2}+\sqrt{2}\lambda})$ . (23)

states the line segment joining the points  $(\frac{\lambda(-b_1 + (\sqrt{2}-1)b_2)}{1-\lambda}, 0)$  and

$(\frac{(\sqrt{2}-1)(b_1+b_2) - \sqrt{2}\lambda b_1}{\sqrt{2}(1-\lambda)}, \frac{(b_1+b_2) - \sqrt{2}\lambda b_2}{\sqrt{2}(1-\lambda)})$  (24) states the line segment joining the points

$(\frac{\lambda(-b_1 + (\sqrt{2}-1)b_2)}{1-\lambda}, 0)$  and  $(\frac{\lambda b_1 + (\sqrt{2}-1)b_2}{\lambda-1}, \frac{b_2}{\lambda-1})$ . (25) gives the line segment joining the

points  $(\frac{\lambda b_1 + (\sqrt{2}-1)b_2}{\lambda-1}, \frac{b_2}{\lambda-1})$  and  $(\frac{(\sqrt{2}-1)(b_1-b_2) - \sqrt{2}\lambda b_1}{\sqrt{2}(1-\lambda)}, \frac{-(b_1-b_2) - \sqrt{2}\lambda b_2}{\sqrt{2}(1-\lambda)})$ . (26) states the

line segment joining the points  $(\frac{-(\sqrt{2}-1)(b_1-b_2) + \sqrt{2}\lambda b_1}{2-\sqrt{2}+\sqrt{2}\lambda}, \frac{-(b_1-b_2) + \sqrt{2}\lambda b_2}{2-\sqrt{2}+\sqrt{2}\lambda})$  and

$(b_1, \frac{-b_1 + \lambda b_2}{\lambda - (\sqrt{2}-1)})$ . (28) gives the line segment joining the points

$(\frac{-(\sqrt{2}-1)(b_1+b_2) + \sqrt{2}\lambda b_1}{2-\sqrt{2}+\sqrt{2}\lambda}, \frac{(b_1+b_2) + \sqrt{2}\lambda b_2}{2-\sqrt{2}+\sqrt{2}\lambda})$  and  $(\frac{\lambda((\sqrt{2}-1)b_1 - b_2)}{\sqrt{2} + (\sqrt{2}-2)\lambda}, \frac{\lambda((\sqrt{2}-1)b_1 - b_2)}{\sqrt{2} + (\sqrt{2}-2)\lambda})$ . (29)

states the line segment joining the points

$(\frac{(\sqrt{2}-1)(b_1+b_2) - \sqrt{2}\lambda b_1}{\sqrt{2}(1-\lambda)}, \frac{(b_1+b_2) - \sqrt{2}\lambda b_2}{\sqrt{2}(1-\lambda)})$  and  $(b_1, \frac{-b_1 + \lambda b_2}{\lambda - (\sqrt{2}-1)})$ . (30) states the line

segment joining the points  $(\frac{(\sqrt{2}-1)(b_1-b_2) - \sqrt{2}\lambda b_1}{\sqrt{2}(1-\lambda)}, \frac{-(b_1-b_2) - \sqrt{2}\lambda b_2}{\sqrt{2}(1-\lambda)})$  and

$(\frac{\lambda((\sqrt{2}-1)b_1 + b_2)}{\sqrt{2}(\lambda-1)}, \frac{\lambda((\sqrt{2}-1)b_1 + b_2)}{\sqrt{2}(\lambda-1)})$ . (33) gives the equation of the line segment

joining points  $(b_1, \frac{(\sqrt{2}-1)b_1 + \lambda b_2}{\lambda-1})$  and  $(\frac{\lambda((\sqrt{2}-1)b_1 - b_2)}{\sqrt{2} + (\sqrt{2}-2)\lambda}, \frac{\lambda((\sqrt{2}-1)b_1 - b_2)}{\sqrt{2} + (\sqrt{2}-2)\lambda})$ . (35)

states the line segment joining the points  $(b_1, \frac{(\sqrt{2}-1)b_1 + \lambda b_2}{\lambda-1})$  and

$(\frac{\lambda((\sqrt{2}-1)b_1 + b_2)}{\sqrt{2}(\lambda-1)}, \frac{\lambda((\sqrt{2}-1)b_1 + b_2)}{\sqrt{2}(\lambda-1)})$ . Since the set  $A_C(A, B; \lambda)$  contains the line segments

in (30) and (35), it is non-convex, as in the previous corollaries. The set  $A_C(A, B; \lambda)$  for this case is shown on Figure 2(c).

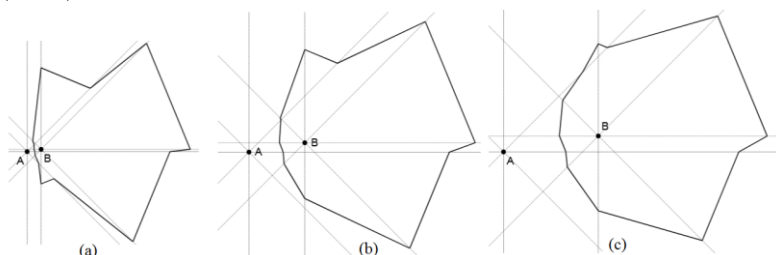


Figure 2  $A_C(A, B; \lambda)$  for  $\lambda < \frac{\sqrt{2}}{1-m}$

When  $\lambda = \frac{\sqrt{2}}{1-m}$ , the endpoints of the line segments in (33) and (35) are coincide. So, the line segments and vertices, except for the line segment

specified in (33) and (35) in the proof of Corollary 3.9, remain the same and the Apollonian set  $A_C(A, B; \lambda)$  consists of ten line segments.

**Corollary 3.10.** Let two distinct points  $A$  and  $B$  be on the same gradual line in  $R_C^2$  and let  $\frac{1}{1-m} < \lambda < \frac{1}{\sqrt{2}}$  where  $m$  is the slope of the line  $AB$ . Then the

Apollonian set  $A_C(A, B; \lambda)$  satisfies the following properties:

i) It constitutes a non-convex polygon composed of ten line segments whose slopes are  $\pm \frac{\lambda+1}{(\sqrt{2}-1)(\lambda-1)}$ ,  $\pm \frac{1}{\sqrt{2}-1}$ ,  $\frac{\lambda-1}{(\sqrt{2}-1)(\lambda+1)}$ ,  $\pm \frac{1+(\sqrt{2}-1)\lambda}{\lambda-(\sqrt{2}-1)}$ ,  $\pm \frac{1-(\sqrt{2}-1)\lambda}{\lambda-(\sqrt{2}-1)}$ .

ii) Eight vertices are on the horizontal line, the vertical line, and the two separator lines through the point  $B$  and the remaining two vertices are on the horizontal line through the point  $A$ .

**Proof.** From the general analysis given above, the following results are immediately observed for the values of  $\lambda$  satisfying the inequality  $\frac{1}{1-m} < \lambda < \frac{1}{\sqrt{2}}$  and the Apollonian set  $A_C(A, B; \lambda)$  is formed by the union of line segments given below:

The equality (20) is the line segment joining the points  $(\frac{\lambda(b_1+(\sqrt{2}-1)b_2)}{\lambda+1}, 0)$  and

$(\frac{-(\sqrt{2}-1)(b_1-b_2)+\sqrt{2}\lambda b_1}{2-\sqrt{2}+\sqrt{2}\lambda}, \frac{-(b_1-b_2)+\sqrt{2}\lambda b_2}{2-\sqrt{2}+\sqrt{2}\lambda})$ . (21) is the line segment joining the

points  $(\frac{\lambda(b_1+(\sqrt{2}-1)b_2)}{\lambda+1}, 0)$  and  $(\frac{\lambda b_1-(\sqrt{2}-1)b_2}{\lambda+1}, b_2)$ . The equality (22) is the line

segment joining the points  $(\frac{\lambda b_1-(\sqrt{2}-1)b_2}{\lambda+1}, b_2)$  and

$(\frac{-(\sqrt{2}-1)(b_1+b_2)+\sqrt{2}\lambda b_1}{2-\sqrt{2}+\sqrt{2}\lambda}, \frac{(b_1+b_2)+\sqrt{2}\lambda b_2}{2-\sqrt{2}+\sqrt{2}\lambda})$ . (23) states the line segment joining the

points  $(\frac{\lambda(-b_1+(\sqrt{2}-1)b_2)}{1-\lambda}, 0)$  and  $(\frac{(\sqrt{2}-1)(b_1+b_2)-\sqrt{2}\lambda b_1}{\sqrt{2}(1-\lambda)}, \frac{(b_1+b_2)-\sqrt{2}\lambda b_2}{\sqrt{2}(1-\lambda)})$  (24) states

the line segment joining the points  $(\frac{\lambda(-b_1+(\sqrt{2}-1)b_2)}{1-\lambda}, 0)$  and  $(\frac{\lambda b_1+(\sqrt{2}-1)b_2}{\lambda-1}, b_2)$ . (25)

gives the line segment joining the points  $(\frac{\lambda b_1+(\sqrt{2}-1)b_2}{\lambda-1}, b_2)$  and

$(\frac{(\sqrt{2}-1)(b_1-b_2)-\sqrt{2}\lambda b_1}{\sqrt{2}(1-\lambda)}, \frac{-(b_1-b_2)-\sqrt{2}\lambda b_2}{\sqrt{2}(1-\lambda)})$ . (26) states the line segment joining the

points  $(\frac{-(\sqrt{2}-1)(b_1-b_2)+\sqrt{2}\lambda b_1}{2-\sqrt{2}+\sqrt{2}\lambda}, \frac{-(b_1-b_2)+\sqrt{2}\lambda b_2}{2-\sqrt{2}+\sqrt{2}\lambda})$  and  $(b_1, \frac{-b_1+\lambda b_2}{\lambda-(\sqrt{2}-1)})$ .

(28) gives the line segment joining the points  $(\frac{-(\sqrt{2}-1)(b_1+b_2)+\sqrt{2}\lambda b_1}{2-\sqrt{2}+\sqrt{2}\lambda}, \frac{(b_1+b_2)+\sqrt{2}\lambda b_2}{2-\sqrt{2}+\sqrt{2}\lambda})$

and  $(b_1, \frac{b_1+\lambda b_2}{\lambda-(\sqrt{2}-1)})$ . (29) states the line segment joining the points

$(\frac{(\sqrt{2}-1)(b_1+b_2)-\sqrt{2}\lambda b_1}{\sqrt{2}(1-\lambda)}, \frac{(b_1+b_2)-\sqrt{2}\lambda b_2}{\sqrt{2}(1-\lambda)})$  and  $(b_1, \frac{-b_1+\lambda b_2}{\lambda-(\sqrt{2}-1)})$ . (30) states the line

segment joining the points  $(\frac{(\sqrt{2}-1)(b_1-b_2)-\sqrt{2}\lambda b_1}{\sqrt{2}(1-\lambda)}, \frac{-(b_1-b_2)-\sqrt{2}\lambda b_2}{\sqrt{2}(1-\lambda)})$  and  $(b_1, \frac{b_1+\lambda b_2}{\lambda-(\sqrt{2}-1)})$ .

Also, the line segment connecting any two points on the line segments in (23) and (24) is outside  $A_C(A, B; \lambda)$ . Therefore, the set  $A_C(A, B; \lambda)$  is non-convex. The set  $A_C(A, B; \lambda)$  for this case is shown on Figure 3(a).

When  $\lambda = \frac{1}{m} - 1$ , since the line segments and vertices, except for the line

segment specified in (27) in the proof of Corollary 3.10, remain the same, the Apollonian set  $A_C(A, B; \lambda)$  consists of nine line segments.

**Corollary 3.11.** Let two distinct points  $A$  and  $B$  be on the same gradual line in  $R_C^2$  and let  $\frac{1}{m} - 1 < \lambda < \frac{1}{m}$  where  $m$  is the slope of the line  $AB$ . Then the

Apollonian set  $A_C(A, B; \lambda)$  satisfies the following properties:

i) It constitutes a non-convex polygon composed of ten line segments whose slopes are  $\frac{\lambda+1}{(\sqrt{2}-1)(\lambda-1)}, \pm \frac{1}{\sqrt{2}-1}, \frac{\lambda-1}{(\sqrt{2}-1)(\lambda+1)}, \pm \frac{1+(\sqrt{2}-1)\lambda}{\lambda-(\sqrt{2}-1)}, \pm \frac{1-(\sqrt{2}-1)\lambda}{\lambda-(\sqrt{2}-1)}, -\frac{1+(\sqrt{2}-1)\lambda}{\lambda+(\sqrt{2}-1)},$

ii) Eight vertices are on the horizontal line, the vertical line, and the two separator lines through the point  $B$  and the remaining two vertices are on the horizontal line through the point  $A$ .

**Proof.** From the general analysis given above, the following results are immediately observed for the values of  $\lambda$  satisfying the inequality  $\frac{1}{m} - 1 < \lambda < \frac{1}{m}$  and the Apollonian set  $A_C(A, B; \lambda)$  is formed by the union of line

segments given below:

(21) is the line segment joining the points  $(\frac{(\sqrt{2}-1)(b_1-b_2)+\sqrt{2}\lambda b_1}{\sqrt{2}(\lambda+1)}, \frac{-(b_1-b_2)+\sqrt{2}\lambda b_2}{\sqrt{2}(\lambda+1)})$  and  $(\frac{\lambda b_1-(\sqrt{2}-1)b_2}{\lambda+1}, b_2)$ . The equality (22) is the line segment joining the points

$(\frac{\lambda b_1-(\sqrt{2}-1)b_2}{\lambda+1}, b_2)$  and  $(\frac{-(\sqrt{2}-1)(b_1+b_2)+\sqrt{2}\lambda b_1}{2-\sqrt{2}+\sqrt{2}\lambda}, \frac{(b_1+b_2)+\sqrt{2}\lambda b_2}{2-\sqrt{2}+\sqrt{2}\lambda})$ . (23) states the line

segment joining the points  $(\frac{\lambda(-b_1+(\sqrt{2}-1)b_2)}{1-\lambda}, 0)$  and

$(\frac{(\sqrt{2}-1)(b_1+b_2)-\sqrt{2}\lambda b_1}{\sqrt{2}(1-\lambda)}, \frac{(b_1+b_2)-\sqrt{2}\lambda b_2}{\sqrt{2}(1-\lambda)})$ . (24) states the line segment joining the

points  $(\frac{\lambda(-b_1+(\sqrt{2}-1)b_2)}{1-\lambda}, 0)$  and  $(\frac{\lambda b_1+(\sqrt{2}-1)b_2}{\lambda-1}, b_2)$ . (25) gives the line segment joining

the points  $(\frac{\lambda b_1+(\sqrt{2}-1)b_2}{\lambda-1}, b_2)$  and  $(\frac{(\sqrt{2}-1)(b_1-b_2)-\sqrt{2}\lambda b_1}{\sqrt{2}(1-\lambda)}, \frac{-(b_1-b_2)-\sqrt{2}\lambda b_2}{\sqrt{2}(1-\lambda)})$ . (26) states the

line segment joining the points  $(b_1, \frac{-b_1+\lambda b_2}{\lambda-(\sqrt{2}-1)})$  and  $(\frac{\lambda((\sqrt{2}-1)b_1+b_2)}{1+(\sqrt{2}-1)\lambda}, 0)$ . (27) states

the line segment joining the points  $(\frac{(\sqrt{2}-1)(b_1-b_2)+\sqrt{2}\lambda b_1}{\sqrt{2}(\lambda+1)}, \frac{-(b_1-b_2)+\sqrt{2}\lambda b_2}{\sqrt{2}(\lambda+1)})$  and

$(\frac{\lambda((\sqrt{2}-1)b_1+b_2)}{1+(\sqrt{2}-1)\lambda}, 0)$ . (28) gives the line segment joining the points

$(\frac{-(\sqrt{2}-1)(b_1+b_2)+\sqrt{2}\lambda b_1}{2-\sqrt{2}+\sqrt{2}\lambda}, \frac{(b_1+b_2)+\sqrt{2}\lambda b_2}{2-\sqrt{2}+\sqrt{2}\lambda})$  and  $(b_1, \frac{b_1+\lambda b_2}{\lambda-(\sqrt{2}-1)})$ . (29) states the line segment joining the points  $(\frac{(\sqrt{2}-1)(b_1+b_2)-\sqrt{2}\lambda b_1}{\sqrt{2}(1-\lambda)}, \frac{(b_1+b_2)-\sqrt{2}\lambda b_2}{\sqrt{2}(1-\lambda)})$  and

$(b_1, \frac{-b_1+\lambda b_2}{\lambda-(\sqrt{2}-1)})$ . (30) states the line segment joining the points

$(\frac{(\sqrt{2}-1)(b_1-b_2)-\sqrt{2}\lambda b_1}{\sqrt{2}(1-\lambda)}, \frac{-(b_1-b_2)-\sqrt{2}\lambda b_2}{\sqrt{2}(1-\lambda)})$  and  $(b_1, \frac{b_1+\lambda b_2}{\lambda-(\sqrt{2}-1)})$ . As in Corollary 3.10, since

the set  $A_C(A, B; \lambda)$  contains the line segments labeled (23) and (24), it is non-convex. The set  $A_C(A, B; \lambda)$  for this case is shown on Figure 3(b).

When  $\lambda = \frac{1}{\sqrt{2}} + 1$ , the endpoints  $(\frac{\lambda(-b_1+(\sqrt{2}-1)b_2)}{1-\lambda}, 0)$  and  $(\frac{(\sqrt{2}-1)(b_1+b_2)-\sqrt{2}\lambda b_1}{\sqrt{2}(1-\lambda)}, \frac{(b_1+b_2)-\sqrt{2}\lambda b_2}{\sqrt{2}(1-\lambda)})$  of the line segment in (23) are coincide. So,

the line segments and vertices, except for the line segment specified in (23) in the proof of Corollary 3.11, remain the same and the Apollonian set  $A_C(A, B; \lambda)$  consists of nine line segments.

**Corollary 3.12.** Let two distinct points  $A$  and  $B$  be on the same gradual line in  $R_C^2$  and let  $\frac{1}{\sqrt{2}} + 1 < \lambda < \frac{1}{m}$  where  $m$  is the slope of the line  $AB$ . Then the

Apollonian set  $A_C(A, B; \lambda)$  satisfies the following properties:

i) It constitutes a non-convex polygon composed of ten line segments whose slopes are  $\frac{\lambda+1}{(\sqrt{2}-1)(\lambda-1)}$ ,  $\pm \frac{1}{\sqrt{2}-1}$ ,  $\frac{\lambda-1}{(\sqrt{2}-1)(\lambda+1)}$ ,  $\pm \frac{1+(\sqrt{2}-1)\lambda}{\lambda-(\sqrt{2}-1)}$ ,

$\pm \frac{1-(\sqrt{2}-1)\lambda}{\lambda-(\sqrt{2}-1)}$ ,  $-\frac{1+(\sqrt{2}-1)\lambda}{\lambda+(\sqrt{2}-1)}$ ,  $\frac{-1+(\sqrt{2}-1)\lambda}{\lambda+(\sqrt{2}-1)}$ ,

ii) Eight vertices are on the horizontal line, the vertical line, and the two separator lines through the point  $B$  and the remaining two vertices are on the horizontal line through the point  $A$ .

**Proof.** From the general analysis given above, the following results are immediately observed for the values of  $\lambda$  satisfying the inequality  $\frac{1}{\sqrt{2}} + 1 < \lambda < \frac{1}{m}$

and the Apollonian set  $A_C(A, B; \lambda)$  is formed by the union of line segments given below:

(21) is the line segment joining the points  $(\frac{(\sqrt{2}-1)(b_1-b_2)+\sqrt{2}\lambda b_1}{\sqrt{2}(\lambda+1)}, \frac{-(b_1-b_2)+\sqrt{2}\lambda b_2}{\sqrt{2}(\lambda+1)})$

and  $(\frac{\lambda b_1-(\sqrt{2}-1)b_2}{\lambda+1}, \frac{b_2}{\lambda+1})$ . The equality (22) is the line segment joining the points

$(\frac{\lambda b_1-(\sqrt{2}-1)b_2}{\lambda+1}, \frac{b_2}{\lambda+1})$  and  $(\frac{-(\sqrt{2}-1)(b_1+b_2)+\sqrt{2}\lambda b_1}{2-\sqrt{2}+\sqrt{2}\lambda}, \frac{(b_1+b_2)+\sqrt{2}\lambda b_2}{2-\sqrt{2}+\sqrt{2}\lambda})$ . (24) states the line

segment joining the points  $(\frac{(\sqrt{2}-1)(b_1+b_2)+\sqrt{2}\lambda b_1}{\sqrt{2}-2+\sqrt{2}\lambda}, \frac{-(b_1+b_2)+\sqrt{2}\lambda b_2}{\sqrt{2}-2+\sqrt{2}\lambda})$  and

$(\frac{\lambda b_1 + (\sqrt{2}-1)b_2}{\lambda-1}, b_2)$ . (25) gives the line segment joining the points  $(\frac{\lambda b_1 + (\sqrt{2}-1)b_2}{\lambda-1}, b_2)$  and  $(\frac{(\sqrt{2}-1)(b_1-b_2) - \sqrt{2}\lambda b_1}{\sqrt{2}(1-\lambda)}, \frac{-(b_1-b_2) - \sqrt{2}\lambda b_2}{\sqrt{2}(1-\lambda)})$ . (26) states the line segment joining the points  $(b_1, \frac{-b_1 + \lambda b_2}{\lambda - (\sqrt{2}-1)})$  and  $(\frac{\lambda((\sqrt{2}-1)b_1 + b_2)}{1 + (\sqrt{2}-1)\lambda}, 0)$ . (27) states the line segment joining the points  $(\frac{(\sqrt{2}-1)(b_1-b_2) + \sqrt{2}\lambda b_1}{\sqrt{2}(\lambda+1)}, \frac{-(b_1-b_2) + \sqrt{2}\lambda b_2}{\sqrt{2}(\lambda+1)})$  and  $(\frac{\lambda((\sqrt{2}-1)b_1 + b_2)}{1 + (\sqrt{2}-1)\lambda}, 0)$ . (28) gives the line segment joining the points  $(\frac{-(\sqrt{2}-1)(b_1+b_2) + \sqrt{2}\lambda b_1}{2 - \sqrt{2} + \sqrt{2}\lambda}, \frac{(b_1+b_2) + \sqrt{2}\lambda b_2}{2 - \sqrt{2} + \sqrt{2}\lambda})$  and  $(b_1, \frac{b_1 + \lambda b_2}{\lambda - (\sqrt{2}-1)})$ . (29) states the line segment joining the points  $(\frac{\lambda((\sqrt{2}-1)b_1 + b_2)}{1 - (\sqrt{2}-1)\lambda}, 0)$  and  $(b_1, \frac{-b_1 + \lambda b_2}{\lambda - (\sqrt{2}-1)})$ . (29') states the line segment joining the points  $(\frac{(\sqrt{2}-1)(b_1+b_2) + \sqrt{2}\lambda b_1}{\sqrt{2}-2 + \sqrt{2}\lambda}, \frac{-(b_1+b_2) + \sqrt{2}\lambda b_2}{\sqrt{2}-2 + \sqrt{2}\lambda})$  and  $(\frac{\lambda(-(\sqrt{2}-1)b_1 + b_2)}{1 - (\sqrt{2}-1)\lambda}, 0)$ . (30) states the line segment joining the points  $(\frac{(\sqrt{2}-1)(b_1-b_2) - \sqrt{2}\lambda b_1}{\sqrt{2}(1-\lambda)}, \frac{-(b_1-b_2) - \sqrt{2}\lambda b_2}{\sqrt{2}(1-\lambda)})$  and  $(b_1, \frac{b_1 + \lambda b_2}{\lambda - (\sqrt{2}-1)})$ . Furthermore, the line segment connecting any two points on the line segments in (26) and (27) is outside  $A_C(A, B; \lambda)$ . Therefore, it is non-convex. The set  $A_C(A, B; \lambda)$  for this case is shown in black in Figure 3(c).

When  $\lambda = \frac{1}{m}$ , the endpoints  $(b_1, \frac{-b_1 + \lambda b_2}{\lambda - (\sqrt{2}-1)})$  and  $(\frac{\lambda((\sqrt{2}-1)b_1 + b_2)}{1 + (\sqrt{2}-1)\lambda}, 0)$  of the line segment in (26) are coincide, and (26) specifies the point  $(b_1, 0)$ . Similarly, the endpoints  $(b_1, \frac{-b_1 + \lambda b_2}{\lambda - (\sqrt{2}-1)})$  and  $(\frac{\lambda(-(\sqrt{2}-1)b_1 + b_2)}{1 - (\sqrt{2}-1)\lambda}, 0)$  of the line segment in (29) are coincide, and (29) specifies the point  $(b_1, 0)$ . So, the line segments and vertices, except for the line segments specified in (26) and (29) in the proof of Corollary 3.12, remain the same and the Apollonian set  $A_C(A, B; \lambda)$  consists of eight line segments. Moreover, the line segment connecting any two points on the set  $A_C(A, B; \lambda)$  lies entirely in the set. Therefore, the set  $A_C(A, B; \lambda)$  is convex. The set  $A_C(A, B; \lambda)$  for this case is shown in blue in Figure 3(c).

**Corollary 3.13.** Let two distinct points  $A$  and  $B$  be on the same gradual line in  $R_C^2$  and let  $\lambda > \frac{1}{m}$  where  $m$  is the slope of the line  $AB$ . Then the

Apollonian set  $A_C(A, B; \lambda)$  satisfies the following properties:

i) It constitutes a convex polygon composed of eight line segments whose slopes are



$$\frac{\lambda+1}{(\sqrt{2}-1)(\lambda-1)}, -\frac{1}{\sqrt{2}-1}, \frac{\lambda-1}{(\sqrt{2}-1)(\lambda+1)}, \frac{1+(\sqrt{2}-1)\lambda}{\lambda-(\sqrt{2}-1)}, -\frac{1+(\sqrt{2}-1)\lambda}{\lambda+(\sqrt{2}-1)}, \frac{1-(\sqrt{2}-1)\lambda}{\lambda-(\sqrt{2}-1)}, \frac{-1+(\sqrt{2}-1)\lambda}{\lambda+(\sqrt{2}-1)},$$

ii) Eight vertices are on the horizontal line, the vertical line, and the two separator lines through the point  $B$ .

**Proof.** From the general analysis given above, the following results are immediately observed for the values of  $\lambda$  satisfying the inequality  $\lambda \geq \frac{1}{m}$  and

the Apollonian set  $A_C(A, B; \lambda)$  is formed by the union of line segments given below:

(21) is the line segment joining the points  $(\frac{(\sqrt{2}-1)(b_1-b_2)+\sqrt{2}\lambda b_1}{\sqrt{2}(\lambda+1)}, \frac{-(b_1-b_2)+\sqrt{2}\lambda b_2}{\sqrt{2}(\lambda+1)})$

and  $(\frac{\lambda b_1-(\sqrt{2}-1)b_2}{\lambda+1}, b_2)$ . The equality (22) is the line segment joining the points

$(\frac{\lambda b_1-(\sqrt{2}-1)b_2}{\lambda+1}, b_2)$  and  $(\frac{-(\sqrt{2}-1)(b_1+b_2)+\sqrt{2}\lambda b_1}{2-\sqrt{2}+\sqrt{2}\lambda}, \frac{(b_1+b_2)+\sqrt{2}\lambda b_2}{2-\sqrt{2}+\sqrt{2}\lambda})$ . (24) states the line

segment joining the points  $(\frac{(\sqrt{2}-1)(b_1+b_2)+\sqrt{2}\lambda b_1}{\sqrt{2}-2+\sqrt{2}\lambda}, \frac{-(b_1+b_2)+\sqrt{2}\lambda b_2}{\sqrt{2}-2+\sqrt{2}\lambda})$  and

$(\frac{\lambda b_1+(\sqrt{2}-1)b_2}{\lambda-1}, b_2)$ . (25) gives the line segment joining the points  $(\frac{\lambda b_1+(\sqrt{2}-1)b_2}{\lambda-1}, b_2)$

and  $(\frac{(\sqrt{2}-1)(b_1-b_2)-\sqrt{2}\lambda b_1}{\sqrt{2}(1-\lambda)}, \frac{-(b_1-b_2)-\sqrt{2}\lambda b_2}{\sqrt{2}(1-\lambda)})$ . (27) states the line segment joining

the points  $(\frac{(\sqrt{2}-1)(b_1-b_2)+\sqrt{2}\lambda b_1}{\sqrt{2}(\lambda+1)}, \frac{-(b_1-b_2)+\sqrt{2}\lambda b_2}{\sqrt{2}(\lambda+1)})$  and  $(b_1, \frac{-b_1+\lambda b_2}{\lambda+(\sqrt{2}-1)})$ . (28) gives the line

segment joining the points  $(\frac{-(\sqrt{2}-1)(b_1+b_2)+\sqrt{2}\lambda b_1}{2-\sqrt{2}+\sqrt{2}\lambda}, \frac{(b_1+b_2)+\sqrt{2}\lambda b_2}{2-\sqrt{2}+\sqrt{2}\lambda})$  and

$(b_1, \frac{b_1+\lambda b_2}{\lambda-(\sqrt{2}-1)})$ . (29') states the line segment joining the points

$(\frac{(\sqrt{2}-1)(b_1+b_2)+\sqrt{2}\lambda b_1}{\sqrt{2}-2+\sqrt{2}\lambda}, \frac{-(b_1+b_2)+\sqrt{2}\lambda b_2}{\sqrt{2}-2+\sqrt{2}\lambda})$  and  $(b_1, \frac{-b_1+\lambda b_2}{\lambda+(\sqrt{2}-1)})$ . (30) states the line segment

joining the points  $(\frac{(\sqrt{2}-1)(b_1-b_2)-\sqrt{2}\lambda b_1}{\sqrt{2}(1-\lambda)}, \frac{-(b_1-b_2)-\sqrt{2}\lambda b_2}{\sqrt{2}(1-\lambda)})$  and  $(b_1, \frac{b_1+\lambda b_2}{\lambda-(\sqrt{2}-1)})$ .

Furthermore, the line segment connecting any two points on the set  $A_C(A, B; \lambda)$  lies entirely in the set. Therefore, the set  $A_C(A, B; \lambda)$  is convex.

The set  $A_C(A, B; \lambda)$  for this case is shown in red in Figure 3(c).

It should be noted here that if the points  $A$  and  $B$  are on a steep line, the Apollonian set  $A_C(A, B; \lambda)$  and its properties can be obtained immediately by applying suitable isometric transformations in the plane  $R_C^2$  together with the corollaries established for the gradual case.

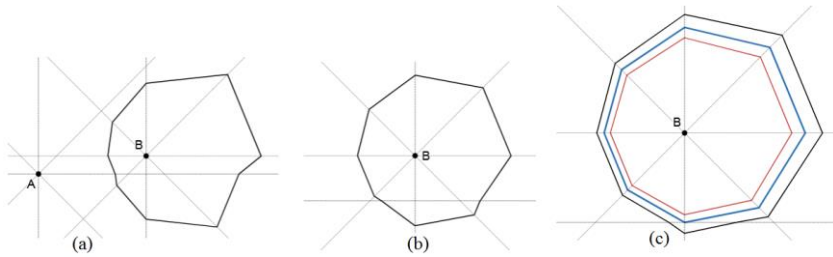


**Figure 3**  $A_C(A, B; \lambda)$  for  $\lambda > \frac{\sqrt{2}}{1-m}$

## CONCLUSION

This study presents a comprehensive analysis of Apollonian sets in the Chinese Checkers plane and extends the classical concept of Apollonian set to a non-Euclidean framework. The research systematically classifies the structure of these sets based on the relative positions of the two distinct points  $A$  and  $B$ , whether they lie on horizontal, vertical, separator, or gradual lines, and examines the influence of the parameter  $\lambda$ . When  $A$  and  $B$  lie on coordinate axes, separator lines, or lines parallel to the axes, the Apollonian set forms a convex octagon composed of eight line segments. For points on a gradual line, the structure becomes more complex, forming piecewise-linear polygons with 8 to 14 segments, depending on the value of  $\lambda$ . For the case where the points lie on a gradual line, the threshold values of the parameter  $\lambda$  related to the number of sides, vertices, and convexity of the set have been determined. Additionally, for points on the coordinate axis, horizontal or vertical line or separator line, the study establishes fundamental properties such as symmetry with respect to the line  $AB$ , vertex distributions along horizontal, vertical, and separator lines through  $B$ , and internal division ratios of diagonals by the point  $B$ . These results are supported by rigorous proofs and detailed case analyses. This work not only extends the concept of Apollonian sets to the Chinese Checkers plane but also offers a geometric classification under this metric. These findings are expected to contribute to the understanding of the Apollonian sets in non-Euclidean geometries and to form a foundation for future studies.

## REFERENCE

- Akça, Z. and Çalış, C. (2021). Voronoi diyagramı ve Taksi düzlemi üzerine. Erzincan Üniversitesi Fen Bilimleri Enstitüsü Dergisi, 14(1), 175–181.
- Akça, Z. and Kaya, R. (2004). On the distance formulae in three dimensional taxicab space. Hadronic J., 27(5), 521–532.
- Akça, Z. and Kaya, R. (1997). On the taxicab trigonometry. J. of Inst. Math. Comput. Sci. Math. Ser., 10(3), 151–159.

- Akça, Z. and Kaya, R. (2004). On the norm in higher dimensional taxicab spaces. *Hadronic J. Suppl*, 19(4), 491–501.
- Bahuaud, E., Crawford, S., Fish, A., Helliwell, D., Miller, A., Nungaray, F., Shergill, S., Tiffay, J. and Velez, N. (2020). Apollonian Sets in taxicab geometry, *Rocky Mountain Journal of Mathematics*, 50(1): 25-39.
- Bayar, A. and Ekmekçi, S. (2006). the Chinese Checker Sine and Cosine Functions. *International Journal of Mathematics and Analysis*, 1(3), 249–259.
- Ekmekçi, S. (2024). On the Generalized Taxicab Apollonian Sets. *Hagia Sophia Journal of Geometry*, 6(2), 1–12.
- Ekmekçi, S. and Yıldırım, D. (2022). On the Maximum Apollonian Sets , *New Trends in Mathematical Sciences*, vol. 10, no. 4, pp. 151-160.
- Gelişgen, Ö. and Rüstem, K. (2015). The isometry group of Chinese Checker space. *International Electronic Journal of Geometry*, 8(2), 82–96.
- Gelişgen, Ö. and Rüstem, Kaya. (2006). CC Analog of the Theorem of Pythagoras. *Algebras, Groups and Geometries*, 23(2), 179–188.
- Gelişgen, Ö., Rüstem, K., and Özcan, M. (2006). Distance Formulae in the Chinese Checker Space. *International Journal of Pure and Applied Mathematics*, 26(1), 35–44.
- Kaya, R., Gelişgen, Ö., Ekmekçi, S., and Bayar, A. (2006). Group Of Isometries Of CC Plane. *Missouri Journal Of Mathematical Sciences*, 18(3), 221–233.
- Kaya, R., Akça, Z., Özcan, M. and Günaltı, İ. (2000). General equation for taxicab conics and their classification. *Mitt. Math. Ges. Hamburg* , 19(0), 135–148.
- Krause, E. F. (1975). *Taxicab geometry*. Menlo Park, California: Addison –Wesley Publishing Company.
- Özcan, M., Ekmekçi, S. and Bayar, A. (2002). A note on the variation of the taxicab lengths under rotations. *The Pi Mu Epsilon Journal*, 11(7), 381–384.
- Pekzorlu, A. and Bayar, A. (2022). On the Chinese Checkers Circular Inversions in the Chinese Checkers Plane. *Hagia Sophia Journal of Geometry*, 4(2), 28–34.
- Pekzorlu, A. and Bayar, A. (2020). On The Chinese Checkers Spherical Inversions In Three Dimensional Chinese Checkers Space. *Commun. Fac. Sci. Univ. Ank. Ser. A1 Math. Stat*, 69(2), 1498–1507.
- Turan, M. and Özcan, M. (2006). General equation for Chinese Checker conics and focus-directrix Chinese Checker Conics. *International Journal of Pure and Applied Mathematics*, 393–401.
- Turan, M. and Özcan, M. (2004). Two-foci Chinese Checker ellipses. *International Journal of Pure and Applied Mathematics*, 119–127.
- Turan, M. and Özcan, M. (2004). Two-foci Chinese Checker hyperbolas. *International Journal of Pure and Applied Mathematics*, 0–0.

